

DEVELOPMENT OF SOLAR ENERGY HARVESTING TEXTILES

ACHALA SAJEEVA SATHARASINGHE

A thesis submitted in partial fulfilment of the requirements of
Nottingham Trent University for the degree of
Doctor of Philosophy

October 2019

Copyright statement

This work is the intellectual property of the author. You may copy up to 5% of this work for private study, or personal, non-commercial research. Any re-use of the information contained within this document should be fully referenced, quoting the author, title, university, degree level and pagination. Queries or requests for any other use, or if a more substantial copy is required, should be directed in the owner of the Intellectual Property Rights.

Acknowledgements

During this exciting journey, I have been fortunate to receive support and encouragements from many people towards the completion of my research work. First of all, I'd like to express my sincere gratitude to Professor Tilak Dias; my Director of Studies, for providing this life-changing opportunity to pursue the studies under his mentorship and guidance, and it was a unique and thoroughly enjoyable experience to work with him. I am grateful to have Dr Theodore Hughes-Riley as my second supervisor whose constant direction and advise was instrumental in meeting the research objectives.

My colleagues and staff members at the Advanced Textiles Research Group were always there for me extending their invaluable support. I am very thankful to Carlos Oliviera, who assisted me in preparing electronic yarns samples throughout the project, Dr. Gayani Nandasiri and Richard Arm who helped me to prepare the silicone moulds for soldering work, Matholo Kgateke and Daisy-Kate Hornsby for their assistance in preparing woven fabric samples, Dr Arash Shahidi for support in conducting testing. evaluations, and many other tasks, and Dr Dorothy Hardy for her support in sourcing miniature solar cells and conducting wash durability tests. I would also like to extend my thanks Dr Pasindu Lugoda, Nour-Al Nashed, Ioannis Anastasopoulos, Dr Varindra Kumar, William Hurley and Zahra Rahematulla for supporting me in their fullest capacities.

I would like to make a special mention about my beloved wife Dinesha and my loving little daughter Vimansie who were behind me unconditionally, making sacrifices to achieve my goals and being close to me throughout this journey. Also, I am grateful to my parents, sister, brother and extended family for their emotional support, and special thank should go to my sister-in-law Dr Dilani and brother-in-law Dr Niroshan who facilitated us during our early days in the UK.

Finally, I must thank the Vice-Chancellor of the university for providing the crucial funding for my PhD work.

Research Activities

Journal articles

SATHARASINGHE, A., HUGHES-RILEY, T. and DIAS, T., 2019., An investigation of a wash durable solar energy harvesting textile. *Progress in photovoltaics, under review*.

SATHARASINGHE, A., HUGHES-RILEY, T. and DIAS, T., 2018. Photodiodes embedded within electronic textiles. *Scientific Reports*, 8 (1): 16205.

Conference Proceedings

SATHARASINGHE, A., HUGHES-RILEY, T. and DIAS, T., 2019., Wearable and washable photovoltaic fabrics. In: 34th European Photovoltaic Solar Energy Conference (EUPVSEC) 2019, Marseille, France, 9 -13 September 2019.

SATHARASINGHE, A., HUGHES-RILEY, T. and DIAS, T., 2019. Photodiode and LED embedded textiles for wearable healthcare applications. In: 19th World Textile Conference (AUTEX 2019), Ghent, Belgium, 11-15 June 2019.

Conference presentations

Oral presentation (Nominated for the student award) - 36th European Photovoltaic Solar Energy conference (EUPVSEC) and Exhibition 2019, 9th -13th September 2019 - Marseille, France. (Linked to above proceedings)

Oral and Poster presentation – 19th World Textiles Conference (AUTEX) 2019, 11-15 June 2019, Ghent, Belgium. (Linked to above proceedings)

Poster presentation (Best poster award) – Innovations in Large Area Electronics (innoLAE) conference 2019, 22-23 January 2019, Cambridge, UK.

Three-minute thesis presentation and digital poster presentation – NTU Doctoral Research Festival 2019, 29th March 2019, Nottingham Trent University, Nottingham, UK

Poster presentation – 35th European Photovoltaic Solar Energy Conference (EUPVSEC) and Exhibition 2018, 24-27th September 2018 - Brussels, Belgium

Conference chair (E-textiles session), Oral and poster presentation – IDTechEx Show Europe 2018 11-12th April 2018, Berlin, Germany.

Poster presentation – NTU Doctoral Research Festival 2018 - 29th March 2018, Nottingham Trent University, Nottingham, UK

Exhibitor and poster presentation – Materials Research Exhibition (MRE) 2018, 12-13 March 2018, London, UK

Exhibitor - Wearable Technology Show 2018, 13th & 14th March 2018, London, UK

Poster presentation - CAADH College Research Conference 2017, 7th July 2017, Nottingham Trent University, Nottingham, UK

Table of Contents

Copyright statement	i
Acknowledgements	ii
Research Activities.....	iii
Table of contents.....	v
Abstract.....	xi
Chapter 1 - Introduction	1
1.1 Background.....	3
1.1.1 Wearable devices	4
1.1.2 Electronic textiles	4
1.1.3 Electronic yarn technology	5
1.2 Motivation	6
1.3 Aim of the research	8
1.4 Research questions	8
1.5 Research objectives	9
1.6 Research methodology	9
1.7 Structure of the thesis.....	14
Chapter 2 - Literature review	17
2.1 Introduction to the chapter.....	19
2.2 Powering wearable devices and E-textiles	19
2.2.1 Existing methods for powering wearables and E-textiles.....	20
2.2.1.1 Batteries	20
2.2.1.2 Supercapacitors	21
2.2.1.3 Textile energy storage devices	22
2.2.2 Sources and methods of energy harvesting for wearables	24
2.2.2.1 Thermoelectric generators for wearables	24
2.2.2.2 Piezoelectric generators for wearables.....	26
2.2.2.3 Triboelectric generators for wearables.....	27
2.2.2.4 Electromagnetic induction-based energy harvesters for wearables.....	28
2.3 Solar energy harvesting.....	29
2.3.1 Photovoltaic effect.....	30

2.3.1.1	Semiconductors.....	30
2.3.1.2	Electron excitation by solar radiation	30
2.3.2	Operating principles semiconductor solar cell.....	32
2.2.3	Types of solar cells.....	35
2.4	Solar energy harvesting for wearable applications	37
2.4.1	Categorization of wearable solar energy harvesters in literature.....	37
2.4.1.1	Attaching flexible solar panels onto fabrics using adhesives or sewing	41
2.4.1.2	Applying flexible photovoltaic films and coatings onto planar textiles	42
2.4.1.3	One dimensional (1D) photovoltaic structures.....	47
2.4.1.3.1	Photovoltaics using non-polymeric fibres or wires.	48
2.4.1.3.2	Photovoltaics using polymeric fibres with multilayered conductive and photovoltaic material coatings	52
2.4.1.4	Textile fabrics made by weaving PV wires, tapes or yarns	53
2.4.1.5	Non-woven PV structures	58
2.4.1.6	Mechanically linked rigid or flexible solar cell arrays.....	59
2.5	Strategies for integrating electronic device within textile fabrics in the form of yarns, threads or tapes	61
2.6	Discussion.....	65
Chapter 3 – Materials and methods.....		67
3.1	Introduction	68
3.2	E-yarn fabrication process	70
3.2.1	Photodiodes and solar cells.....	71
3.2.2	Soldering surface mount devices (SMD) onto fine copper wires	74
3.2.3	Making electrical interconnects between the solder-pads and Cu wires for photodiodes	77
3.2.4	Making electrical interconnects between the solder-pads and Cu wires for solar cells.....	79
3.2.5	Encapsulating the Soldered photocells inside resin micro-pods.....	82
3.2.6	Embedding the micro-pod inside of a fibre sheath and knitted tube	85
3.2.7	Impregnation of the fibrous sheath with clear resin	87
3.3	Evaluating the optoelectronic behaviour of the photocells and photocell yarns	88

3.3.1	Optical test rig	89
3.3.2	Solar simulator	93
3.3.3	Conducting characterisations under different angles of incident light ..	95
3.3.4	Generating characteristic curves for photocells.....	96
3.3.5	Data analysis.....	97
3.4	Summary	97
Chapter 4 - Photodiode embedded electronic yarns.....		99
4.1	Introduction	101
4.2	Modelling the effect of the micro-pod encapsulation.....	103
4.2.1	Generalized ray-tracing model	104
4.2.2	Deriving the electrical parameters using the ray tracing model	105
4.2.3	Simplification of the generalized ray tracing mathematical model.....	106
4.2.4	Application of the mathematical model to photodiodes.....	107
4.3	Empirical study on the effect of resin micro-pod on photodiode performance	109
4.3.1	Variation analysis for TEMD 7000x01 before and after encapsulating inside RMPs.	110
4.3.2	Effect of micro-pod diameter	111
4.3.3	Effect of the depth of positioning the photodiode inside of the resin micro-pod.....	113
4.3.4	Effect of the micro-pod material	115
4.4	Photodiode embedded electronic yarns	117
4.4.1	Performance of photodiode embedded E-yarns.....	119
4.4.2	Individual and combined effect of the components	121
4.4.3	Effect of resin-impregnation.....	123
4.5	Conclusions	124
Chapter 5 – Solar cell embedded yarns.....		125
5.1	Introduction	127
5.2	Preliminary tests using solar cells	128
5.2.1	Characterisation of maiden solar cells	128
5.2.2	Effects of resin micro-pod	129
5.2.2.1	Implications of Fresnel reflection	130
5.2.2.2	Significance of total internal reflection.....	132

5.3	Solar cell embedded yarns	133
5.3.1	Material selection and structure	133
5.3.2	Evaluation of solar-E-yarns using 1.5 mm ×1.5 mm solar cells.....	135
5.3.3	Effect of changing the incident angle of the light source normal to the longitudinal axis of the devices on their optoelectronic properties	137
5.3.4	Individual and combined effects of the components of the solar-E-yarns	139
5.3.5	Theoretical and empirical modelling of the effect of changing the angle of the incident light normal to the longitudinal axis of the devices.....	145
5.3.5.1	Change in the width of incident beam of light with the angle	146
5.3.5.2	Modelling the effect of incident angle on short-circuit current.....	147
5.3.6	Effect of colour of the fibre sheath	154
5.3.7	First prototype of fabric using solar cell yarns.....	150
5.3.8	Optimisation of solar cell length	156
5.4	Solar-E-yarns using 1.5 mm ×3 mm solar cells.....	156
5.4.1	Effect of change in incident angle normal to the polar axis of the device	159
5.4.2	Effect of light intensity on the solar-E-yarns	161
5.4.3	Packing fibres embedded within the micro-pod.....	162
5.4.4	Solar-E-yarns prepared with normal braided outer sheath	164
5.4.5	Solar-E-yarns using bi-facial solar cell concept.....	168
5.5	Conclusions	171
Chapter 6 - Performance under operational conditions		173
6.1	Introduction	174
6.2	Wash durability testing	175
6.2.1	Machine wash testing of solar-E-yarns	177
6.2.2	Machine wash and hand wash testing of woven fabrics with solar-E-yarns and photodiode embedded E-yarns	179
6.3	Tensile strength tests.....	184
6.4	Abrasion resistance test	186
6.5	Mechanical impact testing.....	189
6.6	Effect of temperature, humidity and water	195
6.6.1	Effect of temperature on solar-E-yarns.....	191
6.6.2	Effect of humidity on solar-E-yarns.....	194

6.6.3	Effect of liquid water	192
6.7	Conclusions.....	198
Chapter 7 - Solar energy harvesting fabrics		199
7.1	Introduction	201
7.2	7.2 Fabrication of solar-E-yarns for fabric demonstrators.....	201
7.3	First fabric demonstrator	204
7.3.1	Electrical characterisation of the first fabric demonstrator-yarns	206
7.3.2	Liquid absorption properties of the solar cell (SC) embedded fabric demonstrator	208
7.3.3	Demonstration of energy harvesting capability	209
7.4	Second fabric demonstrator	212
7.5	Fabric demonstrators for comparative tests and field test.....	213
7.5.1	Characterisation of solar-E-yarns and resultant fabrics	215
7.5.2	Field test using the fabric demonstrators	217
7.6	Effect of incident angle and the spacing of the solar-E-yarn within fabrics	220
7.6.1	Evaluating free standing solar-E-yarns	220
7.6.2	Experiments with solar-E-yarns woven into fabrics	221
7.7	Conclusions.....	226
Chapter 8 - Conclusion.....		229
8.1	Conclusions	231
8.2	Contributions to knowledge	232
8.4	Challenges faced during the research.....	233
8.5	Future work.....	233
References.....		235
Appendices.....		257
Appendix 1 - List of research work reported in literature categorized based on the solar cell material type		259
Appendix 2 – Variation of physical dimensions of the solar cells		268
Appendix 3 – Light intensity analysis of the lamp of the optical test rig.....		269
Appendix 4 - Light intensity analysis of the solar simulator		271

Appendix 5 - Full derivation of the mathematical model	272
Appendix 6 – Positioning of the photodiodes inside resin micro-pods.....	277
Appendix 7 – Mathematical model revised to include total internal reflection	278
Appendix 8 – Measured test results of the solar-E-yarns during the wash test	280
Appendix 9 – LabView program for monitoring solar-E-yarns during abrasion tests.	283
Appendix 10 - Preparation and characterisation of supercapacitor embedded E-yarns	284
Appendix 11 - Data acquisition device built to conduct the field tests	286
Annexes	289
Annex 1- Introduction to wearable devices and E-textiles	291
Annex 2 - Full specifications of the photodiodes	304
Annex 3 – Test report provided by the manufacturer for the solar cells before cutting	312
Annex 4 – Material specification of the solder paste	313
Annex 5 - Material specifications of the encapsulation resins	315
Annex 6 - Specifications of the UV curing lamp	327
Annex 7 – Details of the knit-braiding machine.....	329
Annex 8 - Full specification and calibration certificate for the solar simulator	331

Abstract

The Achilles heel of many wearable and electronic textile (E-textile) devices is their power requirement, which has been a major hurdle in the adoption of E-textiles. To keep these devices continuously powered without frequent recharging or bulky energy storage devices, many have proposed integrating energy harvesting capability into clothing. Solar energy harvesting has been one of the most investigated avenues for this due to the abundance of solar energy and maturity of photovoltaic technologies.

This research investigated a novel approach for realising solar energy harvesting with textiles by embedding miniature solar cells (SCs) within the fibres of a yarn, thus delivering a robust and consumer-friendly solution for powering wearable and mobile devices. SCs were first soldered onto fine copper wires and encapsulated inside of resin micro-pods, before being covered by a fibrous sheath, to realise solar cell embedded yarns (solar-E-yarns) that can be readily converted into fabrics with conventional fabric manufacturing processes such as weaving and knitting. Preliminary investigations conducted using miniature photodiode embedded E-yarns laid the foundation for embedding photovoltaic devices within yarns. A mathematical model was also formulated to characterise the performance of photovoltaic devices embedded in yarns and was experimentally validated using photodiodes to evaluate the effects of the resin micro-pod on photovoltaic response.

Subsequently solar-E-yarns were fabricated using silicon SCs. The photovoltaic response of these solar-E-yarns were studied at each stage of the E-yarn fabrication process and under a range of test conditions including different light intensities, incident light angles, ambient temperatures and humidity levels. Solar-E-yarn performance could be further enhanced by impregnating the photoactive sides of the yarns with an optically clear resin, as well as by using bifacial SCs.

A series of fit-for-purpose tests including wash durability tests were conducted on the solar-E-yarns which revealed that the solar-E-yarn embedded fabrics could undergo domestic laundering and maintained ~90% of the original power output after 15 machine wash cycles, which was vastly superior to other solutions proposed in the literature.

To demonstrate the energy harvesting capability, prototype demonstrators were created by weaving solar-E-yarns. A solar fabric demonstrator with ~25cm² active area generated up to ~2.15 mW/cm² under one sun illumination and maintained both the feel and aesthetics of a normal textile. The fabric demonstrator was capable of charging various electronic storage and powering low power mobile devices.

The research has generated a wealth of knowledge on the fabrication, performance and the utility of the solution for regular clothing applications. These attributes will enable these solar fabrics to feature in future wearable electronics and electronic textiles to provide a continuous supply of power, without having to compromise on comfort, aesthetics or wash durability.

Chapter 1

Introduction

This thesis presents a scientific investigation into the development of a wearable solar energy harvesting textiles for powering wearable and mobile electronic devices. The solar energy harvesting textiles were realized by embedding miniature solar cells within the fibres of a textile yarns, enabling the integration of energy harvesting capability within the heart of a textile fabric.

1.1 Background

1.1.1 Wearable devices

Recent advancements in semiconductor devices, electronic sensor technologies, and the Internet of Things (IoT), have made wearable devices an increasingly integral part of modern society. In recent years electronic devices have miniaturised, become cheaper, and also have low power requirements when compared to their 20th century predecessors, mainly to cater the growing demands of mobile phone industry. Smaller, smarter, more efficient, and lower-cost electronic components and sensors have made mobile and wearable devices technically viable and commercially feasible. The International Data Corporation (IDC, 2018) predicts that global wearable device market is expected grow from 122.6 million devices in 2018 to 190.4 million devices in 2022, with an annual compound growth rate of 11.6 %. According to eMarketer (2019) in the United States the number of adults using a wearable devices is expected to grow from 45.8 million in 2017 to 67.0 million by 2022. The wearable device market is currently dominated by wristables (smart watches and activity trackers) with a market share of ~95% for 2018, while apparel based products capturing only 2.4% (IDC, 2018).

Wearable electronic devices and technologies have transformed the future of many industry sectors including sports and wellness, medical, military, consumer electronics, apparel, and communications. The advent of the internet and leaps forward in wireless communication technologies have enabled the users to be part of a massive, interactive, virtual network with a click of a button. These developments have contributed to the new generations of connected wearable and smart mobile devices as we know them today, where many wearable devices are equipped with some form of wireless connectivity such as Wifi, Bluetooth, Zigbee, or Z-wave. Internet driven global megatrends such as social media, digitisation, and e-commerce have also helped to popularise wearable devices.

Generally, wearable devices are regarded as devices with some level of intelligence and smartness (ability to sense external stimuli and respond). However, devices worn on body with electronic or electrical functionality which require human intervention to operate (e.g. wearable head lamp) also fall under the broad category of wearable devices. (Annex 1 provides more details on the definitions and categorisation of wearable devices and electronic textiles). In fact, the very first known application of wearable devices were reported in late 1800s, where ballet dancers illuminated with electric light bulbs on their foreheads performed on stage (The New York Times, 1884).

1.1.2 Electronic textiles

The integration of electronics with textiles has transcended from superficially attached devices on clothing (Fig.1.1(a)) to devices with fabric embedded devices (for example electrodes, stretch sensors or fabric heaters) and interconnects (Fig.1.1(b)). Many E-textiles are used for sensing applications with most sensing techniques related to body vital sign monitoring being based on changes in electrical properties such as a change in electrical resistance, electrical potential, or electrical capacitance that are simple to capture by functionalised textile structures. More advanced types of sensors which involve semiconductor devices, are now available in miniaturised forms that can be integrated within textiles in an unobtrusive manner.

The ideal scenario for an electronic textile (E-textile) can be envisioned as a system that has all of the electronic functionality and components (i.e. sensing, signal processing, data storage, data communication, signal output and power supply) fully embedded within the fabric, discrete from external hardware (Fig.1.1(c)). These textile embedded systems are vastly superior to the superficially attached devices as they are light weight, less bulky and offer the appearance and feel of normal textiles. However, the practicality of such a fully textile integrated system depends on its three-dimensional conformability, aesthetic appeal and mechanical robustness during its use and washing.

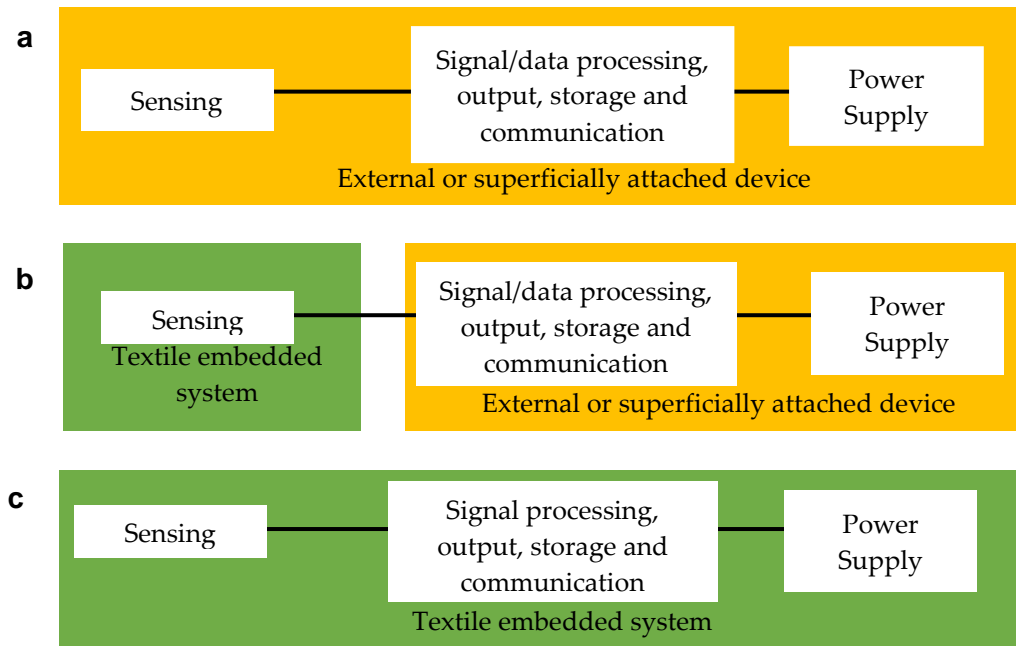


Figure 1.1. – different levels of integrating electronics with textiles (E-textiles) from external or superficially attached devices to fully textile embedded systems. (a) All components superficially attached. (b) Sensing capability integrated within the textile with other components superficially attached. (c) All components integrated within the textile.

1.1.3 Electronic yarn technology

The Advanced Textile Research Group at Nottingham Trent University has pioneered a technology to embed semiconductor devices inside of textile yarns (Dias and Fernando, 2005, Dias and Ratnayake, 2015; Dias and Rathnayake, 2016) to create electronically active yarns (E-yarns). The E-yarn technology enables electronic components and interconnects to be integrated within the core of textile yarns, thus enabling these to be undetectable to the human eye. The E-yarns are fabricated by soldering small-scale (typically around 1.0 mm × 1.0 mm cross section) electronic devices onto fine multi-strand copper wires before encapsulating them individually inside of clear resin micro-pods that hermetically seal the soldered device and solder joints. The encapsulated devices are then covered by a textile fibrous sheath comprising of packing fibres and a tubular warp knitted structure, which consolidates the structure to create the final E-yarn. The unique architecture of these E-yarns shown illustrated in Fig. 1.2 (Dias and Hughes-Riley, 2017) will enable them to be washable and re-useable for multiple cycles while maintaining their electronic properties and all-important textile like haptic and

aesthetic character, which will make them more desirable over superficially attached wearable devices (Dias and Rathnayake, 2016).

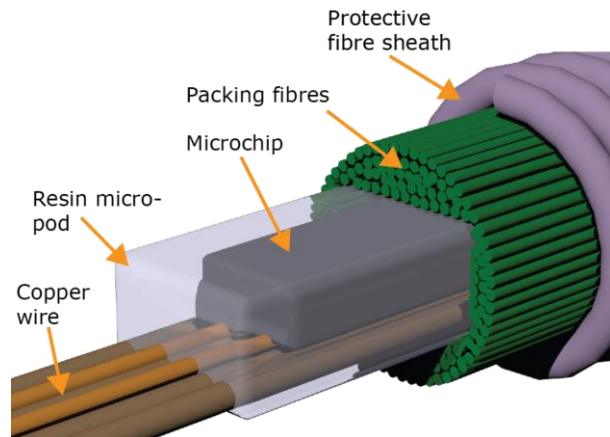


Figure 1.2 – Schematic illustrating the structure of an electronic yarn. (Dias and Hughes-Riley, 2017)

The viability of the E-yarn technology to integrate electronic devices within yarns is already proven for sensing devices (Hughes-Riley and Dias, 2018; Lugoda *et al.*, 2018; Satharasinghe,) and LEDs (Hardy *et al.*, 2018). The next step in the progression of the technology is to embed signal processing (transistors and micro-processors), signal communication (Bluetooth, ZigBee, WiFi) and power supply (batteries, supercapacitors, energy harvesting devices) capabilities within yarns using the E-yarn technology, which will enable a fully self-functioning E-textiles. While several types of multi-terminal devices requiring upto 4 interconnections (e.g. Accelerometers) being achieved with the technology using insulated Cu conductors, in order to achieve E-yarns with more advanced functionality (e.g. micro-processor E-yarns) multi-terminal capability need to be further enhanced to realise more interconnects in a robust manner, which is yet to be achieved.

1.2 Motivation

The Achilles heel for many wearable electronic textiles (E-textiles) is the need for a power supply. Batteries are gaining higher energy densities, becoming smaller and longer lasting, however they are still relatively bulky and must be attached on to clothing in a manner similar to the older forms of electronic textiles such as in pockets or on the surface of clothing. Most commercially available wearable E-textiles are powered by standard solid coin cells, pouch cells, cylindrical cells or prismatic cell batteries of an

Alkaline, Nickel metal hydride (NiMH), Lithium-ion (Li-Ion), or Lithium-ion Polymer (LiPo) type (Davis, 2017). LiPo type batteries are preferred for most wearable applications due to their relative flexibility compared to other types (Tran, 2016). The use of supercapacitors for energy storage for wearable applications has also been considered, however they have limited use due to low energy densities, high-power densities, and high self-discharge rates. These batteries or supercapacitors are typically attached to the garment after assembly, or embedded in a removable module (Fig.1.3) , making the systems bulky and cumbersome to use (Jost, Dion and Gogotsi, 2015). Smaller and lighter batteries require frequent recharging meaning that there is a compromise between battery life and user-friendliness. These deficiencies in the power supply of present-day E-textile systems have affected the adoption rates of E-textile, which is reflected in the small share of the global wearable devices market captured by E-textiles (IDC, 2018).

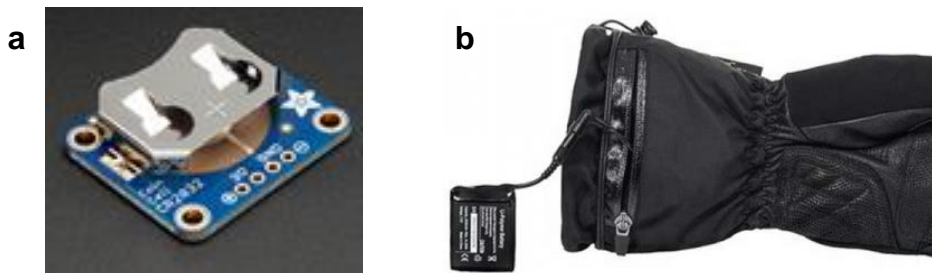


Figure 1.3 – (a) Battery module used to power mobile computing development boards. (Adafruit.com) (b) Heating glove powered by a battery pack. (telford-motorcyclecentre.co.uk)

To counter the challenges posed by energy storage devices, integration of energy harvesting capability into textiles has been considered a promising alternative. Amongst the energy harvesting technologies explored for E-textiles, such as tribo-electric (Pu, Li, *et al.*, 2016; Zhu *et al.*, 2016), piezo-electric (Song, Ahn and Yun, 2015; Ramadan *et al.* 2014; Waqar *et al.* 2015), thermoelectric (Leonov, 2013) or electromagnetic induction (Ylli *et al.*, 2013), solar energy harvesting has been one of the most investigated avenues due to the abundance of solar energy (International Energy Agency IEA, 2011) and the maturity of photovoltaic (PV) technologies (Conibeer and Willoughby, 2014).

The methods proposed in literature for creating wearable solar energy harvesting systems are not practical for regular clothing applications due to their poor normalcy (appearance and hand feel), lack of comfort (softness, breathability and moisture management), and insufficient three-dimensional deformability (drapability). In

addition, most of these proposed solar energy harvesters are incompatible with water and washing. It is envisioned that to address the deficiencies of existing E-textile energy harvesting systems that E-yarn technology can be employed to create photovoltaic textiles that bring a new perspective for incorporating energy harvesting capabilities into textile structures.

1.3 Aim of the research

The aim of this PhD study was to create the knowledge required to craft a solar energy harvesting yarn by embedding miniature photovoltaic cells within the fibres of a textile yarn (Solar E-yarn), which could be used to develop textile structures capable of converting solar energy into electricity to power wearable devices. Here the energy harvesting capability is intended to reduce the need for use of heavy and bulky energy storage devices and the frequency of recharging. This work will herald a significant step-change in E-textiles by incorporated sources of power into the heart of textiles and will pave the way to develop a new generation of wearable devices and E-textiles, mainly for outdoor applications.

1.4 Research Questions

This research focused on how E-yarn technology can be adapted to create miniature solar cell embedded yarns that can be used to construct a wearable and washable textile capable of harvesting solar energy and generating satisfactory levels of electricity (i.e. by maintaining a high conversion efficiency). A clear gap in knowledge was identified in understanding the effects on the opto-electrical behaviour of photovoltaic cells when embedded within the E-yarns structure, and the performance and durability of resultant E-yarns under operational conditions. In order to bridge this knowledge gap, the following research questions were investigated:

- The formation of fine copper wire interconnects with miniature solar cells.
- The effect of the resin micro-pod on the performance of the embedded solar cells.
- The effect of the textile fibre cover on the performance of the embedded solar cells.
- The performance of the solar cell embedded yarns when integrated within a fabric.
- The durability of the solar cell embedded fabrics and yarns against mechanical stresses and washing.

1.5 Research objectives

1. To develop new knowledge on how to embed miniature photovoltaic cells within the fibres of textile yarns using the E-yarn technology.
2. To investigate the photovoltaic response of yarn embedded photovoltaics devices under different electromagnetic spectral ranges, incident angles, and optical interferences, induced by the different components of the yarn.
3. To investigate strategies to improve the power generation capability of the fabricated devices.
4. To study the behaviour of the solar E-yarn under realistic operating conditions.
5. To demonstrate the solar energy harvesting capability of the fabrics crafted with the solar E-yarns.

1.6 Research Methodology

To achieve the aim and these objectives a quantitative research approach has been employed, where the state-of-the-art and knowledge gaps were identified by reviewing the available literature. The available knowledge on relevant methods and theories were employed for the design, development, and characterisation of the solar energy harvesting yarns. The literature review (*Chapter 2*) provides a background on the powering of wearable and E-textile devices using energy storage and harvesting devices. The literature review extensively surveys the state-of-the-art textile based solar energy harvesting devices, while identifying existing challenges in achieving a practical solution. It was envisioned that the E-yarn technology could be employed to create a solar energy harvesting textile that possess the desirable attributes of a normal textile such as normal appearance and hand-feel, comfort drapability and durability, while generating sufficient levels of power. The literature review facilitated the identification of specific knowledge gaps in creating such solar energy harvesting textile based on the E-yarn technology.

The approach proposed to create solar energy harvesting fabrics was to weave miniature solar cell-embedded yarns (solar-E-yarns) together. To achieve a drapable and soft fabric that can endure machine washing, the shear behaviour and a low bending rigidity of the structure had to be maintained. Therefore, the rigid PV elements (solar cells) were

deployed in a discontinuous fashion within the fabric in yarn form. The solar-E-yarns were realized in three steps: First, miniature solar cells (SCs) were soldered in parallel, onto two multistrand copper wires. A new soldering method was developed to conduct this soldering step, since the existing soldering technique employed for previous E-yarn developments was not capable of solder two parallel copper wires onto the type of solar cell available for this work. Next, the soldered SCs were individually encapsulated within clear, cylindrical resin micro-pods. The solar-micro-pod filament containing the encapsulated cells was then covered by packing fibres and a knit-braid to give the final solar-E-yarn a textile-feel and appearance. In some cases, the photoactive side of the solar-E-yarn were impregnated with a polymeric resin to improve the photovoltaic performance. Using this method, the embedding of other types of solar cells, such as organic (Che *et al.*, 2018), perovskite (Feng *et al.*, 2018) or multi-junction (Fraunhofer ISE, 2019) solar cells, within textiles could be possible, however this research focused on crystalline silicon (c-Si) type SCs. The discrete micro-pods and the fibrous sheath resulted in solar-E-yarns with a low bending rigidity and a high degree of porosity enabling the transfer of moisture and heat through the E-yarns and the resultant fabrics. This feature was crucial to prevent discomfort to the user caused by thermal and sweat build-up, especially during warm and sunny conditions (Gibson, 1993).

Preliminary experiments were conducted using two types of miniature photodiodes to prove the technical viability of creating a textile yarn embedded optoelectronic device. Photodiodes were selected for these preliminary tests as they were a readily available and cost-effective alternative to custom developed miniature solar cells (photodiodes follow the same operational principles as solar cells although they are specifically designed and optimised to have higher speed of response and typically used in reverse bias. Solar cells are designed to maximise power and is used in forward bias). To characterise the developed E-yarns in a repeatable manner a bespoke optical test rig was developed. It was understood that the resin micro-pod (RMP) could interfere with the incident light depending on the geometry and optical properties of the resin material of the RMP. In order to theoretically estimate the photovoltaic response of the micro-pod embedded devices, in relation to the optical properties and geometry of the micro-pod, a generalized mathematical model was developed. An empirical study was conducted to experimentally evaluate the individual and cumulative effects of different

components of the E-yarn structure (RMP, packing fibres and knit braid) on the photoelectric output of the embedded photodiode. The generalized model was simplified (to a cylindrical micro-pod geometry) to reflect the empirical study conducted. Subsequently, the experimental data from the empirical study was compared to the estimated values from the mathematical model to confirm the validity of the model within given boundary conditions.

After proving the concept using photodiodes, solar-E-yarns were created by embedding crystalline SCs ($1.5 \text{ mm} \times 1.5 \text{ mm} \times 0.2 \text{ mm}$) and characterised for their photovoltaic output. A fabric prototype comprising five solar-E-yarns (each yarn containing three SCs) was constructed to analyse the viability of weaving solar-E-yarns together to create solar energy harvesting fabrics. Based on the results the SC length was changed from 1.5 mm to 3 mm to improve the production efficiency and power density of the resultant fabrics. An in-depth characterisation of solar-E-yarns prepared with $1.5 \text{ mm} \times 3 \text{ mm} \times 0.2 \text{ mm}$ SCs was conducted. The characterisations included the generation of characteristic curves, and the measurement of short-circuit current and open-circuit voltage of solar-E-yarns at different stages of the fabrication process, as well as under different incident angles and different incident light intensities. A critical factor to understand for a solar energy harvesting solution intended for wearable application was how the angle of incident light effects the functionality of the device: ultimately a wearer of a solar energy harvesting device would move relative to the light source (i.e. the Sun). Theoretical and empirical models were developed based on geometric models and experimental data to predict the effect of incident angle on the performance of the solar-E-yarns. A study of different variants of solar-E-yarns was also conducted, with the aim of optimising the performance. These included the use of resin impregnation of the solar-E-yarns surface fibres and a bi-facial SC concept to enhance the power output of the solar-E-yarns, as well as the possibility of using normal braiding, instead of knit braiding to create the fibrous sheath of the solar-E-yarns.

One of the objectives of the research was to assess the performance of solar-E-yarns during the operational conditions that the solar-E-yarns would be exposed to during normal use. Wash durability was one of the key aspects assessed and this was conducted both in yarn form and fabric form under test conditions with different levels of harshness. These tests provided an indication of the level of mechanical stresses the E-

yarns could withstand before experiencing electrical failure. Other tests included tensile strength measurements in yarn form, impact tests, and abrasion tests in fabric form that provided insights into the durability of the solar-E-yarns under the mechanical interactions that they may get exposed to during use. Additionally, solar-E-yarn performance was evaluated at different temperatures and humidity levels to understand their operational boundary conditions in different environments.

Finally, the solar-E-yarns were woven into a fabric and the performance and the power generation capabilities of the solar-E-yarn fabrics were demonstrated. It was understood that the performance of the solar-E-yarns woven into a fabric can vary depending on the shading effects by the adjacent solar-E-yarns, the albedo effect (effects of light scattered from the background), and the colour of the fabric. These effects were studied by creating solar-E-yarn woven fabrics with different weaving patterns and colours. Five fabric demonstrators were created by weaving multiple solar-E-yarns, each comprising ten SCs. The largest fabric demonstrator comprising a total of 200 SCs had a photoactive area of 44.5 mm × 45.5 mm. This fabric demonstrator was employed to charge various energy storage devices (such as batteries and supercapacitors) and to power small mobile electronic devices (mobile phones, fitness trackers) under simulated sun light. A field study under natural sun light was conducted using four fabric demonstrators that compared the effects of resin impregnation and fabric colour on the power generation.

The findings of this research proved the viability of integrating miniature SCs within a fabric, in the form of solar-E-yarns, to create solar energy harvesting fabrics. This approach will revolutionise the way in which wearable and mobile electronic devices will be powered in the future where the end user will not have to compromise on reusability, appearance or comfort.

The flow of the research is summarized in the flow diagram shown in Fig. 1.4.

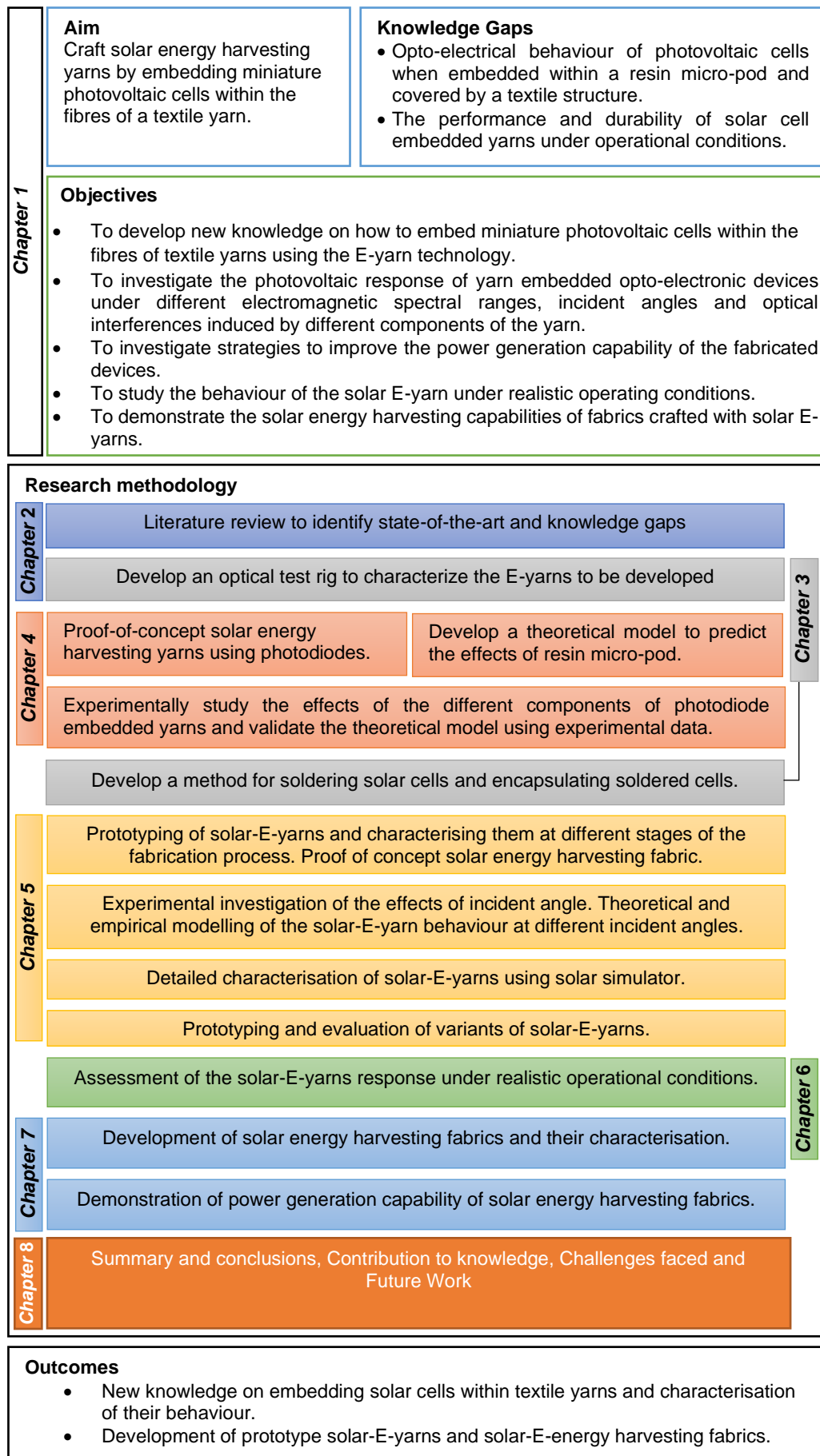


Figure 1.4 – Summary of the progression of the research in a flow diagram.

1.7 Structure of the thesis

The thesis contains eight chapters including the introduction, literature review, materials and methods, four experimental chapters, and conclusion, as outlined below.

Chapter 1 – Introduction and background. This chapter provides a brief background to the topics related to the research (wearable devices, E-textiles, E-yarn technology) and presents the key motivation behind the research. Based on that the aims, objectives, knowledge gaps, and research questions were defined. The research methodology and steps taken to achieve the research objectives of this project were also outlined.

Chapter 2 – Literature review. This chapter opens with an overview of incumbent electrical power storage devices, such as batteries and supercapacitors, and outlines the existing literature on textile based electrical energy storage devices intended for wearable applications. With a view towards addressing the drawbacks of energy storage devices, the state-of-the-art of textile embedded energy harvesting technologies were studied, with an in-depth review on textile integrated and textile based solar energy harvesting devices; mainly from a wearability perspective. The end of the chapter explores prior work related to embedding small-scale electronic components within textile structures.

Chapter 3 – Materials and methods. This chapter reports the materials and methods used to create the opto-electronic device embedded E-yarns studied in this research. This includes the instruments and apparatus employed to create electrical interconnects, resin micro-pods, and to craft the final E-yarns. The chapter also details the experimental procedures followed in order to characterize the opto-electrical performance of the solar-E-yarns and to ensure repeatability of the test results.

Chapter 4 – Photodiode (PD) embedded electronic yarns. The chapter covers the preparation and characterisation of photodiode embedded electronic yarns (PDEY) to prove the technical viability of using solar cell embedded electronic yarns for energy harvesting. The effects of the different components of the E-yarns on the performance of the embedded PDs were investigated. The chapter details the development a generalized theoretical model to predict the effects of the cylindrical resin micro-pod on the photovoltaic output of an embedded photocell. This model was simplified and

validated using experimental data for photodiodes embedded within RMPs of different sizes and materials.

Chapter 5 – Characterisation of solar cell (SC) embedded electronic yarns. The chapter details the characterisation of solar cell embedded electronic yarns (solar-E-yarns) at different stages of the fabrication process, and at different light intensities. The effects of incident angle on the performance of solar-E-yarns were analysed in depth. Theoretical and empirical models were developed based on geometric models and experimental data to predict the effects of incident angle on the performance of the solar-E-yarns. The chapter also investigates the effect of resin impregnation introduced in **Chapter 3** and the use of a bi-facial SC concept to enhance the power output of the solar-E-yarns, as well as the possibility of using normal braiding, instead of knit braiding to create the fibrous sheath of solar-E-yarns.

Chapter 6 – Performance of solar cell embedded yarns in operational conditions. This chapter focuses on the assessment of solar-E-yarns and resultant fabric when exposed to realistic operational conditions that they may encounter during their normal use. These tests include wash durability, both in yarn form and fabric form, under test conditions with different levels of harshness. Other tests include tensile strength measurements in yarn form, and impact tests and abrasion tests in fabric form; these tests provided insight into the durability of the solar-E-yarns under the types of mechanical interaction that they may be exposed to during use. Finally, solar-E-yarn performance was evaluated at different temperatures and humidity levels to understand their boundary conditions for use in different environments.

Chapter 7 – Solar energy harvesting fabrics. This chapter covers the preparation of solar energy harvesting fabrics using solar-E-yarns, and the electrical characterisation of the solar-E-yarn networks in fabric form under different light intensities and incident angles. The chapter details the preparation of solar energy harvesting fabric demonstrators and the evaluation of their capability to charge energy storage devices and power small mobile electronic devices under simulated light. Finally, a field test was conducted under sunlight to compare the performance of solar energy harvesting fabrics made using different coloured yarns and when resin impregnation was used.

Chapter 8 – Conclusion. This chapter concludes the thesis by providing a summary of the study and outlining the main conclusions. Suggestions for future work to be undertaken to optimise the performance of the solar-E-yarns and to further the technology readiness was presented. Finally, the chapter points out the challenges and problems encountered during the course of the research along with steps taken to overcome them.

Chapter 2

Literature Review

2.1 Introduction

Textiles can be considered as one of the best platforms for capturing and storing most forms of energy including solar energy to power wearable devices: They are large surface area structures, providing ample space to interact with the human body and the environment to harness energy (however the viability of harvesting mechanical energy from body kinetics using wearable devices is debatable due to the dependency on human body movements and possible intrusiveness), as well as space to incorporate energy storage/capturing capability. Textiles also have the benefit of being flexible, foldable, conformable and lightweight making them easy to transport. Due to these reasons, there has been an emerging interest and steady growth in research into textile-based energy storage and harvesting technologies during the last few decades (Soin, Anand and Shah, 2016). The chapter begins by briefly covering the incumbent electrical energy storage devices such as batteries and supercapacitors and outlines the existing literature on textile based electrical energy storage devices intended for wearable applications. With a view towards addressing the drawbacks of energy storage devices various approaches of energy harvesting to power wearable devices were reviewed.

Multiple streams of research have focussed on generating electricity by exploiting various sources of freely available ambient energy: This energy can be captured and readily stored or converted into other forms of energy. Important energy harvesting technologies which could be integrated with clothing are discussed in this chapter, with an in-depth review on the textile-based solar energy harvesting devices intended for wearable applications. In addition, the operating principles and fundamentals of the photovoltaic devices will be outlined in this chapter. Finally, prior-art relating to the incorporation of miniature electronic devices within textile yarns is explored, with the aim of identifying candidate technologies for embedding miniature solar cells within the core of textile yarns.

2.2 Powering wearable devices and E-textiles

The need for portable energy solutions, and the impetus for creating an energy harvesting fabric, has been brought about by the proliferation of wearable and mobile devices in recent years. Wearable and mobile devices have a wide range of applications

including telecommunications (Moustafa *et al.*, 2015), non-invasive healthcare monitoring (Piwek *et al.*, 2016), sports (Düking *et al.*, 2016), learning assistance (Sapargaliyev, 2015) and entertainment (Page, 2015): The development of these devices has been catalysed by the advancements in miniature and low powered electronic components originally developed to cater the demands of smart phone industry. For example components such as microcontrollers (e.g. MAX32625 by MAXIM) (Maxim Integrated, 2019), analogue to digital convertor (e.g. ADS7042 by Texas Instruments) (Texas Instruments, 2014), accelerometers (e.g. BMA400 by Bosch) (Bosch Sensortec, 2019) or Bluetooth® modules (e.g. CYBT-213043-02 by CYPRESS) (Cypress Semiconductors, 2019) employed in such electronic devices can operate with only a few milliwatts of power. Generally speaking, the power requirement for similar wearable devices typically range between tens to hundreds of milliwatts (Kalantarian *et al.*, 2015).

There are two main user cases for wearable textile energy solutions; extending the battery life of mobile (or portable) devices, and fully or partially powering wearable electronic textile (E-textile) devices (Min, 2009). Key mobile devices of interest include mobile phones, smart watches and fitness trackers, which require 50 mW - 1000 mW during normal use (Carroll and Heiser, 2010). E-textiles is an emerging field where electronic functionality is integrated with or imparted onto textiles, to realise capabilities such as lighting, sensing, and heating (Hughes-Riley, Dias and Cork, 2018). Despite the unprecedented interest and potential foreseen, providing a robust and user-friendly power supply to them remains an unfulfilled need for many wearable E-textile devices, which is a major hurdle to the wider adoption of E-textiles (Jost, Dion and Gogotsi, 2015).

2.2.1 Existing methods for powering wearables and E-textiles

2.2.1.1 Batteries

Batteries are the most widely used method of supplying power to wearable devices. Batteries directly convert chemical energy stored between their electrodes into electrical energy by undergoing chemical reactions. Battery technology dates back to the late 18th century as detailed by Whittingham (Whittingham, 2012). In 1799, Italian physicist Alessandro Volta created the first battery by stacking alternating layers of zinc, brine-soaked pasteboard or cloth, and silver. The Daniel cell invented in 1836 used a copper

pot filled with copper sulphate solution which was then immersed in an earthenware container filled with sulfuric acid and a zinc electrode. The lead acid battery was the first rechargeable battery which was invented by Gaston Plante in 1859. Nickel-Cadmium (Ni-Cd) batteries were invented by Waldermar Jungner in 1899 helped to pave the way for the development of the modern battery technology (Whittingham, 2012).

The latter half of the 20th century saw rapid developments in battery technology with the invention of alkaline battery in 1950s, Nickel-Metal hydride (NiMH) battery in 1989, and Lithium-ion (Li-ion) battery in 1991 (Visual Capitalists, 2016). The advancements in battery materials, as well as novel charge storage and transfer mechanisms, helped to achieve higher charge densities using low-cost raw materials thereby making the batteries smaller, lighter and cheaper. For example, since their commercialisation in the mid-1990s, energy densities of Li-ion batteries have increased more than threefold, and the cost has reduced by more than eight times (Crabtree, Kócs and Trahey, 2015). These advancements have helped fuel recent technology trends including electric vehicles, mobile electronics, and wearable devices.

Most commercially available wearable systems are powered by standard solid coin cells, pouch cells, cylindrical cells, or prismatic cell batteries of Alkaline, NiMH, Li-Ion or Lithium-Ion Polymer (LiPo) type (Davis, 2017). These batteries are typically attached to the garment after assembly, or embedded in a removable module, making the systems bulky and cumbersome to use (Jost, Dion and Gogotsi, 2015).

2.2.1.2 Supercapacitors

Supercapacitors store electrical energy in the form of ions. There are three main types of supercapacitors; electrochemical double layer capacitors (EDLC), which physically absorb electrolyte ions onto the surfaces of their electrodes, pseudocapacitors which undergo reversible redox reactions, intercalation or electrosorption at or near the surface of electrodes. The third type, hybrid supercapacitors have electrochemical and pseudocapacitor mechanisms (Zhang and Zhao, 2009). Supercapacitors have higher power densities and lower energy densities in comparison to batteries, hence they are ideal for applications requiring fast charging and discharging of electricity (Kularatna, 2014). First versions of supercapacitors were investigated by General Electric in early 1950s. In 1966

Standard Oil of Ohio patented a developed version of a supercapacitor under the title 'electrical energy storage apparatus', which was later licensed to NEC Corporation who finally marketed the results as "supercapacitors" in 1971, to provide backup power for computer memory (Schindall, 2007). The end of the 20th century saw stepped improvements in supercapacitor technologies including a reduction in the internal resistance and an increase in the electrolyte's breakdown voltage (David A. Evans, 2007) which lead to the wide-spread use of supercapacitors for a range of applications where large power density and fast discharge rates were required (Sharma and Bhatti, 2010). Lithium-ion supercapacitors, which were pioneered by FDK in 2007, was a milestone in supercapacitor history where significant improvements in capacitance values and specific energy were achieved (FDK Corporation, 2007).

The relatively low energy densities, high-power densities, and high self-discharge rates of supercapacitors limit their usage to secondary energy storage device and efficient power regulation (Jost, Dion and Gogotsi, 2015).

2.2.1.3 Textile energy storage devices

With the advancements in ultrathin and flexible energy storage materials, conventional batteries and supercapacitors are being transformed for wearable applications for both electrical energy storage and power regulation. Nevertheless, the flexibility and thin profiles of these improved devices need significant upgrades before integration into wearable and E-textile devices (Jost, Dion and Gogotsi, 2015). To address many of the challenges associated with conventional energy storage devices for wearable and E-textile applications, the viability of integrating storage capability within textiles, or fabricating textile-based energy storage devices, have been explored. Textile fibre-based energy storage devices are reported to be superior over their polymer film and paper based counterparts, due to their flexible, pliable nature, which prevents kinking, and ability to recover their shape (Jost *et al.*, 2011).

This has led to the emergence of a new stream of research into textile batteries and supercapacitor systems (Jost, Dion and Gogotsi, 2014, 2015; Kaushik *et al.*, 2015; Zhai *et al.*, 2016), with an aim to improve the appearance and comfort for the wearer. Clothing provides ample space for integrating charge storage capability and therefore is

considered as a viable platform for electrical energy storage systems for powering wearable devices. The first attempts at creating textile batteries and supercapacitors were reported by Yi Cui's group at Stanford University where they realized a single wall carbon nanotube (SWCNT) ink coated textile electrode supercapacitor devices (Hu *et al.*, 2010). In 2011, Jost and co-workers (2011) reported the screen printing of activated carbon onto mass-produced cotton and polyester woven fabrics. The structure of these energy storage devices was categorised based on their physical dimensionality (one-dimensional or two-dimensional textile batteries and supercapacitors) by Zhai *et al.* (2016). One-dimensional structures include conductive textile fibre or yarn (made of conductive fibres or coated with conductive materials) pairs separated by a membrane material twisted or bonded together. Two-dimensional structures were prepared by coating fabrics with conductive material or by weaving or knitting together one-dimensional energy storage structures. Jost, Dion and Gogotsi, (2014) followed a categorisation based on form; namely, coated textiles, fibre and yarns electrodes, and custom woven and knitted fabrics.

In order to reduce the reliance on recharging, several attempts were reported in developing hybrid textile energy systems, where energy storage and energy harvesting capability were harmonized (Lau *et al.*, 2019). The first of these works was reported by Fu *et al.* (2013) where a fibre supercapacitor combined with a triboelectric generator was created to store and harvest energy from body movements. Li *et al.* (2016a) reported a flexible energy-smart ribbon with an organic photovoltaic face and flexible supercapacitor backing, which could simultaneously harvest solar energy and store electricity. Some of these works emphasized the use of supercapacitors to store energy which is simultaneously harvested to minimize the frequency of recharging, while other hybrid systems used the energy storage in the form of supercapacitors to regulate the energy harvested.

While the primary function of these textile energy storage devices should remain storing useful amounts of energy, desirable textile characteristics are critical for their adoption for real life applications. While textile energy storage remains a frontier of research in the field of wearables and energy, existing knowledge on textile energy storage devices may currently be insufficient to practically power wearable devices, owing to poor

durability, washability, appearance and comfort. In addition, any devices containing corrosive liquid electrolytes pose significant safety concerns, which make them prohibitive for wearable applications (Zhai *et al.*, 2016).

In light of these drawbacks, many have proposed integrating energy harvesting capabilities into clothing (Stoppa and Chiolerio, 2014; Bhatnagar and Owende, 2015), to fully or partially power wearable devices using ambient energy available from the surroundings or the human body. Energy harvesting systems are also being widely investigated to minimize the frequency of recharging the energy storage devices using electricity grids or to reduce the size and weight of portable energy storage devices.

2.2.2 Sources and methods of energy harvesting for wearables

Solar energy, wind energy, thermal energy from the body, and kinetic energy due to body movements, are amongst the most widely investigated sources of energy (Beeby, Cao and Almussallam, 2013) for wearable systems, including E-textiles.

2.2.2.1 Thermoelectric generators for wearables

Thermoelectric (TE) generators are semiconductor devices capable of generating an electric current when exposed to a temperature gradient between two surfaces (change in temperature over space) using the Seebeck effect as shown in Fig. 2.1 (Goldsmid, 2017).

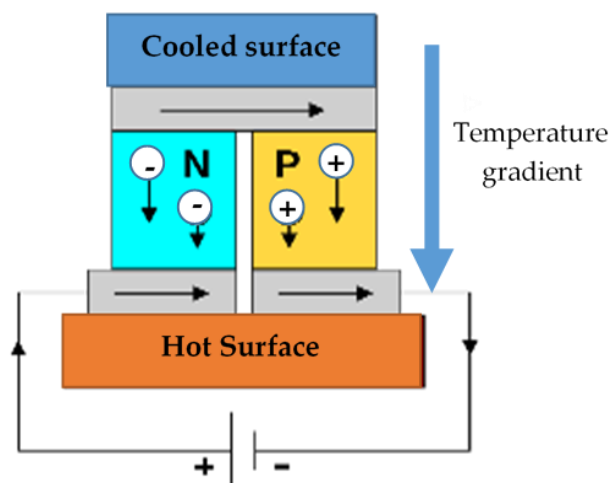


Figure 2.1 - Schematic illustration depicting the operation of a thermoelectric cell.

Electrical energy can be harvested by taking advantage of the energy gradient between the body and environment, with the electrical power generation efficiency being

dependent on this temperature gradient. Several attempts to develop wearable thermoelectric generators have been reported in the literature (Sebald et al. 2009; Stark 2012; Du et al. 2015; Cao et al. 2016; Lee et al. 2016; Li et al. 2016; Lu et al. 2016; Wu & Hu 2016;). Leonov (2013) found that for a wearable TE system, the conversion efficiency is related to many key factors such as ambient temperature, wind speed, clothing thermal insulation and a person's activity; while conversion efficiency was less dependent on the wearer's metabolic rate. He further estimated that the maximum power density attainable was around $60 \mu\text{W}/\text{cm}^2$ indoors ($\sim 20^\circ\text{C}$) and about $600 \mu\text{W}/\text{cm}^2$ when there was an external temperature of 0°C . Seeberg *et al.* (2011) investigated the potential of screen printing commercially available organic conductive polymers such as poly(3,4-ethylenedioxythiophene):poly(4-styrenesulfonate) (PEDOT:PSS) and polyaniline (PANI) as active ingredients to realise thermoelectric devices on woven cotton textiles. While achieving a thermoelectric voltage of about $+10 \mu\text{V}/\text{K}$, the authors identified that the generated voltage exhibited drift and fluctuations which made the devices unreliable. Kim *et al.* (Kim, We and Cho, 2014) realized a textile based TE generator system with a power density of $38 \text{ W}/\text{m}^2$ when there was a temperature gradient of 50 K . In this work, a glass fabric-based flexible TE generator was demonstrated using a screen-printing technique. Self-sustaining structure of this fabric-based TE device did not require top and bottom substrates. However, the above discussed TE generators were fabricated using conventional thermo-electric materials such as Bi_2Te_3 and PbTe which are brittle, toxic, heavy, and therefore undesirable to use for wearable applications (Du et al. 2015; Weng et al. 2016;). Also, it is to be noted that to achieve power conversion efficiencies greater than 1%, the devices reported need to be exposed to temperature gradients in excess of 20 K which are not practical for wearable applications.

Pyroelectric generators can also be employed to convert thermal energy into electricity. In contrast to TE generators, pyroelectric generators rely on temperature fluctuations (change in temperature over time) caused by thermal diffusion, to generate electricity (Sebald, Guyomar and Agbossou, 2009). This was not considered useful for wearable applications due to low levels of skin temperature fluctuation (Du *et al.*, 2015), approximately $\pm 1^\circ\text{C}$ even during strenuous exercising and sweat-induced cooling (Kondo *et al.*, 1997).

2.2.2.2 Piezoelectric generators for wearables

A piezoelectric material is a solid material that can generate an electron flow when it is mechanically deformed. Wearable piezoelectric generators utilize mechanical energy generated by human motion to compress or elongate a piezoelectric material and subsequently generate pulses of electron flow. The direction of the electron flow is dependent on the form of mechanical strain (compression or tensile) undergone by the piezoelectric material (Fig. 2.2).

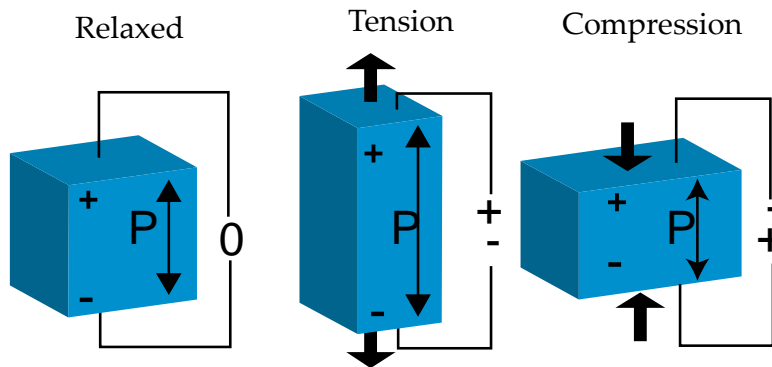


Figure 2.2 - Schematic illustration depicting the piezoelectric effect (Waqar et al. 2015).

Piezoelectric generators can be fixed onto regions on the body where large dynamic compressive forces (directly compressing the material) or tensile forces (indirectly stretching strands of fibres) due to motion are generated, such as the foot. A range of different materials such as piezo ceramics (e.g. Lead zirconate titanate, barium titanate, lead titanate, potassium niobate, lithium niobate), piezo polymers such as Polyvinylidene fluoride (PVDF), piezocomposites consisting nanowires, carbon nanotubes or piezoelectric copolymers have been reported in the literature (Ramadan et al. 2014; Waqar et al. 2015). PVDF has been used extensively in different physical forms (fibres, yarns, films, tapes, nanofibers) for wearable applications due to its mechanical flexibility, good chemical stability, and easiness to handle and the ability to be shaped (Zhao and You, 2014).

A number of research efforts have reported on the development of textile based piezoelectric generators (Chang et al. 2012; Yang & Yun 2012; Zeng et al. 2013; Åkerfeldt et al. 2014; Zampetti et al. 2014; D. Yun et al. 2015; M. Zhang et al. 2015; Song et al. 2015; Anand et al. 2016). Various different types of piezoelectric strands have been made by wrapping or twisting piezoelectric fibres (Zeng et al. 2013), nanofibers or yarns (Chang et al., 2012), or different fibre spinning techniques such as electrospinning (Zampetti,

Bearzotti and Macagnano, 2014), or melt spinning bi-component fibre made with poly(vinylidene fluoride) sheath and conductive high density polyethylene (HDPE)/carbon black (CB) core (Åkerfeldt *et al.*, 2014). These piezoelectric fibres and strands have been converted into various forms of textiles including woven, knitted, braided, spacer fabric structures (Soin *et al.*, 2014; Anand *et al.*, 2016) and non-woven structures for different applications (Waqar, Wang and John, 2015). One of the highest reported power densities for piezoelectric fabrics have been reported as 80 mW/m^2 by Qin *et al.* for a twisted microfiber-TiO₂ nanowire hybrid yarn structure (Qin, Wang and Wang, 2008) however the input power was not provided, hence the efficiency or a realistic comparison of the energy harvesting capability could not be derived. This is a common aspect of prior-art in mechanical energy harvesters.

2.2.2.3 Triboelectric generators for wearables

Triboelectric generators can be used to harness energy from vibrations or frictional forces generated by human motion or wind. A triboelectric generator (TEG) consists of two dielectric material surfaces (A positive dielectric material and a negative dielectric material in the dielectric series) applied onto metal electrodes, mechanically interacting with each other in four different modes as illustrated in Fig. 2.3.

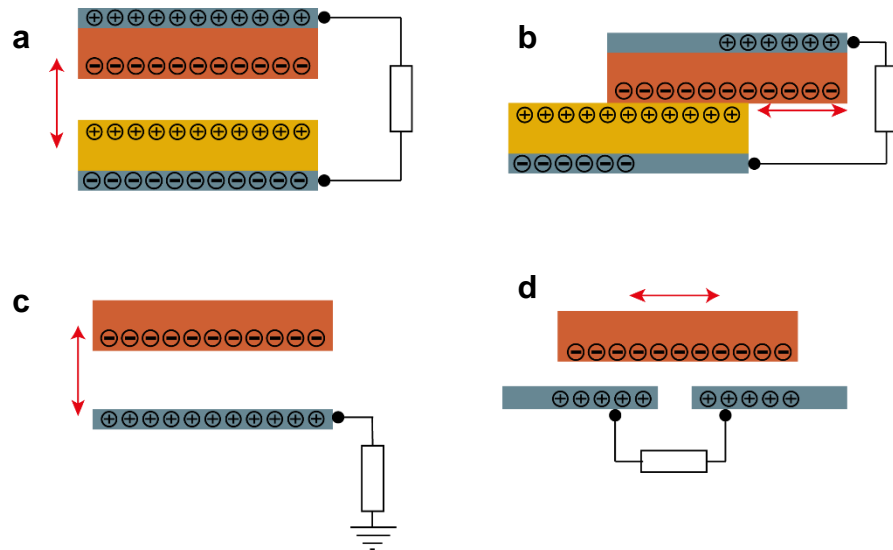


Figure 2.3 - Different triboelectric generation modes. (a) Vertical contact separation mode, (b) contact sliding mode, (c) single electrode mode and (d) free-standing tribo-layer mode.

In the vertical contact-separation mode (Fig. 2.3(a)), the dielectric surfaces generated electrons flow through the external load when alternatively contacted and separated

from each other. The contact sliding mode (Fig. 2.3(b)) used the same electrode structure and the electron generation occurred when the two dielectric layers slide between each other while in direct contact. In the single electrode mode (Fig. 2.3(c)) a dielectric surface and an electrode is present, with electron generation occurring by sliding or separation between the surface and electrode. Finally, in the freestanding triboelectric-layer mode (Fig. 2.3(d)) two equally sized electrodes were induced with a charge imbalance by an external dielectric material (e.g. a shoe with pre-induced electrical charge generated due to walking). In this case, the asymmetric charge distribution of the two electrodes and the nature of approach/departure of the dielectric material off the electrodes create a charge imbalance on the electrodes, resulting in an electron flow.

These systems can generate extremely high power densities of up to 1200 W/m^2 (Wang, 2013), however these high power densities are only instantaneous and result in generating a high electrical potential difference between the triboelectric surfaces with small pulses of current flow. Triboelectric generators are an emerging research topic in the field of energy harvesting, and a number of textile and wearable triboelectric nanogenerator (TENG) systems have been reported in literature (Tang et al. 2014; Cheng et al. 2015; Ha et al. 2015; Lee et al. 2015; Pu et al. 2015; Liu et al. 2016; Pu et al. 2016; Zhao et al. 2016; Zhu et al. 2016). The highest reported power density, 336 W/m^2 , was demonstrated using a composite of aluminium nanoparticles and polydimethyl siloxane (PDMS) (Lee *et al.*, 2015). Despite the high voltage and power density, TENGs are highly volatile and the total energy generated over a time interval was highly unpredictable. Although the TENGs inherently have some energy storage capability in the form of dielectric capacitors (Niu and Wang, 2014; Zhao *et al.*, 2019) this internal capacitance was not sufficient to regulate the power output. Therefore TENGs require sophisticated energy management systems to convert and regulate the power before being used to power devices (Wang, Chen and Lin, 2015).

2.2.2.4 Electromagnetic induction-based energy harvesters for wearables

Electromagnetic (EM) induction is also a technique that has been investigated for wearable devices, (Ylli *et al.*, 2013; Teichmann *et al.*, 2014; Zhang, Wang and Kim, 2015; Cho. *et al.*, 2016; Lee and Roh, 2018) especially for shoes. As with piezoelectric generators and TENGs, the power output of EM inductors is dependent on relative motion. The relative motion between a conductive coil and a permanent magnet can induce an

electric current that can be regulated to power a device; the operating principle of generators used in electric power generation. The reported textile-based devices of this kind are typically heavy and bulky. A typical EM induction energy harvester has a cylindrical permanent magnet in the core which is free to move inside a tubular structure onto which the induction coils are mounted. Power conversion rates reported in literature for devices with thinner ($\sim 10\text{mm}$) profiles (Zhang et al. 2015) are below 1 mW/cm^3 (Input power not quantified), limiting them to low power sensor applications (Teichmann *et al.*, 2014). Therefore, electromagnetic induction has not yet made significant mark in wearable devices or E-textile applications. Also, no noteworthy report on fully textile integrated electromagnetic induction-based device was available in literature.

2.3 Solar energy harvesting

Solar energy can be harnessed by irradiating sunlight upon semiconductor materials that can release free-electrons in order to generate an electron flow. This effect was first observed by French physicist A. E. Becquerel in 1839 which is defined as the photoelectric effect (Becquerel 1839). On average, around 170 W/m^2 of solar radiation is received at the earth's surface after atmospheric losses, of which currently only a small fraction (less than 0.01%) is converted into electricity (World Energy Council, 2013). Solar cell or photovoltaic (PV) technology has come a long way from its first generation of silicon (Si) solar cells, and state-of-the-art, multi-junction solar cells have a power conversion efficiency (PCE) of 38.8 % (Green *et al.*, 2019). Amongst the many wearable solar energy harvesting systems reported, solar cells that can be considered textile based (the PV materials built into the fibres, yarn) have conversion efficiencies far behind the industry benchmarks for industrial scale PVs, with efficiencies below 4% (Xu *et al.*, 2016). Nevertheless, these seemingly modest efficiency levels operate with a higher predictability than other textile-based energy harvesting device that use other energy sources. Considering the non-reliance on human activity (that can provide a truly non-obtrusive user experience) to generate power and availability, solar radiation can provide a good platform for developing a textile-based energy harvesting system, especially for outdoor applications.

2.3.1 Photovoltaic effect

2.3.1.1 Semiconductors

Semiconductors are a group of materials that have electrical conductivity that range between electrical conductors (e.g. metals) and electrical insulators. They can release free electrons when provided with energy above a value (band gap) determined by the specific material type (Conibeer and Willoughby, 2014). Materials with very high band gaps are electrical insulators and the electrical conductors such as metals do not demonstrate a band gap as the conduction and valance bands overlap; therefore, the excited electron-hole pairs recombine readily.

Band gaps of typical semiconductor materials used in electronics are summarised in Table 2.1 (Kettle 1986) below.

Table 2.1 - Semiconductor Band Gaps (Kettle 1986)

Material	Energy gap (eV)	
	0 K (-273°C)	300 K
Si	1.17	1.11
Ge	0.74	0.66
InSb	0.23	0.17
InAs	0.43	0.36
InP	1.42	1.27
GaP	2.32	2.25
GaAs	1.52	1.43
GaSb	0.81	0.68
CdSe	1.84	1.74
CdTe	1.61	1.44
ZnO	3.44	3.2
ZnS	3.91	3.6

As indicated in Table 2.1, the energy band gap will change with the temperature and hence for a given material type the behaviour of the charge carriers (electrons and holes) would depend on the absolute temperature.

2.3.1.2 Electron excitation by solar radiation

Solar radiation contains photons (energy packets) with wide spectrum of wavelengths and energy levels, some of which be partially absorbed by the atmosphere as illustrated in Fig. 2.4. The atmospheric gases (mainly H₂O and CO₂) are responsible for these

absorptions. The energy of a photon (given by $E = h\nu$, where h is the Planck's constant and ν the frequency) is determined by its wavelength.

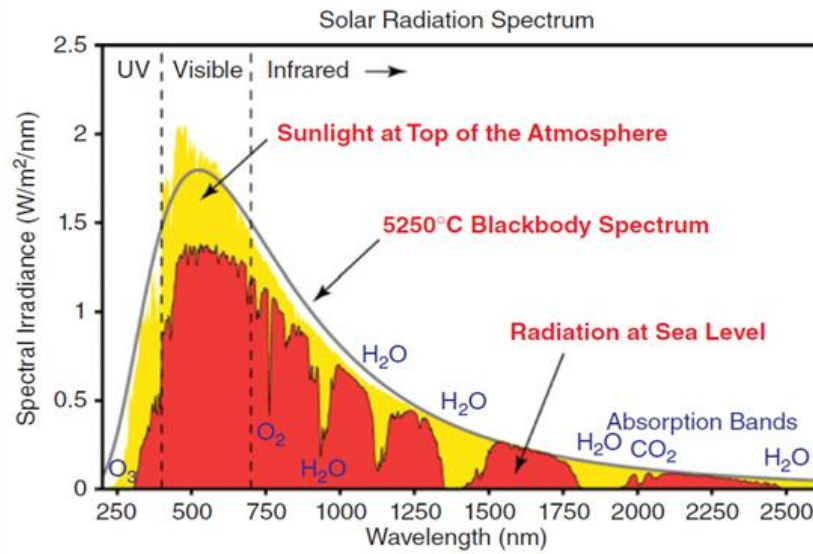


Figure 2.4 - Solar radiation spectrum before and after atmospheric absorption (Guillemoles 2014).

When a semiconductor is irradiated with photons, the photons have the ability to transfer their energy to electrons in the semiconductor lattice and excite them from the valence band to the conduction band (Fig. 2.5).

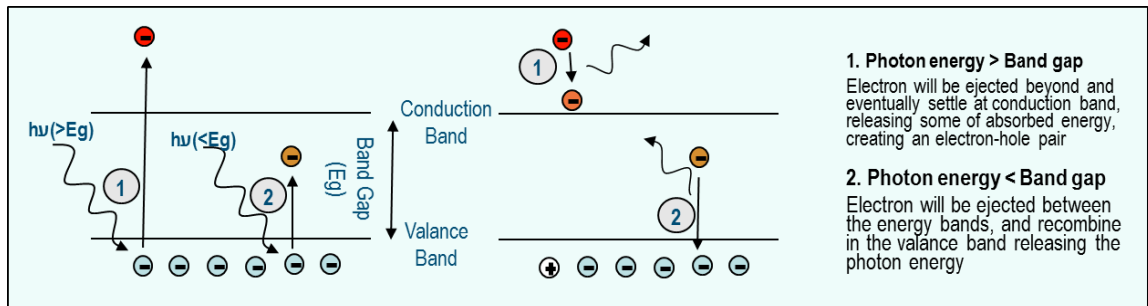


Figure 2.5 - Excitation of electrons by photons inside a semi-conductor due to photons.

Electrons in the valence band contribute to the valence bonds between adjacent semiconductor atoms. When the electrons in the valence band gain sufficient energy to break the valence bonds (determined by the band gap) they become free electrons or enter the conduction band that contribute to an electron flow. If the photon energy is larger than the band gap, then electrons are released from the valence band to the conduction band.

2.3.2 Operating principles semiconductor solar cell

Within a semiconductor, electrons and holes can carry charges. An intrinsic semiconductor, shown in Fig.2.6(a) is a pure semiconductor without any impurities. Intrinsic semiconductors can be doped with electron donor, D (group 15 atoms) in Fig. 2.6(b) or electron acceptor, A (group 13 atoms) in Fig. 2.6(c) impurity atoms to create N-type or P-type semiconductors respectively.

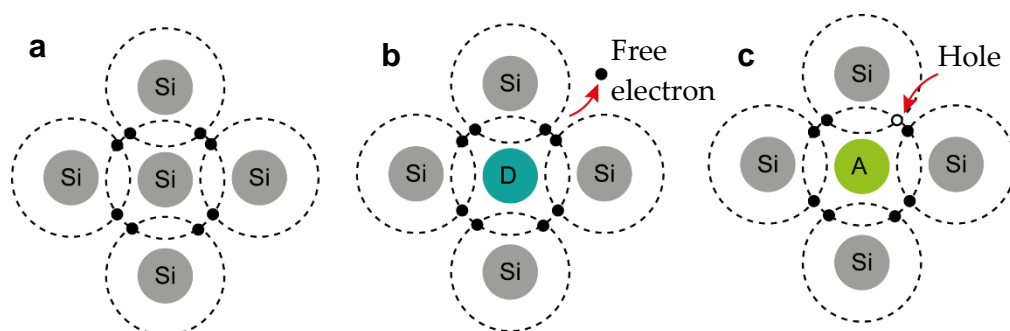


Figure 2.6 – (a) Intrinsic silicon (Si) semiconductor. (b) Intrinsic semiconductor doped with donor (D) atom. (c) Intrinsic semiconductor doped with acceptor (A) atom.

In N-type semiconductors electrons are the majority carriers and holes are the minority carriers, while in P-type semiconductors holes (vacancies of electrons) are the majority carriers and the electrons are the minority carriers. The doped semi-conductors have different band structures and reduced band gaps to the intrinsic semiconductors as shown in Fig 2.7.

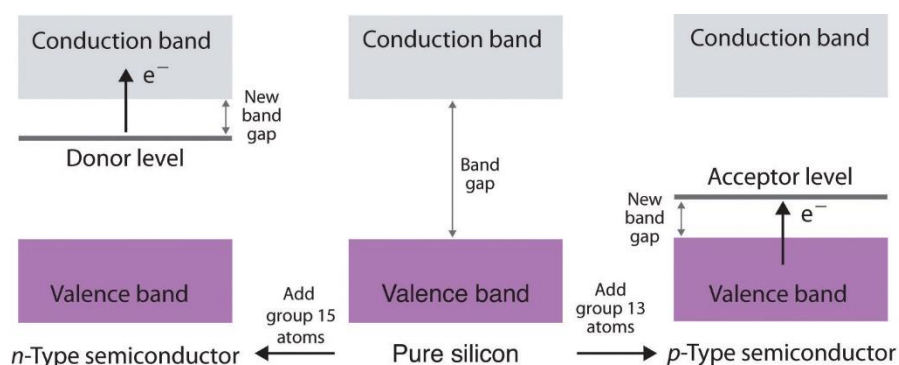


Figure 2.7 – Structures and Band Diagrams of n-Type and p-Type Semiconductors (a) Doping silicon with a group 15 element results in a new filled level between the valence and conduction bands of the host. (b) Doping silicon with a group 13 element results in a new empty level between the valence and conduction bands of the host. (Chemistry Libretext, 2019)

By combining N type and P type semi-conductors a PN junction is formed. At the boundary of the PN junction a depletion region (region where no free charge carriers

exist) is formed by exchange of majority carriers across the boundary of the PN junction developing a small electric field across the boundary of PN junction.

When a semiconductor PN junction is illuminated (Fig 2.8), electron-hole pairs are generated on both the P and N sides of the semiconductor junction. With the increase in carrier concentration, minority carriers on each side (electrons in P side and holes in N side) start to cross the depletion region and drift to the opposite side (electrons to the N side and holes to the P side) due to the electric field across the depletion region. This charge movement increases the majority carrier concentration on both P and N sides. When the PN junction is externally connected with an electrical conductor, the majority carriers in the N side (electrons) flow through the conductor to recombine with majority carrier in the P side (holes), generating an electric current.

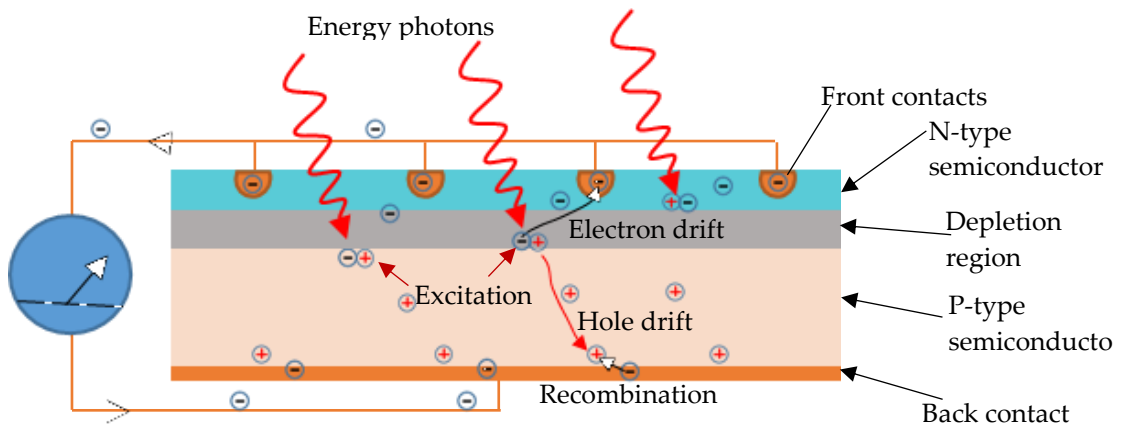


Figure 2.8 - Charge carrier generation and transport within an inorganic PN junction semiconductor solar cell.

Theoretical maximum efficiency of a pn-junction Si solar cell is around 32.33% (Shockley and Queisser, 1961) due to the maximum number of photons in the solar spectrum that can exceed the band gap of 1.1 eV of Si pn junction.

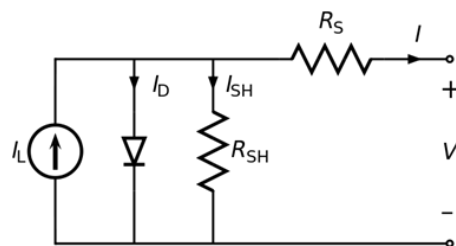


Figure 2.9 - Equivalent circuit for a solar cell (McEvoy et al. 2013).

Solar cell performance can be analysed using an equivalent electronic circuit, which consists of an ideal diode, a current source (I_L) and a resistor (R_{SH}) connected together in parallel to a series resistor (R_S) as illustrated in Fig. 2.9.

The relationship between the output current (I) and voltage (V) of a solar cell can be given by the below equations.

$$I = I_L - I_D - I_{SH} \quad (2.1)$$

Where,

$$I_D = I_o * \left[\exp \left(\frac{V + IR_S}{k_B T} \right) \right] \quad (2.2)$$

And,

$$I_{SH} = \frac{V + IR_S}{R_{SH}} \quad (2.3)$$

Here, I_L , I_D , I_{SH} represent the photon-generated current, diode current and shunt resistor current respectively. I_o is the saturation current of the diode, k_B is the Boltzmann constant, and T is the absolute temperature. A typical characteristic I-V curve for a solar cell is given in Fig. 2.10.

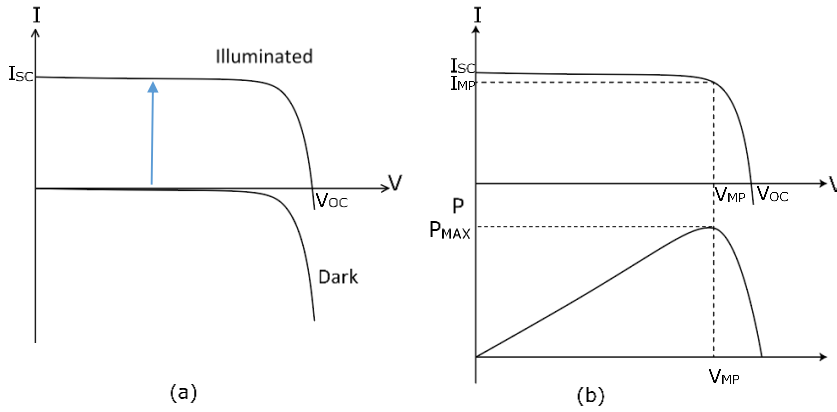


Figure 2.10 - I-V characteristic for a solar cell (a) under dark and illuminated conditions
Equivalent circuit for a solar cell (McEvoy et al. 2013)

In dark conditions a light induced-current will not be generated, and the I-V curve will represent the behaviour of the diode. Once illuminated, a photo current is generated, and the I-V curve will be shifted upwards along the current axis. The intersection point

of the I-V curve on the voltage and the current axis gives the open circuit voltage (V_{OC}) and the short circuit current (I_{SC}) respectively. V_{OC} is the voltage across the solar cell when no connection is made between the terminals (zero current is drawn from the cell), which is the maximum possible voltage. I_{SC} represents the current flow through a zero-resistance conductor when connected between the terminals of the solar cell, which is the maximum possible current.

The voltage (V_{MP}) and current (I_{MP}) at the point where the maximum power (P_{MAX}) is generated is a useful defining characteristic features of a solar cell. Fill Factor (FF), which is a characteristic parameter for a given cell type, indicates the performance of the cell when the maximum power is drawn and is defined below.

$$FF = \frac{V_{MP} * I_{MP}}{V_{OC} * I_{SC}} \quad (2.4)$$

The power conversion efficiency (PCE) of a solar cell is the percentage of incident light energy converted into electric energy by the solar cell (Eq. 2.5). Here, P_{in} is the incident solar/light power received by the solar cell.

$$PCE = \frac{P_{IN}}{V_{MP} * I_{MP}} \times 100\% = \frac{P_{IN}}{FF * V_{OC} * I_{SC}} \times 100\% \quad (2.5)$$

2.2.3 Types of solar cells

Several different types of solar cells have been developed using different types of semiconductor materials; the first generation of solar cells were of mono-crystalline/multi-crystalline single junction type. The most renowned first-generation solar cell type is the crystalline silicon (c-Si) solar cell, which still dominates the commercial solar cell market. These first-generation solar cells are typically rigid and brittle therefore, need to be mounted on rigid frames. The second-generation solar cells were produced as thin films to reduce manufacturing costs (McEvoy, Markvart and Castañer, 2013). The efficiency levels achieved were less than the single crystal types except for gallium arsenide (GaAs) cells. GaAs cells were developed to compete with c-Si solar cells and are more expensive due to the higher cost of raw material. In recent years these second-generation solar cells have been applied onto flexible substrates and have become one of the best options for applications requiring flexibility, conformability to three-dimensional objects, and durability. While research is still ongoing to improve the efficiencies of second generation thin-film cells, the substrate material used to

construct this type of cells are still limited to flexible sheets or films made of metals, ceramics or glass (Feurer *et al.*, 2016; Gerthoffer *et al.*, 2017). The third-generation of solar cell technologies include multi-junction cells, organic photovoltaic (OPV) cells, hybrid solar cells; namely dye-sensitized solar cells (DSSC) and perovskite solar cells which employ inorganic and organic material combinations with different photon absorbing, charge carrier generation, and transport mechanisms. Typically OPVs are made of photovoltaic polymer pairs (electron donor and electron acceptor pairs) such as poly-3-hexylthiophene-2,5-diylpoly(3,4-ethylenedioxythiophene):phenyl-C61-butyric acid methyl ester (P3HT:PCBM) with metallic electrodes (e.g. Ti or Ag) and a transparent counter electrode such as poly(3,4-ethylenedioxythiophene):poly(4-styrenesulfonate) (PEDOT:PSS), indium tin oxide (ITO) or their combinations. DSSCs employ a combination of organic and inorganic active materials where narrow-band gap metal oxide semiconductor nano-particles such as TiO_2 or ZnO are deposited onto a transparent electrode such as PEDOT: PSS or ITO. An organic dye is adsorbed onto the metal oxide layer which is also in contact with a reduction-oxidation (red-ox) couple mediator, which transports photo-generated electrons to the metallic counter electrode. The perovskite cells use materials with a perovskite crystal structure ABX_3 (A = monovalent cation, B = metal cation, X = halide anion) as the photon absorption material, hence the name. These cells are built nearly identical to DSSCs with the active layer consisting from perovskites. Most of these third-generation cell types are yet to make a significant entry into large scale commercial applications due to the challenges faced in scaling up of production, durability or cost. Multi-junction solar cells have successfully managed to enter extra-terrestrial and concentrated photovoltaics (CPV) markets due to their unparalleled conversion efficiencies, however their volumes remain small due to the high cost.

In recent years the organic and hybrid cell concepts have shown great promise in achieving improvements in conversion efficiency and durability which will allow them to compete with first and second generation technologies in the future, especially for application demanding mechanical flexibility (McEvoy, Markvart and Castañer, 2013). In June 2018 Oxford Photovoltaics achieved a perovskite-silicon tandem solar cell with a 28% conversion efficiency that exceeded the 26.7% efficiency world record for a single-

junction silicon solar cell. Table 2.2 outlines the highest levels of Power Conversion Efficiency (PCE) levels achieved in laboratory conditions by the main types of solar cells.

Table 2.2 - Highest reported solar cells efficiency levels as of June 2018 (Green *et al.*, 2019).

Generation	Cell Type	Power Conversion Efficiency (%)	Fill Factor
1 st	Crystalline Si	26.7 ± 0.5	84.9
2 nd Generation	Gallium Arsenide (GaAs) thin film	28.8 ± 0.9	86.5
	Copper indium gallium (di)selenide (CIGS)	22.9 ± 0.5	79.5
	Amorphous Si	10.2 ± 0.3	69.8
3 rd Generation	Perovskite	20.9 ± 0.7	74.5
	Dye sensitised	11.9 ± 0.4	71.2
	Organic	11.2 ± 0.3	74.2
	Five junction cell (bonded)	38.8 ± 1.2	85.2

2.4 Solar energy harvesting for wearable applications

Amongst the other energy harvesting technologies explored for wearables, solar energy harvesting has been one of the most investigated avenues due to the abundance of solar energy (International Energy Agency IEA, 2011) and the maturity of photovoltaic (PV) technologies (Conibeer and Willoughby, 2014).

Integration of photovoltaics into textiles, or fabricating solar cells on textiles, has been driven by several factors, either as an effort to make stiff and rigid solar cells more versatile (ease of transporting, deploying and disassembling) for their conventional use (off-grid or domestic solar applications), by making them flexible, or by opening up new applications such as for powering mobile, wearable or E-textile devices (J. I B Wilson and Mather, 2015). It is to be noted that each approach has inherent challenges. For example, mobile solar units powering off-grid sites need to withstand extreme climate conditions, while E-textile applications demands not only wearability, but also the ability to survive multiple wash and wear cycles (Krebs and Hösel, 2015).

2.4.1 Categorisation of wearable solar energy harvesters in literature

Various methodologies to integrate solar energy harvesting capability into textiles for wearable applications have been explored over the years (Schubert and Werner, 2006;

Kumar, 2011; Mather and Wilson, 2017). These approaches can be categorized based on the photovoltaic material type (Fig. 2.11) or their physical structure (Fig. 2.12).

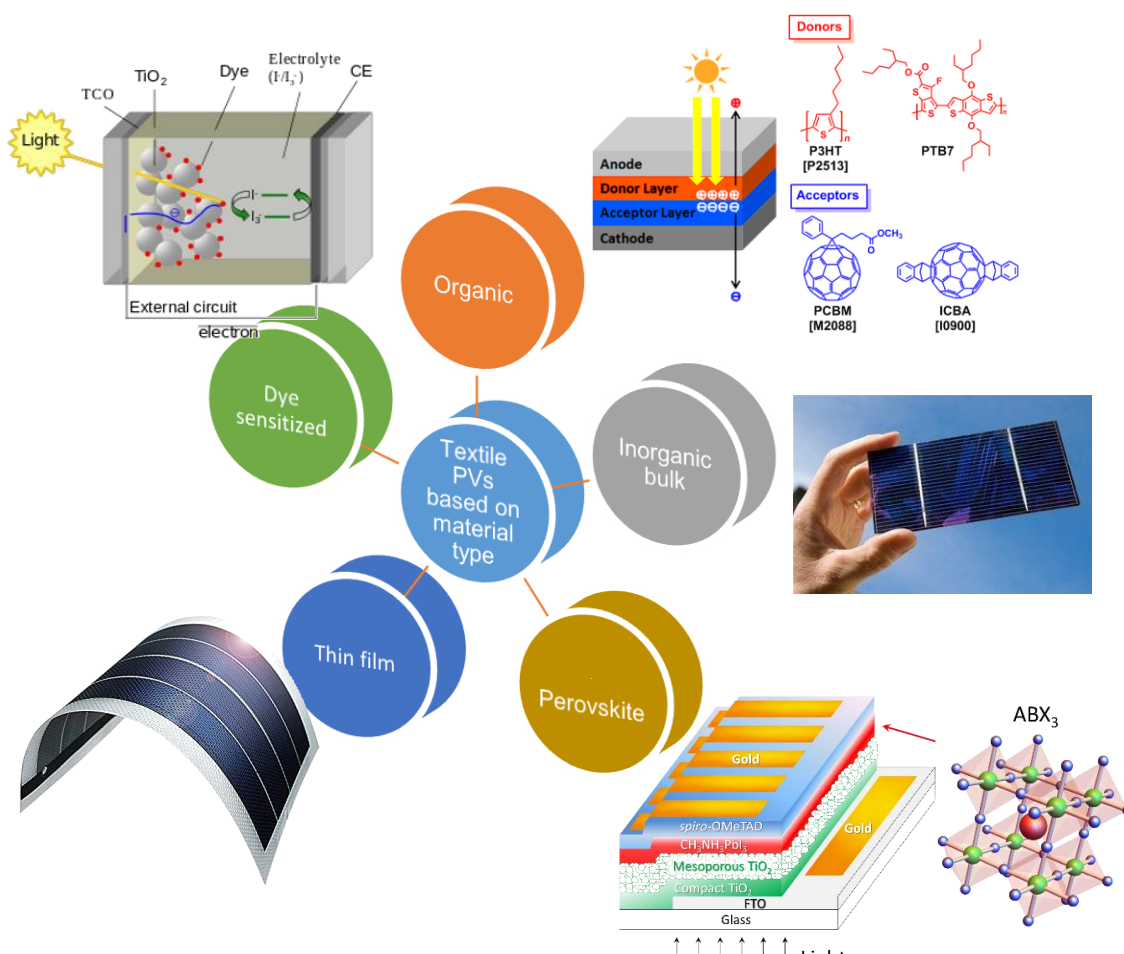


Figure 2.11 - Categorisation of solar cell types used for textile applications based on the photovoltaic material type.

Despite the high efficiency levels and established knowledge which led to their domination for mainstream PV applications, inorganic PV technologies including c-Si, poly-crystalline silicon and other bulk semiconductor PV configurations have seen limited exploration for wearable applications, mainly owing to their lack of mechanical flexibility. The demand for softness and flexibility has made traditional stiff and rigid inorganic solar cells prohibitive for textile-based applications. Only a handful of literature resources present the use of inorganic thin-film semiconductor materials as coatings on textile structures (He *et al.*, 2013; J.I.B. Wilson and Mather, 2015). These textile structures are limited to a few substrate types (e.g. glass, ceramic, etc.) which can withstand high process temperatures used in inorganic semiconductor material processing, hence these are of little use for wearable applications. Additionally, these

coatings are prone to cracking and delamination under mechanical stresses (J.I.B. Wilson and Mather, 2015). However, the application of organic photovoltaics (OPV) (Krebs *et al.*, 2006), hybrid photovoltaics such as dye-sensitized solar cells (DSSCs) (Zhao *et al.*, 2018) and perovskite solar cells (Jung *et al.*, 2018) onto textile substrates have dominated most of the textile based PV research.

Second-generation thin film solar cells applied onto flexible substrates have shown promising results, with mechanical flexibility and durable solar energy harvesting performance. Thin film PV laminates such as copper indium gallium diselenide (CIGS) (Knittel *et al.*, 2010; Nocito and Koncar, 2016) and amorphous thin-film silicon (a-Si, TF-Si) (J. I B Wilson and Mather, 2015; Plentz *et al.*, 2016; Mather and Wilson, 2017) have been explored for textile applications. These thin film PVs have been laminated onto textiles either by means of an adhesive layer or using a printed base-layer onto which the PV film is laminated. In addition to their inherent flexibility, a strong interest towards OPVs, hybrid PVs and thin film PVs has emerged due to their affordability and recent improvements in efficiency. These technologies have already proven themselves as cost effective and mechanically versatile alternatives to inorganic solar cells and are showing great promise for future wearable photovoltaics, however it is important to note that these solutions are still incapable of achieving the efficiencies of inorganic cells (Green *et al.*, 2019). As with any film-based technology, thin-film PVs also cannot be considered ideal due to the non-permeable nature of the monolithic structure of the films. The majority of the materials used for hybrid and organic cells suffer from long term-durability issues, and their performance deteriorates upon prolonged exposure to sun (Chae *et al.*, 2013); this is a key challenge for their mass adoption. DSSCs in particular can suffer from performance deterioration due to electrolyte leakages, and non-reversible chemical degradation. Some research has reported solid-state electrolytes and dye-electrolyte combinations with higher stability for DSSCs, however their efficiencies were not comparable to traditional DSSC cells based on liquid electrolytes and dyes. The most effective electrolytes identified as red-ox couples (e.g. iodine-based) in DSSCs could be corrosive and toxic. In general, the inherent flexibility of these flexible PVs types demands mechanical integrity within and between photoactive and conductive layers. Mechanical failures accumulated during deformations will result in drastic performance

degradations. This is also a key consideration in adapting flexible PV technologies for wearable applications.

A list of research work reported in literature categorized based on the solar cell material type is given in **Appendix 1**.

From a wearability and apparel perspective, the categorisation of PV textiles based on construction and structure is more relevant, since key textile characteristics (three-dimensional conformability, air and moisture permeability, and appearance) are mostly determined by how individual elements of the structure are assembled together. All textiles fabrics are made of yarns made from fibres. During the manufacture of a textile fabric these yarns are bound together physically using interlacing (weaving and braiding) and interloping (knitting) techniques. The type of yarn binding defines the mechanical properties and air and moisture permeability of a textile. The shear behaviour of a textile dominates the three-dimensional conformability, and the air and moisture permeability of a textile structure is determined by the micro-sized capillaries formed during the fabric manufacture.

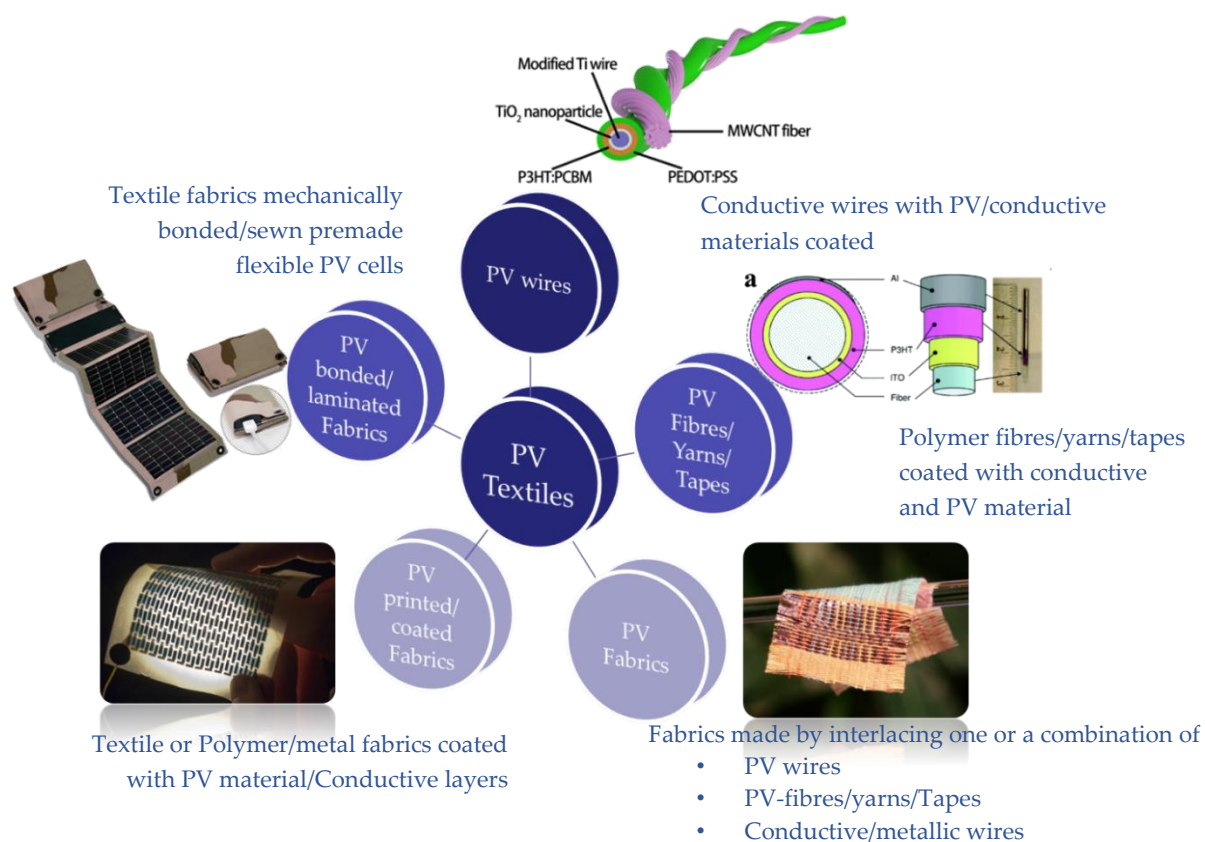


Figure 2.12 - Categorisation of solar cell types used for textile applications based on the photovoltaic material type.

The reported textile-based PV systems can be broadly categorized based on the structure or construction methods shown in Fig. 2.12.

2.4.1.1 Attaching flexible solar panels onto fabrics using adhesives or sewing

The simplest method of adding solar energy harvesting capability to a textile is to superficially attach flexible solar panels onto the surface of a fabric. Attaching flexible solar panels onto fabric surface has been employed to develop many consumer products such as back-packs, hand bags and luggage (Nocito and Koncar, 2016; Mather and Wilson, 2017) in addition to apparels. The attachment of flexible solar panels onto garments provided a convenient alternative to rigid solar panels and power banks for replenishing their mobile devices during outdoor activities. Amorphous silicon and CIGS thin-film solar panels being amongst the most widely used cell types, due to their good efficiency and long-term stability (Mather and Wilson, 2017).



Figure 2.13 - Prototype apparel with pre-fabricated flexible solar panels attached onto the fabric. (a) Tommy Hilfiger's solar powered jacket (Forbes, 2014). (b) Maier Sports' outdoor winter jacket with solar panels (Schubert and Werner, 2006). (c) Solar shirt developed by Pauline van Dongen (van Dongen, 2018).

Early examples include the Maier Sports' prototype of a winter outdoor jacket (Fig.2.13(b)), which was first presented in Munich at the International Trade Fair for Sports Equipment and Fashion (ISPO) 2006 and comprised nine amorphous Si solar modules from Akzo Nobel. The jacket could generate a maximum power output of 2.5 W under full sun (Schubert and Werner, 2006). Tommy Hilfiger's solar powered jacket (Fig.2.13(a)), released for the holiday 2014 season, (Forbes, 2014) used a similar concept, and comprised flexible amorphous silicon solar cells was developed by Pavilion. Pauline van Dongen developed a collection of designer wear with thin film solar cells (van Dongen, 2018) attached which included 'The Solar Shirt' (2014) that can generate 1 W under direct sunlight (Fig. 2.13c)), wearable solar dress (2014), 'The Solar Parka' (2015), 'The solar Windbreaker' (2016): for these garments the thin film solar cells were combined into standardised, functional modules.

These solar cell-attached garment prototypes provided the first glimpse of wearable solar energy harvesters; however, they were limited to heavy-duty outerwear and futuristic fashion prototypes. The appearance, comfort and durability of these were not comparable to regular clothing, hence these products were not appealing to regular consumers. It was evident that in order to achieve satisfactory levels of wearability and washability, new paradigms of PV device fabrication methods need to be explored in order to enable the conformal (drapable and shear deformable) and structural (hierarchical and porous) features that are inherent in textile structures.

2.4.1.2 Applying flexible photovoltaic films and coatings onto planar textiles

Printing (Ayse Bedeloglu *et al.*, 2011; Arumugam *et al.*, 2018), laminating or coating (P. . Du *et al.*, 2013), organic photovoltaics (OPV) (Krebs *et al.*, 2006; Jinno *et al.*, 2017; Jeong *et al.*, 2019), and hybrid photovoltaics such as dye-sensitized solar cells (DSSC) (J. Liu *et al.*, 2018; Liu *et al.*, 2019) and perovskite solar cells (Lam *et al.*, 2017; Jung *et al.*, 2018) onto planar textiles has been widely investigated for textile based PVs (Fig.2.14).

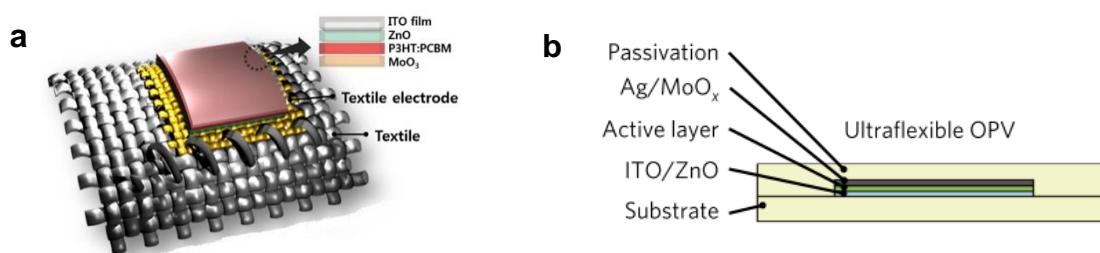


Figure 2.14 – Schematic illustration of the textile based OPV developed by (a) Lee *et al.*, (2014) and (b) Jinno *et al.* (2017).

One of the first reported printed PVs intended for textile fabrics was made by Krebs and co-workers (Krebs *et al.*, 2006) where organic photovoltaic devices were fabricated onto non-transparent polyethylene terephthalate (PET) or Polyethylene (PE) tapes and Indium tin oxide (ITO) coated glasses. Two strategies of fabric integration were explored; in the first method, PET tapes coated with organic PV materials using a doctor blade method were subsequently laminated on to a suitably transparent textile fabric, in the second method PE tapes were first laminated to the fabric prior to the application of the PV coatings and electrodes onto the tape. The power conversion efficiency (PCE) and fill factor of these textile coated PVs were $1.4 \times 10^{-3} \%$ and 25% respectively, and substantial degradation of performance was observed even within two hours of direct

exposure to light (1 Sun intensity). The degradation of performance was mainly attributed to the instability of photovoltaic material under sunlight. Similar work was presented by Bedeloglu and co-workers (Bedeloglu *et al.*, 2009) using polymer PV coatings on six different substrates (PP based and ITO/glass based), where the maximum PCE achieved was $\sim 0.37\%$ for ITO/glass based substrate. Bedeloglu *et al.* subsequently realized a 0.29% PCE for nano-silver coated PP tapes which could be laminated onto textiles.

Sundarrajan *et al.* (Sundarrajan *et al.*, 2010) attempted to fabricate a polymeric PV nanofiber web for textile applications using core-shell electrospinning technique, however the PCE achieved by these PV webs were only 0.087% . In order to make flexible PV films more compliant for wearable applications Lipomi and co-workers (Lipomi *et al.*, 2011) devised a stretchable polymer solar cell by spin coating a pre-strained polydimethyl siloxane (PDMS) film with polymeric PV materials. These stretchable films achieved a PCE of 2% . This strategy of coating pre-strained PDMS, or similar elastic films, was adopted widely in subsequent studies to achieve stretchable PV films. Polymer PV films were prepared by Kaltenbrunner *et al.* (Kaltenbrunner *et al.*, 2012) on $2\ \mu\text{m}$ thin PET foils that exhibited a PCE of 4% . Importantly, the areal density of these PV films was as low as $4\ \text{gm}^{-2}$. It was possible to attach these ultrathin films onto pre-stretched elastomeric films to realize stretchable PV films as previously achieved by Lipomi *et al.* Kylberg *et al.* developed organic PV coatings on woven structures made with a combination of metal and polymeric mono-filaments (Kylberg *et al.*, 2011). One side of the woven structure was coated with a transparent PET filler material (this side was used as the active side to apply a PEDOT: PSS electron transport layer and P3HT: PCBM active material), with the back electrodes coated on the other side of the woven structure. This construction resulted in a flexible polymeric film with a PCE of 2.2% . A stitchable organic photovoltaic cell was proposed (Lee *et al.*, 2014) where a fabric electrode prepared by weaving PE multifilament yarns coated with metal multilayers of Ni-Cu-Ni-Au. The authors presented a construction where at least part of the solar cell was a textile structure. These cells managed to achieve a PCE of 1.8% . A fully spray coated OPV was realized by Arumugam *et al.* (Arumugam *et al.*, 2016) on a polyester cotton blended plain woven fabric, after smoothening the fabric surface using a screen

printed interface layer. The interface layer provided a smooth surface to deposit the OPV coating. This construction, however only yielded a PCE of $20 \times 10^{-3} \%$.

For the first time an organic PV film (Fig.2.14(b)) was presented by Jinno and coworkers for wearable applications which claimed to be waterproof and washable (Jinno *et al.*, 2017). They fabricated the OPV devices on a $1.0\mu\text{m}$ -thick parylene film which was subsequently covered by another $1.0\mu\text{m}$ -thick parylene film (referred to as free standing OPV by the authors). The free standing OPV exhibited a high PCE of 7.9 %. The washability of the free standing OPV was demonstrated by dipping the device in beaker of stirred distilled water for 30 minutes, and in stirred 10% detergent water for 5 minutes. The free standing OPV was sandwiched between two 200 % stretched $500\mu\text{m}$ -thick layers of acrylic elastomer with the aim to achieve stretchability and better compatibility with water. Another test was performed by dipping the free standing and sandwiched devices into distilled water for 120 minutes, which showed ~20% and ~5% reductions in PCE respectively. A recent study on OPVs with a SiO_2 -polymer composite capping-layer encapsulation, developed on a woven fabric (Jeong *et al.*, 2019), has seen more rigorous washability test where the OPV devices were stirred in 2% detergent solution inside of a beaker for 10 minutes after subjecting the device to 1000 bending cycles at a bending radius of 3 mm. This test was repeated up to 20 times for thirty days and the OPV devices showed no significant change in performance after this time. These devices also generated impressive PCE of 7.26 %. This construction however did not yield stretchability, although it could undergo thousands of bending cycles without a deterioration in performance. In comparison to previous reports of flexible OPV devices for wearable E-textile applications, these two liquid-water-compatible devices showed great promise and were clearly are leaps forward in achieving wash durable PVs for wearable applications. However, the washability and water compatibility tests conditions employed in this study were mild, and far from the vigorous hydro-mechanical, thermal and chemical processes undergone by regular clothing in a domestic washing process.

PV films and coatings based on DSSC and perovskite technologies were also explored for wearable applications, however none of these were able to demonstrate levels of mechanical robustness and compatibility to water or washing achieved by some of the OPVs discussed earlier. One of the first studies on textile based DSSC was presented by

Du *et al* (P. Du *et al.*, 2013) where $\sim 3\mu\text{m}$ -long TiO_2/MgO nanorods were physically bound to PET non-woven fabrics using an acrylic binder, onto which the organic dye molecules were adsorbed. These devices demonstrated a PCE of 3.93 %, however the long-term stability was not evaluated. A cotton fabric based DSSC was presented (Xu *et al.*, 2014) where a Ni-polypyrrole coating applied on the cotton fabric was employed as the counter electrode to replace fluorine-doped tin oxides commonly used for DSSCs. This fabric based DSSC was flexible and yielded a PCE of 3.3 %. The PCE was further enhanced up to 3.83 % by the same research team in 2016 by optimizing the surface resistance of the Ni-polypyrrole coating (Xu *et al.*, 2016). DSSCs were prepared on metal wire woven structures without using transparent conducting oxides (Min Ju Yun *et al.*, 2016) by employing float printing deposition onto a plain-weave, which generated PCE of 4.16 %. Opwis *et al.* realized a DSSC on a polyamide-coated glass woven fabric (Klaus Opwis *et al.*, 2016) that generated a PCE of 1.1 %; these were stable in performance for at least seven weeks and showed improved efficiency at lower incident light intensities. A DSSCs was developed on woven polyester cotton fabric (J. Liu *et al.*, 2018) by screen printing an interface layer onto the fabric before coating it with Ag electrode (Fig 2.15).

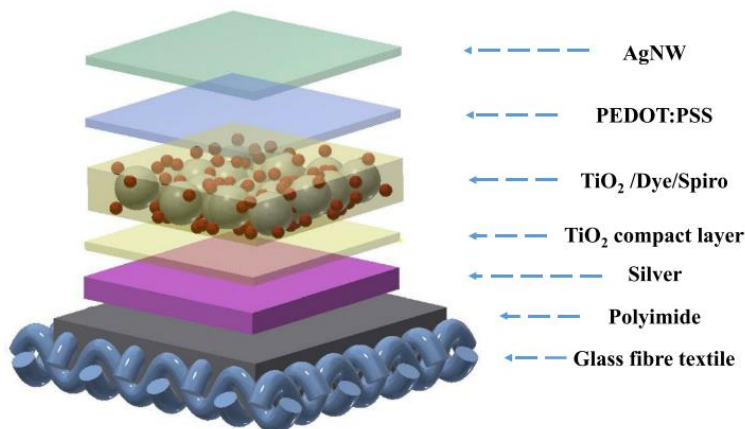


Figure 2.15 – Schematic diagram showing an isometric view of a textile based solid-state DSSC device (J.Liu *et al.* 2018).

This approach was similar to how Arumugam *et al.* prepared the fully spray coated textile based OPVs. The resultant DSSCs exhibited a PCE of 2.78 %. A novel approach to preparing textile DSSCs were presented (Yun *et al.*, 2019) where a three-dimensional structure was developed by sandwiching an electrolyte-infused woven glass-fibre spacer fabric, between two stainless steel woven fabric electrodes using an interlock stitching process. The electrode fabrics were coated with active materials prior to the

sandwiching process. Finally, the sandwich structure was encased inside of a pouch made of a polyester film which was filled with the electrolyte. The prepared DSSC generated a PCE of 1.7 %. A recent report on fully encapsulated liquid electrolyte based DSSC, developed on a woven glass fabric (Liu *et al.*, 2019), revealed that the stability of the developed cells deteriorated from a PCE of 3.24% to 1.03% during three months of exposure to ambient conditions.

Perovskite material coated PV textiles have also been developed recently, where cell architectures similar to the DSSC coated textiles were used: These perovskite PVs generated significantly better power densities and longer stability compared to their DSSCs counterparts. For example, Lam and co-workers (Lam *et al.*, 2017) reported a textile-based perovskite PV laminate using SnO_2/PCBM active layer and an elastomeric encapsulation covering the fabric and active layers with an unmatched PCE of 15 % for a fabric based device. The researchers claimed that the ductile elastomer used for encapsulating the device yielded a good flexibility and potential washability; however experimental evidence to prove these claims were not presented. Jung *et al.* reported perovskite solar cells prepared via low-temperature solution-processing (Jung *et al.*, 2018), adopting a planar heterojunction architecture on a textile substrate. A polyurethane coating on the textile fabric enabled the low-temperature solution processing where the resultant solar cells achieved a good PCE of 5.7 %. CIGS thin film coatings were presented on glass-fibre-woven fabrics by Knittel (Knittel *et al.*, 2010) which achieved an impressive PCE of 8.0 %. A similar amorphous Si thin-film coated glass fabric PV was realized with a PCE of 1.41 % by Plentz *et al.* (2016), however this approach was not suitable for applying PV functionality directly onto standard polymeric textiles substrates such as PA or PET due to high processing temperatures. Despite their future potential, low temperature processed thin-film PV technologies (Hou *et al.*, 2009) are currently not reported for wearable applications. In general, the printed, coated or laminated multi-layered PV structures, are either prepared directly onto a planar textile surface or patched onto the textile surface after partly or fully pre-fabricating the device. The former often requires a fabric surface preparation step to make the fabric surface electrically functional or morphologically smooth (using a coating or by laminating a film) for the application of the PV device. Some methods involve developing PV device on textile surfaces made with inherently functional (e.g.

electrically conductive) fibres or yarns. To achieve long term stability and compatibility with water, the devices have to undergo an encapsulation step using a thin film or a flexible coating (sometimes elastic) with excellent barrier properties. Regardless of the approach followed or the functionality achieved, one thing common to all these planar PVs is the resultant of a non-permeable, non-porous structure. Despite being inherently flexible or stretchable, when applied onto large area textiles (which are inherently porous due to the openness of woven or knitted structures), these PV materials inhibit the air and moisture permeability of the base textile, which is critical for the comfort of the wearer, especially during warm and humid conditions. Also, these PV systems significantly alter the colour and fibrous surface morphology of textile fabrics. For example, most PV films have a smooth glossy surface with a rubbery or foil-like texture and the colours are typically limited to the inherent colours of the photoactive or electrode material. This would significantly change the appearance and hand-feel of the textile fabric. In terms of mechanical behaviour, textile fabrics possess the ability to undergo large deformations, without accumulating structural defects. This is due to the hierarchical fibre entanglement of textile structures, where the yarns have a high degree of freedom to move independently within the macro structure and reorganize, without changing their micro-structure (i.e. yarns can move independently without changing the fabric structure and fibres can deform independently without collapsing the yarn structure). However, when a monolithic coating or a film is applied on to the surface of a textile fabric structure, it permanently binds the textile fibres and yarns together and occupy the empty spaces between individual fibres in yarns; this significantly hinders fibres' and yarns' freedom of movement when external forces are applied.

2.4.1.3 One dimensional (1D) photovoltaic structures

With the aim of addressing the disadvantages of coated or film-like planar PV materials, scientists have been exploring the alternative routes of developing one-dimensional (1D) PV devices in the form of fibres, yarns, wires or tapes (e.g., narrow woven and knitted tapes) for fabricating planar PV devices using a bottom-up approach. Two main routes have been explored for creating such one-dimensional devices with regards to the base material; initially, metal wires, carbon-based fibres (Carbob fibres, CNTs) or conductive polymer filaments were employed as the core with the other layers built on top of them to create PV-fibres. The other method presented in the literature utilized conventional

polymeric textile fibres as the base material to build the 1D devices. The latter approach is more desirable for retaining the textile features of the resultant planar structure due to better flexibility and lower stiffness, while the former allows for a simpler fabrication process and better device performance (in terms of PCE) due to lower electrical resistance of the core electrode.

2.4.1.3.1 Photovoltaics using non-polymeric fibres or wires.

Use of metal wires or carbon-based fibres as the core to craft 1D photovoltaics (PV-fibres) has been investigated, where the conductive material was coated with various photovoltaic material combinations to create organic, hybrid or inorganic co-axial-fibre shaped solar cells. In principle the stacking of PV layer(s) and others onto the fibre surface was similar to the coated, laminated or printed films discussed earlier, with the small cross sections and large aspect ratios allowing them to be woven into fabrics. Literature suggests that, hybrid PV (predominantly DSSCs) technologies have dominated the research on PV-fibres, due to their ease of adaptability to one-dimensional flexible structures. The conformal electrolytes (mostly liquid or gel) used in DSSCs allow these PV-fibres to deform while maintaining the integrity of the PV structure. However, DSSC can suffer performance degradation caused by leakage of electrolyte due to the deficiencies of the encapsulation. A typical DSSC fibre is fabricated on a Ti wire core, where TiO_2 or ZnO nanoparticles or nano-wires are grown on the Ti wire before adsorbing the sensitizer dye (Fig.2.16). It is widely understood that the catalytic performance of both the electrode and counter electrode is instrumental for achieving enhanced PV performance, and therefore nano-scale modifications to the electrodes are often implemented (Cavallo *et al.*, 2017)). In some reports, Ti wire was replaced by stainless steel or carbon nanotube based wires. The counter electrodes have often taken the form of a Ti or Pt wire twisted around the working electrode (other conductive strands such as CNTs were also explored) before encasing the twisted assembly inside of an electrolyte (predominantly liquid based) filled encapsulation.

Early studies of these DSSCs had limited flexibility and mechanical robustness due to the capillary tube encasements employed, and the poor adhesion between the Ti wire and the TiO_2 nano coating (Ramier *et al.*, 2008). Several reports have seen the metal wire counter electrodes being replaced by a transparent conductive metal oxide (e.g. ITO) capillary tubes; these tubes also served the purpose of encapsulating the device,

however, they make the device stiff and rigid which is undesirable for a textile application. Lv *et al.* (Lv *et al.*, 2011) reported a DSSC wire with the twisted working electrode / counter electrode configuration encapsulated by a electrolyte filled capillary tube, which generated a PCE of 5.41 %: The authors further investigated the lensing effect of the capillary tubes employed for encapsulating the device.

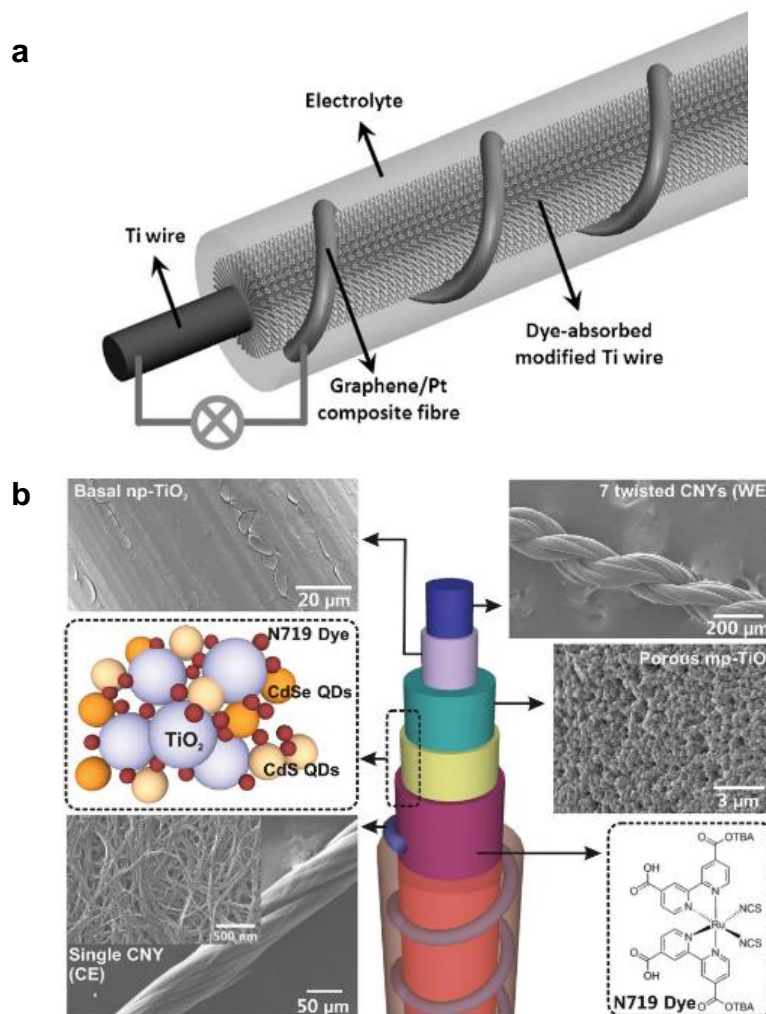


Figure 2.16 – (a) Schematic of a Ti wire metal core based DSSC wire developed by Yang *et al.* (2013). (b) Three-dimensional representation and SEM images of a carbon nanofiber core based DSSC wire realized by Yan *et al.* (2014).

DSSCs fibres with carbon-nanotube (CNT) based working electrodes and counter electrodes have been presented in the literature (Cai, Chen and Peng, 2012; Chen, Qiu, Cai, *et al.*, 2012; Velten *et al.*, 2013; Yan *et al.*, 2014), which resulted in metal free PV-fibre devices, with improved flexibility and weavability. These exhibited power densities ranging between 2 -3 % with the exception of the CdSe/CdS quantum dot modified working electrode and solid electrolyte based twisted DSSC presented by Yan *et al.*

which generated a PCE of 6.24 %. Zhang *et al.* (S. Zhang *et al.*, 2012) proposed a modified CNT based DSSC fibre by replacing the CNT counter electrode with a Pt nanoparticle adsorbed, twisted CNT film which yielded a PCE of 4.85 %. Yang *et al.* (Yang *et al.*, 2013) managed to realize a PCE of 8.45 % with a Ti/TiO₂/Pt working electrode by replacing the Pt counter electrode with a Pt nanoparticle modified graphene oxide (GO) fibre. A multi-working electrode structure with six Ti/TiO₂ working electrodes assembled around a Pt counter electrode was proposed by Liang *et al.* (Liang *et al.*, 2015). The assembly was inserted into a flexible plastic capillary tube filled with an electrolyte. This multi-working electrode structure achieved a PCE of 9.1 %. In 2017 Fu *et al.* (Fu *et al.*, 2018) reported the highest PCE record of 10 % for a DSSC type PV wire, which was created using a core-sheath twisted CNT fiber counter electrode modified with Pt. The authors used a Ti/TiO₂ working electrode as the core of the wire which was treated with a N719 (C₅₈H₈₆N₈O₈RuS₂) sensitizer dye and iodine based red-ox couple. The DSSC fibres showed >80% of its original efficiency after 2000, 90° bending cycles (Bending radius not provided). The long-term stability of the device was not reported. The researchers hand stitched the PV-fibres onto a T-shirt to demonstrate their power generation capability by connecting to a commercial pedometer.

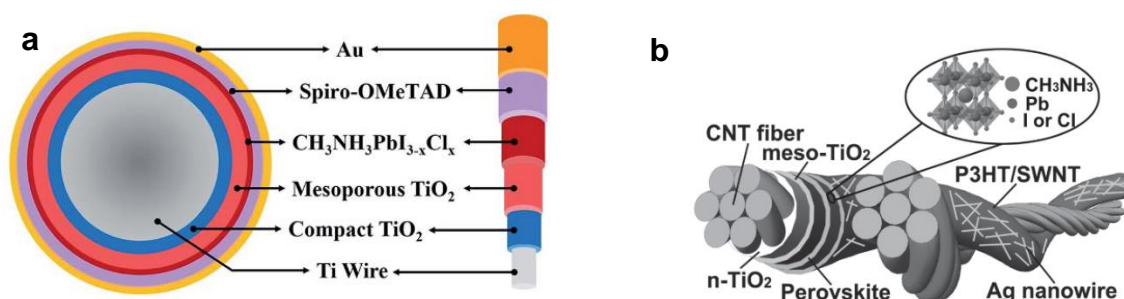


Figure 2.17 – (a) Schematic of a Ti wire metal core based perovskite PV wire developed by Qiu *et al.* (Qiu *et al.*, 2014). (b) Structure of double twisted perovskite PV yarn prepared on carbon nanotube fibre electrodes (Hu *et al.* 2016).

Perovskite based co-axial fibre PV devices (Fig 2.17) have recently emerged, addressing some of the challenges faced by DSSCs while also maintaining some of the favourable structural features of DSSC devices. The co-axial fibre perovskite cells used a similar working electrode and counter electrode configuration to the DSSCs while the dye-electrolyte combination in a DSSC was replaced by a perovskite active material, enabling an all solid-state PV-fibre. One of the first perovskite PV-fibres intended for use in fabrics

was reported by Qiu *et al.* (Qiu *et al.*, 2014). They employed a stainless-steel wire electrode deposited with a mesoporous TiO₂ layer, which was subsequently coated with CH₃NH₃PbI₃ perovskite sensitizer material. A hole transport layer was applied onto the sensitizer-coated working electrode and a CNT sheet was wrapped as the counter electrode to realize the PV-fibre. This construction managed to generate a PCE of 3.3 %. He *et al.* (2015) followed a similar approach where they replaced the TiO₂ layer with a ZnO nano-rods grown on a stainless steel wire. The resultant PV-fibre generated a PCE of 2.61 %. The PV-fibre showed a 7 % change in performance after 200 bending cycles of 30°. A double twisted perovskite yarn was developed by coating one CNT fibre bundle with TiO₂/sensitizer/hole transport layers and twisting it with another CNT fibre bundle. This PV-fibre device realized a maximum PCE of 3.03 % and was stable after 96 hours in ambient condition, and 1000 bending cycles of 30° (bending radius not provided). Hu *et al.* (Hu *et al.*, 2016) reported a fibre-shaped perovskite solar cell using an Au counter electrode in a co-axial construction which resulted in a PCE of 5.3 %. It was clear that amongst the flexible PV technologies explored for co-axial PV-fibre devices, Perovskites show the highest potential for wearable applications, due to their all-solid construction, and excellent mechanical stability; although long-term stability and superior power conversion efficiencies achieved by their planar form devices are yet to be realized.

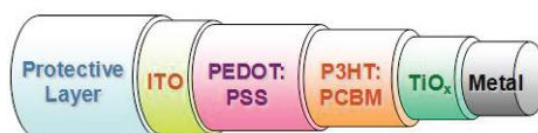


Figure 2.18 – Schematic of a typical design for a metal core based organic PV wire.

(Chuangchote, Sagawa and Yoshikawa, 2011)

Co-axial fibre PV devices have also been created using OPVs (Lee *et al.*, 2009; Chuangchote, Sagawa and Yoshikawa, 2011; Liu *et al.*, 2012) (Fig.2.18), inorganic PVs (Chen, Qiu, Kia, *et al.*, 2012; L. Zhang, Shi, Li, *et al.*, 2012) or thin-film PVs (L. Zhang, Song, *et al.*, 2012); however these have not made significant advancements in performance and have not been frequently explored recently. This may be due to their unsatisfactory flexibility, mechanical robustness, the complexity of the production process, or potentially low power conversion efficiencies (<4%) in comparison to DSSC or Perovskite metal core fibre/wire shape devices.

2.4.1.3.2 Photovoltaics using polymeric fibres with multilayered conductive and photovoltaic material coatings.

While conductive core based co-axial or twisted constructions was the most widely explored route for fibre PV devices, polymer core/substrate-based fibre photovoltaics have also been studied with the aim of achieving improved mechanical robustness and conformability during subsequent processing and use. O'Connor and co-workers (O'Connor, Pipe and Shtein, 2008) used polyimide-coated silica fiber as the core of the PV-fibre to fabricate an OPV fibre. Thin films of conductive material and organic active materials were deposited by vacuum thermal evaporation to devise a PV-fibre with a 0.5 % PCE. An OPV fibre (Toivola *et al.*, 2009) was realized on a polymethyl methacrylate (PMMA) optical fibre which did not generate notable amount of power (PCE < 0.1%). Bedeloglu *et al.* fabricated a polymer PV-fibre (Fig 2.19(a)) starting with a polypropylene (PP) fibre core, which only generated 0.021% PCE (a. Bedeloglu *et al.*, 2010). A stretchable dye-sensitized solar cell was presented by Yang *et al.* where a CNT fibre tape was helically wrapped around a rubber fibre (Fig. 2.20(b)) to be used as the elastic counter electrode (Z Yang *et al.*, 2014). Subsequently, a helical Ti/TiO₂ working electrode adsorbed with the dye-sensitizer was wrapped around the elastic counter electrode. This construction was highly conformable and was able to generate a PCE of 7.13% which was maintained during stretching.

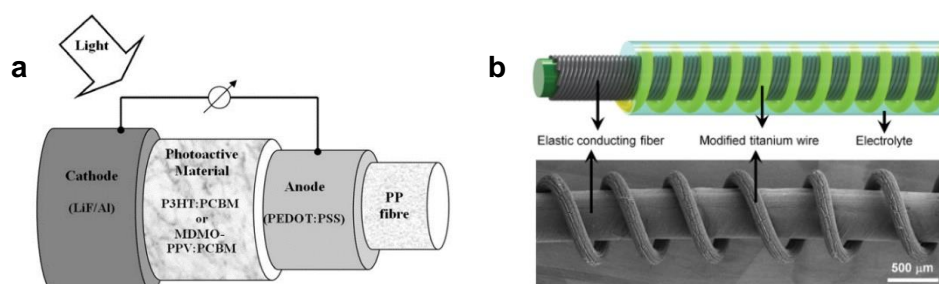


Figure 2.19 – (a) A schematic of a polypropylene fibre core based organic PV wire (a. Bedeloglu *et al.*, 2010). (b) A Schematic (top) and SEM image (bottom) of a stretchable DSSC wire prepared by wrapping CNT fibre tape around a rubber core (Yang *et al.* 2014).

There has been a wide range of work investigating fibre/wire/tape shaped PV devices transformed into planar form (e.g. a woven textile) as discussed in 2.4.1.4. The above discussed fibre-PV devices however, have been only demonstrated in fibre/wire form. Therefore, their performance in planar form (i.e. fabric form) needs further investigation

to establish their feasibility for wearable applications. For example, the feasibility of weaving these in to fabrics and mechanical robustness, aesthetics, and wash durability of these PV-fibres in fabric structures need to be examined. In principle these PV-fibre devices can be used to make fabrics that exhibit limited desirable textile characteristics (e.g. air/vapor permeability and shear deformability), but their appearance, surface texture, and flexibility appear to be significantly different from that of textile fabrics made of conventional textile yarns intended for wearable applications. Hence, it is doubtful that these PV-fibre devices could be adapted for powering wearable or e-textile devices for regular clothing.

2.4.1.4 Textile fabrics made by weaving yarns with PV-fibres.

To understand the drawbacks of coated or laminated planar PV materials is to weave PV coated wires or flexible PV tapes. Woven structures prepared using wires, fibres, yarns or tapes containing PV materials, various non-woven webs comprising PV-fibres or PV-coating, are found in literature that demonstrated flexible planar PV devices (Fig. 2.20).

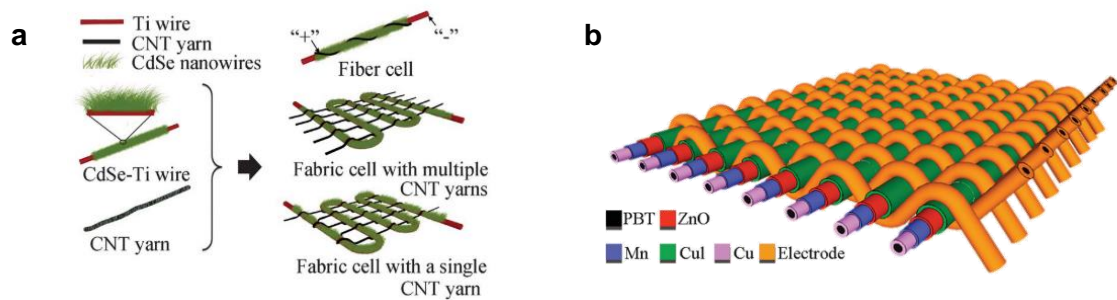


Figure 2.20 – Schematic illustrations of woven photovoltaic fabrics using (a) CdSe coated Ti wire working electrode (L. Zhang, Shi, Ji, *et al.*, 2012), and (b) co-axially coated polybutylene terephthalate (PBT) fibres (Nannan Zhang *et al.*, 2016).

These fabrics woven with PV-yarns (made using PV-fibres) or PV-narrow-tapes benefit from the inherent flexibility and conformability rendered by the interlacing of yarns or narrow-tapes in the woven structure, where the individual elements (wires, fibres or narrow-tapes) of the weave were free to undergo relative deformations due to external stresses even if the individual elements are not stretchable. A woven structure with discrete PV wires or tapes would allow the structure to permeate air and moisture, which is critical for a wearable application. Most of the woven fabrics realised fully functioning

planar PV modules by combining separate working electrode and counter electrode strands. Here the interlacing points within the woven structure provided the electrical interconnects to complete the fully functioning PV cell. Another approach for creating PV woven structures is by using fully functional PV wires or yarns with both the electrodes (working electrode and counter electrode) within the same strand similar to those discussed in 2.4.1.3.

In most cases, these woven devices did not report power densities based on total planar area of the PV wire distribution, but only based on the area covered by the PV elements (wires or narrow tapes). It is important to note that a true comparison of such woven devices can only be made with the actual fabric area-based power densities. Conversion of 1D solar elements to woven fabrics would involve significant shading due to the interlacing points, that will affect the conversion efficiency of the fabrics. However little consideration had been paid to characterise or theoretically estimate these effects in literature. Also, in these studies, any evidence of long term wash and wear durability was not forthcoming.

An early example of a woven PV fabric was reported by interlacing a CdSe coated Ti wire as a working electrode with a set of CNT yarn used as counter electrodes (L. Zhang, Shi, Ji, *et al.*, 2012). This device demonstrated how a photovoltaic planar structure can be fabricated by using interlacing points for electrical contacts. The CdSe coated wires in the fabric structure had a PCE of 1.24 %, which was lower than the same CdSe coated wire twisted with a CNT counter electrode (2.9 %). This was attributed to the comparatively low number of contact points and contact pressure between the two electrodes in the woven structure. Pan *et al.* prepared woven mesh like electrode pairs (Pan *et al.*, 2014) which were stacked together to create a DSSC fabric structure. The working electrode was woven using TiO₂ nanotube grown Ti wires which were subsequently adsorbed with the sensitizer dye. The counter electrode was made using woven CNT yarns. Stacked electrodes were sealed and injected with the electrolyte to realize a DSSC which exhibited a PCE of 3.10%. The PCE of the device showed less dependency on the incident angle in comparison to the planar devices; this behaviour is desirable for mobile applications, where the incident light angle is unpredictable. The reason for this uniformity in performance was due to the circular cross sections of the electrodes and the spacing between the adjacent electrodes in the same plane of the

fabric; this minimized the shading effect of nearby electrodes at higher incident angles. Similar to the coated or laminated PV devices, the need to fully encapsulate the device hindered the permeability and flexibility of the final product. In an effort to improve the textile appearance and feel of PV woven textiles, a few attempts to weave PV-fibre devices along with regular textile yarns have been reported in the literature (Chai *et al.*, 2016; N Zhang *et al.*, 2016; P. Liu *et al.*, 2018). Zhang *et al.* demonstrated a woven fabric solar energy harvester by interlacing all-solid-state co-axial DSSC working electrodes (weft yarns) with metal coated polymer counter electrode (warp yarns) (Nannan Zhang *et al.*, 2016). The working electrodes were prepared by coating Mn/ZnO nano-rod/sensitizer dye/hole-transfer layers onto a polybutylen terephthalate (PBT) fibre. The functioning solar cell was completed by using the warp weft interlacing points for the electrical connections between the two electrodes. A single wire-shaped solar cell unit was reported to have a PCE of 1.3 %, which is lower than some of the core-sheath type DSSC fibres discussed in previous section; however, the demonstration of the woven form energy harvesting capability using a regular tightly woven structure was a novel aspect of this work. Zhang *et al.* conducted mechanical stress analysis of the PV elements within the woven structure and studied the effect of mechanical stress on the PV performance. Further, the effect of counter electrode (warp) density and the woven pattern (plain, twill or satin) on the PV performance was analysed. The results showed that the warp densities and the weave structure which realised the highest number of interlacing points (or the contact points between the warp and weft) yielded the best PCEs. Bending tests were conducted with no significant change in performance observed after 500 cycles (Bending radius not given). Fabrics woven using the aforementioned PV-fibres and wool yarns were also presented, however the energy harvesting capability of the wool blended fabric was not investigated. The same DSSC wire structure was utilized by the team to prepare an all-solid-state textile woven device to simultaneously harvest and store solar energy (Chai *et al.*, 2016). The solar energy harvesting section of the fabric was realized by weaving together DSSC working electrode wires (weft yarns) and Cu coated polymeric counter electrode (warp yarns), in addition cotton yarns were used to fill the gaps between the electrode wires. A PCE of ~1% was reported, however it was not clear whether this was based on the fabric area or the wire area. The researchers reported that the device had a stable performance after two months of exposure to ambient conditions, and after 100 bending cycles of 120° (Bending radius

not provided). The same research team created a similar woven textile that could harvest solar and mechanical energy simultaneously (Chen *et al.*, 2016). The fabric generated a power density of $25\mu\text{W}/\text{cm}^2$ when worn by a human walking under $80\text{mW}/\text{cm}^2$ sun intensity. The solar energy harvesters used in this work were DSSC co-axial type wires identical to that used by Zhang *et al.*

Liu *et al.* reported a woven PV structure (Fig 2.21) realized by weaving OPV working electrode weft wires with counter electrodes as a warp (P. Liu *et al.*, 2018).

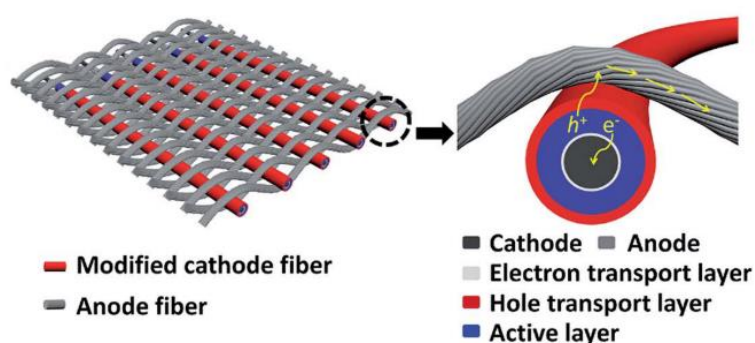


Figure 2.21 – Schematic of woven photovoltaic fabrics using metal wires coated with organic PV layers (Liu *et al.* 2018).

This successfully demonstrated the weaving of fibre shaped PV structures using industry standard weaving loom, which was a key milestone in textile PV devices. This fabric also employed the interlacing technique to achieve electrical interconnections between the working electrodes and counter electrode wires. The co-axial working electrode was prepared on a Ti wire core by coating ZnO buffer layer, PTB7:PC₇₁BM active layer, and a PEDOT: PSS hole transport layer sequentially. Ag-plated nylon was used as the counter electrode. The warp was prepared by alternating Ag-plated nylon and cotton yarns. The resultant woven fabric exhibited a PCE of 1.62% (wire form). The fabric showed a less than 15 % reduction in performance after bending up to 80° (bending radius not provided) and had no deterioration of performance after 1000 bending at 20° and 1000 twisting cycles of 180°, indicating relatively higher stability to other devices of the same type under mechanical deformations. The fabric was very similar to a regular woven fabric in terms of appearance. In summary, this study has demonstrated promising prospects for the future of woven wearable PV devices in many aspects, however the strategies to improve fabric level PCE to compete with coated/laminated

textile PV devices need to be investigated if these woven PV wires or fibres are to have practical applications. It was obvious that by improving the density of working electrodes the PCE of the fabric could be enhanced, however this would have significant implications for the conformability and softness of the fabric, which would need to be considered.

One approach of improving the PCE of woven PV textiles is by replacing PV wires with pre-fabricated PV ribbons (also referred to as tapes) as reported in some of the literature (Krebs and Hösel, 2015; Min Ju Yun *et al.*, 2015; C. Li *et al.*, 2016; Kuhlmann *et al.*, 2018). These ribbons were either complete PV devices or constituted of some of the active PV layers. PV ribbons have a larger active area, and they can cover a significantly larger proportion of the available planar surface compared to PV wires. However, PV ribbons can significantly alter the conformability and appearance of the final fabric depending on of the stiffness of a single ribbon and a number of ribbons per unit length within the fabric. Yun *et al.*, fabricated a woven PV device by inserting a DSSC type PV ribbon (M J Yun *et al.*, 2015) using a conventional weaving machinery. The active substrate of the PV ribbon was made on a perforated stainless-steel tape coated with TiO₂ nano material, which was subsequently adsorbed with sensitizer dye. This ribbon device exhibited a PCE of 2.63 %. Krebs and Hösel (2015) employed pre-fabricated OPV tapes (~2 cm wide) to weave a large area (25 × 25 cm²) woven solar cell textile (Fig 2.23(a)). The solar tapes woven into the structure consisted of 16 serially connected organic solar cells with a PCE of 1%.

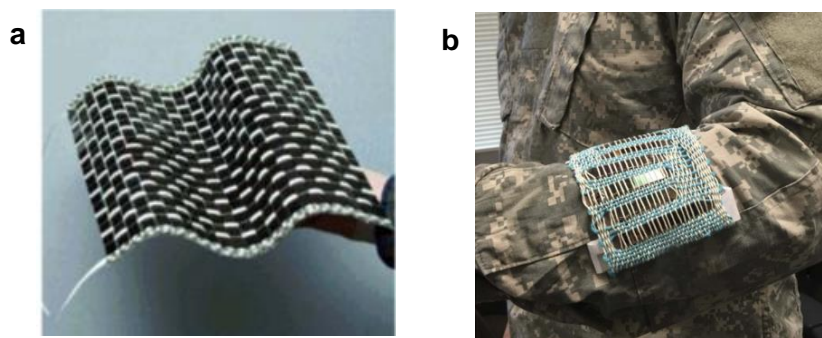


Figure 2.23 – Images of photovoltaic woven structures prepared using (a) organic photovoltaic ribbons (Krebs and Hösel, 2015) and (b) perovskite photovoltaic and supercapacitor composite tapes (C. Li *et al.*, 2016).

A ribbon shaped hybrid device which can synchronously harvest and store solar energy (Fig. 2.23(b)) was reported by C. Li *et al.* (2016). This could be inserted into a woven structure to demonstrate a wearable energy device. The ribbon was prepared by stacking a perovskite flexible PV film onto a thin film electrochemical supercapacitor device. The top electrode of the supercapacitor also acted as the counter electrode of the PV device. The perovskite PV device generated an impressive 10.41 % PCE when the hybrid device was illuminated under one sun intensity. The supercapacitor held an energy density of 4.14 Jcm^{-3} and a power density of 243 mWcm^{-3} . The demonstrated woven device did not resemble a textile material due to larger widths ($>1\text{cm}$) of tapes used in the work.

A textile based solar energy harvesting and storage system was created by weaving pre-fabricated 44 mm-wide CIGS thin-film PV cells and attaching commercially available flexible batteries (solid-state lithium batteries having a thickness of 0.4 mm, with a capacity of 235 mAh at a voltage of 3.75 V) (Kuhlmann *et al.*, 2018). This system could generate a high PCE, however this design was similar to the first-generation solar fabric concepts where solar cells were directly attached to the fabric and cannot be considered suitable for a wearable application due to the lack of flexibility and normalcy. Krebs and Hösel have argued that woven PV tapes are one of the most technically feasible and commercially viable strategies for incorporating PV functionality onto textiles (Krebs and Hösel, 2015), however it is doubtful whether such devices are suitable for the use in future wearable devices intended for day-to-day use, mainly due their lack of normalcy.

Fabrics woven with PV coated wires or flexible PV tapes showed improvements in their shear behaviour and breathability, however, they still looked and felt significantly different to normal textile fabrics. In addition, the electrical interconnections achieved by the interlacing points may not be reliable during the deformations undergone by the resultant garments, and these interconnections could deteriorate during washing and wearing.

2.4.1.5 Non-woven PV structures

Non-woven textile structures such as electro spun nano-fibre webs or fibre membranes (electro spun or wet-laid) were also investigated as a substrate for textile PV devices by few research groups (Sundarrajan *et al.*, 2010; Sun *et al.*, 2015; Juhász Junger *et al.*, 2018). Sundarrajan *et al.* (2010) managed to realise an electrospun polymeric PV web by co-

electrospinning a two component polymer mixture to form a co-sheath structure, where P3HT/PCBM was the core and polyvinyl pyrrolidone (PVP) was the shell. This technique was employed due to the difficulty of electrospinning of pure conjugate polymers. The shell material was subsequently dissolved to realize the P3HT/PCBM, which was used as the active layer of a PV web, sandwiched between transparent conductive electrode films: A notable PCE was not reported for the device. An efficient dye-sensitized solar cell based on a PET membrane (as the medium for liquid electrolyte) was developed by Sun *et al.*, (2015) which reported a PCE of 10.2 %. The PET membrane was prepared by wet laying PET short staple fibres and binding them using a water based binder. The photoanode and counterelectrodes used were monolithic and non-conformable, hence the device was not desirable for a wearable application. A DSSC PV device with textile-based counter electrodes coated by a conducting polymer and working electrodes built on TiO₂ coated Fluorinated tin oxide (FTO) glass dyed with a natural dye were investigated by Junger *et al.* (2018) which showed conformable properties, however the PCE achieved was not noteworthy.

2.4.1.6 Mechanically linked rigid or flexible solar cell arrays

As an effort to make inorganic semiconductor PV materials more attractive for flexible applications, rigid inorganic cells can be mechanically and electrically linked together with flexible materials to create quasi-flexible structures. A number of such embodiments in the form of solar jackets or suites (Haugen 1989; Anon 1996; Jaynes 2007; Orandi 2009;), windable, rollable or retractable solar modules (Hanak *et al.*, 1987; Ma, 2011; Oppizzi, 2014), awning solar modules (Heidenreich 2007; Lambey 2008; Nocito *et al.* 2012), and flexible interconnected solar cell networks based on fabrics (Escoffery 1966; Luch 2009; Forster & Zimmermann 2011; Daniel 2011; Lerner *et al.* 2015; Chen *et al.* 2015; Nance *et al.* 2016) have been proposed in several patents. The products and processes disclosed in these patents appear to be of limited use for practical wearable systems, due to inadequate level of flexibility, lack of shear behaviour, and unsuitability for washing. In addition, the appearance rendered by these fabrics attached devices were not desirable for the use on regular clothing.

Sandia National Laboratories have been working with micro-scale inorganic photovoltaic cells for concentrator photovoltaic (CPV) applications, which were also explored for flexible solar arrays (Cruz-Campa *et al.*, 2011). This micro-enabled

photovoltaic (MEPV) technology has been demonstrated in flexible mouldable concentrator PV (CPV) arrays where the cells are distributed on a concentrator lenses array (Gu *et al.*, 2015), as well as flexible arrays of closely packed cell arrays (Sandia National Laboratories, 2017) mounted on a flexible substrate (Fig. 2.24(a)). The bespoke microscale PV cells have hexagonal shape with back contacts and typically have a thickness of 14 μm and a width from 250 – 500 μm (Fig. 2.24(b)). To minimize the edge recombination losses, the cell boundaries were heavily doped. With the optimized cell design they managed to achieve a PCE of 14.9 %. One advantage of using such micro-scale PV devices for CPV applications is the ability to dissipate heat efficiently which improves the PCE. This work using miniaturize hexagonal solar cells provides evidence of the potential of employing miniaturized PV cells for applications requiring flexibility. Nevertheless, the use of similar miniature solar cells networked and deployed in an aesthetically pleasing and mechanically durable way for wearable applications discussed in this thesis is not reported to date.

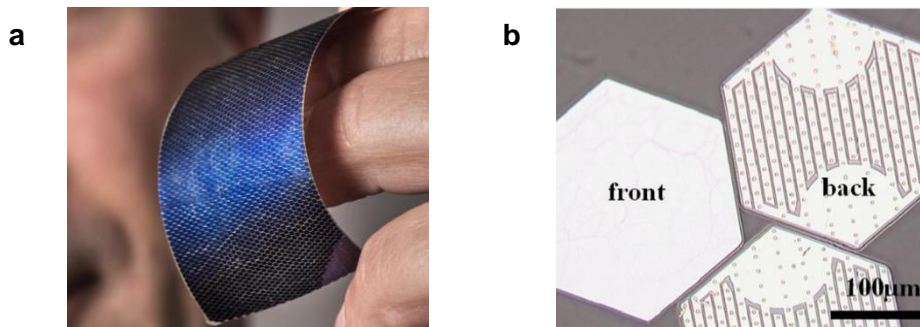


Figure 2.24 – (a) An image of the prototype micro-solar panel developed using micro-enabled photovoltaic technology (MEPV) (Sandia National Laboratories, 2017). (b) Microscopic image of micro-structured PV cells developed by Sandia Laboratories (Cruz-Campa *et al.*, 2011).

It is evident that there is a gap in the knowledge in creating a truly wearable and washable solar energy harvesting system. Hence, a need exists to explore novel approaches in delivering a system that addresses the above-mentioned challenges in order to deliver a viable wearable photovoltaic energy harvesting system for powering mobile electronics, wearable devices, or electronic textiles.

2.5 Strategies for integrating electronic device within textile fabrics in the form of yarns, threads or tapes

A novel approach to create fabrics which can harvest solar energy worth exploring is to incorporate plurality of prefabricated discrete miniature solar cells at a yarn level. The appearance, conformability and mechanical robustness of such fabrics will depend on the method of integration and size of the solar cells. Also, the integration method shall not substantially impede the energy harvesting capability. There have been a number of strategies reported in prior art that aimed to integrate electronic components into yarns or tapes, to be converted to fabrics. (Leonard 2004; Dias & Fernando 2006, Hill et al. 2009; Brun *et al.*, 2009;; Brun et al. 2011; Speich 2011; Brun, Leonard 2013, Vicard, et al. 2014; Brun, Lancon, et al. 2014; Newby & Pedley 2017;). In 2005 Dias and Fernando in their patent disclosed an electronic yarn where an operative device was confined within the fibres of a yarn and the device was then protected using a polymer micro-pod. Staufert (2008) proposed a filamentous structure integrated with electronic components that has textile characteristics. This structure has an electronic filament that consists of conductive wires and small electronic components, along with an additional element for mechanically stabilizing the structure. A textile sheath was wound around the electronic filament, however, a protection mechanism suggested by Dias and Fernando for the integrated devices from external mechanical stresses and chemical agents were not provided. Both these inventions provided a solution to protect the yarn integrated device, however the method of creating electrical connections to the device was not disclosed in detail. The device embedded yarn was intended to be converted to a knitted or a woven fabric. Leonard (2004, 2013) proposed a textile thread or fiber that had electronic elements embedded or encapsulated to create a fabric. The textile thread or fiber comprised of elements interconnected to form a signal processing system. The structure and the details of the architecture of the textile thread or how the individual elements would be electrically and mechanically interconnected within the thread to deliver a mechanically robust system was not presented. A transponder thread that can be integrated with a transponder chip along with an antenna inside of a yarn was proposed by Speich (2011) but also lacked detailed insight into the construction of the thread. Hill *et al.* 2009 disclosed an approach where electronic chips were integrated onto electrically insulated weavable flexible tapes with conductive tracks on them. A woven

structure made using these tapes was also proposed. Zysset *et al.*, (2010) also demonstrated a similar tape-like device integrated within woven structures, where the device was used as weft yarn. A tape could comprise multiple of electronic devices attached along the longitudinal axis (i.e. the length of the tape) which may or may not be electrically interconnected. The primary means of electrical interconnections between devices were the conductive threads used for the warp yarns. These tapes were also a potential platform for integrating miniature solar cells however, the appearance and softness of resultant fabric may not have been best suited for the intended application. Brun *et al.* (2009, 2011) described the assembly of a microelectronic chip onto a pair of conductive wires using a method referred to as 'Diabolo'. The chip was designed to have grooves on the sides close to its contact pads to accommodate the conductive wires. The electrical connection could be secured either after positioning the wire inside of the groove using soldering or by mechanically crimping the groove. Brun, Lancon, *et al.* (2014) extended this concept to prepare a sheathed yarn, with the wire attached chip inserted at the core of the yarn, however a means of providing a protective encapsulation to the chip was not elaborated. A printed yarn system that has a core-sheath structure was presented by Newby & Pedley (2017). Here, an electronic circuitry-incorporated linear substrate was used as the core and the sheath comprised fibres. The core was prepared by printing the electronic circuitry on a tape and attaching electronic component onto the circuitry before concealing (encapsulating) it within a covering material which is typically a polymer resin. While this invention has some structural features similar to the filament device presented by Dias & Fernando (such as the use of a resin to encapsulate the electronic components and use of fibres to surround the core), the printed linear circuitry within the core of the yarn which has the form of a thick tape, may significantly stiffen the final yarn. Rein *et al.* (Rein *et al.*, 2018) realized a diode fibre by drawing a multilayered preform comprising of two tungsten wires, multiple diode chips, and additional polymeric layers which were consolidated in a heated hydraulic press. The electrical interconnections between the diodes and the tungsten wires were physically pressed contacts (instead of soldering or using crimped fixtures, the contact is maintained by sandwiching the wires and diodes between the polymeric layers during the pressing process), therefore the long term stability of the interconnects between the devices and wires need to be investigated.

The robustness of the electrical conductive pathways and interconnects is a critical factor in determining the practicality and utility of a E-textile system for day-to-day applications in addition to the all-important flexibility and ability to conform to 3D contours. The electrical properties (electrical resistance, frequency response, crosstalk) required are often dictated by the application and the mechanical properties (tensile strength, fatigue resistance, abrasion resistance, elastic modulus) are equally important for most applications (Agcayazi *et al.*, 2018). For example for signal transmission (e.g. bio-potential measurements) applications low conductivity is acceptable however for power transmission (e.g. heating and lighting) higher conductivity levels are needed. In literature, various materials and methods have been proposed and studies on the conductive pathways and interconnection methods have often been discussed as a key theme.

Conductive pathways used for E-textiles typically have the form of fibres, yarns, wires or printed lines made of various substrates such as inherently conducting polymers (Grancarić *et al.*, 2017), metals (Tseghai *et al.*, 2020), polymer-metal composites (Chatterjee, Tabor and Ghosh, 2019), conducting polymer composites and metal coated polymers (Ali *et al.*, 2019). Copper is often the preferred choice in terms of conductivity and cost effectiveness. However the use of metals as part of textiles is limited by their relatively high stiffness and low extension to failure compared to fiber-forming polymers. To minimize the stiffness, metal coated or metal composite polymeric fibres are also considered, however there is a compromise of conductivity. Conducting polymers and composites are advantageous due to their tunable electrical conductivity, ease of processing and cost-effectiveness. However, they have poor temperature and environmental (moisture and oxygen) stability and are significantly lower in conductivity compared to metals (Schwarz and Van Langenhove, 2013).

Interconnects are often one of the key factors determining the practicality of a E-textiles systems. Interconnections can take the form of soldered or welded joints (Dias and Ratnayake, 2015; Koshi, Nomura and Yoshida, 2020; Micus, Haupt and Gresser, 2020), mechanical crimp or grip connectors and conductive adhesives. E-textile systems may comprise miniature semiconductor devices typically made of silicon which are stiff and brittle. When joining the semiconductor devices to a relatively flexible conductive pathways, the mechanical properties beside the interconnection point remain

significantly different, exposing the interconnection point to high mechanical stress. While having good electrical conductance the material employed for the interconnection point need to have the correct balance of adherence to both the conductive pathway as well as the terminals of the semiconductor device, to achieve robust mechanical joint. Therefore selection of the right material and technique for the interconnection point is critical for the mechanical and electrical robustness of the e-textile system. The below table compares different interconnection methods as summarized by Agcayazi *et al.*

Table. 2.3 – Comparison of different interconnection methods employed for E-textiles. (Agcayazi *et al.*, 2018)

Interconnection method	Structure	Advantages	Drawbacks
Welding	Melting both metals to make a physical connection	- High conductivity - Strong physical connection	Materials need to withstand high temperatures - Connection is not flexible
Soldering	Introducing a low temperature melt material in between to adhere the two surfaces for an electrical connection	- High conductivity - Strong physical connection - Low melt solders are available	Materials need to withstand high temperatures Connection is not flexible
Relaxed flexible grip	- Looping conductive fiber through a metallic object - Wrapping metallic wires through zigzag sewing	Simplicity and flexibility	Connection quality varies with motion, heat, moisture
Crimping	Crimping the textile using a metallic object	Robust physical and electrical connection	Stiffness
Conductive adhesives	Curable resin doped with conductive particles	Good conductivity and flexibility	deterioration due to humidity, temperature variations

An electronically functional yarn (Dias and Rathnayake, 2016), which has similarities to electronic yarn introduced in 2005 by Dias & Fernando, details a structure that integrate electronic components within the core of textile yarns. These yarns were fabricated by connecting electronic devices onto fine copper wires before encapsulating them inside of polymeric resin micro-pods that hermetically seal the connected devices with the wires extending along the axis of the yarn; a textile fibre sheath surrounding the wires and the micro-pods gives textile features to the completed yarn. The use of copper wires

enable integration of devices requiring power transmission, while interconnection using soldering creates an electrically and mechanically robust connection between the wire and the device. The resin micro-pod covers the solder-joint and creates an area with graduated stiffness between the copper wire and the solder joint, which reduces the accumulation of bending fatigue near the solder joint thereby improving mechanical robustness. These electronic yarns (E-yarns) can be readily integrated into a textile structure either by weaving (interlacing textile yarns) or knitting (inter-looping textile yarns), that is mechanically robust and wash durable. The viability of the E-yarn technology to integrate electronic devices within textiles was proven for sensing devices such as thermistors (Hughes-Riley *et al.*, 2017; Lugoda *et al.*, 2018), acoustic sensors (Hughes-Riley and Dias, 2018) in addition to lighting devices such as LEDs (Hardy *et al.*, 2018).

Whilst some of these methods detailed in the literature could be potential candidates for integrating PV devices within a textile structure in the form of a yarn, the selection criterion should focus on not only the wearability and durability aspects, but also the power conversion efficiency, which is governed by the intensity of light received by the photoactive surface of the solar cell.

2.6 . Discussion

In this chapter the state-of-the-art of textile embedded energy harvesting technologies presented in literature was studied with an in-depth review on various methods disclosing textile integrated and textile based solar energy harvesting devices, mainly from a wearability perspective. While the energy harvesting capability remains important, wearability is decisive for wider adoption of these technologies in regular clothing. In general, the chemistry and micro/nano structure of the materials are crucial for optimizing the photovoltaic performance. In most of the literature, flexibility is considered the prime requirement for wearability, however in reality it is often a combination of many facets such as softness, three-dimensional conformability, normal appearance, air/moisture permeability and wash durability. There exists a gap in knowledge on how these features can be achieved, while maintaining satisfactory levels of power conversion efficiency. Retaining the hierarchical structure present in conventional textile fabrics (i.e. fabric made of yarns that are prepared using plurality of

fibres) is of paramount importance in achieving these desirable features. This research aims to realise a solar energy harvesting fabric that preserves the hierarchical structure by combining textile yarns created by embedding discrete miniature photovoltaic cells within a fibrous structure. Amongst several methods that reported yarns/tapes integrated with electronic devices E-yarn technology pioneered by Dias and co-workers is considered a viable candidate to achieve this. However, the nature and effects of the interferences of sunlight with fibrous structure and encapsulation in the E-yarn structure has not been previously investigated, which is a gap in in knowledge.

Chapter 3

Materials and Methods

3.1 Introduction

This chapter details the methods and procedures followed, and materials used, during the research to fabricate and characterize solar energy harvesting electronic yarns (solar-E-yarns). The methods include step-by-step details of the production process and the equipment and materials used for soldering photocells (here the term ‘photocell’ refers to both solar cells and photodiodes used in the research), encapsulating them inside of resin micro-pods, and covering them within textile fibres to realize the final solar-E-yarns. The chapter also cover the procedures and instruments employed to simulate test conditions and conduct electrical measurements of the photoactive devices during their production process and after converting into fabrics. Some of the contents in this chapter has been included in a journal article by the author (Satharasinghe, Hughes-Riley and Dias, 2018). The methods and materials detailed in this chapter apply to the experiments mentioned throughout this thesis; specific or unique experiments will be detailed in their relevant chapters. Procedures for the fit-for-purpose testing and preparation of E-yarn embedded fabrics will be detailed in Chapter 6 and Chapter 7 respectively.

The E-yarn technology has previously been explored for embedding radio-frequency identification (RFID) devices (Rathnayake, 2015), light emitting diodes (LEDs)(Hardy *et al.*, 2018) and various types of sensors (Hughes-Riley *et al.*, 2017) within the core of textile yarns has been reported previously. This work presents a fundamental shift in how this technology is employed where photoactive devices that respond to light are embedded. The intensity and spectral distribution of light transmitted into the photocell used to embedded in the core of the E-yarn determined photovoltaic output of the yarn. The components in the E-yarn would significantly interfere with the incident light. Therefore, these interferences need to be carefully characterized and understood, to design a solar-E-yarn that generates an optimized and reliable photovoltaic output.

A typical E-yarn production process use standard surface mount device (SMD) type components with the solder pads on the same face of the component that can be soldered onto copper wires; the photodiodes used at the early stages of this research consisted of two solder pads. The miniature photovoltaic cells that were commercially available for use in this work brought new process challenges compared to other E-yarn developed with SMDs. In fact, the solar cells required two parallel copper wires to be soldered onto solder pads which were on front and back sides of the cell. Therefore, several

modifications to the original E-yarn architecture and fabrication process were introduced that are explained in this chapter. In aid of this, prior to initiating the sample preparation using solar cells, the reflow soldering process used in previous E-yarn works was revisited. The aim of this was to gain a better understanding into how the soldering stage of the E-yarn production process could be modified to achieve reliable solder joints with minimum effect on the functionality of the solar cells. Further, a bespoke apparatus was designed and built to achieve precise positioning of the soldered device inside of the resin micro-pod. This not only allowed for consistent solar-E-yarns to be produced but also allowed for the effects of the positioning of the photocell inside the micro-pod to be studied. An additional process of impregnating the solar-E-yarn surface was introduced to enhance the intensity of light received by the photoactive device.

For characterization, an optical test rig was built at the initial stages of the research project to characterize the opto-electronic performance of E-yarns embedded with photoactive devices in comparison to performance of the maiden device (i.e. photodiodes and solar cells before embedding within the yarns). Upon completing the proof-of-concept studies, a standardized solar simulator was employed as the light source for the characterization. The solar simulator provided a light source which allowed the devices to be compared against an absolute measurement scale and prior art. Mechanisms to conduct measurements under varying incident light angles were also devised was use with the optical test rig and the solar simulator.

3.2 E-yarn fabrication process

The basic steps of fabricating photocell embedded yarns are shown in Fig. 3.1. Here the term photocell is used to represent both photodiodes and solar cells. Unless specifically mentioned, the yarn fabrication steps described are applicable for both the photocell types.

The first step of the process was to solder the photocells onto fine copper wires. The soldered device and the solder joints were then encapsulated within a protective resin micro-pod. The micro-pod with soldered photocell along with the copper wires were then sheathed with textile fibres to give the E-yarn a textile-feel and appearance. Optionally, the fibres in the photoactive side of the E-yarn was impregnated with a polymeric resin.

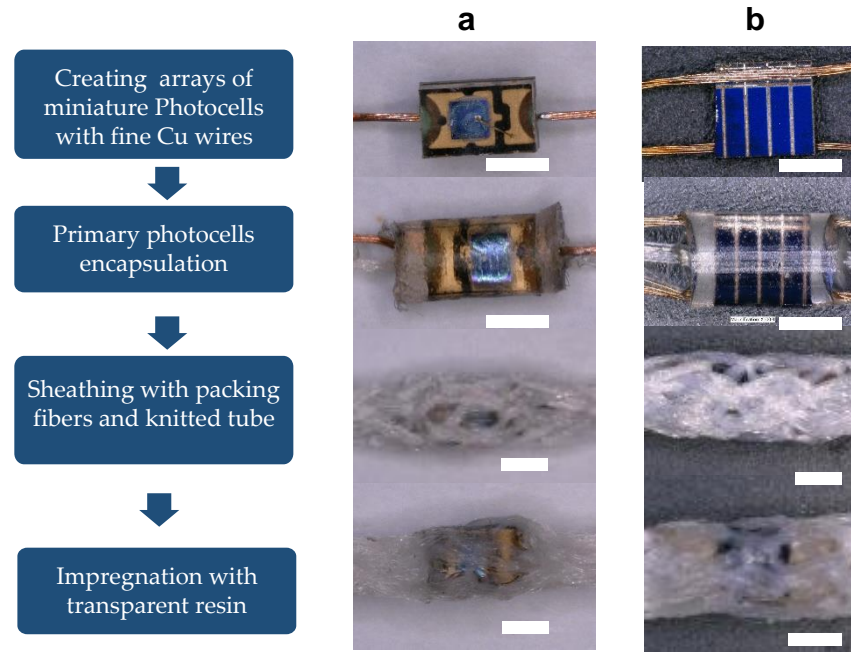


Figure 3.1 - Fabrication process of photocell embedded yarn. (a) Microscopic images of photodiode yarn fabrication at different stages. (b) Microscopic images of solar cell yarns after each step in the fabrication process. (Scalebar indicate 1mm)

3.2.1 Photodiodes and solar cells

In the initial phase of the research, a proof-of-concept for the photocell embedded yarn was developed. In addition, an in-depth investigation into the effects of different components of the yarn on the opto-electronic behavior of the photocell was conducted. Photodiodes were employed as a cost effective and readily available alternative for solar cells to conduct initial testing and demonstrate a proof-of-concept photocell embedded yarn.

Two types of commercial surface mounted device (SMD) miniature silicon P-I-N type photodiodes (PDs) were selected for the initial study and are shown in Fig. 3.2 (TEMD7000x1 and VEMD6060x1 from Vishay Intertechnology Inc., Malvern, PA, USA, the basic specifications are given in Table 3.1 and complete datasheets provided in Annex 2). These photodiodes were responsive to visible and near infra-red regions of the electromagnetic spectrum, which was similar to the spectral distribution of the sunlight.

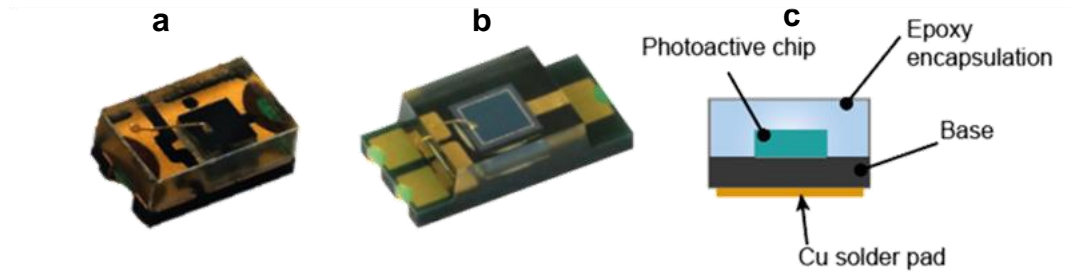


Figure 3.2 – Two photodiode (PD) types used for the first phase of the research. Image of (a) TEMD 7000x01 and (b) VEMD 6060x01. (c) Front view schematic of the PDs. Images are not to scale (Courtesy – Vishay Intertechnology)

The availability of commercially available very small-scale solar cells is limited. Several high efficiency multi-junction solar cell manufacturers were contacted for sourcing miniature solar cells. There existed a challenge in sourcing small batches of cells due to high minimum order quantities defined by the companies. As an alternative, miniature silicon solar cells, cut to required shape and dimensions from a standard crystalline solar cell were eventually sourced from Solar Capture Technologies (Photovoltaic Technology Centre, Blyth, United Kingdom). The specifications of the original large area cells of this type indicated a power conversion efficiency (PCE) level of approximately 18 %. (see the basic specifications in Table 3.1 and test report provided by the supplier in the Annex 3).

Table 3.1 - Specifications of the different photodiode and solar cell types used during this study.

Device Type	Dimensions (mm)	Photoactive Area (mm ²)	Performance
PIN Si Photodiode SMD – Visible and near infrared TEMD7000X01 - Vishay® Intertechnology	2 x 1.25 x .85	0.23	$V_{oc}=350\text{mA}$, $I_{sc}=3\mu\text{A}$ Under $E_e = 1 \text{ mW/cm}^2$, $\lambda = 950 \text{ nm}$
PIN Si Photodiode SMD – Visible and near infrared VEMD6060X01– Vishay® Intertechnology	2 x 4 x 1.05	0.85	$V_{oc}=360\text{mA}$, $I_{sc}=5\mu\text{A}$ Under $E_e = 1 \text{ mW/cm}^2$, $\lambda = 950 \text{ nm}$
crystalline-Si (laser grooved buried contact)	1.6 x 1.6	2	PCE ~ 18% under AM 1.5 -1 sun for the large size cell from which the miniature cells are cut.
	1.6 x 3	4	
	3.2 x 3	8	

These solar cells were of the laser grooved buried contact (LGBC) type where the front side of the cells surface contained an array of parallel Cu bus bars working as the negative electrode (cathode) as shown in Fig. 3.3(a). Each bus bar is connected to the solder pads positioned at one side of the front face of the cell. The positive electrode (anode) was spread throughout the backside of the solar cell (Fig. 3.3(b)).

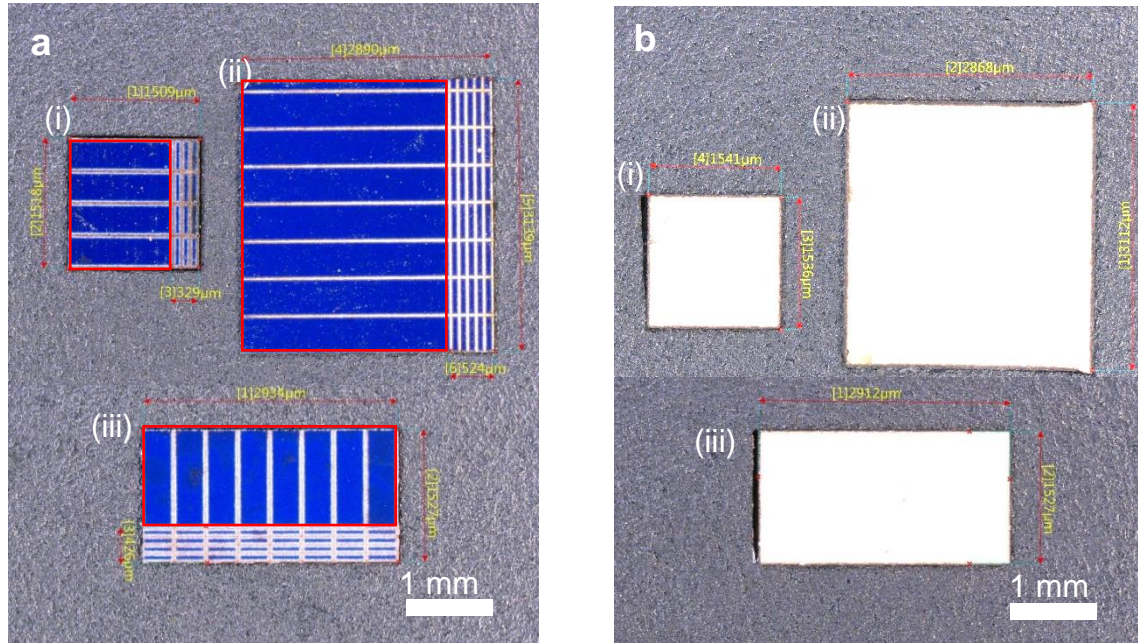


Figure 3.3 – Optical microscopy images of the (a) front and (b) back sides of (i) 1.5 × 1.5 mm, (ii) 3.2 × 3 mm and, (iii) 1.5 × 3 mm solar cells employed in this research. The useable active area of the cell is indicated by the red rectangles.

The first batch of solar cells sourced had dimensions of 1.5 mm × 1.5 mm and 3.2 × 3 mm (Fig. 3.3(a, b)). These dimensions were selected to ensure that the cells width was sufficiently small to be accommodated within the cylinders of the knit braiding machines available the Advanced Textiles Research Group (ATRg) to cover the resin micro-pod. Eventually, the trade-off between the cell area and the fineness of resultant yarn is largely dependent on the end-use. Prior to conducting experiments 30 samples from each cell type were observed under the digital microscope (VHX-5000-Keyence (UK) Limited, Milton Keynes, United Kingdom) to evaluate variations in their size and photoactive area. Cells with a 1.5 mm width and a 3 mm length were subsequent sourced after the initial studies to increase the total active area of solar cell embedded yarns fabricated for preparing woven fabric demonstrators. This also reduced the number of cells needed to generate required amount of power; this would reduce the number of potential points

of failure. Table 3.2 details the variations in active cell area of the three types of cells. The measured values of the full data set are given in Appendix 2.

Table 3.2 – Measured variation in the active area of three solar cell sizes used in the research. Batches of 30 cells were selected from each cell size for this analysis.

	Useable active area (mm ²)		
Cell Type	1.5 mm × 1.5 mm	1.5 mm × 3 mm	3 mm × 3.2 mm
Average	1.756	3.486	7.652
Standard deviation (SD)	0.1066	0.315	0.364
Coefficient of variation (CV)	6.04%	9.03%	4.75%

The results show that the maximum variation in cell size for the tested cells were observed for 1.5 mm × 3 mm cell type. The variation was less than 10%, which was considered acceptable, for further experimentation. No clear relationship between the cell size and the level of size variation was identifiable based on the measured results.

3.2.2 Soldering surface mount devices (SMD) onto fine copper wires

Soldering electronic components onto printed circuit boards (PCBs) using a reflow oven is an established soldering technique in the electronics industry and can be employed to solder circuit boards comprising of many components (Willis, 2003). During a typical reflow soldering process the PCB, solder paste, and solder pads are heated in a controlled manner according to a reflow soldering profile, which has an initial heat ramping phase, preheating phase, ramp to peak phase, reflow phase and a cooling phase as shown in Fig 3.4(a). For situations where individual components need to be soldered or repaired discretely without heating the complete PCB, reflow ovens cannot be used. In such situations IR spot reflow soldering is widely used (Anguiano *et al.*, 2005). Here a beam of IR radiation is directly focused onto the component and only the required component and the PCB footprint around the component is heated according to a reflow profile similar to that of the reflow oven. The E-yarn technology employs this technique for soldering miniature SMDs onto fine copper wires (Rathnayake, 2015) and this technique is also used in this work. Previously, Rathnayake (2015) investigated the use of IR spot reflow soldering to solder SMD type LEDs and resistors (0402 and 0201 sizes)

onto fine eight strand copper wires (single strand diameter 55 μ m). The device was placed with the solder pads facing upwards onto a metal plate covered with black adhesive tape (soldering base), with the Cu wire positioned on top of the two solder pads of the device. A predetermined volume of solder paste was dispensed onto the solder pad areas and exposed to the IR beam using an IR spot reflow soldering station. The IR beam is circular in shape, of which the aperture size and vertical position can be adjusted to achieve a focused IR spot with required diameter. It was identified that a conventional reflow soldering profile was not suitable for this scenario due to the direct application of heat; in conventional printed circuit manufacture the heat is transferred to the solder pads by the circuit board. Several modifications to the reflow profile was trialled and a profile with only two phases (with steep temperature ramping and cooling) was found to be successful (Fig 3.4(b)).



Figure 3.4 - Screen shots of (a) a typical soldering profile used reflow soldering surface mount devices (SMDs) onto printed circuit boards (PCBs). (b) The modified profile for soldering SMD components on to fine copper wires (Rathnayake, 2015).

However, insights on the critical parameters affecting this unique soldering process was not presented in this study. It was identified that to adapt this reflow soldering process for more complex device configurations, similar to the photovoltaic cells used in this study, a better understanding of these critical parameters needs to be gained. Therefore, preliminary tests were conducted on the effects of IR beam parameters (beam diameter, level of beam focus) and the materials used in the process (SMD device, copper wires, copper wires and solder paste). Although a complete comprehension of the effects of the process and material parameters was not within the scope of this work, the general understanding gained from these tests were instrumental in achieving optimized soldering parameters for soldering various types of miniature electronic components developed using the E-yarn technology. A good quality solder joint can be confirmed by a smooth, clean and shiny solder joint and this was verified by optical microscopic images. Temperature variation within the IR heated spot for different spot sizes were observed. The IR beam was directed to a ceramic tile coated with black matt ceramic paint. A k-type thermocouple (Z2-K-1.0-1/0.2-MP-ANSI, Labfacility Ltd, West Sussex, United Kingdom) connected to a temperature logger (RDXL65D Six Channel Handheld Temperature Data Logger, Omega Engineering Limited, Manchester, United Kingdom).

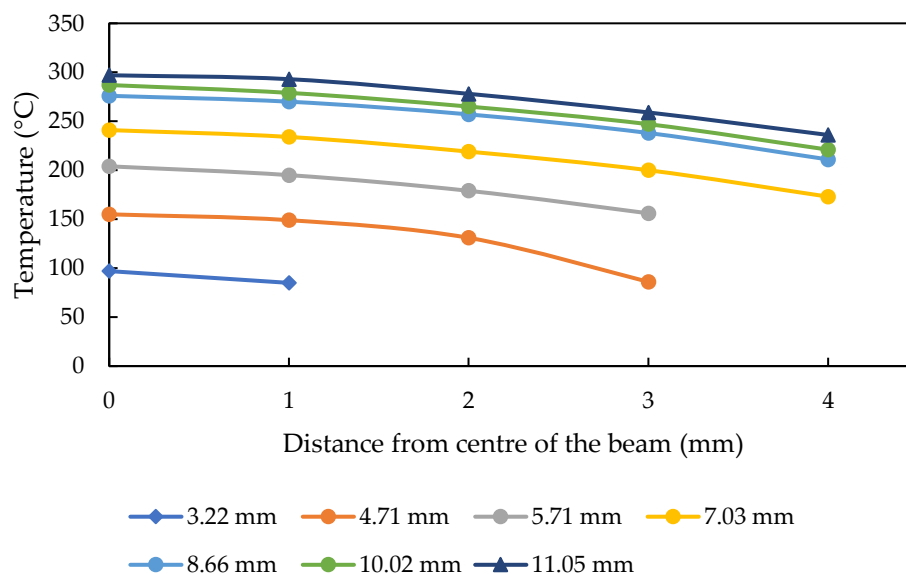


Table 3.5 –Measured temperature for different infrared beam diameters at different distances from the centre of the beam. The measurement was conducted on a matt black ceramic tile surface after one-minute heating at 100% infrared beam power.

The IR spot size was changed by adjusting the aperture size of the IR lamp. The tip of the thermocouple was positioned on ceramic tile at the required distance from the centre

of the spot. The tests revealed that there is a temperature gradient from centre to the perimeter of the IR heated spot, and that the temperature of the heated spot increases with the diameter of the IR beam (Fig. 3.5).

In addition, it was noted that the maximum rate of heating was achieved when the IR beam was in focus with the heated surfaces (i.e. the solder pads and solder paste) which was expected. The rate of heating was also dependent on several other parameters such as the solder pad area of the SMD, total cross-sectional area of the copper wires used, colour and surface roughness (which relates to the thermal absorption coefficient of the material) of the SMD and the soldering base (i.e. the SMD and the platform). It was desirable to have a soldering base with low thermal conductivity and high thermal absorptivity to maintain a high-temperature surrounding in the soldering region. Based on these preliminary tests a soldering base made of black pigmented silicone rubber was selected and the reflow soldering profile was fine-tuned based on the size of the SMD and total copper wire thickness. Silicone has a lower thermal conductivity compared to metals and ceramics (Clemens, 2001). By black pigmentation the thermal absorptivity of silicone can be improved (Tesfamichael *et al.*, 2001). A solder joint with a smooth and shiny surface was considered a good quality solder joint. Complete soldering occurs when all the metal particles in the solder-paste melt and form a non-porous homogeneous solid, resulting a smooth surface that reflect light evenly. To assess the quality of the solder joint optical microscopy was employed.

In summary, it was important to position the device at the centre of the IR spot, with the spot focused at the solder pads to achieve the most efficient soldering process. Larger solder spots resulted in steeper heat ramping. A material with a darker and rougher surface (higher thermal absorption) and low thermal conductivity facilitated the efficient heating of the solder paste. The rate of heating was slower when the total thickness of the Cu wires used was higher (this resulted in higher rates of heat loss from the solder joint via Cu wires).

3.2.3 Making electrical interconnects between the solder-pads and Cu wires for photodiodes

A photodiode (PD) was placed on a flexible base made of black pigmented silicone (Transil 40-1 silicone and 10% black silicone pigment, Mouldlife, Suffolk, United Kingdom) with the two solder pads facing upward towards the IR source (direct

heating) (Fig. 3.6(a)). As previously mentioned, black pigmented silicone facilitated an efficient soldering process, by retaining the thermal energy transmitted by the IR beam around the device.

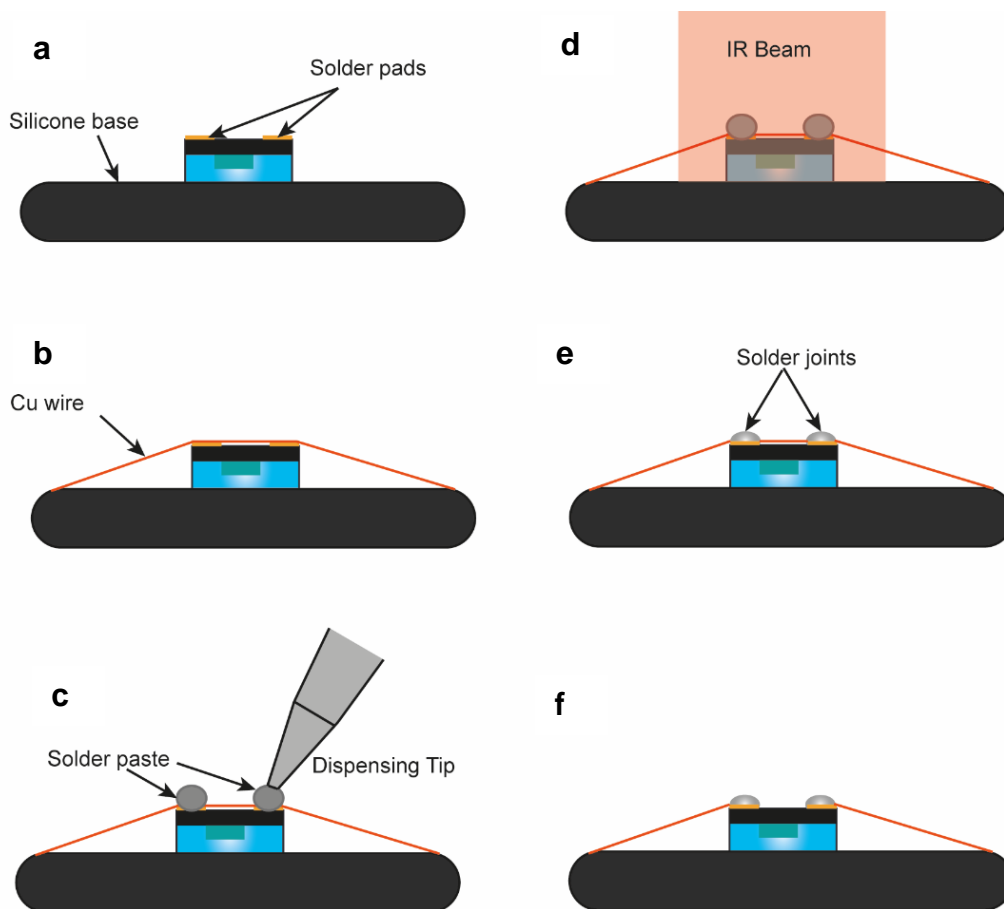


Figure 3.6 – Soldering process for SMD photodiodes (PDs). (a) PD placed on the silicone base with solder pads facing upwards. (b) Cu wire placed over the solder pads of the PD. (c) Solder paste dispensed onto the solder pads and Cu wire at points of contact. (d) Solder pads and solder paste exposed to IR beam. (e) Solder joints formed. (f) Cu wire length between solder joints removed.

A multi-strand Cu wire with seven twisted Cu monofilaments (seven strand, linear density = 120 mg/m, single strand diameter = 50 μm , Knight Wire, Potters Bar, UK) was placed on top of the two solder pads (Fig. 3.6(b)). Approximately 3.0 μl of lead free solder paste (SolderPlus® S965D500A6, Nordson EFD, Dunstable, UK) was dispensed onto the Cu wire at the solder pad (Fig. 3.6(c)) using a pneumatic dispensing system (EFD Ultimus II dispenser system, Nordson EFD, Dunstable, United Kingdom), and reflow soldered using IR spot reflow soldering system (PDR IR-E3 Rework System, PDR-Design & Manufacturing Centre, Crawley, UK). The reflow system settings (reflow

profile, beam diameter) were adjusted to optimise the soldering to achieve robust electrical and mechanical connection between solder-pads and copper wires (Fig. 3.6(d, e)). Finally, the Cu wire length between the solder joints was removed by cutting the Cu wire at the inner edges of the solder pads (Fig. 3.6(f)) using a scalpel (0.5 mm blade thickness).

3.2.4 Making electrical connections between the solder-pads and Cu wires for solar cells

Unlike the PDs, the solar cells had the solder pads on either side of the cells. Therefore, the E-yarn soldering process had to be modified to enable the reflow soldering on both sides of the cell onto two parallel positioned Cu wires simultaneously. The soldered pad on the front of the cell consisted of array of Cu buried contacts. These were positioned on the photoactive (face) side of the cell close to one edge of the cell. The entire backside of the cell is solderable (see Fig. 3.7).

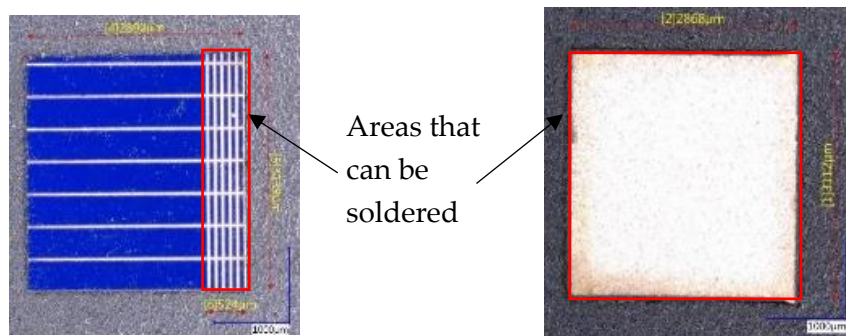


Figure 3.7 – Areas that can be soldered on the front (*left*) and back (*right*) contacts of a solar cell (3.2 mm × 3.0 mm).

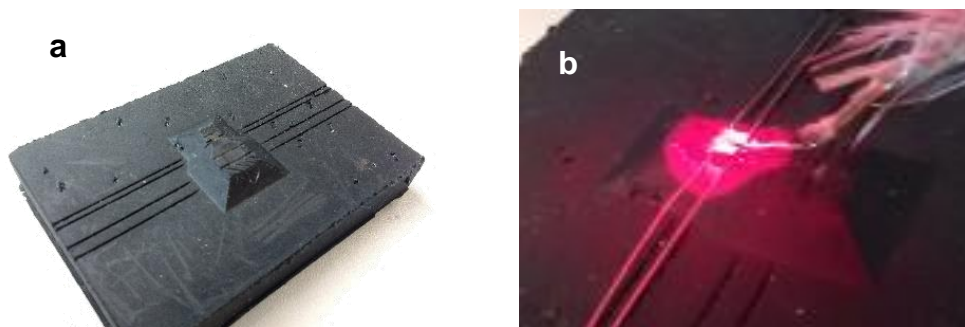


Figure 3.8 – Black pigmented silicone used as the soldering platform for solar cells. (a) Photograph of the mould. (b) Magnified view of the soldering process.

A bespoke mould was fabricated (Fig. 3.8) using the same silicone material used for the PD soldering base. The mould was designed to position two parallel aligned Cu wires onto the front and back solder pads, located on either side of the SC. All the other materials and parameters were the same as for the PD soldering.

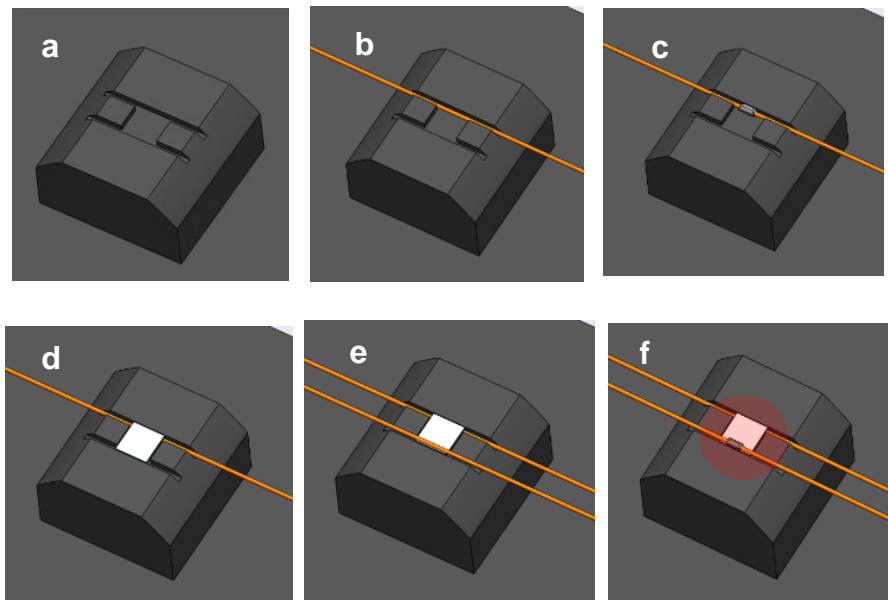


Figure 3.9 - Soldering process for solar cells (SCs). (a) The bespoke mould design. (b) The Cu wire positioned on the mould. (c) Solder paste was dispensed onto the first Cu wire. (d) The SC was positioned on the mould with the front contact touching the first Cu wire. (e) The second Cu wire was positioned on the mould and back side of the SC. (f) Solder paste was dispensed onto the second Cu wire and IR beam was applied.

The steps for soldering a solar cell onto a pair of Cu wires is illustrated in Fig. 3.9. Initially, one Cu wire was placed in one of the two wire positioning grooves (Fig. 3.9(b)). Solder paste was then dispensed onto the wire, where the front solder pad would be soldered onto the Cu wire (Fig. 3.9(c)). The solar cell was positioned into the groove, with the front solder pad in contact with the solder paste/Cu wire (Fig. 3.9(d)). The second Cu wire was positioned onto the back contact of the solar cell (Fig. 3.9(e)) and a solder paste volume was dispensed where the back contact and Cu wire made contact. Once the positioning was complete, IR reflow soldering was conducted (Fig. 3.9(f)). The solar cell was positioned in this orientation (back contact directly facing the IR beam) to minimize the detrimental effects of direct heat exposure on the photoactive area. The solder base facilitated indirect heat transfer to the front contact, allowing simultaneous soldering of both front and back contacts of the solar cell. For connecting multiple cells onto the same pair of Cu wires, with predetermined gaps between cells, a mould with

multiple grooves with required cell spacing was prepared (further details on soldering multiple solar cells are provided in Chapter 7.)

Observations under the microscope showed that a dark colour patch appeared on the photoactive side of the solar cell near the solder joint during the soldering process. This dark patch could be attributed to the charred residues of the solder-paste remaining on the front surface of the solar cell. Therefore, a test was conducted to determine any adverse effects of the IR reflow soldering process on the performance of the solar cells. Five 3.2 mm × 3.0 mm solar cells (which were otherwise identical to the solar cells used throughout the rest of this work), were soldered onto fine copper wires using the IR reflow soldering unit at 250°C. The soldered cells were subsequently exposed to five heating cycles of 230°C (with same cycle time as the soldering). The measurements of the control samples were conducted (Fig. 3.10(b)) using a conductive copper adhesive tape (1181 Tape Copper Foil with Conductive Adhesive, 3M United Kingdom PLC, UK). The results showed (Fig.3.10(a)) that the cells underwent a 5% change in short-circuit current (I_{sc}) even after excessive heating of upto 5 times longer than the normal soldering process. No significant change in open-circuit voltage (V_{oc}) was observed at the end of the test. Microscopic images show clear evidence of residue after the soldering, which did not change significantly afterwards.

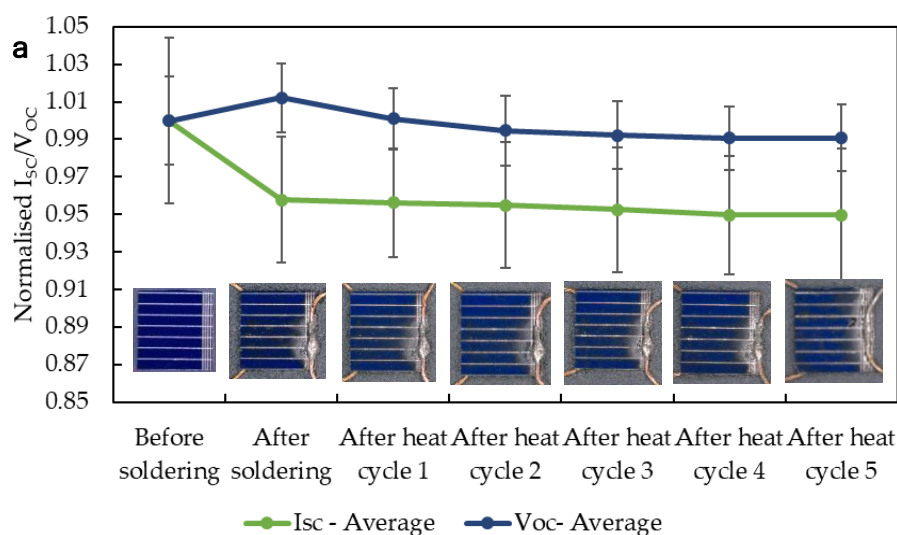


Figure 3.10 - Change in performance of solar cells after soldering and exposure to heat. (a) Change in short-circuit current (I_{sc}) and (open-circuit voltage) V_{oc} after soldering and each subsequent heating cycle. (b) Setup for measuring the control sample, using copper adhesive tape.

3.2.5 Encapsulating the Soldered photocells inside resin micro-pods

Encapsulation of the soldered photocell is a key step of the E-yarn fabrication process and provides protection to the photocell during its use and washing. As in the previous work on E-yarns, an optically clear, ultra-violet curable, electronic grade flexible resin was used to create the resin micro-pods in this study. Micro-pods with a circular cylindrical shape was prepared throughout this study although it was known that other cross-sectional shapes such as parabolic or elliptic can have different effects on how incident light is refracted in the micro-pod. It was important to have the ability to control the depth of the photocell inside of the cylindrical micro-pod to ensure consistency when fabricating the yarns with photocells as well as to conduct an empirical study on the effect of the depth of positioning of the photocell inside of the micro-pod on the performance of the micro-pod-embedded photocell. In order to achieve this a bespoke encapsulation apparatus was devised (Fig. 3.11).

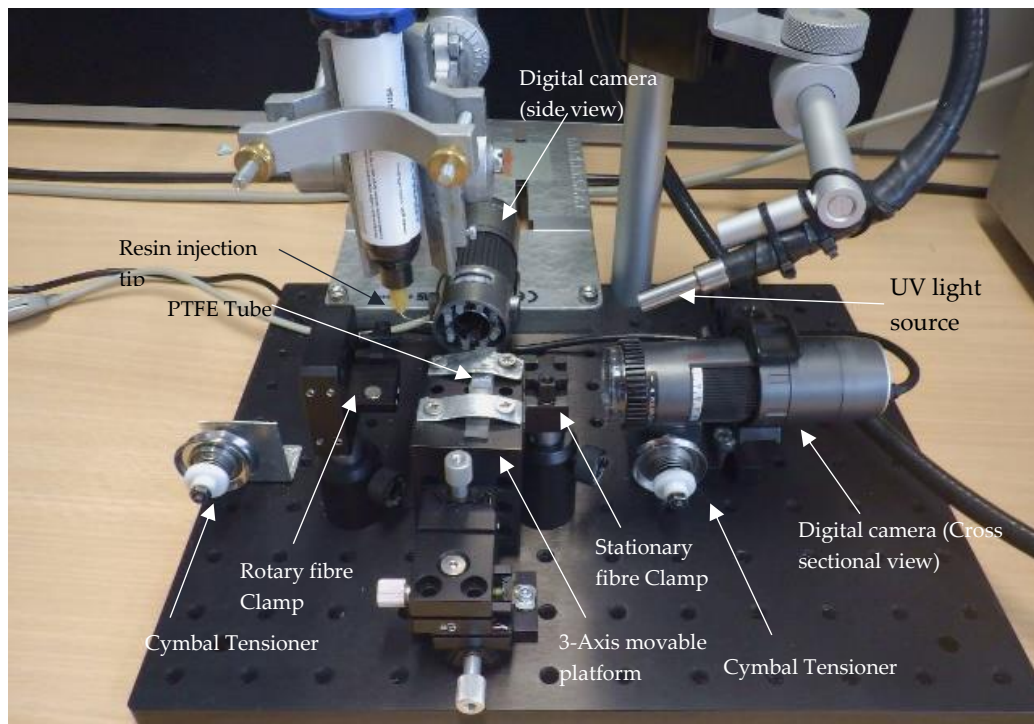


Figure 3.11 - The apparatus for positioning and encapsulating photocells inside of cylindrical resin micro-pods.

The encapsulation apparatus consisted of one rotary and one stationary wire clamp and two cymbal tensioners, before and after the two tensioners; these securely positioned the soldered photocell inside of a PTFE (polytetrafluoroethylene) (Adtech Polymer Engineering Ltd., Gloucester, UK) or a silicone tube (Advanced Fluid Solutions Ltd., Essex, UK) during the resin injection and curing process. PTFE or silicone was employed as the mould as they allowed the micro-pod to be easily released from the mould, as detailed in the literature (Nashed *et al.*, 2019). Due to their flexibility and elasticity, silicone tubes showed the ability to better release the micro-pod. Therefore, silicone tubes were employed for the experiments with photocells. The tube was mounted on to an adjustable platform with three degrees of freedom (XYZ planes). The tube's circular cross section was aligned concentric with the centre of the rotary fibre clamp. A digital camera was positioned behind the stationary clamp concentric to the tube with the focal length adjusted to obtain a clear view of the inner perimeter of the tube. The soldered photocell-Cu wire strand was reinforced by using a 20f/ 110dtex Vectran yarn (Vectran™, Kuraray America Inc., Houston, TX, USA) and guided through the tube with the photocell positioned approximately centrally inside of the tube.

The Vectran™ strand provided strength to the Cu wires to prevent breakages during subsequent processing. The strand was maintained under tension using the cymbal tensioners before the rotary clamp was fastened onto the strand. The photocell positioning was adjusted using the rotary clamp and XYZ movable platform with the operator observing the position through the camera to ensure that the intended orientation of the photocell inside the resultant micro-pod was achieved (Fig. 3.12(a)).

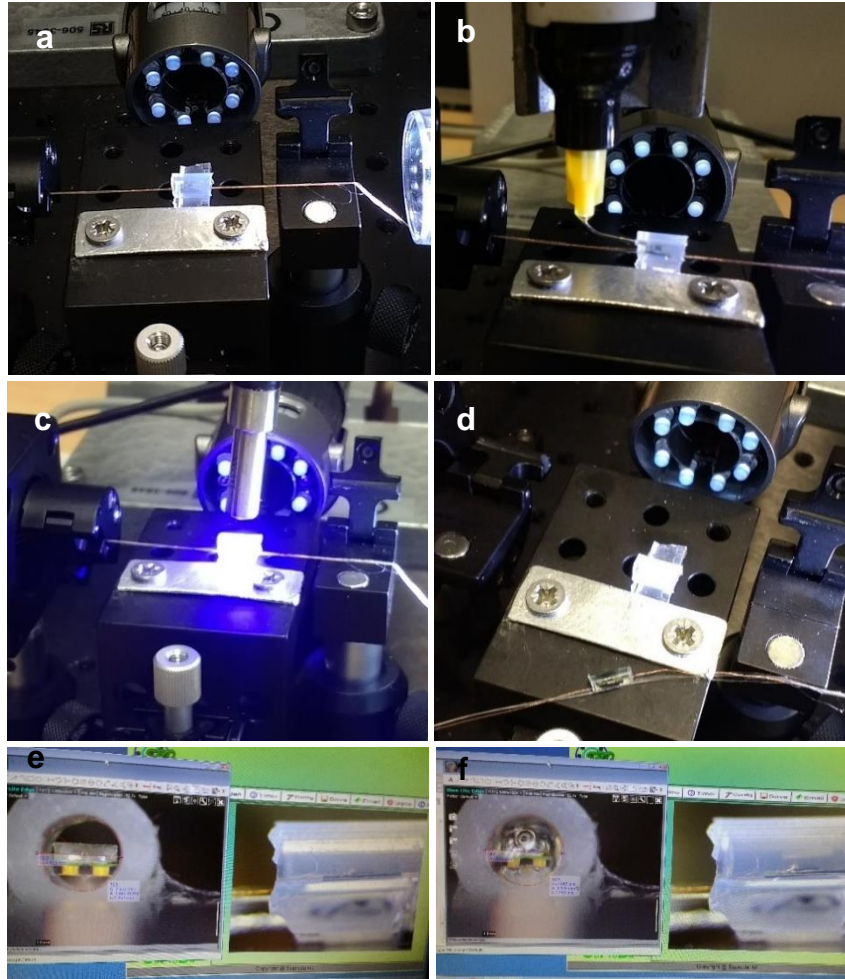


Figure 3.12– The steps for encapsulating the soldered devices. (a) Positioning the device inside of the silicone tube. (b) Dispensing the resin into the tube. (c) Curing the resin using UV light. (d) The cured micro-pod released from the tube. Views from the digital microscopes (e) after positioning the device inside the tube and (f) while dispensing the resin.

Once the positioning was complete, a predetermined volume of UV curable resin (Specifications provided in Annex 5) was injected into the tubular-mould (silicone tube) (Fig. 3.12(b)). The resin volume was controlled to create a cylindrical micro-pod with a length 2.0-3.0 mm longer than the length of the photocell (1.0-1.5 mm longer on each side). Extra care was taken to ensure that the resin was free of air bubbles and that the

photocell was completely surrounded by the resin. The resin was then exposed to UV light (BlueWave™ 50, Dymax Corporation, Torrington, CT, USA, Specification provided in Annex 6) for sixty seconds until it was fully cured (Fig. 3.12(c)). In the case of larger-sized ($> 3.0\text{mm}$ diameter) resin micro-pods multiple UV exposure cycles (four cycles for the largest micro-pods mentioned in this thesis) were carried out. Finally, the strand was released from the clamps and the cymbal tensioners, by forcing the cured micro-pod and Cu wire strand (referred to as micro-pod-Cu strand) out of the tube by pulling the Vectran yarn (Fig. 3.12(d)).

3.2.6 Embedding the micro-pod inside of a knitted fibre sheath

After the encapsulation process, the micro-pod-Cu strand was wrapped within a sheath of textile fibres to provide the textile appearance and hand feel. The fibre wrapping or covering provided additional protection to the micro-pod, copper wires and the embedded photocell. There are three possible routes available to wrap a fibre sheath around the micro-pod; braiding (multiple number of yarns are interlaced at an angle $< 90^\circ$, to form a tubular structure), circular warp knitting (interlooping multiple number of yarns in the length direction direction to create a small diameter tubular knitted structure), and yarn covering (by wrapping one or two yarns around a core yarn in a spiral shape without interlacing or interlooping). However, in the research a small diameter warp knitting machine (RIUS MC-Knit braider, Barcelona, Spain- Specification provided in Annex 7) was utilised to craft a knit -braided structure to prepare the E-yarns embeded with photocels (Fig.3.13(a)).

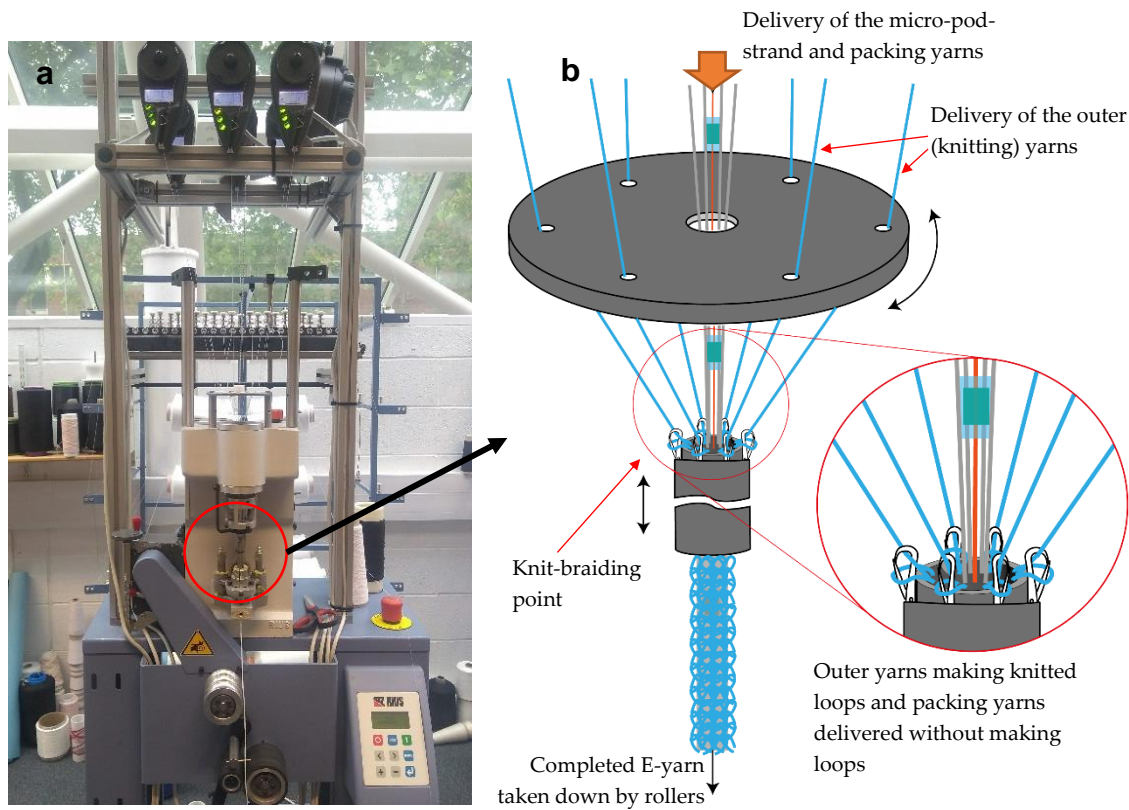


Figure 3.13 – Knit braiding process using the RIUS MC machine equipped with a 2.0 mm inner diameter hollow cylinder. (a) Photograph of the knit braiding machine used for completing the E-yarns. (b) Schematic illustration of the delivery of the yarns and micro-pod strand and yarns to the knit-braiding point and the output of the process.

Warp knit braiding was considered the more conducive method for preparing optically active devices, due to its more open structure of the knit-braid, in comparison to conventional interlaced braiding. This will be further discussed in section 5.4.4. In addition knit braiding has been employed for previous E-yarn developments which accumulated substantial knowledge on preparing E-yarns using knit-braiding (Rathnayake, 2015; Nashed *et al.*, 2019). Two small diameter circular warp-knitting machines (RIUS MC-Knit braiders with 2.0 and 4.0 mm inner diameter hollow cylinders with six and eight needles respectively, outer diameters of the hollow needle cylinders were 10.0 mm; RIUS, Barcelona, Spain) were used to hold the fibres of the packing yarns (fibre sheath) around the micro-pod and Cu wire, which were consolidated by the tubular knitted structure formed by interloping the yarns surrounding the packing yarns. Two sets of yarns were simultaneously delivered to the knitting head of the machine along with the photocell-Cu/Vectran strand that was delivered as the core yarn. One set of white 48f/167 dtex texturized polyester (PET) packing fibres were delivered

straight through the inside of the hollow needle cylinder with the RMP, copper wires and Vectran yarn, thus these did not form loops. The second set of white PET yarns (48f/167 dtex) were delivered to the knitting needles on the outer surface of the needle cylinder, which formed the warp knitted structure (1/1 single bar tricot knitted structure) around the packing fibres, creating the final E-yarn (Fig.3.13(b)). The packing fibres were used to retain the RMP and copper wires centrally in the E-yarn and fill the spaces in the core of the knit braid between the micro-pods, thereby maintaining a regular thickness along the resultant E-yarn, i.e. minimise the thick-places of the yarn.

For making the knit braid for RMPs with diameters larger than 1.5 mm, the braiding machine fitted with eight needle hollow cylinder, with a 4.0 mm inner diameter, was selected. In this case, eight PET yarns (48f/167dtex) were used for packing fibres while eight PET yarns were fed to the knitting-needles to form the knit-braid structure. For 1.5 mm diameter RMPs a six-needle hollow cylinder with a 2.0 mm inner diameter was selected, and six PET yarns (48f/167dtex) were used to form the knit-braid. Four PET yarns were used as packing fibres.

3.2.7 Impregnation of the fibrous sheath with clear resin

In some cases, the photoactive side of the photocell embedded yarn was impregnated with the same resin used to create the resin micro pod by dispensing the resin onto the fibrous sheath (Fig. 3.14).



Figure 3.14 – Photograph of the resin impregnation on a solar cell embedded E-yarn.

This process was intended to improve the light penetration to the resin micro-pod by minimizing the light scattering due to the fibre sheath. It was evident that when the air trapped between the fibres were replaced by a material with a similar refractive index of the fibres, the Fresnel reflection at the fibre surface was minimised. The volume of the

resin dispensed was controlled to achieve a full impregnation of the spaces between the fibres all the way down to the resin micro-pod, while leaving only a thin layer of resin on the outer most layer of fibres. The resin absorption was also facilitated by the capillary action of the fibres. Finally, the non-cured resin was exposed to the UV light source for forty seconds to achieve a complete curing of the resin.

Some relevant optical and mechanical properties of the polymeric material employed during this research are summarized as below (Table 3.3).

Table 3.3 – Optical and mechanical properties of the polymeric material employed for E-yarns. (RI- Refractive Index, TS – Tensile strength, HD – Hardness). These values have been used in all modelling and calculations.

Material	Material group	HD	RI	TS
9001 EV-3.5 (Dymax Corporation, USA)	Acrylated urathane (UV curable)	D45	1.51	5.2 MPa
OP 29 (Dymax Corporation, USA)	Acrylated urathane (UV curable)	D60	1.50	22 MPa
OPT 4200 (Intertronics, UK)	Polyurathane	A75	1.47	15 MPa
OPT 7020 (Intertronics, UK)	Silicone	A75	1.41	4.8 MPa
OPT 5200 (Intertronics, UK)	Epoxy	D82	1.56	-
Texturized PET yarn (Stretchline UK)	Polyester yarn	-	1.54 (Morton et al., 2008)	84 cN/tex
Vetran® (Kuraray USA)	Liquid crystal polymer	-	-	229 cN/tex

3.3 Evaluating the optoelectronic behaviour of the photocells and photocell E-yarns

The fabricated samples were evaluated for the opto-electronic behaviour under a predetermined lighting condition. The main objective of the evaluation was to study the opto-electronic parameters (open circuit voltage and short-circuit current) of the photocells embedded inside of the RMPs relative to the bare (without any RMP or fibre coverage) photocells. To achieve this, a bespoke optical test rig was developed that could generate a reliable and reproducible light beam with a suitable spectral and irradiance

output. The test rig also provided a means of using light filters and mechanism to position the specimens in a repeatable manner. The sample holder of the test rig was later modified to allow exposure of the photocell-E-yarns at various incident angles.

3.3.1 Optical test rig

The test rig (Fig. 3.15(a)) consisted of a quartz tungsten halogen lamp (QTH10/M Thorlabs Inc., Ely, United Kingdom) coupled with a glass diffuser and a concave lens resulting in a 50 mm diameter circular beam output. The diameter of the output from the lamp was reduced to 25 mm to match the size of the light filters subsequently aligned to the light beam using an adjustable filter holder wheel. Next to the filter holder, a frame with a removable sample holder was mounted. The backside of the sample holder was attached with a polymeric sheet (Transparent PET sheet; ~0.5mm thickness) on which the test sample was mounted. The polymeric sheet was marked with vertical and horizontal grid lines to enable precise positioning of the test sample in the sample holder. It was observed that the beam of light caused the temperature of the sample and surrounding area to rise, with temperatures as high as 35°C being observed. Therefore, in order to maintain the temperature of the test samples around 25°C, a Peltier cooler (Supercool® PE-161-12-15, Gothenburg, Sweden) and thermocouple-based feedback-controlled temperature control system was employed. The thermocouple (Z2-K-1.0-1/0.2-MP-ANSI, Labfacility Ltd, West Sussex, United Kingdom) of the temperature control system (CN7500, Omega Engineering Limited, Manchester, United Kingdom) was positioned adjacent to the test sample in the sample holder. The Peltier cooling tile was attached behind the sample holder (cooling face adjacent to the sample holder) which was affixed to an aluminium block which acted as a heat sink. Two cooling fans were provided; one at the back side of the lamp and the other one behind the aluminium block to prevent overheating of the lamp and the Peltier cooler. The lamp and the Peltier cooler were powered by a laboratory DC power supply (Fig. 3.15(b)), and the cooling fans were powered by a 12V AC/DC converter power pack.

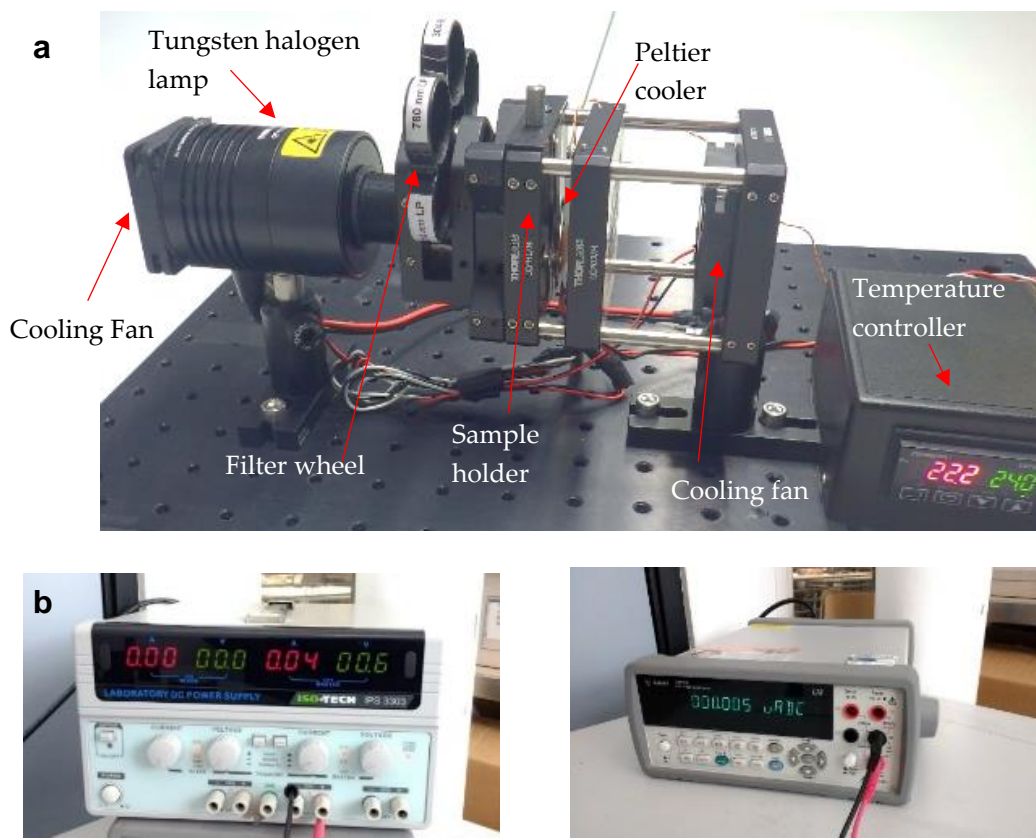


Figure 3.15 – (a) Image of the optical test rig and light source used to evaluate the photocells and resultant samples. (b) Variable DC power source (ISO-TECH IPS 3303, RS Components Ltd. Northants, United Kingdom). (c) Digital multi-meter (34410A 6 $\frac{1}{2}$, Agilent Technologies LDA UK Limited, Stockport, United Kingdom) used for evaluation experiments.

The test samples were mounted onto the polymeric sheet using electrical insulation tape, with the centre of photoactive area of the photocell aligned to the centre point of the line grid (with 1.0 mm vertical and horizontal divisions) and the photoactive plane parallel to the surface of the polymeric sheet. The cells could be observed through the fibres on close inspection with naked eye, and the positioning was adjusted manually whenever needed by trial and error. The sample holder assembly was then placed inside of the holder frame with the Cu wire connectors extending outwards from the top and bottom sides of the holder frame. The Cu wires were connected to the leads of a high precision digital multi-meter (34410A 6 $\frac{1}{2}$, Agilent Technologies LDA UK Limited, Stockport, UK) using small alligator clips. Each test sample was conditioned inside of the sample holder for about 30 seconds before reading measurements from the multi-meter (Fig. 3.15(c)).

In some cases the measurements were conducted under a filtered beam of light using different optical filters (305-485 nm band pass, 485 nm long-pass and 780 nm long pass)

to ascertain the behaviour of the photocells and resultant yarns when exposed with different bands of the light spectrum. Unless specified the lamp was powered with ~ 12V / 0.89A supply.

A dedicated VEMD 6060×1 type photodiode was employed as a baseline to monitor any variations in the light intensity at the sample holder over time. The I_{sc} reading of the photodiode was considered for this due to the linear dependency between the light intensity and I_{sc} . The baseline reading was conducted after every ~ 50 readings to ensure that the light intensity at the centre of the sample holder was within $\pm 2\%$ of the initial measurement. Any variations outside of the tolerance was rectified by adjusting the input voltage to the lamp. The electromagnetic spectrum of the lamp provided by the manufacturer is given in Fig.3.16(a). The output spectrum and power of the light beam generated by the lamp was analysed using a spectrum analyser (LabSpec 4 Benchtop Analyzer, Malvern Panalytical, UK) and a power meter (13PEM001 Broadband Power/Energy Meter, Melles Griot, IDEX Health & Science LLC, WA, USA) without an optical filter (full beam) and with the three optical filters mentioned previously.

Fig. 3.16(b) shows the spectra under the three optical filters normalized to the full spectrum values. The normalized spectral outputs for the optical filters confirmed a close match with spectral data provided by the supplier. The light power output measured at the sample holder at different lamp voltages under different filters is shown in Fig. 3.16(c). The power output of the lamp was observed to be non-linear to the supply voltage (V), which is also explained by theory, where power output P is given by $P = V^2/R$, where R is the resistance of the lamp which varies based on the filament temperature.

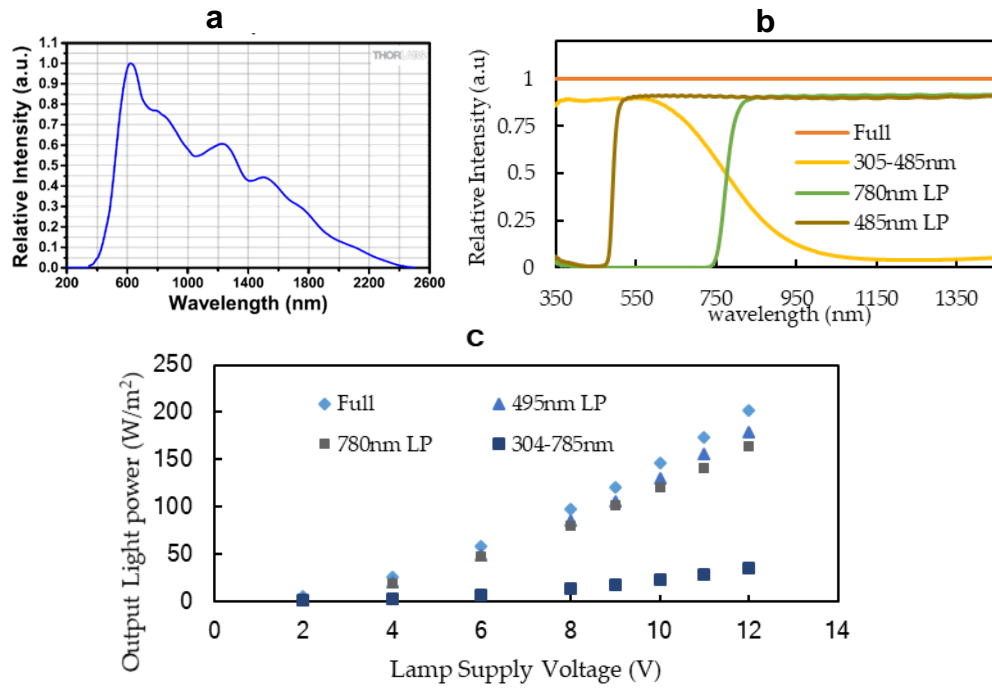


Figure 3.16 – Optical test rig and light source settings. (a) Image of the optical test rig. (b) Manufacturers specification for the emission spectrum of the tungsten halogen lamp (Courtesy - Thorlabs Inc.). (c) Transmission spectra for different filters employed. (d) Relationship between supply voltage and optical output of the lamp through different light filters.

It was important to study the uniformity of the light distribution incident at the sample holder, to ascertain how variations in the positioning of the device might affect the measurements. A photodiode of the type VEMD 6060×1 was positioned on each grid point (the grid had 1mm × 1mm divisions) to map the light intensity at the sample holder as given below in Table 3.4.

Table 3.4 – Short-circuit current (I_{sc}) variation measured at the sample holder of the optical test rig, without optical filters. Values given are normalized to the I_{sc} measured at the centre point of the beam.

Area (mm)	Normalized I_{sc} measured (%)					
	No diffuser		Diffuser close to the sample		Diffuser between the lens and the bulb	
	Avg	CV	Avg	CV	Avg	CV
9	96.0	2.88	96.9	1.67	99.7	0.99
25	91.3	5.62	94.4	3.38	97.8	2.64
49	87.0	7.71	92.1	4.65	96.1	3.19
81	82.5	10.4	88.4	7.42	94.3	4.41

It was observed that the coefficient of variation of the measured current (I_{sc}) was <1% within a 3 mm × 3mm square from the centre of the grid (Table 3.3) when the diffuser is

fixed between the bulb and the convex lens of the lamp. (Appendix 3 provides full details on this intensity analysis).

3.3.2 Solar simulator

The optoelectronic properties of solar cells vary depending on the incident light intensity and spectral distribution. Conducting experiments according to the standard test methods, using a standardised solar simulator, was crucial in order to obtain a realistic and comparable estimation of the behaviour of any type of solar cell or solar device. The solar textile was not intended for indoor applications hence tests were not conducted at light intensities observed indoors. In order to characterize the solar cells a solar simulator was sourced to provide repeatable, reliable and globally comparable input conditions. After considering a range of models available from different solar simulators manufacturers, a model (Fig. 3.17) with class ABA rating (Class A for spectral match, Class B for uniformity and class A for temporal stability) was selected (LSH-7320 ABA LED solar simulator, Newport Corporation, 150 Long Beach Blvd., Stratford, CT 06615, USA) as the most suitable (fulfilling the minimum requirements) and cost effective (low maintenance and running costs) option. Complete specification of the solar simulator and the calibration certificate is provided in the Annex 8.

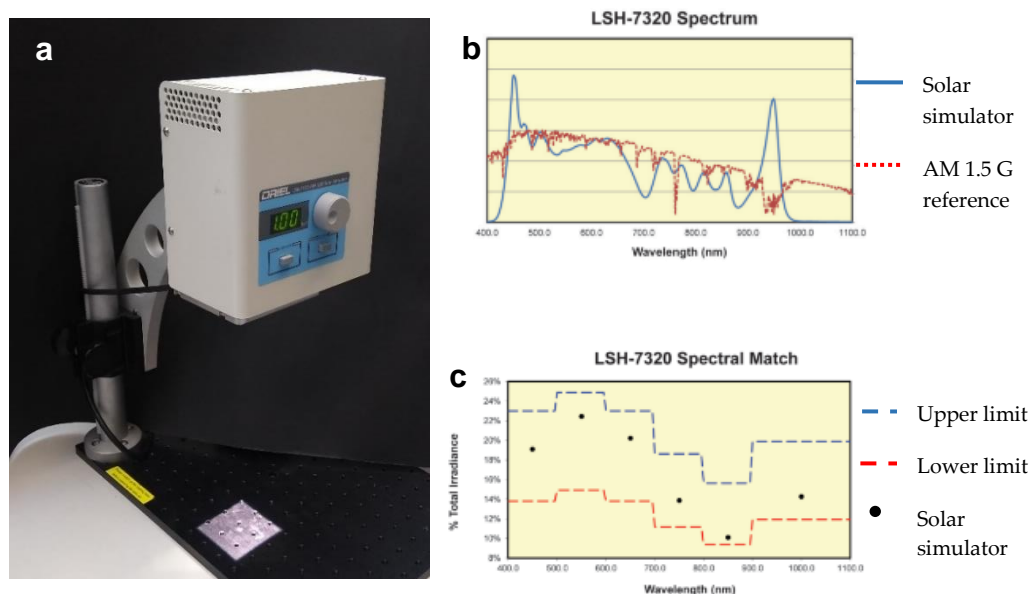


Figure 3.17 – A photograph of the solar simulator employed in this research. (a) Image of the solar simulator in operation (b) spectral distribution and (c) spectral match of the incident light against the standard. (Courtesy – Newport Corporation, USA).

Unless specified otherwise characterisations were conducted under one sun (1000 W/m^2) intensity 1.5 AM global solar spectrum settings. The intensity variation of the beam of light at the measurement plane was evaluated using the VEMD 6060x1 photodiode, using a similar procedure employed for the optical test rig (full details of provided in Appendix 4). The results confirmed that the intensity distribution within the $5 \text{ mm} \times 5 \text{ mm}$ area at the centre of the beam is $< 0.3\%$ (Table 3.5).

Table 3.5 – Short-circuit current (I_{sc}) variation measured under the of the beam of light generated by the solar simulator at one sun intensity. Values given are normalized to the I_{sc} measured at the centre point of the beam.

Measured area (cm ²)	Normalized I _{sc} measured	
	Average	CV
9	99.867	0.205
16	99.69	0.311
25	99.708	0.274

An enclosure was used to isolate the sample from external lighting. A feedback-controlled cooling system (similar to the system used in the optical test-rig, prepared using identical components) was built to maintain the test sample within $\pm 2^\circ\text{C}$ of a set temperature. The Peltier cooler and the cooling fan was controlled by a temperature controller based on the feedback given by a thermocouple positioned on top of the temperature-controlled platform as shown in Fig. 3.18.

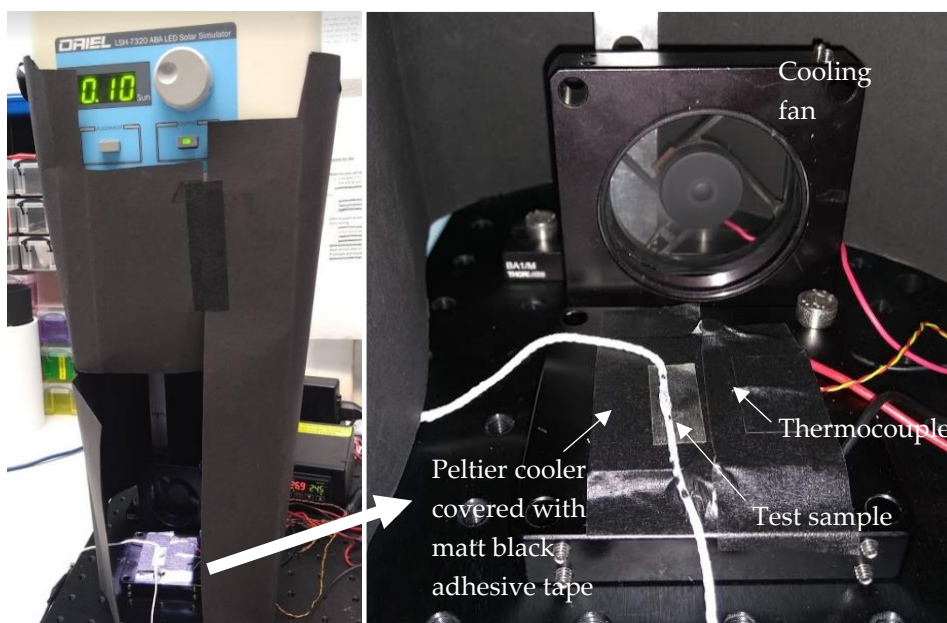


Figure 3.18 – Photographs of the enclosure employed for conducting measurements using solar simulator.

3.3.3 Conducting characterisations under different angles of incident light

It was important to understand how the incident angle of light affected the performance of the embedded photocells. Incident angle of light varies throughout the day for a conventional fixed solar panel. The incident light intensity on a fixed flat panel solar cell varies with the cosine of the angle of tilt (Balenzategui and Chenlo, 2005). Fresnel reflection (caused by the partial reflection at the cell-air boundary) also varies with the incident angle. Solar tracking devices are used to align the solar panels to the direction of the moving sun that minimized the effect of change in incident angle. When it comes to wearable or mobile applications the incident angle is unpredictable, and it is impracticable to envision any form of tracking mechanism, unless the device is stationary for relative longer periods. Therefore, a desirable feature of a wearable or mobile solar energy harvesting system would be uniformity of performance at different incident angles. For conducting measurements under different incident angles using the optical test rig, the sample holder was modified with a Teflon tube affixed with a goniometer, with 5° angle divisions as shown in Fig.3.19. An opening was cut in the Teflon tube as shown in Fig 3.19(a)) to allow the inserted photo cell embedded E-yarn to be fully exposed to light between approximately -100° to 100° incident angles.



Figure 3.19 – Photographs of the modified sample holder to conduct measurements at different incident angles using the optical test rig. (a) Teflon tube attached to the goniometer. (b) Front and (c) back views of the sample holder after the modification.

To conduct measurements when light was exposed from the front side (front half circle), the photocell E-yarn was positioned inside of the tube of the sample mount, to have the photo-active side of the photo cell facing the centre of the opening in the tube. Exposure from behind the photoactive side of the photocell E-yarn (back half circle) was simulated by positioning the back side of the photocell E-yarn facing the opening in the tube. The

photocell E-yarn was secured to the Teflon tube at its the top and bottom ends and inserted inside of the sample holder. The incident angle was changed in steps of 5° to the required value by rotating the dial before recording the I_{sc}/V_{oc} measurements.

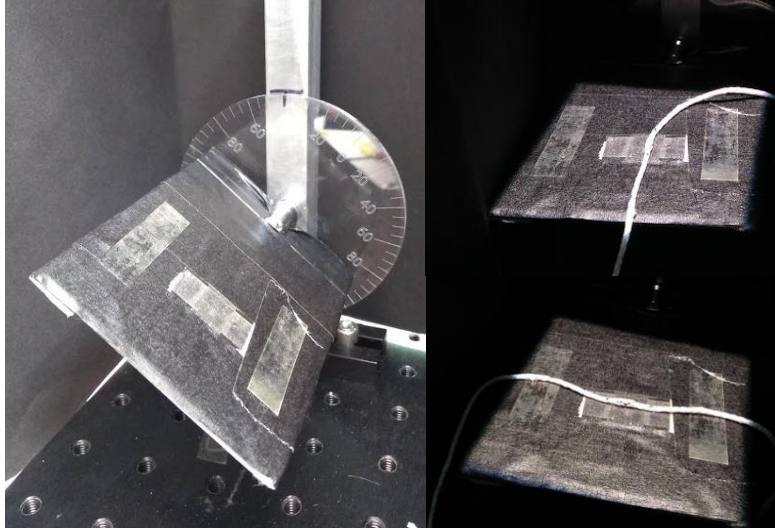


Figure 3.20 – (a) The rotary sample holder devised measurements at different incident angles using the solar simulator. Solar-E-yarn positioned on the sample holder (b) at varying incident angles in the radial direction and (c) at varying incident angles in the longitudinal direction.

Similarly, a rotary sample holder was devised to conduct measurements at different incident angles under the solar simulator (Fig 3.20). The rotary axis of the sample holder was held horizontal by an aluminium pole. A goniometer with 5° angle divisions was fixed to the rotary sample holder to measure the angle relative to the beam of light from the solar simulator.

3.3.4 Generating characteristic curves for photocells

Construction of the characteristic curves (IV and power curves) for the photocells were conducted using a fixed resistor array network (Fig. 3.21) with a resistance range from $1\ \Omega$ to $100\ M\Omega$ utilised. To generate data points, photocells were exposed to the light source (optical test rig or solar simulator) and then the Cu wires were attached to the resistor network. The voltages across the resistor array were measured for each data point under the selected incident light condition. Resistance value across the resistance array was also recorded for each data point to include any changes in the contact resistance of the network. The current through the resistor network was calculated using

the Ohm's law and the current-voltage (I-V) and power-voltage (P-V) curves were generated based on the measured voltages and calculated current values.

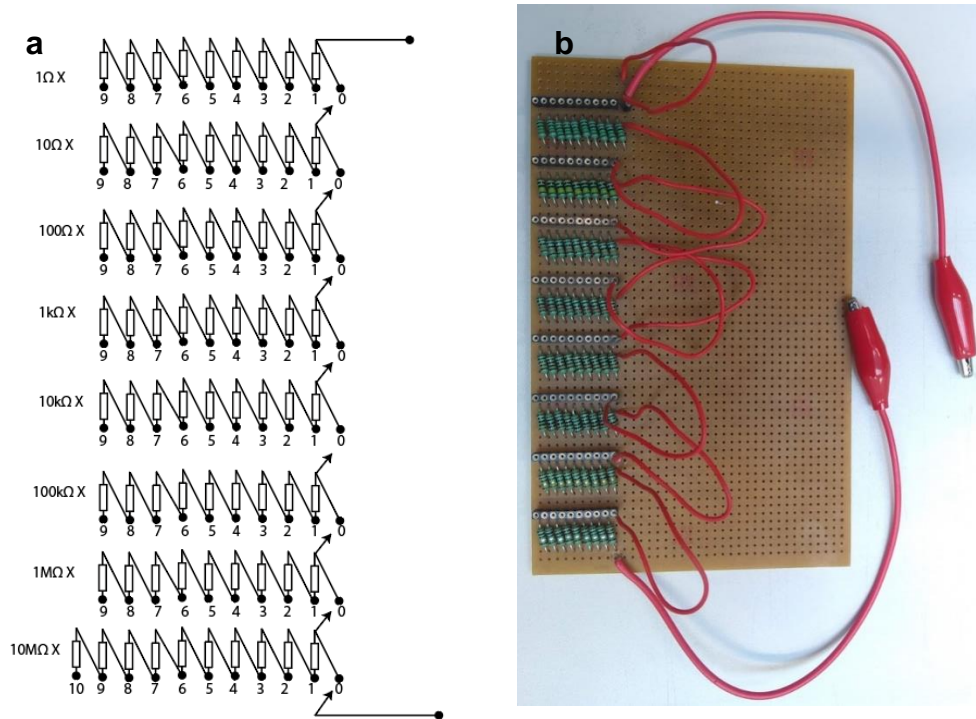


Figure 3.21 – (a) Circuit diagram and (b) photograph of the fixed resistor network used as the variable resistor for developing IV curves.

3.3.5 Data analysis

In general, for each data point reported in this thesis minimum of five measurements were conducted on five test specimen and the average value has been presented. In some instances (e.g. for evaluating the solar fabric demonstrator) five repeat measurements were conducted on the same test specimen. Standard deviation (SD) of the five measurements was given for each data point to indicate the spread of measurements, which is graphically represented as error bars. Any exception to the above is explicitly mentioned under the relevant experimental sections.

3.4 Summary

This chapter reports the types of materials and methods followed to create the photocell embedded E-yarn specimens studied in this research. This includes the instruments and apparatus employed to create electrical connections (soldered copper wires), resin micro-pods and final E-yarns. The chapter also details the experimental procedures followed in order to characterize the opto-electrical performance of the photocell E-yarns and to ensure repeatability of the test results. Here, the equipment and apparatus

employed to generate repeatable lighting (optical test rig and solar simulator) and test conditions (temperature control system and dark enclosures) were outlined to ensure repeatability of measurements. The general methods and procedures mentioned in this chapter may be modified in specific ways to conduct detailed characterisations (e.g. to evaluate the effect of change in temperature and liquid moisture), which will be elaborated in the relevant experimental sections in the following chapters of this thesis.

Chapter 4

Photodiode Embedded Electronic Yarns

4.1 Introduction

In the first phase of this research, PDs were considered for the proof-of-concept of a solar energy harvesting textile yarn, as they were a readily available alternative to miniature solar cells. Photodiodes (PDs) are semiconductor based opto-electronic sensing devices that follow similar operating principles as solar cells. For typical applications, PDs can be connected under forward bias (photovoltaic mode) or reverse bias (photoconductive mode) (Yotter and Wilson, 2003). They are extensively used in a number of commercial products including cameras, medical devices, safety equipment, optical communication devices, position sensors, bar code scanners, automotive sensors, and surveying instruments (Yotter and Wilson, 2003; Farahi, 2014). Their wide-spread employment has resulted in the development of small, low-cost PD devices. PDs also have been employed for energy harvesting in the literature (Cemine, Sarmiento and Blanca, 2008; Moayeri Pour, Benyhesan and Leon-Salas, 2014).

The packaging of the photoactive chip of a typical SMD type photodiode is designed for a shorter response time and high precision. Therefore, the size of the photoactive area of the device is only a fraction of the total device area: This results in a maximum power density significantly lower than that of a solar cell. Nevertheless, the knowledge generated by creating the photodiode embedded yarns (PDEY) would be directly applicable for a new branch of studies into optical sensing and solar energy harvesting E-yarns, which had not previously been explored. Finally, the possibility of enhancing the photovoltaic output of the PDEY by impregnating the fibrous sheath with a clear polymer resin was evaluated.

The use of the E-yarn technology to embed optically sensitive electronic devices, such as a photodiode or a solar cell, within the core of a textile yarn could have implications on how the embedded device would respond to the incident light. In this chapter an in-depth study on how the individual components of the E-yarn (the resin micro-pod and the fibrous sheath) affect the photovoltaic output of the embedded device was studied using miniature photodiodes. The study provided a close representation of how E-yarn embedded solar cells would respond to incident light, in comparison to a maiden (non-embedded) solar cell, which was critical in assessing the technical viability of this approach for creating solar energy harvesting textiles.

It was understood that the resin micro-pod (RMP) could interfere with the incident light depending on the geometry and optical properties of the resin material of the micro-pod. These effects may have significant implications on the intensity of light received by the photoactive area of the embedded photocell (the term photocell was generally used to represent for photoactive chip of the photodiode or solar cell), and hence the electrical output of the device. In order to theoretically estimate the electrical output of the micro-pod embedded photonic devices, in relation to the optical properties and geometry of the micro-pod, a generalized mathematical model is presented in this chapter. An empirical study was conducted to validate the model based on a cylindrical micro-pod shape. Subsequently, the experimental data from the empirical study was compared against the estimated values from the mathematical model (simplified for a cylindrical micro-pod shape) to confirm the validity of the model within the given boundary conditions. The textile fibres of the packing yarns would scatter the incident light and have a significant influence on the amount of light received by the RMP, and eventually the photoactive surface of the embedded device, which would determine the photovoltaic output of the photocell E-yarn. The empirical study further investigated the individual and cumulative effects of the packing fibres and a knit-braid structure used to consolidate the packing fibres on the electrical output of the PDEY.

The results presented in this chapter provide a proof-of-concept for a solar energy harvesting textile yarn and pave the way to the next stage of the research where solar cells will be embedded with yarns. The PDEYs discussed in this chapter reappear in the chapters 5 and 6 where they were subjected to further tests along with the solar cell embedded yarns. The work presented in this chapter is previously featured in a publication titled 'Photodiodes embedded within electronic textiles' by the author (author list: Achala Satharasinghe, Theodore Hughes-Riley and Tilak Dias) (Satharasinghe, Hughes-Riley and Dias, 2018), which discussed the application of the PDEY for sensing applications, although these results are equally important and relevant for energy harvesting applications.

4.2 Modelling the effect of the micro-pod encapsulation

In order to understand and characterise the effects of the resin micro-pod on the opto-electronic performance of the embedded device a generalized mathematical model was proposed (Fig. 4.1).

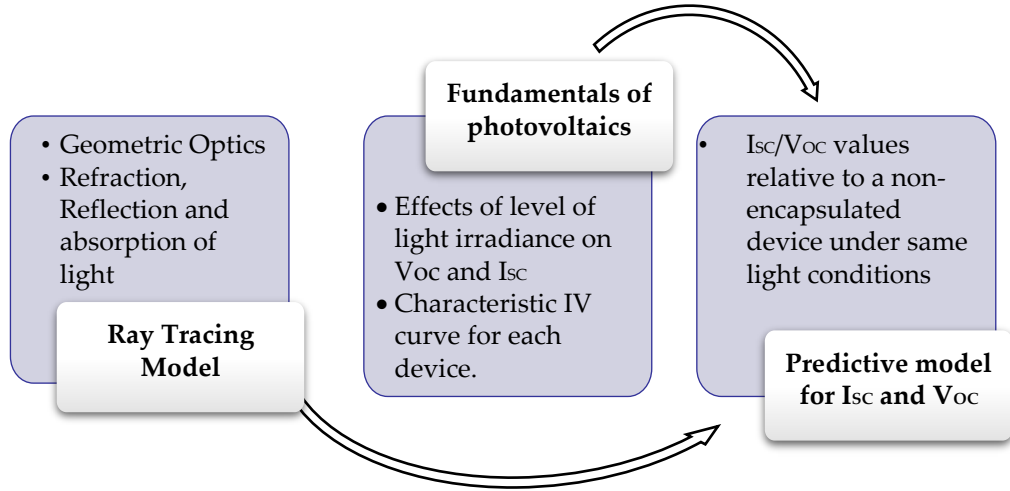


Figure 4.1 – Predictive model development based on ray tracing model and fundamentals of photovoltaics.

A generalized mathematical model was proposed to estimate the effects of the geometry of the cylindrical RMP (selected due to the cylindrical geometry of fibres and yarns), optical properties of the resin, and incident lighting conditions on photovoltaic performance of the photocells. The model was derived based on geometrical optics (Keating, 2002; Malacara-Hernández and Malacara-Hernández, 2013) and the fundamentals of photovoltaics (Cemine, Sarmiento and Blanca, 2008; Markvart and Castañer, 2012; Vincent *et al.*, 2015). First, a ray tracing model was defined based on a cylindrical RMP with uniform cross section. The ray-tracing model estimated the light intensity at a photoactive plane defined inside of the RMP. The light intensity was governed by the shape of the RMP and the optical properties of the micro-pod material as explained by the fundamental laws of refraction, reflection and absorption of light. Based on the estimated light intensity at the photoactive plane and the photovoltaic performance of a non-embedded photocells, the short-circuit current (I_{sc}) and open-circuit voltage (V_{oc}) of a photocell embedded inside the RMP could be predicted.

This generalized model can be extended to incorporate RMPs with non-uniform three-dimensional features (e.g. hemispherical) which were not within the scope of this work.

The generalized model was simplified to represent the experimental scenarios of interest in this work, with experimental results compared against the model-estimated results.

4.2.1 Generalized ray-tracing model

A right-angled cylinder (with its bases given by a function $y=g(x)$) representing the RMP was defined with respect to a three-axis rectangular co-ordinate system (XYZ) as given in Fig. 4.2(a). The intersection between the cylindrical RMP and a plane orthogonal to the bases of the cylinder (parallel to the XZ plane) was defined as the plane of measurement.

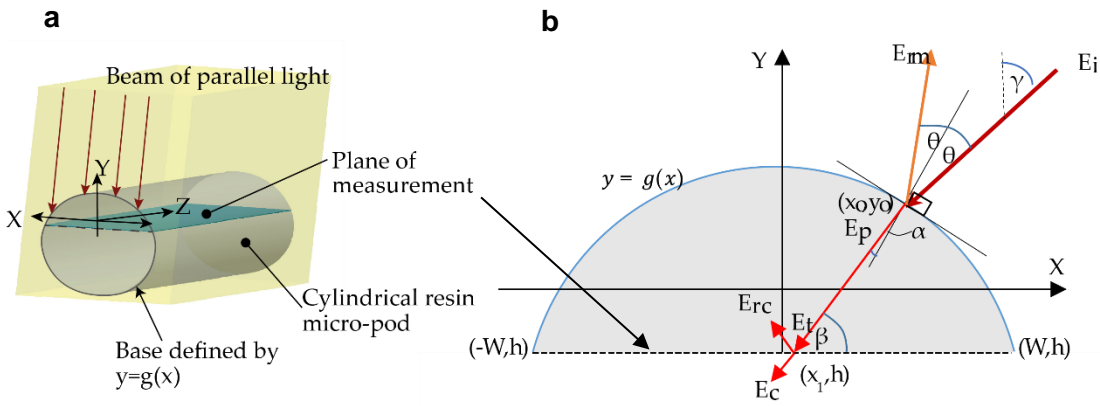


Figure 4.2 – Development of the ray tracing model. (a) Defining the micro-pod geometry and plane of measurement. (b) Illustration of the ray tracing model for a cross section of the micro-pod. The plane of measurement is indicated by green colour.

A single ray of incident light can be considered, as illustrated in Fig. 4.2(b). The ray had an intensity E_i and an angle γ to the vertical axis, which met the boundary of the cylindrical micro-pod defined by $y=g(x)$ at co-ordinates x_0, y_0 . A fraction of the incident ray was reflected (E_{rm}) at the boundary surface and the remaining fraction (E_p) of light was refracted into the RMP. The refracted ray was partially absorbed (attenuated) during its travel inside of the RMP before reaching the plane of measurement (E_t).

Based on the selected geometry, Snell's law for refraction was used to determine the intersection point of the refracted ray and the photoactive plane as given in equation (1).

$$x_1 = x - \left[\frac{g(x)-h}{\tan\beta} \right] \quad (1)$$

Where β was the angle between the transmitted ray E_t and the photoactive plane, which was determined by incident angle of the ray (γ), the tangent angle at the boundary

surface (dy/dx at x_0, y_0) and the refractive index of the micro-pod material (n_r); h was the distance between X-axis and the plane of measurement.

A fraction of the ray (E_{rc}) was partially reflected at the plane of measurement, and the residual ray (E_c) was transmitted to the photocell.

Based on the geometry of the RMP and theory of light absorption, the light transmitted (Keating, 2002) to the photocell at (x_1, h) was given by equation (2).

$$E_c = E_i * (1 - k_m)(1 - k_c) * 10^{-\mu * ([g(x_0) - h] \csc \beta)} \quad (2)$$

where μ was the decadic attenuation coefficient for the micro-pod material, k_m was the fraction of light reflected at the air-micro-pod boundary surface and k_c was the fraction of light reflected at the micro-pod-measurement plane respectively. k_m and k_c were derived using Fresnel equation (Keating, 2002) as shown below.

$$k_m = \left(\frac{1}{2}\right) * \left\{ \left[\frac{\cos \theta - n_r \sqrt{1 - (\sin \theta / n_r)^2}}{\cos \theta + n_r \sqrt{1 - (\sin \theta / n_r)^2}} \right]^2 + \left[\frac{n_r \cos \theta - \sqrt{1 - (\sin \theta / n_r)^2}}{n_r \cos \theta + \sqrt{1 - (\sin \theta / n_r)^2}} \right]^2 \right\} \quad (3.1)$$

$$k_c = \left(\frac{1}{2}\right) * \left\{ \left[\frac{n_r \sin \beta - n_c \sqrt{1 - \left(\frac{n_r}{n_c} \cos \beta\right)^2}}{n_r \sin \beta + n_c \sqrt{1 - \left(\frac{n_r}{n_c} \cos \beta\right)^2}} \right]^2 + \left[\frac{n_p \sin \beta - n_r \sqrt{1 - \left(\frac{n_r}{n_c} \cos \beta\right)^2}}{n_c \sin \beta + n_r \sqrt{1 - \left(\frac{n_r}{n_c} \cos \beta\right)^2}} \right]^2 \right\} \quad (3.2)$$

Here, θ was the angle made by the incident ray to the normal of $y = g(x)$ at x_0, y_0 $\beta x_1, h$ and n_c was the refractive index of the photoactive surface.

The average light intensity (E_{AVG}) between two points (x_a, h) and (x_b, h) on the plane of measurement was given by:

$$E_{Avg} = \frac{\int_{x_a}^{x_b} E_c \sin \beta dx}{x_b - x_a} \quad (4)$$

4.2.2 Deriving the electrical parameters using the ray tracing model

For a photodiode with a rectangular photo-active area embedded inside of an RMP, that has a width equal to the measurement plane discussed in the above ray tracing model, the irradiance intensity on the photodiode E (synonymous to the term E_{AVG} used in the ray tracing model) can be estimated.

The relationships between short-circuit current and irradiance intensity is linear for a photocell (Chegaar *et al.*, 2013). Therefore, the short circuit current for an arbitrary irradiance intensity level E can be given based on a baseline irradiance intensity E_n and the resultant short circuit current I_{scn} as:

$$I_{sc} = I_{scn} \times \left(\frac{E}{E_n} \right) \quad (5.1)$$

For a given irradiance intensity, open-circuit voltage V_{oc} can be given based on a baseline irradiance intensity E_n and the resultant open circuit voltage V_{ocn} as:

$$V_{oc} = V_{ocn} + \frac{nkT}{q} \times \ln \left(\frac{E}{E_n} \right) \quad (5.2)$$

Where n, k, q and T represent the ideality factor for the photocell, Boltzmann Constant, electron charge and absolute temperature respectively (Chegaar *et al.*, 2013).

The performance of a soldered PD without RMP or further modifications was considered the baseline (E_n, I_{scn}, V_{ocn}) for generating theoretically estimated I_{sc} and V_{oc} values. The derived model was subsequently validated experimentally to provide a generalised solution for the encapsulation of optical devices within similar micro-pods. Full details of the mathematical model are provided in Appendix 5.

4.2.3 Simplification of the generalized ray tracing mathematical model

In order to generate theoretical values to compare with the experimental data, the generalized mathematical model was simplified to a cylindrical RMP with a right-angled circular base as illustrated in Fig. 4.3(a), where the diameter of the cylinder was R . The centre of the cylinder in the circular plane was taken as the origin and the boundary surface of the RMP was given by equation (6.1).

$$y = g(x) = \sqrt{(R^2 - x^2)} \quad (6.1)$$

The incident beam of light was normal to the photoactive plane therefore $\gamma = 0$. Based on the defined circular geometry.

$$\theta = \sin^{-1} \left(\frac{x}{R} \right) \quad (6.2)$$

$$\beta = \sin^{-1} \left\{ \frac{\sqrt{(R^2 - x^2)(n_r^2 R^2 - x^2)} + x^2}{n_r R^2} \right\} \quad (6.3)$$

The estimated light intensity distribution at the photoactive plane for PD1 embedded inside of cylindrical RMPs (with circular bases) of different diameters is shown in Fig. 4.3(b).

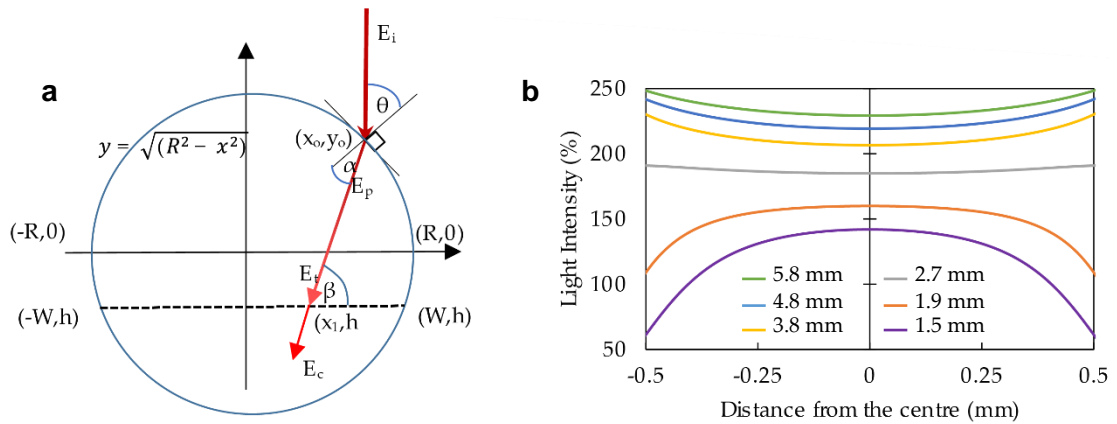


Figure 4.3 – Simplification of the ray-tracing model for a right-circular cylindrical micro-pod. (a) Ray tracing model for a right-circular cylindrical micro-pod. (b) Intensity variation at the measurements plane estimated using the simplified model, for micro-pods with different diameters.

Equations (6.1) - (6.3) were used to simplify the generalized ray tracing model given by equations (4.1) - (4.4) to a micro-pod with circular cross section. To arrive at the estimated I_{SC} and V_{OC} values equations (5.1) - (5.2) were substituted with the corresponding E , E_n , I_{SCN} and V_{OCN} values. The constant nkT/q was derived using the IV curves for the non-embedded devices.

4.2.4 Application of the mathematical model to photodiodes

The photodiodes employed in the study had an epoxy encapsulation window for the protection of the photocell. For simplicity in calculations when applying the mathematical model, the PDs were considered to have an epoxy window with negligible thickness although the actual thickness of this layer was ~ 0.5 mm. Therefore, the use of the simplified model for the PD with negligible epoxy window thickness in the above developed mathematical model needed to be justified. The calculation below verifies that when the effects of optical reflection, refraction and absorption were considered, this simplification made an insignificant difference on the irradiance intensity at the photoactive plane for all scenarios discussed within this chapter.

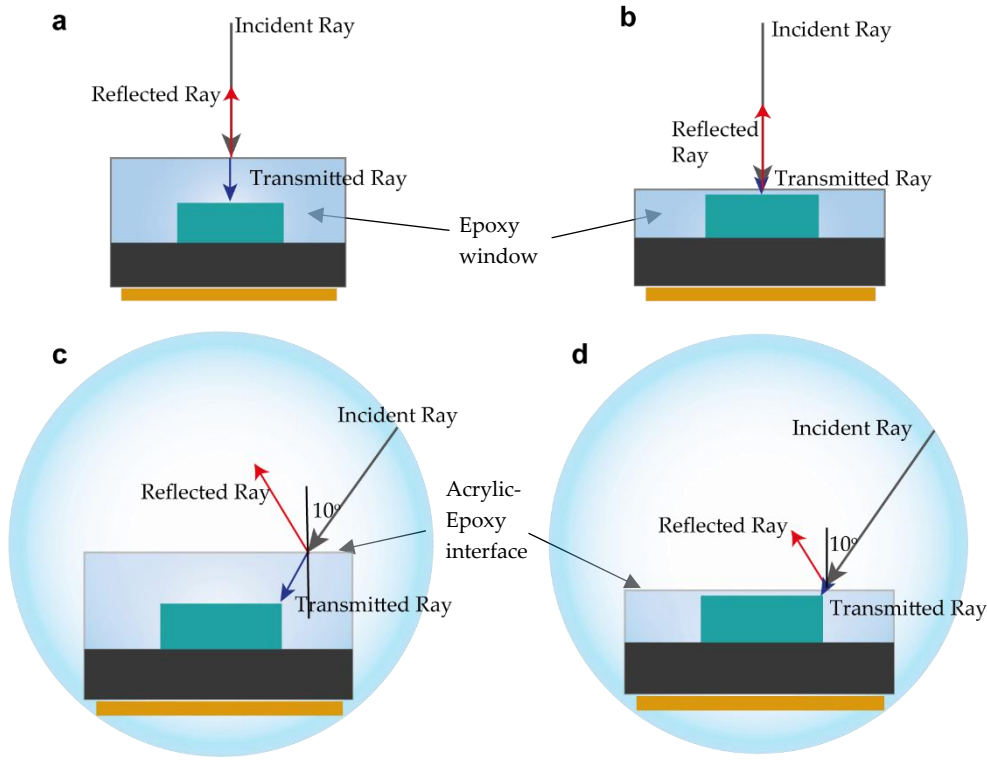


Figure 4.4 - Comparison photodiode (PD) configurations. (a) Actual PD before encapsulation. (b) Model defined PD before encapsulation. (c) Actual PD after encapsulation. (d) Model defined PD after encapsulation.

Before encapsulation

When the actual PD and model defined PD configurations were compared before encapsulation, the loss in transmission due to Fresnel reflection (partial reflectance at material interfaces) was the same due to the same acrylic-epoxy material interfaces present in both the cases. The reduction of intensity due to absorption of light by the epoxy material for actual PD configuration is given as:

$$\begin{aligned} &\% \text{ optical absorption by the epoxy layer with } 0.5\text{mm thickness} \\ &= (1 - 10^{-(.5 \times 0.0001)}) * 100 = 0.0115\% \end{aligned}$$

The model-defined configuration only had a fraction of the above loss due to the thinness of the epoxy layer.

After encapsulation

If a ray which passes the air-acrylic resin interface, enters the acrylic material, reaching an edge of the photoactive material is considered, calculations show that the ray reaches

the acrylic material at an angle no more than 10° to the vertical axis, for all the scenarios discussed in this thesis for both PD types. Both the rays shown in Fig 4.4(c) and Fig 4.4(d) cross the same material interfaces, therefore the reduction in transmittance due to Fresnel reflectance is the same. Since the epoxy layer in the simplified consideration is very thin, the effect of refraction can be neglected.

From Snell's law the angle of a transmitted ray into the epoxy material is given by θ as below.

$$1.51 \sin(10^\circ) = 1.55 \sin \theta \Rightarrow \theta = 9.74^\circ$$

The deflection (d) of the incident ray due to refraction within the PD can be calculated as below for an epoxy layer thickness of 0.5 mm (the actual epoxy layer thicknesses of PDs are less 0.5 mm).

$$d = 0.5(\tan 10^\circ - \tan 9.74^\circ) \Rightarrow d = 0.00234 \text{ mm}$$

This deflection was negligible compared to the width (0.92 mm) of the photoactive material (less than 0.25%) of the photo cell. Additionally, similar attenuation coefficients for the acrylic and epoxy materials resulted in a negligible difference in losses due to optical absorption.

Based on the above calculations, it can be concluded that the physical differences between the actual PDs and simplified PD configuration used for estimations had a negligible difference on light intensity calculated at the photoactive plane.

4.3 Empirical study on the effect of resin micro-pod on photodiode performance

Experiments were conducted using two types of commercial surface mount device (SMD) silicon P-I-N type PDs (TEMD7000x1 and VEMD6060x1 from Vishay Intertechnology Inc., Malvern, PA, USA), hereafter referred to as PD1 and PD2 respectively. The effect of RMP size, resin type, position of the PD inside of the RMP, and the fibrous sheath on short circuit current (I_{sc}) and open-circuit voltage (V_{oc}) of the PDs in photovoltaic mode (zero bias) (Deen and Basu, 2012; Saito, 2012) were experimentally determined.

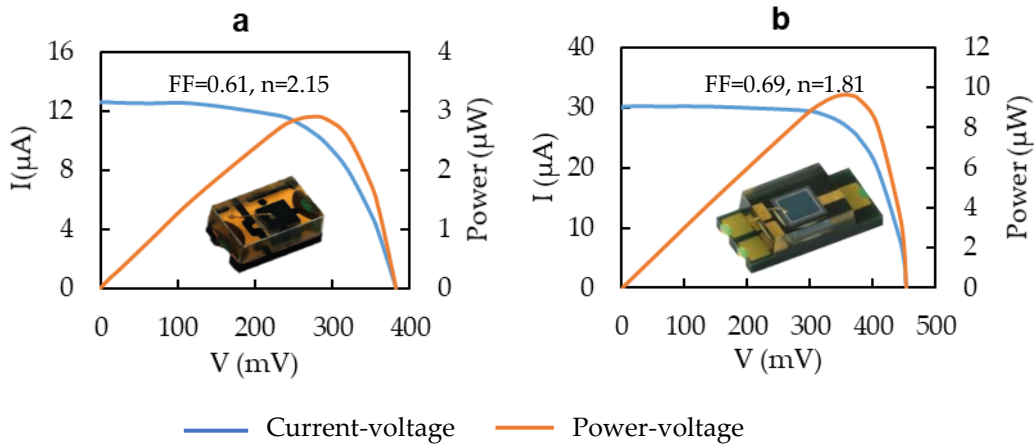


Figure. 4.5 - Characteristic curves for the two photodiode (PD) types employed in the experiments. (a) TEMD 7000 × 01 (PD1). (e) VEMD 6060 × 01 (PD2).

Fig. 4.5 depicts typical characteristic curves (current-voltage and power-voltage) for the two PD types, generated under the optical test-rig at base line test conditions produced by supplying a 12 V/0.89 A input to the lamp and without using light filters along with the corresponding fill factors (FF) of and ideality factors. PD2 had a larger area to perimeter ratio, and showed a ~13% higher fill factor and a lower ideality factor compared to PD1, this was possibly due to lower edge recombination of charge carriers (Fell *et al.*, 2018).

4.3.1 Variation analysis for TEMD 7000x01 before and after encapsulating inside RMPs.

Thirty samples created using PD1 were tested using the optical test rig under baseline test conditions, with I_{sc} and V_{oc} recorded. The soldered PDs showed an average, standard deviation (SD) and co-efficient of variation (CV) of 12.87 μA, 1.14 μA and 8.86 % for I_{sc} (Fig. 4.6(a)) and 0.381 V, 0.0045 V and 1.18 % for V_{oc} values (Fig. 4.6(b)).

Twenty of the thirty soldered PDs were randomly selected and encapsulated inside of cylindrical RMPs with a ~2.7mm diameter using the Dymax 9001E-V3.5 acrylated urethane resin (Dymax, 9001E-V3.5, Dymax Corporation, Torrington, CT, USA; this resin was used throughout this work unless otherwise specified). The PDs were encapsulated at the lowest possible level of the resultant RMP. The encapsulated samples had average, SD and CV values of 23.20 μA, 1.88 and 8.12 % for I_{sc} (Fig. 4.6(a)) and 0.4101 V, 0.0040 and 0.97 % for V_{oc} (Fig. 4.6(b)). From these results, it was clear that there was a significant increase in I_{sc} and V_{oc} values after the encapsulation, which

provided evidence of a light concentrator effect of the RMP. There was a variation in the I_{sc} values before the encapsulation process, which remained unaltered after the encapsulation, indicating that no measurable variation was introduced to the I_{sc} values by the encapsulation process. These variations were within the manufacturer's specifications and therefore strict quality checking was not considered a requirement.

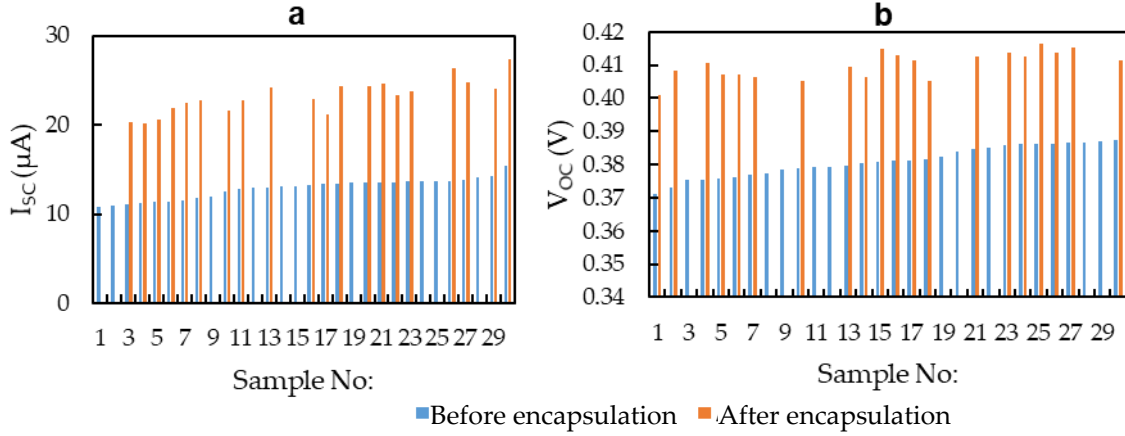


Figure 4.6 - Variation analysis of TEMD 7000 \times 1 Photodiode before and after encapsulation inside 2.7mm micro-pods in standard PD configuration. (a) Short circuit current. (b) Open circuit voltage.

4.3.2 Effect of micro-pod diameter

Sets of PD1s soldered onto fine copper wires were encapsulated with 1.5 mm, 1.9 mm, 2.7 mm, 3.8 mm, 4.8 mm and 5.8 mm diameter RMPs using the clear acrylated urethane resin. Similarly, sets of PD2s were soldered onto fine copper interconnects and were then encapsulated creating PD2s encapsulated within RMPs with 2.7 mm, 3.8 mm, 4.8 mm and 5.8 mm diameters. A 5.8 mm outer diameter RMP would produce a final E-yarn that was significantly larger than desirable for a wearable application, therefore larger RMP sizes were not investigated. The PDs were positioned at the bottom of the resultant RMP (hereafter referred to as the standard PD configuration): Therefore, the exact depth of the PD within the RMP also varied with the micro-pod diameter as depicted in Appendix 6.

The I_{sc} and V_{oc} values were recorded and are illustrated in Fig. 4.7, along with the values predicted by the mathematical model. Both the I_{sc} and V_{oc} values for PD1 showed an increase in values up to a 4 mm diameter RMP, which plateaued afterwards. In the case

of PD2, despite the increase in I_{sc} and V_{oc} values, the plateau effect was indistinct for the RMP sizes tested for this experiment.

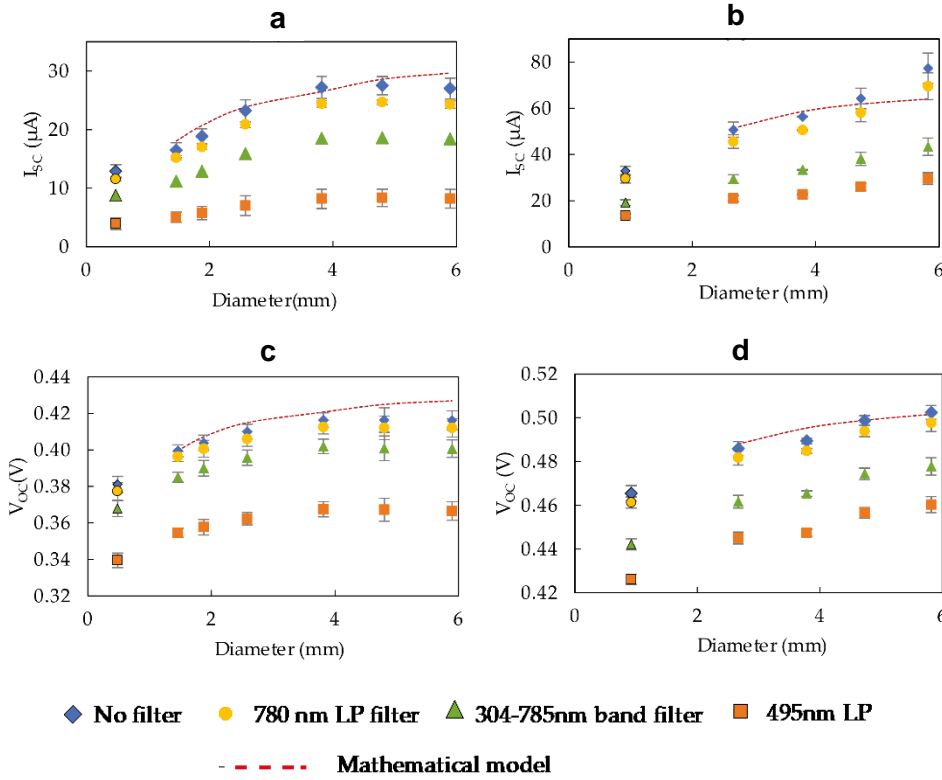


Figure 4.7 - Effect of micro-pod diameter on short-circuit current (I_{sc}) and open-circuit voltage (V_{oc}) for photodiodes (PDs) embedded in the standard configuration under different optical filters. (a) I_{sc} compared to RMP diameter for TEMD 7000 $\times 1$. (b) I_{sc} compared to RMP diameter for VEMD 6060 $\times 1$. (c) V_{oc} compared to RMP diameter for TEMD 7000 $\times 1$. (d) V_{oc} compared to RMP diameter for VEMD 6060 $\times 1$. In all the cases the first data point of each data series (demarcated using a marker with a black border) indicated the I_{sc} and V_{oc} values against the width of the photoactive area for non-encapsulated PDs.

Fig. 4.8 showed I_{sc} and V_{oc} measurements under three different optical filters normalized to the corresponding measurement without an optical filter for PD1 and PD2. These values remained constant for both the PDs before and after encapsulation inside RMPs of different diameters. This indicated that the spectral band of the light received by the photoactive chip of the PD did not change with the diameter of the RMP. This was an important result as different spectral wavelengths could be relevant to different use cases. The incident light spectrum may vary based on the ambient conditions, and in some instances the available light source may not be direct sunlight (e.g. artificial lighting that has a different light spectrum). Also, the fibre sheath and micro-pod could take different colours based on the aesthetic requirements that act as a light filter.

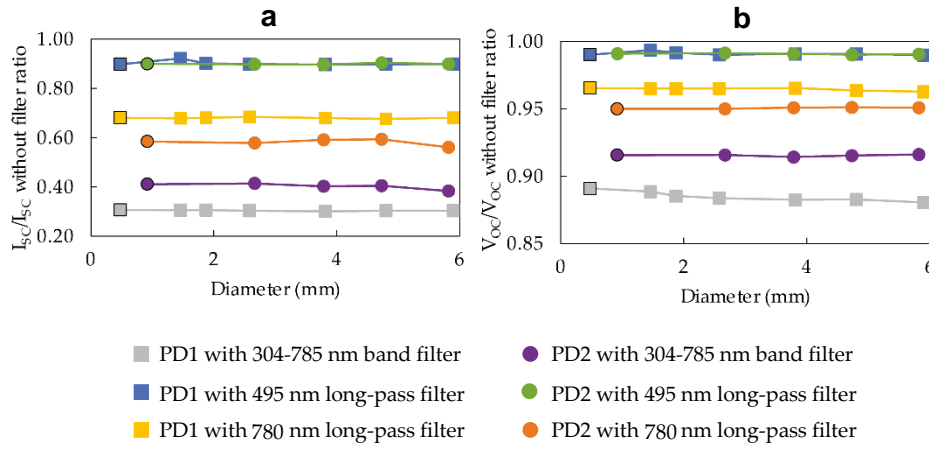


Figure 4.8 - (a) The ratio between I_{sc} with and without optical filter compared to the micro-pod diameter. (b) The ratio between V_{oc} with and without optical filter compared to the micro-pod diameter. In all the cases, first data point of each data series (demarcated with a black border) indicate the I_{sc} and V_{oc} values against the width of the photoactive area for non-encapsulated photodiodes (PD1-TEMD 7000 \times 01, PD2 - VEMD 6060 \times 01).

An estimation of I_{sc} and V_{oc} values were calculated using the mathematical model and compared with the experimental data points, with a mean average percentage error (MAPE) subsequently calculated. The mathematical model estimated values exhibited a close fit with the experimental data with MAPEs of 7.38% for I_{sc} and 1.40% for V_{oc} for PD1 and 8.13% for I_{sc} and 0.43% for V_{oc} for PD2, considering all RMP sizes. When RMP sizes up to 4.8 mm were considered for PD2, the MAPEs improved to 5.57% for I_{sc} and 0.33% for V_{oc} indicating the better fit of the model within these boundary conditions. Therefore, it can be concluded that the developed mathematical model was suitable for predicting I_{sc} and V_{oc} values for both PD types within the given error percentages, providing a useful general solution.

4.3.3 Effect of the depth of positioning the photodiode inside of the resin micro-pod

PDs were embedded inside of 2.7 mm diameter RMPs at three depth levels (the standard PD configuration of extreme bottom, at the extreme top, and at the centre). Microscopic images of the RMPs confirmed that the level of accuracy of the PDs positioning inside RMPs to be within $\sim \pm 5\%$ (detailed in Appendix 6). The experimental results for I_{sc} and V_{oc} are presented against the depth to RMP diameter ratio (hereafter referred to as DDR) in Fig. 4.8 along with predicted values from the mathematical model for different RMP diameters (1.5 mm, 2.7 mm, and 5.8 mm for PD1 and 2.7 mm, and 5.8 mm for PD2).

The results (Fig. 4.9) confirmed that the depth of the photocell within the RMP was a key determining factor in the opto-electronic performance. The mathematical model predicted values showed a good fit with the experimental data with a MAPE of 7.41% and 6.25% for I_{sc} and 1.36% and 0.80% for V_{oc} for PD1 and PD2 respectively. This further confirmed the utility of the mathematical model for accurate predictions of I_{sc} and V_{oc} values.

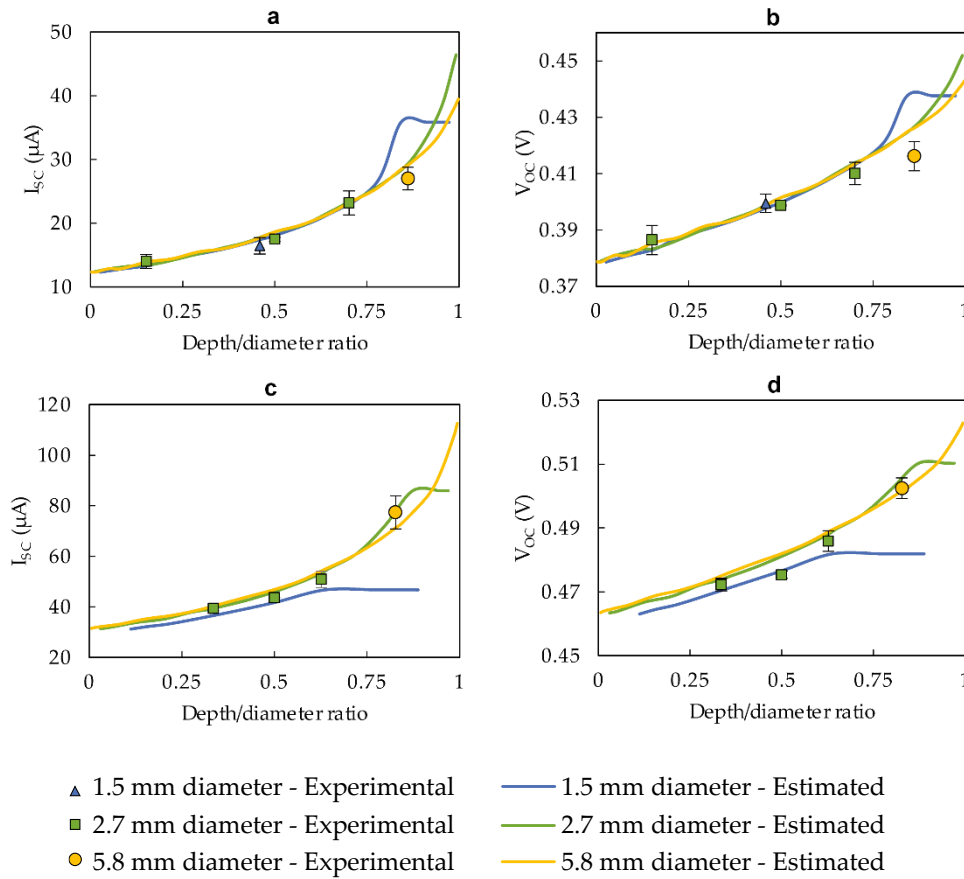


Figure 4.9 - Effect of depth on short-circuit current (I_{sc}) and open-circuit voltage (V_{oc}) for photodiode embedded resin micro-pods with different diameters. Experimental and mathematical model estimated values given for (a) I_{sc} compared to depth/diameter ratio for TEMD 7000 $\times 1$, (b) V_{oc} against depth/diameter ratio for TEMD 7000 $\times 1$, (c) I_{sc} against depth/diameter ratio for VEMD 6060 $\times 1$ and (d) V_{oc} against depth/diameter ratio for VEMD 6060 $\times 1$. Measurements conducted using the optical test rig without optical filters.

Based on the predicted values, it was clear that the PD diameter did not have a direct effect on the I_{sc} and V_{oc} for up to a ~ 0.75 DDR for PD1. The model predicted that for PD1, a 1.5 mm diameter RMP would yield maximum I_{sc} and V_{oc} at around ~ 0.85 DDR. In the case of PD2, the 2.7 mm diameter RMPs generated the maximum values for I_{sc} and V_{oc} , at a DDR of around 0.87. For PD2, it was not possible to fabricate 1.5 mm RMPs

since the SMD packaging of PD2 was 2.0 mm wide. Nevertheless, the mathematical model predicted that the I_{sc} and V_{oc} values for the photoactive chip (~0.9mm wide) of the PD2 embedded inside of a 1.5 mm RMP would reach a maximum value at around a DDR of 0.65. These values were significantly lower than the corresponding maximum values of PD2 embedded within 2.7 mm and 5.8 mm diameter RMPs.

These experimental results along with the mathematical model estimations indicated that DDR was a key parameter when optimising opto-electronic characteristic: DDR showed a greater direct influence on the PD performance than the absolute values of depth or the diameter of the micro-pods. In general, higher DDRs yielded higher values for I_{sc} and V_{oc} . Nevertheless, in certain cases there existed peak I_{sc} and V_{oc} points beyond which a marginal decrease in I_{sc} and V_{oc} was observed. This was attributed to the diversion of rays away from the photoactive area of the PD and an increase in the path length of the light inside the RMP (leading to greater light absorption). As mentioned previously, in practical scenarios, it was not always possible to achieve DDRs that yield the theoretical maximum I_{sc}/V_{oc} value due to the thickness and width of the PD.

When the results for PD1 and PD2 were compared it was clear that the RMP diameters that realised the highest I_{sc}/V_{oc} values were different for each PD type. This was an indication that the width of the photoactive plane was also a key determining factor in selecting the size of the RMP. The RMP should be large enough to accommodate the photoactive device and there may exist a practical maximum RMP diameter value owing to the design constraints governed by the end applications and process parameters. It is important to examine how the I_{sc} and V_{oc} values behave within these limits to determine the most suitable RMP diameter.

4.3.4 Effect of the micro-pod material

The effects of the material properties of elements used in optical systems are well understood: They can define how electromagnetic waves reflect, refract and get absorbed, for an optical element with a given geometry.

Experiments were conducted using five different types of resins (including the standard resin) by embedding PD1 type within RMPs of 2.7 mm diameter (in the standard PD configuration). These resins had refractive indices ranging from 1.404 to 1.560 (this was

the widest range of refractive indices for a clear polymer resin readily available commercially). Except for the 9001 EV-3.5 and OP 29 which were UV curable acrylic resins, the other resin types used were room-temperature vulcanized (RTV) resins. Therefore, resin micro-pods using the RTV resins were prepared by letting the resin cure at an elevated temperature ($\sim 40^{\circ}\text{C}$) for ~ 4 hours after injecting the resins into a mould. All the resins tested have been utilised by the electronic industry and have been specifically developed for encapsulating and bonding electronic or optic devices. As the resultant RMPs exhibited different levels of shrinkages after UV curing, experimental results were normalized based on the diameter of the RMP produced with standard resin to provide comparable I_{sc} and V_{oc} values. The results were plotted against the refractive indices as depicted in Fig. 4.10. In addition, the mathematical model estimated I_{sc} and V_{oc} values were indicated in the same figures.

The results indicated an overall increasing trend in I_{sc} and V_{oc} values with the increase in the refractive index. The silicone-based resin OPT 7020 yielded the lowest I_{sc} while the optical grade acrylated urethane resin OP29 exhibited the highest I_{sc} values, which was $\sim 15\%$ higher than the standard resin (9001 EV-3.5). Nevertheless, considering the proven suitability for electronic applications (better resistance to moisture and thermal cycling), lower hardness, and price the 9001 EV-3.5 resin was continued as the material used for preparing micro-pods in further work.

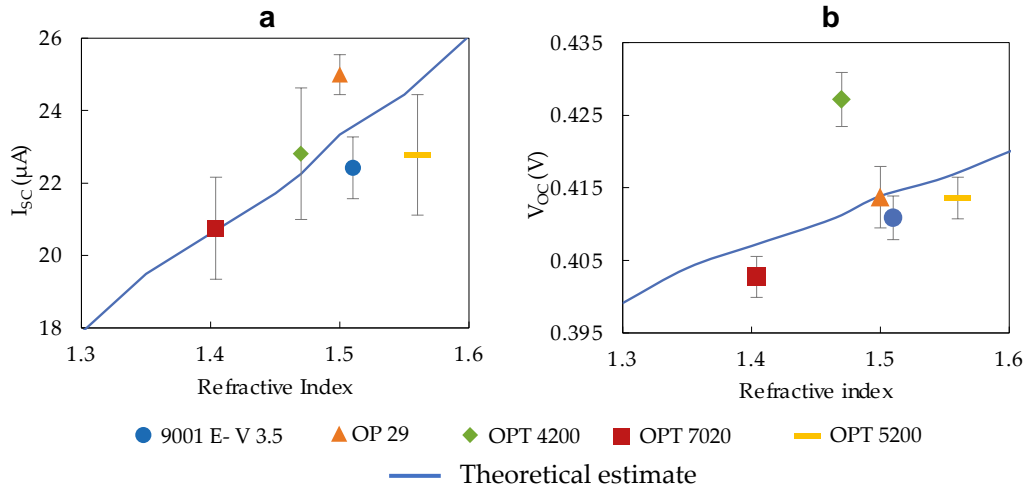


Figure 4.10 - Effect of resin material type on short-circuit current (I_{sc}) and open-circuit voltage (V_{oc}) for photodiode embedded resin micro-pods. Experimental and mathematical model estimated values given for TEMD 7000 $\times 1$ embedded inside 2.7mm diameter micro-pod in the standard configuration. (a) I_{sc} compared to refractive index. (b) V_{oc} compared to refractive index. The blue line indicates the mathematical model predicted values with a decadic attenuation coefficient of 0.0001 dB/mm.

It was noteworthy that for the RMP geometries considered in this study, the refractive index had a significantly higher impact than the attenuation coefficient on the irradiance intensity measured at the photoactive plane. The refractive index governs the ray concentrating effects, while also defining the reflective losses (at material boundaries), which are significant in magnitude. As an example, in the case of a 2.7 mm diameter RMP made of the standard resin (1.51 refractive index and 0.0001 dB/mm attenuation coefficient), theoretical values for the percentage of light reflected at the surface of the RMP and the percentage absorbed by the RMP were $\sim 4\%$ and less than 0.05 % respectively. The model-estimated values for each data point were calculated based on the assumption that all of the resins absorbed light in a similar way, which may not have been the case (Knoll, 2006), as detailed information on attenuation coefficient of all the resin-types was not forthcoming in the literature. When compared with the experimental data, the mathematical model exhibited a MAPE of 6.03 % and 1.44 % for I_{sc} and V_{oc} values respectively, which indicated a good fit.

4.4 Photodiode embedded electronic yarns

PD E-yarns (PDEY)s with PD1 and PD2 type devices were realized by encapsulating them inside of 2.7 mm diameter RMPs in the standard PD configuration and finally

integrating them within a fibrous sheath (2.7 mm was the smallest RMP size that could be employed for both PD types) as depicted in Fig. 4.10. PDEYs with 1.5 mm diameter RMPs were prepared only using PD1 type devices.

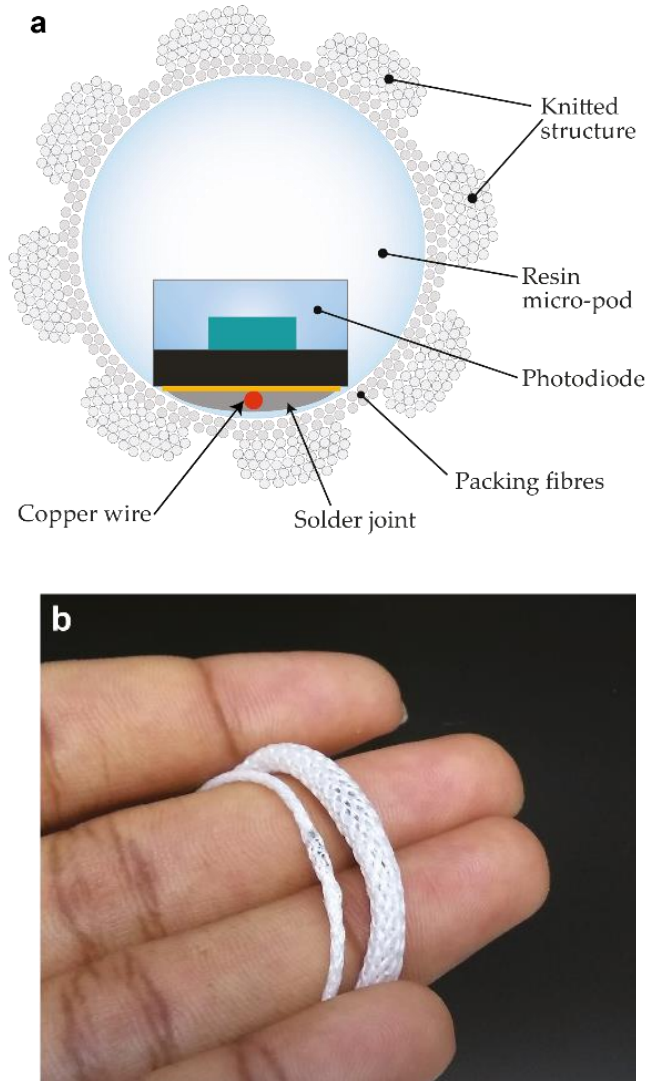


Figure 4.11 – (a) Cross sectional illustration of photodiode embedded yarn. (b) Image of two photodiode embedded yarns (Thin yarn – TEMD 7000 embedded in 1.5mm micropod and in 2mm knit braid. Thick yarn – VEMD 6060 embedded in 5.8mm micro-pod and 6mm knit braid).

The structure of the PDEYs and images of the devices after each step in the fabrication process are given in Fig. 4.11 (a-g). The finalized PDEY had a maximum outer diameter of ~4.4 mm and a minimum diameter of ~4mm.

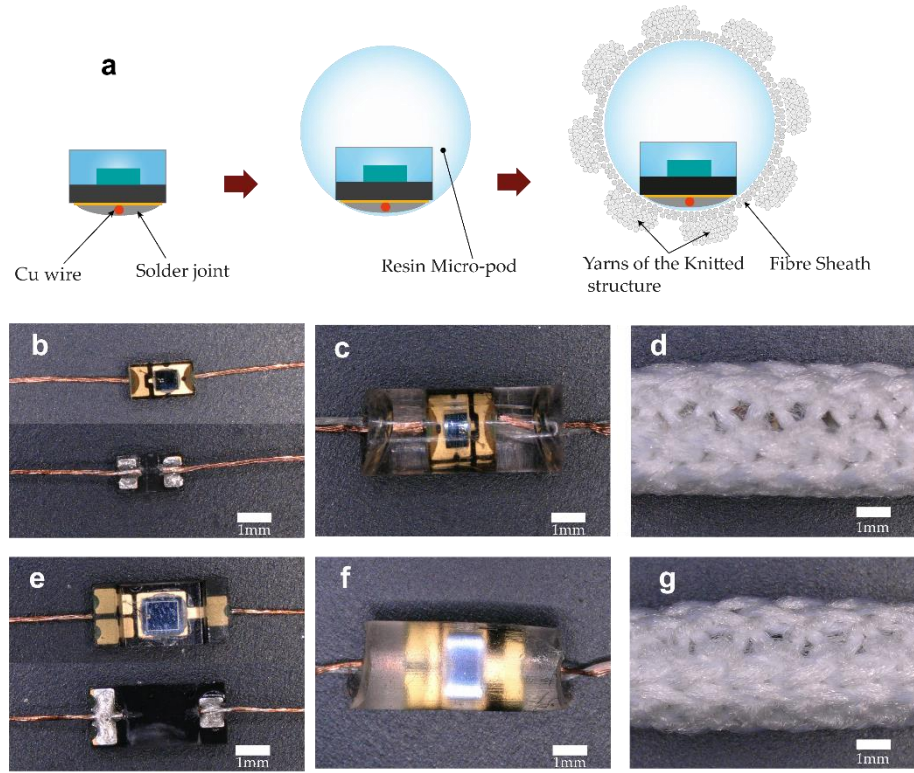


Figure 4.12 – Appearances of photodiode (PD) embedded yarns at different stages of the fabrication process. (a) Schematic cross-sectional view of PD devices, top view images of (b-d) TEMD 7000 ×1 type and (e-g) VEMD 6060 ×1 type PD devices after being soldered to copper wires, after being embedded inside of resin micro-pods, and in the completed yarn form respectively.

4.4.1 Performance of photodiode embedded E-yarns

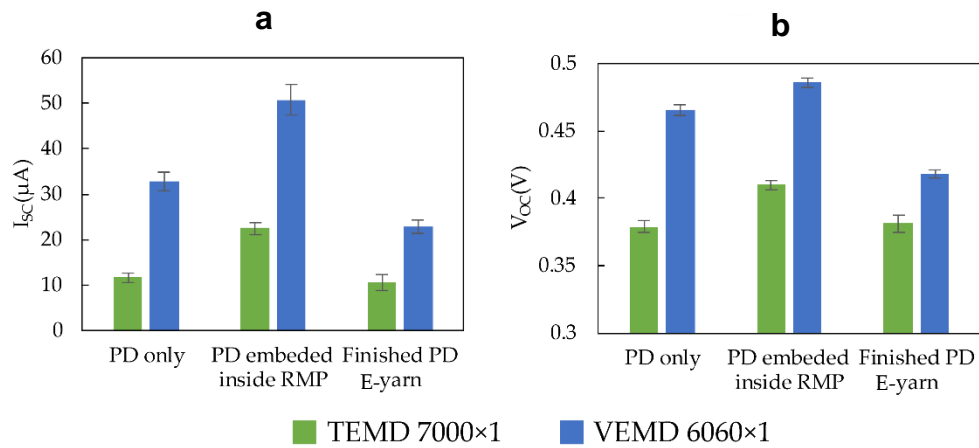


Figure 4.13 – Comparison of experimental (a) short-circuit current (I_{sc}) and (b) open-circuit voltage (V_{oc}) TEMD 7000 ×1 and VEMD 6060 ×01 before encapsulation, after embedding inside resin micro-pods of 2.7mm diameter (standard resin in the standard PD configuration), and for the completed PD yarn (with the same RMP, sheathing fibres and knitted structure). Measurements conducted using the optical test rig at baseline conditions.

It was evident that the sheathing fibres and knit-braid structure had a negative effect on the I_{sc} and V_{oc} , due to the reduction of light flux on to the RMP caused by scattering (Aliaga *et al.*, 2017) and absorption (Pelton, 2002) of light by the fibres (see comparative results in Fig. 4.13. Nevertheless, the finished PDEY generated I_{sc} and V_{oc} values comparable to the original PDs.

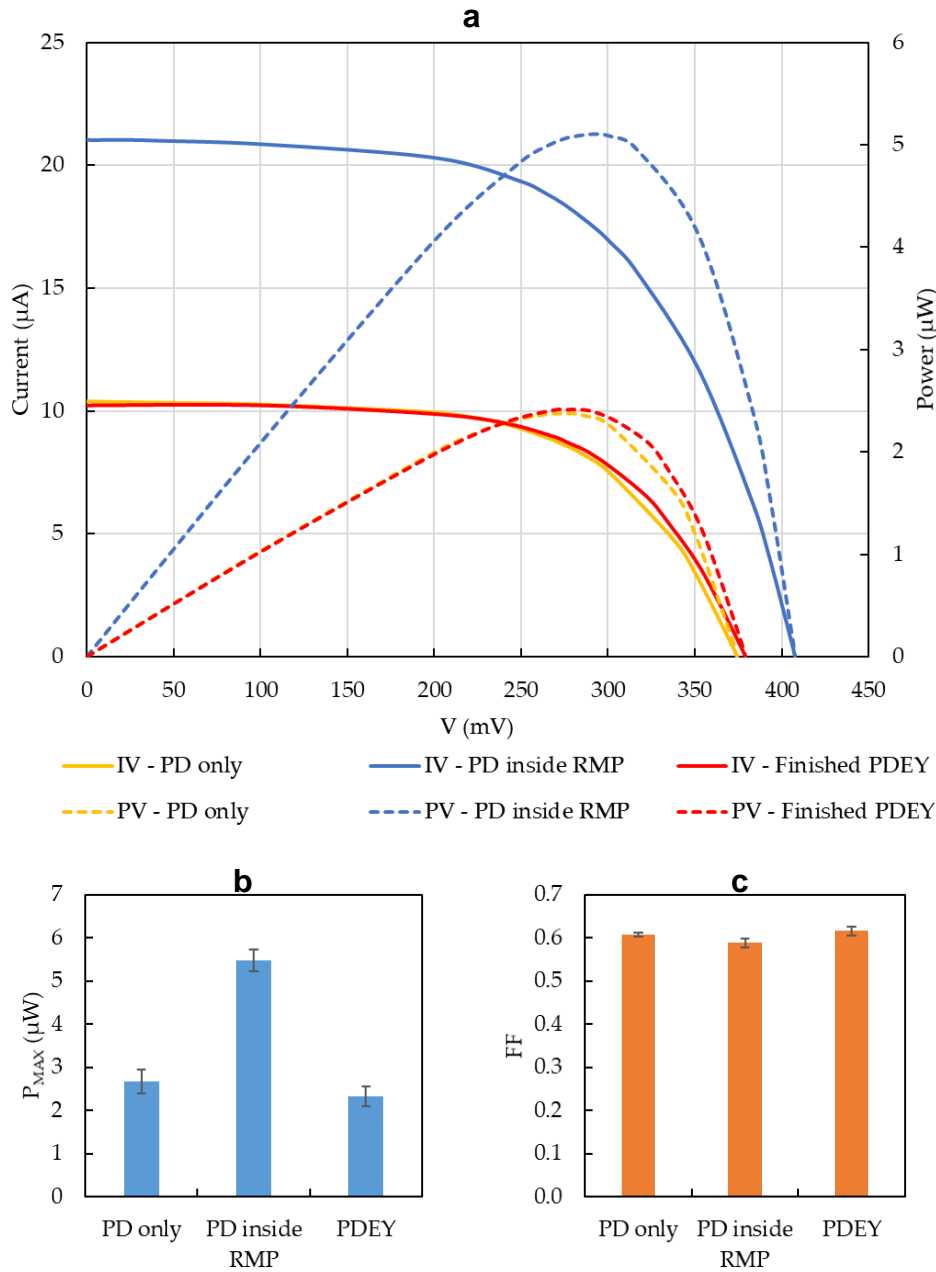


Figure 4.14 – (a) Example current-voltage (IV) and power-voltage (PV) curves for one sample. (b) Maximum power (P_{MAX}), and (c) fill factor (FF) for TEMD 7000 \times 1 photodiode (PD) devices at different stages of the PD E-yarn (PDEY) fabrication process based on five IV and PV curves. Resin micro-pod (RMP) diameter 2.7 mm and yarn thickness was 4mm.

A further analysis was conducted for PD1 by generating I-V and P-V under the standard test conditions using the optical test rig at different stages of the PDEY fabrication process (Fig 4.14). The maximum power output (P_{MAX}) and FF (fill factor) were estimated using the data from Fig. 4.14(a) showing example I-V and P-V curves for one sample and derived P_{MAX} and FF values based on five IV and PV curves in Fig. 4.14(b-c).

The results clearly show the positive effects of the RMP on the power output, and subsequent reduction in power output due to the fibrous sheath. Nevertheless, in comparison to the un-embedded device, the PDEY showed no significant change in P_{MAX} , suggesting that the micro-pod and the fibrous sheath had approximately equal but opposite effect on the power density at the photoactive area of the PD.

4.4.2 Individual and combined effect of the components

To understand the individual effects of the RMP, packing fibres and the knit-braided structure on the performance of the PDEYs, a series of PD1 embedded devices with different constructions were fabricated and I_{sc} measurements were conducted, as shown in Fig. 4.14 below. These yarns had an RMP of 1.5 mm (with the PD in standard PD configuration) and final E-yarn thickness of ~2.0 mm. A 1.5 mm diameter RMP was used for these experiments, as this was the smallest possible yarn diameter achievable for PD1 out of the RMP sizes tested.

As discussed previously, the light concentrating effects of the RMP were evident with a 23 % increase in I_{sc} for PD with the RMP (Fig. 4.13 a (ii)) compared to PD only (Fig. 4.13 a (i)). This was reduced by around 48% after covering the RMP with the knit-braided fibrous sheath (Fig. 4.13a (v)). When the E-yarn was made without packing fibres (Fig. 4.13a (iv)) the I_{sc} values were ~29% lower than the PD with the RMP values. When the E-yarn was made without a micro-pod (Fig. 4.13a (iii); the soldered PD was manually inserted into a knit-braid structure), the I_{sc} values were 39% lower than for the PD only (Fig. 4.13a (i)) value, which showed the combined shading effect of the packing fibres and the knit-braid on the PD.

These results provided a clear indication of the individual and combined effects of the RMP, packing fibres and the knit-braid structure on the amount of light transmitted to the photosensitive area of the PD. The knit-braid (linear density of the knit-braid ~385mg/m) showed a higher shading effect than the packing fibres (linear density of

packing fibres $\sim 70\text{mg/m}$), due to the higher fibre density created by the loop structure of the knit.

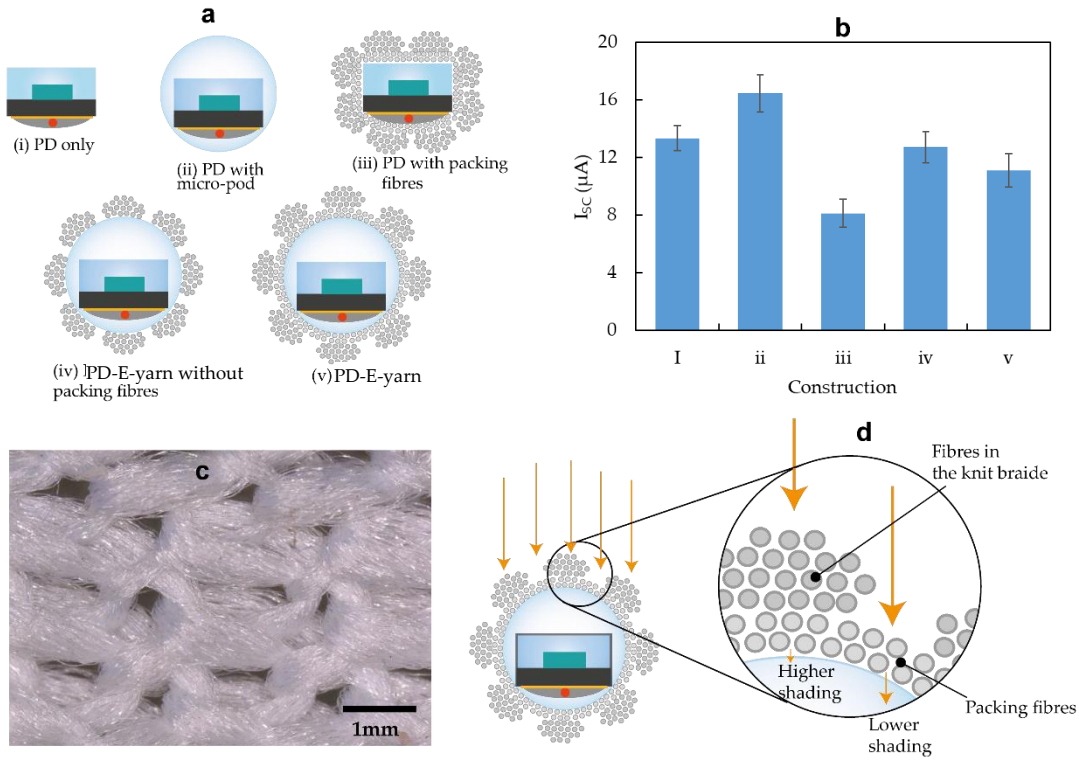


Figure 4.15 – Individual effect of different components of the PD embedded yarn on the short circuit current (I_{sc}). (a) Schematic cross-sectional view of different yarn constructions with PD1. (b) The I_{sc} values for each yarn construction under full spectral incident light using the optical test rig. (c) Microscopic image of the knit braid structure. (d) Schematic depicting the transmission of light through the packing fibres and knit braid structure in the fibrous sheath.

The shading effect of the composite fibrous sheath can be attributed to the amount of light scattered and absorbed (attenuated) by the fibres in the sheath. The knit-braid has a semi-open tubular structure (Fig. 4.13c) where a proportion of the light can be directly transferred to the interior (packing fibre layer) of the PD-E-yarn through the openings without scattering or absorption. The degree of openness of a knitted structure is defined by the porosity (Gong, 2015), which is dependent on the thickness of the yarns and loop structure of the knitted fabric. A proportion of the light that was received by the yarns in the knit-braid was partially reflected or scattered at the surface of the fibres of the yarn. Each individual fibre will scatter a fraction of incident light depending on the refractive index of the fibre material. Therefore, the total amount of light transmitted

through the knit-braided sheath and packing fibres would decay exponentially with fibre density as further discussed in *Chapter 5*. Polyester fibres typically have an refractive index of ~ 1.54 (Morton *et al.*, 2008) meaning that 4 - 5 % of the incident light was reflected by a single fibre.

Light penetrating into the fibre was absorbed by the polymer and delustrants present within the fibre (Morton *et al.*, 2008). The light absorption contributed significantly less than the light scattering, especially for the fine and white/light colour fibres employed in this study. Due to these phenomena, only a proportion of the incident light would be transferred through the bundle of fibres to the inner layer of the yarn. The same effect, with a lower magnitude, was given by the packing fibres since the number of fibres were smaller than that of the knit-braid.

4.4.3 Effect of resin-impregnation

It was clear that the Fresnel reflection at the fibre surfaces caused light scattering, resulting in a reduction in the light penetrating into the core of the PDEY. According to theory this was caused by the difference in refractive indices of the materials on either side of the material boundaries, which in this case were the refractive indices of polyester and air. A preliminary experiment was conducted by impregnating the fibrous sheath with the optically clear resin, thereby replacing the air pockets between the fibres with the resin which had a refractive index similar to the fibre material. The results showed a significant enhancement of I_{sc} , it was speculated that this enhancement of light transmission was caused by reduced Fresnel reflection.

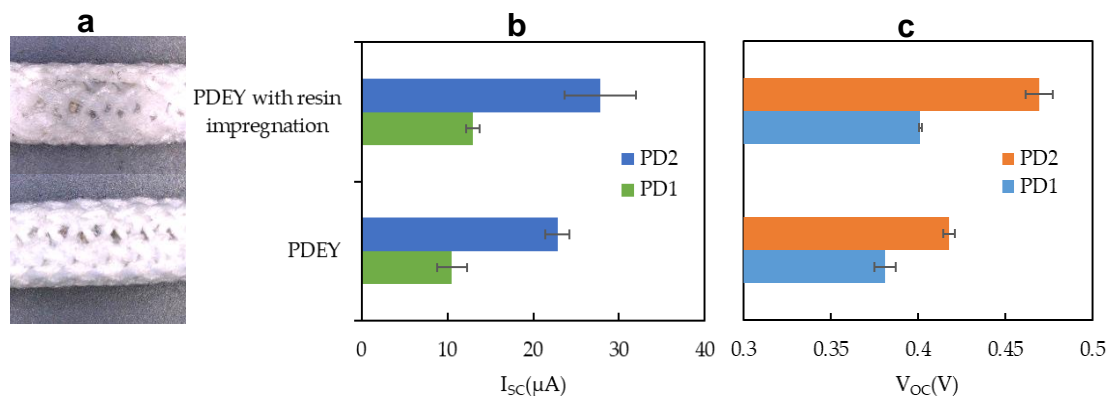


Figure 4.16 – Change in (a) appearance, (b) short-circuit current (I_{sc}) and (c) open-circuit voltage (V_{oc}) after resin impregnation for photodiode embedded E-yarns (PDEY) prepared with TEMD 7000 $\times 1$ (PD1) and VEMD 6060 $\times 1$ (PD2) 2.7 mm diameter resin micro-pods and 4 mm diameter fibrous sheath. Measurements conducted using the optical test rig at

4.5 Conclusions

The effects of the RMP geometry and material on the opto-electronic properties (short circuit current and open circuit voltage) of the PD E-yarns were investigated in detail empirically and by using a mathematical model. The experimental data exhibited a good fit with the mathematical model, which proved the utility of the model in establishing design rules for the PD E-yarns within given constraints. The results indicated that for the two PD types discussed in this work, the depth (represented as a ratio of the diameter of the micro-pod) at which the photoactive plane of the PD was positioned inside the RMP was a key factor in determining the I_{sc} and V_{oc} values. The experiments conducted with PD embedded within micro-pods made from a series of resin types (with a range of refractive indices) showed the positive effect that higher refractive indexes had on I_{sc} and V_{oc} .

The results of the experiments conducted with the PD embedded E-yarns revealed that the I_{sc} and V_{oc} values of the finished yarn were comparable to the values produced by bare PDs, and lower than the values of PDs embedded inside the micro-pods. The knit-braid structure of the fibrous sheath was the main reason for this reduction, while the packing fibres also contributed. This reduction in performance could be minimized by impregnating the fibrous sheath with a clear polymeric resin, reducing Fresnel reflection. In general, I_{sc} was highly sensitive to the variations in the geometry and material type of the yarn components (due to the linear relationship between I_{sc} and light intensity), while V_{oc} values varied modestly with similar variations (due to the logarithmic relationship between V_{oc} and light intensity).

With the results obtained for PD embedded E-yarns using this technique, there was no doubt that the integration of various types of photocells inside of textile yarns was a technically viable proposition for applications including energy harvesting and optical sensing. Further, the development of a generalised theoretical model allows for the creation of optimised E-yarn designs for other miniaturized opto-electronic devices and textile based optical sensing.

Chapter 5

Solar Cell Embedded Yarn

5.1 Introduction

This chapter builds on the work demonstrated in *Chapter 4* by embedding solar cells (SCs) within textile yarns, which is a critical step towards the development of a solar energy harvesting textile. Due to the unavailability of sufficiently small SCs (small enough to be embedded within a yarn), custom-made miniature SCs (MSC) were prepared in collaboration with a photovoltaic cell manufacturer (Solar Capture Technologies, UK), who laser cut standard size crystalline silicon SCs to the required specifications. The photodiodes employed in the preliminary work had a small photoactive footprint relative to the size of the device (device footprint = 2.5 mm^2 , photoactive area = 0.23 mm^2); in contrast, most part of the front face of the MSCs employed in this work were photoactive. The MSCs also had a significantly different solder-pad configuration to the surface mount device (SMD) photodiodes, with solder-pads on both the front and back side of the MSC. Therefore, the soldering techniques employed to solder PDs had to be modified to successfully create electrical connections between the solder pads and the copper wires. Using SCs embedded in micro-pods with different diameters, the mathematical model developed in *Chapter 4* was further validated. However, the micro-pod diameter was maintained at 1.6 mm for most of the experimental work presented in the chapter due to design and process boundary conditions.

The majority of the work in this chapter presents the characterisation of solar-E-yarns that contain a single embedded MSC. The characterisation included both the generation of characteristic curves and the measurement of short-circuit current and open-circuit voltage of solar-E-yarns. Characterisation was conducted at different stages of the solar-E-yarn fabrication process, when the solar-E-yarn was integrated within woven fabrics, and under different test conditions (different light intensities, different incident angles). The chapter also investigated the effect of resin impregnation, introduced in *Chapter 4*, the use of a bi-facial MSC concept to enhance the power output of the solar-E-yarns, and the possibility of using braiding, instead of knit braiding, to create the fibrous sheath of the solar-E-yarns.

5.2 Preliminary tests using solar cells

5.2.1 Characterisation of maiden miniature solar cells

The current-voltage (IV) curves were generated using the baseline setting for the optical test rig for two different sizes of MSC (1.5×1.5 mm and 3.2×3.0 mm); these IV curves were used to derive corresponding power-voltage (PV) curves, short-circuit current (I_{sc}), and open-circuit voltage (V_{oc}) as shown in Fig. 5.1.

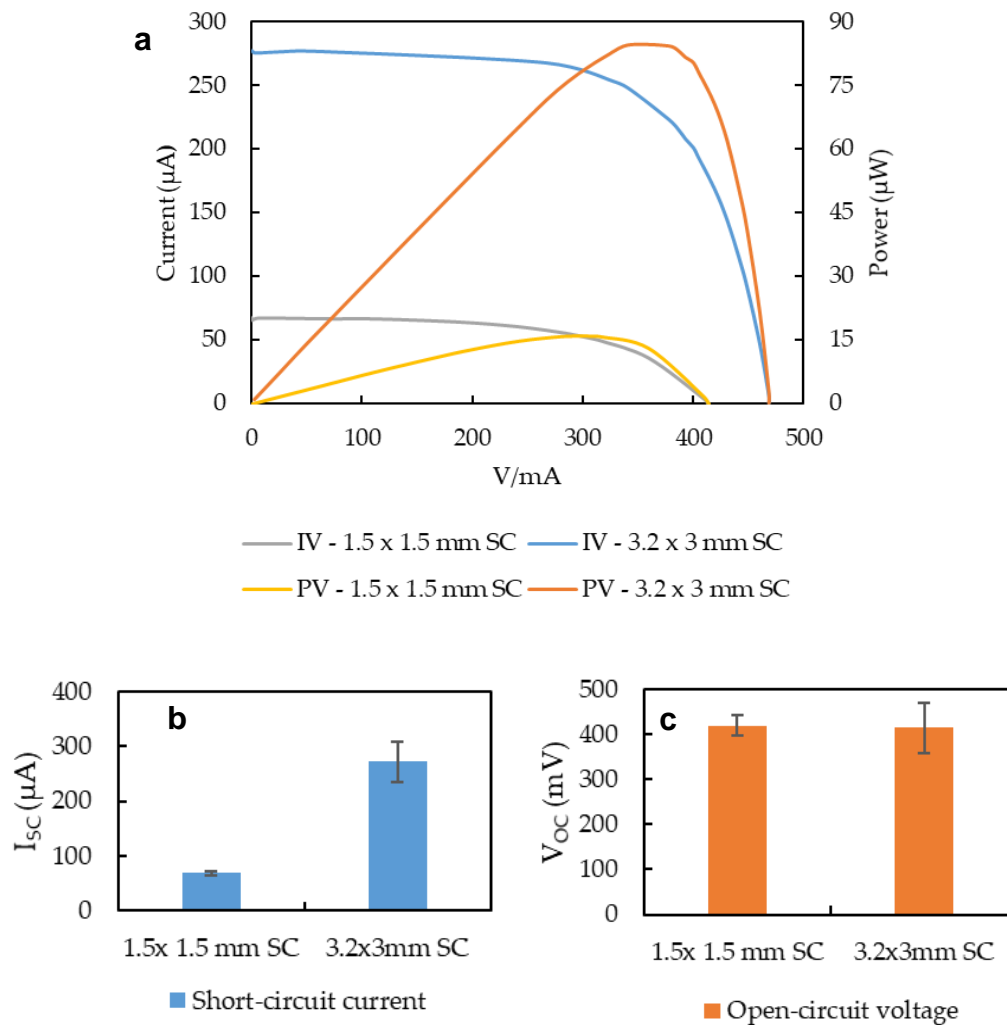


Figure 5.1 – (a) Characteristic curves, (b) short-circuit current and (c) open-circuit voltage measurements for 1.5×1.5 mm and 3.2×3.0 mm solar cells. Measurements conducted using optical test rig at base-line test conditions.

Theoretically, the short circuit current (I_{sc}) of a solar cell should scale linearly with the photoactive area of the device, however practically this may vary due to irregularities in manufacturing process. Therefore, another test was conducted to verify the linear relationship between the photoactive area and the I_{sc} using the 3.2×3 mm MSCs;

different photoactive areas were achieved by covering the front face of the MSCs using masks made of black opaque tape.

The results showed (Fig. 5.2) that I_{sc} was linear with the photoactive area, which agrees with theory (Chegaar et al., 2013). Importantly the 1.5×1.5 mm MSC data closely agreed with the trend obtained by covering regions of the 3.2×3.0 mm MSC, proving that any manufacturing discrepancies introduced negligible difference for MSCs of this size.

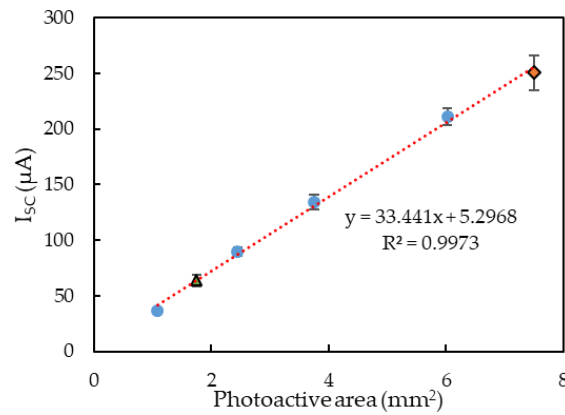


Figure 5.2 – Change in short-circuit current (I_{sc}) with the photoactive area. The blue circles show the photo active area exposed on 3.2×3.0 mm solar cells by using black tape masks. The green triangle and orange diamond represent the fully exposed 1.5×1.5 mm and 3.2×3.0 mm solar cells respectively.

5.2.2 Effects of resin micro-pod

The 1.5 mm \times 1.5 mm MSCs were embedded within resin micro-pods (RMP) with 1.6 mm, 2.7 mm, 3.2 mm and 4.8 mm outer diameters, with the MSC positioned at the bottom of the RMP (the standard configuration). RMP embedded MSCs were evaluated using the optical test rig (described in *Chapter 3*, pages 81-85) under the full beam of the optical test rig with and without optical filters; the results are shown in Fig 5.3. The mathematical model developed in *Chapter 4* was applied to the different micro-pod diameters to verify the validity of the model for MSCs.

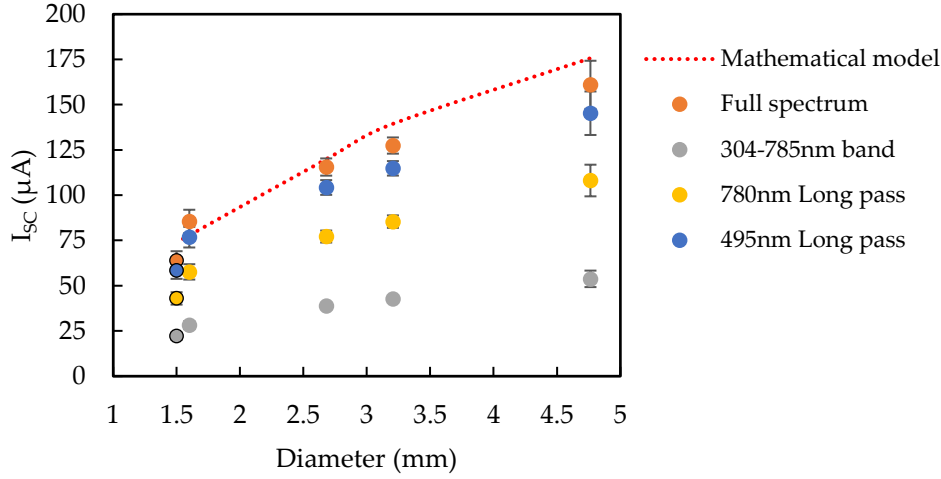


Figure 5.3 – Change in short-circuit current (I_{sc}) with the micro-pod diameter for the 1.5×1.5 mm solar cells, tested under different spectral inputs using optical test rig. The first data-point (with black outline) of each data series shows the value for the maiden solar cell.

Figure 5.3 showed that the behaviour of the MSCs embedded within RMPs was similar to the data collected for PDs (*Chapter 4*): I_{sc} increased with the diameter of the RMP, and different light spectra only reduced the observed I_{sc} , however did not change the relationship between I_{sc} and diameter. The mathematical model compared well to the experimental data and was shown to have a mean absolute percentage error of 8.5%.

5.2.2.1 Implications of Fresnel reflection

The RMP introduced an intermediate material layer between the MSC and air that has a different refractive index (RI) that significantly influence the amount of light reflected at the MSC surface; unlike the PD scenario where the pre-existing encapsulation had a similar RI to the RI of the RMP material. In adapting the mathematical model for MSCs, the Fresnel reflection (FR) at the MSC surface, as given by Fresnel equation (Eq. 5.1), was considered.

$$R_f = \left(\frac{1}{2}\right) \left\{ \left[\frac{n_1 \cos \theta - n_2 \sqrt{1 - \left(\frac{n_1}{n_2} \sin \theta\right)^2}}{n_1 \cos \theta + n_2 \sqrt{1 - \left(\frac{n_1}{n_2} \sin \theta\right)^2}} \right]^2 + \left[\frac{n_2 \cos \theta - n_1 \sqrt{1 - \left(\frac{n_1}{n_2} \sin \theta\right)^2}}{n_2 \cos \theta + n_1 \sqrt{1 - \left(\frac{n_1}{n_2} \sin \theta\right)^2}} \right]^2 \right\} \quad 5.1$$

Here n_1 and n_2 are the refractive indices (RIs) of the materials on either side of the material boundary (i.e. the MSC-RMP boundary) and θ is the angle made by the incident ray to the normal of the boundary surface. According to the Fresnel equation (Eq. 5.1), the partial reflection (R_f) increases with the difference between the RIs (n_1 and n_2) of the two materials on either sides of the boundary (Keating, 2002). For the MSC-RMP

boundary the RIs of the materials on either side of the boundary were, 1.9 (RI for the SiN anti-reflective coating of the MSC surface denoted by n_c) and 1.51 (RI for the resin material of the RMP denoted by n_r) respectively. For the maiden MSC surface the RI at the boundary was 1.9 (n_c) and 1 (RI for air denoted by n_a).

Experimental results showed an 18% increase in I_{sc} for MSC embedded inside of a 1.6 mm diameter RMP (as shown in Figure 5.3). In this case, the RMP diameter was only ~7% wider than the MSC, therefore the increase in I_{sc} could not be explained by the lensing effect alone. Theoretical estimates calculated using the Fresnel equation (Eq. 5.1) showed that the total light reflected at the resin-air interface and resin-MSC interface when using a 1.6 mm diameter RMP (Fig. 5.4(b)) was ~7 %. In the case of the maiden MSC (Fig. 5.4(a)) the estimated FR at the MSC surface was ~9.7 %.

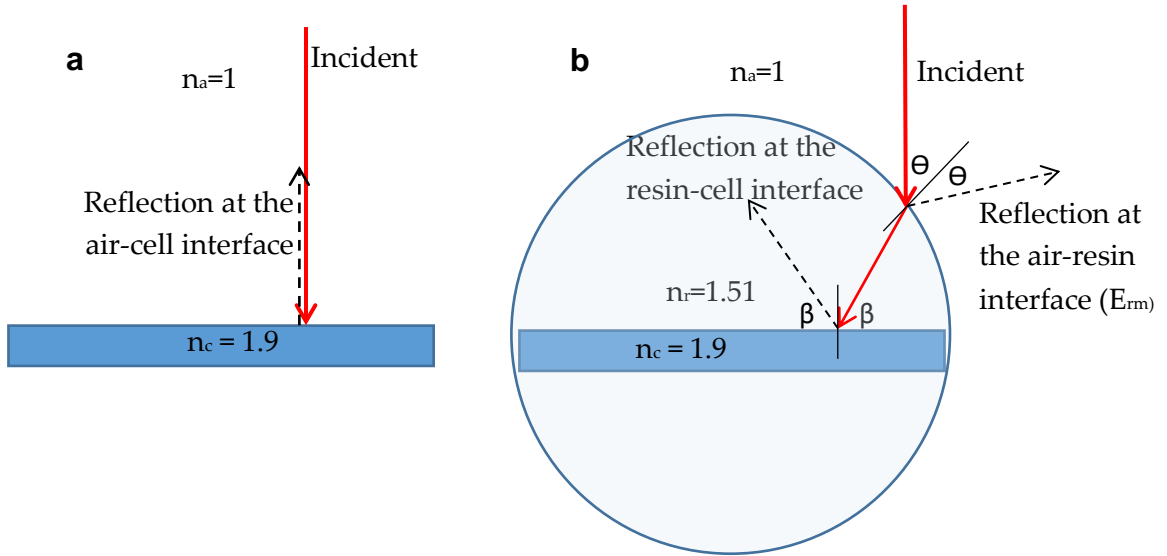


Figure 5.4 – Comparison of the effects of Fresnel reflection for the (a) maiden miniature solar cell and (b) a miniature solar cell embedded within 1.6 mm diameter resin micro-pod with a 1.5 mm wide miniature solar cell.

Based on this estimate it was clear that the reduction in FR at the MSC surface was the main contributor for the enhancement of the I_{sc} after encapsulation within the RMP. This enhancement was especially evident for the MSC embedded within a 1.6 mm diameter RMP, because the light enhancement due to lensing effect was the lowest for 1.6 mm diameter RMP.

The theory suggested that to minimize the FR at an interface of two materials with significantly different refractive indices (n_a and n_c), a layer of a third material with an intermediate RI could be employed. The RI of the RMP material (n_r) that minimise FR can be given as (Keshavarz Hedayati and Elbahri, 2016):

$$n_r = \sqrt{n_a \times n_c} \quad 5.2$$

Therefore, for the MSCs with SiN anti-reflective coatings the ideal RI of the RMP material that minimize FR is ~ 1.38 . In this respect one of the best candidate materials for the RMP would be Poly(1,1,1,3,3,3-hexafluoroisopropyl methacrylate) that has excellent optical clarity and RI close to 1.38 (Sigma-Aldrich, no date). It should be noted that these calculations assumed that all material surfaces were smooth, however in reality, this is often not the case.

5.2.2.2 Significance of total internal reflection

At the MSC surface a fraction of the incident light received is reflected, as previously explained using the Fresnel equation. This reflected fraction of light can be subjected to total internal reflection (TIR) at the micro-pod-air interface resulting in light being trapped inside of the micro-pod (Fig. 5.5). This light trapping can contribute towards an enhancement in I_{sc} of the embedded MSC.

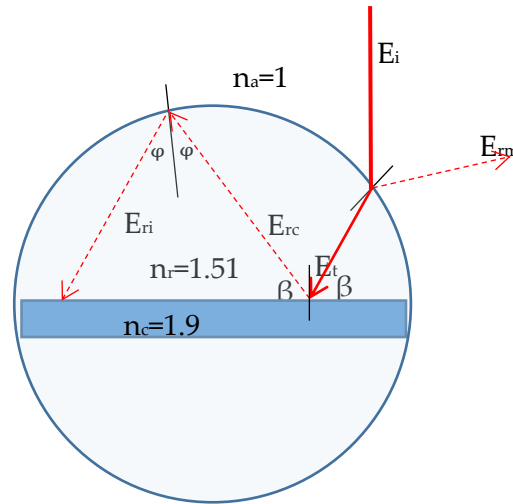


Figure 5.5 – Illustration of the occurrence of the total internal reflection of a ray of light within a 1.6 mm micro-pod embedded with a 1.5 mm wide solar cell.

The previously presented mathematical model assumed that the effects of TIR would be negligible. While this is a valid assumption for a photodiode (since the photoactive width was significantly smaller than the micro-pod diameter), the implications of TIR on the total light flux received were reconsidered for an MSC; this could be significant

for scenarios where MSC width is similar to RMP diameter where internally reflected light has a high probability of reaching the MSC surface.

The conditions for total internal reflection at the RMP-air interface are determined by the relative refractive indices of the material interface as given in Eq 5.3.

At the critical angle:

$$\sin \varphi = \frac{n_a}{n_r} \quad 5.3$$

For the micro-pod-air interface:

$$\begin{aligned} \sin \varphi &= \frac{1}{1.51} \\ \varphi &= 41.47^\circ \end{aligned}$$

Therefore, any ray reaching the RMP-air interface making angle beyond 41.47° to the normal at the micro-pod surface will be subjected to TIR.

The magnitude of the TIR can be approximated by the sum of all of the rays reflected at the MSC-RMP interface (E_{rc}) that make an angle between 41.47° and 90° to the RMP-air boundary surface. The previous version of the mathematical model was extended to capture the TIR for MSCs embedded within RMPs as given in Appendix 7. Based on the extended mathematical model the influence of TIR for $1.5 \text{ mm} \times 1.5 \text{ mm}$ MSCs, embedded at within RMPs of different diameters were estimated, and it was found that TIR caused less than 0.15 % of the total light directly received (E_t) by the MSC. This estimation confirmed the validity of the assumption that TIR had a negligible effect on I_{sc} , even for scenarios where photocell widths are similar to micro-pod diameter.

5.3 Micro solar cell embedded yarns

5.3.1 Material selection and structure

The performance of the MSC was evaluated at different stages of the fabrication process. The width of the MSCs to be used was a key consideration in achieving the optimum balance between the E-yarn thickness and the power density of the resultant photovoltaic fabrics. A larger width for the MSC would be desirable to achieve higher power densities but would result in thicker fabrics. Therefore, most of the proceeding work was limited to using micro-pods with a diameter of 1.6 mm to accommodate the widest possible MSCs (1.5 mm wide) within $\sim 2.0 \text{ mm}$ diameter E-yarn (which was the

smallest diameter achievable using the available knit-braiding machine). Initially, 1.5 mm × 1.5 mm size MSCs were used for preparing the solar cell embedded E-yarns (solar-E-yarns) and the first prototype of a solar cell embedded woven fabric.

Considering the need for creating the thinnest possible yarn using existing machinery and available MSC sizes, specifications given in Table 5.1 were selected as the baseline for creating solar-E-yarns.

Table 5.1 - Specification for the solar-E-yarns prepared for evaluations and experiments.

Component/Parameter	Description
Cell size	1.5 × 1.5 × 0.2 mm (measured dimensions, width and length 1.54±0.04 × 1.55±0.03 mm)
Cu wire type	7 × 50 µm multi strand twisted Cu wire
Micro-pod geometry and size	Cylindrical with a 1.6 mm diameter circular base and 2.5-3.0 mm length
Micro-pod resin type	Dymax 9001E-V3.5 acrylated urethane
Packing fibres	Four texturized polyester packing yarns (yarns with 48 filaments and a liner density of 167 dtex)
Knitted sheath	2.0 mm diameter warp knitted tube with six texturized polyester yarns (yarns with 48 filaments and a liner density of 167 dtex)

The cross-sectional and isometric views of the solar-E-yarn prepared according to above specifications are schematically illustrated in Fig. 5.6 below. The key differences of the solar-E-yarn structure in comparison to the PDEYs discussed in previous chapter are evident in the illustrations (such as the use of two parallel running copper wires and solder pads on both front and back sides of the solar cells).

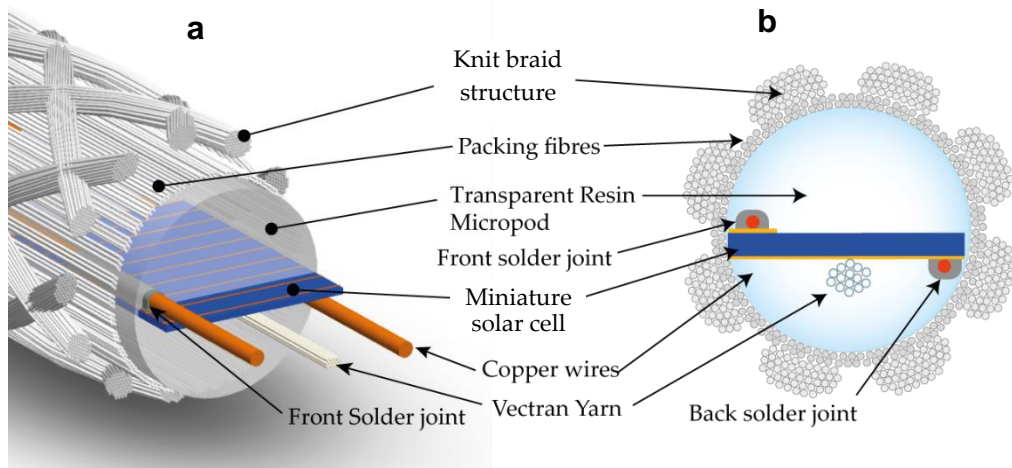


Figure 5.6 – Schematic illustrations of (a) isometric and (b) cross sectional view of solar cell embedded yarns.

An additional resin impregnation step was introduced to the normal E-yarn fabrication process in preparing Solar-E-yarns. For this the Dymax 9001E-V3.5 acrylated urethane resin was used and fibres covering front side of the solar cells in the micro-pod regions were selectively impregnated. The selective impregnation helped to minimize the change in surface texture of the solar-E-yarn.

5.3.2 Evaluation of solar-E-yarns using 1.5 mm ×1.5 mm solar cells

The solar-E-yarns were prepared according to the specifications detailed in Section 5.3.1 (above) and were evaluated at each stage of the E-yarn fabrication process using the optical test rig (using both methods; no optical filter and with optical filters). The measurement of I_{sc} and V_{oc} at different stages of the fabrication process are given in Fig. 5.7.

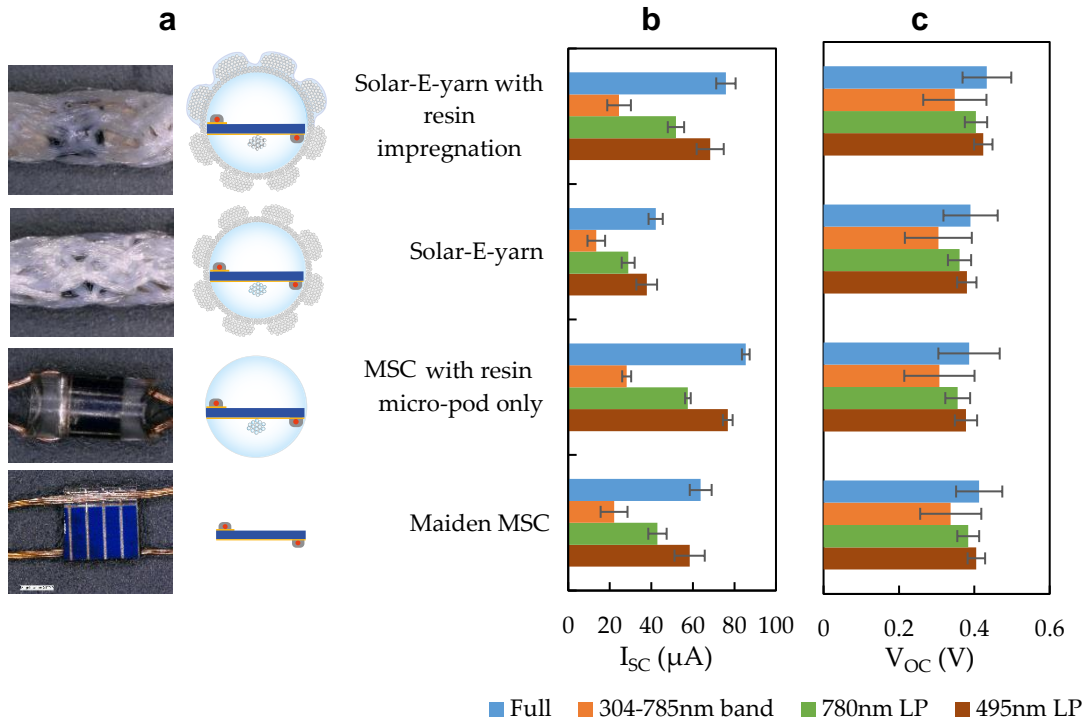


Figure 5.7 - Change in the short circuit current (I_{sc}) and open circuit voltage (V_{oc}) at different stages in the fabrication process for 1.5×1.5 mm solar cell embedded yarns, tested using optical test rig full beam under different optical bands.

The changes in I_{sc} confirmed the enhancement of light intensity at the photoactive surface by the RMP, the shading effect of the fibrous sheath and the improvement in light penetration due to the resin impregnation.

In comparison to the maiden MSC values, a 34 % increase in I_{sc} was observed after embedding the MSC inside of the RMP and a 26 % reduction in I_{sc} was seen after covering the RMP with a fibrous sheath (combination of packing fibres and knit braid). The resin impregnation enhanced the I_{sc} by ~16% compared to the maiden MSC. As observed in previous experiments using PDs, I_{sc} changed significantly due to the changes transpired during the E-yarn fabrication process, while in comparison there was only a modest change in V_{oc} . Therefore, these results were consistent with the results observed for PDEY discussed in *Chapter 4*.

To compare the change in MSC performance at different stages of the fabrication process, under different spectral bands of incident light, the I_{sc} and V_{oc} values were generated using filtered light. The results were normalised to the corresponding values without any optical filters (full spectrum) as shown in Fig. 5.8.

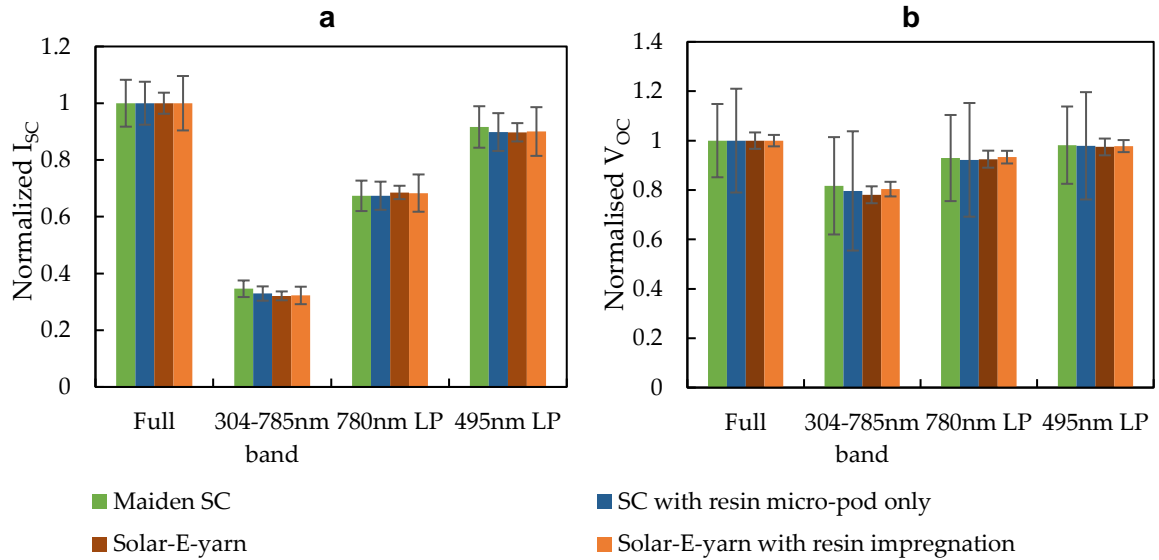


Figure 5.8 - Change in short circuit current (I_{sc}) and open circuit voltage (V_{oc}) at different stages in the fabrication process for 1.5 x 1.5 mm solar cell embedded yarns under different optical filters. The values are normalised to the results with no-optical filter for each stage of the process.

The results showed that at all the stages of the solar-E-yarn fabrication process the device performance was consistent for different optical bands. In other words, the RMP and the fibrous sheath interact with light consistently and proportionately across different parts of the incident light spectrum (ultraviolet, visible and infrared).

5.3.3 Effect of changing the incident angle of the light source normal to the longitudinal axis of the devices on their optoelectronic properties

For any solar energy harvesting system, having an understanding about the effect of the angle of the incident light on the power conversion efficiency is vital. For fixed applications (i.e. fixed solar panels installed outside) the angle of the incident light would vary based on the position of the Sun. To minimize the variation in power generation during the day, solar panels are often mounted onto solar tracking systems that follow the sun to achieve direct light exposure onto the solar panel. However, these solar trackers increase the capital investment of the system (Hafez, Yousef and Harag, 2018) and maintenance costs. In the case of wearable systems, the incident angle of the light relative to the solar energy harvesting textile would vary unpredictably based on

the movement of the wearer relative to the light source (Sun). Therefore it was important to study the response of the solar cell embedded yarns at range of different incident angles.

The initial experiments were conducted using 1.5×1.5 mm SCs and TEMD 7000×1 photodiodes (PD1) with 2.7mm RMPs and 4.0 mm fibrous sheaths. PDs were also included in the investigations to fully comprehend the effects of the E-yarn structure at different incident angles for different photocell types. I_{sc} measurements were taken for different angles normal to the longitudinal axis of the solar E-yarn (-180° to 180° where 0° was the exposure normal to the photoactive plane facing the photoactive side) at 5° increments. In the first set of experiments the MSCs and PDs were studied in their maiden form, with RMPs, and in the final yarn form (without resin impregnation). The experiments were conducted using the optical test rig under baseline settings. Fig. 5.9 illustrates how I_{sc} output changed with the incident angle.

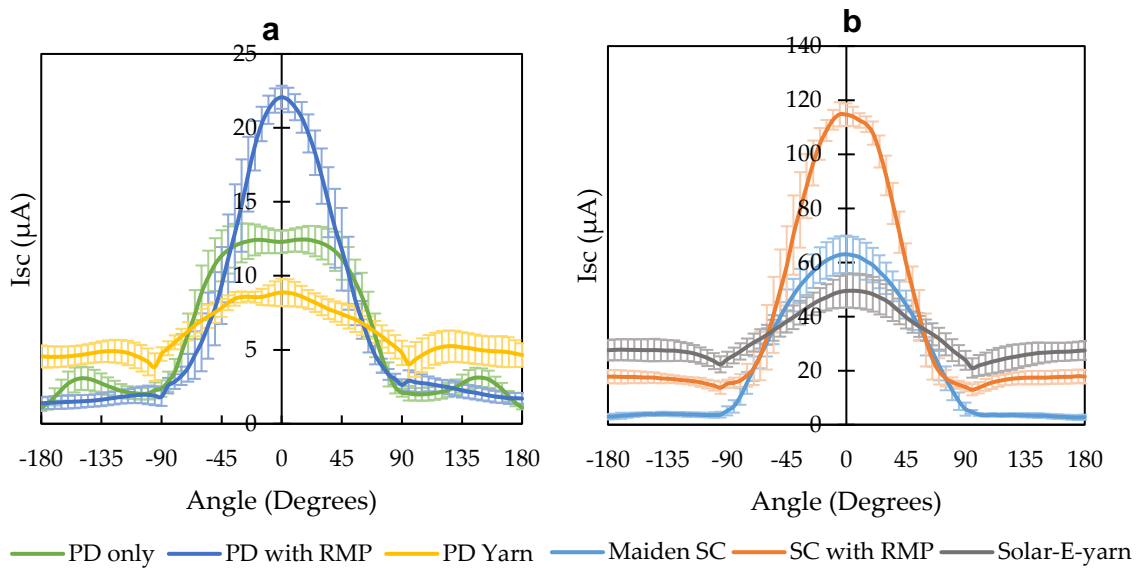


Figure 5.9 – Change in short circuit current (I_{sc}) at different the incident angles for (a) TEMD 7000×1 (PD1) type photodiodes and (b) 1.5×1.5 mm solar cells.

The result showed that the I_{sc} profiles varied significantly with the incident angle at different stages of the E-yarn fabrication process for both the PD (Fig. 5.9(a)) and MSC (Fig. 5.9(b)). In the case of maiden MSC a significant I_{sc} response was observed only in the front half circle (from -90° to 90°) due to the flatness and mono-faciality (single photoactive face) of the maiden MSC. The shape of this curve was sinusoidal which followed the cosine of the incident light beam. In the case of the bare PD the shape of the curve was not sinusoidal; this was due to the effects of built in epoxy encapsulation

(window) in the PD device. The rectangular cuboid shaped window in the PDs can induce internal reflections resulting in a plateau in the front half circle and peaks in photocurrents in back half circle ($<-90^\circ$ and $>90^\circ$). The curves were similar in shape for both the SCs and PDs after encapsulation within the RMP. The peak I_{sc} was enhanced due to the lensing effect of the RMP, which has been discussed in detail in the previous chapter. In comparison to the maiden MSC, the encapsulated MSC showed an increase in I_{sc} when the back half circle of the RMP was exposed to light, this was possibly due to diffusion of the light trapped by the RMP to the opposite side (photosensitive side) of the MSC as a result of internal reflections. After covering the RMPs with a fibrous sheath, the shape of the I_{sc} curve became flatter and the variation in I_{sc} with the angle significantly reduced. The peak I_{sc} for the PDEYs and solar-E-yarns reduced in comparison with the maiden PD and MSC in the front half circle, and the opposite effect was evident in the back half circle. This can be explained by the combined light trapping and light diffusion effects of the fibrous sheath and RMP, which redistributed the incident light around the cross section of the E-yarn. This was an interesting observation since the PD and MSC embedded yarns generated significant photocurrents even when illuminated from the backside. This effect is advantageous in solar energy conversion when the incident angle is unpredictable (due to dynamic nature of the light source and the harvester). In addition, this effect is beneficial when converting these solar-E-yarns into fabric, where yarn to yarn performance variations caused by angular positioning discrepancies would be significantly nullified.

5.3.4 Individual and combined effects of the components of the solar-E-yarns

In the previous chapter, the effects of each of the components that make-up an E-yarn on the performance of embedded PDs were discussed. In order to distinguish between the effects of each of the components on the solar-E-yarns, similar experiments were conducted with MSCs incorporated into different constructions as listed below. All the components were constructed according to the specifications given in Table 5.1 (i.e. 1.6 mm RMP and ~2.0 mm knit braid). Tests were conducted using the optical test rig with experiments performed for incident angles between -180° and 180° in 5° increments as shown in Fig. 5.10.

- I. Maiden MSC
- II. MSC with RMP only
- III. MSC with knitted-braid only (No packing fibres)
- IV. MSC with RMP and knitted-braid (No packing fibres)
- V. MSC with packing fibres and knitted-braid (No micro-pod)
- VI. MSC with RMP, packing fibres and knitted-braid (Solar-E-yarn)
- VII. Solar-E-yarn with resin impregnation
- VIII. MSC with RMP, knitted-braid and resin impregnation (No packing fibres)

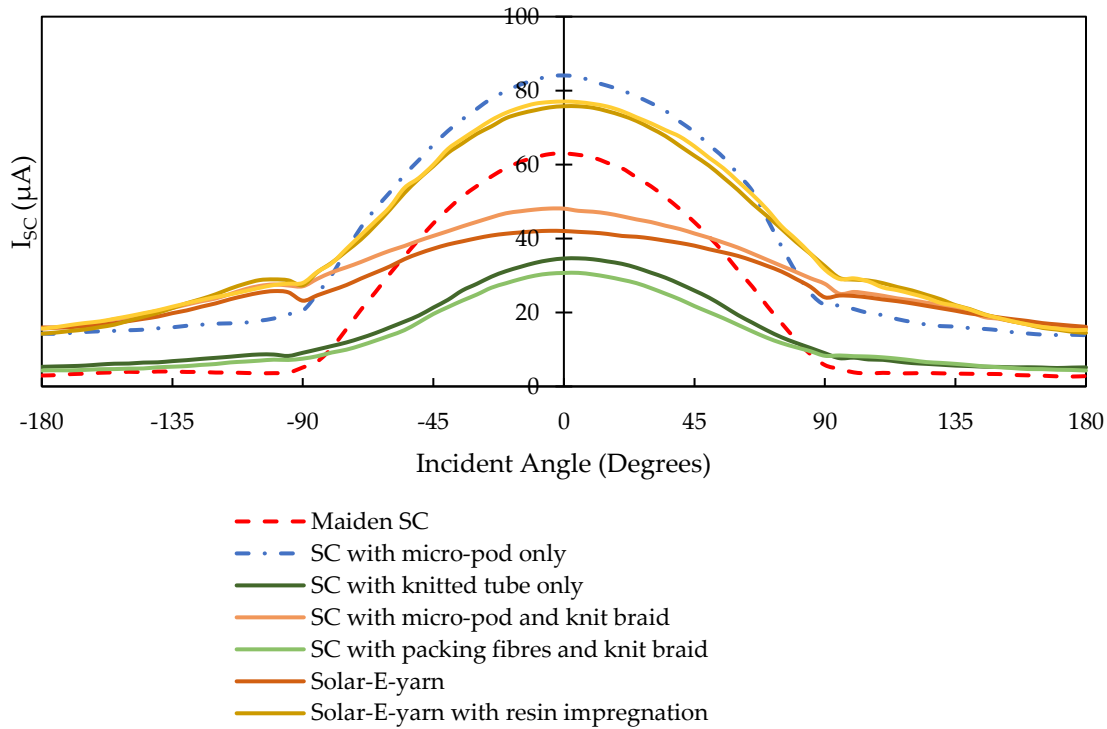


Figure 5.10 – Change in short circuit current (I_{sc}) with the incident angle for different solar cell (MSC) embedded device constructions evaluated under the baseline test settings using the optical test rig.

The results shown in Fig. 5.10 further confirmed how the RMP and fibrous sheath changed the I_{sc} at different incident angles measured normal to the longitudinal axis of the device. This experiment revealed the individual effects of each component including the packing fibres and resin impregnation as well as the synergistic effects of the components.

The results suggested that the shading effect of the packing fibres was significantly smaller than that of the knitted-braid (warp knitted tubular structure). This could be attributed to a smaller number of fibres and the orderly orientation of the layer of packing fibres around the RMP. In contrast, the knitted- braid structure had a

comparatively higher number of fibres and irregular fibre orientation, which could result in significantly higher light scattering and absorption away from the core of the yarn. After resin impregnation the shading effect of the packing fibres was negligible. The resin impregnation clearly enhanced the I_{sc} by ~23% compared to maiden MSC value, proving the effectiveness of the resin impregnation in improving light transmission through the fibrous sheath to the RMP.

When the results for the MSC with RMP only, MSC with fibrous sheath (packing fibres and warp knitted tube) only, and solar-E-yarn were compared, it was observed that only the solar-E-yarn exhibited the improved uniformity of I_{sc} over the range of incident angles. This gave clear evidence of the synergistic effects yielded by the combination of the RMP and fibrous sheath that was not present in the individual cases. The above-mentioned individual and synergistic effects can be theoretically explained as below, without detailed mathematical modelling.

At oblique incident angles, the maiden MSC (Fig 5.11(a)) received the least amount of direct light flux since the light receiving surface is flat. Nevertheless, the total light flux received is directed for the power conversion. When embedded inside of the RMP (Fig 5.11(b)), the micro-pod received a higher amount of direct light flux due to its circular cross section. This light received was collected and directed to the photoactive area yielding higher I_{sc} values compared to the maiden MSC.

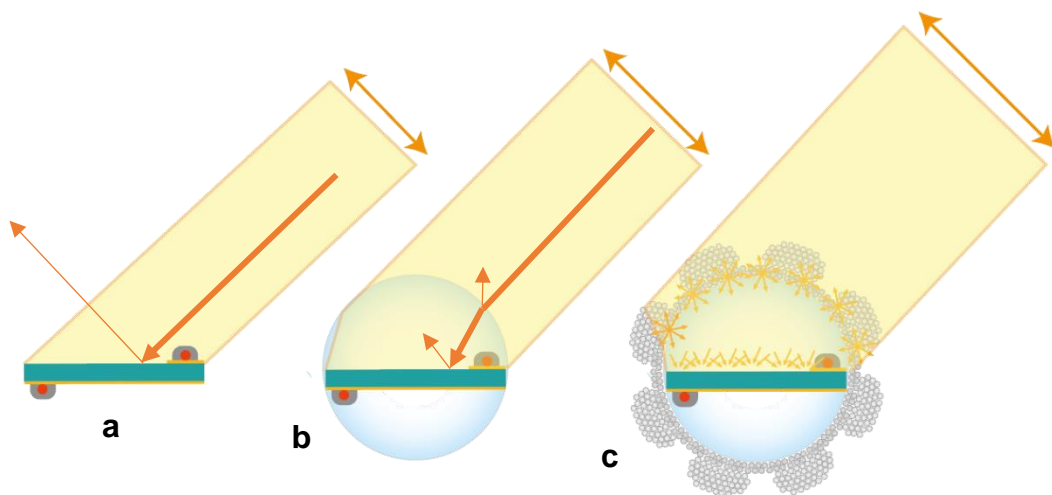


Figure 5.11 – Cross sectional illustration of light flux received at the photoactive plane for (a) a maiden MSC, (b) a MSC embedded within a resin micro-pod and (c) a solar-E-yarn at oblique incident angles.

In the case of a yarn embedded with MSC without resin impregnation (Fig 5.11(c)), the

light flux received by the yarn surface was the highest due to the increase in the effective diameter. However, only a proportion of the light flux received at the yarn surface was directed to the RMP, resulting in lower overall I_{sc} than for the maiden MSC: This was due to the light scattered by the fibrous sheath.

After the fibres in the front side of the solar-E-yarn were impregnated with the resin the proportion of light transferred through the fibrous sheath significantly increased, leading to higher overall I_{sc} values compared to the maiden MSC. This phenomenon can be further explained using Fig. 5.12.

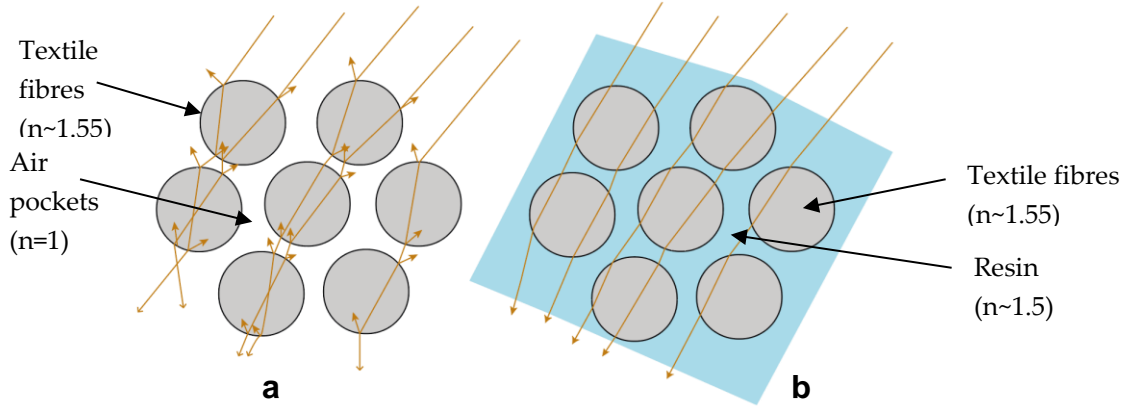


Figure 5.12 – Cross sectional illustration of light transmission through a bundle of fibres in the sheath of the MSC yarn (a) before resin impregnation and (b) after resin impregnation.

Light reflects partially each time it confronts a fibre-air interface. When a single fibre is considered, a ray is reflected twice by the fibre. When the reflections of a ray by a series of fibres is considered, if the reflections by the i^{th} fibre is given by $r_{i(1)}$ and $r_{i(2)}$ (the first and second reflection respectively) the relative intensity of a beam of light after being scattered (I_r/I) by n number of fibres can be given as:

$$\frac{I_r}{I} = (1 - r_{1(1)})(1 - r_{1(2)})(1 - r_{2(1)})(1 - r_{2(2)}) \dots \dots \dots (1 - r_{n(1)})(1 - r_{n(2)}) \quad 5.3$$

The according to the Fresnel equation smallest amount of reflection occurs when the incident angle is 0° because at this point FR can be given as:

$$R_{f(0)} = \left[\frac{n_1 - n_2}{n_1 + n_2} \right]^2 \quad 5.4$$

In the scenario where the incident angle is 0° the smallest possible reflection by n fibres (with circular cross sections) would occur when the centres of the fibre cross sections are on a straight line, along which the ray travels through the fibres (Fig. 5.13). Although, the probability of fibre cross-sections aligning on a straight line is small due to the

randomness of fibre orientation in the fibrous sheath, this hypothetical scenario would be useful, to understand the effect of resin impregnation. For this analysis effects of light absorption (attenuation) by the fibre and resin material is considered negligible.



Figure 5.13 – Cross sectional illustration of a ray travelling through a series of fibre cross sections arranged in a straight line.

In this case:

$$r_{(i)1} = r_{(i)2} = R_{f(0)} \Rightarrow \frac{Ir}{I} = \left\{ 1 - \left[\frac{n_1 - n_2}{n_1 + n_2} \right]^2 \right\}^{2n} \quad 5.5$$

Before resin impregnation (Fig 5.12(a)), $n_1=1$ and $n_2=1.55$.

$$\frac{Ir}{I} = \{0.953479\}^{2n} \quad 5.6$$

After resin impregnation (Fig 5.12(b)) $n_1=1.51$ and $n_2=1.55$.

$$\frac{Ir}{I} = \{0.999829\}^{2n} \quad 5.7$$

The change in $\frac{Ir}{I}$ with n can be plotted for the two scenarios as shown in Fig. 5.14.

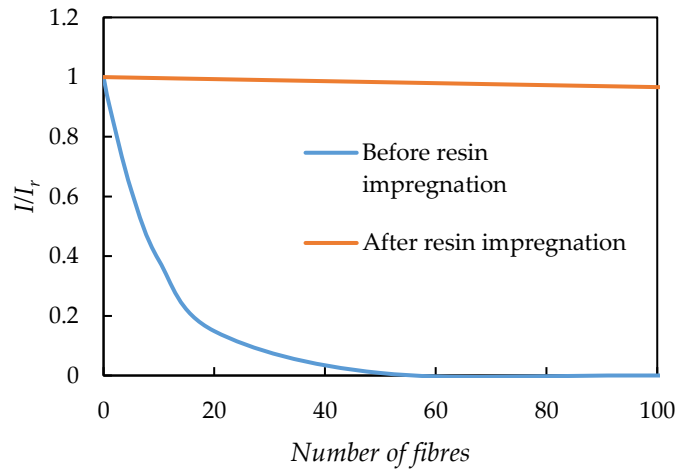


Figure 5.14 – Estimated change in the transmitted light intensity for a ray travelling through multiple fibres (n) in a straight line before and after the spaces between the fibres are impregnated with resin.

For all other cases where a light ray would take a staggered path ($\theta > 0$), the enhancement in I_{sc} due to resin impregnation should be more evident. Based on this analysis the enhancement due to resin impregnation can be directly attributed to the reduction in Fresnel reflection.

The average I_{sc} values for maiden MSC, solar-E-yarn, and solar-E-yarn with resin impregnation was calculated for the full circle around the E-yarn (-180° to 180°) and front half circle (-90° to 90°), as depicted in Fig. 5.15. The average I_{sc} provided a good indication about the comparative power conversion efficiency across a range of incident angles for different wearable photovoltaic systems.

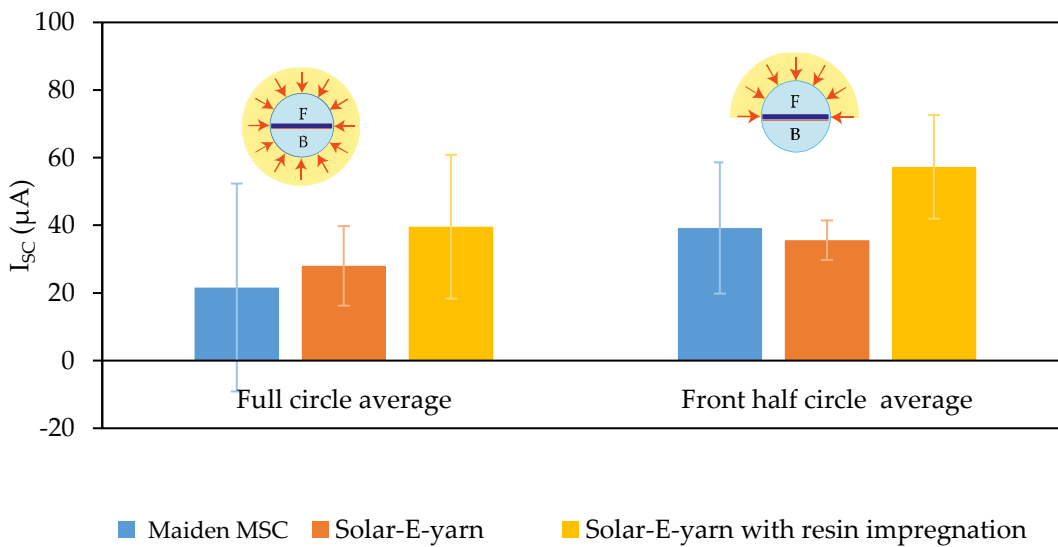


Figure 5.15 – Average short circuit current (I_{sc}) value calculated for the full circle (-180° to 180°) and front half circle (-90° to 90°) for a maiden MSC, a solar-E-yarn, and a solar-E-yarn after resin impregnation, based on the measurements conducted at different incident angles using the optical test rig. The error bars show the standard deviation of the I_{sc} values across the angles measured.

The average I_{sc} of the full circle exposure is an indication of how the MSC yarn performs when the incident light is exposed uniformly around the yarn in a circular manner. Front-half circle exposure was representative of a free standing solar-E-yarn with the photoactive side of the yarn directed to North on a sunny day. When the full circle mean value is considered, the maiden MSC exhibited the lowest value, due to negligible I_{sc} generated by the back half circle. In this case, the solar-E-yarn with resin impregnation yielded mean values, which were ~45% and ~38.5% higher than the mean values of maiden MSC and solar-E-yarn, respectively. In the case of the front half circle mean

values, the solar-E-yarns with resin impregnation exhibited 31.6 % and 56.7 % higher values than the values for maiden MSC and solar-E-yarn, respectively. The front half circle means values clearly showed that the solar-E-yarns had a similar overall performance to the maiden MSCs. Solar-E-yarns with resin impregnation exhibit superior performance to the maiden MSCs and the solar-E-yarns across all of the incident light angles. It is to be noted that this behaviour may not be present when the solar-E-yarns are deployed within fabrics due to the shading effects present at larger incident angles due to fibres of neighbouring yarns; this will need further investigation in fabric form.

These results confirmed the contributions the RMP, fibrous sheath, and resin impregnation in combination have in optimizing overall performance of solar-E-yarns for solar energy harvesting applications.

5.3.5 Theoretical and empirical modelling of the effect of the angle of the incident light normal to the longitudinal axis of the devices

The generalised ray-tracing model developed in *Chapter 4* encompassed the effects of incident angle (γ) on the light intensity at the photoactive plane of a photocell embedded inside a micro-pod geometry defined by a function $f(x)$. It is useful to understand how the incident light is propagated through the fibrous sheath after scattering, attenuation and polarisation by the fibres, so that an estimation of the effects of the fibrous sheath on the photovoltaic output of the solar-E-yarn can be obtained. However, a similar ray-tracing approach used in *Chapter 4* for the micro-pod cannot be followed to study the effect of the fibrous sheath, due to the complex nature of light propagation through the randomly oriented fibrous structure. Theoretical estimations of the polarisation, scattering, and propagation of light within fibrous structures have been presented in the literature using techniques such as Monte-Carlo simulations (Green, Lamberg and Lumme, 2000; Peng, Ding and Wang, 2012). However, such detailed study is not an object of this work. Instead, an empirical model was derived based on the width of the beam of light captured by the solar-E-yarn, and the incident angle of light, to estimate the I_{sc} of the solar-E-yarn at varying incident angles.

5.3.5.1 Change in the width of incident beam of light with the angle

The width of the beam of light captured by the front side (front-half circle) of the device at higher incident angles were significantly different for the above three cases (maiden MSC, MSC embedded within RMP, solar E-yarn). This was due to the change in the geometry after the encapsulation and after being covered with fibres. Simplified ray tracing models for maiden MSC, MSC inside RMP and solar-E-yarns are depicted in Fig 5.16.

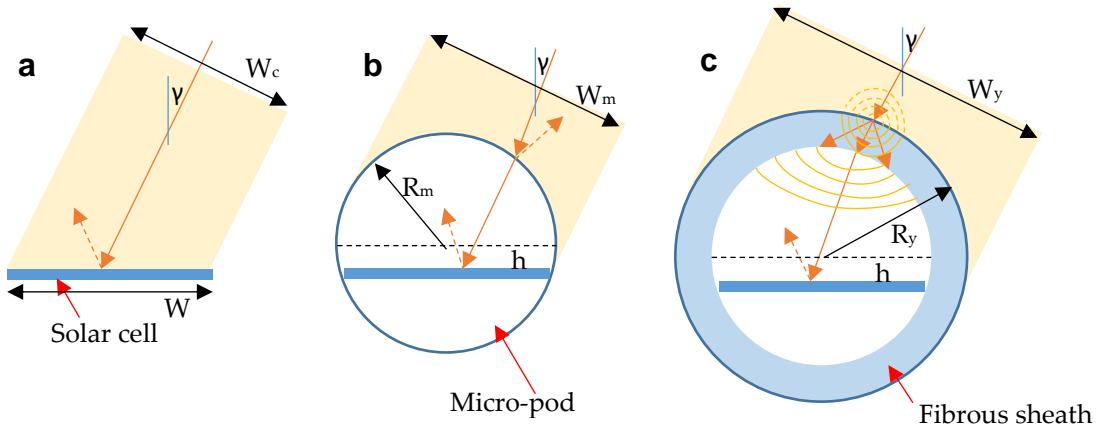


Figure 5.16 – Cross sectional illustration of light flux received at the photoactive plane for (a) a maiden MSC, (b) a MSC embedded within a resin micro-pod and (c) a solar-E-yarn at higher incident angles.

The theoretical values for the width of the beam of light captured by the front face of the MSC device in each case, for an incident angle γ can be calculated as shown below.

The width of the beam captured by the maiden MSC (Fig 5.16(a)):

$$W_c = W \cos \gamma \quad 5.8$$

Where W is the width of the maiden MSC.

The width of the beam captured by the RMP (Fig 5.16(b)):

$$W_m = R_m + \sqrt{(R_m^2 - h^2)} \cos \gamma + h \sin \gamma \quad 5.9$$

Where R_m is the radius of the RMP and h is the depth from the centre of the micro-pod to the MSC.

The width of the beam captured by the solar-E-yarn (Fig. 5.16(c)):

$$W_y = R_y + \sqrt{(R_y^2 - h^2)} \cos \gamma + h \sin \gamma \quad 5.10$$

Where R_y is the mean radius of the RMP and h is the depth from the centre of the micro-pod to the MSC.

For the experimental scenarios considered here $h = 0$, therefore:

$$W_m = R_m + \sqrt{(R_m^2 - h^2)} \cos \gamma - h \sin \gamma = R_m(1 + \cos \gamma) \quad 5.11$$

And:

$$W_y = R_y + \sqrt{(R_y^2 - h^2)} \cos \gamma - h \sin \gamma = R_y(1 + \cos \gamma) \quad 5.12$$

By substituting measured values into the equations, with $W = 1.5$ mm, $R_m = 1.6$ mm and $R_y = 2.0$ mm, the change in the effective width of the collected beam for different incident angles were calculated (Fig. 5.17).

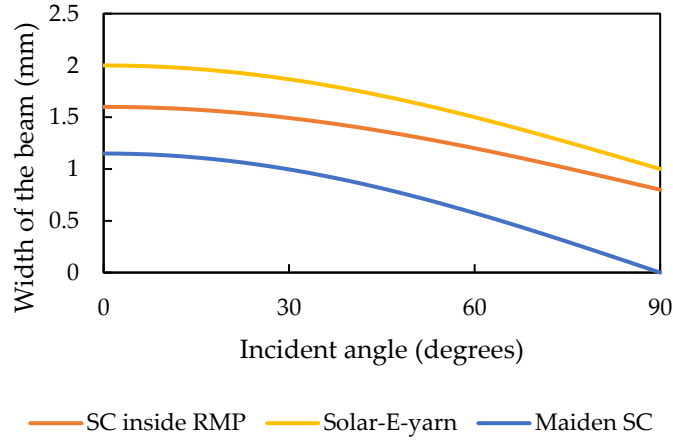


Figure 5.17 – Theoretical values for the effective width of the beam captured by the maiden miniature solar cell (MSC), MSC embedded within a resin micro-pod, and solar-E-yarn. Here the diameter of the solar-E-yarn is assumed to be constant.

5.3.5.2 Modelling the effect of incident angle on short-circuit current

The theoretical values given in Fig. 5.17 showed that when the front half circle of the individual MSC devices were considered, both the RMP and solar-E-yarn captured a significant amount of light even when illuminated at 90°. By applying the ray tracing model developed, and the Fresnel equation for the reflection at the MSC surface, the

theoretical values for the light captured by the maiden MSC and the MSC embedded inside of an RMP with different incident angles of light can be estimated and compared with the experimental results (Fig 5.18). In both cases the measured I_{sc} value at 0° incident angle for the maiden MSC was considered the baseline (i.e. theoretical and experimental I_{sc} values at 0° for maiden MSC were assumed to be equal). A complete derivation and calculation of the generalized ray tracing model is given in Appendix 5.

Unlike in the previous cases, theoretical estimations for the light absorbed by the MSC embedded within the solar-E-yarns required more advance modelling techniques, such as Monte-Carlo simulations, where the light intensity at a given point in the fibrous sheath space is defined using a probability density function (PDF) to encompass the complexities of light propagation (due to reflection, refraction and polarisation) through multi-fibre structures (Green, Lamberg and Lumme, 2000; Peng, Ding and Wang, 2012). In its simplest forms the PDF was derived based on the optical properties of the fibre material, geometry of the fibres, the fibre density and relative fibre orientation within the fibrous structure. In this work instead of developing a generalized model based on the properties of the fibrous sheath, the relationship between the incident light angle and I_{sc} was empirically modelled for solar-E-yarns, based on the width of the beam of light captured by a solar-E-yarn.

The basis for this empirical model is the assumption that the I_{sc} the solar-E-yarn can be given as (based on the Eq .5.11):

$$I_{sc} = f(\gamma)W_y = f(\gamma)R_y(1 + \cos \gamma) \quad 5.13$$

Where $f(\gamma)$ is defined as a trigonometric function in the form of sum of sines given in Eq. 5.14:

$$f(\gamma) = \sum_{i=1}^n a_i \sin (b_i \gamma + c_i) \quad 5.14$$

Here, the first, second, and third order sum of the sines were evaluated for the empirical model based on the goodness of fit given by R^2 (co-efficient of determination).

First order form:

$$f(\gamma) = a_1 \sin (b_1 \gamma + c_1) \quad 5.15$$

The second order form:

$$f(\gamma) = a_1 \sin (b_1 \gamma + c_1) + a_2 \sin (b_2 \gamma + c_2) \quad 5.16$$

Third order form:

$$f(\gamma) = a_1 \sin(b_1\gamma + c_1) + a_2 \sin(b_2\gamma + c_2) + a_3 \sin(b_3\gamma + c_3) \quad 5.17$$

Here $a_1, b_1, c_1, a_2, b_2, c_2, a_3, b_3,$ and c_3 were fitting constants, for the given scenarios.

The curve fitting was conducted using the Matlab® curve-fitting toolbox, to arrive at the fitting coefficients and R^2 for the first-order, second-order and third-order form for the solar-E-yarn. Using the same approach, an empirical model was generated and examined to estimate the I_{sc} for the MSC embedded in RMP as given by Eq. 5.18:

$$I_{sc} = g(\gamma)R_m(1 + \cos \gamma) \quad 5.18$$

Where $g(\gamma)$ is a sum of sines series.

The results of the curve-fitting are given in the Table 5.2.

Table 5.2 – Results of the curve-fitting for short-circuit current (I_{sc}) using Matlab®.

Device type	Sum of sines order	Fitting coefficients			R^2
		a	b	c	
For the solar-E-yarn	First order	$a_1 = 365.5$	$b_1 = 0.006057$	$c_1 = 0.06309$	0.8058
	Second order	$a_1 = 7911$ $a_2 = 7887$	$b_1 = 1.259$ $b_2 = 1.261$	$c_1 = 0.4809$ $c_2 = 3.621$	0.9741
	Third order	$a_1 = 39.91$ $a_2 = 24.17$ $a_3 = 9.124$	$b_1 = 1.057$ $b_2 = 2.312$ $b_3 = 2.968$	$c_1 = 0.4414$ $c_2 = 2.441$ $c_3 = 4.963$	0.9923
For the MSC embedded within an RMP	First order	$a_1 = 53.35$	$b_1 = 0.8757$	$c_1 = 1.21$	0.9528
	Second order	$a_1 = 3779$ $a_2 = 3727$	$b_1 = 1.294$ $b_2 = 1.304$	$c_1 = 1.595$ $c_2 = 4.737$	0.9848
	Third order	$a_1 = 70.11$ $a_2 = 1780$ $a_3 = 1762$	$b_1 = 1.581$ $b_2 = 3.722$ $b_3 = 3.733$	$c_1 = 0.4588$ $c_2 = 1.505$ $c_3 = 4.634$	0.9851

Based on the R^2 values the third order sum of sines series were selected for the empirical model, for the solar-E-yarn. In the case of MSC inside RMP, there was no significant different in the R^2 values from second-order to third-order model. Therefore second-order sum of sines series was selected in this case. The empirical models for I_{sc} for the solar-E-yarn (I_{scy}) was given by:

$$I_{scy} = W_y[39.91 \sin (1.057\gamma + 0.4414) + 24.17 \sin (2.312\gamma + 2.441) + 9.124 \sin (2.968\gamma + 4.963)](1 + \cos \gamma) \quad 5.19$$

Similarly, the empirical model for the MSC embedded within an RMP (I_{scm}) was given by

$$I_{scm} = W_m[3779 \sin (1.294\gamma + 1.595) + 3727 \sin (1.304\gamma + 4.737)](1 + \cos \gamma) \quad 5.20$$

The experimental and model-estimated data for maiden MSC, MSC embedded within an RMP, and the solar-E-yarn are shown in Fig 5.18.

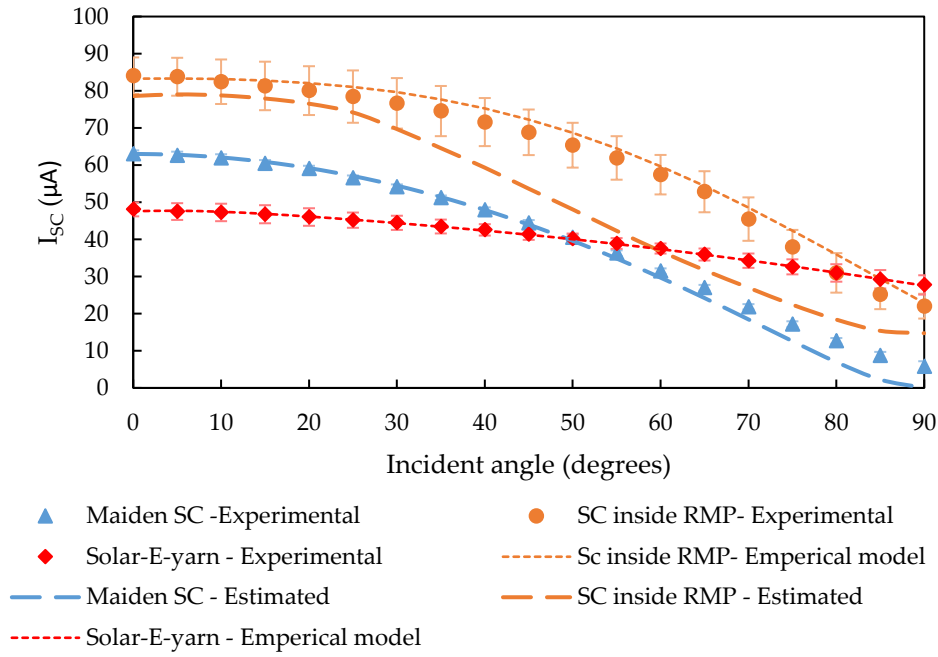


Figure 5.18 – Experimental and estimated values for the short-circuit current for maiden MSC), MSC embedded within resin micro-pod (RMP) and solar-E-yarns for different incident angles in the front half circle.

5.3.6 Effect of colour of the fibre sheath

The colour of large scale solar panels employed for applications such as building integrated photovoltaics (BIPV) is also an important consideration, as the solar energy harvesting capability should harmonize with the architectural and aesthetic features of its surroundings (Halme and Mäkinen, 2019). The colour of the solar panels are typically modified by colouring the encapsulation material (Hardy *et al.*, 2013), or halftone (colour dot pattern) printing (Kamelolone Solar, 2018). Halme and Mäkinen in their theoretical study on efficiency limits for single-band solar cells with different colours suggested that a green-yellow would be the optimum colour for a Si solar cell material. As

discussed in *Chapter 2*, in most cases, the textile-based solar energy harvesters presented in the literature were limited to the colour of the photoactive material employed within the cell.

The colour of the solar-E-yarns could be a key design consideration depending on their end-user application, especially for outerwear products. The fibre sheath of the solar-E-yarn determines its colour. For this research white textile fibres were mainly employed to craft solar-E-yarns. However, it is important to investigate the viability of creating solar-E-yarns with different colours that expand the application area of the solar-E-yarns. Therefore, solar-E-yarns were prepared using fibrous sheaths in two additional colours (red and black) and were studied to analyse the effect of colour on their photovoltaic output (I_{sc} and V_{oc}). The $1.5\text{ mm} \times 1.5\text{ mm}$ SCs encapsulated within 1.6mm micro-pods were covered using texturized polyester yarns, of the same yarn characteristics mentioned in previous experiments, in white, red and black as shown in Fig 5.19.

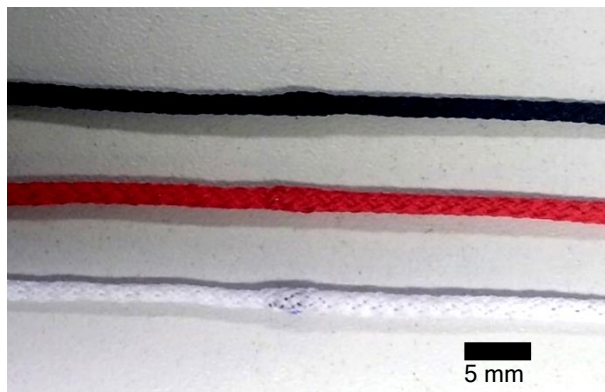


Figure 5.19 – Photograph of solar-E-yarns with packing yarns and tubular warp knitted structure made using black, red, and white textured polyester yarns for the knit braid. The packing fibres were white coloured.

The I_{sc} and V_{oc} values of the solar-E-yarns were evaluated using optical test rig under different optical filters to study the effect of coloured fibre sheath under different optical spectra (Fig. 5.20). The I_{sc} for each solar-E-yarn type at different incident angles were also studied.

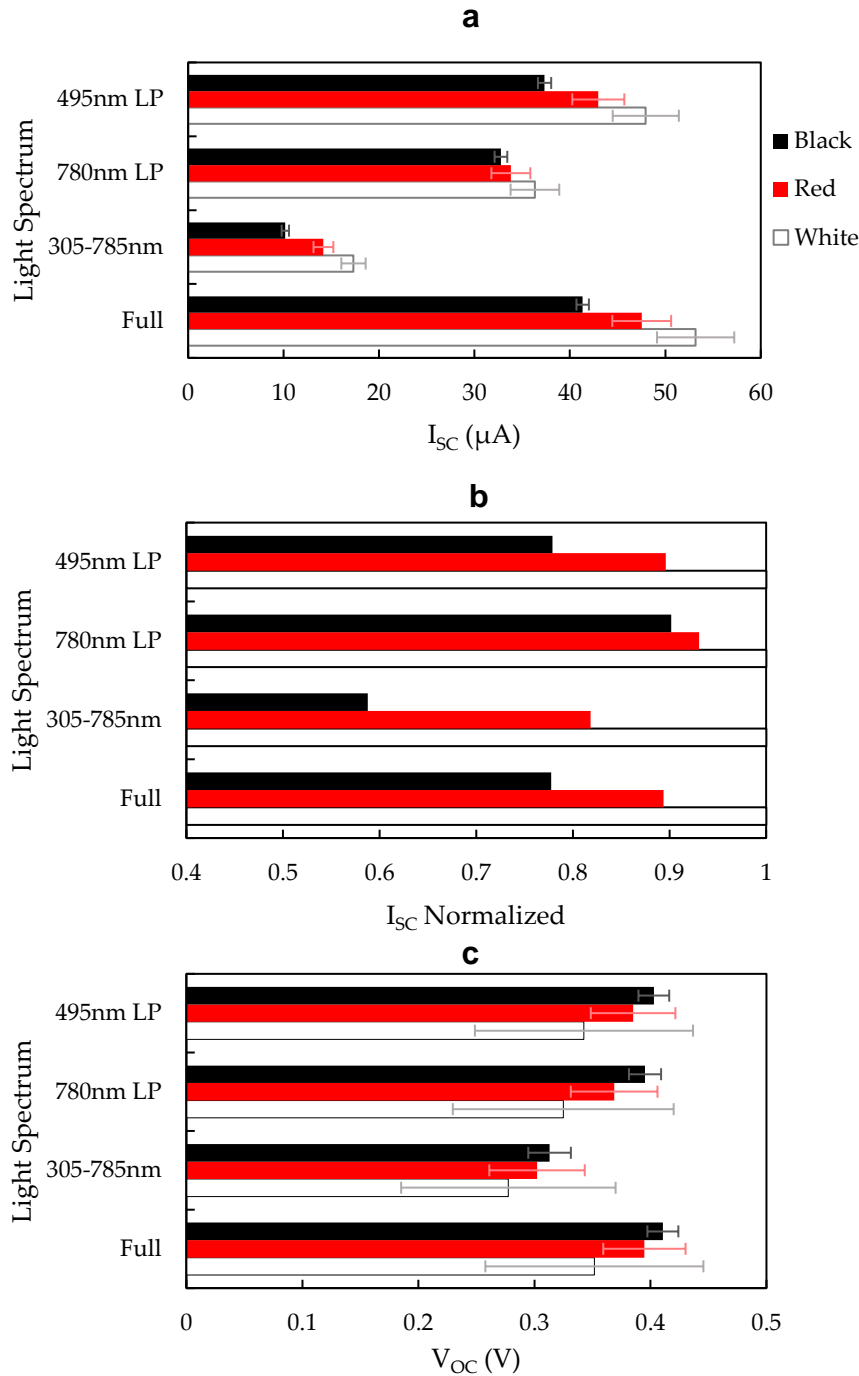


Figure 5.20 – Results for the solar-E-yarns with black, red and white outer sheaths. (a) Short-circuit current (I_{sc}); (b) normalized I_{sc} , and (c) open-circuit voltage (V_{oc}). In (b) the results were normalized to the I_{sc} for white solar-E-yarn for each spectral band.

When red and black fibrous sheaths were used the solar-E-yarns showed I_{sc} value of $89.4 \pm 5.8\%$ and $77.7 \pm 1.2\%$ compared to the normal solar-E-yarn (white sheath) respectively (See Fig.5.20(a)) under the full light spectrum. The data for V_{oc} values (Fig 5.20(b)) did not show a significant difference for three different colours tested. These results

suggested that the colour of the knit braid did influence the I_{sc} value although this effect did not significantly compromise the performance of the solar-E-yarns. This also provided evidence that the light penetration into the RMP predominantly occurred through the spaces between the fibres. When the I_{sc} values from the red and black solar-E-yarns were normalized to the white solar-E-yarn values, it was clear that the measurements under 305-785 nm band (ultraviolet and visible band) filter resulted in the largest difference in relative I_{sc} value.

This observation could be explained by the higher light absorption by black and red fibre sheath in comparison to white in the visible range. When the 780 nm long-pass (infra-red range) filter was used the difference between the I_{sc} values were the smallest (Figure 5.20 (a)), possibly due to the similar absorption of infra-red energy by all three-colours of knit-braids.

I_{sc} measurements were also conducted with different incident light angles normal to the longitudinal axis of solar-E-yarns made with black, red and white knit braids (Fig. 5.21).

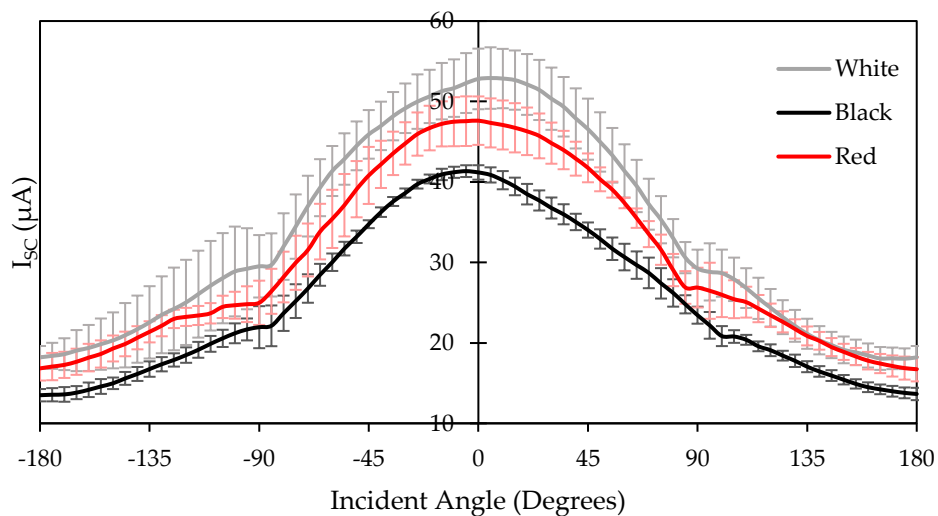


Figure 5.21 – Change in short-circuit current (I_{sc}) at different incident angles for solar-E-yarns with white, red and black outer sheaths. Measurements were conducted using the optical test rig with no optical filters.

All of the solar-E-yarns showed similar behaviour at different angles of incident light regardless of the colour of the outer textile sheath.

5.3.7 First prototype of fabric using solar cell yarns

In-order to confirm the feasibility of converting the solar-E-yarns into a fabric form, a set of yarns with multiple MSC embedded were fabricated. The solar-E-yarn each included three embedded MSCs ($1.5 \text{ mm} \times 1.5 \text{ mm}$) which were soldered onto a pair of copper wires in parallel. Gaps between the two adjacent MSCs were maintained at 2.0 mm after considering four factors; maximise the power density of the solar-E-yarn, maintaining a sufficient spacing between the MSCs to produce discrete RMPs that could hermetically seal the MSCs, retain the bendability of the resultant fabric, and to prevent short-circuiting of the two parallel copper wires (as this Cu wire was not electrically insulated). The soldered MSCs were individually encapsulated in 1.6 mm diameter cylindrical RMPs of $\sim 2.5 \text{ mm}$ length and were finished according to the baseline specifications given in Table 5.1 (page 124) as shown in Fig. 5.22(a). Five of these solar-E-yarns were then woven into a fabric swatch in combination with cotton yarns as shown in the Fig. 5.22(b).

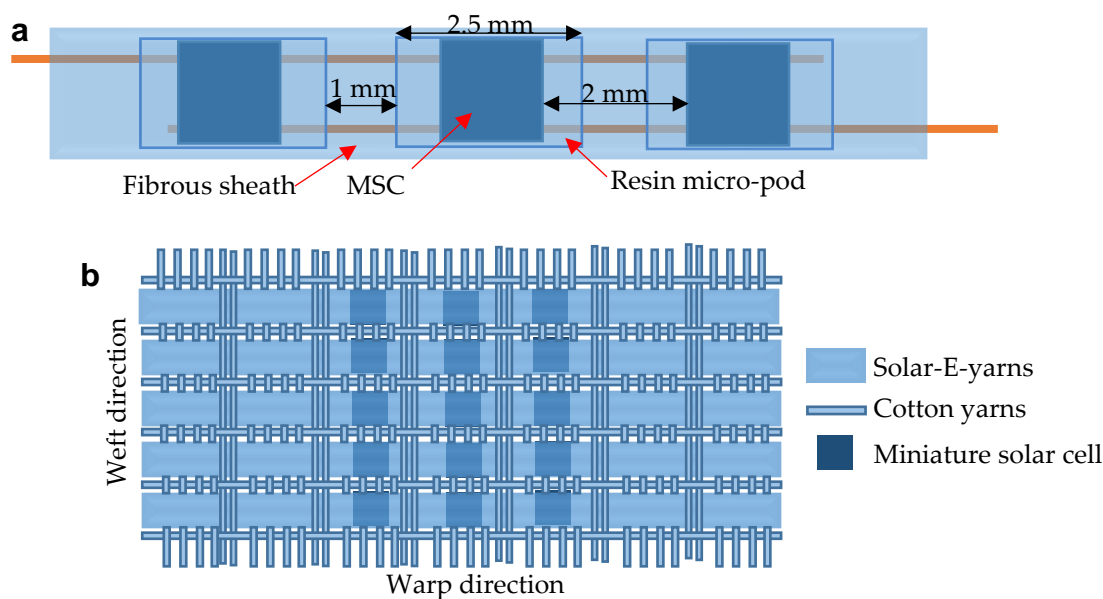


Figure 5.22 – Schematic depiction of (a) a solar-E-yarns prepared with three $1.5 \times 1.5 \text{ mm}$ solar cells and (b) the fabric woven with solar-E-yarns and cotton yarns.

The solar cell region covered a rectangular area of $\sim 1.0 \times 1.4 \text{ mm}$ ($\sim 1.4 \text{ cm}^2$) as shown in Fig. 5.23(a). The five individual yarns were then connected in series to create a network of 15 MSCs as illustrated in Fig. 5.23(b).

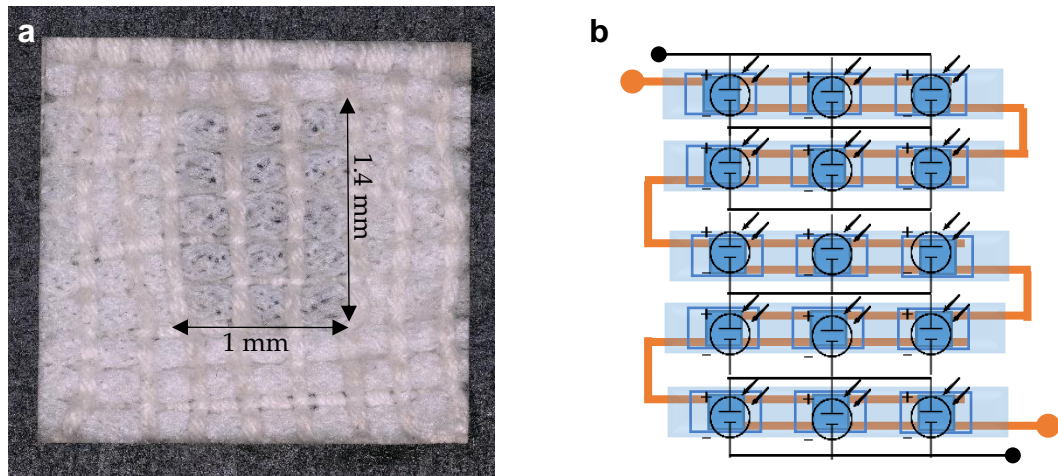


Figure 5.23 – First fabric prototype developed with solar cell embedded yarn. (a) Microscopic image of the fabric. (b) Electrical network of solar-E-yarns within the fabric.

The prototype was tested under direct sunlight (Fig 5.24) on a sunny day and under one sun illumination (1000 W/m^2 , AM 1.5 Global spectrum) using the solar simulator mentioned in *Chapter 3*; the results obtained are given in Table 5.3. The solar simulator was introduced and employed for subsequent evaluations of the solar-E-yarns and resultant fabrics under standard one sun illumination to generate globally comparable test results. The solar simulator also provided closer representation of the conditions prevailing in most real-life applications.



Figure 5.24 – Measurement of short-circuit current and open-circuit voltage of the first solar energy harvesting prototype fabric under direct sunlight.

Table 5.3 – Output from the prototype solar energy harvesting fabric under direct sunlight and using the solar simulator.

Lights source	Isc (mA)	Voc (V)	Estimated power (mW) at FF = 0.65
Direct Sunlight	1.42	2.62	2.42
Solar Simulator (1000 W/m^2 , AM 1.5 G)	1.53	2.65	2.64
Theoretical estimation based on single cell performance	1.56	2.71	2.75

These experiments confirmed the viability of developing solar energy harvesting fabrics woven with solar-E-yarns. The first prototype exhibited an estimated power density of 1.88 mW/cm^2 which would be adequate for powering wearable or low-powered mobile electronic devices when applied for an outerwear product such as a jacket. Compared to the theoretical estimates based on single cell solar-E-yarns were slightly higher than the experimental figures probably due to mismatch losses and cell mis-alignment losses. In addition the fabric surrounding would also have a positive effect on the solar-E-yarn performance. These will be further discussed in *Chapter 7*.

5.3.8 Optimisation of solar cell length

Based on the evaluations conducted using $1.5 \text{ mm} \times 1.5 \text{ mm}$ SCs the possibility of increasing the length of the MSC as a strategy to improve power density was considered. This would also reduce the number of MSCs required to produce the same amount of energy, which will improve the manufacturing efficiency. The length of the MSC dictates the length of the micro-pod which directly influenced the bending radius the solar-E-yarn. Therefore to achieve an optimum balance between bendability and power density of the solar-E-yarn the cell length was revised to 3.0 mm . It was estimated that by using 3.0 mm long cells, the maximum power density of a solar-E-yarn integrated woven fabrics can be enhanced by $\sim 30\%$, as shown in the Table 5.4. The table also shows the estimated power density of resultant fabric prepared with resin impregnated solar-E-yarns for both the MSC sizes.

Table 5.4 – Estimated maximum power densities for fabrics woven using solar-E-yarns prepared with different MSC sizes.

Solar-E-yarn type	Maximum number of solar cells in 1 cm^2	Maximum power density in fabric form (mW/cm^2)
$1.5 \times 1.5 \text{ mm}$	12	1.88 (Measured)
$1.5 \times 3 \text{ mm}$	8	2.50 (Estimated)
$1.5 \times 1.5 \text{ mm}$ with resin impregnation	12	3.29 (Estimated)
$1.5 \times 3 \text{ mm}$ with resin impregnation	8	4.38 (Estimated)

5.4 Solar-E-yarns using $1.5 \text{ mm} \times 3.0 \text{ mm}$ solar cells

The production process and material employed for preparing solar-E-yarns using $1.5 \text{ mm} \times 3 \text{ mm}$ MSCs was identical to that of solar-E-yarns with $1.5 \text{ mm} \times 1.5 \text{ mm}$ MSCs, as

mentioned in Table 5.1. Fig 5.25 shows microscopic images of the different stages of the solar-E-yarn process when using $1.5\text{mm} \times 3\text{ mm}$ MSCs were used (Fig 5.25).

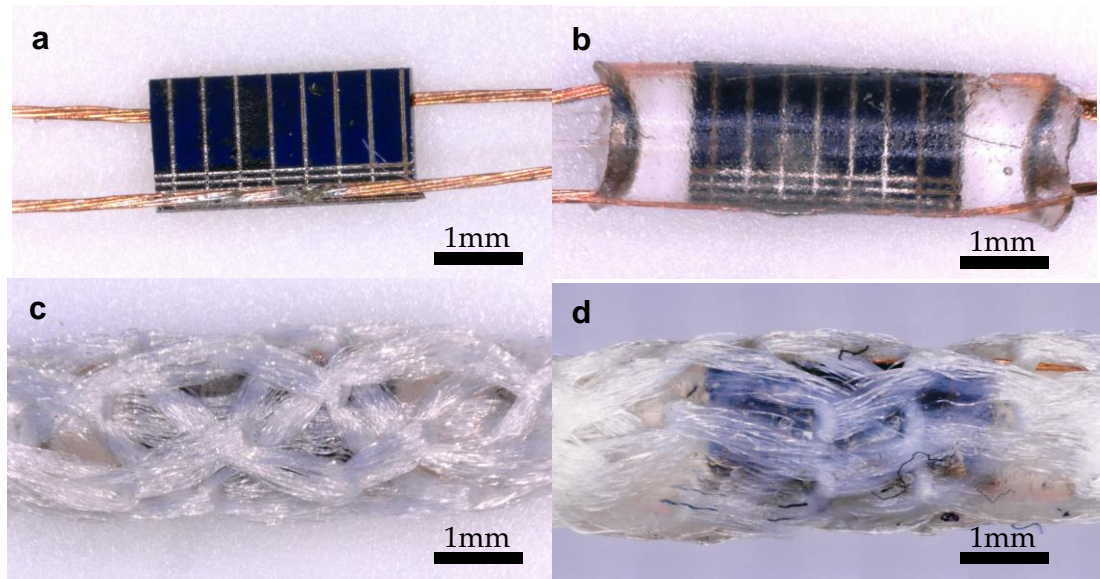


Figure 5.25 – Microscopic images of $1.5 \times 3.0\text{ mm}$ MSC (a) soldered onto Cu wires, (b) embedded inside 1.6mm resin micro-pod, (c) solar-E-yarn and (d) solar-E-yarn with resin impregnation.

Characterisation was conducted using the solar simulator at one sun intensity (AM 1.5 global spectrum, $1000\text{W}/\text{m}^2$). In this case a detailed study of device performance was performed by generating current-voltage (I-V) and (P-V) power voltage curves (Fig. 5.26(a)) from which I_{SC} , V_{OC} , FF, and P_{MAX} were derived.

The linear relationship between light intensity and I_{SC} explains the clear change in I_{SC} of the MSC during the yarn fabrication process. On the other hand, V_{OC} showed a modest change due to its logarithmic relationship with light intensity (Chegaar *et al.*, 2013).

When the MSCs were encapsulated within the RMPs the I_{SC} and P_{MAX} values increases by 18.3% and 21.7% respectively. After covering the MSC in RMP with a fibrous sheath the I_{SC} and P_{MAX} values decreased by 29.3% and 32.5% (relative to the values of maiden MSCs) due to shading and light absorbance effects of the fibrous sheath as observed previously. After resin impregnation the I_{SC} and P_{MAX} values were enhanced by ~66.5% compared to the values for solar-E-yarn before resin impregnation. In comparison to the maiden MSC, the resin impregnated solar-E-yarn had a 12.8 % higher P_{MAX} . The V_{OC} did not change significantly due to the fabrication process. FF was reduced by ~4.6% from the maiden MSC to solar-E-yarn, which recovered to original values after resin impregnation.

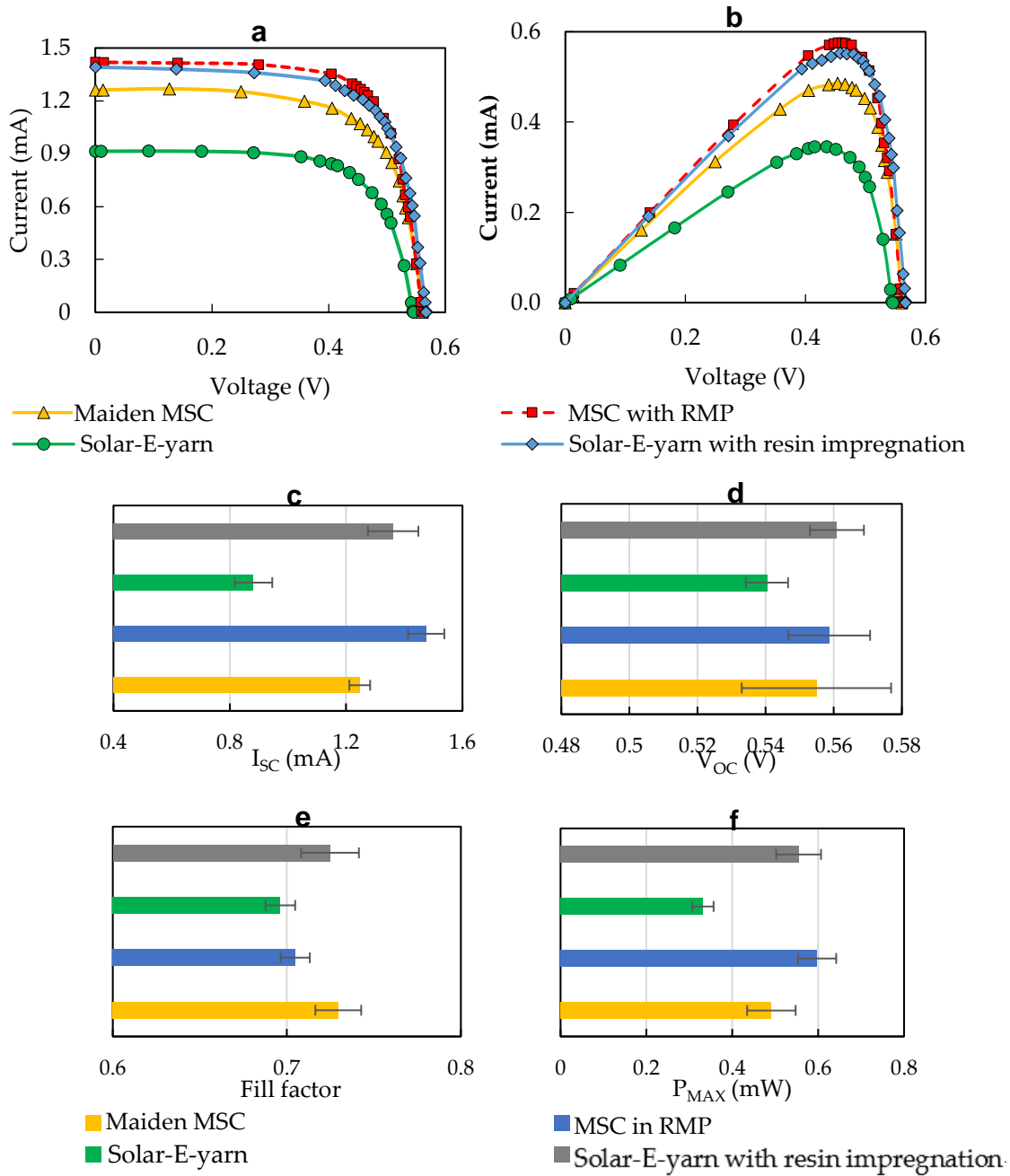


Figure 5.26 – Opto-electronic characterisation of the solar-E-yarns with a single $1.5\text{mm} \times 3\text{mm}$ single cell at different stages of the fabrication process, under one sun (AM 1.5 global spectrum, $1000\text{W}/\text{m}^2$) intensity: (a) Current-voltage curves (IV), (b) power-voltage (P-V) curves, (c) short-circuit current (I_{sc}), (d) open-circuit voltage (V_{oc}), (e) fill factor and (f)

In summary these results agreed with the results observed for the experiments conducted using $1.5\text{mm} \times 1.5\text{mm}$ MSCs. Further experiments on the preparation and characterisation of the solar-E-yarns and resultant fabrics prepared with multiple $1.5\text{mm} \times 3.0\text{mm}$ MSCs are discussed in *Chapter 7*.

5.4.1 Effect of change in incident angle normal to the width direction of the solar-E-yarns

As mentioned in *Chapter 3*, the solar simulator introduced the possibility of conducting measurements at different incident angles normal to both longitudinal axis and width direction of the solar-E-yarns. An experiment was conducted to measure the change in the I_{sc} of solar-E-yarns normal to the width direction of the MSC and resultant solar-E-yarns using the solar simulator. These results, along with the previous tests of solar-E-yarns at varying incident angles normal to the longitudinal axis generated using the optical test rig (discussed previously in 5.3.3 and 5.3.4) provided a complete picture of the performance of solar-E-yarns at varying incident angles in three-dimensional space.

When the angle of incident light changed normal to the width direction, the I_{sc} reached zero at 90° and -90° angles. This was possibly due to the complete self-shading of light when the beam of light was parallel to the photoactive plane of the MSC. The normalized I_{sc} values at each stage in the solar-E-yarn fabrication process closely followed the cosine law. This provided clear evidence that the effects of the different components of the solar-E-yarn did not vary with the change in incident angle normal to the width direction of the embedded MSC.

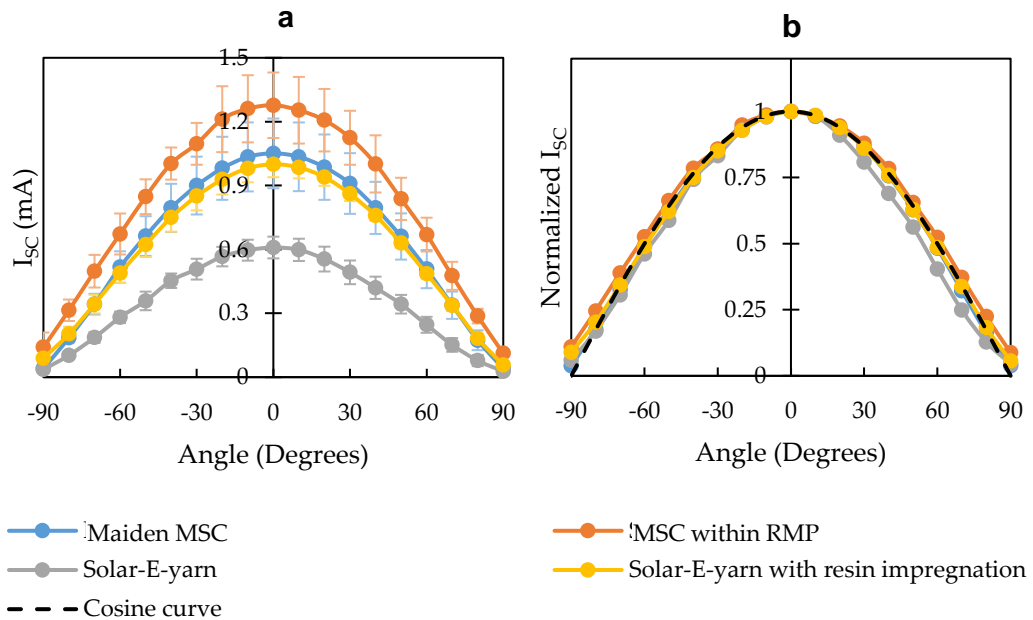


Figure 5.27 –Change in short-circuit current (I_{sc}) at different incident angles normal to the width direction of the MSCs in the front half circle, for solar-E-yarns at different stages of the fabrication process. (a) Absolute I_{sc} values. (b) Normalized I_{sc} values (normalized to the value at zero-degree angle, at each stage).

In a real-life application not only would the azimuth and altitude of the sun change but also the orientation of the solar-E-yarns is unpredictable due to the movement by the wearer of the clothing embedded with solar-E-yarns. Based on the results of the above experiments and empirical models given by Eq 5.8, 5.19 and 5.20, change in I_{sc} with incident angle variations in three-dimensional hemispherical space can be empirically estimated as:

$$I_{SC (Maiden SC)} = kW \cos \gamma_1 \cos \gamma_2 \quad 5.21$$

$$I_{SC (SC in RMP)} = R_m [3779 \sin (1.294\gamma_1 + 1.595) + 3727 \sin (1.304\gamma_1 + 4.737)] (1 + \cos \gamma_1) \cos \gamma_2 \quad 5.22$$

$$I_{SC (Solar-E-yarn)} = R_y [39.91 \sin (1.057\gamma_1 + 0.4414) + 24.17 \sin (2.312\gamma_1 + 2.441) + 9.124 \sin (2.968\gamma + 4.963)] (1 + \cos \gamma_1) \cos \gamma_2 \quad 5.23$$

Where W , R_m and R_y are the width of the SC, radius of the RMP, and radius of the solar-E-yarn. γ_1 and γ_2 are the angles to the vertical axis made by the two orthogonal projections of an incident ray as indicated in Fig 5.28.

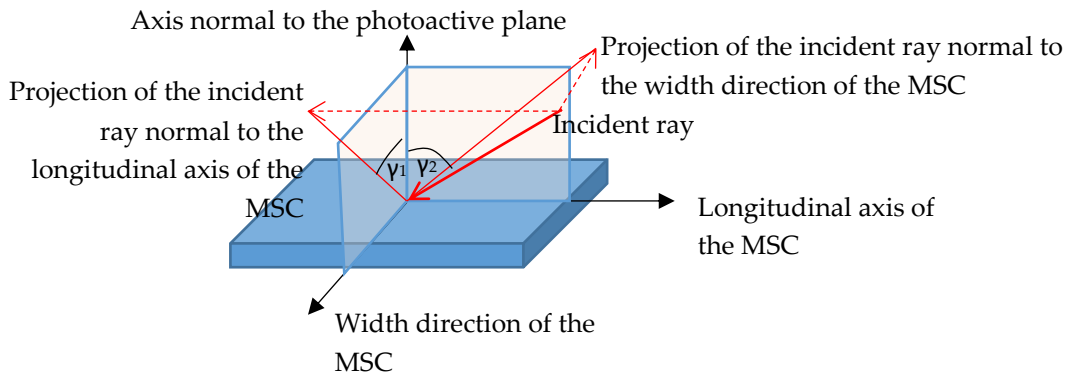


Figure 5.28 – Illustration of an incident ray defined in three-dimensional space relative to the photoactive surface of a MSC.

In summary the I_{sc} showed higher uniformity with change in incident angle normal to the longitudinal direction compared to the I_{sc} with change in incident angle normal to the width direction of the solar-E-yarn. Therefore, in practical applications it would be best to position the solar-E-yarns vertically on the final garment when designing products for use in the polar regions and vice-versa (position the solar-E-yarns horizontally) for use in the tropical regions of the globe.

5.4.2 Effect of light intensity on the solar-E-yarns

In practical scenarios, the intensity of light received by the solar energy harvesters may change over time: This could be due to atmospheric changes such as the nature of cloud cover, the change in altitude and azimuth of Sun, or the motion of the wearer. According to theory I_{sc} of MSCs have linear relationship with intensity of light, while the V_{oc} changes logarithmically with the light intensity (Chegaar *et al.*, 2013) as given in Eq. 5.24:

$$V_{oc} = \left(\frac{k_B T}{q} \right) \ln \left(\frac{I_{ph}}{I_0} + 1 \right) \quad 5.24$$

Where $\frac{k_B T}{q}$ is a constant for a given temperature (k_B - boltzman constant, T - absolute temperature, q -electron charge), I_{ph} is the photo-generated current, and I_0 is the dark current. According to the equation, when the MSC is in the dark V_{oc} approaches zero.

When the MSC is embedded inside of the E-yarn the fibrous sheath and the RMP interfere with the incident light. An experiment was conducted to study the effects of the components of the solar-E-yarns on the I_{sc} and V_{oc} were consistent at different light intensities in comparison with maiden MSCs (Fig. 5.29).

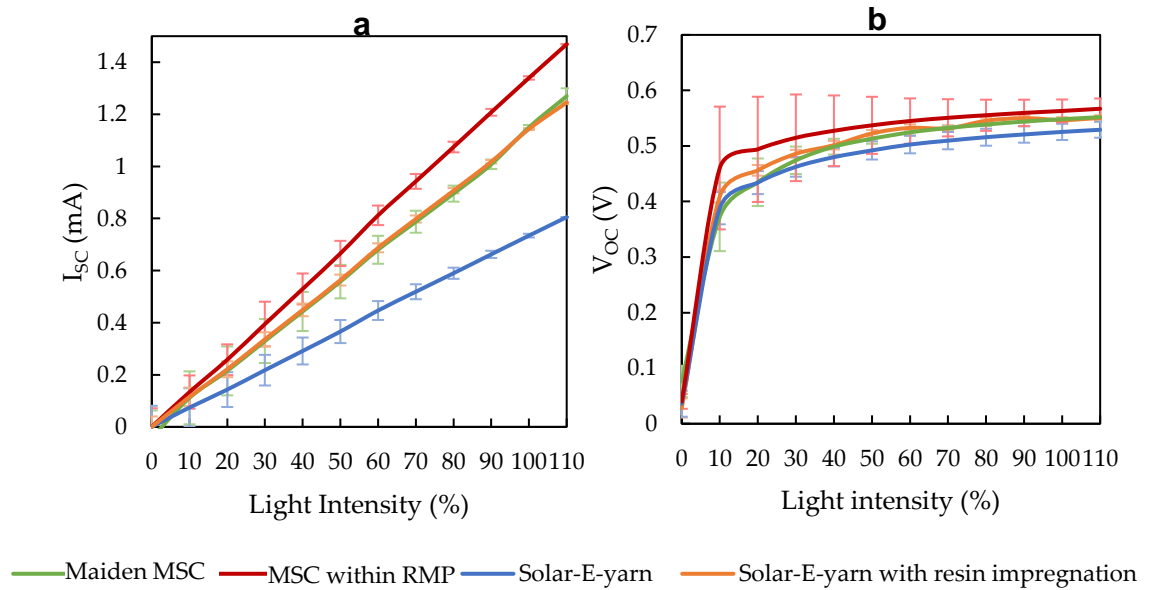


Figure 5.29 – Change in (a) short-circuit current (I_{sc}) and (b) open-circuit voltage (V_{oc}) with light intensity for solar-E-yarns at different stages of the fabrication process. 100% represents one sun intensity.

The results confirmed that the linear relationship between I_{sc} and light intensity is preserved at every stage of the solar-E-yarn fabrication process. The current per input

power values (Table 5.5) given by the gradient of the lines of Fig. 5.29(a) show that the effects of RMP, fibrous sheath and resin impregnation on the current, at different light intensities were proportionate to the light intensity.

Table 5.5 – Estimated short-circuit current (I_{sc}) per incident light power using the experimental I_{sc} values at different light intensities current.

Device type	Short-circuit current (I_{sc})/input power density (mA/mWcm ⁻²)
Maiden MSC	0.0114
MSC embedded within an RMP	0.0134
Solar-E-yarn	0.0074
Solar-E-yarn with resin impregnation	0.0116

The experimental V_{oc} values for the MSCs at each stage in the solar-E-yarn fabrication process fit closely with the logarithmic relationship (Eq.5.25) given by:

$$V_{oc} = a \ln(bx + 1) \quad 5.25$$

as given in table 5.6. Here x is the light intensity and a and b are fitting constants.

Table 5.6 – Results of the curve-fit for open-circuit voltage (V_{oc}) against light intensity for solar-E-yarns at different stages of the fabrication process. Curve-fitting was conducted using the Matlab® curve-fitting tool.

Device type	Fitting constants	R ²
Maiden MSC	a = 0.07446, b = 17.46	0.9788
MSC inside RMP	a=0.04418, b = 3612	0.9956
Solar-E-yarn	a = 0.05869, b =82.13	0.9922
Solar-E-yarn with resin impregnation	a = 0.05847, b = 123.3	0.9892

Although the V_{oc} value should reach zero at zero light intensity, the experimental results at this point was slightly higher than zero, probably due to imperfect dark conditions.

5.4.3 Packing fibres embedded within the micro-pod

The use of texturized yarns for packing fibres was crucial to improve the uniformity in thickness of E-yarns along the length direction, where the texturized yarns can bulk-up by crimping when the E-yarn relaxes. In the regions without RMPs, the packing fibres readily crimp and occupy the empty spaces in the core of the E-yarn. However, the

packing fibres are compacted between the RMP and knit-braided structure in the regions with the RMP therefore, do not crimp and volumize. To enhance the uniformity of the E-yarns it was suggested that the packing fibres could be embedded inside of the RMP with the soldered MRC during the encapsulation process. This was expected to reduce the diameter of solar-E-yarns at the RMP, as illustrated in Fig 5.30.

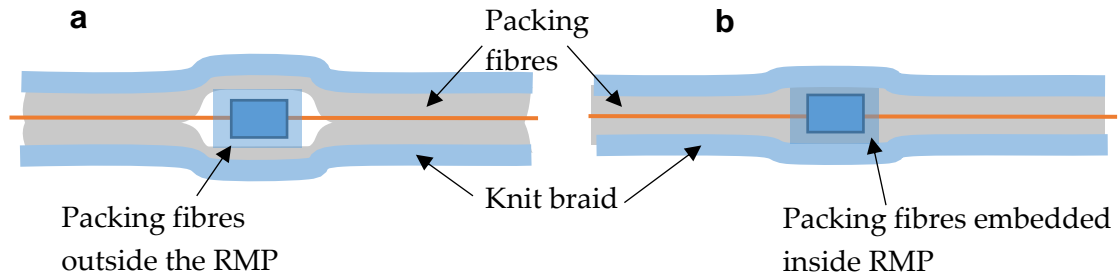


Figure 5.30 – Schematic of the longitudinal sections of solar-E-yarns prepared with packing fibres (a) outside of the resin micro-pod (RMP) and (b) embedded within the RMP.

To evaluate the viability and benefits of embedding packing fibres within the RMP for solar-E-yarns, the encapsulation process was modified to position packing fibres (four 167dtex/48f packing yarns) within the encapsulation tube surrounding the soldered MSC.

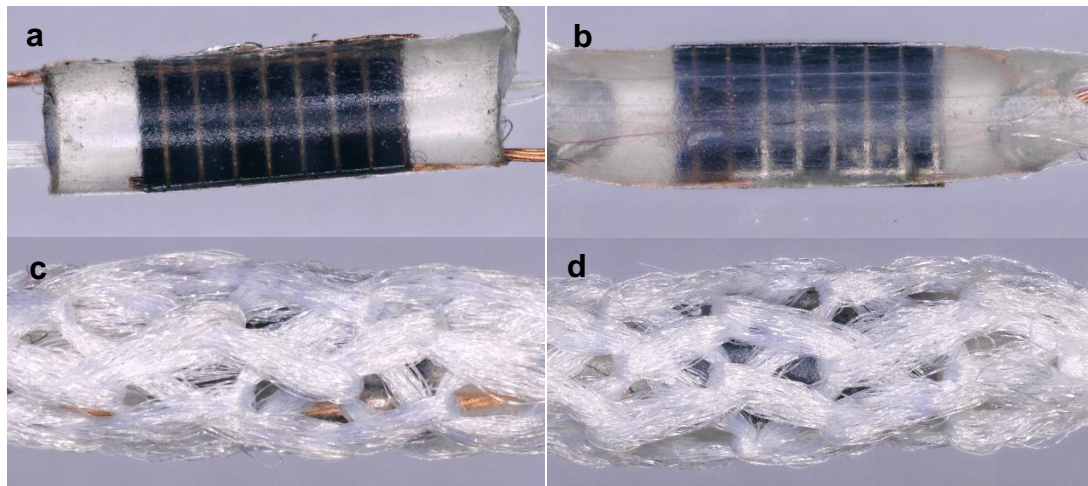


Figure 5.31 – Microscopic images of (a) MSC embedded within a resin micro-pod (RMP) (b) MSC and packing fibres embedded within RMP, and the resultant solar-E-yarns with (c) packing fibres outside of the RMP and (d) packing fibres within the RMP.

The microscopic images of the RMPs prepared with packing fibres embedded in RMP (Fig. 5.31) showed that, the RMP embedded with packing fibres appeared slightly

translucent compared with the RMP without packing fibres. On the other hand, in the microscopic images for standard solar-E-yarns (prepared with packing fibres outside of the RMP) the layer of packing fibres was clearly visible through the knit-braid.

I_{sc} measurements taken using solar-E-yarns with the two different packing fibre configurations showed that at the RMP stage there was a ~9% reduction when the packing fibres were embedded within the RMP, possibly due to light scattering occurring at the fibre-RMP interfaces; There was no significant difference in the I_{sc} for the solar-E-yarns as shown in Fig 5.32, confirming that embedding the packing fibres within the RMP did not enhance the photovoltaic performance of solar-E-yarn. There was a ~9 % reduction in the thickness (~0.2 mm) of the solar-E-yarn when the packing fibres were embedded inside the RMP (Fig. 5.32(b)), confirming that the uniformity of the solar-E-yarn was marginally improved.

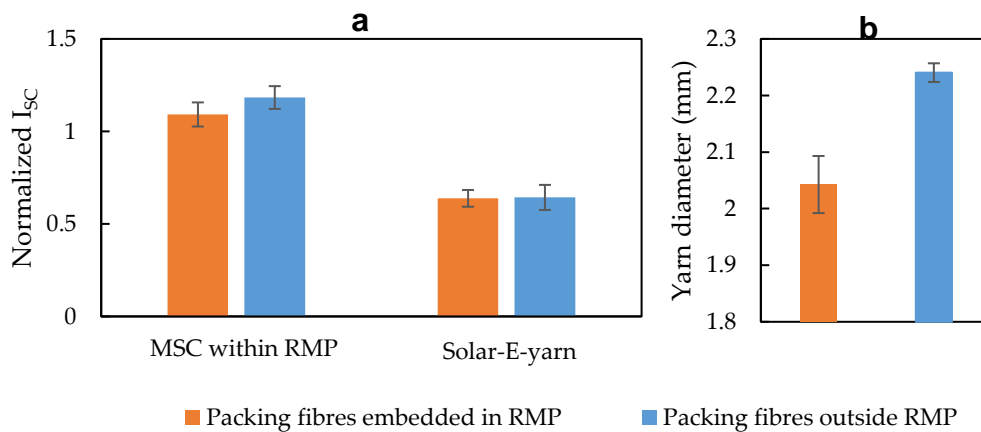


Figure 5.32 – (a) Comparison of normalized short-circuit current (I_{sc}) when the packing fibres were outside of the resin micro-pod (RMP) and packing fibres embedded within the RMP; at the RMP stage and solar-E-yarn stage. The results are normalized to maiden MSC measurements. (b) Change in thickness of the solar-E-yarn when packing fibres were embedded within the RMP.

5.4.4 Solar-E-yarns prepared with normal braided outer sheath

The knit braided structure of the solar-E-yarns can be replaced by a normal braided structure which is prepared using a different technique. Unlike the knit braid, where the tubular structure is prepared by inter-looping yarns, a normal braided structure is formed by interlacing several sets of yarns at different braid angles. The tubular structures prepared by normal braiding have several structural differences compared to knit-braided yarns, such as lower tube wall thickness, higher compactness and higher

cover factor. These features impart an even and smooth surface appearance to the normal braided structure that could be advantageous for applications requiring smooth fabric surfaces. The cover factor of the tubular structure determines the proportion of incident light that can be directly transmitted to the core of the yarns. Higher cover factor of normal braiding means, higher interference with incident light that may reduce the I_{sc} and power output of the solar-E-yarn. From a process standpoint, unlike knit braiding, normal braiding is a semi-continuous process where the yarn carrier bobbins cannot be replenished while the machine is running. In the normal braiding process, the main structural parameter that can be adjusted is the lay length. Lay-length determines the braid angle (the angle made to the longitudinal direction of the braided tube by the individual yarns). It was observed that with braid angle the cover factor and the diameter of the braided tube changed, and this could change the light intensity received by the embedded RMP. A series of solar-E-yarns were prepared with varying lay lengths (8 mm to 20 mm; Fig. 5.33(b)) using Herzog textile braiding machine (RU/12480, Herzog GmbH, Germany) (Fig. 5.33(a)) to observe the relationship between the lay-length, E-yarn diameter, and the I_{sc} generated by the solar-E-yarns.

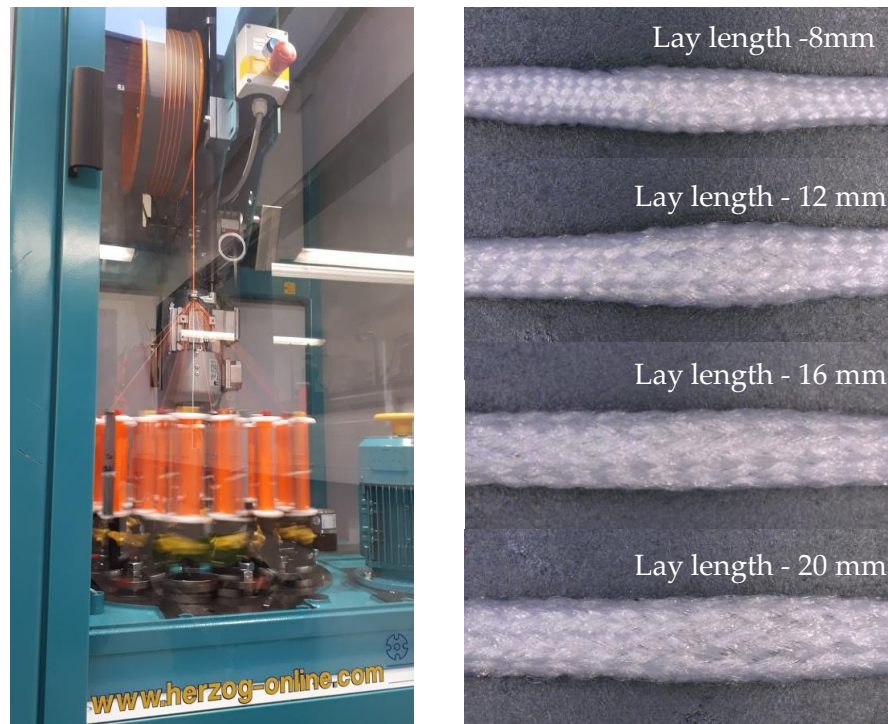


Figure 5.33 – (a) The Herzog braiding machine used for preparing the solar-E-yarns. (b) Microscopic images of the solar-E-yarns prepared with different lay lengths.

These solar-E-yarns used $1.5 \text{ mm} \times 3.0 \text{ mm}$ MSCs embedded within 1.6 mm diameter RMP with no packing fibres. One set of solar-E-yarns were prepared with packing fibres (four 167dtex/48f texturized polyester packing yarns) embedded within the RMP and 12 mm lay length. The braid structure was prepared using 24 texturized polyester (167dtex/48f) yarns.

The result for solar-E-yarns prepared using the braid with a 12 mm lay length (Fig. 5.34(a)), with and without the inclusion of packing fibres, confirm that there was no significant effect of the packing fibres on I_{sc} . The I_{sc} showed a positive linear relationship with the lay length and braid angle, clearly indicating the increased openness of the braid with a higher lay length as shown in literature (Kyosev and Aurich, 2016). It was estimated that a normal braided solar-E-yarn with $\sim 14.0 \text{ mm}$ lay length would generate an I_{sc} values generated by a, solar-E-yarn with a knit braided sheath of 2.0 mm diameter.

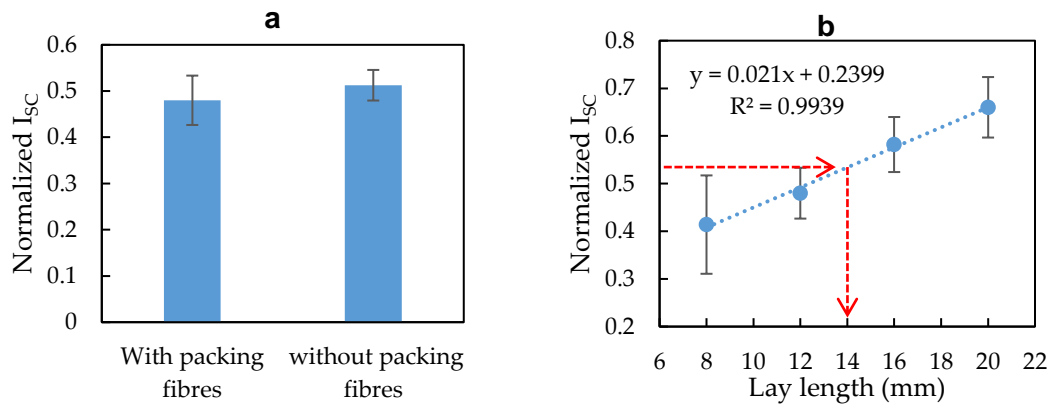


Figure 5.34 – Measurements from the solar-E-yarns made with normal braid outer sheath. (a) Effect of packing fibres on the normalized short-circuit current. (b) Effect of braid lay length on the normalized short-circuit current. The data shown has been normalized to the maiden MSC I_{sc} . The red dashed line indicates the corresponding value for a solar-E-yarn with a knit-braided sheath. Measurements were conducted under one sun intensity.

The normal braiding process can be more versatile over the knit braiding process where the diameter of the E-yarn is limited by the inner diameter of the knitting cylinder. Also, the appearance of the normal braided sheath is smooth due to the highly ordered interlacing structure in contrast to the heterogeneous yarn orientation within the interlooped knit-braided structure (Fig.5.35).

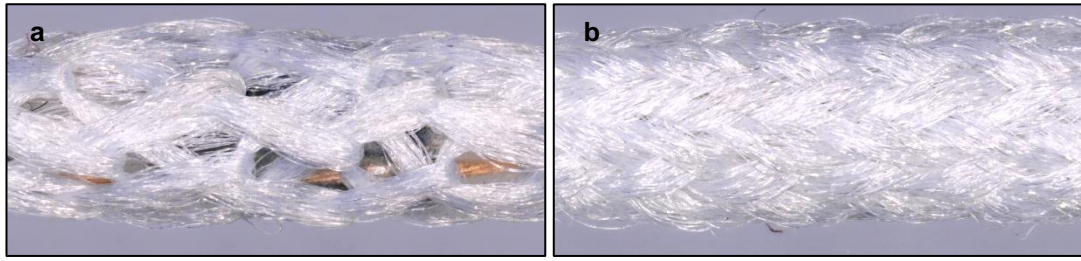


Figure 5.35 – Side-by-side visual comparison of the solar-E-yarns prepared with (a) a knit-braided sheath and (b) a normal braided sheath.

The results confirmed that diameter of the braid was changing with the lay length (Fig. 5.36). It was estimated that the diameter of the braid increased beyond 2.0 mm for lay lengths higher than ~9 mm. However, at this lay length the I_{sc} value for the normal braided solar-E-yarn was estimated ~20% lower than a corresponding knit-braided solar-E-yarn. It was observed that the core of the solar-E-yarn (micro-pod-wire filament) was loose and unstable within the braid for lay lengths beyond 8 mm.

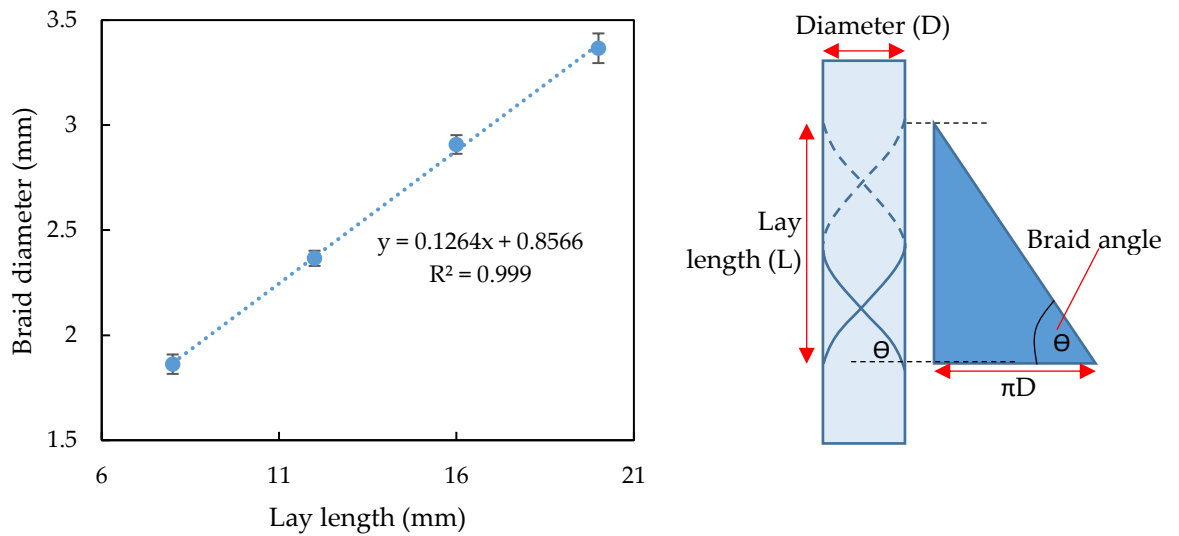


Figure 5.36 – Change in diameter of the braid with lay length for the solar-E-yarns.

While some freedom for movement of the micro-pod within the sheath is desirable to maintain flexibility and conformability of the E-yarn, excessive space between the braid and the core would create instability causing significant rotational misalignment of the RMP. This misalignment would be detrimental to the performance of the solar-E-yarn embedded fabrics, due to the possible electrical mismatch losses caused by irregular shading. In summary, while the normal braided solar-E-yarn had a more desirable appearance, photovoltaic output of a stable solar-E-yarn prepared was lower than the solar-E-yarns prepared using knit-braiding.

5.4.5 Solar-E-yarns using bi-facial solar cell concept

Originating at Bell Labs in 1954, in last decade, bifaciality has emerged as a concept with a potential to enhance power generation capability of SCs (Kopecek *et al.*, 2015). Bifacial cells have transparent faces that allow light to reach the photoactive material from both the front and back of the cell (conventional cells only have front active surface). This is achieved by using localized arrays of back contacts that are similar to the front contacts (Fig 5.33(b)). These bifacial cells can increase the power generated by gathering scattered light from the background, that lower the cost per unit power (Kopecek *et al.*, 2015). Bifacial technology has allowed for the deployment of vertical mount solar panels that are more efficient, versatile, and robust than tilted mono-facial panels (Guo, Walsh and Peters, 2013).

It was expected that the efficiency of solar-E-yarn could be significantly improved by using the bifacial cells. Also, further improvements of incident angle independency were foreseen. Since bifacial cells of the required size were not available, a bifacial equivalent cell was fabricated by attaching two individual MSCs back-to-back (Fig. 5.33(c)).

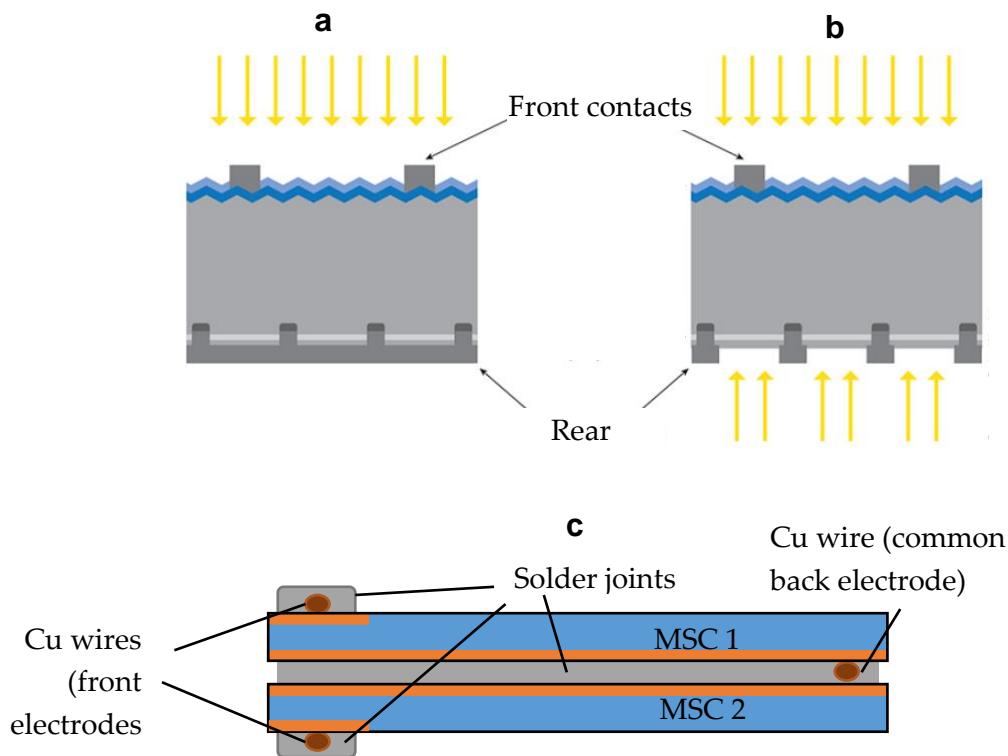


Figure 5.36 – Schematic of a typical electrode configuration of (a) a mono-facial and (b) a bifacial MSC. (c) Schematic illustrating the bi-facial equivalent solar cell prepared using two 1.5 mm × 3 mm solar cells.

The MSCs were soldered as shown in Fig. 5.36 and were encapsulated inside of 1.6 mm diameter resin micro pods, covered inside of a 2.0 mm diameter fibrous sheath, and the surface fibres were impregnated with the encapsulation resin. The I_{sc} and V_{oc} were measured (Fig. 5.37) for the samples made with bifacial cells at different stages of the fabrication process at one sun intensity at 0° incident angle. The results for the direct angle measurements showed no significant improvement in I_{sc} or V_{oc} for bi-facial solar-E-yarns compared to the conventional solar-E-yarns.

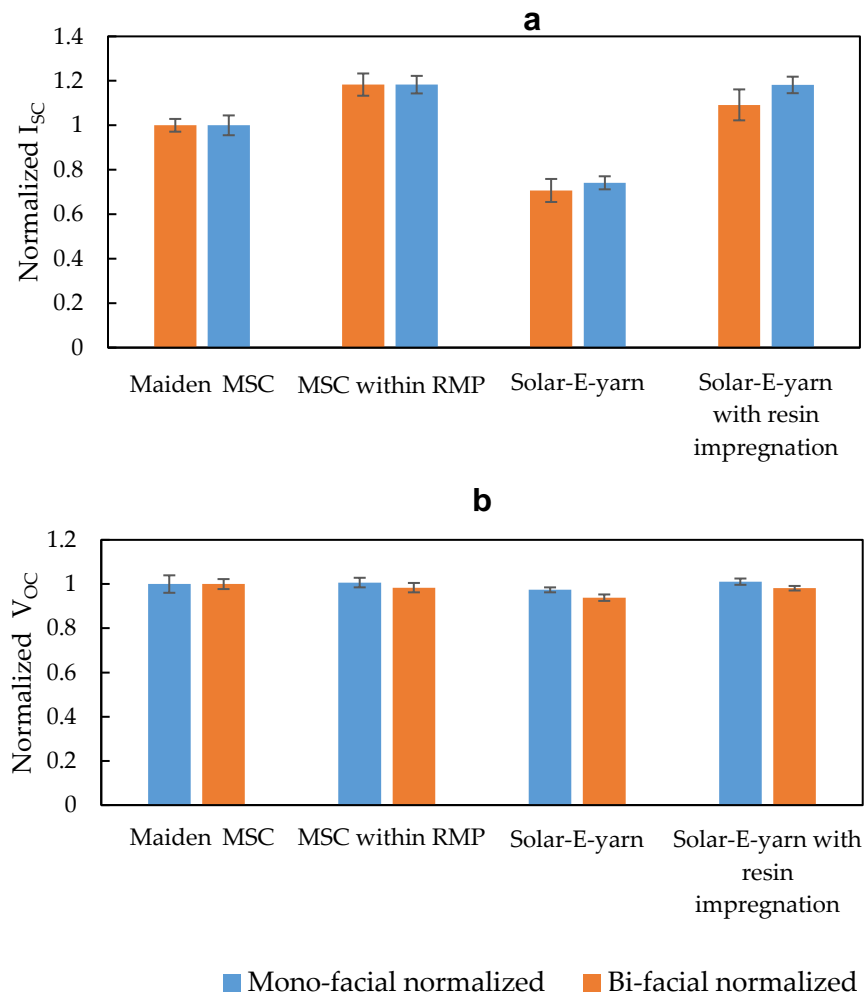


Figure 5.37 – The (a) normalized I_{sc} and (b) normalized V_{oc} for the bi-facial equivalent solar cell prepared with two $1.5\text{ mm} \times 3\text{ mm}$ solar cells. The values indicated are normalized to the results for maiden MSCs.

The change in I_{sc} with incident angle for the bi-facial solar-E-yarns was analysed using the optical test-rig and compared against the results for the solar-E-yarns made using mono-facial MSCs, as shown in Fig. 5.38.

The results showed a clear enhancement of I_{sc} at higher incident angles for solar-E-yarns and solar-E-yarns with resin impregnation prepared with bi-facial cells. This provided evidence of the light diffusing to the opposite face of the MSCs when the incident angle increased. At a 90° incident angle the solar-E-yarns generated (both before and after resin impregnation) an I_{sc} that was ~65% of the value at direct (0°) exposure. As expected, the behaviour of the bifacial devices at the back half circle (90° - 180°) were identical to the front half circle.

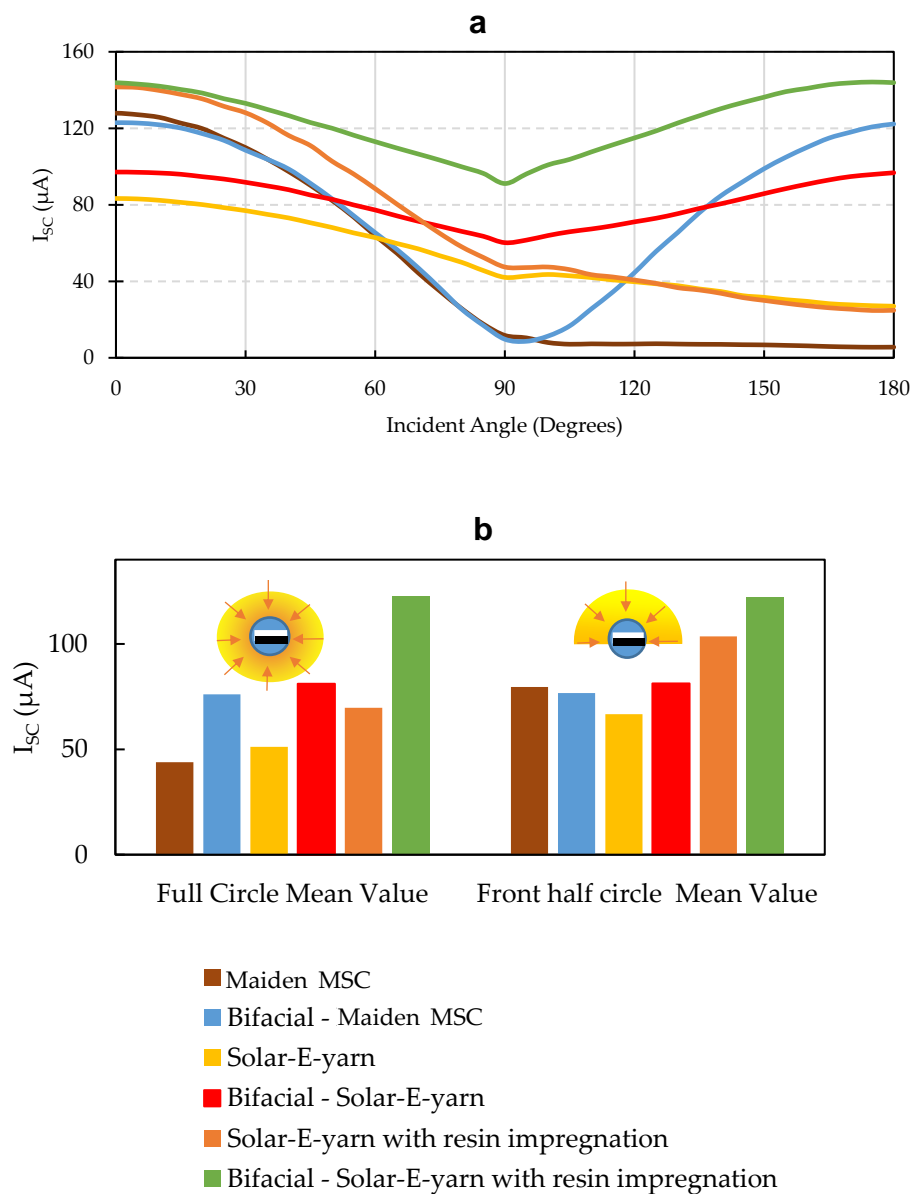


Figure 5.38- Bifacial solar-E- yarn performance. (a) Short circuit current (I_{sc}) and (b) open circuit voltage (V_{oc}) at different stages of the production process. (c) Change in I_{sc} with incident angle and (d) mean I_{sc} values in full circle and front half circle for bifacial and mono-facial (standard) solar-E-yarns.

When average I_{sc} was considered across the front half circle for the bifacial solar-E-yarn and bifacial solar-E-yarn with resin impregnation there was a ~22 % and ~19 % increase in I_{sc} respectively when compared to their mono-facial counterparts. Overall, the combined effects of bifaciality and resin impregnation on solar-E-yarns imparted an 83 % increase in average I_{sc} in the front-half circle.

As seen in Fig. 5.38(b) the increase in the full circle (0° - 180°) average I_{sc} values from mono-facial devices to bifacial devices were significantly higher than respective increases for half-circle values, however the half-circle values are more relevant for practical applications.

5.5 Conclusions

The experimentally observed effects of light scattering due to the fibrous sheath on the solar-E-yarn performance closely aligned with the values theoretically estimated using the mathematical model. The resin impregnation enhanced the short-circuit current of solar-E-yarn by ~70 % and compensated for the negative effects of the fibrous sheath, however the appearance and surface properties of the solar-E-yarn was modified by the resin impregnation. The solar-E-yarn appeared to have a more uniform response at different incident angles compared to the maiden MSCs especially when the incident light was normal to the length direction of the yarn. The comparison studies conducted using white, black and red fibrous sheaths confirmed that the solar-E-yarns can respond to any colour without a significant compromise on their performance. The fabric prototype prepared by weaving together solar-E-yarns (with 1.5 mm × 1.5 mm embedded solar cells) to prove the viability. This fabric generated a power density of 1.88 mW/cm². This was proof of the viability of the technology for developing solar energy harvesting fabrics. To improve the power density of the solar-E-yarns and process efficiency, the cell length was changed from 1.5 mm to 3.0 mm after initial investigations. The experiments conducted using 1.5 mm × 3.0 mm solar cells verified the results of the previous experiments conducted with 1.5 mm × 1.5 mm embedded solar cells. The change in the short-circuit current and open-circuit voltage for the solar-E-yarns at different light intensities exhibited consistent behaviour when compared to the maiden MSCs.

Embedding the packing fibres within the resin-micro pod did improve the uniformity of the yarn and reduced the solar-E-yarn thickness by ~9%, while not affecting the solar-E-yarn performance. A normal braided sheath resulted in a smooth, regular and uniform looking solar-E-yarn, however, this compact structure affected the photovoltaic performance of the solar-E-yarn. The bi-faciality concept was implemented by bonding two mono-facial MSCs together, that created bi-facial solar-E-yarns with superior performance to the solar-E-yarns prepared using mono-facial MSCs, especially at higher incident angles. It was observed that by combining the bi-facial concept and resin impregnation, the normal solar-E-yarn performance could be enhanced by about 83 % when front half of the solar-E-yarn was considered.

Chapter 6 of the thesis covers the evaluation of the solar-E-yarns with relation to various external factors (temperature, humidity, moisture) and processes (washing and drying); which the solar-E-yarns would be exposed to during their use.

Chapter 6

Performance of solar-E-yarns under operational conditions

6.1 Introduction

The importance of understanding the behaviour of any E-textile product during its regular use is clear: The practicality of solar energy harvesting textiles will largely depend on whether they could withstand the mechanical and physical stresses or chemical agents that they would encounter during daily use without a significantly deterioration in their photovoltaic functionality. As discussed in *chapter 2* assessments of textile-based solar energy harvesters under operational conduction (such as performance after washing) reported in literature could not be considered satisfactory or realistic. This chapter focuses on assessing the reliability of the solar-E-yarns when exposed to various conditions that they would encounter during their regular use as part of a wearable product. This will help to define the boundary conditions within which the solar-E-yarns can operate in a satisfactory manner and identify the durability aspects of the solar-E-yarn that require improvements.

In this research the assessment of durability after washing and performance under different ambient conditions (change in temperature and humidity) was conducted. In addition, the effects of mechanical stresses such as tensile forces, abrasion and impact were also assessed. Due to the absence of dedicated test methods and standards for testing of E-textiles, some of the existing test standards and procedures designed for regular textiles (in apparel applications) were adapted in a suitable manner to conduct the relevant evaluations such as wash durability, tensile strength and abrasion resistance. Other evaluations were conducted by designing controlled experiments with little or no specific reference to existing test standards. Assessments of test samples were conducted considering both the textile aspects (e.g. appearance) and photovoltaic output (e.g. short-circuit current). It is logical to assume that the electrical functionality is more susceptible to deterioration during use due to the higher probability of electrical conductivity/interconnect failures. Previous work has identified copper wire breakages as the first mode of failure of many E-yarns (Hardy *et al.*, 2018). Some of the durability tests covered in this chapter were previously presented in the publication 'Photodiodes embedded within electronic textiles' by the author (Satharasinghe, Hughes-Riley and Dias, 2018).

6.2 Wash durability testing

Wash durability is a key determinant for the robustness of an apparel product intended for regular clothing application. Machine washing and hand washing are the practical methods of cleaning clothes, where clothes are exposed to multiple different thermal, hydro-mechanical and chemical conditions over the duration of the wash cycle. Machine washing using detergents and hot water provide an efficient means to removal of dirt and impurities from textile materials. However, these harsher and extreme conditions could be detrimental to clothing with embedded electronic system. Hand washing could be more forgiving to the electronics embedded systems due to the mild hydro-mechanical conditions of the process.

Three tests were conducted to assess the wash durability of solar-E-yarns using machine washing and hand washing methods. The machine wash tests were conducted in two forms; in E-yarn form where the solar-E-yarns were attached onto a T-shirt using embroidery and in fabric form where the solar-E-yarns were woven into fabrics and washed using a wash bag. Use of a wash bag for washing high-value/delicate textile/apparel products is a common practice, that preserve the appearance and functionality of the product. Wash bag prevents the garmets from excessive abrasion, bending fatigue and entanglement with other clothing. The machine wash tests were conducted, closely following the procedure 4N outlined in the British standard BS EN ISO 6330:2012; Textiles - Domestic washing and drying procedures for textile testing (BSI Standards Publication, 2012), using a domestic front-loading washing machine (Bosch Logixx 8 VarioPerfect, BSH Home Appliances Ltd, UK) and 20g of detergent (Persil Non Bio, Unilever UK Ltd, UK) for 25 cycles along with cotton ballasts (100% cotton white T-shirts were used as ballasts to create a total wash load of 2.00 ± 0.01 kg). The samples were tumble dried with ballasts inside a front-loading condenser type domestic tumble-drier (Bosch Classixx 8, BSH Home Appliances Ltd, Milton Keynes, United Kingdom). The wash and tumble dry programmes were selected for the washing and drying machines gave approximately similar settings to the wash and tumble dry cycles prescribed in the wash standard as mentioned in the Table 6.1.

Table 6.1 - Wash test conditions specified in the test standards and set conditions during the experiments.

	Parameter	Directed in the standard	Settings and conditions employed in the test
Machine washing (BS EN ISO 6330:2012)	Temperature	40±3°C	40°C
	Washing time	15 minutes	15 minutes
	Rinsing time	10 minutes	10 minutes
	Spinning time	5 minutes	6 minutes
	Spinning RPM	800±20	800
Hand washing (AATCC Monograph M5)	Temperature	As agreed,	50°C
	Washing	3 repeats of 2 minutes soaking and 1-minute gentle squeezing cycles with 7.6L of detergent water inside a 19L container.	3 repeats of 2 minutes soaking and 1-minute gentle squeezing cycles with 1L of 1% detergent water inside of a 2L container.
	Rinsing	3 repeats of 2 minutes soaking and 1-minute gentle squeezing cycles with 7.6L of tap water inside of a 19L container.	3 repeats of 2 minutes soaking and 1-minute gentle squeezing cycles with 1L of tap water inside of a 2L container.
Tumble drying	Temperature, RPM and Time	Drying time selected to achieve ~2% final relative humidity.	Drying program set to Sportswear (1 hour 47 minutes)
Line drying	Drying apparatus and conditions	Lay flat on a perforated shelf or hung on a garment hanger without blowing air.	Line dried for 2 hours at room temperature (20-25°C) by blowing a stream of air generated by a pedestal cooling fan.

Hand washing of the fabric samples was conducted with 10g of detergent (same type of detergent used in the machine wash test) for 25 cycles (total washing time of 7.5 hours), by closely following the AATCC Monograph M5 for Standardization of Hand Laundering for Fabrics and Apparel (American Association Of Textile Chemists And Colourists, 2010) as given in Table 6.1. Both washing and rinsing were conducted with $50 \pm 2^\circ\text{C}$ tap water (recorded using a digital temperature meter connected with a k-type thermocouple). The samples were line dried under accelerated conditions using a domestic cooling fan to reduce the drying time without applying mechanical or thermal influences. Hand washing and line drying for high-value or delicate apparel products is a regular practice and is a viable proposition for apparel integrated with solar-E-yarns. In the case of outerwear (such as coats, blazers or jackets) hand washing or dry-cleaning (which is even more mechanically forgiving) is the recommended method of cleaning.

6.2.1 Machine wash testing of solar-E-yarns

The first set of machine-wash tests were conducted on solar-E-yarns in yarn form where the solar-E-yarns were stitched onto rectangular fabric swatches (~10.0 cm × 20.0 cm single jersey cotton fabrics) using a zig-zag stitch pattern. The photoactive sides of the E-yarns were aligned to the front side of the fabric swatch during the stitching process. For the wash durability tests, 2.0 mm diameter solar-E-yarns with 1.6 mm RMPs were prepared embedding 1.5 mm × 1.5 mm MSCs, 1.5 mm × 3.0 mm MSCs, and the PD1 type photodiodes (TEMD 7000x01) as listed below. Single E-yarn had one MSC or one PD embedded within it.

- i. 1.5×1.5 mm MSC embedded solar-E-yarn - 10 samples
- ii. 1.5×1.5 mm MSC embedded solar-E-yarn with resin impregnation - 5 samples
- iii. 1.5×3.0 mm MSC embedded solar-E-yarn - 10 samples
- iv. 1.5×3.0 mm MSC embedded solar-E-yarn with resin impregnation - 5 samples
- v. 1.5×1.5 mm 3.0 MSCs parallel connected solar-E-yarn - 5 samples
- vi. TEMD7000×1 photodiode embedded E-yarn (PDEY) – 5 samples
- vii. TEMD7000×1 PDEY with resin impregnation – 5 samples

Each fabric swatch included five solar E-yarns or PDEY of the same type, with ~1.0 cm gaps between the adjacent yarns. The fabric swatches were affixed onto cotton T-shirts using press studs as shown in Fig. 6.1.

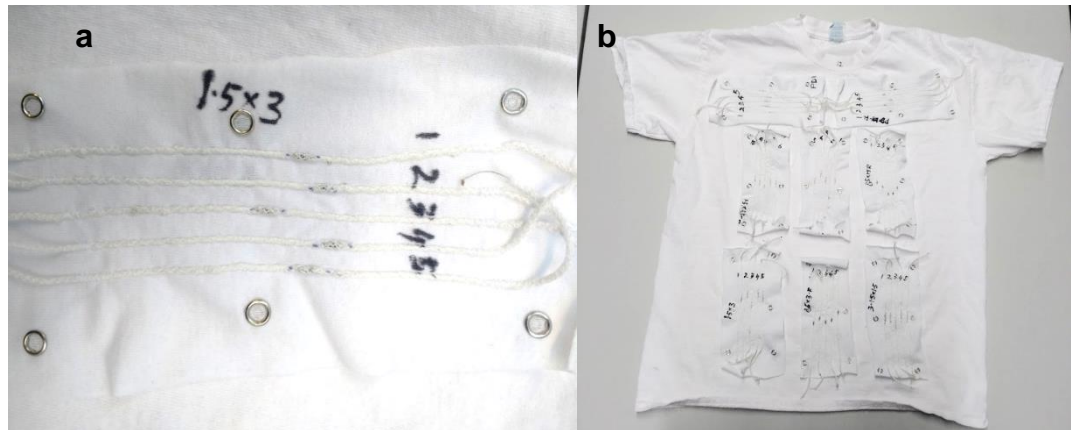


Figure 6.1 – Preparation of test samples for the wash durability tests of the solar E-yarns and PD embedded E-yarns. (a) Five solar E-yarns or PDEYs were stitched onto each fabric swatch. (b) Solar-E-yarn or PDEY embroidered fabric swatches were attached onto a cotton T-shirt using press studs.

The I_{sc} and V_{oc} of each sample was measured before washing, and after 1, 2, 3, 4, 5, 10, 15, 20 and 25 wash and dry cycles to characterise their performance. The performance of the

solar-E-yarns and PDEYs were assessed by removing the fabric swatches from the T-shirt and exposing them to one sun intensity using the solar simulator. Samples with significant (>10 %) changes in their performance compared to previous assessment cycles were considered to have failed. The failed E-yarn samples were removed from the fabric swatches prior to performing the next wash cycle. Full details of the I_{sc} and V_{oc} measurements are given in Appendix 8. Based on this criterion, the number of fully functional solar-E-yarns after the respective number of washes are given in Fig 6.2.

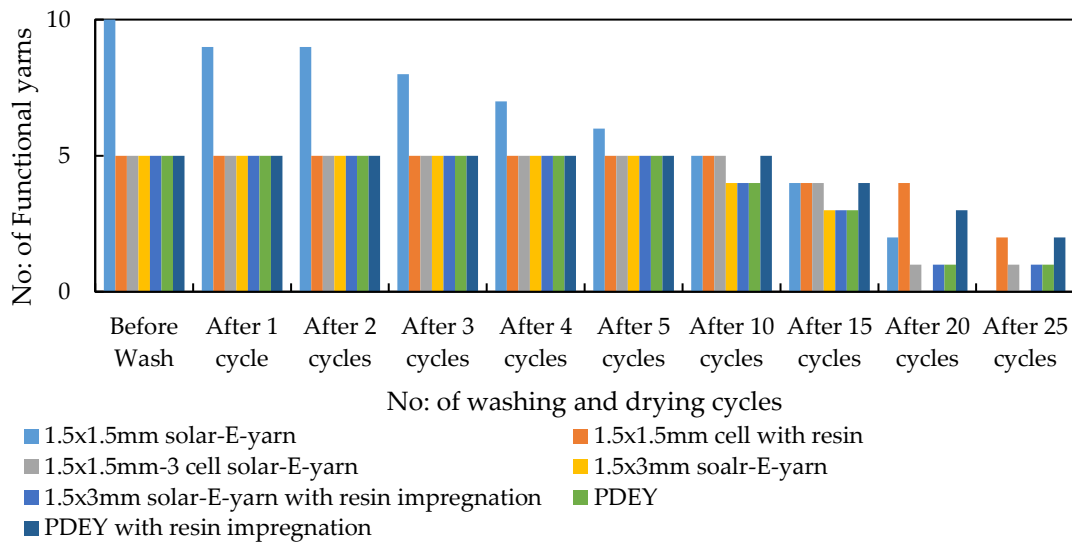


Figure 6.2 – Number of correctly functioning solar-E-yarns and PDEYs after machine washing and tumble-drying cycles.

The results indicated that the solar-E-yarns prepared with 1.5 ×1.5 mm MSC failed at a higher rate compare to the other types of solar-E-yarns. Except for 1.5 ×1.5 mm solar-E-yarns, all other types of solar-E-yarns and PDEYs survived at least 5 cycles of machine washing and tumble drying. However, none of the solar-E-yarns and PDEYs were particularly durable beyond 10 cycles. After 15 wash/dry cycles 62.5 % of the solar-E-yarns and PDEYs functioned correctly. After 25 washes only 17.5 % of the total 40 yarns tested had survived. This result showed that the solar-E-yarns and PDEYs were not able to survive repeated machine laundry and tumble drying beyond 5-10 cycles.

The failed solar-E-yarns were dissected and analysed for their cause of failure using optical microscopy. This included identifying failures in the copper wire and possible micro-cracks or the ingress of water through the RMP. The analysis showed that with the exception of one failure, all of the other failures were due to copper wire breakages. More than 93% of the copper wire breakages had occurred close to the RMP (Fig. 6.3(a)). No

indication of moisture ingress into the RMP was observed. When the broken ends of the multi-filament copper wires were closely analysed, evidence of solder wicking through the capillaries between the individual Cu strands were noticed (Fig 6.3(b)).

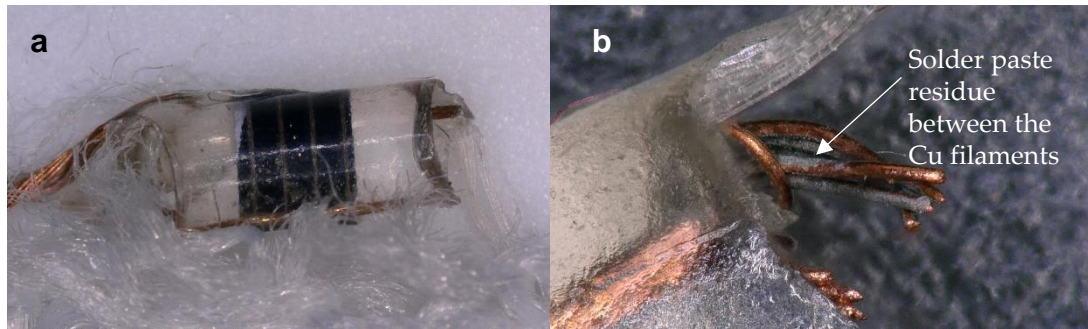


Figure 6.3 – Analysis of cause of failure after washing. (a) Dissected solar-E-yarn with a copper wire breakage close to the resin micro-pod. (b) Magnified image of the copper wire breakage point showing solder wicking through the capillaries.

This wicking process of solder paste can occur when the solder alloy is in a liquid state during the soldering process. It was noticed that the stiffness of the broken Cu wire ends was significantly higher than the maiden Cu wire, possibly due to the solder wicking. This Cu wire stiffening may have resulted in localisation of fatigue stress on the Cu wire close to the RMP during the washing process eventually causing it to break. Therefore, it was of interest to analyse the possibility of reducing the Cu wire breakage close to the RMP by minimizing the solder wicking; however, this analysis is not within the scope of this research programme.

6.2.2 Machine wash and hand wash testing of woven fabrics with solar-E-yarns and photodiode embedded E-yarns

The second and third wash tests were conducted on solar-E-yarns and PD-E-yarns (PDEY) that had been woven into a fabric structure; the fabrics with solar-E-yarns are denoted as solar-fabrics and fabrics woven with PDEYs are named PD-fabrics hereafter. The objective of these tests was to assess the durability of the solar-E-yarns when integrated into a woven fabric and after undergoing machine washing and hand washing. Wash testing the solar-fabric and PD-fabrics would be more representative of how they would be used and washed in real-life. The machine wash tests were conducted after inserting the samples inside a wash bag to provide more protection to the samples of solar-fabrics and PD-fabrics). In contrast to the solar-yarns and PDEYs where the wash tests were followed by tumble drying, the solar-fabric and PD-fabric

samples were line dried. Although these conditions were milder compared to the previous test conditions, this was also a practical and viable method for cleaning a high value-added product such as a solar-fabric.

The solar-fabric and PD-fabric samples were constructed by weaving either solar-E-yarns or PDEYs and cotton yarns in a basket weave structure as shown in Fig. 6.4. Cotton yarns (100% cotton spun yarns, 38.9×2 tex; Elton Vale Yarns Ltd, UK) were used as the warp and solar-E-yarns or PDEY were inserted as the weft, with the photoactive side of the solar-E-yarns or PDEY fully exposed. Between two adjacent solar-E-yarns or PDEYs, five knit braided yarns without a core (the fibrous sheath of these yarns was identical to the solar-E-yarns or PDEYs, however without the RMP and copper wires) and cotton weft yarns were inserted in an alternating order as shown in the Fig. 6.4.

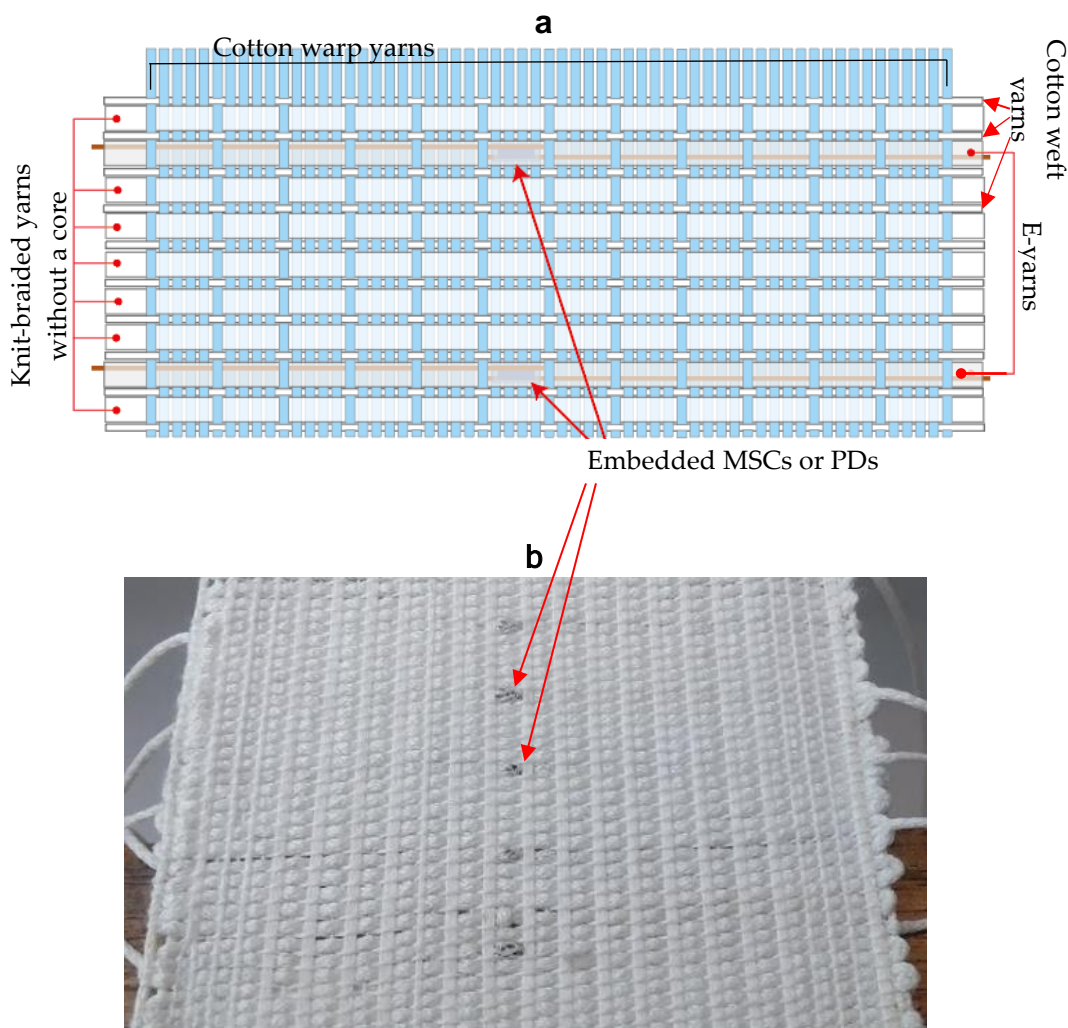


Fig. 6.4 - Woven fabrics containing solar-E-yarns prepared for wash durability and abrasion tests. (a) Schematic illustration of the fabric samples. (b) Photograph of the woven fabric prepared for testing.

The fabrics were machine washed (similar to the first wash test) inside of a wash bag and line-dried at room temperature as detailed in Table 6.1. Below six different types of E-yarns were woven into the fabrics (a total of twelve fabric samples and sixty E-yarns) and were subjected to machine washing (following the method given in Table 6.1).

- i. 1.5 × 1.5mm MSC embedded solar-E-yarns – 5 samples
- ii. 1.5 × 1.5mm MSC embedded solar-E-yarns with resin impregnation -5 samples
- iii. 1.5 × 3.0 mm MSC embedded solar-E-yarns -5 samples
- iv. 1.5 × 3.0 mm MSC embedded solar-E-yarns with resin impregnation - 5 samples
- v. TEMD7000×1 type photodiode embedded PDEYs - 5 samples
- vi. TEMD7000×1 type photodiode embedded PDEYs with resin impregnation - 5 samples

Hand washing was also conducted on another set of fabric samples prepared with the same types of solar-E-yarns and PDEYs.

Both the I_{sc} and V_{oc} of the solar-E-yarns and PDEYs were recorded before washing, and after 1, 2, 3, 4, 5, 10, 15, 20 and 25 wash and dry cycles using the solar simulator (one sun intensity), similar to the previous wash test. In addition to the I_{sc} and V_{oc} measurements the IV and PV curves were also generated before washing and after 25 washes using correctly functioning E-yarns. The results of the wash durability test (Fig. 6.5) showed that the solar-E-yarns and PDEYs in the washed and tumble-dried fabric samples, had a survival rate of over 90 % after 15 wash cycles. After 25 cycles 67 % of the solar-E-yarns and PDEYs still functioned correctly. In this case 92 % of the failures were due to Cu wire breakages close to the RMP.

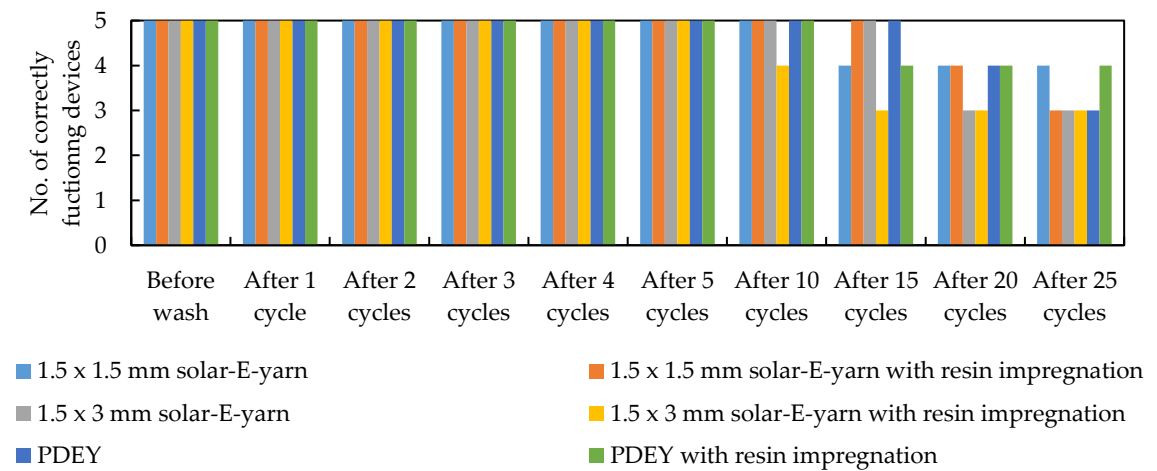


Figure 6.5 – Number of correctly functioning E-yarns woven into fabrics after machine washing and tumble-drying cycles.

In the case of hand washing tests all solar-E-yarns and PDEYs in woven fabrics survived 25 cycles of washing and drying. This was a drastic improvement from the results observed for solar-E-yarns and PDEYs tested in yarn form as shown in Fig. 6.6.

The results confirm that the combined effects of integrating solar-E-yarns and PDEYs within a woven fabric, washing inside a wash bag and line drying are considerable. It is understood that this was possibly due to the structural support given to the solar-E-yarns and PDEYs by the woven structure, additional protection provided by the wash bag that prevented the woven fabric from excessive torsional and tensile stresses during machine washing and, the absence of tumble drying significantly reduced the mechanical stresses on the solar-E-yarns and PDEYs. The individual effects of the integrating the solar-E-yarns and PDEYs within a woven structure, washing using a wash bag and line drying were not separately investigated in this study.

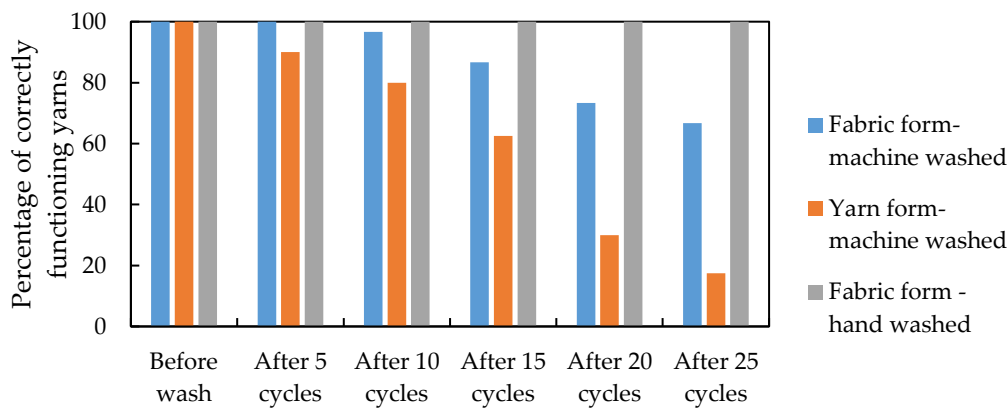


Figure 6.6 – Comparison of the test results after wash testing for the solar-E-yarns and solar-fabrics .

The average of normalized I_{SC} and V_{OC} measurements and, maximum power (P_{MAX}), and fill factor (FF) of the solar-E-yarns that survived 25 washes in fabric form are shown in Fig. 6.7. The normalized I_{SC} and V_{OC} values (normalized to their values before washing) showed that the I_{SC} reduced by ~3 % and ~6 % after 25 hand wash and machine wash cycles respectively. The FF values showed insignificant changes after 25 hand or machine washes. The P_{MAX} values reduced by ~13.5 % and ~10.4 % after 25 machine wash cycles and 25 hand wash cycles (Fig. 6.7(b)), which was the compound effect of changes in I_{SC} , V_{OC} , and FF. The minor reductions in output power observed was possibly due to the migration of the textile fibres in the fibrous sheath during washing, which could increase the shading effect.

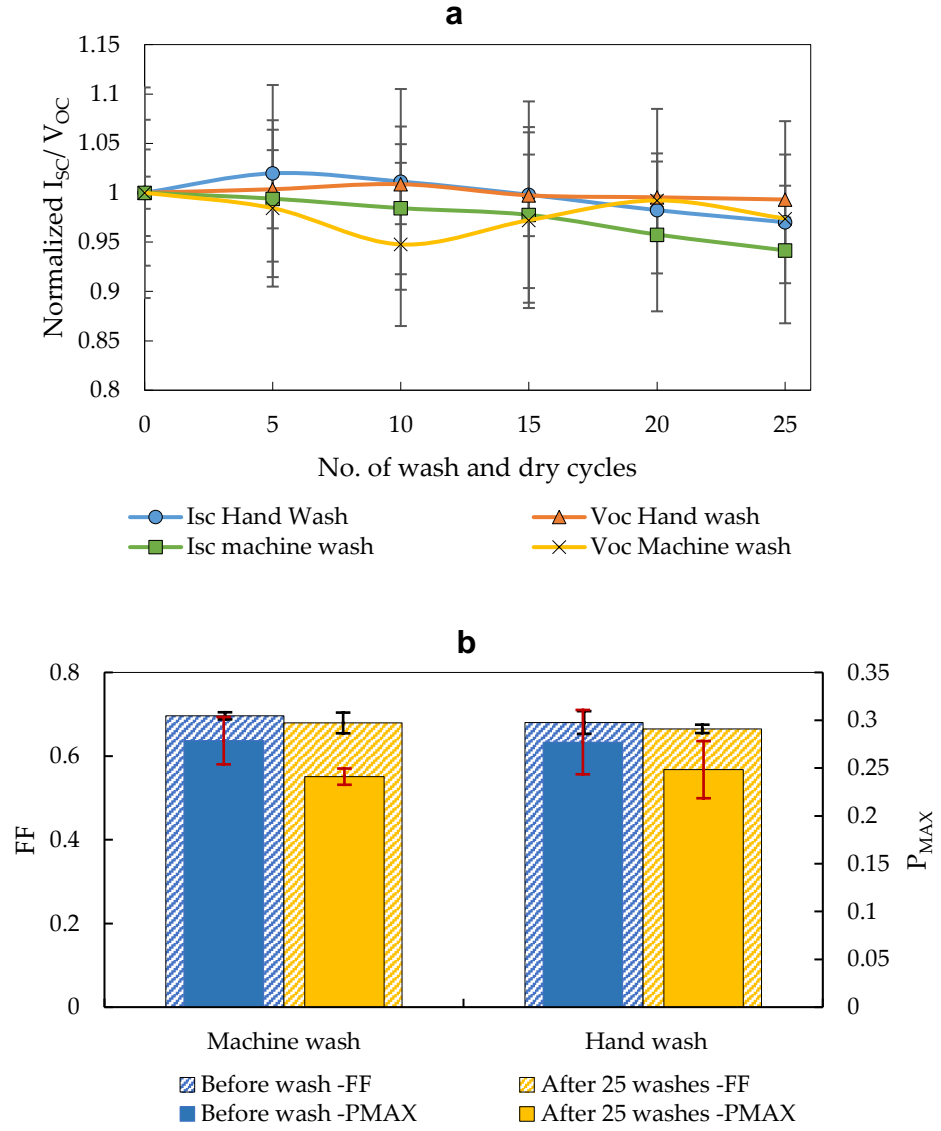


Fig. 6.7. Wash durability of solar-E-yarns embedded within woven fabrics. (a) Change in short circuit current (I_{sc}) and open circuit voltage (V_{oc}) after washing (normalized to before wash values) and (b) change in fill factor (FF) and maximum power output (P_{MAX}) after 25 wash cycles for machine washed and hand washed solar-E-yarns. Two sets of five solar-E-yarns were woven into solar-fabrics and subjected to machine washing and hand washing. The average output of the fully functioning solar-E-yarns indicated with error bars show the SD of the full functioning solar-E-yarns.

The results suggested that the photovoltaic performance of the embedded MSCs did not deteriorated significantly due to the exposure to the combination of water, detergents, heat, and liquid. While the solar-E-yarns are not suitable for machine washing beyond 15 cycles in its current form, hand washing which is a practical and viable method for cleaning high-value clothing can be readily used for apparel integrated with solar-E-yarns. The observed levels of durability of MSCs in solar-E-yarns can be attributed to the discrete micro-pod structure that protected the MSCs from the water-detergent mix

in the wash-bath and degree of freedom for the movement of the individual RMPs within the solar-E-yarns structure, as the micro-pods are not bound to the fibrous sheath. The fibrous sheath provided tensile reinforcement to the solar-E-yarn. The fabrics woven with solar-E-yarns has an architecture that was inherently flexible allowing the solar-E-yarns to move independently (by shear deformation) when under mechanical stress. Considering these advantageous structural features, the durability of the woven solar-E-yarns when machine washed should largely improve simply by enhancing the mechanical properties (bending and torsional fatigue) of the copper wire and optimising the soldering process to minimize the solder wicking during soldering.

6.3 Tensile strength tests

The tensile strength of the solar-E-yarns were evaluated to assess their ability to withstand the tensile forces that may be applied during subsequent manufacturing processes (i.e. weaving, knitting or embroidery) or regular use. Previous work had analysed the tensile properties of E-yarns with LEDs and showed a breaking strength of 54.93–67.46 N (Nashed *et al.*, 2019). In the case of solar-E-yarns, the geometry of the embedded device (MSC), solder pads and the solder joints are significantly different to the LED yarn. Also, it is important to understand the point of electrical failure under tensile loading, which is relevant to the photovoltaic functionality of the solar-E-yarns.

Therefore, an experimental procedure was defined to measure the points of mechanical failure and electrical failure of solar-E-yarns as shown in Fig. 6.8.

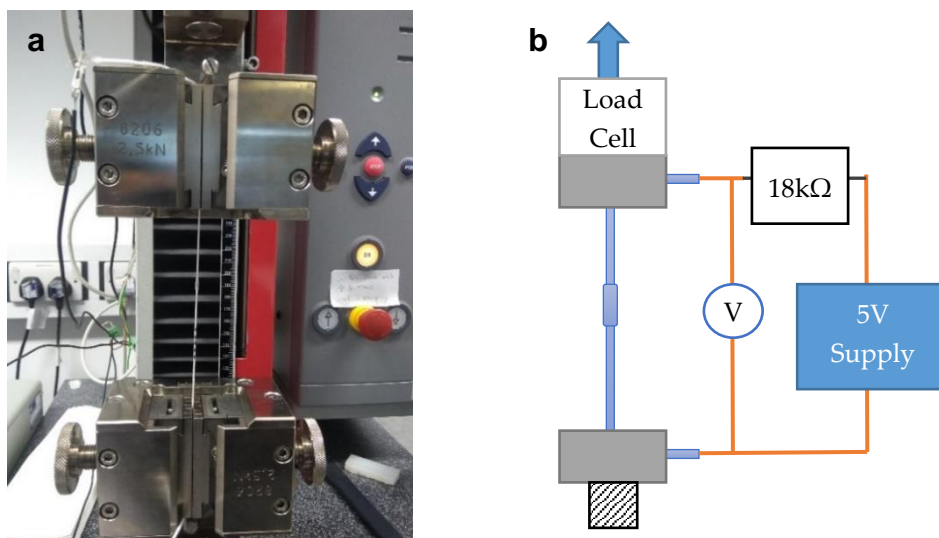


Figure. 6.8 - (a) Image of the test apparatus and (b) a schematic of the voltage divider circuit used for the solar-E-yarns tensile test.

Five solar-E-yarns embedded with 1.5×3.0 mm MSCs were fabricated with 1.5 mm diameter RMP and a 2.0 mm diameter knitted sheath. The solar-E-yarns were tested using the Zwick tensile tester with a 2.5 kN load cell and 100 mm grip to grip separation (Fig.6.8(a)) until the (complete) mechanical breakage of the solar-E-yarn. The ends of the copper wires of each solar-E-yarn were connected to a voltage divider circuit as indicated in the Fig.6.8(b). The tensile load, strain, and the voltage across the yarn were simultaneously recorded with the Zwick software as given in Figure 6.9(a). An analysis of the failure points is given in Fig. 6.9(b). Also, the breaking strengths of the components of the solar-E-yarns (Cu wire, Vectran® yarn, and fibre sheath) were individually measured.

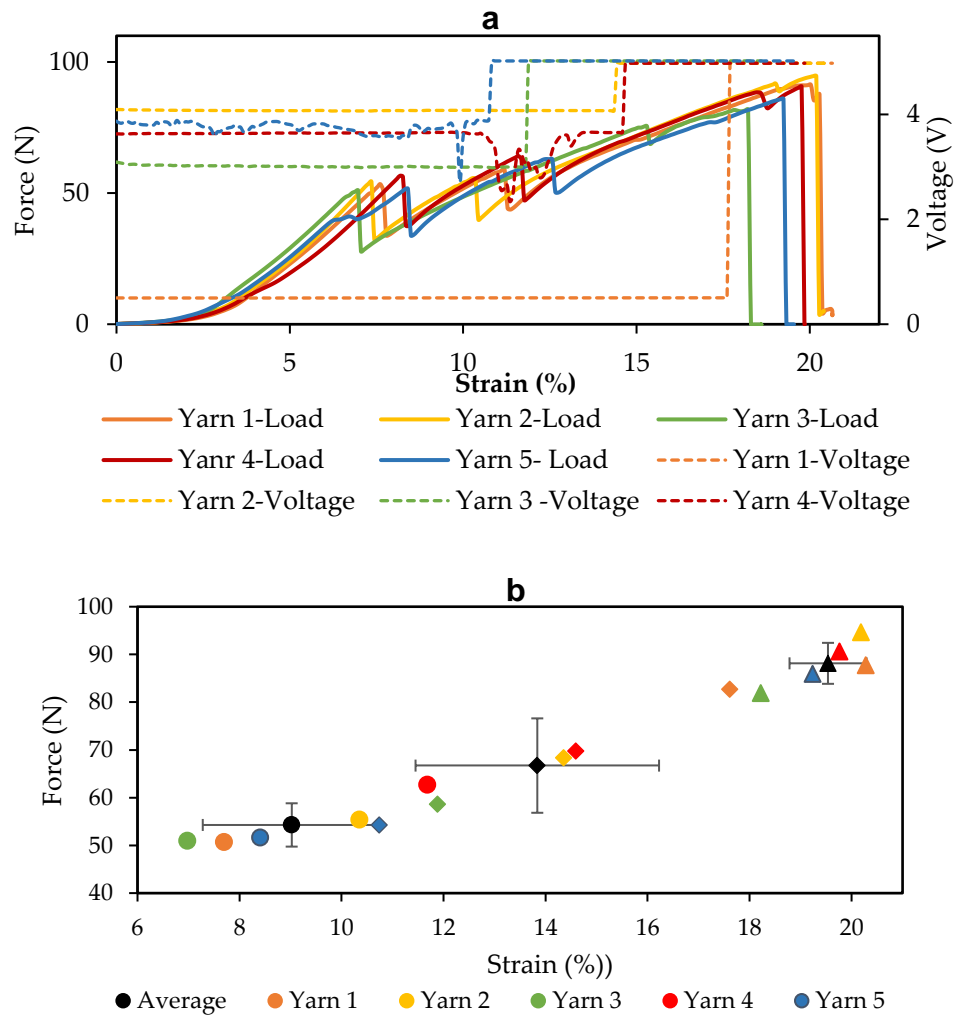


Figure 6.9 - (a) Test results and (b) analysis of failure points under tensile load (circles – first mechanical failure, diamonds-electrical failure and triangles-complete breakage).

The force-strain curve showed a jagged pattern with four distinct drops (Fig 6.9(a)). These drops can be attributed to the failures of individual components of the solar-E-

yarns. Tensile tests were conducted for individual components of the Solar-E-yarn and the results were compared against the Solar-E-yarn elongation test results. The breaking strength of the Vectran® yarns (24.3 ± 2.0 N) was approximately comparable to the drop in load at the first failure point (~ 19.7 N). Therefore, the breakage of the Vectran® yarn within the solar-E-yarn can be assigned to the first failure point. Similarly the third failure point (drop in force ~ 3.7 N) can be assigned to the breakage of the Cu wire that had a breaking strength of 3.26 ± 0.26 N. Based on the results (Fig 6.9(b)) it was clear that the solar-E-yarns can withstand tensile loads of above 54.3 ± 4.5 N before the initial mechanical failure occurred. The electrical failure of the solar-E-yarns was observed at 66.7 ± 9.9 N, which occurred before the mechanical failure of Cu (third mechanical failure point) wire. The final mechanical failure (complete breakage) occurred around 88.1 ± 4.3 N with the breakage of the knit braid. The test was terminated at this point. The sequence of the failure of different components of the E-yarn can be attributed to the amount of slack and the level of elongation before breakage for each component. For example although Cu wire has a lower breaking strength than Vectran® yarn, it has a higher strain at breakage (19.46 ± 0.39 %) compared to Vectran® yarn (10.66 ± 2.05 %) hence the electrical failure occurs after the Vectran® yarn breakage. According to literature, in a typical weaving process the maximum tension applied on a single warp end is less than 20N (Shih *et al.*, 1995). Therefore, based on the results confirmed that the electrical and mechanical robustness of the solar-E-yarns under tensile loading was sufficient to survive subsequent processing and normal use.

6.4 Abrasion resistance test

During their regular use textile fabrics are subjected to rubbing (abrasion) against the various surfaces and this can affect their appearance (fibre breakage and pilling) and mechanical integrity (loss of material, fabric structural failures). The solar-E-yarns would be positioned on regions of the garment that are consistently exposed to light, such as front or back of a jacket, that may be less susceptible to abrasion. On the other hand, due to the higher stiffness of the RMPs, the solar-E-yarns may be more vulnerable to fibre breakages even under lower number of abrasion cycles. Therefore, the impact of abrasion on the appearance and performance of solar-fabric was evaluated. To analyse these effects on solar-fabrics, abrasion tests were conducted using a Martindale abrasion tester (902 Mini Martindale, James Heal Ltd, England). The five solar-E-yarns made with

1.5 × 3.0 mm MSCs, 1.5 mm diameter RMPs and 2.0 mm diameter knitted sheaths were woven into a fabric, identical to that used for wash testing in 6.2.2. The fabric sample was subjected to abrasion testing for 6000 cycles (12000 rubs) according to *BS EN ISO 12947-2:2016* (BSI Standards Publication, 2016). A standard rubbing cloth (SM25 Martindale Abrasive Cloth, James Heal Ltd, England) with a 9 kPa rubbing load was used for the test. These abrasion conditions are representative of the level of abrasion, a low-abrasion risk region an outerwear may undergo during its normal use. The voltage of each solar-E-yarn was monitored during the test under constant lighting conditions (achieved by using an LED table lamp), to identify any abnormal changes in electrical properties, using a USB data logger (NI USB DAQ 6008, National instruments Inc, USA) and a bespoke program (see Appendix 9) based on LabView® (National instruments Inc, USA). Microscopic images were taken before the start of the tests and after every 1000 cycles while the test sample were fixed to the abrasion tester. The I_{sc} and V_{oc} were measured for each solar-E-yarn before and after the abrasion tests under one sun intensity.

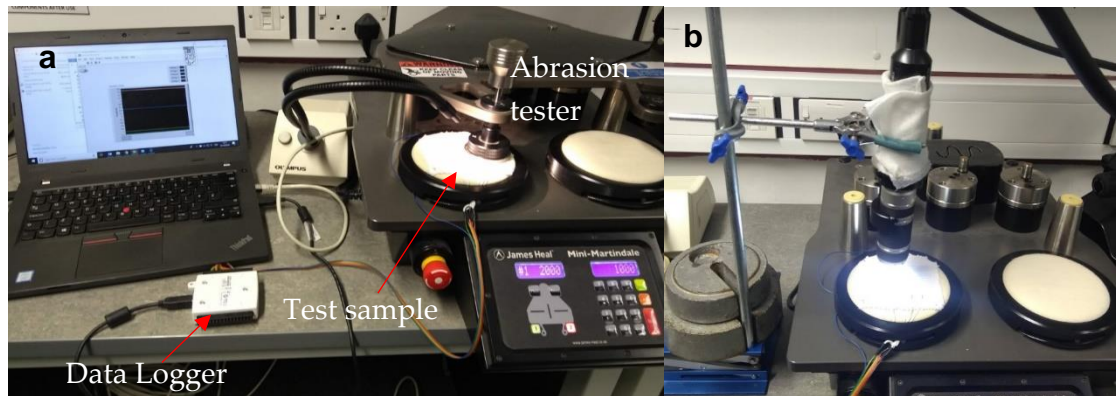


Figure 6.10 - (a) Experimental setup for conducting the abrasion testing. (b) Set-up for the microscopic imaging of the test sample at intervals of 1000 abrasion cycles.

Continuous voltage readings from 0 to 6000 abrasion cycles did not indicate any abnormalities during the test. However, a gradual change in voltage within each 1000 cycle period was observed; at the beginning of the next 1000 cycle, the voltage returned to a value similar to the initial voltage, indicating that this change was temporary. This change may be caused by factors such as increase in temperature (subsequently increasing wire resistance) or accumulation of static electricity due to the rubbing action.

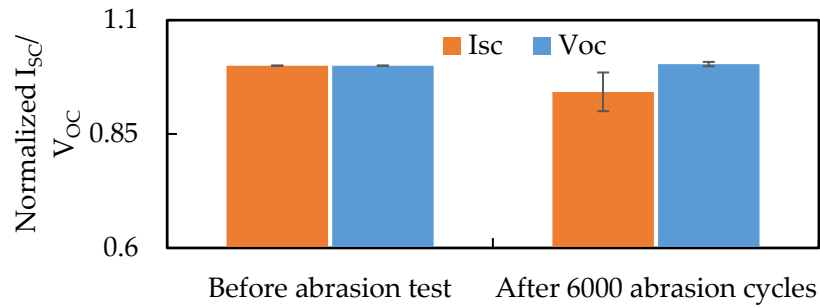


Figure 6.11 – Normalized short-circuit current (I_{sc}) and open-circuit voltage (V_{oc}) of solar-E-yarn embedded fabrics before and after undergoing 6000 abrasion cycles, tested when exposed to one sun intensity with solar simulator.

Table 6.2 – Microscopic images of the five solar-E-yarns during the abrasion test.

	Number of abrasion cycles						
	0 cycles	1000 cycles	2000 cycles	3000 cycles	4000 cycles	5000 cycles	6000 cycles
Sample 1							
Sample 2							
Sample 3							
Sample 4							
Sample 5							

The microscopic images before the test and after each 1000 abrasion cycles (Table 6.2) showed minor changes in surface fibre distribution and small levels of fibre breakages, which were not clearly visible to the naked eye. Based on the results it is clear that despite the change in stiffness in the micro-pod regions the solar-E-yarns maintained a satisfactory appearance and photovoltaic performance after 6000 abrasion cycles (12000 rubs), that may be sufficient for a region of an outerwear that has low abrasion risk. It is to be noted that, based on the specific applications the abrasion test may need to be varied to represent the real-life scenario.

6.5 Mechanical impact testing

For completeness, experiments were conducted to assess the capability of solar-E-yarns to survive mechanical impact. Solar-E-yarns (constructed using one 1.5 ×3.0 mm MSC per yarn) were woven into a fabric (the same fabric structure used for previous durability tests) and were subjected to mechanical impact using a wire impact tester (DVT SAH KAB Cable Impact Tester) with a 10 cm drop height (Fig 6.17).

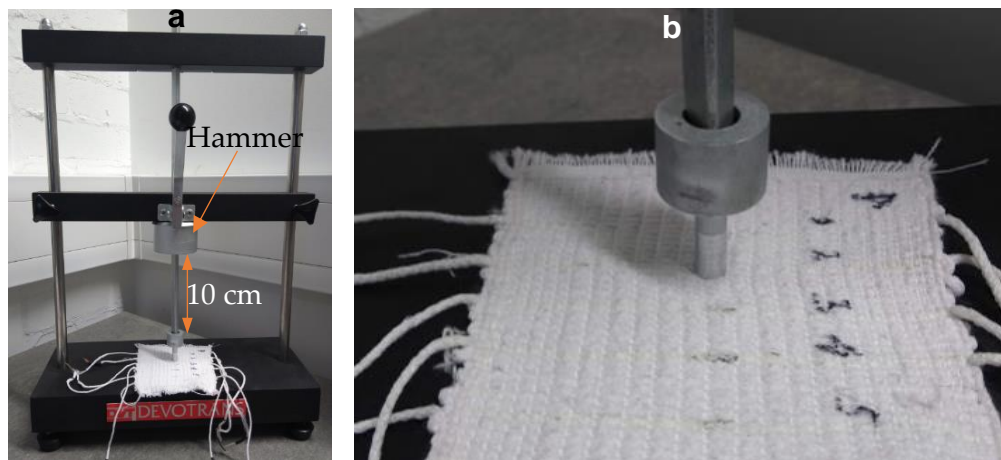


Figure 6.17 - Mechanical impact tests on the solar-fabric. (a) Image of the mechanical impact test apparatus with the wire impact tester conducted on solar-fabric sample. (b) Magnified image of the impact head positioned on the solar-fabric.

The mechanical test performed would be more severe than the nature of mechanical forces encountered during their use (when worn on body or during washing), however this gave an indication about the maximum impact the solar-E-yarn could survive without sustaining substantial deterioration in performance (i.e. the boundary conditions for use). A preliminary test was conducted to determine the maximum impact weight at which the yarn retained at least 50% of its functionality (>50 % of the original short circuit current) after one impact cycle. Hammer weights from 100 g to 500 g (in 100

g increments) were used for the preliminary test. Then five solar-fabric samples were subjected to 25 impact cycles using the hammer weight determined by the preliminary test. The I_{sc} and V_{oc} values were measured using the solar simulator under one sun intensity.

The preliminary test (Fig. 6.18(b)) showed that the solar-E-yarns retained their functionality (here defined as I_{sc} above the 50% of the original value) only when a 100g hammer was used. Tests with multiple impact cycles of the 100g mass were conducted up to 25 cycles, and the I_{sc} and V_{oc} values were recorded at 1, 2, 3, 4, 5, 10, 15, 20 and 25 impact cycles. After 3 impact cycles using the 100 g hammer, the I_{sc} value of the solar-E-yarns reduced below 50% of the original value. The impact energy of a single impact cycle can be estimated by:

$$E = mgh \quad 6.1$$

Where m is the mass of the hammer, g is the gravity constant and h is the falling height of the hammer.

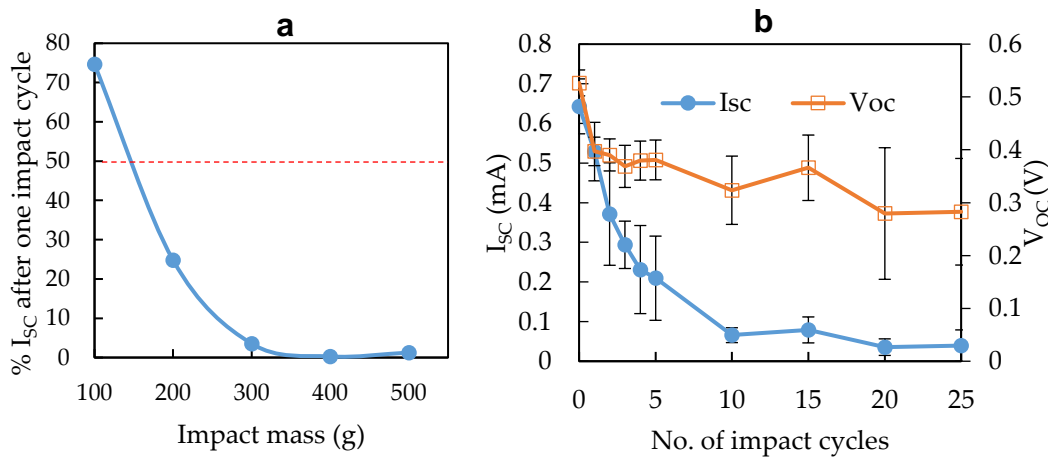


Figure 6.18 – (a) Results of the preliminary test to determine the maximum impact weight at which that solar-E-yarn remained functional. **(b)** Performance of the solar-E-yarns after multiple impact cycles using the 100 g hammer.

For a 100g hammer falling from 10 cm height the impact energy was therefore ~98 mJ. This level of impact is significantly lower than the impact energy absorbed by human joints for example during a fall (10.5J on the knee joint during a fall) (Schwarze, Hurschler and Welke, 2019) hence the solar-E-yarns in its current form will not be suitable for positioning on the areas of the garments that are prone to mechanical impact. The mechanical impact durability of the solar-E-yarns could be improved by increasing

the RMP diameter, which may provide a greater level of protection to the embedded solar cell. However, this may not be desirable due to the increase in yarn thickness, which will impact appearance and wearability. The material properties of the RMP may also be modified, that could improve the impact absorption properties, which is not investigated in this study.

6.6 Effect of temperature and humidity

The environmental conditions the solar energy harvesting textile may have to experience during its normal use may vary vastly. Therefore, the effect of changes in temperature and humidity are two key parameters that need to be considered in this respect.

6.6.1 Effect of temperature on solar-E-yarns

The effect of temperature on the photovoltaic behaviour of solar cells (SC) are well known. According to the theory, with increase in temperature, V_{oc} of an SC reduces approximately linearly and the I_{sc} would show a small logarithmic increase (McEvoy, Markvart and Castañer, 2013; Chander *et al.*, 2015). It was important to understand whether the MSCs embedded within the solar-E-yarn structure had a similar behaviour when compared with the maiden MSC, as the RMP and fibrous sheath would impede heat flow to the cell (Hughes-Riley *et al.*, 2017). Therefore, the change in I_{sc} and V_{oc} with temperature for solar-E-yarns at different stages of the fabrication process was investigated. Solar-E-yarns were prepared with 1.5×3.0 mm MSCs, 1.6 mm diameter RMPs and 2.0 mm diameter knit braided structure using the standard material types employed throughout this chapter. The solar-E-yarns were positioned on the temperature-controlled chilling/heating plate (EchoTherm™ IC50 digital chilling/heating plate, Torrey Pines Scientific Inc., Carlsbad, CA, USA) as shown in Fig. 6.12; with temperature adjusted from 0°C to 60°C in 5 °C steps.

A matt black tube was placed on the chilling/heating plate to cover the solar-E-yarns from ambient light. The actual temperature close to the devices were monitored using a thermocouple (Z2-K-1.0-1/0.2-MP-ANSI, Labfacility Ltd, West Sussex, United Kingdom) connected to a temperature logger (RDXL65D Six Channel Handheld Temperature Data Logger, Omega Engineering Limited, Manchester, United Kingdom). Once the system had reached an equilibrium, measurements were conducted under one sun intensity. I_{sc}

and V_{oc} values were plotted against the temperature measured by the thermocouple for the solar-E-yarns at each stage of the fabrication process (Fig. 6.13).

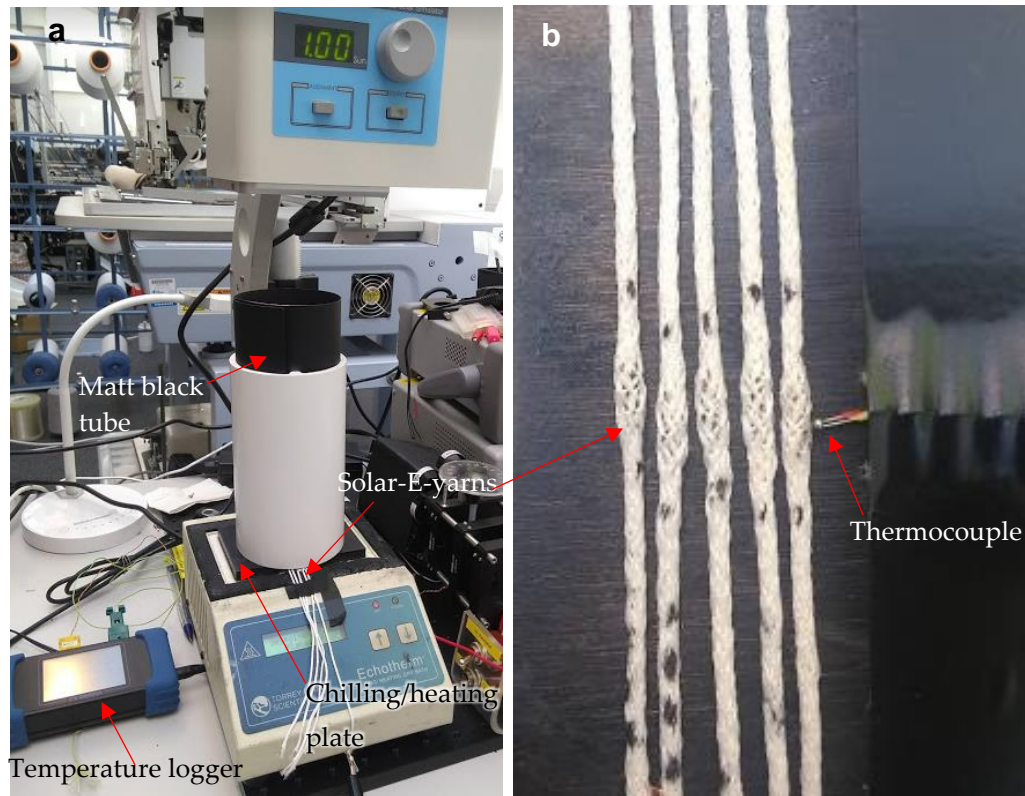


Figure 6.12 - (a) Experimental setup for monitoring the effect of temperature on the photovoltaic behaviour of solar-E-yarns. (b) Close-up image of the solar-E-yarns positioned on the chilling/heating plate with the thermocouple.

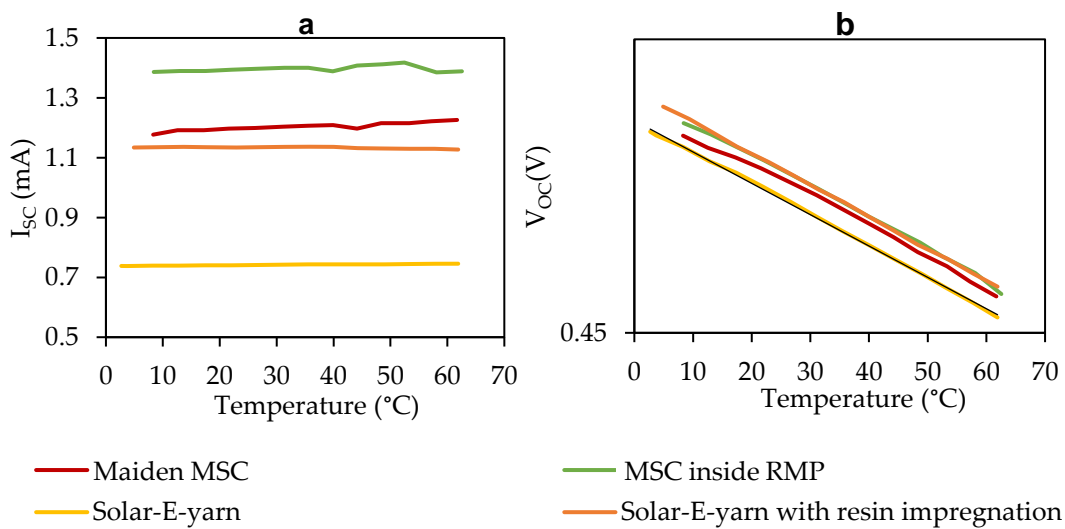


Figure 6.13 - The effect of temperature on the short circuit current (I_{sc}) open circuit voltage (V_{oc}) of solar-E-yarns at different stages of the fabrication process, measured at one sun intensity.

According to the theory (Wu and Chen, 1982);

$$V_{OC} \simeq \frac{k_B T}{q} [\ln(I_{SC}/I_0) + 1] \quad 6.2$$

Where T is the absolute temperature, k_B is the Boltzman constant, q is the electron charge, I_0 is the reverse dark current. However, it was suggested (Singh and Singal, 1983) that this temperature dependent behaviour of V_{OC} can be empirically represented as;

$$V_{OC} = V(0)_{OC} + \alpha T \quad 6.3$$

Where $V(0)_{OC}$ is the open-circuit voltage at 0 K and is constant. T is the absolute temperature. The theoretical analysis of the effect of temperature on I_{SC} is often lengthy and complex (Krawczyk, Jakubowski and Zurawska, 1981) and therefore, is not discussed in detail in this work. As the experimental results and theory suggested, in its simplest form I_{SC} and T can also be defined with a linear relationship within a specific temperature range (Eq. 6.3), where the gradient of the curve gave the temperature coefficient of I_{SC} (i.e. change in I_{SC} for a unit change in temperature).

$$I_{SC} = a_1 + b_1 T \quad 6.4$$

The curve fitting was conducted using the Matlab® curve-fitting toolbox, with the results shown in Table 6.3. The coefficient of variation (R^2) indicated the goodness of the data fit of the selected curve types.

Table 6.3 – Curve fitting the data for short-circuit current (I_{SC}) and open circuit voltage (V_{OC}) at different temperatures.

Device type	Fit coefficients for I_{SC}			Fit coefficients for V_{OC}		
	a1	b1	R^2	$V(0)_{OC}$	α	R^2
Maiden MSC	0.979829	0.000727	0.8601	1.1651	- 0.0021	0.9876
MSC with RMP	1.336365	0.000195	0.1054	1.1944	-0.0021	0.9976
Solar-E-yarn	0.703129	0.000127	0.9646	1.1816	-0.0021	0.9991
Solar-E-yarn with resin impregnation	1.168668	-0.000116	0.5098	1.2057	-0.0022	0.9998

The results of the curve-fitting confirm a that the temperature and V_{OC} had a close linear relationship, with a gradient of -0.0021 approximately meaning that for a 1 K increase in temperature, there was ~2.1 mV reduction in V_{OC} at all stages of the solar-E-yarn fabrication process. This value is defined as the temperature coefficient of open-circuit voltage, which showed a close agreement with the values reported in literature (2.1-2.4 mV/K) for Si solar cells (Wu and Chen, 1982; Cotfas, Cotfas and Machidon, 2018). The

results of the curve-fitting for the I_{sc} were not conclusive and the temperature coefficient of I_{sc} could not be accurately estimated, possibly due to the small and irregular changes in I_{sc} with temperature.

6.6.2 Effect of humidity on solar-E-yarns

Humidity in the atmosphere could affect the performance of a solar-E-yarn especially at high humidity levels in two ways. Firstly, it could change the optical properties of different components of the solar-E-yarns by creating thin layers of liquid droplets. Secondly, the liquid layers could change the electrical resistance between the two electrodes of the device. To assess the behaviour of solar-E-yarns at different relative humidity (RH) levels, a solar-E-yarn characterisation apparatus was setup inside a temperature/humidity controllable chamber (Thermotron SM-1.0-8200 Benchtop Environmental Chamber, Thermotron Industries, USA) as shown in Fig 6.14.

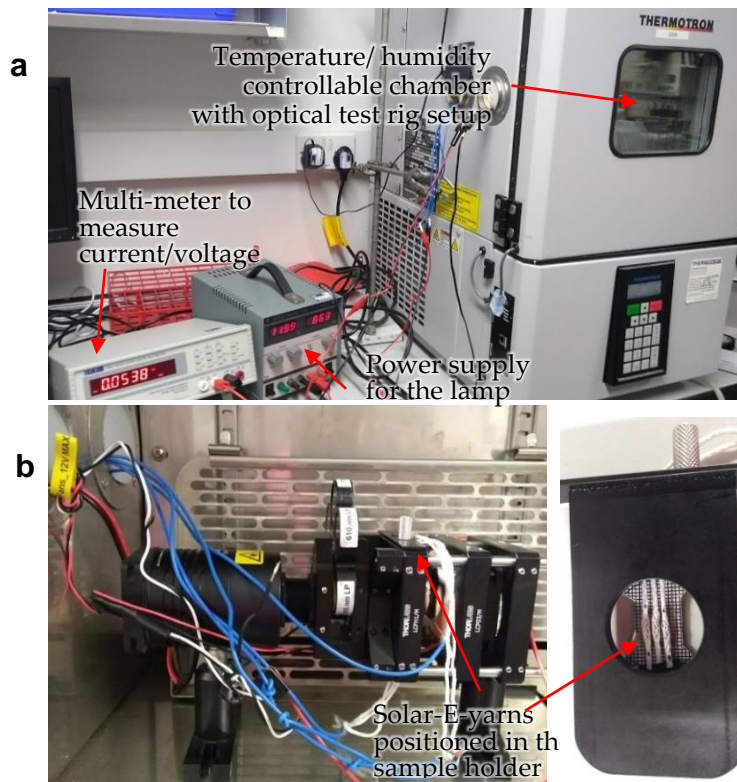


Figure 6.14 - (a) Experimental setup for monitoring the effect of humidity on the photovoltaic behaviour of solar-E-yarns. (b) Image of the optical test rig positioned inside the temperature/humidity-controlled chamber with the solar-E-yarns mounted in the sample

Since it was not possible to use the solar simulator inside of the humidity-controlled chamber (due to its size), for this experiment the optical test rig with full beam settings was employed, with solar-E-yarns positioned in the sample holder as before.

The RH value inside the chamber was changed from 30% to 90% at 15% steps while the temperature was maintained 25 ± 2 °C. The results show insignificant change in I_{sc} or V_{oc} within the RH range tested, suggesting that the solar-E-yarns were not susceptible to fluctuations in photovoltaic performance over RH values (Fig.6.15).

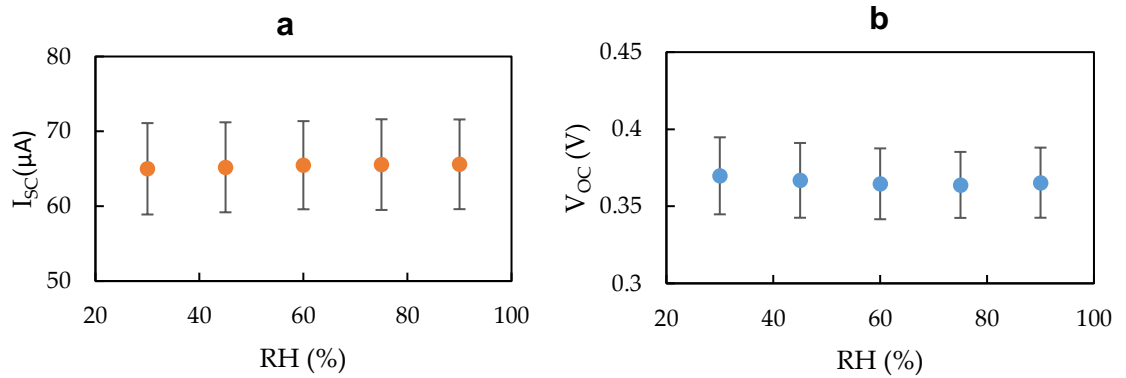


Figure 6.15 – Change in (a) short-circuit current (I_{sc}) and (b) open-circuit voltage (V_{oc}) with relative humidity (RH) for solar-E-yarns at 25 °C measured under optical test rig at full beam.

In this experiment the effects of change in humidity in the near surrounding of the solar-E-yarns was considered. Due to the low moisture However, in real life scenarios, humidity changes in the atmosphere has a direct effect on the incident light intensity. With the increase in humidity, the moisture vapour droplets in atmosphere scatter and absorb significant amount of light resulting in a reduction in incident light intensity measured at the surface of the earth (Gwandu and Creasey, 1995).

6.6.3 Effect of liquid water on solar-E-yarns

In addition to the effect of water in vapour form, the solar-E-yarns could occasionally encounter liquid water during their use. To evaluate the effect of liquid water, the solar-E-yarns fabricated with bare Cu wires were not suitable due to short-circuiting. Therefore, the bare Cu wires were replaced by insulated Cu wires (BXL2001, OSCO Ltd, UK) for the solar-E-yarns used in this experiment. The insulated Cu wire had seven twisted strands of Cu individually enamelled with Polyurethane coating. The electrical properties of these Cu wires were similar to the bare Cu wires used in other experiments. The twisted strands were also covered with a Nylon fibre wrapping that protected the enamel from abrasion and reinforced the wires. To solder the MSCs onto these insulated Cu wires, the Nylon cover and the enamel were manually stripped using a soldering

iron, Pb-solder wire (RS PRO 0.81mm Wire Lead Free Solder, +228°C Melting Point, RS Components, UK) and solder flux (Flux for soft soldering, Power Craft, UK). Special care was given to maintain a stripping length to 3.0-4.0 mm. It was observed that this manual stripping process resulted in a few millimetres of melted nylon serve on either side of the stripped region (Fig. 6.16), which was not desirable for preparing solar-E-yarns with multiple solar cells.

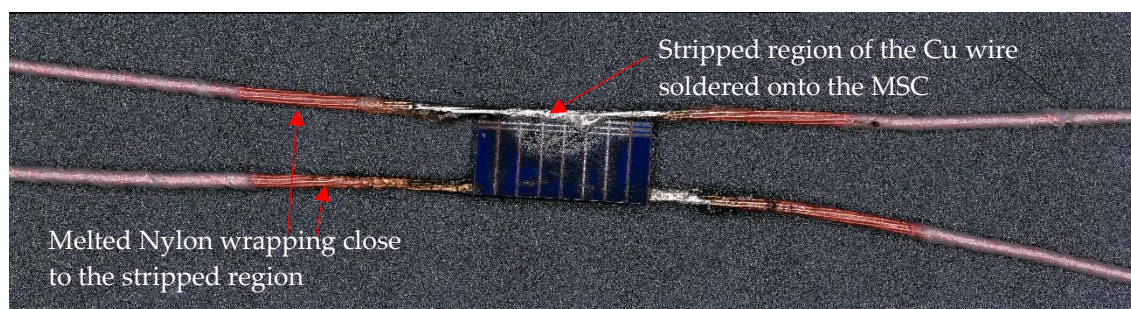


Figure 6.16 – A MSC soldered onto a pair of insulated Cu wires after removing the polyurethane enamel and Nylon wrapping.

However, for this experiment this was considered acceptable since the solar-E-yarns were prepared with single MSCs. The MSCs were soldered onto the prepared Cu wires using the same soldering method employed in previous experiments. Solar-E-yarns with 1.6 mm diameter RMP and 2.0 mm diameter knit braided sheaths were prepared to complete the yarn.

Five solar-E-yarns prepared as mentioned above, were woven into a solar-fabric sample using the same methods and materials used for the preparing samples for the wash durability testing. The I_{sc} and V_{oc} measurements of the solar-E-yarns of the solar-fabric sample were measured under one sun intensity at dry condition (Fig. 6.17(a)), after soaking with tap water (Fig. 6.17(b)) and after being immersed in tap water (Fig. 6.17(c)).

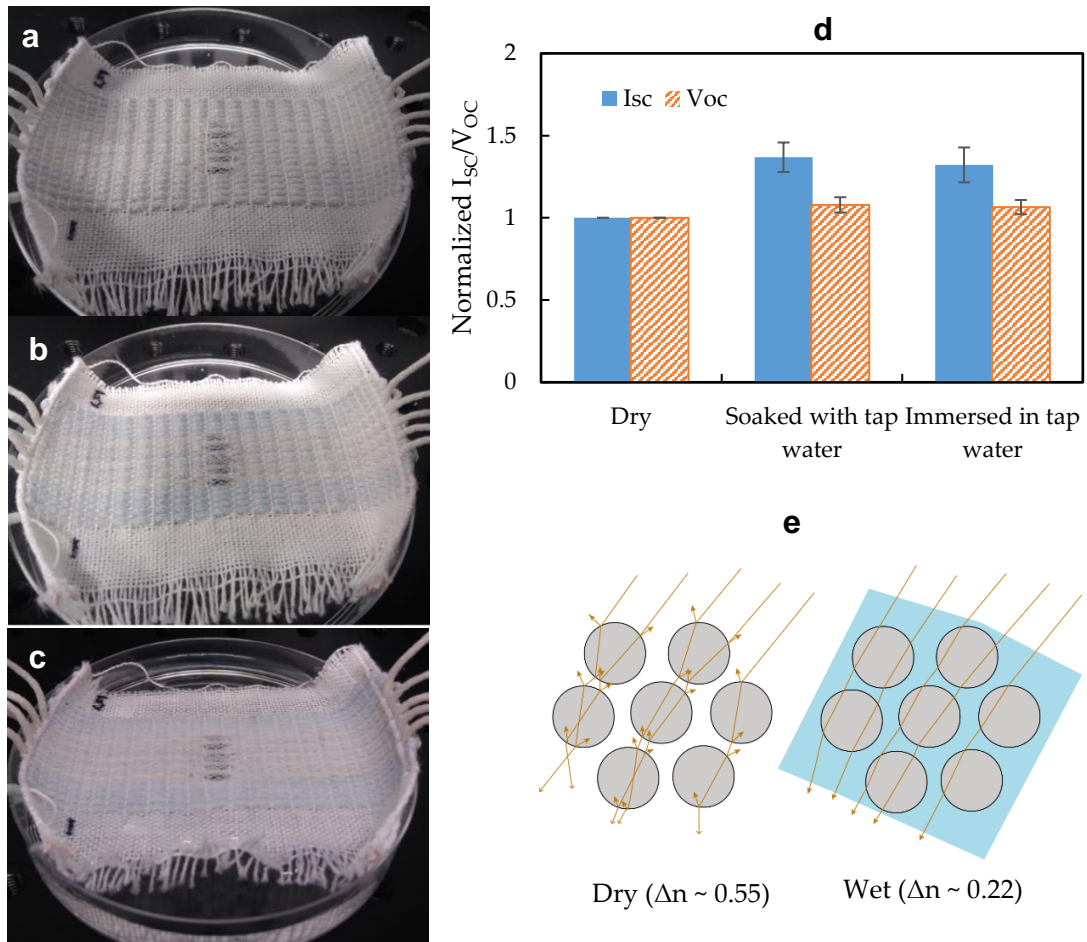


Figure 6.17 – Solar-fabric sample with five solar-E-yarns constructed using electrically insulated copper wires under (a) dry condition, (b) after soaking with tap water and (c) after immersing in tap water. (d) The normalized I_{sc} and V_{oc} values for the five solar-E-yarns when dry, after soaking with tap water and after immersing in tap water. (e) A diagram representing the effect of water on the light transmission through the fibrous sheath of the solar-E-yarns.

The results (Fig. 6.16(d)) clearly show that the solar E-yarns made using insulated copper wires functioned correctly when soaked or immersed in tap water. It was noticed that the I_{sc} values had a ~35 % increase in comparison to the values shown under dry conditions. This could be explained by how water interacts with textile fibres of the fibrous sheath: The amount of light scattered by individual fibres in the sheath is a function of the differences in refractive indices (Δn) of the fibre material and the spaces between fibres. According to the Fresnel equation, a higher Δn will result in a greater amount of light scattering. When the solar-E-yarn is dry Δn value is 0.55 (refractive index of the fibre ~1.55, air 1). When the solar-E-yarn is wet the Δn value is 0.22 (refractive index of water ~1.33). Due to lower amount of scattering under wet conditions, the MSC received a higher light flux, resulting in higher I_{sc} values. This effect was similar to how

resin impregnation enhanced the performance of solar-E-yarns as discussed in chapter 5.

6.7 Conclusions

The results of these experiments confirmed that the solar-E-yarns exhibited satisfactory levels of performance under different operational conditions that they may encounter during their regular use. Wash durability tests of solar-E-yarns confirmed that the solar-E-yarns in a woven structure could survive 15 machine wash cycles and beyond 25 hand wash cycles. The reduction in maximum power after 25 wash cycles was ~13.5 % and ~10.4 % for machine washing and hand washing respectively. The solar- fabrics showed no significant changes in performance or appearance after 6000 abrasion cycles. The solar-E-yarns retained their normal functionality beyond 50 N in uniaxial tensile tests which exceeded the tensile forces encountered during garment manufacture or normal use. The performance of solar-E-yarns significantly deteriorated beyond three impact cycles of 98 mJ. While this impact test would provide an understanding of the limits of the impact that the solar-E-yarns could withstand, further tests may be needed to simulate a more representative mechanical impact scenario.

The experiments conducted at different temperatures confirmed that the solar-E-yarns behaved similarly to the maiden miniature solar cells with change in temperature, where the V_{oc} reduced linearly with the temperature with a temperature coefficient of 21 mW/°K. As predicted, a small increase in I_{sc} was observed with temperature changes, however the results were not conclusive and an accurate temperature coefficient could not be obtained. The tests under different relative humidities showed no significant change in the solar-E-yarn performance with changes in relative humidity in the localised surrounding, although according to literature the change in humidity in atmosphere significantly affects the intensity of incident light. The test conducted with solar-E-yarns prepared with insulated Cu wire confirmed that the functionality of the solar-E-yarns did not deteriorate in the presence of liquid water. Soaking the solar-E-yarns with tap water, or immersing them in tap water, improved the I_{sc} by ~35 %, possibly due to the reduction in the light scattering in the fibrous sheath.

Chapter 7

Solar Energy Harvesting Fabrics

7.1 Introduction

This chapter presents the preparation, characterisation, and demonstration of solar energy harvesting fabrics prepared using solar-E-yarns. For practical applications the solar-E-yarns (one dimensional) need to be deployed in fabrics (two dimensional), in this research woven fabric constructions are considered. The fabrics were prepared using a table loom that represented a pilot scale weaving process.

Six fabric demonstrators were prepared using solar-E-yarns (each containing ten, 1.5×3 mm solar cells) and tested under simulated sunlight and/or natural sunlight. The first fabric demonstrator comprised of 200 MSCs and was employed to demonstrate the capability of the technology to charge various energy storage devices and power small mobile electronic devices. The second fabric demonstrator comprising 200 MSCs had two independently networked modules; one prepared with resin impregnated solar-E-yarns, and the other with normal solar-E-yarns. Another four fabric demonstrators each comprising 50 SCs were prepared to conduct a comparative test of the effect of resin impregnation and colour of fibre sheath in fabric form. Towards the end of the chapter, a study into the effect of incident light angle on the photovoltaic performance of the fabrics has been presented. A study into how different distribution of the solar-E-yarns within the fabric effect photovoltaic performance has also been performed. This study was aimed at defining the design rules and operational boundary conditions for the solar energy harvesting fabric.

7.2 Fabrication of solar-E-yarns for fabric demonstrators

To prepare the solar energy harvesting fabrics, solar-E-yarns were prepared with multiple 1.5×3 mm SCs connected in parallel. Most of the physical dimensions the solar-E-yarns were based on practical implications: The positioning of the solder pads on opposite faces of the solar cell made parallel connection the most practical approach for creating a solar-E-yarns using multiple SCs. An important parameter in the yarn design was the gap between two adjacent SCs. To achieve the maximum power density the cells needed to be soldered without any spacing between each other, however this was not viable due to the process and design constraints: To be able create discrete RMPs that hermetically sealed the soldered SCs, using the current method, a minimum gap of ~ 2 mm was required between SCs. In addition, smaller gaps between RMPs would have

had an adverse effect on the flexibility and bendability of the final solar-E-yarn. Considering these factors, a 2 mm gap between adjacent SCs were maintained at the soldering stage. Ten parallel connected solar cells with 2 mm gaps between adjacent SCs resulted in a solar-E-yarn with a length of ~5 cm. 5 cm was the maximum length of yarn that could be characterised using the solar simulator and therefore, 10 SCs per yarn were used for all of the yarns prepared for the demonstrator fabrics. To solder ten SCs according to the specifications mentioned above, a mould was prepared with black-pigmented silicone (Fig. 7.1). The process for soldering multiple SCs was similar to the process for soldering a single SC, where all ten SC were positioned on the grooves of the mould before laying the second Cu wire onto the back contact of the SCs.

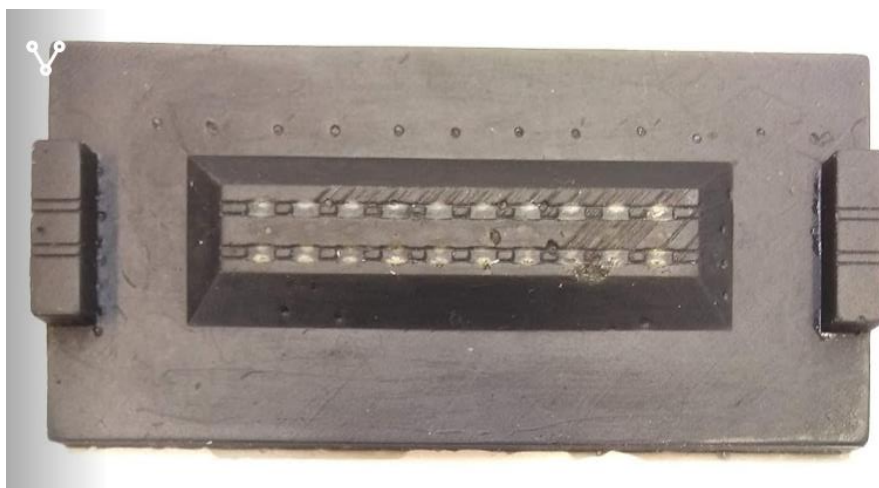


Figure 7.1 – The mould employed for soldering ten solar cells onto a pair of Cu wires.

After dispensing the solder paste onto the Cu wire the MSCs were individually soldered using the process described in section 3.2.4 of Chapter 3. The encapsulation process for the individual soldered MSCs used the process described in section 3.2.5 (Dymax 9001E-V3.5 resin was used). The micro-pod had a diameter of 1.6 mm and a length of ~4 mm (1 mm longer than the MSC, which was positioned at the centre of the RMP). The process and materials for covering the solar-micro-pod is described in section 3.2.6.

Microscopic images of the solar-E-yarns at different stages of the fabrication process are shown in Fig. 7.2.

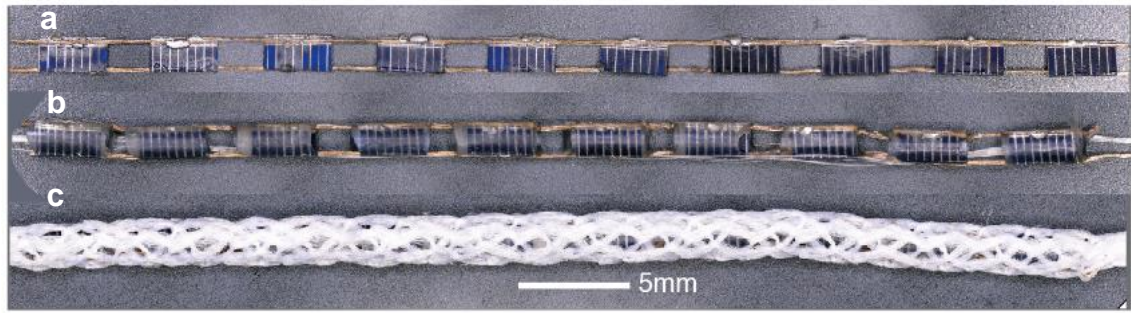


Figure 7.2 – Preparation of solar-E-yarns with ten solar cells. (a) Ten solar cells soldered onto pair of parallel Cu wires. (b) The soldered solar cells individually encapsulated within cylindrical resin micro-pods. (c) The completed solar-E-yarns with ten solar cells.

The short circuit current (I_{sc}) and open-circuit voltage (V_{oc}) values at each stage of the process for twenty solar-E-yarns was measured under one sun light intensity (Fig. 7.3).

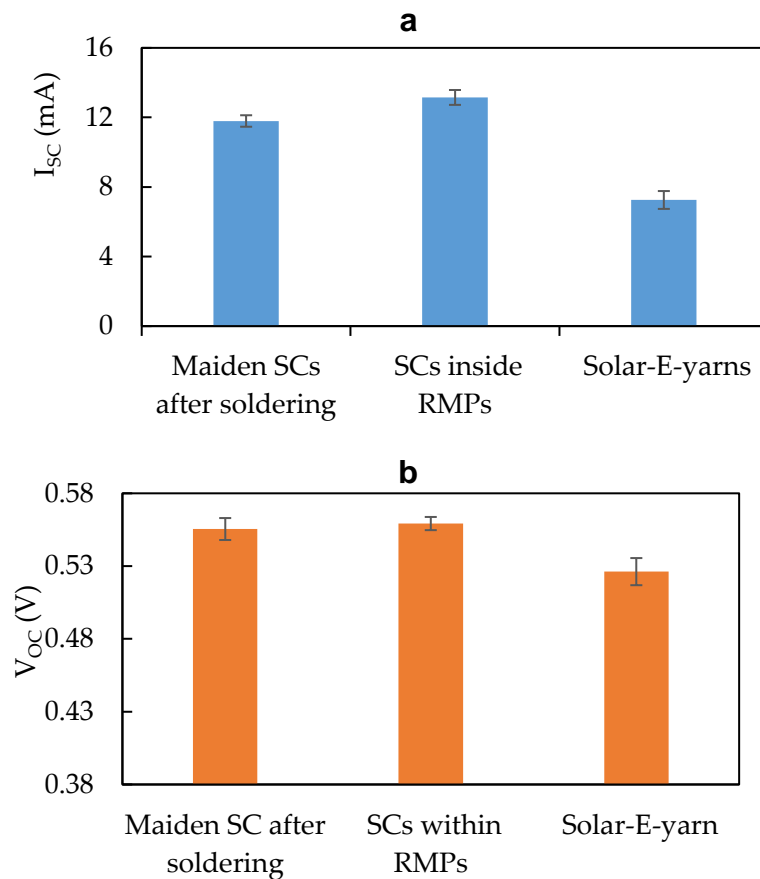


Figure 7.3 – (a) Short-circuit current (I_{sc}) and (b) open-circuit voltage (V_{oc}) for solar-E-yarns prepared with ten solar cells. Here the results show the average and standard deviation of 20 samples.

The change in I_{sc} and V_{oc} values per cell in the above tested samples were similar to the results obtained for the solar-E-yarn with single solar cell, given in 5.4 of chapter 5.

7.3 First fabric demonstrator

To construct the first MSC embedded demonstrator fabric, 20 solar-E-yarns with ten MSCs per yarn were used. A table top weaving loom (four shafts, 24" width; Harris Looms, UK) was prepared (Fig. 7.4(a)) with a 12 cm wide sheet of warp yarns (-10 yarns per centimetre) using white cotton yarns (38.9 × 2 tex; Elton Vale Yarns Ltd, UK). The warp yarns were threaded to achieve a four by one shedding pattern (a basket weave). The woven fabric was created (Fig 7.4(b)) using these solar-E-yarns inserted in the weft direction. The solar-E-yarns were inserted in such a manner that the photoactive side was fully exposed on the front surface of the fabric. The SC embedded region of the fabric (the photoactive area) had a footprint of 44.5 mm × 45.5 mm.

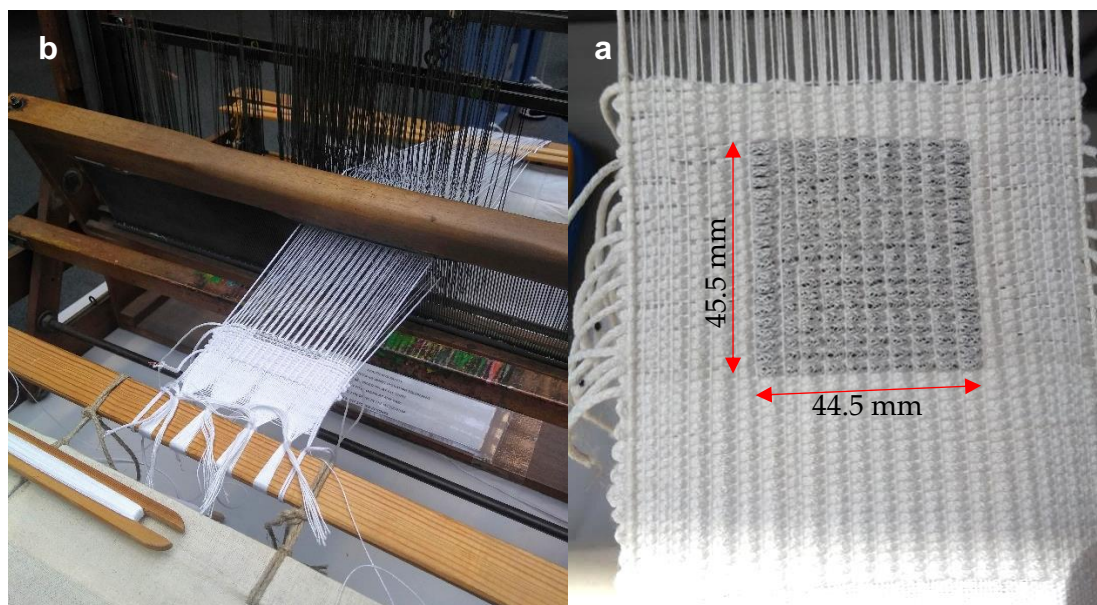


Figure 7.4 – (a) Image of the weaving loom during the solar-E-yarn weaving process. (b) The first solar-E-yarn demonstrator after completing the weaving process.

Fig. 7.5(a) illustrates the woven structure employed for preparing demonstrator fabrics. Cotton yarns (same type used for the warp) were used as weft yarns to fill the gaps between the solar-E-yarns. One cotton weft yarn was inserted between each of the solar-E-yarns. Four mini-modules, each consisting of five solar-E-yarns, were created by connecting five solar-E-yarns in series. The electrical connections between the five solar-E-yarns within each mini-module is indicated in Fig. 7.5(a), with the circuit diagram of the solar cell network within each mini-module shown in Fig. 7.5(b).

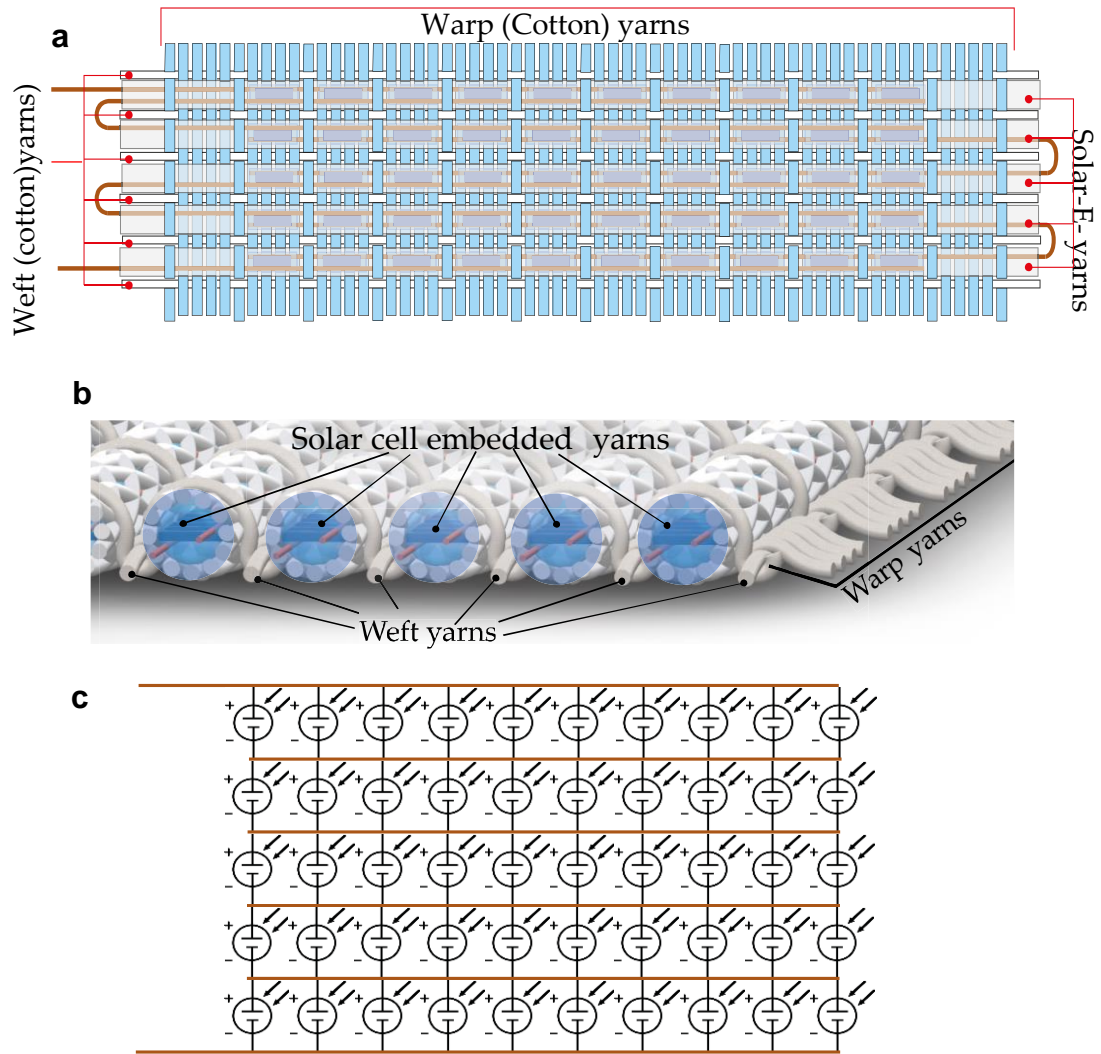


Figure 7.5 – (a) The woven fabric structure of the solar energy harvesting fabric demonstrators and the solar-E-yarn connections of a single mini-module. (b) Three-dimensional illustration of the side view of the solar energy harvesting fabric structure. (c) Electrical circuit diagram of the network of solar cells in a single mini-module.

The mini-modules produced an I_{sc} and V_{oc} of ~ 7.5 mA and ~ 2.6 V respectively. The four mini-modules were connected in different configurations that generated I_{sc} values ranging between 7.5 – 30.1 mA and V_{oc} values ranging between 2.6 – 10.2V as shown in Fig 7.6.

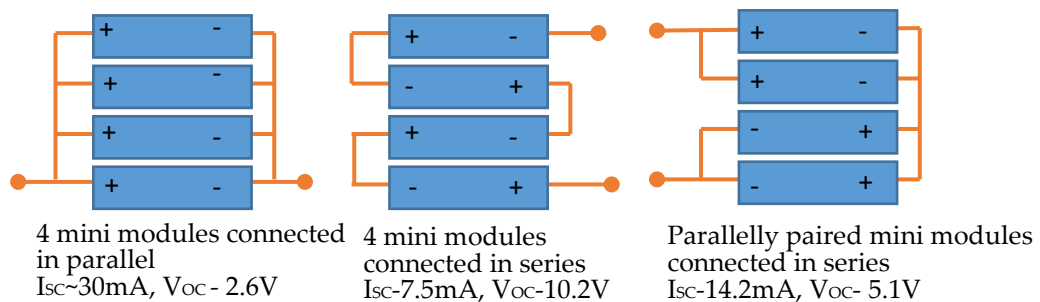


Figure 7.6 – Different network configurations of the four mini-modules of the solar energy harvesting fabric, with their short-circuit current and open-circuit voltage values.

Since most battery types and small mobile devices were compatible with a ~5V supply, the four mini-modules were permanently wired according to the configuration that generated I_{sc} - 14.2mA, V_{oc} - 5.1V (Fig.7.7).

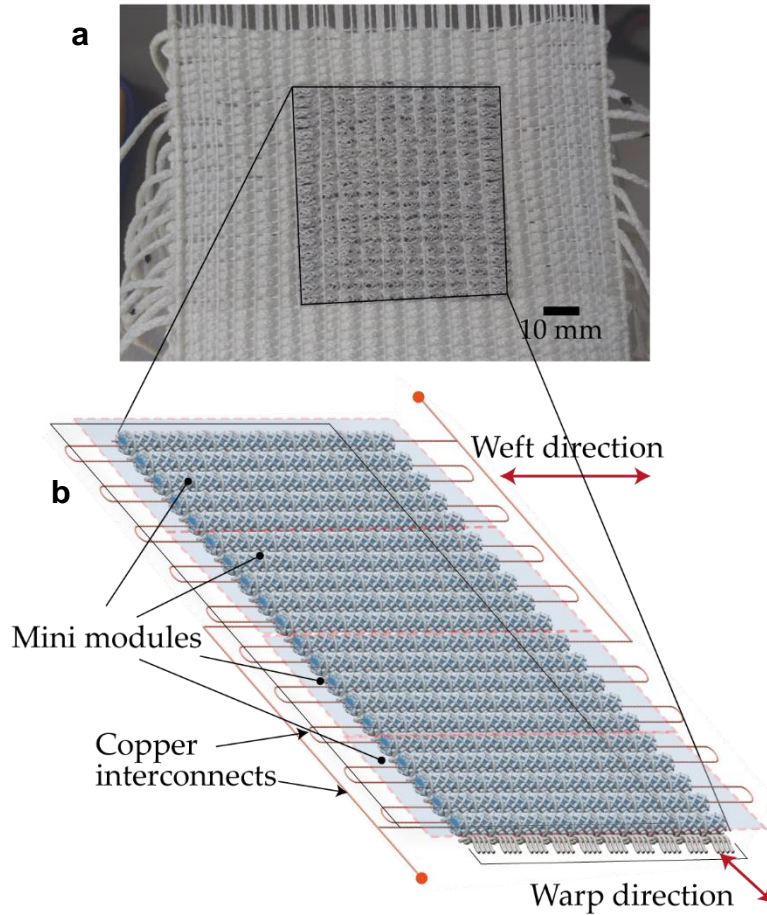


Figure 7.7 – (a) Image of the solar cell embedded fabric (black box indicating solar cell footprint) and (b) three-dimensional schematic of the solar cell fabric demonstrator showing how the solar-E-yarns and mini-modules were connected.

7.3.1 Electrical characterisation of the first fabric demonstrator

The first fabric demonstrator was characterised using the solar simulator. The I-V curves were generated for the fabric demonstrator under four different light intensities of AM 1.5 G solar spectrum. The P-V curves, I_{sc} , V_{oc} , P_{MAX} and FF were derived using the I-V data.

The solar energy harvesting fabric demonstrator generated P_{MAX} values of 43.4 ± 0.29 mW, 31.00 ± 0.38 mW, 18.60 ± 0.25 mW and 7.62 ± 0.17 mW under 100%, 75%, 50% and 25% of one sun illumination (100 mW/cm^2 , 1.5 AM spectrum) respectively, as shown in Fig. 7.8(a, c).

At one sun intensity I_{sc} , V_{oc} , FF, and power density values of 14.14 ± 0.05 mA, 5.14 ± 0.02 V, 0.598 ± 0.004 and 2.146 ± 0.014 mW/cm² were observed respectively (Fig. 7.8(b, c)).

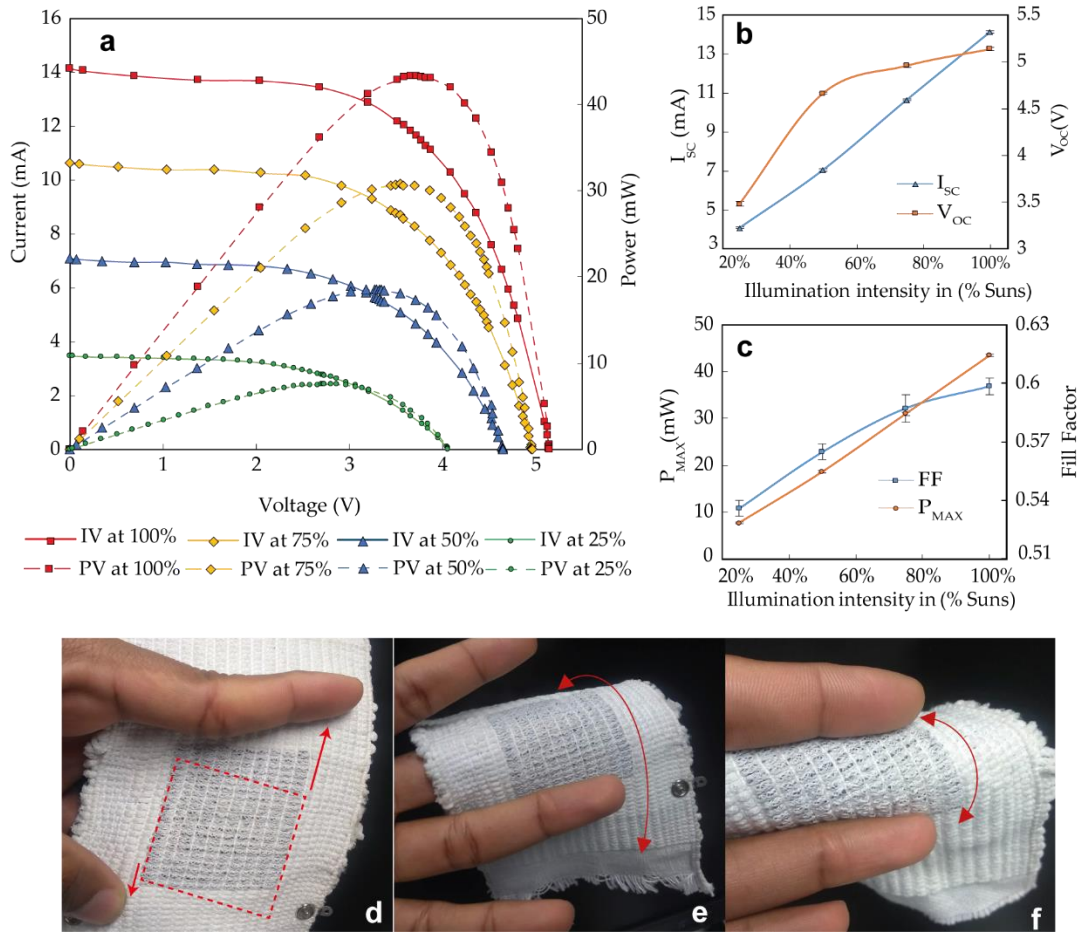


Figure. 7.8 - Performance of miniature solar cell embedded fabric demonstrator. (a) Current-voltage (IV) and power-voltage (PV) characteristics, (b) short circuit current (I_{sc}) and open circuit voltage (V_{oc}) and (c) fill factor (FF) and maximum power (P_{MAX}) for solar cell embedded fabric demonstrator at different sun intensities, (100% = one sun intensity with 1.5 AM standard solar spectrum). Error bars indicate the SD of five repeat experiments. Performance of the solar cell embedded fabric demonstrator under (d) shear deformation, (e) draping on a finger and (f) bending around a finger. Error bars show the standard deviation of five repeat measurements using one sample.

Overall, the I_{sc} and P_{MAX} values showed a close linear relationship with the light intensity level, indicating a behaviour equivalent to a typical c-Si SC network (Chegaar *et al.*, 2013). The P_{MAX} per solar-E-yarn when woven into the fabric was $217.3 \mu\text{W}$, -4.5 % lower than the average P_{MAX} values of 20 individual solar-E-yarns ($227.5 \pm 17.5 \mu\text{W}$), owing to current/voltage mismatches caused due to cell-to-cell variations (Kaushika and Rai, 2007) and variations in angular position of the embedded MSCs relative to the fabric's surface. Part of these losses would get compensated by the increase in light flux due to

the specular reflectance (albedo effect) for the fabric surrounding which is investigated in detail in section 7.6.

When worn, a solar energy harvesting fabric may undergo mechanical deformation, therefore the effects of deformation on the electrical performance under these conditions was important to understand. When subjected to shear deformation (Fig. 7.8(d)), draping (Fig. 7.8(e)) and bending (Fig. 7.8(f)), the demonstrator fabric showed I_{sc} values of 13.83 mA, 11.06 mA and 2.32 mA respectively under one sun intensity. These results provided clear evidence that the SC embedded fabric could generate power while undergoing various forms of deformation. The I_{sc} after bending significantly differed from the I_{sc} before deformation (14.14 mA), due to the lower surface area exposed to the light source (less than 30 % of the photoactive area was exposed), which is also curved (incident angle varies across the exposed curved area). The modest reduction in I_{sc} after draping on hand was due to the curvature of the photoactive area. There was an insignificant change in I_{sc} after shear deformation. These results indicated that the changes were likely caused by the change in incident angles, not due to electro-mechanical effects within the cells and cell network, when subjected to deformations. When the fabric was returned to its original shape the measured I_{sc} recovered to its pre-deformed values in all cases. These results provided evidence of the viability of the solar-E-yarns for wearable applications as clothing would be exposed to different levels of sunlight and has to undergo various mechanical deformations during its regular use.

7.3.2 Liquid absorption properties of the solar cell (SC) embedded fabric demonstrator

An experiment was conducted to assess the liquid absorption properties of the solar fabric demonstrator, to compare its liquid moisture management performance against a control fabric without solar-E-yarns. The control fabric was woven using knit-braided yarns without the MSC-RMP-Cu wire core (all other material and process parameters remaining identical to the solar-E-yarns) The was prepared using identical woven structure, process parameters and additional cotton yarns to the demonstrator fabric for a comparison test. The solar cell embedded demonstrator fabric containing 200 SCs and the control fabric were tested using the Gravimetric Absorbance Test System (GATS – M/K systems Inc, USA), as shown in Fig. 7.8(a). The backside of the fabrics was covered by a thin polyethene film with a 45 mm × 45 mm window, to selectively expose the back

side of the cell embedded area of the fabric to the porous plate of the GATS. The fabrics were placed on the porous plate of the GATS and an absorption test was conducted according to TAPPI T561 (Sorptive Rate and Capacity Using Gravimetric Principles) with distilled water, until the fabric was saturated.

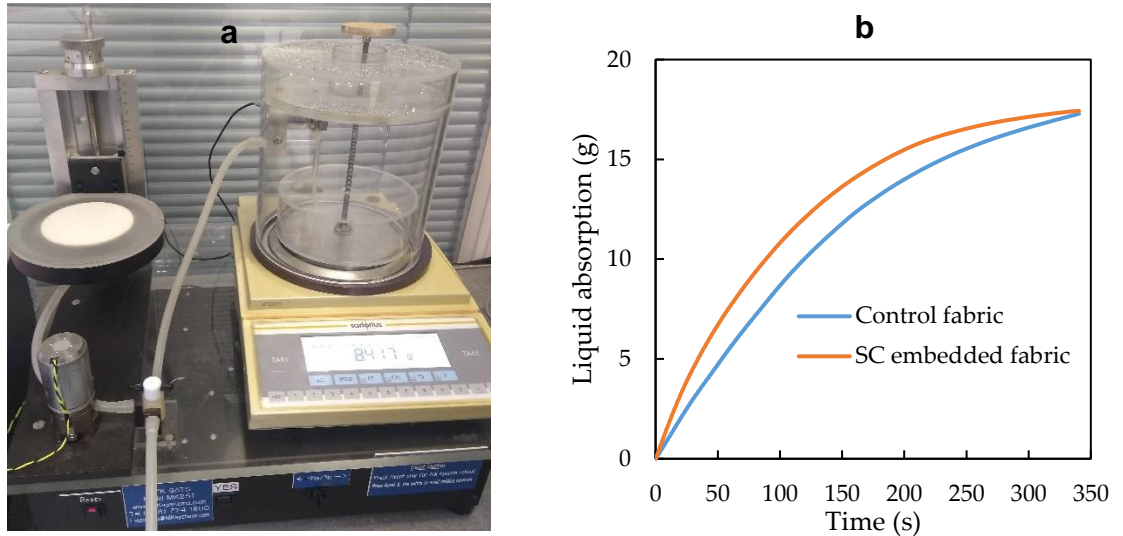


Figure 7.9- (a) Image of the GAT System used for liquid absorption measurements. (b) Liquid absorption of the solar cell embedded fabric and the control fabric.

The results for the liquid absorption test are given in Fig. 7.9(b). The fabric demonstrator showed saturated water capacity of 17.43 g which was similar to the results for the control fabric sample (saturated water capacity of 17.29 g). The solar fabric demonstrator showed a higher absorption rate (up to 50% higher) than the control fabric during the first 50s of the tests. This may be due to the increased wicking action caused by the higher tightness (resulting smaller capillary radii) of the fabric structure in the solar cell embedded area. Tighter woven structure leads to small capillary radii between individual fibres, that increase the rate of the wicking action.

7.3.3 Demonstration of energy harvesting capability

The ability of the MSC embedded fabric demonstrator to charge different types of electrical devices was explored, as ultimately the SC embedding fabric was designed to charge wearable devices. To demonstrate the possibility of creating fully fabric integrated energy harvesting and storage systems, an array of supercapacitor embedded E-yarns were prepared using, CPH3225A supercapacitors (11mF, 3.3V, $3.2 \times 2.5 \times 0.9$ mm, Seiko Instruments Inc, Japan). Each of the E-yarns comprised of ten supercapacitors connected to two parallel Cu wires and individually embedded within cylindrical RMPs

of 3.2 mm diameter before being covered with a 4 mm knit braided structure (Fig 7.10). The supercapacitor embedded yarn had a resultant capacitance of 110 mF. Further details of preparation and characterisation of supercapacitor embedded E-yarns are provided in Appendix 10.

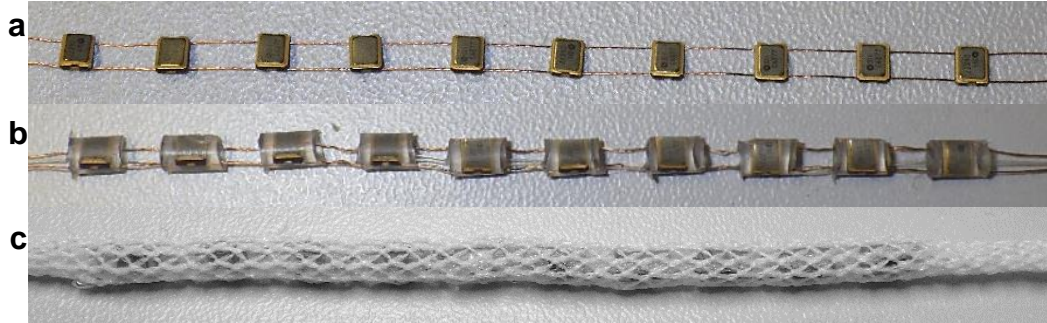


Figure 7.10- Supercapacitor embedded textile yarns. (a) Supercapacitors soldered onto copper wires. (b) Supercapacitor strands after the supercapacitors were encapsulated inside of 3.2 mm diameter micro-pods. (c) Supercapacitor embedded textile yarn after covering with a 4 mm diameter fibrous sheath.

An experiment was conducted where the above supercapacitor embedded yarns were charged by the solar fabric demonstrator using the solar simulator. A single supercapacitor yarn was connected to the solar fabric demonstrator and charging was performed under 100%, 75%, 50%, 25% and 10% of one sun intensity (Fig. 7.11).

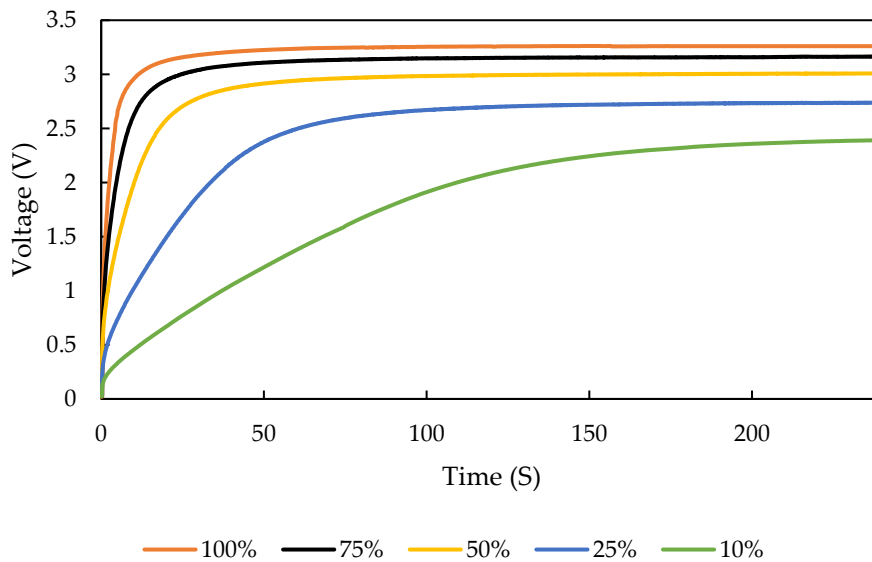


Figure. 7.11 - Charging supercapacitor embedded E-yarns using the solar energy harvesting fabric demonstrator at different solar intensity levels generated by solar simulator.

The charging voltages and the time taken to reach the voltages at corresponding sun intensities are given in Table 7.1.

Table. 7.1 – Charged voltage and charging time for supercapacitor embedded E-yarns using the solar energy harvesting fabric demonstrator at different solar intensity levels generated by solar simulator.

Light intensity (% one sun)	Charged voltage (V)	Charging time (s)
100 %	3.2	37
75 %	3.1	46
50 %	3.0	160
25 %	2.73	187
10 %	2.4	261

A 47 mF (5.5 V) supercapacitor (KEMET Electronic Components, USA) was charged using the solar fabric under 100%, 75%, 50% and 25% of one sun illumination; the supercapacitor reached its maximum voltage within 15s and 60s under 100% and 25% sun intensity respectively ((Fig. 7.12(a)).

Under 100 % sun intensity the fabric woven with solar-E-yarns was able to charge a 15 mAh (3.7 V) Li-ion battery to ~ 3.7 V within 10 minutes ((Fig. 7.12(b)) and charged a 380 mAh (3.7 V) Li-polymer battery from 3.1 V to 3.55 V within 60 minutes ((Fig. 7.12(c)).

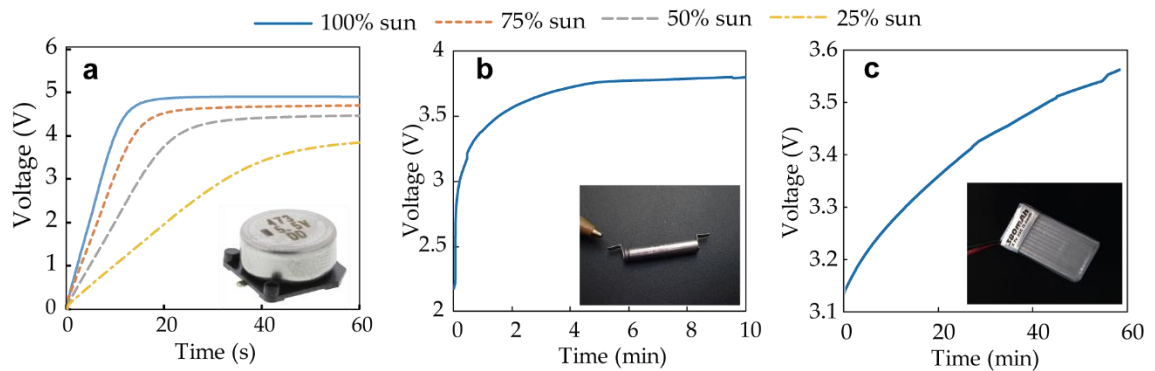


Table. 7.12 – Charging and powering devices using the solar cell embedded fabric. Evaluating the charging behaviour of (a) a 47 mF, 5.5 V super capacitor, (b) a 15 mAh, 3.7 V miniature Li-ion battery and (c) a 380 mAh, 3.7 V Li-polymer battery using the solar cell embedded fabric.

The solar fabric demonstrator was also capable of charging a basic mobile phone with 1000 mAh battery (Fig. 7.13(a)), a fitness tracker with a 50 mAh battery ((Fig. 7.13(b)) and a LED fabric demonstrator ((Fig. 7.13(c)) that contained 10 flashing LEDs E-yarns. These demonstrations provided clear evidence of the utility of the solar energy harvesting

fabric for use within regular clothing as a power source for wearable devices, which often have a power requirement around tens to a few hundreds of milliwatts.

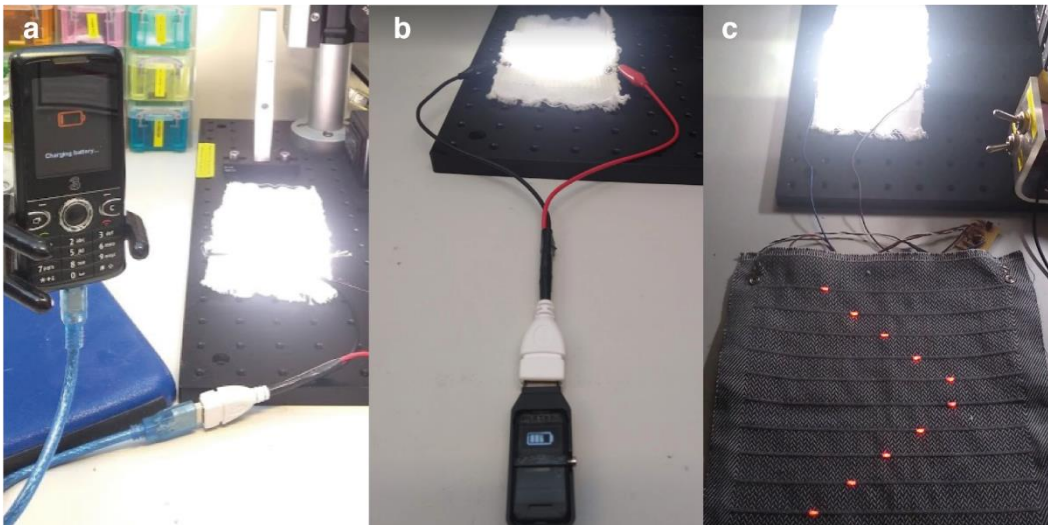


Figure. 7.13 - Demonstrating the charging of (a) a basic mobile phone with a 1000 mAh, 3.7 V battery, (b) a fitness tracker with 50 mAh, 3.7 V battery and (c) powering an LED embedded fabric demonstrator developed using E-yarn technology.

7.4 Second fabric demonstrator

A second fabric demonstrator was prepared in a similar fashion to the first fabric demonstrator, however here half of the solar-E-yarns were impregnated with the Dymax 9001 E-V3.5 resin (Fig 7.14(b)). The solar-E-yarns with resin impregnation and without resin impregnation were separately serially networked into two modules (Fig 7.14(a)).

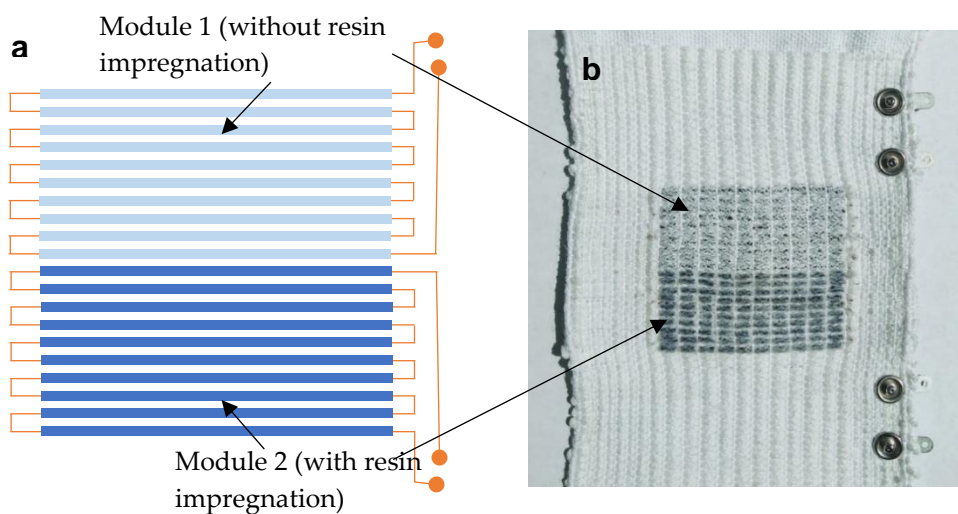


Figure. 7.14 – Second fabric demonstrator prepared using solar-E-yarns with and without resin impregnation. (a) Schematic illustration of the two separately networked modules. (b) Image of the second fabric demonstrator.

The second fabric demonstrator was characterised under one sun using the solar simulator (Fig. 7.15), and the results are summarized in Table 7.2

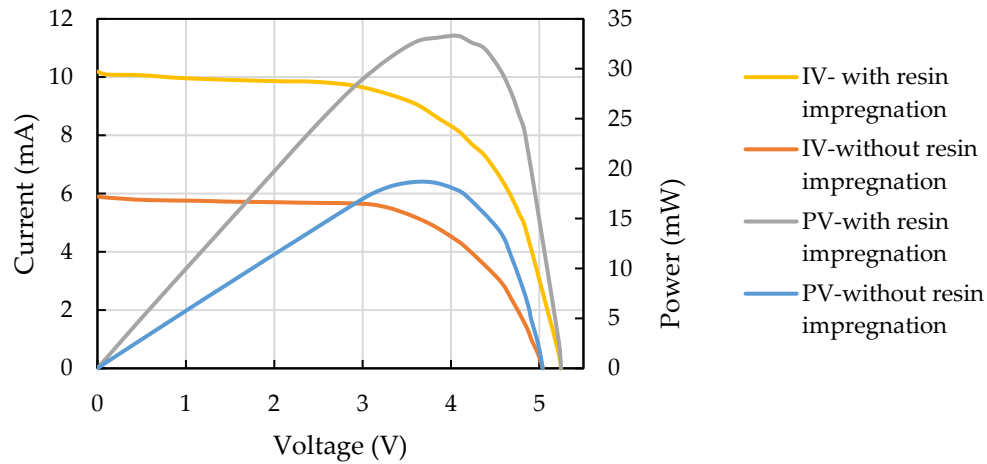


Figure. 7.15 – IV and PV characteristics for module 1 (no resin impregnation) and module 2 (with resin impregnation), under one sun illumination.

The results for the resin impregnated module confirmed the enhancement brought about by using resin impregnation, with a ~78 % increase in P_{MAX} with resin impregnation.

Table. 7.2 – Summary of the results for the module 1 (no resin impregnation) and module 2 (with resin impregnation) for second fabric demonstrator under one sun illumination.

Parameter	Module 1	Module 2
I_{SC} (mA)	5.90	10.19
V_{OC} (V)	5.04	5.24
P_{MAX} (mW)	18.68	33.33
FF	0.63	0.62

7.5 Fabric demonstrators for comparative tests and field test

A third set of solar fabrics were prepared to conduct a comparison test under the solar simulator and a field test under natural sun light. Four solar fabric demonstrators were prepared using solar-E-yarn types given below (Fig 7.16).

- Solar-E-yarns prepared with white textile fibres.
- Solar-E-yarns prepared with white textile fibres and with resin impregnation.
- Solar-E-yarns prepared with red textile fibres.
- Solar-E-yarns prepared with black textile fibres.

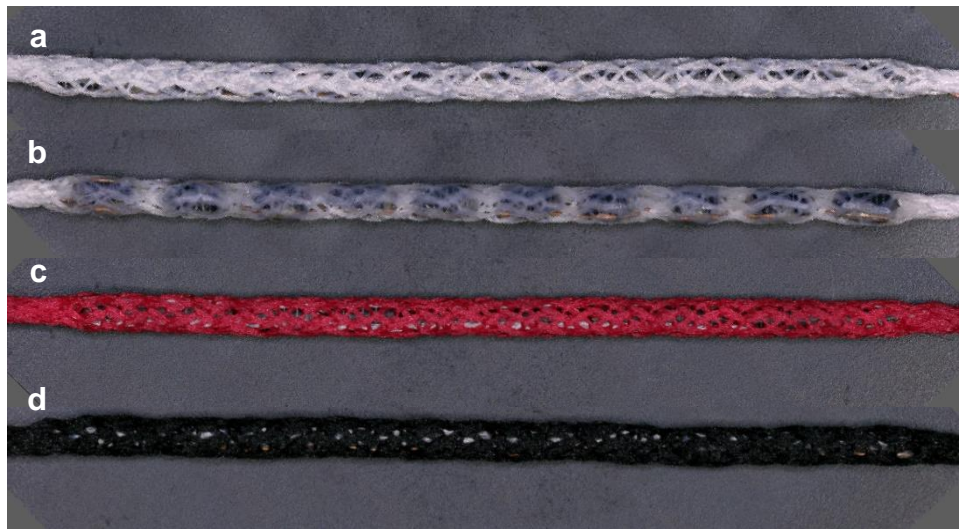


Figure. 7.16 – Microscopic images of the solar-E-yarns prepared for producing the third set of solar fabric demonstrators. (a) Solar-E-yarns prepared with white textile fibres. (b) Solar-E-yarns prepared with white textile fibres and with resin impregnation. (c) Solar-E-yarns prepared with red textile fibres. (d) Solar-E-yarns prepared with black textile fibres.

Each fabric comprised of five solar-E-yarns (each solar-E-yarn contained ten SCs as detailed in 6.1) woven together (Fig. 7.17) in a fashion similar to fabric demonstrators one and two.

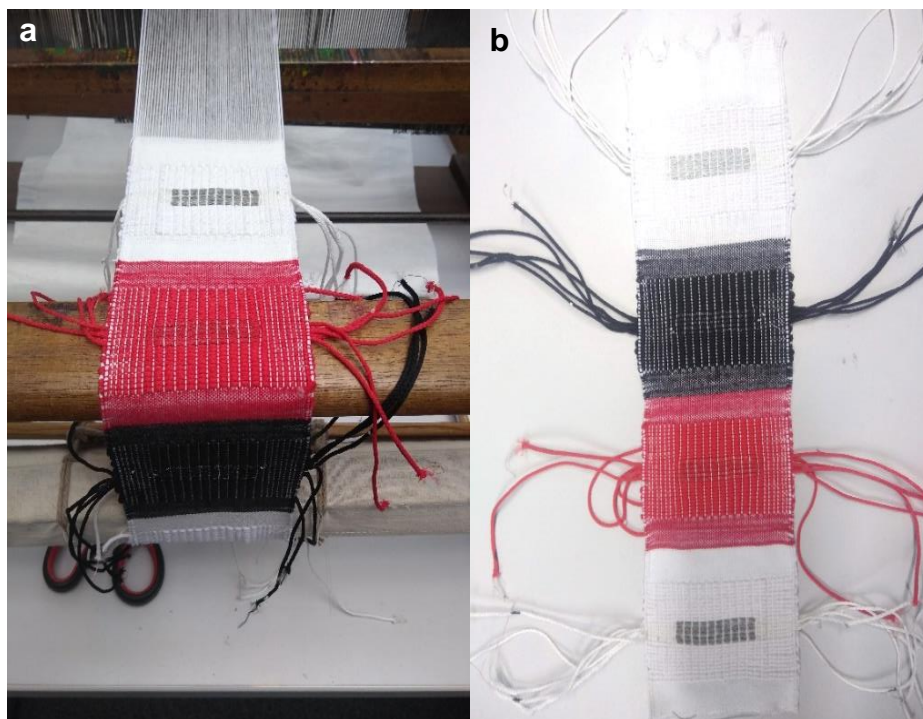


Figure. 7.17 – Image of the third set of solar fabric demonstrators (a) during and (b) after the weaving process.

7.5.1 Characterisation of solar-E-yarns and resultant fabrics

The individual solar-E-yarns were evaluated for I_{sc} and V_{oc} under one sun intensity before weaving (free standing form) and in within woven fabric (Fig. 7.18).

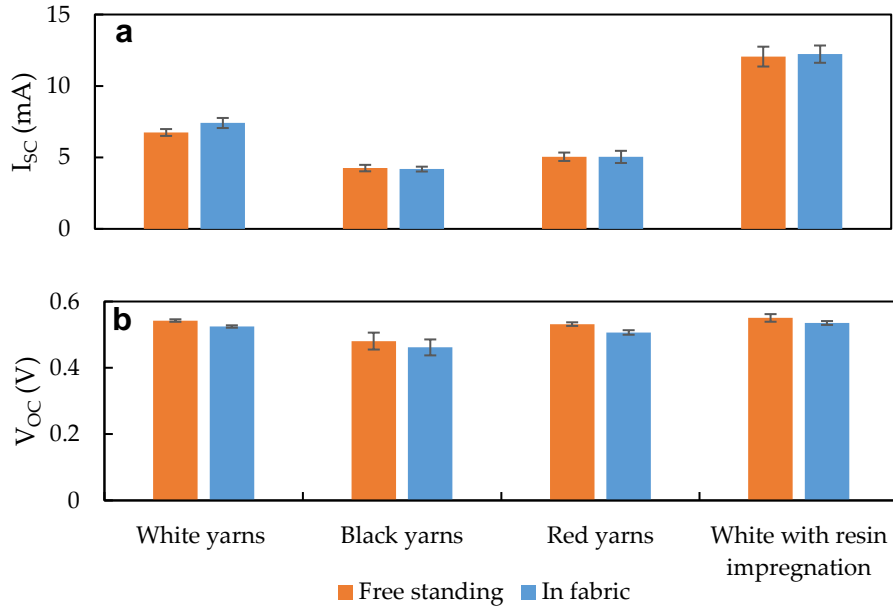


Figure. 7.18 – The (a) short-circuit current (I_{sc}) and (b) open-circuit voltage (V_{oc}) of solar-E-yarn prepared for the third set of fabric demonstrators in free standing and fabric form.

When the yarns in free standing form were considered, the black and red yarns showed a 37 % and 25 % reduction in I_{sc} respectively in comparison to white yarns, while after resin impregnation the I_{sc} improved by ~79 %. The V_{oc} for the black and red yarns were 11.4 % and 2.0 % lower than for the white yarns; after resin impregnation the V_{oc} increased by 1.5 %. When the yarns in free standing form and fabric form were compared a ~10 % increase in I_{sc} was observed for white yarn, while in the other cases the increase in I_{sc} in fabric form was insignificant. Any changes in performance of solar-E-yarns after weaving into fabric could be attributed to two factors. Firstly, any angular misalignments of the yarns after embedding within the fabric would cause a reduction in performance. Secondly, the enhancement of incident light caused by scattered light off the fabric surface surrounding the solar-E-yarns (the albedo effect) (Brennan *et al.*, 2014). The significance of the albedo effect is governed by the specular reflectivity of the surrounding surfaces. The higher enhancement of I_{sc} due to albedo effect in the case of white yarns can be explained by the significant specular reflectivity by the surrounding white fibres. In the case of the red, and black solar-E-yarns, as well as the solar-E-yarns

with resin impregnation, the specular reflectivity of the surrounding was significantly lower, therefor the I_{sc} enhancement may not be apparent after the losses due to angular misalignments are considered. The V_{oc} values showed a reduction between 2.8 % - 4.8 % from free standing form to fabric form across all four yarn types. The reason for this reduction was not clear.

Five-individual solar-E-yarns of each type were networked in series to create four solar fabric demonstrators (white, red, black and white with resin impregnation) and were characterised under one sun intensity using the solar simulator (Fig. 7.19).

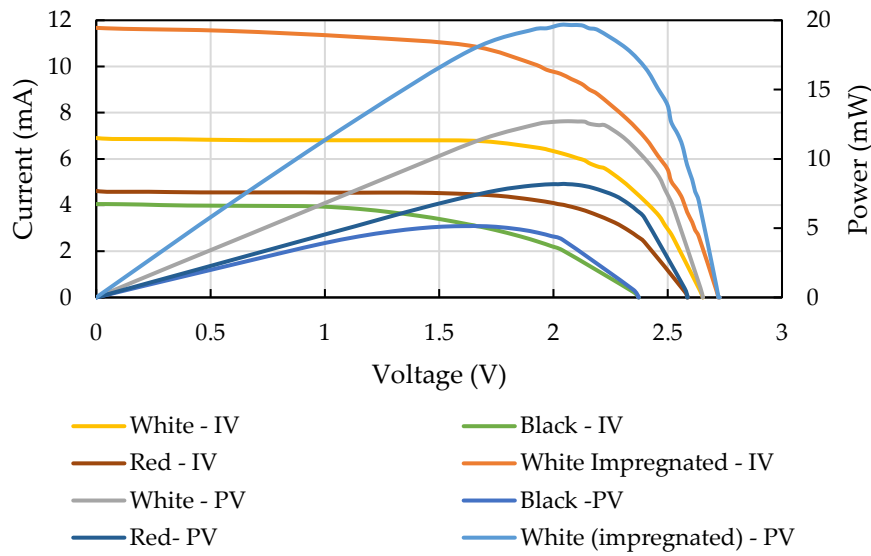


Figure. 7.19 – I-V and P-V curves for the four solar energy harvesting fabrics generated under one sun intensity using solar simulator.

The I_{sc} , V_{oc} , P_{MAX} and FF data were derived from the IV and PV curves as given in the Table 7.3.

Table. 7.3 – Summary of the results for the third set of fabric demonstrators, under one sun illumination, using solar simulator.

Parameter	White	Black	Red	White with resin impregnation
I_{sc} (mA)	6.90	4.04	4.61	11.67
V_{oc} (V)	2.65	2.37	2.59	2.73
P_{MAX} (mW)	12.72	5.16	8.20	19.67
FF	0.69	0.54	0.69	0.62

The module I_{sc} values were between 3.4 % - 8.4 % lower than the yarn form I_{sc} values across the four solar-E-yarn types, indicating that mismatch losses possibly due to the variations caused by angular misalignments. The P_{MAX} values for the black and red demonstrators were 59 % and 39 % lower (respectively) than the corresponding value for white fabric, and the resin impregnated white fabric was ~55 % higher.

These results revealed that the colour of the fibrous sheath has a significant detrimental effect on the power output of the solar fabrics and confirmed the enhancement of power due to resin impregnation. The implication of the significant performance differences for different coloured-yarns will be significant when preparing modules with multiple colours. In the extreme case, the number of cells per yarn may need to be increased by ~60% for black colour yarns if they are to be networked in series with white yarns.

7.5.2 Field test using the third set of fabric demonstrators

A field test under natural sunlight to evaluate the comparative behaviour of the third set of solar energy harvesting demonstrators was designed. An autonomous mobile data acquisition device (DAQ) was built to conduct the field tests as detailed in Appendix 10. The DAQ was designed to record the voltage across fixed load resistors connected to the four solar fabric modules and a commercially available flexible solar module (MPT4.8-75, flexible solar module with 0.24W peak power, PowerFilm solar Inc., USA) (Fig. 7.20). The fabric modules and the commercial solar module were attached onto a fabric using press studs.

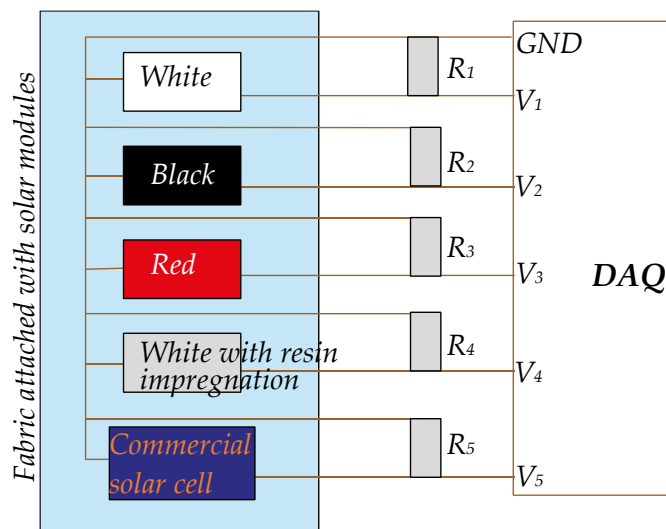


Figure 7.20 – Schematic illustration of the experimental setup for conducting field tests for the third set of solar fabric demonstrator using a data acquisition (DAQ) device.

1 k Ω load resistors (R_1 , R_2 , R_3 , R_4 and R_5 , the measured resistance values were $\sim 990\Omega$) were used for all five solar modules the field test, to generate comparable test data (a 1 k Ω load resistor value did not match the load resistance at the maximum power point for the modules, therefore the modules did not operate close to the maximum power point during the test). The modules were attached onto the back side of a white T-shirt. The solar fabrics were positioned onto the T-shirt with the individual solar-E-yarns of the solar fabrics positioned vertically. The T-shirt was dressed onto a mannequin and placed outdoors (Fig. 7.21), with the solar modules facing the North, on a bright sunny day without clouds (17th of September 2019 from 1.00 PM and 2.30 PM, in Nottingham).

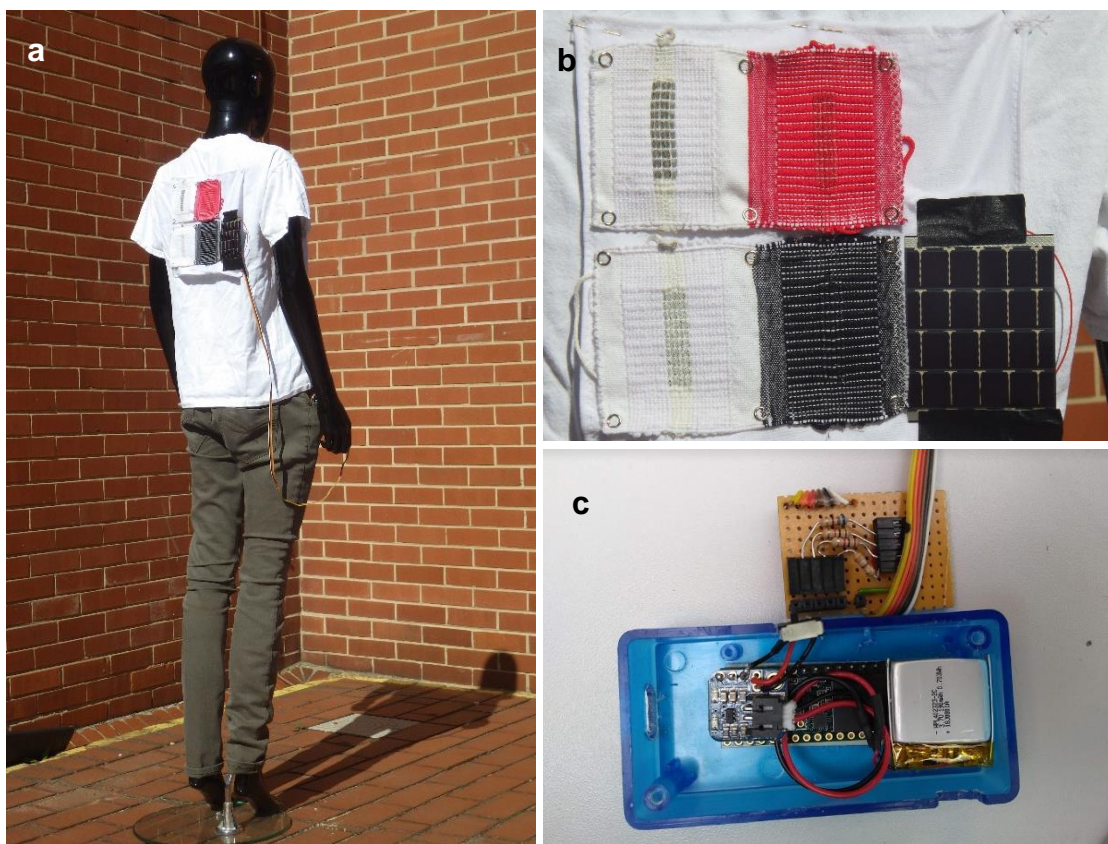


Figure 7.21 – (a) The field test conducted with solar fabric modules and commercial solar module attached onto a T-shirt that was dressed onto a mannequin. (b) Image of the solar modules attached to the T-shirt. (c) The mobile data logging device developed for recoding the performance of the solar modules.

The power density generated by each module during the test period of ~ 85 minutes is given in Fig. 7.22 and the average test results are summarized in Table 7.4.

The results provide evidence that the white fabric solar modules show comparable power density to the commercial flexible solar module. The enhancement due to resin

impregnation was apparent in the test results, where the resin impregnated solar module generated a power density 35.3 % and 24.3 % higher than the white fabric module and commercial solar module respectively. The black and red fabric solar modules generated a power density that were 54.4 % and 23.5 % lower than the white fabric module. The results of the field test confirm that the fabric modules prepared using solar-E-yarns were suitable for generating power under natural sun light.

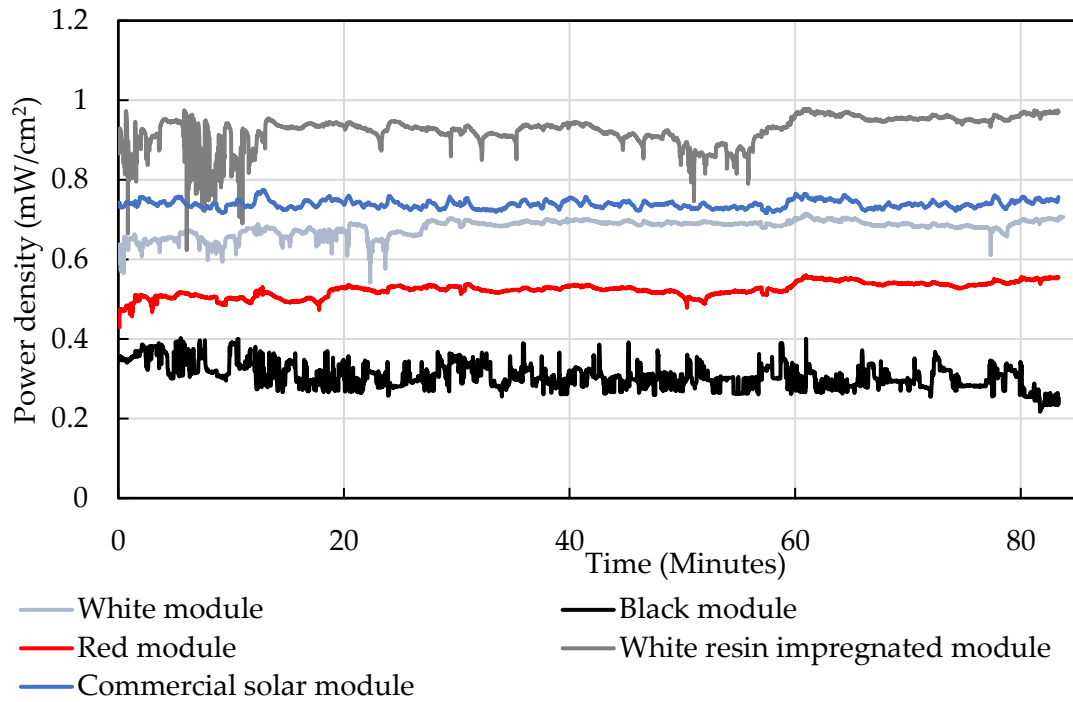


Figure 7.22 – Schematic illustration of the experimental setup for conducting field tests using the third set of solar fabric demonstrator using a data acquisition (DAQ) device.

Table 7.4 – The average results of the field study for each solar module

	V (V)	I (mA)	J (mA/cm ²)	P (mW)	Power density (mW/cm ²)
White module	1.93	1.95	0.353	3.76	0.68
Black module	1.30	1.305	0.235	1.69	0.31
Red module	1.69	1.715	0.310	2.89	0.52
White resin impregnated module	2.25	2.275	0.412	5.11	0.92
Commercial solar module	6.41	6.48	0.115	41.53	0.74

7.6 Effect of incident angle and the spacing of the solar-E-yarn within fabrics

The solar fabric demonstrators prepared earlier in this work were designed to achieve the maximum power density. For some applications maximising power density may not be critical but achieving the maximum power output per cell may be more desirable. In other instances, achieving better flexibility and drapability may be advantageous. Therefore, it would be beneficial to evaluate the effects of distributing the solar-E-yarns on a fabric may have on their performance under direct and at oblique illumination angles. For these experiments solar-E-yarns with a diameter of 2 mm containing a single $1.5 \text{ mm} \times 3 \text{ mm}$ SC were prepared using white textile fibres.

7.6.1 Evaluating free standing solar-E-yarns

Solar-E-yarns were positioned with different spacing's between the adjacent yarns (0 mm - 4 mm gaps) in a free-standing form on the sample holder, as shown in Fig. 7. 23(a), and the I_{sc} was recorded at different incident angles (the solar-E-yarn positioned at the centre was evaluated) under one sun intensity. The results were normalized to the I_{sc} values for a solar-E-yarn without adjacent yarns as shown in Fig. 7. 23(b).

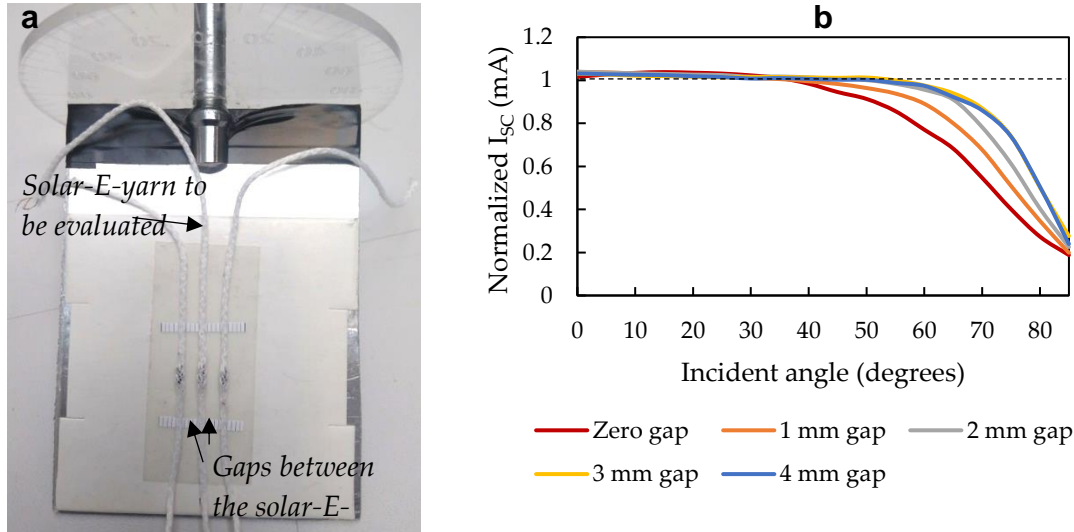


Figure 7.23 – (a) Image of three solar-E-yarn positioned on the rotary sample holder with specific gaps between each other for conducting I_{sc} measurement at different incident angles. (b) I_{sc} measurements were conducted under one sun intensity at different incident angles for solar-E-yarns with different gaps between adjacent yarns. (Results normalized to the values of solar-E-yarn with no adjacent yarns).

The results clearly indicated the shading effects of adjacent yarns with relation to the gaps between the adjacent yarns. These results can be explained with a simple geometric

model (Fig.7.24), which shows the relationship between the gaps between adjacent yarns (l), and the critical angle (θ) at which the shading was initiated with respect to the diameter (D) of the E-yarns.

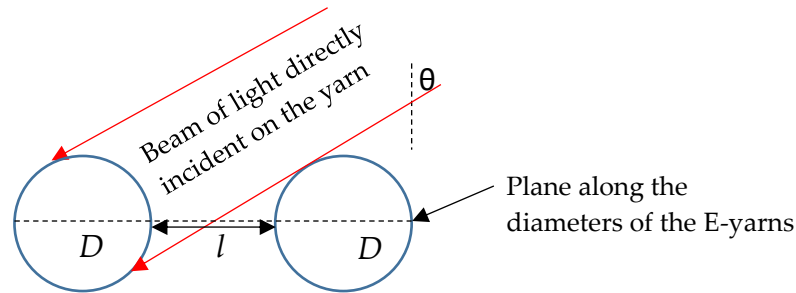


Figure 7.24 – Cross sectional geometric model for determining the critical angle at which the shading from adjacent solar-E-yarns occurred.

$$\theta = \cos^{-1} \left(\frac{D}{D+l} \right) \quad 7.1$$

Based on the geometrical model the critical angles for a 2 mm diameter solar-E-yarns with zero, 1 mm, 2 mm 3 mm and 4 mm gaps were estimated as 0°, 48.2°, 60°, 66.4° and 70.5° respectively. These estimated values indicate an agreement with the empirical results (i.e. the angles at which the data series cross the dotted line in Fig. 7.23(b)).

7.6.2 Experiments with solar-E-yarns woven into fabrics

For the second set of experiments, fabrics with different spacings between the solar-E-yarns were prepared (Fig. 7.25), with five solar-E-yarns included in each fabric sample. Before preparing the fabrics the I_{sc} values for each solar-E-yarn were measured in free standing form at different incident angles. To realize different gaps between adjacent solar-E-yarns a specific number of cotton weft yarns were inserted between solar-E-yarns (Table 7.5).

Table. 7.5 – Number cotton yarns inserted as weft between solar-E-yarns when preparing solar-E-yarn fabrics with specific gaps between adjacent E-yarns.

Approximate gap between two adjacent E-yarns (mm)	Number of cotton weft yarns inserted between E-yarns
0	1
1	3
2	7
3	11
4	15

When required, cotton yarns were used as weft yarns to add extra length to the fabric samples. The woven structure and weaving procedure were similar to the other woven fabrics prepared in this chapter.

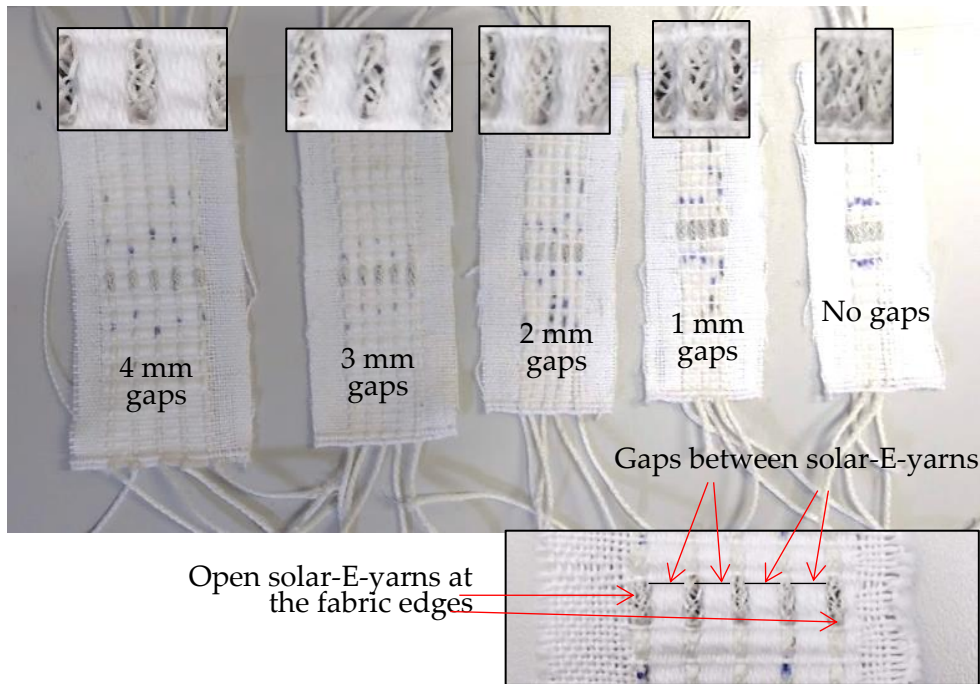


Figure 7.25 – Five fabric samples prepared with different gaps between the individual solar-E-yarns.

In this case the critical angle at which the shading from the adjacent yarn was initiated would be dependent on the fabric thickness (t) as well. The critical angle (θ) can be geometrically modelled based on D , l and t as shown in Fig. 7.26. Here it was assumed that the solar-E-yarns were embedded halfway within the fabric.

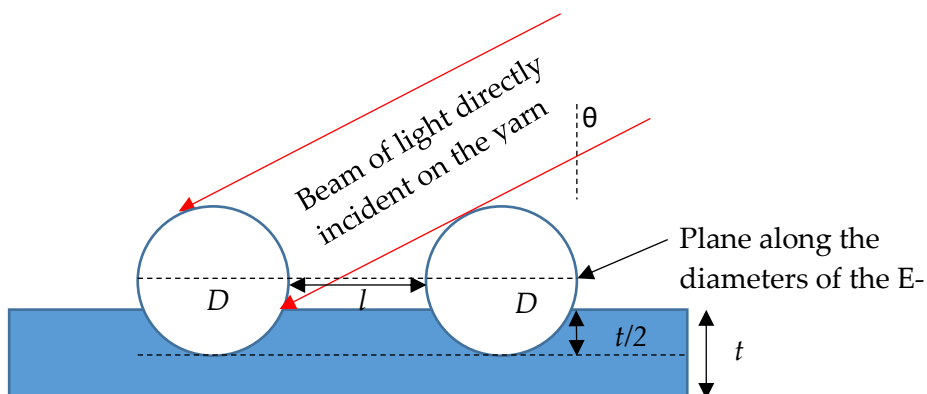


Figure 7.26 – Cross sectional geometric model for determining the critical angle at which the shading from adjacent solar-E-yarns would occur in fabric form.

Based on the geometrical model there existed a shading caused by the fabric thickness independent of the gaps between yarns.

For $\cos^{-1}\left(\frac{D}{D+l}\right) < \sin^{-1}\left(\frac{D-t}{D}\right)$ the critical angle would be given by

$$\theta = \cos^{-1}\left(\frac{D}{D+l}\right) \quad 7.2$$

Else

$$\theta = \sin^{-1}\left(\frac{D-t}{D}\right) \quad 7.3$$

Considering this shading due to the fabric with a thickness of ~ 0.4 mm, the critical angles for 2 mm diameter solar-E-yarns with zero, 1 mm and 2 mm gaps were approximated as 0° , 48.2° , 60° . In all other cases the critical angle was 64.2° .

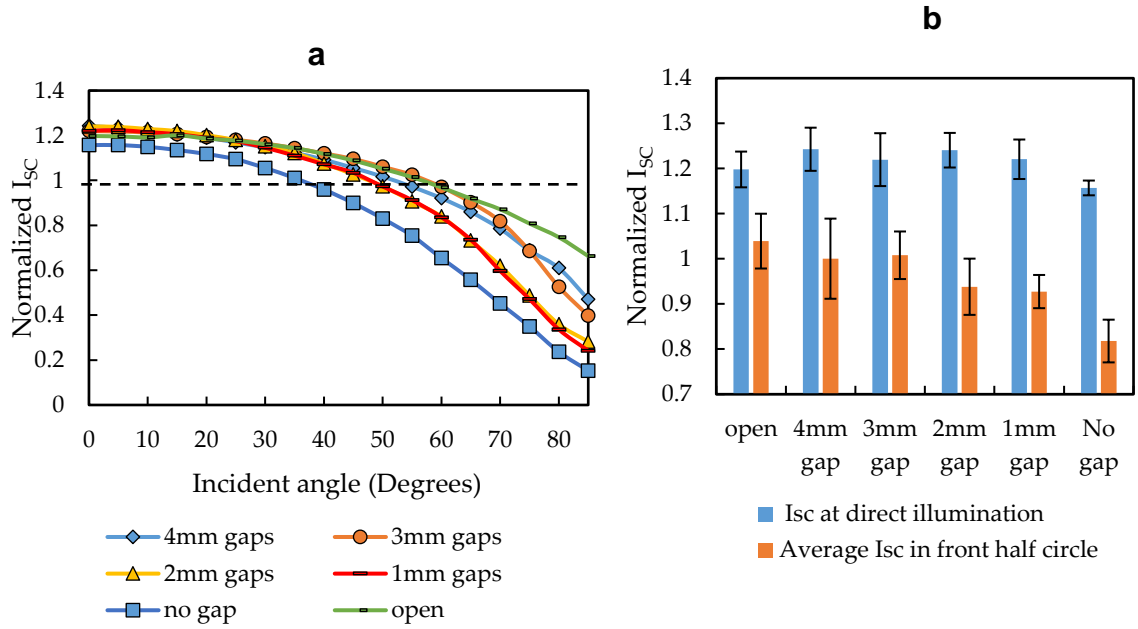


Figure 7.27 – (a) Change in I_{sc} with incident angle (b) I_{sc} at direct illumination and averaged in the front half circle for solar-E-yarns embedded in fabrics with different gaps between adjacent yarns (Results normalized to the values of free standing solar-E-yarn with no adjacent yarns).

The solar-E-yarns were individually characterized for I_{sc} at different incident angles (0° – 85°) by positioning the fabric samples onto the rotary sample holder and using the solar simulator under one sun illumination. The results were normalized to the free-standing individual yarn form values, measured for comparability, (Fig. 7.27). The estimated critical angles for different gaps showed a similar trend to the empirical results (i.e. the angles at which the data series crossed the dotted line in Fig. 7.27(b)).

In all of the cases explored, the solar-E-yarns within the woven structures showed higher I_{sc} values than the corresponding free-standing values for small incident angles, and lower I_{sc} values for higher incident angles. Overall, the average I_{sc} for the front half circle increased with the gap between the solar-E-yarns. It is believed that this effect was due to the significant albedo effect (Brennan *et al.*, 2014) (from the surrounding fabric at smaller incident angles, as shown in Fig. 7.28. When the incident angle increased the adjacent solar-E-yarn started to shade part of the incident light Fig. 7.28(b). By studying the cross-sectional geometry of the woven structure, it was clear that the angle at which the direct shading from yarns started to occur increased with the gaps size, which supported the experimental results. When the incident angle increased, the light flux reaching the solar-E-yarn reduced due to direct shading (from neighbouring solar-E-yarns) as well as a diminished albedo effect (as the gaps between the solar-E-yarns were also shaded), this is illustrated in Fig. 7.28(b).

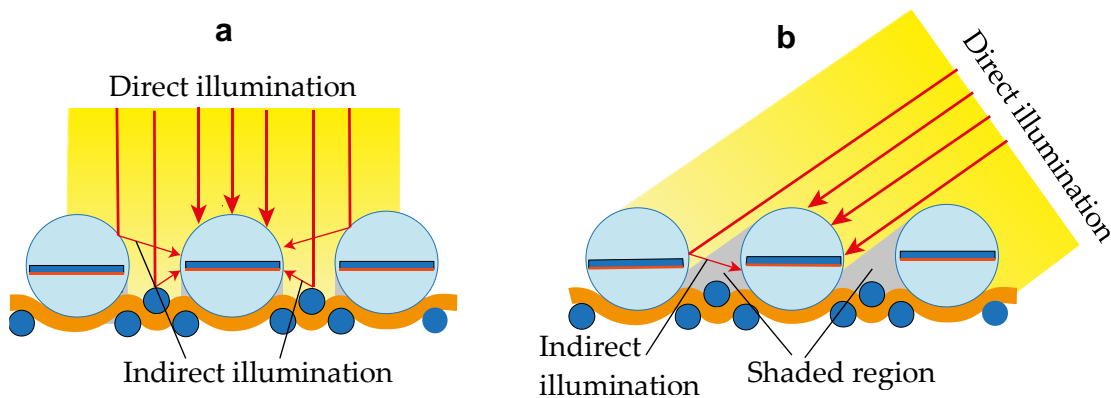


Figure 7.28 – Illustration of the effect of direct and indirect illumination received by woven solar-E-yarns at (a) direct incident light and (b) illumination where the incident light was at an oblique angled.

The impact of the albedo effect due to the surrounding fabric was investigated empirically by covering the solar-E-yarn gaps (rectangular spaces on the fabric between the active regions of adjacent solar-E-yarns) and outer surrounding (complete surrounding except for the gaps). Experimental results using a woven sample with 3.0 mm gaps between the solar-E-yarns showed (Fig. 7.29) that the albedo enhancement from the solar-E-yarn gaps were higher and more angle dependent in comparison to the albedo enhancement by the outer surrounding. The albedo enhancement due to the gaps disappeared completely at incident angle of 55 - 60°, as approximated by in the geometrical model.

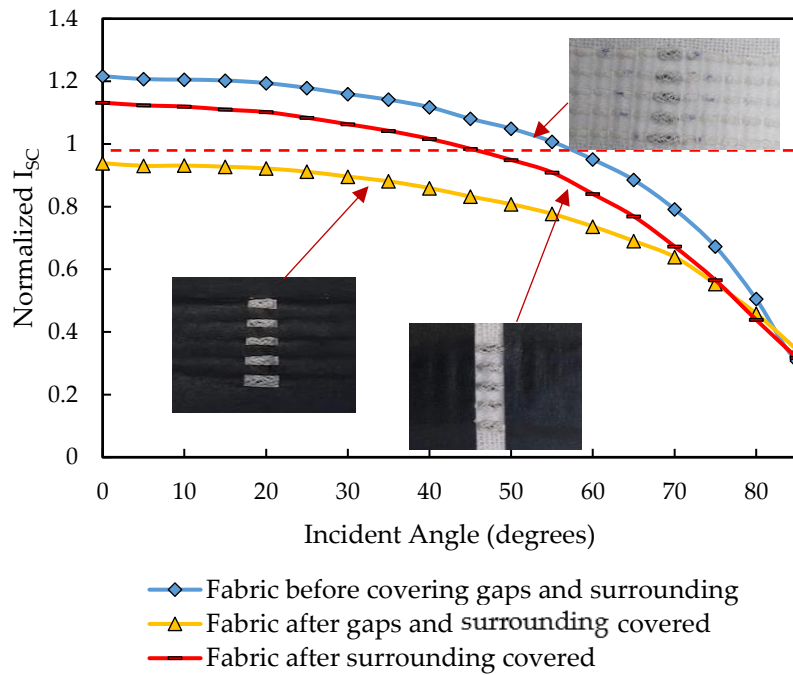


Figure 7.29 – Change in normalized I_{sc} (normalized to free-standing I_{sc} values) with incident angle for woven solar-E-yarns with 3.0 mm spacing, when the surrounding of the solar-E-yarns area was covered with black, non-reflective tape. The red dashed line shows the results for a free standing solar-E-yarn.

Another experiment was conducted to understand the relationship between the illuminated area and the albedo effect on solar-E-yarns when woven into fabrics. For this experiment fabrics identical to those prepared for the wash durability tests in Chapter 6 were employed. The I_{sc} of the individual solar-E-yarns woven into the fabric were measured under one sun intensity with matt black windows exposing different fabric areas surrounding the active area of the solar-E-yarn (Fig. 7.30).

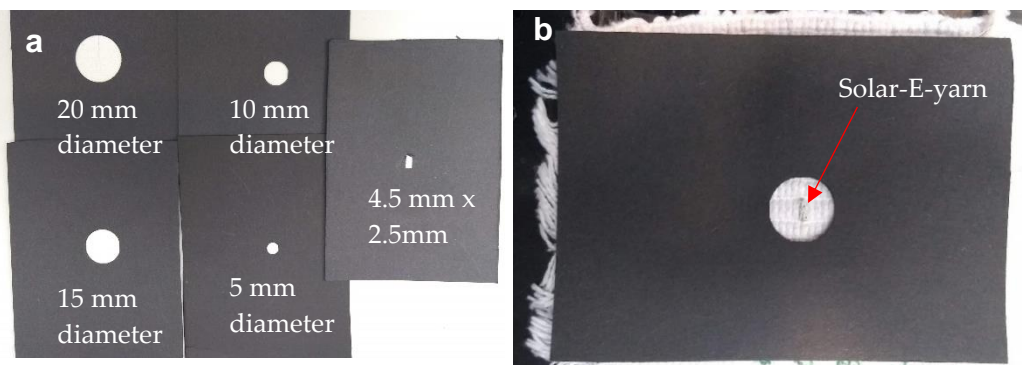


Figure 7.30 – (a) Matt black windows prepared for conducting the experiments different illumination areas. (b) An example of a window positioned on the fabric sample before conducting measurements under the solar simulator.

The 4.5 mm × 2.5 mm window fully covered the surrounding of the solar-E-yarn active area, and this measurement was considered the baseline for comparison. The I_{sc} values generated with 5 mm, 10 mm, 15 mm and 20 mm windows and without a window (in this case illumination area ~50 mm × 50 mm) were normalised to the baseline value and plotted against the exposed area as illustrated in Fig. 7.31.

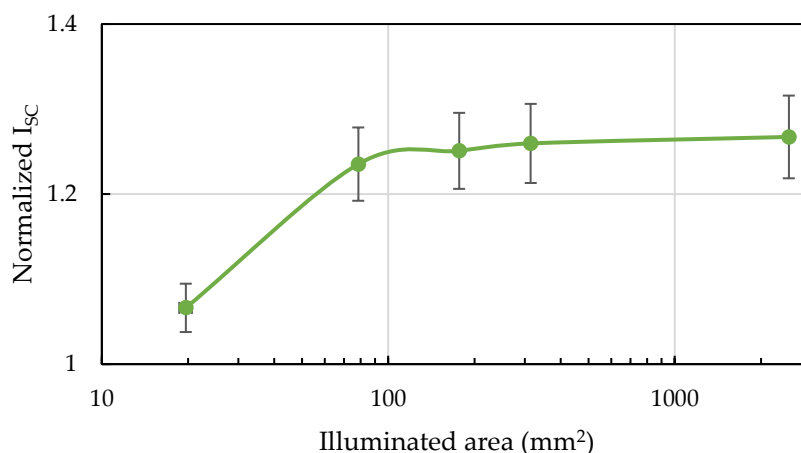


Figure 7.31 – The normalized I_{sc} for a solar-E-yarn embedded in woven fabric, exposed to one sun intensity with different sized windows. Results normalized to the I_{sc} value of 4.5 mm × 2.5 mm window measurement.

Based on these results it was clear that the albedo effect resulted in a significant increase (23.5 %) when up to a 10 mm diameter window was used, beyond which the incremental enhancement was less than 3 %. This result would be useful in designing solar-E-yarn embedded fabrics with different coloured fabrics, where light-coloured margins around the photoactive region is advantageous in enhancing the photovoltaic performance. The width of the margin may vary depending on the fabric structure and type of yarns of the fabric.

7.7 Conclusions

The first solar fabric comprised 200 solar cells, which generated a short-circuit current, open-circuit voltage and a power density of 14.14 mA, 5.14 V and 2.146 mW/cm² respectively. Using this fabric, the charging of energy storage devices suitable for wearable and mobile electronic device such as Li-ion batteries, Li-polymer batteries, and supercapacitors, was demonstrated successfully under simulated light of one sun intensity. In addition, the first solar fabric demonstrator was capable of powering a small

mobile phone, a fitness tracker and an E-textile with ten embedded LEDs E-yarns. The second solar fabric comprised two solar-E-yarn modules each prepared with ten solar-E-yarns (100 solar cells). The solar-E-yarns of one of these modules were resin-impregnated. The results confirmed that the resin impregnation enhanced the power generation by ~78 %, as observed in studies conducted with free-standing solar-E-yarns. A third set of solar fabrics were prepared using the solar-E-yarns with white (standard), red, and black knitted sheath, and a resin impregnated white sheath. Each fabric comprised of 50 solar cells (five solar-E-yarns). The comparison study conducted with these four fabric modules indicated that red and black knitted sheaths caused a reduction in the short-circuit current by 3.7% and 25 % respectively when compared to white yarns. A comparative field test conducted using this third set of solar fabric demonstrators, and a commercial flexible solar module, revealed that the solar fabric demonstrators were capable of generating a comparable level of power density to the commercial module under natural sunlight. It was observed that the albedo effect and the shading by adjacent yarns have a significant effect on the performance. The woven solar-E-yarns showed a higher power output than the free standing solar-E-yarns at smaller (0° - 55°) incident angles. Also, the power generated by the woven solar-E-yarns increased with the gap between individual solar-E-yarns; these observations were attributed to the increase in albedo effect caused by the surrounding fabric. A significant reduction in power was observed at higher incident angles due to shading by adjacent yarns. The relationship between the solar-E-yarn performance and illuminated area of the fabric was studied and the short-circuit current showed an increase with the area, which eventually reached a saturation point. This meant that it was desirable to have specific gaps between the solar-E-yarns in a solar fabric to maximise the power generated per yarn and minimize shading at higher incident angles.

Chapter 8

Conclusion

8.1 Conclusions

In light of the aim, objectives and research questions outlined in *Chapter 1*, this thesis draws the below conclusions on the behaviour and utility of solar-E-yarns and resultant fabrics intended for wearable applications.

The E-yarn technology provides a robust and versatile platform for creating solar energy harvesting textile yarns. The discrete micro-pod structure, and porous fibrous sheath meant that the solar-E-yarns are flexible, breathable and appeared and felt like a normal textile structure. When converted into planer form (fabrics), the solar-E-yarns impart the same desirable properties to the fabrics; these characteristics that are critical for retaining the comfort, aesthetics and durability suitable for regular clothing.

As with the conventional solar energy harvesters, the power generation capability remained the primary determinant of the utility of solar-E-yarns: The solar-E-yarn exhibited a comparable energy harvesting capability compared to the maiden miniature solar cells, which confirmed the technical viability of the solar-E-yarn technology for converting solar energy to electricity. The solar-E-yarn fabrication process, and individual components of the solar-E-yarns, imparted positive and negative effects to the energy conversion performance. The resin micro-pod (in general) improved the performance of the embedded miniature solar cell; the size, geometry and optical properties of the resin micro-pod was decisive to the level of enhancement. In practical applications these resin-micro-pod parameters may be dictated by design constraints such as the thickness of the fabric. The textile fibre sheath provided textile appearance and feel however, had a negative effect on the energy harvesting performance mainly due to light scattering caused by Fresnel reflection. The resin impregnation process substantially nullified the negative effects of the fibre sheath, resulting in an output that exceeded the performance of the embedded maiden miniature solar cell. This enhancement can be attributed to the lensing effect created by the resin micro-pod in combination with the resin impregnation.

The solar-E-yarns and resultant fabrics were sufficiently durable and robust to survive domestic washing, various external mechanical forces, and changes in environmental conditions that they may be subjected during their regular use in clothing applications.

The solar energy harvesting fabrics developed using the solar-E-yarns demonstrated their utility in charging small energy storage devices and powering small mobile electronic devices. The demonstrations revealed the true potential of the technology for powering larger and more powerful devices, using a fabric with larger photoactive area.

8.2 Contribution to knowledge

This research generated new knowledge and insights into the design rules, fabrication techniques, boundary conditions for use, and performance characteristics of photovoltaic devices embedded in textile structures that include:

- A detailed design for a solar energy harvesting textile yarns based on the existing E-yarn technology;
- The specific fabrication techniques needed to develop a solar-E-yarns with multiple parallel connected cells;
- A comprehensive empirical and theoretical study on the effects of a geometry, size and optical properties of a cylindrical-shaped clear resin micro-pod on the opto-electric performance of a photovoltaic device embedded within the resin micro-pod;
- A comparative study on the individual and combined effects and interference of the resin micro-pod, textile fibrous sheath, and resin impregnation on the opto-electric performance of a miniature solar-cell under direct and oblique angled illumination;
- Evaluation of the opto-electric performance of solar-E-yarns when exposed to domestic washing, abrasion, mechanical impact, uniaxial tensile loading and during changes to environmental conditions (temperature, humidity and liquid water);
- Performance characterisation of solar-E-yarn in woven fabrics designed to generate the maximum possible power density, and demonstration of the power generation capability in fabric form;

The implications of the albedo and shading effects on the performance of the solar-E-yarns by investigating the distribution of the solar-E-yarns, angle of incident light, and the illumination area.

8.3 Challenges encountered

Various operational and technical challenges were encountered during the project that largely relates to the availability of material and instruments .

Firstly, solar cells with suitable dimension were not readily available. Therefore, the preliminary studies were conducted using miniature photodiodes until a supplier of custom-cut miniature solar cells was found. With regards to the equipment for characterisation, during the first phase of the project a bespoke optical test rig had to be developed to conduct the characterisation of E-yarns embedded with photodiodes until a standard solar simulator was provided by a sponsor. Due to this the results generated at the early phase of the project were not directly comparable with global standards. In addition, for I-V curve tracing a fixed resistor array was devised which made the process cumbersome and time consuming.

With regards to the challenges related to the fabrication of solar E-yarns, the sourced miniature solar cells had their contact pads on front and back sides of the cell, which was not solderable with the soldering method employed in E-yarn technology. A modified method that allowed the solar cell to be soldered onto a pair of parallel running copper wires had to be developed. Since the diameter of the resin micro-pod was largely dictated by the available internal diameter of the cylinder of the knit-braiding machine used to create the fibre sheath. Due to this the scope for optimising the micro-pod size was limited. Finally, the existing semi-automated E-yarn fabrication process was not adaptable to fabricate solar-E-yarns and therefore the preparation of solar energy harvesting fabrics consisting of hundreds of solar cells, took substantial number of man-hours.

8.4 Future work

This work explored the fundamentals and the viability of creating solar energy harvesting yarns and fabrics using the E-yarns technology.

Further work may be required to enhance the readiness of the technology to ensure commercial viability and fitness for specific applications that include:

- Development of a pilot manufacturing line that can achieve a scalable, repeatable, and cost-effective output.
- Development of a cost effective, reliable, supply of miniature solar cells which will be critical in achieving commercial viability.
- Improvement of the mechanical robustness of the copper wires at the point of entry into the resin micro-pod need to be addressed in order to augment the durability of

the solar-E-yarns under repeated machine washing. More specific mechanical test procedures may need to be employed to simulate such strenuous mechanical processes.

Several avenues of in-depth study is also desirable to identify the boundaries of the capability while enhancing the utility of the technology for various applications.

Further explorations into the fundamentals on the effect of the solar-E-yarns density and distribution on a woven fabric would be beneficial to enhance the utility of the technology for various applications. It may be desirable to optimise the flexibility and drapability (three-dimensional conformability), which may be critical for applications requiring improved comfort and aesthetics. Computational simulation and modelling techniques are suggested for such optimisations to minimising the need for physical prototypes. Using the developed generalized theoretical model, cylindrical resin micro-pods with a non-circular base (e.g. elliptic or parabolic) may be evaluated. The mathematical model may be further extended to non-uniform cross-sectional shapes defined in three-dimensional space (here the surface of the micro-pod would be defined by a surface function, instead of a linear function) to facilitate the creation of optimized geometries for resin micro-pods suitable for different miniature solar cell sizes or specific applications.

Detailed evaluations using textile fibres with different thickness, cross sectional shapes (e.g. trilobal, rectangular, oval and hollow), materials (e.g. photoluminescent), and levels of texturization may be useful in developing a comprehensive knowledgebase on the effect of the fibrous sheath on the performance of the solar-E-yarn. Studies in to how the resin micro-pod can be engineered to survive mechanical impact may be necessary for designing solar-E-yarns for products that are prone to collisions with rigid objects.

Finally, application of the core technology across different photovoltaic cell types would also be desirable, that would require the sourcing/development of different types of miniature solar cells and the creation of robust electrical and mechanical connections between the cell and wire.

References

- Adafruit (2017) *Celebrating 10 Years of the Lilypad Arduino #WearableWednesday #wearabletech #Arduino #tech* « Adafruit Industries – Makers, hackers, artists, designers and engineers! Available at: <https://blog.adafruit.com/2017/10/11/celebrating-10-years-of-the-lilypad-arduino/> (Accessed: 2 March 2019).
- Adafruit, (n.d) '20mm Coin Cell Breakout Board' Available at <https://www.adafruit.com/product/1870> (Accessed: 20 March 2019)
- Agcayazi, T. *et al.* (2018) 'Flexible Interconnects for Electronic Textiles', *Advanced Materials Technologies*, 3(10), pp. 1–32. doi: 10.1002/admt.201700277.
- Åkerfeldt, M. *et al.* (2014) 'Textile piezoelectric sensors – melt spun bi-component poly(vinylidene fluoride) fibres with conductive cores and poly(3,4-ethylene dioxothiophene)-poly(styrene sulfonate) coating as the outer electrode', *Fashion and Textiles*, 1(1), pp. 1–17. doi: 10.1186/s40691-014-0013-6.
- Ali, A. *et al.* (2019) 'Metal Coating on Ultrafine Polyester Non-woven Fabrics and Their Ageing Properties', *Fibers and Polymers*, 20(7), pp. 1347–1359. doi: 10.1007/s12221-019-1078-z.
- Aliaga, C. *et al.* (2017) 'An Appearance Model for Textile Fibers', *Computer Graphics Forum*, 36(4), pp. 35–45. doi: 10.1111/cgf.13222.
- American Association Of Textile Chemists And Colourists (2010) *AATCC M5 - Standardization of Hand Laundering for Fabrics and Apparel*. Available at: <https://www.aatcc.org/wp-content/uploads/2015/01/M05-2007.pdf> (Accessed: 15 January 2019).
- Anand, S. *et al.* (2016) 'Energy harvesting "3-D knitted spacer" based piezoelectric textiles', *IOP Conference Series: Materials Science and Engineering*, 141(1), p. 12001. doi: 10.1088/1757-899X/141/1/012001.
- Anguiano, C. *et al.* (2005) 'Influence of intermetallic compounds growth on properties of lead-free solder joints', *Modern Optical Engineering*, 8(C), pp. 175–176. doi: 10.1364/OE.21.023851.
- Arumugam, S. *et al.* (2016) 'Fully spray-coated organic solar cells on woven polyester cotton fabrics for wearable energy harvesting applications', *Journal of Materials Chemistry A*, 4(15), pp. 5561–5568. doi: 10.1039/c5ta03389f.
- Arumugam, S. *et al.* (2018) 'Solution Processed Organic Solar Cells on Textiles', *IEEE Journal of Photovoltaics*, 8(6). doi: 10.5258/SOTON/D0153.
- Balenzategui, J. L. and Chenlo, F. (2005) 'Measurement and analysis of angular response of bare and encapsulated silicon solar cells', *Solar Energy Materials and Solar Cells*, 86(1), pp. 53–83. doi: 10.1016/j.solmat.2004.06.007.
- Barmag, O. and Neumag, O. (2015) *The car of the future will be wearing more textiles*.
- Bedeloglu, a. *et al.* (2010) 'A Photovoltaic Fiber Design for Smart Textiles', *Textile Research Journal*, 80(11), pp. 1065–1074. doi: 10.1177/0040517509352520.

- Bedeloglu, A. *et al.* (2009) 'A flexible textile structure based on polymeric photovoltaics using transparent cathode', *Synthetic Metals*, 159(19–20), pp. 2043–2048. doi: 10.1016/j.synthmet.2009.07.019.
- Bedeloglu, A. *et al.* (2010) 'A photovoltaic fiber design for smart textiles', *Textile Research Journal*, 80(11), pp. 1065–1074. doi: 10.1177/0040517509352520.
- Bedeloglu, Ayse *et al.* (2011) 'Photovoltaic textile structure using polyaniline/carbon nanotube composite materials', *Journal of the Textile Institute*, 102(10), pp. 857–862. doi: 10.1080/00405000.2010.525816.
- Bedeloglu, A. C. *et al.* (2010) 'Development of energy generating photovoltaic textile structures for smart applications', *Fibers and Polymers*, 11(3), pp. 378–383. doi: 10.1007/s12221-010-0378-0.
- Beeby, S. P., Cao, Z. and Almussallam, A. (2013) 'Kinetic, thermoelectric and solar energy harvesting technologies for smart textiles', in Kirstein, T. (ed.) *Multidisciplinary Know-How for Smart-Textiles Developers*. 1st edn. Oxford: Woodhead Publishing Limited., pp. 306–328. doi: 10.1533/9780857093530.2.306.
- Beecham Research (2019) *Wearable Technology Application Chart - Beecham Research*. Available at: <http://www.beechamresearch.com/download.aspx?id=36> (Accessed: 28 February 2019).
- Bhatnagar, V. and Owende, P. (2015) 'Energy harvesting for assistive and mobile applications', *Energy Science & Engineering*, 3(3), pp. 153–173. doi: 10.1002/ese3.63.
- Bosch Sensortec (2019) *BMA400 acceleration sensor*. Available at: https://www.bosch-sensortec.com/bst/products/all_products/bma400_1 (Accessed: 7 June 2019).
- Brennan, M. P. *et al.* (2014) 'Effects of spectral albedo on solar photovoltaic devices', *Solar Energy Materials and Solar Cells*, 124, pp. 111–116. doi: 10.1016/J.SOLMAT.2014.01.046.
- Brun, J. *et al.* (2009) 'Packaging and wired interconnections for insertion of miniaturized chips in smart fabrics', in *2009 European Microelectronics and Packaging Conference*, pp. 2–6.
- Brun, J. *et al.* (2011) 'Method and device for fabricating an assembly of at least two microelectronic chips'. US8012795. Available at: <https://www.google.com/patents/US8012795>.
- Brun, J., Lancon, L. and Vicard, D. (2014) 'Inclusion of chip elements in a sheathed wire'. US8814054. Available at: <https://www.google.com/patents/US8814054>.
- Brun, J., Vicard, D. and Verrun, S. (2014) 'Assembly of a wire element with a microelectronic chip with a groove comprising at least one bump securing the wire element'. US8723312. Available at: <https://www.google.com/patents/US8723312>.
- BSI Standards Publication (2012) *BS EN ISO 6330: 2012 Textiles — Domestic washing and drying procedures for textile testing*. Available at: <https://shop.bsigroup.com/> (Accessed: 15 December 2017).
- BSI Standards Publication (2016) *BS EN ISO 12947-2:2016 — Determination of the abrasion resistance of fabrics by the Martindale method Part 2: Determination of specimen breakdown (ISO 12947-2:2016)*. Available at: <https://shop.bsigroup.com/> (Accessed: 15 January 2019).

- Cai, F., Chen, T. and Peng, H. (2012) 'All carbon nanotube fiber electrode-based dye-sensitized photovoltaic wire', *Journal of Materials Chemistry*, 22(30), pp. 14856–14860. doi: 10.1039/c2jm32256k.
- Cao, Z. *et al.* (2016) 'Screen Printable Flexible BiTe-SbTe-Based Composite Thermoelectric Materials on Textiles for Wearable Applications', *IEEE Transactions on Electron Devices*, PP(99), pp. 4024–4030. doi: 10.1109/TED.2016.2603071.
- Carroll, A. and Heiser, G. (2010) 'An analysis of power consumption in a smartphone', *Proceedings of the 2010 USENIX conference on USENIX annual technical conference*. USENIX Association, pp. 21–21. Available at: <https://dl.acm.org/citation.cfm?id=1855861> (Accessed: 7 June 2019).
- Carron., A. I. (1911) 'Electrically heated gloves'. Available at: <https://patents.google.com/patent/US1011574A/en> (Accessed: 1 March 2019).
- Cassill, N., Carroll, K. and Suh, M. (2010) 'Critical Review on Smart Clothing Product Development', *Journal of Textile and Apparel Technology and Management (JTATM)*, 6(4), pp. 1–18.
- Cavallo, C. *et al.* (2017) 'Nanostructured Semiconductor Materials for Dye-Sensitized Solar Cells', *Journal of Nanomaterials*, 2017, pp. 1–31. doi: 10.1155/2017/5323164.
- Cemine, V. J., Sarmiento, R. and Blanca, C. M. (2008) 'High-resolution mapping of the energy conversion efficiency of solar cells and silicon photodiodes in photovoltaic mode', *Optics Communications*, 281(22), pp. 5580–5587. doi: 10.1016/j.optcom.2008.07.086.
- Chae, Y. *et al.* (2013) 'All-solid, flexible solar textiles based on dye-sensitized solar cells with ZnO nanorod arrays on stainless steel wires', *Materials Science and Engineering B: Solid-State Materials for Advanced Technology*, 178(17), pp. 1117–1123. doi: 10.1016/j.mseb.2013.06.018.
- Chai, Z. *et al.* (2016) 'Tailorable and Wearable Textile Devices for Solar Energy Harvesting and Simultaneous Storage', *ACS Nano*, p. acsnano.6b05293. doi: 10.1021/acsnano.6b05293.
- Chander, S. *et al.* (2015) 'Impact of temperature on performance of series and parallel connected mono-crystalline silicon solar cells', *Energy Reports*, 1, pp. 175–180. doi: 10.1016/J.EGYR.2015.09.001.
- Chang, J. *et al.* (2012) 'Piezoelectric nanofibers for energy scavenging applications', *Nano Energy*, 1(3), pp. 356–371. doi: 10.1016/j.nanoen.2012.02.003.
- Chatterjee, K., Tabor, J. and Ghosh, T. K. (2019) 'Electrically conductive coatings for fiber-based E-Textiles', *Fibers*, 7(6), pp. 1–45. doi: 10.3390/fib7060051.
- Che, X. *et al.* (2018) 'High fabrication yield organic tandem photovoltaics combining vacuum- and solution-processed subcells with 15% efficiency', *Nature Energy*, 3(5), pp. 422–427. doi: 10.1038/s41560-018-0134-z.
- Chegaar, M. *et al.* (2013) 'Effect of illumination intensity on solar cells parameters', *Energy Procedia*. doi: 10.1016/j.egypro.2013.07.084.
- Chemistry Libretexts (2019) 'Metals and Semiconductors.' Available at: <https://chem.libretexts.org/@go/page/23910> [Accessed March 20, 2019].

- Chen, J. *et al.* (2016) 'Micro-cable structured textile for simultaneously harvesting solar and mechanical energy', *Nature Energy*, 1(September), p. 16138. doi: 10.1038/nenergy.2016.138.
- Chen, M. T., Wu, C. A. and Ou, Z. H. (2015) 'Flexible photovoltaic apparatus'. US20150059852. Available at: <https://google.com/patents/US20150059852>.
- Chen, T., Qiu, L., Kia, H. G., *et al.* (2012) 'Designing aligned inorganic nanotubes at the electrode interface: Towards highly efficient photovoltaic wires', *Advanced Materials*, 24(34), pp. 4623–4628. doi: 10.1002/adma.201201893.
- Chen, T., Qiu, L., Cai, Z., *et al.* (2012) 'Intertwined aligned carbon nanotube fiber based dye-sensitized solar cells', *Nano Letters*, 12(5), pp. 2568–2572. doi: 10.1021/nl300799d.
- Chen, X. *et al.* (2014) 'A novel "energy fiber" by coaxially integrating dye-sensitized solar cell and electrochemical capacitor', *Journal of Materials Chemistry A*, 2(6), pp. 1897–1902. doi: 10.1039/c3ta13712k.
- Cheng, X. *et al.* (2015) 'Wearable electrode-free triboelectric generator for harvesting biomechanical energy', *Nano Energy*, 12, pp. 19–25. doi: 10.1016/j.nanoen.2014.12.009.
- Cho, H. *et al.* (2016) 'An Exploratory Study on the Feasibility of a Foot Gear Type Energy Harvester Using a Textile Coil Inductor', *Journal of Electrical Engineering Technology*, 11(5), pp. 1210–1215.
- Chuangchote, S., Sagawa, T. and Yoshikawa, S. (2011) 'Design of Metal Wires-based Organic Photovoltaic Cells', *Energy Procedia*, 9, pp. 553–558. doi: 10.1016/J.EGYPRO.2011.09.064.
- Clemens, J. M. L. (2001) *The thermal conductivity of rubbers/elastomers* | *Electronics Cooling*. Available at: <https://www.electronics-cooling.com/2001/11/the-thermal-conductivity-of-rubbers-elastomers/> (Accessed: 5 August 2019).
- Conibeer, G. and Willoughby, A. (2014) *Solar Cell Materials: Developing Technologies*. Edited by G. Conibeer and A. Willoughby. John Wiley & Sons, Inc. doi: 10.1002/9781118695784.
- Cotfas, D. T., Cotfas, A. and Machidon, O. M. (2018) 'Study of Temperature Coefficients for Parameters of Photovoltaic Cells'. doi: 10.1155/2018/5945602.
- Coyle, S. and Diamond, D. (2016) 'Medical applications of smart textiles', *Advances in Smart Medical Textiles*, pp. 215–237. doi: 10.1016/B978-1-78242-379-9.00010-4.
- Crabtree, G., Kócs, E. and Trahey, L. (2015) 'The energy-storage frontier: Lithium-ion batteries and beyond', *MRS Bulletin*, 40(12), pp. 1067–1078. doi: 10.1557/mrs.2015.259.
- Cruz-Campa, J. L. *et al.* (2011) 'Microsystems enabled photovoltaics: 14.9% efficient 14 micrometer thick crystalline silicon solar cell', *Solar Energy Materials and Solar Cells*, 95(2), pp. 551–558. doi: 10.1016/j.solmat.2010.09.015.
- Cypress Semiconductors (2019) CYBT-213043-02: EZ-BT™ MODULE, 2019. Available at: <https://www.cypress.com/documentation/datasheets/cybt-213043-02-ez-bt-module> (Accessed: 7 June 2019).
- Daniel, J. H. (2011) 'Photovoltaic modules on a textile substrate'. US20110290304. Available at: <https://google.com/patents/US20110290304>.
- Das, S. C. *et al.* (2013) 'Smart Textiles- New Possibilities in Textile Engineering',

2013(November), pp. 1–3.

David A. Evans (2007) *The Littlest Big Capacitor - an Evans Hybrid*. Available at: <http://www.evanscap.com/isdlc5-2.htm> (Accessed: 29 May 2019).

Davis, N. (2017) *Powering wearables: battery types, current challenges, and energy harvesting - Power Electronics*. Available at: <https://www.powerelectronicsnews.com/technology/powering-wearables-battery-types-current-challenges-and-energy-harvesting> (Accessed: 7 March 2019).

Deen, M. J. and Basu, P. K. (2012) 'Silicon Photodetectors', in Arthur Willoughby, Capper, P., and Kasap, S. (eds) *Silicon Photonics*. John Wiley & Sons, Ltd, pp. 197–247. doi: 10.1002/9781119945161.ch8.

Dias, T. and Fernando, A. (2006) 'Operative devices installed in yarns'. Available at: <https://patents.google.com/patent/EP1882059B1/en?q=operative&q=devices&q=installed&q=yarns&oq=operative+devices+installed+in+yarns> (Accessed: 10 October 2019).

Dias, T. and Fernando, A. (2009) 'Operative devices installed in yarns'. US20090139198. Available at: <https://www.google.com/patents/US20090139198>.

Dias, T. K. and Rathnayake, A. (2016) 'Electronically functional yarns'. WO2016038342A1. Available at: <https://www.google.com/patents/WO2016038342A1?cl=en>.

Dias, T. and Ratnayake, A. (2015) 'Integration of micro-electronics with yarns for smart textiles', in Dias, Tilak (ed.) *Electronic Textiles*. Woodhead Publishing Limited, pp. 109–116. doi: 10.1016/B978-0-08-100201-8.00006-0.

Dias, T. and Hughes-Riley, T. , (2017) 'Electronically functional yarns transform wearable device industry.' *R&D Magazine*, 59 (2), pp. 19-21.

van Dongen, P. (2018) *Wearable Solar Dress — Pauline van Dongen*. Available at: <http://www.paulinevandongen.nl/project/wearable-solar/> (Accessed: 26 February 2019).

Du, P. *et al.* (2013) 'A photovoltaic smart textile and a photocatalytic functional textile based on co-electrospun TiO₂/MgO core-sheath nanorods: Novel textiles of integrating energy and environmental science with textile research', *Textile Research Journal*, 83(16), pp. 1690–1702. doi: 10.1177/0040517513490062.

Du, Y. *et al.* (2015) 'Thermoelectric fabrics: toward power generating clothing.', *Scientific reports*, 5, p. 6411. doi: 10.1038/srep06411.

Düking, P. *et al.* (2016) 'Comparison of Non-Invasive Individual Monitoring of the Training and Health of Athletes with Commercially Available Wearable Technologies', *Frontiers in Physiology*, 7, p. 71. doi: 10.3389/fphys.2016.00071.

Electronically Functional Yarns Transform Wearable Device Industry - Research & Development World (no date). Available at: <https://www.rdworldonline.com/electronically-functional-yarns-transform-wearable-device-industry/> (Accessed: 20 March 2021).

eMarketer (2019) *Wearables 2019 - eMarketer Trends, Forecasts & Statistics*. Available at: <https://www.emarketer.com/content/wearables-2019> (Accessed: 28 February 2019).

Escoffery, C. A. (1966) 'Flexible fabric support structure for photovoltaic cells'.

- US3255047. Available at: <https://www.google.com/patents/US3255047>.
- Farahi, F. (2014) 'Overview of Optical Sensing', in Santos, J. L. and Farahi, F. (eds) *Handbook of Optical Sensors*. CRC Press, pp. 3–12. doi: 10.1201/b17641-3.
- FDK Corporation (2007) *Development of a new large-capacity capacitor 'EneCapTen' - Continuous use in high temperature environment* - FDK. Available at: <http://www.fdk.co.jp/whatsnew-j/release070919-j.html> (Accessed: 29 May 2019).
- Fell, A. *et al.* (2018) 'Modeling Edge Recombination in Silicon Solar Cells', *IEEE Journal of Photovoltaics*, 8(2), pp. 428–434. doi: 10.1109/JPHOTOV.2017.2787020.
- Feng, J. *et al.* (2018) 'Record Efficiency Stable Flexible Perovskite Solar Cell Using Effective Additive Assistant Strategy', *Advanced Materials*, 30(35), p. 1801418. doi: 10.1002/adma.201801418.
- Fernández-Caramés, T. *et al.* (2018) 'Towards The Internet-of-Smart-Clothing: A Review on IoT Wearables and Garments for Creating Intelligent Connected E-Textiles', *Electronics*, 7(12), p. 405. doi: 10.3390/electronics7120405.
- Feurer, T. *et al.* (2016) 'Progress in thin film CIGS photovoltaics - Research and development, manufacturing, and applications', *Progress in Photovoltaics: Research and Applications*. doi: 10.1002/pip.2811.
- Forbes (2014) *Tommy Hilfiger's Solar-Powered Jacket - Wearable Tech in Review*. Available at: <https://www.forbes.com/sites/mitsubishiheavyindustries/2019/02/11/new-collar-manufacturing-a-new-fit-for-vietnam-as-a-next-generation-hub/#40fa21fc24f7> (Accessed: 26 February 2019).
- Forster, U. and Zimmermann, J. H. (2011) 'Method for Attaching Flat Electronic Components Onto a Flexible Surface Structure'. US20110240091. Available at: <https://google.com/patents/US20110240091>.
- Fraunhofer ISE (2019) *Photovoltaic Trend: Tandem Solar Cells Record Efficiency for Silicon-based Multi-junction Solar Cell* - Fraunhofer ISE. Available at: <https://www.ise.fraunhofer.de/en/press-media/press-releases/2019/photovoltaic-trend-tandem-solar-cells-record-efficiency-for-silicon-based-multi-junction-solar-cell.html> (Accessed: 5 March 2019).
- Fu, X. *et al.* (2018) 'A fiber-shaped solar cell showing a record power conversion efficiency of 10%', *Journal of Materials Chemistry A*, 6(1), pp. 45–51. doi: 10.1039/c7ta08637g.
- Fu, Y. *et al.* (2013) 'Integrated power fiber for energy conversion and storage', *Energy & Environmental Science*, 6(3), p. 805. doi: 10.1039/c3ee23970e.
- Gaudiana, R. *et al.* (2006) 'Photovoltaic fibers', in *Proceedings of SPIE - The International Society for Optical Engineering*. doi: 10.1117/12.683130.
- Gerthoffer, A. *et al.* (2017) 'CIGS solar cells on ultra-thin glass substrates: Determination of mechanical properties by nanoindentation and application to bending-induced strain calculation', *Solar Energy Materials and Solar Cells*, 166, pp. 254–261. doi: 10.1016/j.solmat.2016.11.022.
- Gibson, P. W. (1993) 'Factors Influencing Steady-State Heat and Water Vapor Transfer Measurements for Clothing Materials', *Textile Research Journal*, 63(12), pp. 749–764. doi: 10.1177/004051759306301208.

- Goldsmid, H. J. (2017) 'Thermoelectric refrigerators and generators', in *The Physics of Thermoelectric Energy Conversion*. IOP Publishing. doi: 10.1088/978-1-6817-4641-8ch9.
- Gong, R. H. (2015) 'Yarn to Fabric: Specialist Fabric Structures', in *Textiles and Fashion*. Woodhead Publishing, pp. 337–354. doi: 10.1016/B978-1-84569-931-4.00014-3.
- Gopalsamy, C. *et al.* (1999) 'The Wearable Motherboard?: The first generation of adaptive and responsive textile structures (ARTS) for medical applications', *Virtual Reality*, 4(3), pp. 152–168. doi: 10.1007/BF01418152.
- Grancarić, A. M. *et al.* (2017) 'Conductive polymers for smart textile applications', *Journal of Industrial Textiles*, 48(3), pp. 612–642. doi: 10.1177/1528083717699368
- Green, K., Lamberg, L. and Lumme, K. (2000) 'Stochastic modeling of paper structure and Monte Carlo simulation of light scattering', *Applied Optics*, 39(25), p. 4669. doi: 10.1364/AO.39.004669.
- Green, M. A. *et al.* (2019) 'Solar cell efficiency tables (Version 53)', *Progress in Photovoltaics: Research and Applications*, 27(1), pp. 3–12. doi: 10.1002/pip.3102.
- Gu, T. *et al.* (2015) 'Micro-concentrator Module for Microsystems-enabled Photovoltaics: Optical Performance Characterization, Modeling and Analysis, in the proceeding of IEEE PVSC 2015'.
- Guo, S., Walsh, T. M. and Peters, M. (2013) 'Vertically mounted bifacial photovoltaic modules: A global analysis', *Energy*, 61, pp. 447–454. doi: 10.1016/J.ENERGY.2013.08.040.
- Gwandu, B. A. L. and Creasey, D. J. (1995) 'Humidity: A factor in the appropriate positioning of a photovoltaic power station', *Renewable Energy*, 6(3), pp. 313–316. doi: 10.1016/0960-1481(95)00073-S.
- H. Lee Wainwright (2019) *The Grandfather of E-Textiles* | H. Lee Wainwright. Available at: <http://www.hleewainwright.com/> (Accessed: 2 March 2019).
- Ha, M. *et al.* (2015) 'Triboelectric Generators and Sensors for Self-Powered Wearable Electronics', *ACS Nano*, 9(4), pp. 3421–3427. doi: 10.1021/acsnano.5b01478.
- Hafez, A. Z., Yousef, A. M. and Harag, N. M. (2018) 'Solar tracking systems: Technologies and trackers drive types – A review', *Renewable and Sustainable Energy Reviews*, 91, pp. 754–782. doi: 10.1016/J.RSER.2018.03.094.
- Halme, J. and Mäkinen, P. (2019) 'Theoretical efficiency limits of ideal coloured opaque photovoltaics', *Energy & Environmental Science*, 12(4), pp. 1274–1285. doi: 10.1039/C8EE03161D.
- Hanak, J. J. *et al.* (1987) 'Retractable power supply'. US4636579. Available at: <https://google.com/patents/US4636579>.
- Hardy, D. *et al.* (2013) *Improving the Aesthetics of Photovoltaics Through Use of Coloured Encapsulants*. Available at: http://irep.ntu.ac.uk/id/eprint/20641/1/220569_PubSub2588_Hardy.pdf (Accessed: 13 August 2019).
- Hardy, D. *et al.* (2018) 'Engineering a Costume for Performance Using Illuminated LED-Yarns', *Fibers*, 6(2), p. 35. doi: 10.3390/fib6020035.
- He, R. *et al.* (2013) 'Silicon p-i-n junction fibers', *Advanced Materials*, 25(10), pp. 1461–

1467. doi: 10.1002/adma.201203879.

He, S. *et al.* (2015) 'Radically grown obelisk-like ZnO arrays for perovskite solar cell fibers and fabrics through a mild solution process', *Journal of Materials Chemistry A*, 3(18), pp. 9406–9410. doi: 10.1039/c5ta01532d.

Heidenreich, D. C. (2007) 'Photovoltaic awning structures'. US20070277867. Available at: <https://google.com/patents/US20070277867>.

Hill, I. G. *et al.* (2009) 'Woven electronic textile, yarn and article'. US7592276. Available at: <https://www.google.com/patents/US7592276>.

Hou, W. W. *et al.* (2009) 'Low-temperature processing of a solution-deposited CuInSSe thin-film solar cell', *Thin Solid Films*, 517(24), pp. 6853–6856. doi: 10.1016/J.TSF.2009.06.032.

Hu, H. *et al.* (2016) 'Fiber-shaped perovskite solar cells with 5.3% efficiency', *Journal of Materials Chemistry A*, 4(10), pp. 3901–3906. doi: 10.1039/C5TA09280A.

Hu, L. *et al.* (2010) 'Stretchable, porous, and conductive energy textiles', *Nano Letters*, 10(2), pp. 708–714. doi: 10.1021/nl903949m.

Hughes-Riley, T. *et al.* (2017) 'A study of thermistor performance within a textile structure', *Sensors (Switzerland)*, 17(8). doi: 10.3390/s17081804.

Hughes-Riley, T. and Dias, T. (2018) 'Developing an Acoustic Sensing Yarn for Health Surveillance in a Military Setting', *Sensors*, 18(5), p. 1590. doi: 10.3390/s18051590.

Hughes-Riley, T., Dias, T. and Cork, C. (2018) 'A Historical Review of the Development of Electronic Textiles', *Fibers*, 6(2), p. 34. doi: 10.3390/fib6020034.

Hyoung Park, J. *et al.* (2012) 'Organic photovoltaic cells with nano-fabric heterojunction structure', *Applied Physics Letters*, 100(7). doi: 10.1063/1.3679097.

IDC (2018) *IDC Forecasts Slower Growth for Wearables in 2018 Before Ramping Up Again Through 2022*. Available at: <https://www.idc.com/getdoc.jsp?containerId=prUS44276818> (Accessed: 28 February 2019).

International Electrotechnical Committee (2018) *Strategic business plan -Wearable electronic devices and technologies-SMB/6488/SBP*. Available at: <https://www.iec.ch/public/miscfiles/sbp/124.pdf>.

International Energy Agency IEA (2011) *Solar Energy Perspectives, Solar Energy Perspectives*. doi: 10.1787/9789264124585-en.

Járó, M. (1990) 'Gold embroidery and fabrics in europe: XI – XIV centuries', *Gold Bulletin*, 23(2), pp. 40–57. doi: 10.1007/BF03214711.

Jaynes, S. (2007) 'Solar powered survival suit'. US20070151593. Available at: <https://google.com/patents/US20070151593>.

Jeong, E. G. *et al.* (2019) 'Textile-based washable polymer solar cells for optoelectronic modules: toward self-powered smart clothing', *Energy & Environmental Science*. doi: 10.1039/C8EE03271H.

Jinno, H. *et al.* (2017) 'Stretchable and waterproof elastomer-coated organic photovoltaics for washable electronic textile applications', *Nature Energy*. doi: 10.1038/s41560-017-0001-3.

Jost, K. *et al.* (2011) 'Carbon coated textiles for flexible energy storage', *Energy &*

- Environmental Science*, 4(12), p. 5060. doi: 10.1039/c1ee02421c.
- Jost, K., Dion, G. and Gogotsi, Y. (2014) 'Textile energy storage in perspective', *Journal of Materials Chemistry A*, 2(28), p. 10776. doi: 10.1039/c4ta00203b.
- Jost, K., Dion, G. and Gogotsi, Y. (2015) 'Garment Devices: Integrating Energy Storage into Textiles', in Barfield, W. (ed.) *Fundamentals of Wearable Computers and Augmented Reality*. 2nd edn. CRC Press, pp. 639–660. doi: 10.1201/b18703-29.
- Juhász Junger, I. *et al.* (2018) 'Dye-Sensitized Solar Cells with Electrospun Nanofiber Mat-Based Counter Electrodes', *Materials*, 11(9), p. 1604. doi: 10.3390/ma11091604.
- Jung, J. W. *et al.* (2018) 'Fully solution-processed indium tin oxide-free textile-based flexible solar cells made of an organic–inorganic perovskite absorber: Toward a wearable power source', *Journal of Power Sources*, 402, pp. 327–332. doi: 10.1016/J.JPOWSOUR.2018.09.038.
- Kalantarian, H. *et al.* (2015) *Power Optimization for Wearable Devices*. Available at: <http://www.nalshurafa.com/assets/papers/12.pdf> (Accessed: 17 June 2019).
- Kaltenbrunner, M. *et al.* (2012) 'Ultrathin and lightweight organic solar cells with high flexibility', *Nature Communications*, 3. doi: 10.1038/ncomms1772.
- Kamelolone Solar (2018) *About colored solar panels: what are the options - Kameleon Solar*. Available at: <https://kameleonsolar.com/colored-solar-panels-info/> (Accessed: 13 August 2019).
- Kaushik, V. *et al.* (2015) 'Textile-Based Electronic Components for Energy Applications: Principles, Problems, and Perspective', *Nanomaterials*, 5(3), pp. 1493–1531. doi: 10.3390/nano5031493.
- Kaushika, N. D. and Rai, A. K. (2007) 'An investigation of mismatch losses in solar photovoltaic cell networks', *Energy*, 32(5), pp. 755–759. doi: 10.1016/J.ENERGY.2006.06.017.
- Keating, M. P. (2002) 'Scattering, Absorption, Dispersion, and Polarization', in *Geometric, Physical, and Visual Optics*. 2nd edn. Elsevier, pp. 523–543. doi: 10.1016/B978-0-7506-7262-7.50027-8.
- Keshavarz Hedayati, M. and Elbahri, M. (2016) 'Antireflective Coatings: Conventional Stacking Layers and Ultrathin Plasmonic Metasurfaces, A Mini-Review', *Materials*, 9(6), p. 497. doi: 10.3390/ma9060497.
- Kim, S. J., We, J. H. and Cho, B. J. (2014) '[15] A wearable thermoelectric generator fabricated on a glass fabric', *Energy & Environmental Science*, 7(6), p. 1959. doi: 10.1039/c4ee00242c.
- Knittel, D. *et al.* (2010) 'Coatings on textiles for Cu(In,Ga)Se₂ photovoltaic cell formation on textile carriers: Preparation of Cu(In,Ga)Se₂ solar cells on glass-fiber textiles', *Journal of Applied Polymer Science*, 115(5), pp. 2763–2766. doi: 10.1002/app.30349.
- Knoll, W. (2006) 'Optical Properties of Polymers', in *Materials Science and Technology*. Wiley-VCH Verlag GmbH & Co. KGaA. doi: 10.1002/9783527603978.mst0143.
- Koncar, V (2016) 'Introduction to smart textiles and their applications', in Koncar, Vladan (ed.) *Smart Textiles and their Applications*. 1st edn. Oxford: Woodhead Publishing (Woodhead Publishing Series in Textiles), pp. 1–8. doi:

<https://doi.org/10.1016/B978-0-08-100574-3.00001-1>.

- Kondo, N. *et al.* (1997) 'The effect of change in skin temperature due to evaporative cooling on sweating response during exercise', *International Journal of Biometeorology*, 40(2), pp. 99–102. doi: 10.1007/s004840050026.
- Kopecek, R. *et al.* (2015) 'Bifaciality: One small step for technology, one giant leap for kWh cost reduction', *Photovoltaics International*, 26, pp. 1–11. Available at: http://www.silfabsolar.com/wp-content/uploads/2015/01/PVI26_Paper_01_ISC-Konstanz-ENDGU%23U0308LTIG.pdf (Accessed: 17 August 2019).
- Koshi, T., Nomura, K. I. and Yoshida, M. (2020) 'Electronic component mounting for durable e-textiles: Direct soldering of components onto textile-based deeply permeated conductive patterns', *Micromachines*, 11(2), pp. 19–21. doi: 10.3390/mi11020209.
- Krawczyk, S. K., Jakubowski, A. and Zurawska, M. (1981) 'Temperature dependence of the short-circuit current in mis solar cells', *Solar Cells*, 4, pp. 187–194.
- Krebs, F. C. *et al.* (2006) 'Strategies for incorporation of polymer photovoltaics into garments and textiles', *Solar Energy Materials and Solar Cells*, 90(7–8), pp. 1058–1067. doi: 10.1016/j.solmat.2005.06.003.
- Krebs, F. C. and Hösel, M. (2015) 'The Solar Textile Challenge: How It Will Not Work and Where It Might', *ChemSusChem*, 8(6), pp. 966–969. doi: 10.1002/cssc.201403377.
- Kuhlmann, J. *et al.* (2018) 'Development of a Universal Solar Energy Harvesting System Suited for Textile Integration Including Flexible Energy Storage', *Journal of Fashion Technology & Textile Engineering*, s4, pp. 10–12. doi: 10.4172/2329-9568.s4-012.
- Kularatna, N. (2014) *Energy Storage Devices for Electronic Systems: Rechargeable Batteries and Supercapacitors*, *Energy Storage Devices for Electronic Systems: Rechargeable Batteries and Supercapacitors*. Available at: <https://books.google.com/books?id=6CCOAwwAAQBAJ&pgis=1>.
- Kumar, M. (2011) 'Flexible Photovoltaic Textiles for Smart Applications', in *Solar Cells - New Aspects and Solutions*. InTech. doi: 10.5772/19950.
- Kwon, S. *et al.* (2018) 'Weavable and Highly Efficient Organic Light-Emitting Fibers for Wearable Electronics: A Scalable, Low-Temperature Process', *Nano Letters*, 18(1), pp. 347–356. doi: 10.1021/acs.nanolett.7b04204.
- Kylberg, W. *et al.* (2011) 'Woven electrodes for flexible organic photovoltaic cells', *Advanced Materials*, 23(8), pp. 1015–1019. doi: 10.1002/adma.201003391.
- Kyosev, Y. and Aurich, M. (2016) 'Investigations about the braiding angle and the cover factor of the braided fabrics using Image Processing and Symbolic Math Toolbox of Matlab', *Advances in Braiding Technology*, pp. 549–569. doi: 10.1016/B978-0-08-100407-4.00023-5.
- Lam, J.-Y. *et al.* (2017) 'A stable, efficient textile-based flexible perovskite solar cell with improved washable and deployable capabilities for wearable device applications', *RSC Advances*, 7(86), pp. 54361–54368. doi: 10.1039/C7RA10321B.
- Lambey, J. (2008) 'Blind or Awning Photo-Generator'. US20080163984. Available at: <https://google.com/patents/US20080163984>.
- Lau, D. *et al.* (2019) 'Hybrid solar energy harvesting and storage devices: The promises

- and challenges', *Materials Today Energy*, 13, pp. 22–44. doi: 10.1016/J.MTENER.2019.04.003.
- Lee, H. and Roh, J.-S. (2018) 'Wearable electromagnetic energy-harvesting textiles based on human walking', *Textile Research Journal*, p. 004051751879734. doi: 10.1177/0040517518797349.
- Lee, J. A. *et al.* (2016) 'Woven-Yarn Thermoelectric Textiles', *Advanced Materials*, 28(25), pp. 5038–5044. doi: 10.1002/adma.201600709.
- Lee, M. R. *et al.* (2009) 'Solar Power Wires Based on Organic Photovoltaic Materials', *New Series*, 324(5924), pp. 232–235. doi: 10.1126/science.1169544.
- Lee, S. *et al.* (2014) 'Stitchable organic photovoltaic cells with textile electrodes', *Nano Energy*, 9, pp. 88–93. doi: 10.1016/j.nanoen.2014.06.017.
- Lee, S. *et al.* (2015) 'Triboelectric energy harvester based on wearable textile platforms employing various surface morphologies', *Nano Energy*, 12, pp. 410–418. doi: 10.1016/j.nanoen.2015.01.009.
- Leonard, P. (2004) 'Electronic systems incorporated into textile threads or fibres'. US20040115430. Available at: <https://www.google.com/patents/US20040115430>.
- Leonard, P. N. (2013) 'Electronic systems incorporated into textile threads or fibres'. US8536075. Available at: <https://www.google.com/patents/US8536075>.
- Leonov, V. (2013) 'Thermoelectric energy harvesting of human body heat for wearable sensors', *IEEE Sensors Journal*, 13(6), pp. 2284–2291. doi: 10.1109/JSEN.2013.2252526.
- Lerner, R., Dalland, T. and Touhey, C. (2015) 'Systems and methods for applying flexible solar panels to flexible underlying membranes'. US20150365046. Available at: <https://encrypted.google.com/patents/US20150365046>.
- Li, C. *et al.* (2016) 'Wearable energy-smart ribbons for synchronous energy harvest and storage', *Nature Communications*, 7(1), p. 13319. doi: 10.1038/ncomms13319.
- Li, P. *et al.* (2016) 'Single-walled carbon nanotubes/polyaniline-coated polyester thermoelectric textile with good interface stability prepared by ultrasonic induction', *RSC Advances*, 6(93), pp. 90347–90353. doi: 10.1039/C6RA16532J.
- Li, R. *et al.* (2015) 'Wearable Double-Twisted Fibrous Perovskite Solar Cell', *Advanced Materials*, 27(25), pp. 3831–3835. doi: 10.1002/adma.201501333.
- Li, X. *et al.* (2014) 'Hybrid heterojunction and solid-state photoelectrochemical solar cells', *Advanced Energy Materials*, 4(14). doi: 10.1002/aenm.201400224.
- Liang, J. *et al.* (2015) 'High efficiency flexible fiber-type dye-sensitized solar cells with multi-working electrodes', *Nano Energy*, 12, pp. 501–509. doi: 10.1016/J.NANOEN.2015.01.023.
- Lim, J. H. *et al.* (2015) 'Improvement in light harvesting of dyesensitized solar cells with antireflective and hydrophobic textile PDMS coating by facile soft imprint lithography', *Optics Express*, 23(3), pp. A169–A179. doi: 10.1364/OE.23.00A169.
- Lipomi, D. J. *et al.* (2011) 'Stretchable Organic Solar Cells', *Adv. Mater.*, 23, pp. 1771–1775. doi: 10.1002/adma.201004426.
- Liu, D. *et al.* (2012) 'Solid-state, polymer-based fiber solar cells with carbon nanotube electrodes', *ACS Nano*, 6(12), pp. 11027–11034. doi: 10.1021/nn304638z.

- Liu, J. *et al.* (2018) 'Screen Printed Dye-Sensitized Solar Cells (DSSCs) on Woven Polyester Cotton Fabric for Wearable Energy Harvesting Applications', *Materials Today: Proceedings*, 5(5), pp. 13753–13758. doi: 10.1016/J.MATPR.2018.02.015.
- Liu, J. *et al.* (2019) 'Flexible Printed Monolithic-Structured Solid-State Dye Sensitized Solar Cells on Woven Glass Fibre Textile for Wearable Energy Harvesting Applications', *Scientific Reports*, 9(1), p. 1362. doi: 10.1038/s41598-018-37590-8.
- Liu, L. *et al.* (2016) 'A triboelectric textile templated by a three-dimensionally penetrated fabric', *Journal of Materials Chemistry*, 4(16), pp. 6077–6083. doi: 10.1039/C6TA01166G.
- Liu, P. *et al.* (2018) 'Polymer solar cell textiles with interlaced cathode and anode fibers', *Journal of Materials Chemistry A*, 6(41), pp. 19947–19953. doi: 10.1039/C8TA06510A.
- Lu, Z. *et al.* (2016) 'Silk fabric-based wearable thermoelectric generator for energy harvesting from the human body', *Applied Energy*, 164, pp. 57–63. doi: 10.1016/j.apenergy.2015.11.038.
- Luch, D. (2009) 'Collector grid and interconnect structures for photovoltaic arrays and modules'. US20090107538. Available at: <https://google.com/patents/US20090107538>.
- Lugoda, P. *et al.* (2018) 'A Wearable Textile Thermograph', *Sensors*, 18(7), p. 2369. doi: 10.3390/s18072369.
- Ly, Z. *et al.* (2011) 'Large size, high efficiency fiber-shaped dye-sensitized solar cells', *Physical Chemistry Chemical Physics*, 13(21), pp. 10076–10083. doi: 10.1039/c1cp20543a.
- Ma, J. S. (2011) 'Power generation umbrella'. US20110290288. Available at: <https://google.com/patents/US20110290288>.
- Malacara-Hernández, D. and Malacara-Hernández, Z. (2013) 'Geometrical Optics Principles', in *Handbook of Optical Design*. 3rd edn. CRC Press, pp. 1–34. doi: 10.1201/b13894-2.
- Markvart, T. and Castañer, L. (2012) 'Principles of Solar Cell Operation', in Markvart, T. and Castañer, L. (eds) *Practical Handbook of Photovoltaics*. 2nd edn. Elsevier Ltd, pp. 7–31. doi: 10.1016/B978-0-12-385934-1.00001-5.
- Mather, R. and Wilson, J. (2017) 'Fabrication of Photovoltaic Textiles', *Coatings*, 7(5), p. 63. doi: 10.3390/coatings7050063.
- Maxim Integrated (2019) *MAX32625 Ultra-Low-Power Arm Cortex-M4 with FPU-Based Microcontroller (MCU) with 512KB Flash and 160KB SRAM - Maxim*. Available at: <https://www.maximintegrated.com/en/products/microcontrollers/MAX32625.html> (Accessed: 7 June 2019).
- Micus, S., Haupt, M. and Gresser, G. T. (2020) 'Soldering electronics to smart textiles by pulsed Nd:YAG laser', *Materials*, 13(11). doi: 10.3390/ma13112429.
- Mbise, E., Dias, T. and Hurley, W. (2015) 'Design and manufacture of heated textiles', *Electronic Textiles*, pp. 117–132. doi: 10.1016/B978-0-08-100201-8.00007-2.
- McEvoy, A. J., Markvart, T. and Castañer, L. (2013) *Solar cells : materials, manufacture and operation*. Elsevier. Available at: <http://www.sciencedirect.com/science/book/9780123869647> (Accessed: 25 April 2017).
- Min, G. (2009) 'Power supply sources for smart textiles', in *Smart Clothes and Wearable*

- Technology*, pp. 214–231. doi: 10.1533/9781845695668.2.214.
- Moayeri Pour, G., Benyhesan, M. K. and Leon-Salas, W. D. (2014) 'Energy harvesting using substrate photodiodes', *IEEE Transactions on Circuits and Systems II: Express Briefs*, 61(7), pp. 501–505. doi: 10.1109/TCSII.2014.2327371.
- Morton, W. E. *et al.* (2008) 'Optical properties', in *Physical Properties of Textile Fibres*. Woodhead Publishing, pp. 690–708. doi: 10.1533/9781845694425.690.
- Moustafa, H. *et al.* (2015) 'Mobile wearable communications', *IEEE Wireless Communications*, 22(1), pp. 10–11. doi: 10.1109/MWC.2015.7054713.
- Münzenrieder, N. *et al.* (2017) 'Oxide Thin-Film Transistors on Fibers for Smart Textiles', *Technologies*, 5(2), p. 31. doi: 10.3390/technologies5020031.
- Nance, D. S. *et al.* (2016) 'Photovoltaic assembly and associated methods'. EP2901498A4. Available at: <https://google.com/patents/EP2901498A4?cl=en>.
- Nashed, M.-N. *et al.* (2019) 'A Novel Method for Embedding Semiconductor Dies within Textile Yarn to Create Electronic Textiles', *Fibers*, 7(2), p. 12. doi: 10.3390/fib7020012.
- Newby, B. and Pedley, M. (2017) 'Printed system yarns'. WO2017021719A1. Available at: <https://www.google.com/patents/WO2017021719A1?cl=en>.
- Niu, S. and Wang, Z. L. (2014) 'Theoretical systems of triboelectric nanogenerators', *Nano Energy*, pp. 1–32. doi: 10.1016/j.nanoen.2014.11.034.
- Nocito, C. and Koncar, V (2016) 'Flexible photovoltaic cells embedded into textile structures', in Koncar, Vladan (ed.) *Smart Textiles and their Applications*. 1st edn. Oxford: Woodhead Publishing (Woodhead Publishing Series in Textiles), pp. 401–422. doi: <https://doi.org/10.1016/B978-0-08-100574-3.00018-7>.
- Nocito, C., Raymond, L. and Boussu, F. (2012) 'Awning type solar protection device equipped with an electrical power production system'. US20120073624. Available at: <https://google.com/patents/US20120073624>.
- O'Connor, B., Pipe, K. P. and Shtein, M. (2008) 'Fiber based organic photovoltaic devices', *Applied Physics Letters*, 92(19). doi: 10.1063/1.2927533.
- Oppizzi, D. (2014) 'Photovoltaic Blind'. US20140027069. Available at: <https://google.com/patents/US20140027069>.
- Opwis, Klaus *et al.* (2016) 'Preparation of a Textile-Based Dye-Sensitized Solar Cell', *International Journal of Photoenergy*, 2016, pp. 1–11. doi: 10.1155/2016/3796074.
- Opwis, K *et al.* (2016) 'Preparation of a Textile-Based Dye-Sensitized Solar Cell', *International Journal of Photoenergy*, 2016. doi: 10.1155/2016/3796074.
- Orandi, K. (2009) 'Solar powered motorcycle jacket'. US20090144887. Available at: <https://www.google.com/patents/US20090144887>.
- Page, T. (2015) 'A Forecast of the Adoption of Wearable Technology', *International Journal of Technology Diffusion (IJTD)*, 6(2), pp. 12–29. doi: 10.4018/IJTD.2015040102.
- Pan, S. *et al.* (2014) 'Wearable solar cells by stacking textile electrodes', *Angewandte Chemie - International Edition*, 53(24), pp. 6110–6114. doi: 10.1002/anie.201402561.
- Pelton, M. (2002) 'The lustre of textile fibres and a method of measurement', *Transactions of the Optical Society*, 184. doi: 10.1088/1475-4878/31/4/302.

- Peng, B., Ding, T. and Wang, P. (2012) 'Propagation of polarized light through textile material'. Available at: https://www.osapublishing.org/DirectPDFAccess/9F77A916-ED21-5B24-658F8292904F31D9_241238/ao-51-26-6325.pdf?da=1&id=241238&shib=963446&seq=0&mobile=no (Accessed: 9 August 2019).
- Piwek, L. *et al.* (2016) 'The Rise of Consumer Health Wearables: Promises and Barriers', *PLOS Medicine*, 13(2), p. e1001953. doi: 10.1371/journal.pmed.1001953.
- Plentz, J. *et al.* (2016) 'Amorphous silicon thin-film solar cells on glass fiber textiles', *Materials Science and Engineering B: Solid-State Materials for Advanced Technology*, 204, pp. 34–37. doi: 10.1016/j.mseb.2015.11.007.
- Post, E. R. *et al.* (2000) 'E-broidery: design and fabrication of textile-based computing', *IBM Systems Journal*, pp. 840–860. doi: 10.1147/sj.393.0840.
- Postrel, V. (2017) *E-Textiles & Interiors*. Available at: <https://vpostrel.com/articles/e-textiles-interiors> (Accessed: 1 March 2019).
- Pu, X. *et al.* (2015) 'A Self-Charging Power Unit by Integration of a Textile Triboelectric Nanogenerator and a Flexible Lithium-Ion Battery for Wearable Electronics', *Advanced Materials*, 27(15), pp. 2472–2478. doi: 10.1002/adma.201500311.
- Pu, X., Song, W., *et al.* (2016) 'Wearable Power-Textiles by Integrating Fabric Triboelectric Nanogenerators and Fiber-Shaped Dye-Sensitized Solar Cells', *Advanced Energy Materials*, 6(20), pp. 1601048–n/a. doi: 10.1002/aenm.201601048.
- Pu, X., Li, L., *et al.* (2016) 'Wearable Self-Charging Power Textile Based on Flexible Yarn Supercapacitors and Fabric Nanogenerators', *Advanced Materials*. doi: 10.1002/adma.201504403.
- Qin, Y., Wang, X. and Wang, Z. L. (2008) 'Microfibre-nanowire hybrid structure for energy scavenging', *Nature*, 451(February), pp. 809–13. doi: 10.1038/nature06601.
- Qiu, L. *et al.* (2014) 'Integrating Perovskite Solar Cells into a Flexible Fiber', *Angewandte Chemie International Edition*, 53(39), pp. 10425–10428. doi: 10.1002/anie.201404973.
- Ramadan, K. S., Sameoto, D. and Evoy, S. (2014) 'A review of piezoelectric polymers as functional materials for electromechanical transducers', *Smart Materials and Structures*, 23(3), p. 033001. doi: 10.1088/0964-1726/23/3/033001.
- Ramier, J. *et al.* (2008) 'Mechanical integrity of dye-sensitized photovoltaic fibers', *Renewable Energy*, 33(2), pp. 314–319. doi: 10.1016/j.renene.2007.05.029.
- Rathnayake, A. S. (2015) *Development of the core technology for the creation of electronically-active, smart yarn*. Nottingham Trent University. Available at: <https://core.ac.uk/download/pdf/74207226.pdf> (Accessed: 9 July 2019).
- Rein, M. *et al.* (2018) 'Diode fibres for fabric-based optical communications', *Nature*, 560(7717), pp. 214–218. doi: 10.1038/s41586-018-0390-x.
- Saito, T. (2012) 'Spectral Properties of Semiconductor Photodiodes', in Gian Franco, D. B. (ed.) *Advances in Photodiodes*. Intech, pp. 111–133. doi: 10.5772/711.
- Sandia National Laboratories (2017) *Sandia's solar glitter closer to market with new licensing agreement*. Available at: <https://phys.org/news/2017-02-sandia-solar-glitter-closer-agreement.html> (Accessed: 2 July 2019).
- Sapargaliyev, D. (2015) 'Learning with Wearable Technologies: A Case of Google

- Glass', in Brown, T. H. and Merwe, H. J. van der (eds) *The Mobile Learning Voyage - From Small Ripples to Massive Open Waters. mLearn 2015*. Springer, Cham, pp. 343–350. doi: 10.1007/978-3-319-25684-9_25.
- Satharasinghe, A., Hughes-Riley, T. and Dias, T. (2018) 'Photodiodes embedded within electronic textiles', *Scientific Reports*, 8(1), p. 16205. doi: 10.1038/s41598-018-34483-8.
- Schindall, J. (2007) *The Charge of the Ultra-Capacitors - IEEE Spectrum*. Available at: <https://spectrum.ieee.org/transportation/advanced-cars/the-charge-of-the-ultra-capacitors> (Accessed: 29 May 2019).
- Schubert, M. B. and Werner, J. H. (2006) 'Flexible solar cells for clothing', *Materials Today*, 9(6), pp. 42–50. doi: 10.1016/S1369-7021(06)71542-5.
- Schwarz, A. and Van Langenhove, L. (2013) 'Types and processing of electro-conductive and semiconducting materials for smart textiles', in *Multidisciplinary Know-How for Smart-Textiles Developers*. Woodhead Publishing Limited, pp. 29–69. doi: 10.1533/9780857093530.1.29.
- Schwarze, M., Hurschler, C. and Welke, B. (2019) 'Force, impulse and energy during falling with and without knee protection: an in-vitro study', *Scientific Reports*, 9(1), p. 10336. doi: 10.1038/s41598-019-46880-8.
- Sebald, G., Guyomar, D. and Agbossou, A. (2009) 'On thermoelectric and pyroelectric energy harvesting', *Smart Materials and Structures*, 18(12), p. 125006. doi: 10.1088/0964-1726/18/12/125006.
- Seeberg, T. M. *et al.* (2011) 'Printed organic conductive polymers thermocouples in textile and smart clothing applications', *Proceedings of the Annual International Conference of the IEEE Engineering in Medicine and Biology Society, EMBS*, (0314), pp. 3278–3281. doi: 10.1109/IEMBS.2011.6090890.
- Sharma, P. and Bhatti, T. S. (2010) 'A review on electrochemical double-layer capacitors', *Energy Conversion and Management*, 51(12), pp. 2901–2912. doi: 10.1016/J.ENCONMAN.2010.06.031.
- Shih, Y. *et al.* (1995) 'Analysis of Beat-up Force During Weaving', *Textile Research Journal*, 65(12), pp. 747–754. doi: 10.1177/004051759506501207.
- Shockley, W. and Queisser, H. J. (1961) 'Detailed Balance Limit of Efficiency of p-n Junction Solar Cells', *Journal of Applied Physics*, 32(3), pp. 510–519. doi: 10.1063/1.1736034.
- Sigma-Aldrich (no date) *Materials for High and Low Refractive Index Coatings* | Sigma-Aldrich. Available at: <https://www.sigmaaldrich.com/technical-documents/articles/materials-science/organic-electronics/refractive-index-coatings.html> (Accessed: 19 September 2019).
- Simon, E. P. *et al.* (2012) 'Development of a multi-terminal crimp package for smart textile integration', in *2012 4th Electronic System-Integration Technology Conference*. IEEE, pp. 1–6. doi: 10.1109/ESTC.2012.6542057.
- Singh, R. V. and Singal, C. M. (1983) 'Temperature dependence of the open-circuit voltage of an N+-P-P+ silicon solar cell under high illumination levels', *Solar Cells*. doi: 10.1016/0379-6787(83)90016-9.
- Soin, N. *et al.* (2014) 'Novel "3-D spacer" all fibre piezoelectric textiles for energy harvesting applications', *Energy Environ. Sci.*, 7(5), pp. 1670–1679. doi: 10.1039/C3EE43987A.

- Soin, N., Anand, S. C. and Shah, T. H. (2016) 'Energy harvesting and storage textiles', *Handbook of Technical Textiles*, pp. 357–396. doi: 10.1016/B978-1-78242-465-9.00012-4.
- Solomon, P. M. *et al.* (2002) 'Active devices using threads'. US6437422. Available at: <https://www.google.com/patents/US6437422>.
- Song, S., Ahn, Y. and Yun, K. S. (2015) 'Scalable textile energy harvester in woven piezoelectric structures', *2015 Transducers - 2015 18th International Conference on Solid-State Sensors, Actuators and Microsystems, Transducers 2015*, pp. 708–709. doi: 10.1109/Tranceducers.2015.7181021.
- Speich, F. (2011) 'Transponder-Thread and Application Thereof'. US20110147462. Available at: <https://www.google.com/patents/US20110147462>.
- Stark, I. (2012) 'Integrating Thermoelectric Technology into Clothing for Generating Usable Energy to Power Wireless Devices', in *Proceedings of the Conference on Wireless Health*. New York, NY, USA: ACM (WH '12), pp. 17:1–17:2. doi: 10.1145/2448096.2448113.
- Starner, T. *et al.* (1995) *Wearable Computing and Augmented Reality*. Available at: <https://pdfs.semanticscholar.org/c04a/eb6910c8d0e7cae03afdaa38120b449fdacf.pdf> (Accessed: 2 March 2019).
- Starner, T. *et al.* (1996) *Augmented Reality Through Wearable Computing*. Available at: <https://www.cc.gatech.edu/~thad/p/journal/augmented-reality-through-wearable-computing.pdf> (Accessed: 2 March 2019).
- Staufert, G. (2008) 'Filament'. WO2008080245A3. Available at: <https://www.google.com/patents/WO2008080245A3?cl=en>.
- Stoppa, M. and Chiolerio, A. (2014) 'Wearable Electronics and Smart Textiles: A Critical Review', *Sensors*. doi: 10.3390/s140711957.
- Sun, K. C. *et al.* (2015) 'Highly efficient and durable dye-sensitized solar cells based on a wet-laid PET membrane electrolyte', *Journal of Materials Chemistry A*, 4(2), pp. 458–465. doi: 10.1039/c5ta07720f.
- Sundarrajan, S. *et al.* (2010) *Fabrication of P3HT/PCBM solar cloth by electrospinning technique*, *Materials Letters*. doi: 10.1016/j.matlet.2010.07.054.
- Tang, W. *et al.* (2014) 'A power-transformed-and-managed triboelectric nanogenerator and its applications in a self-powered wireless sensing node.', *Nanotechnology*, 25(22), p. 225402. doi: 10.1088/0957-4484/25/22/225402.
- Tao, X. (2001) 'Smart technology for textiles and clothing – introduction and overview', in Tao, X. (ed.) *Smart Fibres, Fabrics and Clothing*. Woodhead Publishing, pp. 1–6. doi: 10.1533/9781855737600.1.
- Teichmann, D. *et al.* (2014) 'The MAIN Shirt: a textile-integrated magnetic induction sensor array.', *Sensors (Basel, Switzerland)*, 14(1), pp. 1039–1056. doi: 10.3390/s140101039.
- Tesfamichael, T. *et al.* (2001) 'Optical characterization and modeling of black pigments used in thickness-sensitive solar-selective absorbing paints', *Solar Energy*, 69, pp. 35–43. doi: 10.1016/S0038-092X(01)00016-0.
- Teslasuit (2017) *Detailed wearables classification by Teslasuit team* | Teslasuit blog. Available at: <https://teslasuit.io/blog/wearables/detailed-wearables-classification-by-teslasuit-team> (Accessed: 28 February 2019).

- Texas Instruments (2014) *ADS7042 12-Bit 1MSPS Ultra-Low-Power Ultra-Small-Size SAR ADC With SPI Interface* | TI.com. Available at: <http://www.ti.com/product/ADS7042#> (Accessed: 7 June 2019).
- The New York Times (1884) *Electric Girls*, *The New York Times*. Available at: <https://www.nytimes.com/1884/04/26/archives/electric-girls.html>.
- Thorp, E. O. (1998) 'The invention of the first wearable computer', in *Digest of Papers. Second International Symposium on Wearable Computers (Cat. No.98EX215)*. IEEE Comput. Soc, pp. 4–8. doi: 10.1109/ISWC.1998.729523.
- Toivola, M. *et al.* (2009) 'Photovoltaic fiber', *Thin Solid Films*, 517(8), pp. 2799–2802. doi: 10.1016/j.tsf.2008.11.057.
- Toprakci, H. A. K. and Ghosh, T. K. (2015) 'Textile Sensors', in *Handbook of Smart Textiles*. Singapore: Springer Singapore, pp. 357–379. doi: 10.1007/978-981-4451-45-1_37.
- Torah, R. *et al.* (2018) 'Energy-harvesting materials for smart fabrics and textiles', *MRS Bulletin*, 43(3), pp. 214–219. doi: 10.1557/mrs.2018.9.
- Tran, R. (2016) *How to Select the Right Battery for Wearables & Consumer Electronics*. Available at: <https://www.ecnmag.com/article/2016/08/how-select-right-battery-wearables-consumer-electronics> (Accessed: 1 August 2019).
- Tseghai, G. B. *et al.* (2020) 'Integration of conductive materials with textile structures, an overview', *Sensors (Switzerland)*, 20(23), pp. 1–28. doi: 10.3390/s20236910.
- Uddin, M. J. *et al.* (2013) 'Solid state dye-sensitized photovoltaic micro-wires (DSPMs) with carbon nanotubes yarns as counter electrode: Synthesis and characterization', *Solar Energy Materials and Solar Cells*, 108, pp. 65–69. doi: 10.1016/j.solmat.2012.09.003.
- Velten, J. *et al.* (2013) 'Weavable dye sensitized solar cells exploiting carbon nanotube yarns', *Applied Physics Letters*, 102(20). doi: 10.1063/1.4807891.
- Vincent, J. D. *et al.* (2015) 'Classical Photon Detectors: Simple Photoconductor and Photovoltaics', in Vincent, J. D. *et al.* (eds) *Fundamentals of Infrared and Visible Detector Operation and Testing*. 2nd edn. John Wiley & Sons, Inc, pp. 105–148. doi: 10.1002/9781119011897.ch4.
- Visual Capitalists (2016) *The Evolution of Battery Technology*. Available at: <https://www.visualcapitalist.com/evolution-of-battery-technology/> (Accessed: 7 March 2019).
- Wagner, M. (2013) 'Automotive applications of smart textiles', *Multidisciplinary Know-How for Smart-Textiles Developers*, pp. 444–467. doi: 10.1533/9780857093530.3.444.
- Wang, X. *et al.* (2016) 'Wire-shaped perovskite solar cell based on TiO₂ nanotubes', *Nanotechnology*, 27(20). doi: 10.1088/0957-4484/27/20/20LT01.
- Wang, Z. L. (2013) 'Triboelectric nanogenerators as new energy technology for self-powered systems and as active mechanical and chemical sensors', *ACS Nano*, 7(11), pp. 9533–9557. doi: 10.1021/nm404614z.
- Wang, Z. L., Chen, J. and Lin, L. (2015) 'Progress in triboelectric nanogenerators as a new energy technology and self-powered sensors', *Energy Environ. Sci.*, 8(8), pp. 2250–2282. doi: 10.1039/C5EE01532D.
- Waqar, S., Wang, L. and John, S. (2015) 'Piezoelectric energy harvesting from intelligent

- textiles', in *Electronic Textiles*. Elsevier Ltd., pp. 173–197. doi: 10.1016/B978-0-08-100201-8.00010-2.
- Weng, W. *et al.* (2016) 'Smart electronic textiles', *Angewandte Chemie - International Edition*, 55(21), pp. 6140–6169. doi: 10.1002/anie.201507333.
- Whittingham, M. S. (2012) 'History, evolution, and future status of energy storage', *Proceedings of the IEEE*, 100(SPL CONTENT), pp. 1518–1534. doi: 10.1109/JPROC.2012.2190170.
- Willis, B. (2003) *Reflow Soldering Processes and Troubleshooting SMT, BGA, CSP and Flip Chip Technologies, Soldering & Surface Mount Technology*. Emerald Group Publishing Limited. doi: 10.1108/ssmt.2003.21915aae.003.
- Wilson, J. I B and Mather, R. R. (2015) 'Photovoltaic energy harvesting for intelligent textiles', in Dias, T. (ed.) *Electronic Textiles: Smart Fabrics and Wearable Technology*. 1st edn. Woodhead Publishing Limited., pp. 155–171. doi: 10.1016/B978-0-08-100201-8.00009-6.
- Wolf, E. (1996) 'Outer clothing item with an attached solar cell'. DE4436246A1. Available at: <https://www.google.com/patents/DE4436246A1?cl=en>.
- World Energy Council (2013) 'Energy Resources: Solar', *World Energy Council 2013 World Energy Resources: Solar*, pp. 1–28. doi: https://www.worldenergy.org/wp-content/uploads/2013/10/WER_2013_8_Solar_revised.pdf.
- Wu, C.-Y. and Chen, J.-F. (1982) 'Temperature coefficients of the open-circuit voltage of p-n junction solar cells', *Junction Solar Cells Journal of Applied Physics*, 53, p. 5001. doi: 10.1063/1.331129.
- Wu, Q. and Hu, J. (2016) 'Waterborne polyurethane based thermoelectric composites and their application potential in wearable thermoelectric textiles', *Composites Part B: Engineering*, 107, pp. 59–66. doi: 10.1016/j.compositesb.2016.09.068.
- Xu, J. *et al.* (2014) 'A flexible polypyrrole-coated fabric counter electrode for dye-sensitized solar cells', *Journal of Power Sources*, 257, pp. 230–236. doi: 10.1016/j.jpowsour.2014.01.123.
- Xu, Q. *et al.* (2016) 'Polypyrrole-coated cotton fabrics prepared by electrochemical polymerization as textile counter electrode for dye-sensitized solar cells', *Organic Electronics: physics, materials, applications*, 29, pp. 107–113. doi: 10.1016/j.orgel.2015.11.007.
- Yan, J. *et al.* (2014) '3D Wire-Shaped Dye-Sensitized Solar Cells in Solid State Using Carbon Nanotube Yarns with Hybrid Photovoltaic Structure', *Advanced Materials Interfaces*, 1(6). doi: 10.1002/admi.201400075.
- Yang, B. and Yun, K. S. (2012) 'Piezoelectric shell structures as wearable energy harvesters for effective power generation at low-frequency movement', *Sensors and Actuators, A: Physical*, 188, pp. 427–433. doi: 10.1016/j.sna.2012.03.026.
- Yang, Z. *et al.* (2013) 'Photovoltaic wire derived from a graphene composite fiber achieving an 8.45 % energy conversion efficiency', *Angewandte Chemie - International Edition*, 52(29), pp. 7545–7548. doi: 10.1002/anie.201301776.
- Yang, Z *et al.* (2014) 'Stretchable, wearable dye-sensitized solar cells', *Advanced Materials*, 26(17), pp. 2643–2647. doi: 10.1002/adma.201400152.

- Yang, Zhibin *et al.* (2014) 'Stretchable, wearable dye-sensitized solar cells', *Advanced Materials*, 26(17), pp. 2643–2647. doi: 10.1002/adma.201400152.
- Ylli, K. *et al.* (2013) 'Design, fabrication and characterization of an inductive human motion energy harvester for application in shoes', *Journal of Physics: Conference Series*, 476, p. 12012. doi: 10.1088/1742-6596/476/1/012012.
- Yoon, J. *et al.* (2008) 'Ultrathin silicon solar microcells for semitransparent, mechanically flexible and microconcentrator module designs.', *Nature materials*, 7(11), pp. 907–915. doi: 10.1038/nmat2287.
- Yotter, R. A. and Wilson, D. M. (2003) 'A review of photodetectors for sensing light-emitting reporters in biological systems', *IEEE Sensors Journal*, pp. 288–303. doi: 10.1109/JSEN.2003.814651.
- Yun, D., Park, J. and Yun, K.-S. (2015) 'Highly stretchable energy harvester using piezoelectric helical structure for wearable applications', *Electronics Letters*, 51(3), pp. 284–285. doi: 10.1049/el.2014.3400.
- Yun, M. J. *et al.* (2014) 'Highly flexible dye-sensitized solar cells produced by sewing textile electrodes on cloth', *Scientific Reports*, 4. doi: 10.1038/srep05322.
- Yun, Min Ju *et al.* (2015) 'Highly Flexible Dye-sensitized Solar Cells Produced by Sewing Textile Electrodes on Cloth', *Scientific Reports*, 4(1), p. 5322. doi: 10.1038/srep05322.
- Yun, M J *et al.* (2015) 'Insertion of Dye-Sensitized Solar Cells in Textiles using a Conventional Weaving Process', *Scientific Reports*, 5. doi: 10.1038/srep11022.
- Yun, Min Ju *et al.* (2016) 'Float printing deposition to control the morphology of TiO₂ photoanodes on woven textile metal substrates for TCO-free flexible dye-sensitized solar cells', *RSC Adv.*, 6(71), pp. 67331–67339. doi: 10.1039/C6RA09457K.
- Yun, M.J. *et al.* (2016) 'Float printing deposition to control the morphology of TiO₂ photoanodes on woven textile metal substrates for TCO-free flexible dye-sensitized solar cells', *RSC Advances*, 6(71), pp. 67331–67339. doi: 10.1039/c6ra09457k.
- Yun, M J *et al.* (2016) 'Monolithic-Structured Single-Layered Textile-Based Dye-Sensitized Solar Cells', *Scientific Reports*, 6. doi: 10.1038/srep34249.
- Yun, M. J. *et al.* (2019) 'Three-Dimensional Textile Platform for Electrochemical Devices and its Application to Dye-Sensitized Solar Cells', *Scientific Reports*, 9(1), p. 2322. doi: 10.1038/s41598-018-38426-1.
- Zampetti, E., Bearzotti, A. and Macagnano, A. (2014) 'Flexible piezoelectric transducer based on electrospun PVDF nanofibers for sensing applications', *Procedia Engineering*, 87, pp. 1509–1512. doi: 10.1016/j.proeng.2014.11.585.
- Zeng, W. *et al.* (2013) 'Highly durable all-fiber nanogenerator for mechanical energy harvesting', *Energy & Environmental Science*, 6(9), pp. 2631–2638. doi: 10.1039/c3ee41063c.
- Zhai, S. *et al.* (2016) 'Textile energy storage: Structural design concepts, material selection and future perspectives', *Energy Storage Materials*, 3, pp. 123–139. doi: 10.1016/J.ENS.2016.02.003.
- Zhang, L., Shi, E., Ji, C., *et al.* (2012) 'Fiber and fabric solar cells by directly weaving carbon nanotube yarns with CdSe nanowire-based electrodes', *Nanoscale*, 4(16), pp.

4954–4959. doi: 10.1039/c2nr31440a.

Zhang, L., Song, L., *et al.* (2012) 'Flexible fiber-shaped CuInSe₂ solar cells with single-wire-structure: Design, construction and performance', *Nano Energy*, 1(6), pp. 769–776. doi: 10.1016/j.nanoen.2012.07.022.

Zhang, L., Shi, E., Li, Z., *et al.* (2012) 'Wire-supported CdSe nanowire array photoelectrochemical solar cells', *Physical Chemistry Chemical Physics*, 14(10), pp. 3583–3588. doi: 10.1039/c2cp00024e.

Zhang, L. L. and Zhao, X. S. (2009) 'Carbon-based materials as supercapacitor electrodes', *Chemical Society Reviews*, 38(9), p. 2520. doi: 10.1039/b813846j.

Zhang, M. *et al.* (2015) 'A hybrid fibers based wearable fabric piezoelectric nanogenerator for energy harvesting application', *Nano Energy*, 13, pp. 298–305. doi: 10.1016/j.nanoen.2015.02.034.

Zhang, N *et al.* (2016) 'A Wearable All-Solid Photovoltaic Textile', *Advanced Materials*, 28(2), pp. 263–269. doi: 10.1002/adma.201504137.

Zhang, Nannan *et al.* (2016) 'A Wearable All-Solid Photovoltaic Textile', *Advanced Materials*, 28(2), pp. 263–269. doi: 10.1002/adma.201504137.

Zhang, Q., Wang, Y. and Kim, E. S. (2015) 'Electromagnetic Energy Harvester with Flexible Coils and Magnetic Spring for 1-10 Hz Resonance', *Journal of Microelectromechanical Systems*, 24(4), pp. 1193–1206. doi: 10.1109/JMEMS.2015.2393911.

Zhang, S. *et al.* (2012) 'Porous, platinum nanoparticle-adsorbed carbon nanotube yarns for efficient fiber solar cells', *ACS Nano*, 6(8), pp. 7191–7198. doi: 10.1021/nn3022553.

Zhang, Z. *et al.* (2014) 'A Lightweight Polymer Solar Cell Textile that Functions when Illuminated from Either Side', *Angewandte Chemie - International Edition*, 53(43), pp. 11571–11574. doi: 10.1002/anie.201407688.

Zhang, Z. *et al.* (2015) 'Stretchable polymer solar cell fibers', *Small*, 11(6), pp. 675–680. doi: 10.1002/smll.201400874.

Zhao, C. *et al.* (2018) 'Recent Development of Fabricating Flexible Micro-Supercapacitors for Wearable Devices', *Advanced Materials Technologies*, 3(9), p. 1800028. doi: 10.1002/admt.201800028.

Zhao, J. and You, Z. (2014) 'Models for 31-mode PVDF energy harvester for wearable applications.', *TheScientificWorldJournal*, 2014, p. 893496. doi: 10.1155/2014/893496.

Zhao, K. *et al.* (2019) 'Nanogenerator-Based Self-Charging Energy Storage Devices', *Nano-Micro Letters*, 11(1), p. 19. doi: 10.1007/s40820-019-0251-7.

Zhao, Z. *et al.* (2016) 'Machine-Washable Textile Triboelectric Nanogenerators for Effective Human Respiratory Monitoring through Loom Weaving of Metallic Yarns', *Advanced Materials*, 28(46), pp. 10267–10274. doi: 10.1002/adma.201603679.

Zhu, M. *et al.* (2016) '3D spacer fabric based multifunctional triboelectric nanogenerator with great feasibility for mechanized large-scale production', *Nano Energy*, 27, pp. 439–446. doi: 10.1016/j.nanoen.2016.07.016.

Zysset, C. *et al.* (2010) 'Woven electronic textiles: An enabling technology for health-care monitoring in clothing', *Proc. 5th Int. Workshop Ubiquit. Health Wellness*, pp. 1–4. Available at:

http://www.researchgate.net/publication/228905737_Woven_Electronic_Textiles_An_Enabling_Technology_for_Health-Care_Monitoring_in_Clothing/file/9c960527a7a4f82fa2.pdf.

Zysset, C. *et al.* (2012) 'Integration Method for Electronics in Woven Textiles', *IEEE Transactions on Components, Packaging and Manufacturing Technology*, 2(7), pp. 1107–1117. doi: 10.1109/TCPMT.2012.2189770.

Appendices

Appendix 1 - List of research work reported in literature categorized based on the solar cell material type

Category	Description	Performance/Remarks
DSSC textile fibre and fabric	All-solid, dye-sensitized solar cell (DSSC) textile fibre and fabric which is tailorable and wearable (Chai et al, 2016).	The cells are 100% made of solids and can be cut/sewn. Power conversion efficiency (PCE) are well below liquid based DSSC (only around 1 %) Good bending performance.
DSSC printed fabric	TCO-free flexible dye-sensitized solar cells coated/printed on fabrics (M.J. Yun et al, 2016).	PCE of 4.16 %.
Perovskite solar cell yarn	Wire-shaped perovskite solar cell yarn based on TiO ₂ nanotubes (Wang et al, 2016).	Integrated Ti/TiO ₂ nanotube/perovskite/CNT solar cell wire exhibited a PCE of 1.16 %.
Fabric electrode based DSSC	Polypyrrole-coated cotton fabrics as textile counter electrode for dye-sensitized solar cells (Xu et al, 2016).	Pt-free, PCE of 3.83%, low cost, and biodegradable.
DSSC fabric	Monolithic-structured, single-layered, textile-based, dye-sensitized solar cells (M J Yun et al, 2016)	Initial PCE (0.35 %) decreased to 0.21 % and 0.18 % after 5 and 7 days, respectively, for the fabric.
DSSC coated fabric	Textile-based dye-sensitized solar cells using glass-fibre fabrics (Opwis et al, 2016).	PCE of 1.8 % lasts for 7 weeks.
Perovskite solar cell yarn	Wearable double-twisted fibrous perovskite solar cell (Li et al, 2015) .	PCE of 3.03 %, bending stability exceeding 1000 cycles, and maintain 89 % efficiency after 96 h.
DSSC tape and woven fabric	Insertion of dye-sensitized solar cells in textiles using a conventional weaving process (Yun et al, 2015).	PCE of 2.63% for inserted cells.
DSSC woven fabric	PDMS woven textile imprinted transparent layer for DSSC (Lim et al, 2015).	Compared to the bare FTO/glass, the textile PDMS increased the total transmittance from 82.3 to 85.1% and its diffuse transmittance was significantly increased from 5.9 to 78.1 % at a 550 nm wavelength.
DSSC non-woven fabric	Dye-sensitized solar cells based on a wet-laid PET membrane electrolyte (Sun et al, 2015).	Non-woven based DSSC with a PCE of 10.248 % and better lifetime with plasma treatment.

Perovskite solar wire and woven fabric	Woven structures made of ZnO perpendicularly grown (stainless steel) wire, perovskite solar cell (He et al, 2015).	PCE of 3.8 % achieved. photovoltaic fibres and fabrics can be twisted in three dimensions without obvious damage to the structure.
DSSC Fibre/yarn	3D solid-state wire-shaped DSSC with a hybrid photovoltaic structure (Yan et al, 2014).	All Solid state DSSC with PCE of 7.39 % using a CNT, QD hybrid structure. Relatively steady cell performance up to 100 irradiation cycles for up to 50 h.
DSSC fibre	Stretchable, wearable dye-sensitized solar cell textile (Yang et al, 2014).	7.13 % PCE with stretchability by wrapping a wire around an elastic monofilament fibre.
Hybrid woven solar fabric	Graphene woven fabric based Hybrid solar cell with solid state electrolyte and n-Si (Li et al, 2014)	PCE of 11 %.
DSSC yarn	Sewable DSSC on Glass fibre/Ti wire based electrodes (Yun et al, 2014).	Sewable onto regular textiles. Flexibility and high performance under 4 mm radius of curvature for over thousands of deformation cycle. PCE 5.8 %.
Woven electrode for DSSC	Cotton woven fabric based Nickel/Polypyrrolle coated counter electrode for DSSC (Xu et al, 2014).	PCE of 3.30 %.
DSSC fibre	DSSC/electrochemical capacitor with coaxially arranged, TiO ₂ coated, Ti wire and CNT sheets as two electrodes (Chen et al, 2014).	PCE of 2.73% achieved by DSSC, capacitor energy storage efficiency reached 75.7 % with specific capacitances up to 3.32 mF/cm ² and power densities up to 0.27 mW/cm ² at 50 mA.
DSSC solar fabric	DSSC textile with Ti woven electrode and woven CNT counter electrode, stacked together (Pan et al, 2014)	Maximum PCE of 3.10%. Maintained good energy conversions even with bending for 100 cycles and deformed form a rectangle to a parallelogram.
Graphene composite DSSC fibre	Photovoltaic wire derived from a graphene composite fibre. (Yang et al, 2013)	PCE of 8.45% achieved at fibre level.
DSSC wire	All-solid, flexible solar textiles based on dye-sensitized solar cells with ZnO nanorod arrays on stainless steel wires (Chae et al, 2013).	PCE of 2.57 %.
DSSC yarn	TiO ₂ /Pt coated, CNT spun yarn based DSSC (Velten et al, 2013).	PCE of 3.1 %.

DSSC yarn	Flexible DSSC based on ITO and Pt/Ti coated PEN electrodes and electro spun TiO ₂ /MgO core-sheath nanorods (Du et al, 2013).	TiO ₂ /MgO core sheath structure showed a better performance compared with TiO ₂ only structures.
CNT based DSSC yarn	All carbon nanotube fibre electrode-based, dye-sensitized, photovoltaic wire (Cai, Chen and Peng, 2012).	Maximum PCE 3.9 % achieved with modification of working electrodes with TiO ₂ .
CNT based DSSC yarn	Intertwined aligned CNT based (TiO ₂ coated and non-coated) twisted DSSC yarn (Chen et al, 2012).	PCE of 2.94 % achieved. Good strength and flexibility.
CNT based DSSC yarn	Solid electrolyte Ti-TiO ₂ , CNT yarn based DSSC yarn (Uddin et al, 2013).	All Solid State. PCE of 0.1959 % with prolonged-time stability. Highly flexible.
DSSC fibre	Large size, high efficiency fibre-shaped dye-sensitized solar cells (Lv et al, 2011).	PCE of 5.41 % achieved.
DSSC fibre	DSSC fibre base on a cladding less optical fibre (Gaudiana et al, 2006).	PCE is very low (<0.001 %)
Coated OPV fabric	Spray coated organic solar cells on woven polyester/cotton fabrics (Arumugam et al, 2016).	PCE of 0.02 % achieved.
OPV fibre	Stretchable fibre shaped polymeric solar cell on an elastic substrate and a spring-like structure (Z. Zhang et al, 2015).	Maximum PCE of 1.23 % with PCEs that vary less than 10 % after being bent for 1000 times and under stretching at a strain of above 30 %.
OPV yarn	Textile-based OPV as a stitchable power source (Lee et al, 2014).	OPV showed an enhanced short circuit current density of 13.11 mA/cm ² , which was higher than that of a typical OPV. The corresponding PCE reached to about 1.8 %.
Woven OPV fabric	A lightweight polymer solar cell textile that functions when illuminated from either side (Zhang et al, 2014).	Maximum PCE of 1.08 %.
OPV fibre	Organic photovoltaic cells containing electron-transporting organic nanofibers made of bis(octyl)-perylene diimide (PDI-C8) in the form of nano-fabrics (Hyoung Park et al, 2012).	An increase in fill factor is observed for photovoltaic cells incorporating the nano-fabric heterojunctions.

OPV yarn	Solid-state, polymer-based, fibre solar cells with carbon nanotube electrodes (Liu et al, 2012).	PCE of 2.3 %.
OPV fabric	Photovoltaic textile structure using polyaniline/carbon nanotube composite materials (Bedeloglu et al, 2011).	PCE of 0.023 % for photovoltaic tapes and 0.04 % for ITO-coated glass-based solar cells.
OPV woven fabric	Transparent and flexible electrode based on a metal and polymer fibres woven mesh, and a PEDOT:PSS based solar cell fabricated on the same mesh (Kylberg et al, 2011).	Flexible woven fabric-based cells with PCE of 2.2 %.
Coated OPV tape	P3H:PCBM based organic solar cell coated on Polypropylene tape with PEDOT:PSS anode and metallic cathode (A. C. Bedeloglu et al, 2010).	PCE of 0.29 %.
OPV fibre	MDMO-PPV:PCBM and P3H:PCBM based organic solar cell coated on polypropylene fibres, with PEDOT:PSS anode and metallic cathode (A. Bedeloglu et al, 2010).	PCE of 0.021 % and 0.01 % achieved for MDMO-PPV: PCBM and P3H: PCBM based solar cell fibres respectively.
Electro spun OPV fabric	Fabrication of P3HT/PCBM solar cloth by electrospinning core-shell nanofibers made of a conducting polymer or PVP as the shell (Sundarrajan et al, 2010).	Continuous P3HT or P3HT/PCBM nanofiber solar fabric with 8.7×10^{-8} % PCE.
Coated OPV tape	Flexible textile based organic photovoltaic devices fabricated onto non-transparent PP tapes and ITO coated glasses (Bedeloglu et al, 2009).	Maximum PCE of 0.33 % was observed with an Ag coated PP tape substrate.
OPV fibre	Fiber-shaped organic photovoltaic cell, utilizing concentric thin films of small molecular organic compounds (O'Connor, Pipe and Shtein, 2008).	PCE of 0.5 %.
OPV decorative coating	Incorporating organic solar cells into garments and textiles by coating a polyethylene terephthalate (PET) substrate with PEDOT electrode using	The total area of the device on PET was typically much smaller than the active area due to the decorative design of the aluminium electrode.

	doctor blade and screen-printing methods (Krebs et al, 2006).	The maximum module output power was found to be 0.27 μ W.
Si Based PV sheet laminated fabric	Amorphous Si based flexible semi-conductor sheets laminated onto textiles (Nocito and Koncar, 2016).	Flexible textile-based fabrics with good manufacturability and utility. PCEs were four times lower than c-Si.
Amorphous Si PV layer coated woven fabric	Amorphous Si based p-i-n solar cells printed on glass fibre woven structures (Plentz et al, 2016).	PCE of 1.4 % achieved, which increased by 5 % with a transparent conductive oxide
Inorganic PV fibre and woven fabric	Photovoltaic woven textile with all solid inorganic solar cell fibre (Zhang et al, 2016).	PCE of 1.3 % for a single cell unit.
Hybrid triboelectric and solar yarns woven fabric	Micro-cable inorganic/polymer hybrid material structured textile for simultaneously harvesting solar and mechanical energy (Chen et al, 2016).	Combined power generation of 0.5 mW ($4 \times 5\text{cm}^2$ area) for a human walking under 0.8 sun illumination.
Si based PV fibre	Si p-i-n junction photodiode junction for photovoltaics (He et al, 2013).	PCE of 0.5 %.
CdSe-CNT PV yarn	Semiconductor solar cell fibre with CdSe-CNT Nanowires (Zhang, Shi, Li, et al, 2012).	Highly flexible semiconductor solar cell yarn with PCE of around 1-2 %.
CuInSe ₂ PV wire	Flexible fibre-shaped CuInSe ₂ solar cells with single-wire-structure (Zhang, Song, Tian, et al, 2012).	PCE of 2.31 %, which varied between 2.16–2.32 % during rotation (0-360°), bending (0-360°), and long-time aging (stored at 60 °C for 600 h) processes.
CIS based woven PV fabric	Inorganic CIS PV cell on a glass fibre woven fabric (Knittel et al, 2010).	High level of flexibility achieved. PCE was higher than 8 %.
Si based PV cell printed fabric	Printed arrays of Si microcells on flexible substrate, with concentrator lens arrays (Yoon et al, 2008).	PCE of 6 % was achieved under 1 sun illumination, highly bendable, and performance changing only slightly with bending.
Inorganic-CNT nanowire-based PV fibre and woven PV fabric	Fibre and fabric solar cells by directly weaving carbon nanotube yarns with CdSe nanowire-based electrodes (Zhang, Shi, Ji, et al, 2012).	PCE in the range 1 % to 2.9 % at yarn level.

CNT/Ti wire electrodes for PV fibre	Porous, platinum nanoparticle-adsorbed carbon nanotube yarns for efficient fibre solar cells (Zhang, Ji, Bian, et al, 2012).	PCE of 4.85 % at yarn level.
-------------------------------------	--	------------------------------

References

- Arumugam, S. *et al.* (2016) 'Fully spray-coated organic solar cells on woven polyester cotton fabrics for wearable energy harvesting applications', *Journal of Materials Chemistry A*, 4(15), pp. 5561–5568. doi: 10.1039/c5ta03389f.
- Bedeloglu, A. *et al.* (2009) 'A flexible textile structure based on polymeric photovoltaics using transparent cathode', *Synthetic Metals*, 159(19–20), pp. 2043–2048. doi: 10.1016/j.synthmet.2009.07.019.
- Bedeloglu, A. *et al.* (2010) 'A photovoltaic fiber design for smart textiles', *Textile Research Journal*, 80(11), pp. 1065–1074. doi: 10.1177/0040517509352520.
- Bedeloglu, A. *et al.* (2011) 'Photovoltaic textile structure using polyaniline/carbon nanotube composite materials', *Journal of the Textile Institute*, 102(10), pp. 857–862. doi: 10.1080/00405000.2010.525816.
- Bedeloglu, A. C. *et al.* (2010) 'Development of energy generating photovoltaic textile structures for smart applications', *Fibers and Polymers*, 11(3), pp. 378–383. doi: 10.1007/s12221-010-0378-0.
- Cai, F., Chen, T. and Peng, H. (2012) 'All carbon nanotube fiber electrode-based dye-sensitized photovoltaic wire', *Journal of Materials Chemistry*, 22(30), pp. 14856–14860. doi: 10.1039/c2jm32256k.
- Chae, Y. *et al.* (2013) 'All-solid, flexible solar textiles based on dye-sensitized solar cells with ZnO nanorod arrays on stainless steel wires', *Materials Science and Engineering B: Solid-State Materials for Advanced Technology*. Elsevier B.V., 178(17), pp. 1117–1123. doi: 10.1016/j.mseb.2013.06.018.
- Chai, Z. *et al.* (2016) 'Tailorable and Wearable Textile Devices for Solar Energy Harvesting and Simultaneous Storage', *ACS Nano*, p. acsnano.6b05293. doi: 10.1021/acsnano.6b05293.
- Chen, J. *et al.* (2016) 'Micro-cable structured textile for simultaneously harvesting solar and mechanical energy', *Nature Energy*, 1(September), p. 16138. doi: 10.1038/nenergy.2016.138.
- Chen, T. *et al.* (2012) 'Intertwined aligned carbon nanotube fiber based dye-sensitized solar cells', *Nano Letters*, 12(5), pp. 2568–2572. doi: 10.1021/nl300799d.
- Chen, X. *et al.* (2014) 'A novel "energy fiber" by coaxially integrating dye-sensitized solar cell and electrochemical capacitor', *Journal of Materials Chemistry A*, 2(6), pp. 1897–1902. doi: 10.1039/c3ta13712k.
- Du, P. *et al.* (2013) 'A photovoltaic smart textile and a photocatalytic functional textile based on co-electrospun TiO₂/MgO core-sheath nanorods: Novel textiles of integrating

- energy and environmental science with textile research', *Textile Research Journal*, 83(16), pp. 1690–1702. doi: 10.1177/0040517513490062.
- Gaudiana, R. *et al.* (2006) 'Photovoltaic fibers', in *Proceedings of SPIE - The International Society for Optical Engineering*. doi: 10.1117/12.683130.
- He, R. *et al.* (2013) 'Silicon p-i-n junction fibers', *Advanced Materials*, 25(10), pp. 1461–1467. doi: 10.1002/adma.201203879.
- He, S. *et al.* (2015) 'Radically grown obelisk-like ZnO arrays for perovskite solar cell fibers and fabrics through a mild solution process', *Journal of Materials Chemistry A*, 3(18), pp. 9406–9410. doi: 10.1039/c5ta01532d.
- Hyoung Park, J. *et al.* (2012) 'Organic photovoltaic cells with nano-fabric heterojunction structure', *Applied Physics Letters*, 100(7). doi: 10.1063/1.3679097.
- Knittel, D. *et al.* (2010) 'Coatings on textiles for Cu(In,Ga)Se₂ photovoltaic cell formation on textile carriers: Preparation of Cu(In,Ga)Se₂ solar cells on glass-fiber textiles', *Journal of Applied Polymer Science*, 115(5), pp. 2763–2766. doi: 10.1002/app.30349.
- Krebs, F. C. *et al.* (2006) 'Strategies for incorporation of polymer photovoltaics into garments and textiles', *Solar Energy Materials and Solar Cells*, 90(7–8), pp. 1058–1067. doi: 10.1016/j.solmat.2005.06.003.
- Kylberg, W. *et al.* (2011) 'Woven electrodes for flexible organic photovoltaic cells', *Advanced Materials*, 23(8), pp. 1015–1019. doi: 10.1002/adma.201003391.
- Lee, S. *et al.* (2014) 'Stitchable organic photovoltaic cells with textile electrodes', *Nano Energy*, 9, pp. 88–93. doi: 10.1016/j.nanoen.2014.06.017.
- Li, R. *et al.* (2015) 'Wearable Double-Twisted Fibrous Perovskite Solar Cell', *Advanced Materials*, 27(25), pp. 3831–3835. doi: 10.1002/adma.201501333.
- Li, X. *et al.* (2014) 'Hybrid heterojunction and solid-state photoelectrochemical solar cells', *Advanced Energy Materials*, 4(14). doi: 10.1002/aenm.201400224.
- Lim, J. H. *et al.* (2015) 'Improvement in light harvesting of dyesensitized solar cells with antireflective and hydrophobic textile PDMS coating by facile soft imprint lithography', *Optics Express*, 23(3), pp. A169–A179. doi: 10.1364/OE.23.00A169.
- Liu, D. *et al.* (2012) 'Solid-state, polymer-based fiber solar cells with carbon nanotube electrodes', *ACS Nano*, 6(12), pp. 11027–11034. doi: 10.1021/nn304638z.
- Lv, Z. *et al.* (2011) 'Large size, high efficiency fiber-shaped dye-sensitized solar cells', *Physical Chemistry Chemical Physics*, 13(21), pp. 10076–10083. doi: 10.1039/c1cp20543a.
- Nocito, C. and Koncar, V. (2016) 'Flexible photovoltaic cells embedded into textile structures', in Koncar, V. (ed.) *Smart Textiles and their Applications*. 1st edn. Oxford: Woodhead Publishing (Woodhead Publishing Series in Textiles), pp. 401–422. doi: <https://doi.org/10.1016/B978-0-08-100574-3.00018-7>.
- O'Connor, B., Pipe, K. P. and Shtein, M. (2008) 'Fiber based organic photovoltaic devices', *Applied Physics Letters*, 92(19). doi: 10.1063/1.2927533.

- Opwis, K. *et al.* (2016) 'Preparation of a Textile-Based Dye-Sensitized Solar Cell', *International Journal of Photoenergy*, 2016. doi: 10.1155/2016/3796074.
- Pan, S. *et al.* (2014) 'Wearable solar cells by stacking textile electrodes', *Angewandte Chemie - International Edition*, 53(24), pp. 6110–6114. doi: 10.1002/anie.201402561.
- Plentz, J. *et al.* (2016) 'Amorphous silicon thin-film solar cells on glass fiber textiles', *Materials Science and Engineering B: Solid-State Materials for Advanced Technology*, 204, pp. 34–37. doi: 10.1016/j.mseb.2015.11.007.
- Sun, K. C. *et al.* (2015) 'Highly efficient and durable dye-sensitized solar cells based on a wet-laid PET membrane electrolyte', *Journal of Materials Chemistry A*, 4(2), pp. 458–465. doi: 10.1039/c5ta07720f.
- Sundarrajan, S. *et al.* (2010) *Fabrication of P3HT/PCBM solar cloth by electrospinning technique*, *Materials Letters*. doi: 10.1016/j.matlet.2010.07.054.
- Uddin, M. J. *et al.* (2013) 'Solid state dye-sensitized photovoltaic micro-wires (DSPMs) with carbon nanotubes yarns as counter electrode: Synthesis and characterization', *Solar Energy Materials and Solar Cells*, 108, pp. 65–69. doi: 10.1016/j.solmat.2012.09.003.
- Velten, J. *et al.* (2013) 'Weavable dye sensitized solar cells exploiting carbon nanotube yarns', *Applied Physics Letters*, 102(20). doi: 10.1063/1.4807891.
- Wang, X. *et al.* (2016) 'Wire-shaped perovskite solar cell based on TiO₂ nanotubes', *Nanotechnology*, 27(20). doi: 10.1088/0957-4484/27/20/20LT01.
- Xu, J. *et al.* (2014) 'A flexible polypyrrole-coated fabric counter electrode for dye-sensitized solar cells', *Journal of Power Sources*, 257, pp. 230–236. doi: 10.1016/j.jpowsour.2014.01.123.
- Xu, Q. *et al.* (2016) 'Polypyrrole-coated cotton fabrics prepared by electrochemical polymerization as textile counter electrode for dye-sensitized solar cells', *Organic Electronics: physics, materials, applications*, 29, pp. 107–113. doi: 10.1016/j.orgel.2015.11.007.
- Yan, J. *et al.* (2014) '3D Wire-Shaped Dye-Sensitized Solar Cells in Solid State Using Carbon Nanotube Yarns with Hybrid Photovoltaic Structure', *Advanced Materials Interfaces*, 1(6). doi: 10.1002/admi.201400075.
- Yang, Z. *et al.* (2013) 'Photovoltaic wire derived from a graphene composite fiber achieving an 8.45 % energy conversion efficiency', *Angewandte Chemie - International Edition*, 52(29), pp. 7545–7548. doi: 10.1002/anie.201301776.
- Yang, Z. *et al.* (2014) 'Stretchable, wearable dye-sensitized solar cells', *Advanced Materials*, 26(17), pp. 2643–2647. doi: 10.1002/adma.201400152.
- Yoon, J. *et al.* (2008) 'Ultrathin silicon solar microcells for semitransparent, mechanically flexible and microconcentrator module designs.', *Nature materials*, 7(11), pp. 907–915. doi: 10.1038/nmat2287.
- Yun, M. J. *et al.* (2014) 'Highly flexible dye-sensitized solar cells produced by sewing textile electrodes on cloth', *Scientific Reports*, 4. doi: 10.1038/srep05322.
- Yun, M. J. *et al.* (2015) 'Insertion of Dye-Sensitized Solar Cells in Textiles using a

Conventional Weaving Process', *Scientific Reports*, 5. doi: 10.1038/srep11022.

Yun, M. J. *et al.* (2016) 'Float printing deposition to control the morphology of TiO₂ photoanodes on woven textile metal substrates for TCO-free flexible dye-sensitized solar cells', *RSC Advances*. Royal Society of Chemistry, 6(71), pp. 67331–67339. doi: 10.1039/c6ra09457k.

Yun, M. J. *et al.* (2016) 'Monolithic-Structured Single-Layered Textile-Based Dye-Sensitized Solar Cells', *Scientific Reports*, 6. doi: 10.1038/srep34249.

Zhang, L., Shi, E., Ji, C., *et al.* (2012) 'Fiber and fabric solar cells by directly weaving carbon nanotube yarns with CdSe nanowire-based electrodes', *Nanoscale*, 4(16), pp. 4954–4959. doi: 10.1039/c2nr31440a.

Zhang, L., Song, L., Tian, Q., *et al.* (2012) 'Flexible fiber-shaped CuInSe₂ solar cells with single-wire-structure: Design, construction and performance', *Nano Energy*, 1(6), pp. 769–776. doi: 10.1016/j.nanoen.2012.07.022.

Zhang, L., Shi, E., Li, Z., *et al.* (2012) 'Wire-supported CdSe nanowire array photoelectrochemical solar cells', *Physical Chemistry Chemical Physics*, 14(10), pp. 3583–3588. doi: 10.1039/c2cp00024e.

Zhang, N. *et al.* (2016) 'A Wearable All-Solid Photovoltaic Textile', *Advanced Materials*, 28(2), pp. 263–269. doi: 10.1002/adma.201504137.

Zhang, S., Ji, C., Bian, Z., *et al.* (2012) 'Porous, platinum nanoparticle-adsorbed carbon nanotube yarns for efficient fiber solar cells', *ACS Nano*, 6(8), pp. 7191–7198. doi: 10.1021/nn3022553.

Zhang, Z. *et al.* (2014) 'A Lightweight Polymer Solar Cell Textile that Functions when Illuminated from Either Side', *Angewandte Chemie - International Edition*, 53(43), pp. 11571–11574. doi: 10.1002/anie.201407688.

Zhang, Z. *et al.* (2015) 'Stretchable polymer solar cell fibers', *Small*, 11(6), pp. 675–680. doi: 10.1002/sml.201400874.

Appendix 2 – Variation of physical dimensions of the solar cells.

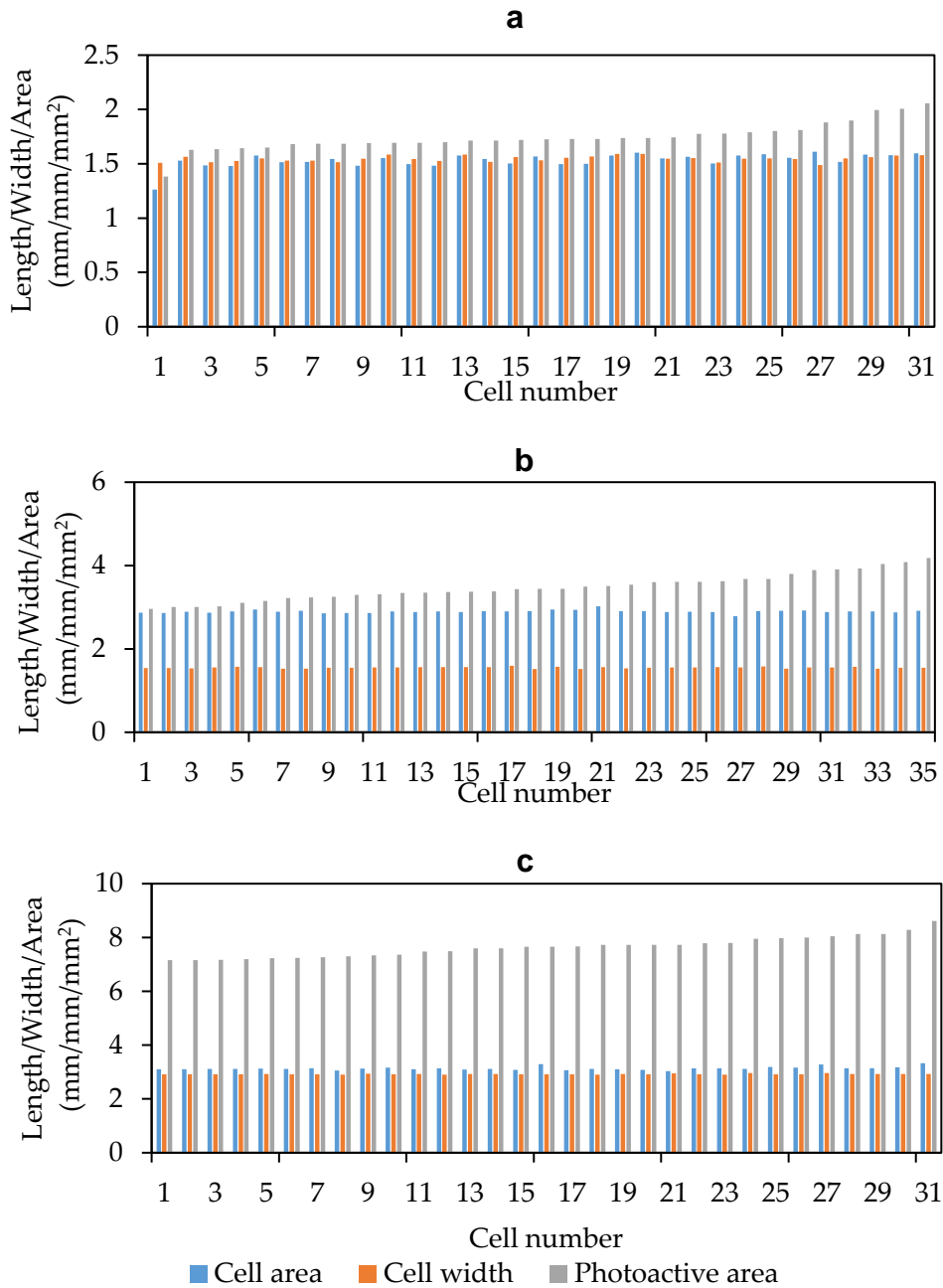


Figure Ap1 – Variation in the physical dimensions of the (a) 1.5×1.5 mm, (b) 1.5×3.0 mm and (c) 3.0×3.2 mm solar cells in batches of 30 cells measured using a digital optical microscope.

Appendix 3 – Light intensity analysis of the lamp used in the optical test rig with and without diffusers.

To evaluate the intensity distribution a VEMD 6060×1 photodiode was positioned on the sample holder. The sample holder was demarcated with a grid of 1 mm × 1 mm unit cells. The I_{sc} values were then recorded on the grid space for four different scenarios, with the lamp of the optical test-rig being supplied with 12 V and 0.89 A. First the measurements were conducted without using a light diffuser.

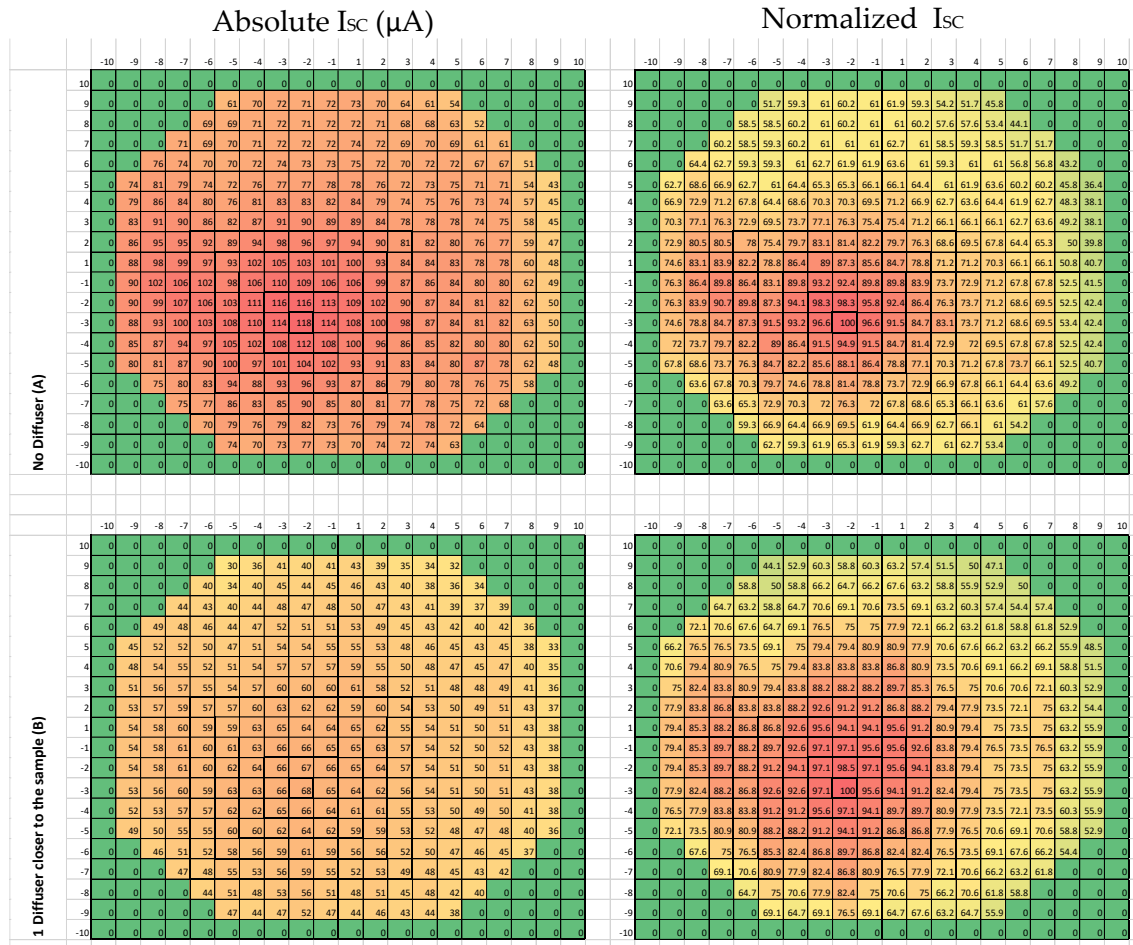


Figure Ap2.1 – Variation of light intensity reaching the sample holder of the optical test rig without a light diffuser and with one light diffuser positioned between the lamp and the sample holder, close to the sample holder. Normalized data presented are based on the I_{sc} measured at the centre.

Appendix 4 - Light intensity analysis of the solar simulator.

The light intensity of the beam of light generated by the solar simulator at one sun intensity was measured using a VEMD 6060×1 photodiode at the measurement plane on a grid of 1 mm × 1 mm unit cells, close to the centre point of the beam.

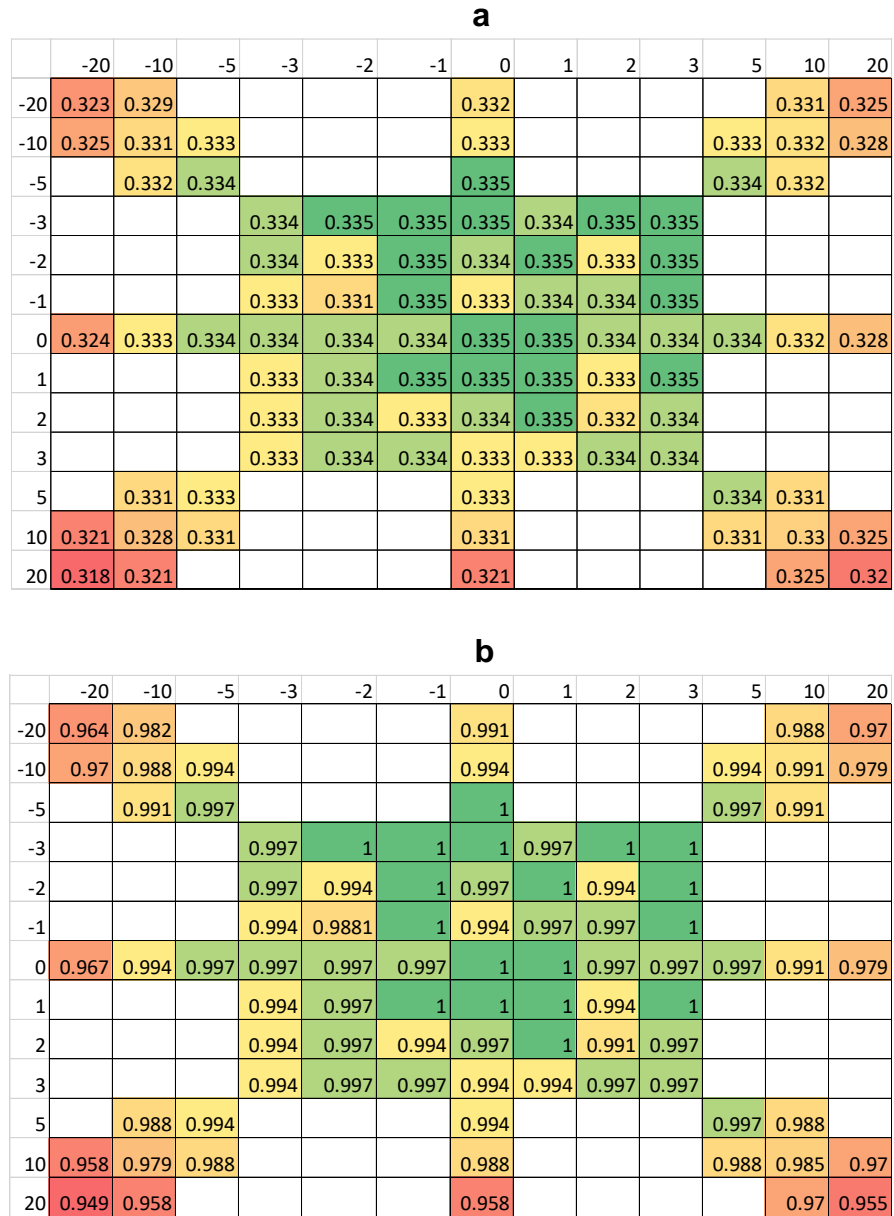


Figure Ap3 – Variation of light intensity at the (a) absolute and (b) normalized short-circuit current measurements for the solar simulator when generating a beam of light at one sun intensity. The normalized data presented is based on the I_{sc} value measured at the centre of the grid.

Appendix 5 - Full details of the mathematical model

In order to understand and characterise the effects observed for an encapsulated PDs a generalized ray tracing mathematical model, which predict the light intensity within the RMP, was proposed.

Generalized Ray Tracing Model

In its simplest terms, a single ray incident of light can be considered. The ray had an intensity E_i and angle γ to the vertical axis, which met the boundary of the cylindrical micro-pod defined by $y = g(x)$ at co-ordinates x_0, y_0 , as illustrated in Fig. Ap. 4. A fraction of the incident ray was reflected (E_r) at the boundary surface and the remaining fraction (E_p) was refracted into the RMP. The refracted ray was attenuated during its travel inside of the RMP before reaching the plane of measurement (E_t). A fraction of the ray (E_{rc}) was partially reflected at the photocell surface, and the residual ray (E_c) was transmitted to the semiconductor.

- E_i - Intensity of incident ray
- E_{rm} - Intensity of reflected ray at air micro-pod boundary
- E_{rp} - Intensity of reflected ray at the plane of measurements
- E_p -Intensity of the ray penetrated through the micro-pod
- E_t -Intensity of transmitted ray at the plane of measurement
- E_c -Intensity of transmitted to the photocell
- γ - Angle of incident light to the vertical axis
- $g(x)$ -Boundary surface function of the material
- n_r - Refractive index of the resin material relative to air
- n_p - Refractive index of the photocell material relative to air
- μ - decadic attenuation coefficient of the material
- θ - Angle of incident light to the normal of the boundary surface
- α - Angle of refracted light to the normal of the boundary surface
- β - Angle of transmitted light to the horizontal axis

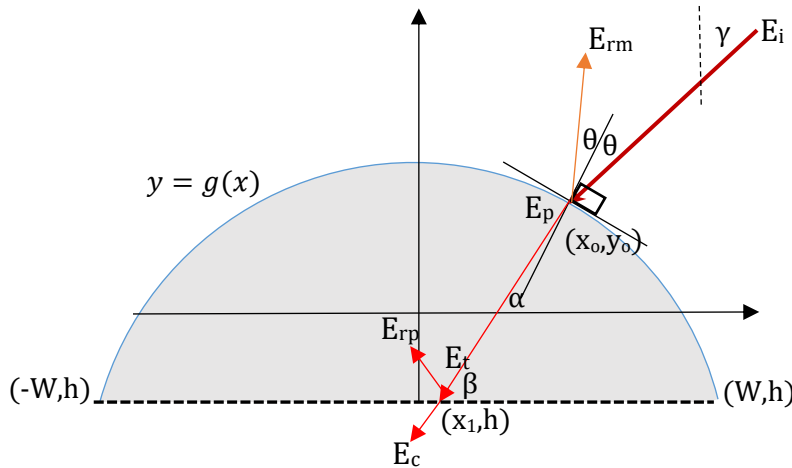


Figure Ap4 - Generalized ray-tracing model depicting the cross-sectional view of the cylindrical micro-pod.

$$E_p = E_i - E_{rm} \quad (I)$$

Based on the geometry:

$$\alpha + \beta + \gamma - \theta = \frac{\pi}{2}$$

$$\left(\frac{dy}{dx}\right) = -\cot(\beta + \alpha)$$

$$x_1 = x_0 - \left\lfloor \frac{g(x_o) - h}{\tan \beta} \right\rfloor \quad (II)$$

From Snell's law of refraction:

$$n_r * \sin \alpha = \sin \theta$$

From Fresnel equation for partial reflection of non-polarized light at the boundaries of non-magnetic material:

$$\frac{E_{rm}}{E_i} = \left(\frac{1}{2}\right) * \left\{ \left[\frac{\cos \theta - n_r \sqrt{1 - (\sin \theta / n_r)^2}}{\cos \theta + n_r \sqrt{1 - (\sin \theta / n_r)^2}} \right]^2 + \left[\frac{n_r \cos \theta - \sqrt{1 - (\sin \theta / n_r)^2}}{n_r \cos \theta + \sqrt{1 - (\sin \theta / n_r)^2}} \right]^2 \right\} \quad (III)$$

Based on the theory of absorption of electromagnetic radiation inside a homogeneous material:

$$E_t = E_p * 10^{(-\mu l)} \quad (IV)$$

Where: $l = [g(x_o) - h] \operatorname{cosec} \beta$

Using the Fresnel equation for the partial reflection of non-polarized light at the boundaries of non-magnetic material, the reflection at the micro-pod-photocell boundary can be given as:

$$\frac{E_{rp}}{E_t} = \left(\frac{1}{2}\right) * \left\{ \left[\frac{n_p \sin \beta - n_r \sqrt{1 - \left(\frac{n_r}{n_p} \cos \beta\right)^2}}{n_r \sin \beta + n_p \sqrt{1 - \left(\frac{n_r}{n_p} \cos \beta\right)^2}} \right]^2 + \left[\frac{n_p \sin \beta - n_r \sqrt{1 - \left(\frac{n_r}{n_p} \cos \beta\right)^2}}{n_p \sin \beta + n_r \sqrt{1 - \left(\frac{n_r}{n_p} \cos \beta\right)^2}} \right]^2 \right\} \quad (V)$$

The intensity of the ray transmitted to the photocell:

$$E_c = E_t - E_{rp}$$

The average Intensity between two points (x_a, h) and (x_b, h) on the horizontal plane along (x_1, h) are given by:

$$E_{AVG} = \left(\int_{x_a}^{x_b} E_c \sin \beta \cdot dx / (x_b - x_a) \right) \quad (VI)$$

Simplification of the generalized model for a circular cross section

In order to generate comparative values with the experimental data, the generalized mathematical model was simplified to an RMP with a circular basis.

Incident light is uniform and parallel to the vertical axis. The boundary surface is circular, and the width of the section is equal to the diameter (se Fig. Ap. 5).

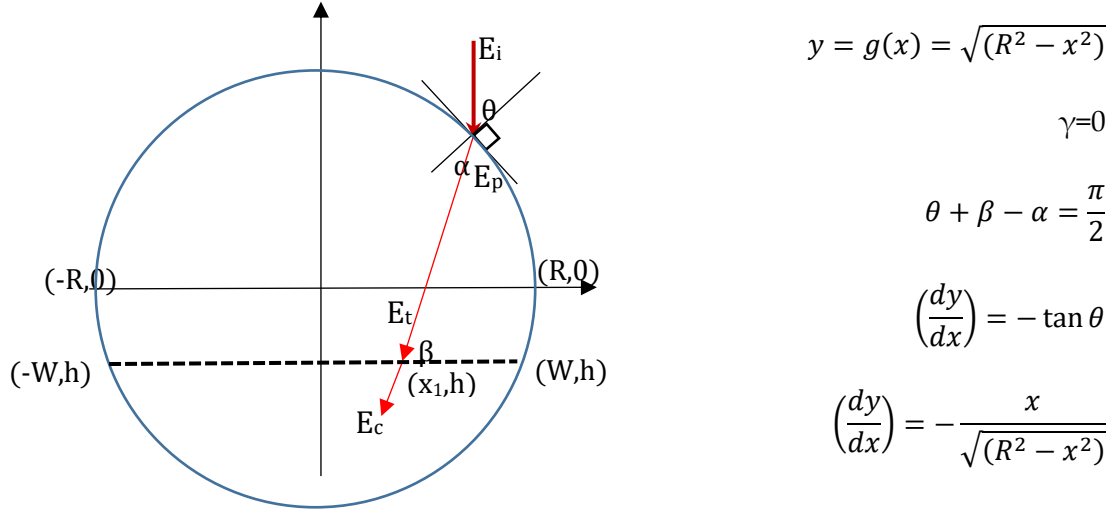


Figure Ap.5 - Simplified ray tracing model for a circular cross section.

$$\tan \theta = \frac{x}{\sqrt{(R^2 - x^2)}} \Rightarrow \sin \theta = \frac{x}{R}, \cos \theta = \left(\frac{\sqrt{(R^2 - x^2)}}{R} \right) \text{ and}$$

$$n_r * \sin \alpha = \sin \theta \Rightarrow \sin \alpha = \left(\frac{x}{n_r R} \right), \cos \alpha = \frac{\sqrt{(n_r^2 R^2 - x^2)}}{nR}$$

$$\sin \beta = \sin \left(\frac{\pi}{2} - \theta + \alpha \right) = \cos(\alpha - \theta) = \frac{\sqrt{(R^2 - x^2)(n_r^2 R^2 - x^2)} + x^2}{nR^2}$$

$$\cos \beta = \cos \left(\frac{\pi}{2} - \theta + \alpha \right) = \sin(\theta - \alpha) = x(\sqrt{(n_r^2 R^2 - x^2)} - \sqrt{(R^2 - x^2)}) / (R^2 * n_r)$$

$$\tan \beta = \frac{\sqrt{(R^2 - x^2)(n_r^2 R^2 - x^2)} + x^2}{x(\sqrt{(n_r^2 R^2 - x^2)} - \sqrt{(R^2 - x^2)})}$$

$$\Rightarrow x_1 = x_0 - \left[\frac{g(x_0) - h}{\tan \beta} \right] = x_0 \left[1 - \left(\sqrt{(R^2 - x_0^2)} - h \right) * \frac{\left(\sqrt{(n_r^2 R^2 - x_0^2)} - \sqrt{(R^2 - x_0^2)} \right)}{\sqrt{(R^2 - x_0^2)(n_r^2 R^2 - x_0^2)} + x_0^2} \right] \quad (\text{VII})$$

$$\Rightarrow l = [g(x_0) + h] \csc \beta = \frac{R^2 n_r (\sqrt{(R^2 - x^2)} - h)}{\sqrt{(R^2 - x^2)(n_r^2 R^2 - x^2)} + x^2}$$

$$\frac{E_{rm}}{E_i} = \left(\frac{(1-n_r^2)^2}{2} \right) * \left\{ \left[\frac{R}{\sqrt{(n_r^2 R^2 - x^2)} + \sqrt{(R^2 - x^2)}} \right]^4 + \left[\frac{n^2(R^2 - x^2) - x^2}{(\sqrt{(n_r^2 R^2 - x^2)} + n^2 \sqrt{(R^2 - x^2)})^2} \right]^2 \right\} \quad (VIII)$$

Estimating short circuit current and open circuit voltage for a crystalline photovoltaic cell encapsulated inside of an RMP

The intensity estimates were converted into estimated I_{sc} and V_{oc} values using the fundamentals of semiconductor photovoltaics. For a crystalline silicon photovoltaic cell embedded inside of an RMP that has a rectangular photo-active area with a width equal to the width of the measurement plane, the irradiance intensity on the photovoltaic cell E can be given as the:

$$E = E_{AVG}$$

Based on the theory the relationships between short-circuit current (I_{sc}) and irradiance intensity E for a photovoltaic cell can be given as:

$$I_{sc} = K_E * E$$

Where K_E is a constant that characterizes the relative variation of short circuit current as a function of irradiance intensity.

The nominal values for short circuit current (I_{scn}) and open circuit voltage (V_{ocn}) of the photovoltaic cell are determined experimentally under nominal irradiance intensity (E_n) before encapsulating inside an RMP.

Using the above equations, the short circuit current I_{sc} for an irradiance intensity E can be estimated as:

$$I_{sc} = I_{scn} * \left(\frac{E}{E_n} \right) \quad (IX)$$

Also, the open circuit voltage V_{oc} for a given irradiance intensity E can be given as:

$$V_{oc} = V_{ocn} + \frac{nkT}{q} * \ln \left(\frac{E}{E_n} \right) \quad (X)$$

Here k - Boltzmann Constant ($1.380649 \times 10^{-23} \text{ JK}^{-1}$)

n - Ideality factor

q - Electron charge

T- Absolute temperature

The ideality factor (n) for the photocell is determined using the IV curve of the photocell under nominal irradiance condition E_n . The IV curve is fitted to an exponential function in the below form:

$$I = \alpha - \beta e^{\gamma V}$$

Where I is the current V is the voltage and α , β and γ are constants. According to theory the ideality factor is given by:

$$n = \frac{q}{\gamma k T}$$

Appendix 6 – Positioning of the photodiodes inside of resin micro-pods

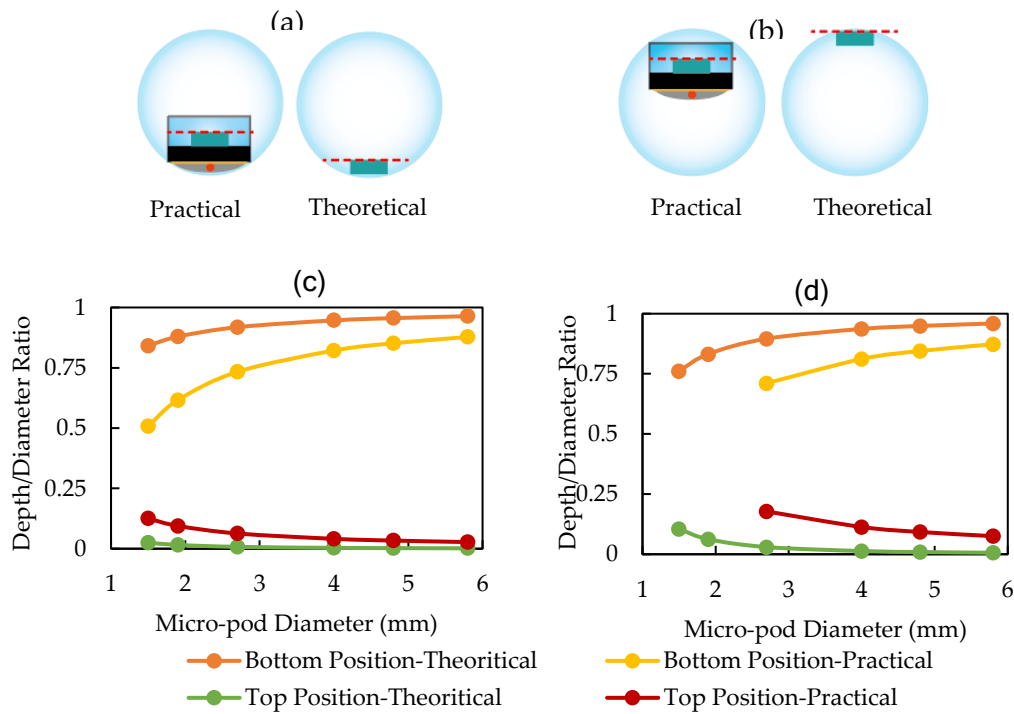


Figure Ap. 6 - Theoretical and practical the depths of positioning for the photoactive plane of photodiodes inside of resin micro-pods. (a) Schematic of the PD in the bottom position. (b) Schematic of PD in the top position. (c, d) Depth to diameter ratio for top and bottom positions against micro-pod diameter for: (c) TEMD 7000x01 (d) VEMD 6060x01.

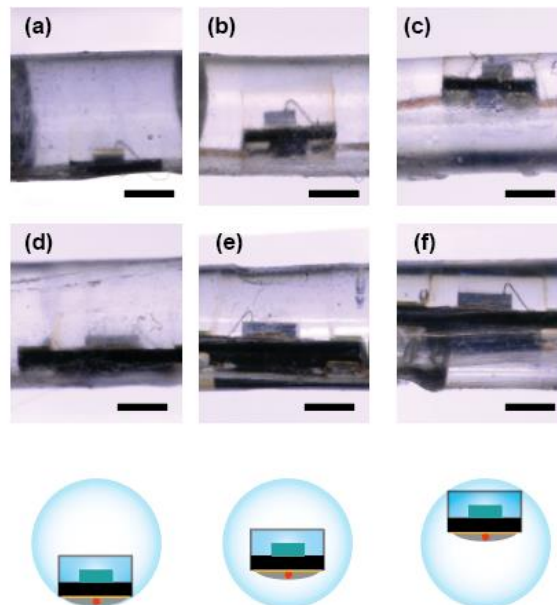


Figure Ap. 7 - Images showing the positioning of the photodiodes inside of 2.7 mm diameter resin micro-pods. (a) TEMD7000x01 embedded at the bottom position. (b) TEMD7000x01 embedded at centre position. (c) TEMD7000x01 embedded at top position. (d) VEMD6060x01 embedded at the bottom position, (e) VEMD6060x01 embedded at the centre position. (f) VEMD6060x01 embedded at top position. (bottom) Schematics of the three PD positions.

Appendix 7 – Mathematical model revised to include total internal reflection.

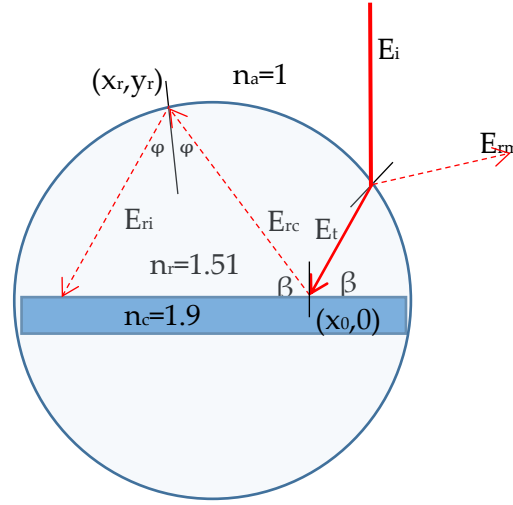


Figure Ap. 8 – Illustration of the occurrence of the total internal reflection of a ray of light within a 1.6 mm micro-pod embedded with a 1.5 mm wide solar cell.

When a refracted ray approaching the solar cell surface (E_t), making an angle β to the photoactive surface is considered, the intensity of the partially reflective light E_{rc} can be given as;

$$\frac{E_{rc}}{E_t} = \left(\frac{1}{2}\right) * \left\{ \left[\frac{n_r \sin \beta - n_p \sqrt{1 - \left(\frac{n_r}{n_c} \cos \beta\right)^2}}{n_r \sin \beta + n_p \sqrt{1 - \left(\frac{n_r}{n_c} \cos \beta\right)^2}} \right]^2 + \left[\frac{n_c \sin \beta - n_r \sqrt{1 - \left(\frac{n_r}{n_c} \cos \beta\right)^2}}{n_c \sin \beta + n_r \sqrt{1 - \left(\frac{n_r}{n_c} \cos \beta\right)^2}} \right]^2 \right\}$$

The equation for the linear path flowed by the reflected ray at the photoactive surface can be given as:

$$y = -\tan \beta (x - x_0)$$

Based on this, the co-ordinates of the point at which the reflected ray reaches the micro-pod air boundary (x_r, y_r) can be given as:

$$x_r = x_0 \sin^2 \beta \pm (\sqrt{r^2 - x^2 \sin^2 \beta}) \cos \beta$$

$$y_r = \sin \beta (\cos \beta \pm \sqrt{r^2 - x^2 \sin^2 \beta})$$

The angle of the normal drawn at (x_r, y_r) to the micro-pod-air boundary can be given as:

$$\tan^{-1}\left(-\frac{x}{y}\right) + \pi/2$$

The acute angle made by the reflected ray to the normal drawn at (x_r, y_r) to the micro-pod-air boundary is given as:

$$\varphi = \pi - (\beta + \frac{\pi}{2} + \tan^{-1}(-x_r/y_r))$$

$$\varphi = \frac{\pi}{2} - \beta + \tan^{-1}(x_r/y_r)$$

Based on Snell's law at the critical angle of total internal reflection (TIR) at the micro-pod-air boundary:

$$\sin \varphi = \frac{n_a}{n_r}$$

$$\varphi = \sin^{-1}\left(\frac{n_a}{n_r}\right)$$

For TIR:

$$\varphi > \sin^{-1}\left(\frac{n_a}{n_r}\right)$$

$$\frac{\pi}{2} - \beta + \tan^{-1}(x_r/y_r) > \sin^{-1}\left(\frac{n_a}{n_r}\right)$$

$$\beta < \frac{\pi}{2} + \tan^{-1}(x_r/y_r) - \sin^{-1}\left(\frac{n_a}{n_r}\right)$$

By summing the reflected rays fulfilling the above requirement, the intensity of total internal reflection can be approximated.

Appendix 8 – Measured test results of the solar-E-yarns during the wash test.

Table Ap. 1 – Measured values for the solar-E-yarns after machine washing and tumble drying in yarn form.

Tested Samples	Before wash		After Wash/Dry 1		After Wash/Dry 2		After Wash/Dry 3		After Wash/Dry 4		After Wash/Dry 5		After Wash/Dry 10		After Wash/Dry 15		After Wash/Dry 20		After Wash/Dry 25	
	Isc (A)	Voc (V)	Isc (A)	Voc (V)	Isc (A)	Voc (V)	Isc (A)	Voc (V)	Isc (A)	Voc (V)	Isc (A)	Voc (V)	Isc (A)	Voc (V)	Isc (A)	Voc (V)	Isc (A)	Voc (V)	Isc (A)	Voc (V)
Yarn	S1	0.000542	0.5296	0.000535	0.5301	0.000593	0.5222	0.000534	0.5394	0.000544	0.5347	0.00052	0.5463	0.000542	0.5328	0.000538	0.5352	0.000524	0.5115	
	S2	0.000499	0.5383	0.000523	0.536	0.000492	0.5305	0.00047	0.5349	0.00051	0.5222	0.000539	0.5279	0.000509	0.5322	0.000503	0.5279	0.000503	0.5322	
	S3	0.000448	0.5219	0.000445	0.5234	0.000457	0.5234	0.000471	0.526	0.000466	0.5376	0.000485	0.5281	0.000458	0.533	0.000458	0.533	0.000474	0.5132	
	S4	0.000533	0.4989	0.000495	0.4896	0.00048	0.4895	0.000445	0.4986	0.000479	0.501									
	S5	0.000444	0.5322	0.000461	0.5384	0.000432	0.5294	0.000458	0.5435	0.000447	0.5351	0.000458	0.5473	0.000462	0.536	0.000436	0.5412			
	S6	0.000492	0.5388	0.000531	0.5431	0.000498	0.5397	0.000531	0.5494	0.000527	0.5429	0.000524	0.5501							
	S7	0.000327	0.5046	0.00036	0.5094	0.000487	0.5363	0.000353	0.5159											
	S8	0.000451	0.3991																	
	S9	0.000412	0.5543	0.000434	0.556	0.000412	0.5521													
	S10	0.000383	0.536	0.000424	0.5437	0.00038	0.5333	0.000392	0.5482	0.000391	0.5411	0.000414	0.5578	0.000399	0.5432					
1.5x1.5mm SC	S1	0.000797	0.5565	0.000758	0.5596	0.000802	0.5559	0.000753	0.5597	0.000763	0.5546	0.000768	0.5671	0.000778	0.5532	0.000743	0.5625	0.000761	0.5454	
	S2	0.000829	0.5553	0.000887	0.5552	0.000836	0.542	0.000844	0.5615	0.000836	0.5585	0.000825	0.5714	0.000824	0.5566	0.000857	0.5645	0.000839	0.5486	0.000729
	S3	0.000685	0.5389	0.000662	0.5365	0.000627	0.5275	0.000649	0.5445	0.00068	0.5413	0.000647	0.5495	0.000644	0.5333	0.000645	0.5454	0.000607	0.5267	
	S4	0.000759	0.5528	0.000769	0.5501	0.000771	0.5443	0.000759	0.5582	0.000762	0.5533	0.00078	0.5683	0.000793	0.5547	0.000746	0.5585	0.000754	0.5412	0.000783
	S5	0.000652	0.5677	0.000628	0.5727	0.000612	0.5731	0.000629	0.5762	0.000606	0.5746	0.000647	0.5835	0.000601	0.5666					0.5548
3-1.5mm SC	S1	0.00174	0.5193	0.001793	0.5228	0.001864	0.5183	0.001808	0.5264	0.001785	0.5233	0.001799	0.5363	0.001816	0.5244	0.000637	0.5416	0.000626	0.5244	0.00062
	S2	0.001131	0.4983	0.00133	0.5073	0.001314	0.4964	0.001338	0.5161	0.001269	0.5083	0.001287	0.5217	0.001272	0.504	0.001327	0.5077	0.000465	0.5042	0.000457
	S3	0.001415	0.5319	0.001395	0.5316	0.001412	0.5246	0.001381	0.5377	0.001367	0.5339	0.001373	0.5488	0.001368	0.5334	0.001388	0.5384	0.001409	0.5249	0.000448
	S4	0.001484	0.5249	0.001624	0.5429	0.001605	0.5393	0.001638	0.5449	0.001637	0.5463	0.001656	0.5496	0.001638	0.5366	0.001642	0.5443	0.001088	0.5377	0.001075
	S5	0.001365	0.527	0.001291	0.5334	0.001251	0.5286	0.001329	0.5347	0.001259	0.5326	0.001245	0.5463	0.001249	0.5382	0.001253	0.5386	0.000465	0.5235	0.001252
1.5x3mm SC	S1	0.000978	0.5415	0.00097	0.5433	0.000971	0.5369	0.000919	0.5465	0.000925	0.5439	0.000956	0.552							
	S2	0.00092	0.533	0.000934	0.5402	0.000939	0.5365	0.000936	0.5455	0.000927	0.5421	0.000906	0.5589	0.000897	0.5384	0.000857	0.544			
	S3	0.000731	0.538	0.00086	0.5508	0.000875	0.5486	0.000882	0.5504	0.000852	0.5531	0.00084	0.5576	0.000848	0.5177					
	S4	0.000975	0.523	0.000971	0.5286	0.000976	0.5243	0.000919	0.5328	0.000964	0.5284	0.000929	0.5436	0.000941	0.5282	0.000647	0.5394			
	S5	0.000768	0.5274	0.000757	0.5263	0.000804	0.5245	0.000777	0.534	0.00078	0.5337	0.000767	0.5442	0.000788	0.5378	0.000749	0.5355			
1.5x3mm SC	S1	0.001419	0.5581	0.001252	0.5643	0.001268	0.5469	0.00126	0.5558	0.001316	0.5553	0.001306	0.5674	0.001275	0.5504	0.00125	0.5547	0.001249	0.5423	0.001282
	S2	0.001258	0.546	0.001338	0.5678	0.001314	0.5487	0.001289	0.5567	0.001295	0.559	0.001298	0.5623							
	S3	0.001454	0.5632	0.001427	0.5723	0.001466	0.5609	0.001424	0.5615	0.001412	0.5619	0.001456	0.5746	0.001534	0.5676					
	S4	0.00159	0.5633	0.001581	0.5819	0.00158	0.5711	0.001614	0.5705	0.001535	0.5735	0.001557	0.5804	0.001552	0.5677	0.00161	0.5762			
	S5	0.001293	0.5462	0.001335	0.5601	0.0013	0.5478	0.001323	0.5558	0.001288	0.5537	0.001265	0.5571	0.001303	0.5509	0.001226	0.5525			
PD TEMD-7000	S1	0.000114	0.4797	0.000126	0.5025	0.000131	0.497	0.000128	0.493	0.000129	0.4953	0.000133	0.5036	0.000132	0.4931	0.000129	0.498			
	S2	0.000121	0.4811	0.000115	0.4953	0.000114	0.4863	0.000121	0.4936	0.000118	0.4896	0.000124	0.5032	0.000132	0.4886					
	S3	0.000128	0.481	0.000121	0.4976	0.000122	0.4899	0.000123	0.4889	0.000119	0.4899	0.000125	0.499							
	S4	0.000109	0.4743	0.00011	0.4924	0.000109	0.4843	0.000114	0.49	0.00011	0.4848	0.000109	0.4962	0.00011	0.4846	0.00011	0.4881			
	S5	9.03E-05	0.4627	0.000118	0.4901	0.000115	0.4877	0.000129	0.4937	0.000122	0.4934	0.000123	0.4983	0.00012	0.485	0.000122	0.4972	0.000123	0.4877	0.000118
PD TEMD-7000 coating	S1	0.00012	0.4806	0.000161	0.5088	0.000148	0.4983	0.000154	0.5027	0.000163	0.5031	0.000133	0.5053	0.000137	0.4969	0.000151	0.501	0.000146	0.4947	0.000164
	S2	0.000109	0.4838	0.000155	0.5098	0.000155	0.5041	0.000159	0.503	0.000149	0.5041	0.00016	0.5124	0.000152	0.4877	0.000164	0.5139	0.000166	0.5044	0.000147
	S3	0.00013	0.4817	0.00013	0.4931	0.000135	0.4923	0.000138	0.4967	0.000137	0.4934	0.000131	0.5001	0.000143	0.4986					
	S4	0.000132	0.4836	0.000128	0.4935	0.00016	0.5029	0.000167	0.506	0.000154	0.5047	0.000169	0.5107	0.000166	0.5032	0.000159	0.51			
	S5	0.00013	0.4837	0.000162	0.5081	0.000152	0.4976	0.000161	0.5077	0.000161	0.5054	0.000168	0.5138	0.000159	0.5053	0.000185	0.5137	0.000166	0.5024	

Table Ap. 2 – Measured values for the solar-E-yarns after machine washing and line drying in woven fabric form.

Sample Type	Before wash		After 1 wash		After 2 washes		After 3 washes		After 4 washes		After 5 washes		After 10 washes		After 15 washes		After 20 washes		After 25 washes	
	Isc (A)	Voc (V)	Isc (A)	Voc (V)	Isc (A)	Voc (V)	Isc (A)	Voc (V)	Isc (A)	Voc (V)	Isc (A)	Voc (V)	Isc (A)	Voc (V)	Isc (A)	Voc (V)	Isc (A)	Voc (V)	Isc (A)	Voc (V)
1.5x1.5mm SC Yarn	S1	0.000616	0.536	0.000641	0.54	0.000682	0.5459	0.000628	0.5372	0.000646	0.5363	0.000639	0.534	0.000646	0.5115	0.000645	0.5304	0.000646	0.5456	0.000641
	S2	0.000194	0.5023	0.000185	0.4898	0.000296	0.5156	0.000189	0.4864	0.000196	0.4917	0.000197	0.4874	0.000196	0.4635	0.000204	0.4899	0.0002	0.5016	0.000201
	S3	0.000486	0.5315	0.000528	0.5383	0.000556	0.543	0.000496	0.5261	0.000502	0.5254	0.000508	0.5213	0.000496	0.4887	0.000512	0.5124	0.000495	0.5215	0.000509
	S4	0.000468	0.4886	0.000476	0.494	0.000513	0.4982	0.000471	0.4802	0.000474	0.4855	0.000472	0.4829	0.00047	0.4651	0.000477	0.4855	0.000468	0.4978	0.000465
	S5	0.000485	0.555	0.000461	0.5528	0.000479	0.5554	0.000487	0.5488	0.00048	0.5459	2.01E-08	0.12705	0.000459	0.5265					
1.5x1.5mm SC Yarn with resin	S1	0.000731	0.5699	0.000761	0.5681	0.00079	0.5744	0.000762	0.5684	0.000753	0.5629	0.000749	0.5598	0.000777	0.5576	0.000765	0.5611			
	S2	0.000762	0.568	0.000803	0.571	0.000797	0.5708	0.000809	0.5673	0.000814	0.5629	0.00082	0.5654	0.00081	0.5569	0.000804	0.5599	0.000802	0.5752	0.000803
	S3	0.00075	0.5631	0.000784	0.5628	0.000788	0.5663	0.000788	0.5624	0.000797	0.5584	0.000784	0.5572	0.000799	0.5538	0.000783	0.5565	0.000795	0.5695	
	S4	0.000536	0.2616	0.00054	0.2739	0.00054	0.2717	0.000541	0.2724	0.000551	0.276	0.000547	0.2751	0.000572	0.2948	0.00058	0.2991	0.000551	0.2953	0.000587
	S5	0.000641	0.5371	0.000683	0.5384	0.000698	0.5419	0.000666	0.5345	0.000696	0.5301	0.000659	0.5282	0.000666	0.5185	0.000671	0.5218	0.000692	0.5392	0.000698
1.5x3mm SC Yarn	S1	0.000736	0.5333	0.000746	0.532	0.000744	0.532	0.00076	0.53	0.00076	0.5257	0.000759	0.5277	0.00074	0.5052	0.000751	0.5179	0.00075	0.532	0.000732
	S2	0.000668	0.53	0.000683	0.5281	0.000699	0.5315	0.000694	0.5268	0.0007	0.5197	0.000701	0.5197	0.000686	0.488	0.00067	0.5129	0.000695	0.53	0.000684
	S3	0.000893	0.5538	0.000857	0.5548	0.00087	0.5546	0.000846	0.5485	0.000866	0.5448	0.000842	0.5467	0.000845	0.5304	0.000842	0.5408			
	S4	0.000708	0.5372	0.0007	0.5338	0.000689	0.5367	0.000688	0.532	0.000692	0.5255	0.000689	0.526	0.000693	0.5087	0.000673	0.5203			
	S5	0.0007	0.5467	0.000711	0.549	0.000696	0.5479	0.000698	0.5453	0.000702	0.5391	0.000691	0.5387	0.000683	0.5273	0.000685	0.534	0.000683	0.546	0.000676
1.5x3mm SC Yarn with resin	S1	0.001531	0.5649	0.001488	0.5671	0.001552	0.5689	0.001534	0.5638	0.001579	0.5576	0.00156	0.5593	0.001568	0.5547	0.001577	0.5573	0.001543	0.5718	0.001519
	S2	0.001452	0.5673	0.001453	0.567	0.001425	0.5669	0.001461	0.5656	0.001467	0.5612	0.001451	0.5594	0.001424	0.5431					
	S3	0.001238	0.5409	0.001286	0.5496	0.001312	0.5465	0.001288	0.5442	0.001293	0.5372	0.001272	0.5377							
	S4	0.001376	0.5654	0.001413	0.5652	0.001426	0.5653	0.001416	0.5652	0.001433	0.557	0.001402	0.557	0.001421	0.5478	0.001409	0.5541	0.001407	0.5687	0.001406
	S5	0.00126	0.5573	0.001276	0.5623	0.001297	0.5595	0.00132	0.5536	0.001289	0.5445	0.00126	0.5438	0.00129	0.5319	0.001259	0.5372	0.001277	0.5543	0.00127
PD TEMD-7000 Yarn	S1	7.2E-05	0.4639	7.54E-05	0.4638	7.69E-05	0.4667	7.58E-05	0.4625	7.6E-05	0.4633	7.51E-05	0.4567	7.49E-05	0.4564	7.53E-05	0.4617	7.72E-05	0.4731	7.65E-05
	S2	0.000128	0.4914	0.000132	0.4954	0.000131	0.4922	0.000132	0.4908	0.00013	0.4871	0.000127	0.4832	0.000129	0.4856	0.000132	0.4908	0.000134	0.5026	0.000133
	S3	9.78E-05	0.4802	0.000118	0.4859	0.000121	0.4914	0.000119	0.488	0.000114	0.482	0.000113	0.4771	0.000126	0.4819	0.000105	0.4767	0.000112	0.491	0.000113
	S4	0.000132	0.4922	0.000156	0.5035	0.00016	0.505	0.000155	0.4981	0.000152	0.4943	0.000152	0.4951	0.000157	0.4942	0.000155	0.4989	0.000126	0.5067	
	S5	0.000155	0.5074	0.000159	0.5039	0.000163	0.5108	0.000159	0.5044	0.000143	0.4924	0.000144	0.4926	0.000141	0.4895	0.000149	0.4961			
PD TEMD-7000 Yarn with resin coating	S1	0.000119	0.4845	0.000123	0.4881	0.000114	0.483	0.00013	0.4902	0.000121	0.4766	0.000123	0.479	0.000134	0.4895	0.000132	0.4852	0.00012	0.4906	0.000119
	S2	0.000121	0.4862	0.000144	0.4999	0.000145	0.495	0.000145	0.4953	0.000142	0.4862	0.000141	0.4895	0.000141	0.49					
	S3	0.000114	0.4888	0.000129	0.4902	0.000128	0.4887	0.000129	0.4924	0.000128	0.4818	0.000128	0.4837	0.000128	0.4832	0.00013	0.4849	0.000131	0.4979	0.000128
	S4	0.000114	0.4815	0.000131	0.4931	0.000131	0.4883	0.000131	0.4874	0.000129	0.4791	0.000125	0.4811	0.000132	0.4824	0.000128	0.4836	0.000133	0.4972	0.00013
	S5	0.000164	0.5039	0.000169	0.5042	0.000169	0.502	0.000172	0.5034	0.000166	0.4932	0.000171	0.4963	0.000172	0.4978	0.000173	0.4988	0.000169	0.5099	0.000166

Table Ap3 – Measured values for the solar-E-yarns after hand washing and line drying in woven fabric form.

Yarn sample	Before wash		After 5 wash		After 10 washes		After 15 washes		After 20 washes		After 25 washes		
	Isc (A)	Voc (V)	Isc (A)	Voc (V)	Isc (A)	Voc (V)	Isc (A)	Voc (V)	Isc (A)	Voc (V)	Isc (A)	Voc (V)	
1.5x1.5mm SC Yarn	S1	0.0007	0.544087	0.000715	0.5435	0.000685	0.5414	0.000662	0.5351	0.000629	0.5321	0.000631	0.5339
	S2	0.000673	0.501768	0.000705	0.5054	0.0007	0.5081	0.000702	0.5022	0.000702	0.5017	0.000693	0.5008
	S3	0.000688	0.548733	0.000706	0.5462	0.000711	0.5539	0.000707	0.5455	0.000697	0.5486	0.000686	0.5468
	S4	0.000835	0.562267	0.000888	0.5655	0.000885	0.567	0.000875	0.5648	0.000873	0.5671	0.000865	0.5665
	S5	0.000758	0.529442	0.000768	0.5275	0.000772	0.5342	0.000759	0.5259	0.000745	0.5198	0.000737	0.5174
	S6	0.000749	0.498738	0.000708	0.5082	0.0007	0.508	0.00069	0.5031	0.000681	0.501	0.00066	0.4977
SC Yarn with resin 1.5x3	S1	0.001303	0.563	0.001198	0.5639	0.001173	0.5705	0.001163	0.5665	0.001167	0.5683	0.001135	0.569
	S2	0.001167	0.5519	0.001047	0.558	0.001026	0.5614	0.001021	0.5555	0.001011	0.5491	0.000984	0.5524
	S3	0.001309	0.5479	0.001168	0.5491	0.001153	0.5549	0.001136	0.5425	0.001137	0.5399	0.001097	0.5429
	S4	0.001167	0.5578	0.001044	0.5642	0.001026	0.566	0.001007	0.5566	0.000995	0.5538	0.000972	0.5552
	S5	0.001155	0.5457	0.001037	0.553	0.00103	0.5569	0.001008	0.5455	0.001012	0.5465	0.000995	0.5491
PD TEMD-7000 Yarn	S1	0.00012	0.4869	0.00011	0.4954	0.000118	0.4999	0.000106	0.4914	0.000115	0.4942	0.000113	0.4959
	S2	9.5E-05	0.4713	0.000111	0.4963	0.000109	0.4983	0.00011	0.4931	0.00011	0.4924	0.00011	0.4961
	S3	0.000113	0.4852	0.000111	0.4948	0.000111	0.4976	0.00011	0.4956	0.000109	0.4915	0.00011	0.4948
	S4	0.000121	0.4847	0.000121	0.5007	0.000122	0.5033	0.000115	0.4945	0.00012	0.4968	0.000122	0.5009
	S5	0.000145	0.4984	0.000138	0.5048	0.000139	0.5085	0.000135	0.5051	0.000141	0.5031	0.000137	0.5061
PD TEMD-7000 Yarn with resin coating	S1	0.000169	0.5024	0.000163	0.5136	0.000162	0.5152	0.000159	0.5108	0.000157	0.5101	0.000156	0.5133
	S2	0.000157	0.5006	0.000157	0.5104	0.000155	0.5116	0.000153	0.5092	0.000155	0.5074	0.000153	0.5103
	S3	0.000141	0.4919	0.000159	0.5127	0.000162	0.5148	0.000163	0.5123	0.000162	0.5107	0.00016	0.5151
	S4	0.000173	0.508	0.00017	0.5143	0.000172	0.5175	0.000169	0.5163	0.000169	0.5122	0.000168	0.5157
	S5	0.000103	0.4766	9.65E-05	0.4895	9.53E-05	0.4903	9.48E-05	0.484	9.46E-05	0.4847	9.3E-05	0.4886

Appendix 9 – LabView program for monitoring solar-E-yarns during abrasion tests.

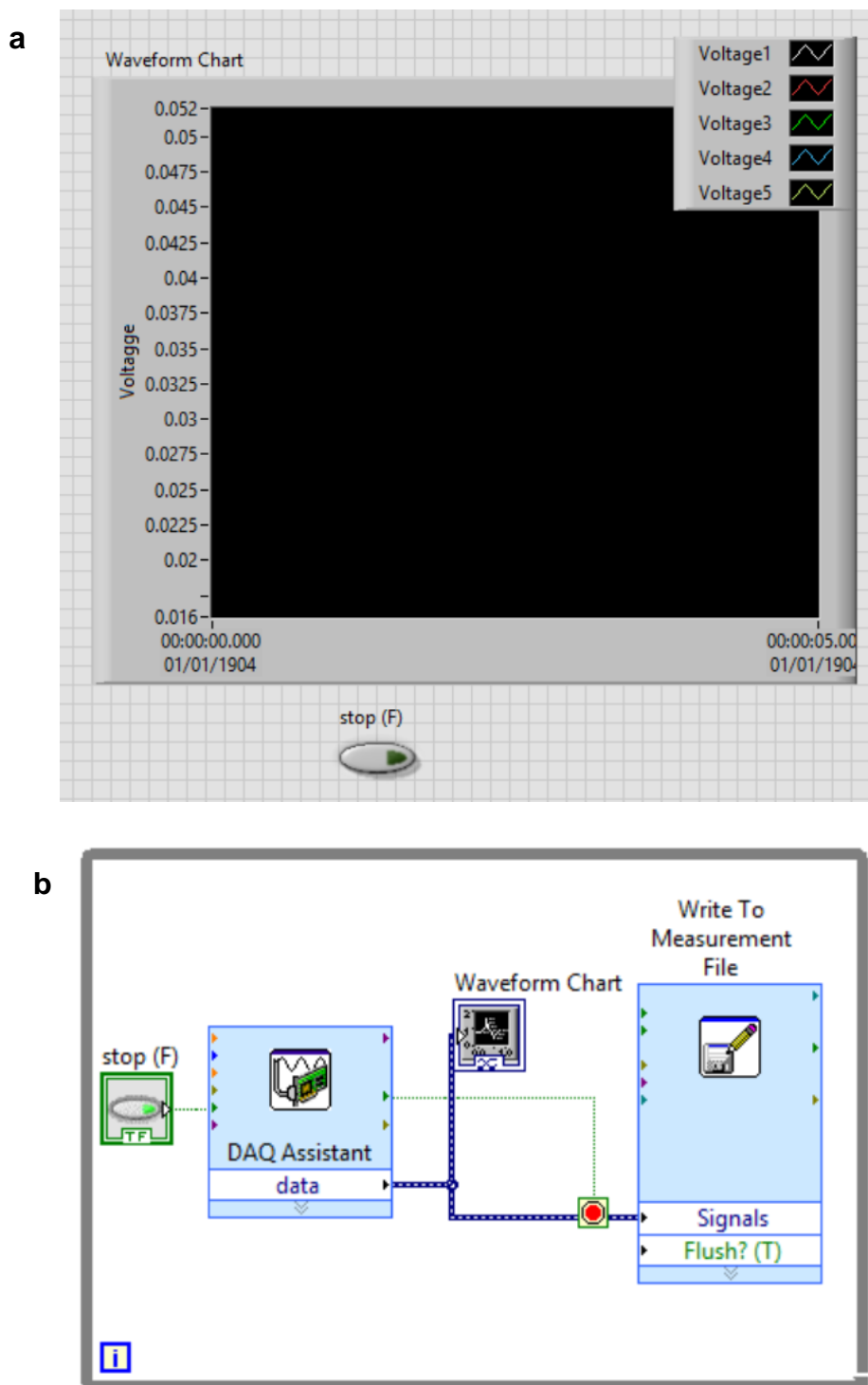


Figure Ap. 9 –Image of the (a) output interface and (b) visual programming code of the LabView program developed for monitoring the voltages of the solar-E-yarns during the abrasion test.

Appendix 10 - Preparation and characterisation of supercapacitor embedded E-yarns.

Ap. 10.1 Basic characterization of supercapacitors

Characterisation of a small-scale supercapacitor (CPH3225A, Seiko Instruments Inc., 11mF, 3.3V, $3.2 \times 2.5 \times 0.9$ mm) was initiated. The super capacitors were soldered onto seven strand Cu wires using reflow soldering with lead-free solder and encapsulated inside of a 3.2 mm diameter resin micro-pod using Dymax 9001E-V3.5 resin.

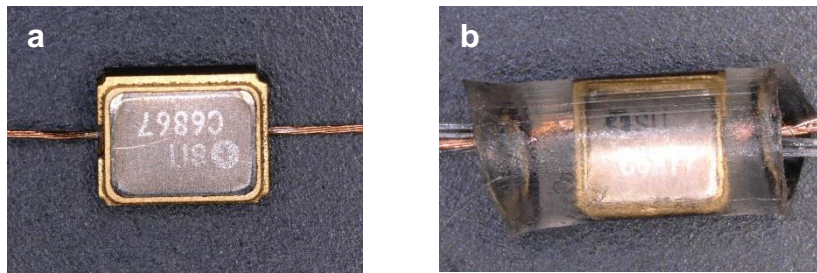


Figure Ap. 10 –Image of the CPH3225A supercapacitors (a) soldered onto seven strand Cu wires and (b) after encapsulating within 3.2mm diameter resin micro-pod.

Measurements were conducted on the maiden supercapacitors and encapsulated supercapacitors. Their charge discharge characteristics were assessed: Charging was conducted by applying a 3V DC voltage and the discharging was conducted through 50Ω resistor.

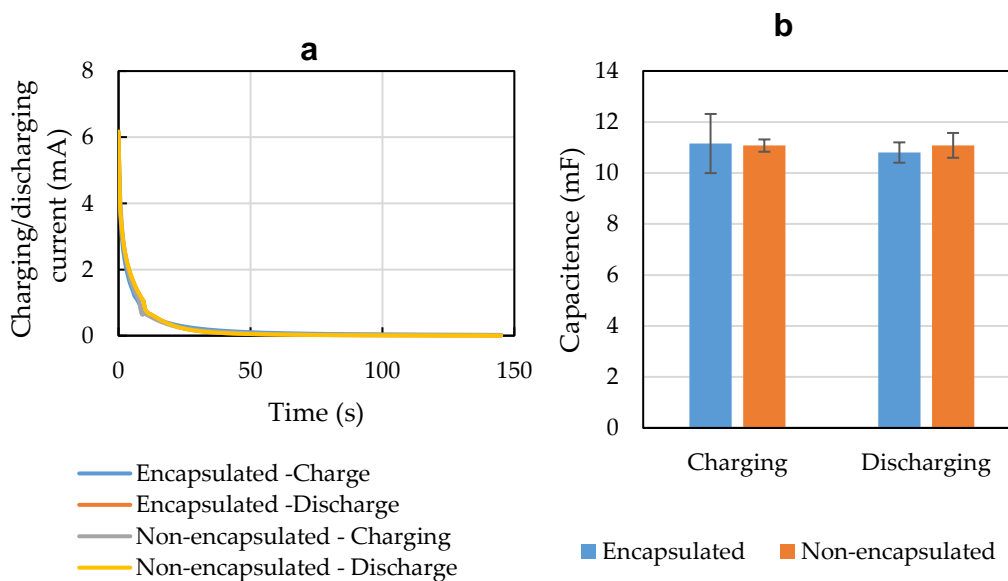


Figure Ap. 11 – (a) Charging and discharging curves for the supercapacitors. (b) Estimated capacitance values for the supercapacitors before and after encapsulating within a resin micro-pod.

Using the charge discharge curves the capacitance (C) of the supercapacitors were estimated using the below equation.

$$C = (\sum It) / \Delta V$$

Where I is the charging/discharging current and ΔV is the charging/discharging voltage difference. The results confirmed (Fig. Ap. 10) that the resin micro-pod had no significant effect on the charging-discharging behaviour or the capacitance.

Ap. 10.2 Supercapacitor embedded e-yarns

To develop an energy storage capability for the solar energy harvesting fabric, supercapacitor embedded textile yarns were fabricated. First, CPH3225A (3.2mm × 2.5 mm) supercapacitors were soldered in parallel onto fine copper wire using a reflow soldering process to create strands including ten supercapacitors each. The gap between two adjacent devices was kept to ~5 mm (see Fig. Ap. 11(a)). The soldered supercapacitors were then individually encapsulated with Dymax 9001-EV 3.5 resin using a silicone tube with a 3.2 mm inner diameter. The micro-pod length was maintained ~5-5.5 mm (see Fig. Ap. 11(b)). A 4 mm diameter fibrous sheath was then used to cover the encapsulated strands using a RIUS knit braiding machine with 4 mm inner-diameter cylinder (8 needles/8 knitting yarns and 6 packing yarns; see Fig. Ap. 11(c)).

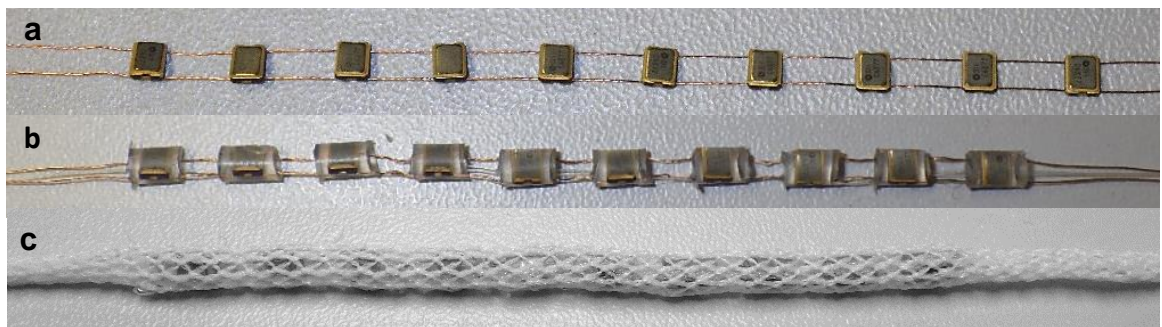


Figure Ap. 12- Supercapacitor embedded textile yarns. (a) Supercapacitors soldered onto copper wires. (b) Supercapacitor strands after the supercapacitors were encapsulated inside of 3.2 mm diameter micro-pods. (c) Supercapacitor embedded textile yarn after covering with a 4 mm diameter fibrous sheath.

Appendix 11 - Data acquisition device built to conduct the field tests.

Ap. 11.1 Hardware

A data acquisition unit was built based on the Teensy 3.5, Arduino compatible, development board (PJRC Electronic Projects) which featured a 32-bit 120 MHz ARM Cortex-M4 processor with floating point unit. All digital pins were 5 V tolerant. The development board comprised of a microSD card slot that allowed for remote data capture and stored.

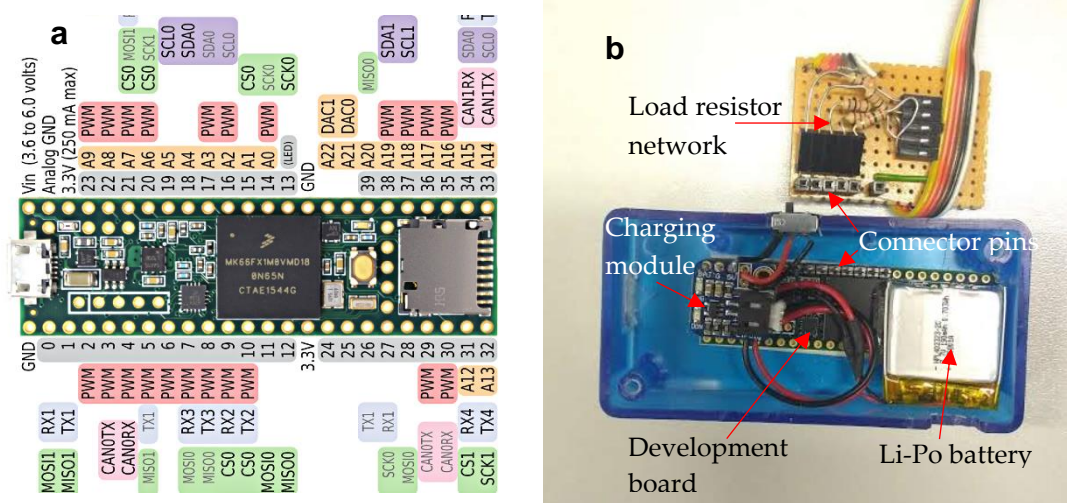


Figure Ap13- (a) Image of the Teensy 3.5 development board with the pinouts. (b) Assembly of the development board, charging module, battery

For powering the data acquisition unit, a Lithium-polymer battery (3.7 V, 190 mAh; Mikroelektronika D.O.O., Serbia) was connected through a charging module (Adafruit LiIon/LiPoly Backpack Add-On for Pro Trinket/ItsyBitsy, Adafruit Industries LLC, USA). The output from each solar fabric module was connected to a 1 k Ω load resistor network and the voltage across each resistor was connected an individual input pin (pins 14-18 were used).

Ap. 11.2 Programming the Teensy 3.5 board

An Arduino 1.8.9 (Arduino LLC, USA) programming platform was employed to configure the analogue data inputs pins 14-18 (A0-A4) and program the data storage onto the micro-SD card (see programming script below).

The board was programmed to capture voltage values from five inputs sequentially in 0.2 s intervals, so that voltage was read from each input at a sample rate of 1 Hz. The program also converted the voltages to current and power values based on the load resistor values. After each reading cycle (every second), a string of data was written to the SD card that contained a time stamp, input channel number, voltage, current, and power values for all five inputs.

The data was stored onto a text file in the below format, that could be transferred to an excel file directly.

0.41	0	0.86	0.87	0.74	1	0.27	0.27	0.07	2	0.56	0.57	0.32	3	1.30	1.32	1.71	4	2.07	6.26	12.94
1351	0	0.85	0.86	0.73	1	0.27	0.27	0.07	2	0.55	0.56	0.31	3	1.30	1.32	1.72	4	2.07	6.26	12.92
2358	0	0.85	0.86	0.73	1	0.27	0.27	0.07	2	0.56	0.57	0.32	3	1.30	1.32	1.71	4	2.07	6.26	12.93
3364	0	0.84	0.85	0.72	1	0.27	0.27	0.07	2	0.56	0.57	0.32	3	1.30	1.32	1.72	4	2.07	6.26	12.94

Time stamp

Data sets for five inputs

Ap. 11.3 Arduino Code

```
#include <SD.h> //libraries
#include <SPI.h>
const int chipSelect = BUILTIN_SDCARD;
double R,V,I,P;
void setup()
{
    analogReadRes(13); //define resolution
    //Serial.begin(9600); //initialize serial
    if (!SD.begin(chipSelect)){
        return;
    }
}
void loop()
{
    String dataString = "";
    dataString += millis();
    dataString += "\t";
    //Serial.println("time stamp");
    for (int analogPin = 0; analogPin < 5; analogPin++)
    {
        int reading = analogRead(analogPin);
        V =(0.0004035*reading + 0.0011938);
        if (analogPin == 0)
        {
```

```
R = 0.998;
}
else if (analogPin == 1)
{
R = 0.9955;
}
else if (analogPin == 2)
{
R = .9889;
}
else if (analogPin == 3)
{
R = 0.3855;
}
else if (analogPin == 4)
{
R = 0.33;
}
I = V/R;
P = V*I;
dataString += analogPin;
dataString += "\t";
dataString += V;
dataString += "\t";
dataString += I;
dataString += "\t";
dataString += P;
dataString += "\t";
delay(200);
}
File dataFile = SD.open("datalog.txt", FILE_WRITE); //Opening the data file
if (dataFile)
{
dataFile.println(dataString);
dataFile.close();
Serial.println(dataString);
}
else
{
}
```

Annexes

Annex 1 - Introduction to wearable devices and E-textiles

1.1 Categorisation of wearable devices

While wearable electronic devices and technologies have many different applications and forms, they share common characteristics; they always stay close to the user's body, collecting data with the aim to improve how users interact with the external environment. The most common classifications of wearables are based on their form factor and end-use. The International Electrotechnical Committee (IEC), which works closely with the industry and academia on providing standardisation for wearable devices, has broadly categorised wearables into accessories, electronic textiles (E-textiles), patchable devices, and implantable devices (International Electrotechnical Committee, 2018). While the vast majority of commercially available devices fit into the accessories category (e.g. wristables, eyewear), devices classified as implantables have only just started to emerge for medical applications. Teslasuit, a start-up company developing smart clothing apparel with haptic feedback, motion capture, climate control and biometric feedback systems has categorised wearable devices (Teslasuit, 2017) based on the physical form-factor, as shown in Fig. An1.1.



Figure An1.1 - Categorisation of wearable devices based on the form proposed by Teslasuit (2017).

The Beecham group has proposed the most widely used categorisation of wearables and IoT (Beecham Research, 2019) based on the industry sectors and application groups (Fig. An1.2). This categorisation broadly covers the applications which are mapped with the relevant features (functions) and form factors (assets).

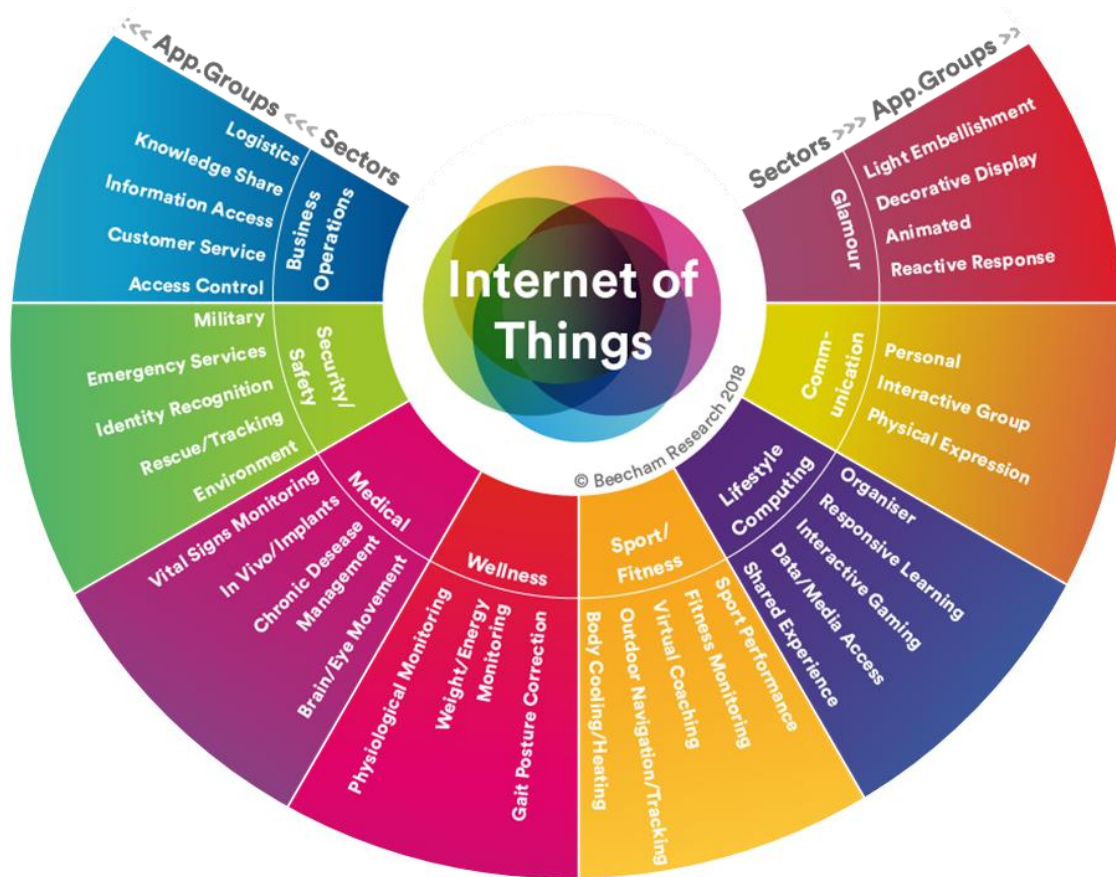


Figure An1.2 - Categorisation of wearable devices based on function and application proposed by Beecham Research (2019).

1.2.3 E-textiles and smart textiles

1.2.3.1 Terminology

The term electronic textiles (commonly abbreviated as E-textiles) is loosely defined as textiles with some form of electronic functionality. E-textiles are often discussed with regards to wearability and their use in for clothing and accessories, however E-textiles have also proven their use in other industries such as automotive (Wagner, 2013; Barmag and Neumag, 2015), furnishing (Postrel, 2017) aerospace and medical textiles

(Coyle and Diamond, 2016). In addition, E-textiles have opened up unimaginable opportunities in energy, protective gear and security fields (Koncar, 2016) where the use of textiles historically had a limited scope. This demonstrates the versatility and practicality of employing textiles as a platform to integrate electronics.

Several other terminologies such as smart textiles, intelligent textiles or interactive textiles can be associated with E-textiles. These can often refer to an intelligent or smart functionality which may not involve adding an electronic functionality with textiles, and hence do not fall under the category of E-textiles. For example, a shape memory polymer textile, although considered a smart textile, does not possess any electronic functionality. The below Venn diagram (Fig. An1.3) illustrates how several related domains overlap within the space of textiles, electronics and functional materials.

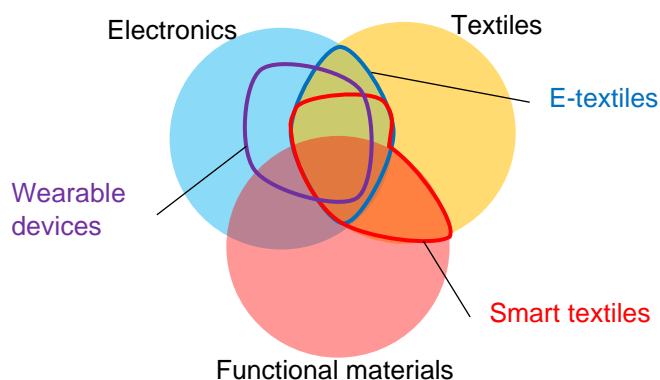


Figure An1.3 - Venn diagram illustrating overlapping domains related to electronics, textiles and functional material.

While many E-textiles can have smart functionality built within the structure of the textile, some E-textiles require constant human interventions to operate, and hence cannot be considered smart. A heated glove which is switched on by the user on-demand is an example for such E-textile device without smart functionality. In contrast to E-textiles, smart textiles are defined as textile structures which can sense and respond to the changes in the environment. Tao (2001) defined smart textiles as intelligent textile structures or fabrics that can sense and react to environmental stimuli, which may be mechanical, thermal, chemical, biological, and magnetic amongst others. Smart textiles are broadly categorized according to the nature of responsiveness to external stimuli; passive smart textiles which can only sense the stimuli, active smart textiles which can

sense and react to stimuli and very smart textiles which can sense, understand external stimuli, and provide adaptive response (Das *et al.*, 2013).

1.2.3.2 Evolution of E-textiles and wearable devices

Historically, textiles embellished with metallic fibres and yarns, which are commonly used in E-textiles have been in existence for over 1000 years. For example, gowns made for royals who lived in Elizabethan era were known to be embroidered with threads wrapped with gold tapes (Járó, 1990). However, due to the absence of active electronic functionality in such garments they are not considered E-textiles. The origin of E-textiles dates back to late 19th century where the first reports of E-textiles were described as “ballet girls with electric lights on the foreheads and batteries concealed in the recesses of their clothing” (The New York Times, 1884). Then in 1911 the first patent disclosing an electrically heated glove was filed by Carron (1911). Between this patent and the mid-1980’s a number of new E-textile innovations were developed including the electric blanket. H. Lee Wainwright saw a fibre-optic lamp and realized he could add animation to apparel. With this inspiration he created the first fibre-optic animated shirt in 1985 (H. Lee Wainwright, 2019). These inventions scattered across almost a century however, could not proliferate wearable device technologies until the inception of wearable computing after 1985.

In the mid-1990s MIT researchers Ed Thorp and Claude Shannon designed a cigarette pack-sized analogy device to improve the odds on roulette wheels (Thorp, 1998) paving the way to the first wearable computers. MIT Media Lab initiated by Steve Mann, Thad Starner and Alex P. Pentland pioneered the field of wearable computing (Starner *et al.*, 1995) in late 20th century. Their vision was to design a networked, multimedia computer that can be worn as clothing or built into the user’s clothes, where power of computing can assist everyday tasks (Starner *et al.*, 1996). Concurrently at Georgia Tech a team led by Jayaraman developed a textile based wearable interface called ‘Wearable Motherboard™’ using woven textile and metal conductive wires. Further, they proposed a detailed framework for designing wearable systems, where performance requirements were mapped to design parameters (Gopalsamy *et al.*, 1999). Another team at the MIT Media Lab explored ways to harmonize wearable computers to clothing in a soft and graceful manner by investigating the possibility of integrating digital

electronics with conductive fabrics using embroidery techniques (Post *et al.*, 2000) to develop E-textiles ranging from embroidered keyboards to fashion technology garments. As a result, one of the first commercially available wearable microcontrollers for E-textile applications, the Lilypad Arduino, was created by Leah Buechley at the MIT Media Lab in 2007 (Adafruit, 2017). Within the space of a century, E-textiles with primitive functionality has transformed into objects of intelligence and cognition. The field of E-textiles have seen unparalleled progress with regards to form and functionality, thanks to the advancements in electronics, material science, information technology and textile technology as well as the growing consumer interest to embrace wearable devices. Today, E-textiles are not only intelligent and miniaturised, but also, have started to look and feel similar to regular textiles and clothing.

1.2.3.3 Categorisation of E-textiles: a textiles perspective

From a textile perspective, components of E-textile systems can be broadly categorized into three generations based on its form (Hughes-Riley, Dias and Cork, 2018) as shown in Table An1.1. This categorisation is highly relevant in assessing the wearability and normalcy of E-textiles. Regardless of the degree of complexity and intelligence built into clothing, wearability and normalcy of E-textiles can play a decisive role in their adoption by users, as most users would favour a familiar and normal textile appearance. Users may also not be willing to compromise on the fit, mobility and comfort (tactile, thermal) delivered by regular textile fabrics (Cassill, Carroll and Suh, 2010).

1.2.3.4 Components of E-textile systems

The functionality and the level of intelligence in an E-textiles system can offer a wide range from user controlled reactive systems to fully autonomous adaptive systems. Depending on the complexity of the desired E-textile system the nature of the components in it will vastly vary as shown in Fig. An1.4. While the above is valid for any wearable system in general, focus will be given for E-textiles based wearable systems in this work. A typical E-textile system can comprise of one or more components outlined below.

Conductive pathways

Conductive pathways can be defined as electrically conductive bus bars running between other components within a textile. They can either transmit power or communicate analogue or digital signals between other components.

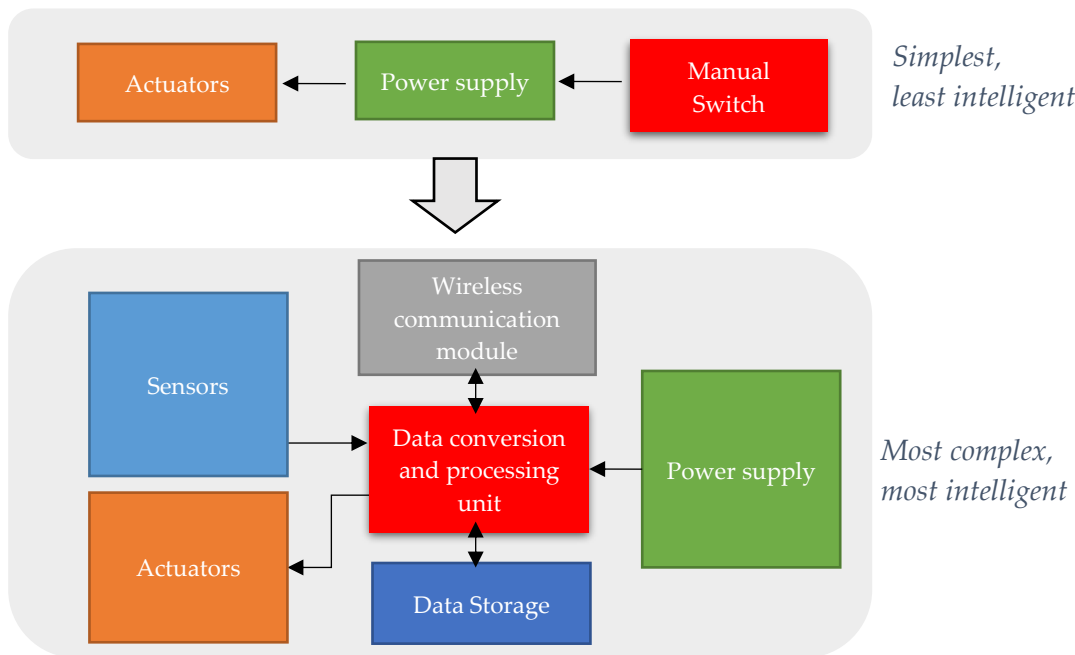


Figure An1.4 - Components of an e-textiles system based on the level of complexity and intelligence.

Actuators

Actuators in the context of E-textiles can be defined as micro-devices generating a mechanical, audio, visual or electro-magnetic output in response to an electrical input. These are mostly prefabricated micro-devices attached onto textiles.

Power supply

Power supplies provide electrical energy required for the functioning of the electronic devices in an E-textiles system. These can comprise of a combination of electrical energy storage, energy conversion or ambient energy harvesting devices. A power supply is an essential component for a wearable system, regardless of its complexity or function.

Sensors

Sensors selectively and quantitatively detect an external stimulus to induce a

Table An1.1 - Generations of E-textiles and their

	1st generation	2nd generation	3rd generation
Description	<i>Electronic components superficially attached onto the surface of fabrics and clothing.</i>	<i>Electronic functionality incorporated in the textile structure during fabric manufacture.</i>	<i>Electronic functionality embedded into yarns (E-yarns)</i>
Examples	<i>Conventional electronic components. Printed electronic components. Flexible PCBs. Functional thin films.</i>	<i>Electrodes and conductive pathways in knitted and woven fabrics.</i>	<i>LED E-yarns, Thermistor E-yarns.</i>
Fabrication techniques	<i>Conventional electronics device fabrication. Printing. Chemical surface functionalisation or etching.</i>	<i>Incorporation of fine metal wires and/or conductive yarns during the knitting and weaving processes.</i>	<i>Chemical functionalisation or etching. Co-extrusion of functional layers. E-yarn technology.</i>
Integration techniques	<i>Adhesive bonding, stitching, lamination. Printing. Various mechanical fastening techniques such as press studs, magnetic fasteners mechanical plugs and clips. Stitching, embroidery or adhesive bonding of the electronic components onto the textile.</i>	<i>Insertion of conductive yarns and/or metal wires as the weft during weaving. Use of intarsia techniques to create conductive areas during knitting.</i>	<i>Weaving, knitting, stitching or embroidery.</i>
Advantages	<i>Established development and manufacturing, simple to integrate. High level of intelligence wide range of functionality available.</i>	<i>Established development and manufacturing. Some normalcy and comfort for wearable applications. However, the electrically conductive areas are visible on the fabric</i>	<i>Lightweight, and discrete. Excellent normalcy and comfort for wearable applications. Potential for high level of functionality and durability.</i>
Disadvantages	<i>Heavy and bulky. Poor normalcy and comfort. Poor shear behaviour. Poor durability of the permanently integrated systems.</i>	<i>Limited functionality and low levels of intelligence.</i>	<i>Manufacturing technology commercially not available.</i>

proportional change in electrical properties such as resistance, inductance, and capacitance, or generate an electric current or a voltage. Textile sensors are amongst the most investigated components for wearable systems.

Data conversion and processing unit

The complexity and functionality of a data conversion and processing unit can vary from basic signal amplification or switching to a level of multi-tasking including signal conversion and processing, computing, power management, and graphical representation.

Data storage

These are the memory devices used to store collected raw data, processed data, or programs containing instructions for the autonomous function of the system. These could be a combination of ROM, RAM and removable flash memory.

Wireless communication module

Wireless communication modules send and receive data and information between the E-textile system and an external system. The external system may be in close proximity (mobile phone) or distant (communication satellites) and may have direct network connectivity (e.g. internet connectivity via a telecommunication network). The frequency of connection, data transfer rate, maximum coverage distance will have implications on the size of the module and power requirement, and therefore it is important to optimize the design specification for the communication module for a given application.

Initially, E-textiles were constructed by attaching electronic components onto the surface of textiles, or into concealed pockets, affecting both the comfort and aesthetics of the textile (Fernández-Caramés *et al.*, 2018). This led to investigations into methodologies for integrating electronics within textiles to create wearable systems that retain their tactile properties (drapability, softness) and other properties which are critical to the comfort of the wearer (breathability, moisture transfer characteristics). This led to the next generation of E-textiles where conductive metal wires or conductive yarns integrated with the structure of textile fabric; these could be used to create interconnections (Stoppa and Chiolerio, 2014), textile heaters (Mbise, Dias and Hurley, 2015), and electrode-based sensors (Toprakci & Ghosh 2015; Brun *et al.* (2009) introduced the "Diabolo" process with

an aim to directly connect a semiconductor chip assembly to conductive wires that can be woven into fabrics. The same diabolio approach was utilized in the European project PASTA (Simon *et al.*, 2012) to integrate RFID and lighting functionality at yarn level. Zysset *et al.* investigated the integration of digital silicon based temperature sensors (2010) and LEDs (2012) onto weavable textile bands. Electronic yarns (E-yarns) have seen small electronic chips integrated into the core of a textile yarn (Dias and Fernando, 2009; Dias and Rathnayake, 2016) to embed electronic functionality within textile yarns as mentioned previously. Recent research has seen electronic components integrated at fibre extrusion level (Münzenrieder *et al.*, 2017; Kwon *et al.*, 2018; Rein *et al.*, 2018), however the practicality of these solutions will depend on their ability to withstand fibre drawing process and robustness during washing and wearing.

Commercially available E-textiles and systems proposed in the literature are not complete textile systems, instead focus on one or few textiles embedded aspect such as sensing or actuation. Ideally, all the components of an E-textile system require to be fully textile based (third generation) to provide the greatest comfort and wearability to the user. However, even the most advanced E-textiles based wearable systems, currently available commercially are limited to either sensors or actuators only. The power supply, data processing, storage, and wireless communication are provided by an external hardware module, which is often rigid and bulky, compromising the appearance and the wearer's comfort.

References

- Adafruit (2017) *Celebrating 10 Years of the Lilypad Arduino #WearableWednesday #wearabletech #Arduino #tech* « Adafruit Industries – Makers, hackers, artists, designers and engineers! Available at: <https://blog.adafruit.com/2017/10/11/celebrating-10-years-of-the-lilypad-arduino/> (Accessed: 2 March 2019).
- Barmag, O. and Neumag, O. (2015) *The car of the future will be wearing more textiles*.
- Beecham Research (2019) *Wearable Technology Application Chart - Beecham Research*. Available at: <http://www.beechamresearch.com/download.aspx?id=36> (Accessed: 28 February 2019).
- Brun, J. *et al.* (2009) 'Packaging and wired interconnections for insertion of

miniaturized chips in smart fabrics', in *2009 European Microelectronics and Packaging Conference*, pp. 2–6.

Carron., A. I. (1911) 'Electrically heated gloves'. Available at: <https://patents.google.com/patent/US1011574A/en> (Accessed: 1 March 2019).

Cassill, N., Carroll, K. and Suh, M. (2010) 'Critical Review on Smart Clothing Product Development', *Journal of Textile and Apparel Technology and Management (JTATM)*, 6(4), pp. 1–18.

Coyle, S. and Diamond, D. (2016) 'Medical applications of smart textiles', *Advances in Smart Medical Textiles*. Woodhead Publishing, pp. 215–237. doi: 10.1016/B978-1-78242-379-9.00010-4.

Das, S. C. *et al.* (2013) 'Smart Textiles- New Possibilities in Textile Engineering', 2013(November), pp. 1–3.

Dias, T. and Fernando, A. (2009) 'Operative devices installed in yarns'. US20090139198. Available at: <https://www.google.com/patents/US20090139198>.

Dias, T. K. and Rathnayake, A. (2016) 'Electronically functional yarns'. WO2016038342A1. Available at: <https://www.google.com/patents/WO2016038342A1?cl=en>.

Fernández-Caramés, T. *et al.* (2018) 'Towards The Internet-of-Smart-Clothing: A Review on IoT Wearables and Garments for Creating Intelligent Connected E-Textiles', *Electronics*. Multidisciplinary Digital Publishing Institute, 7(12), p. 405. doi: 10.3390/electronics7120405.

Gopalsamy, C. *et al.* (1999) 'The Wearable Motherboard?: The first generation of adaptive and responsive textile structures (ARTS) for medical applications', *Virtual Reality*. Springer-Verlag, 4(3), pp. 152–168. doi: 10.1007/BF01418152.

H. Lee Wainwright (2019) *The Grandfather of E-Textiles* | H. Lee Wainwright. Available at: <http://www.hleewainwright.com/> (Accessed: 2 March 2019).

Hughes-Riley, T., Dias, T. and Cork, C. (2018) 'A Historical Review of the Development of Electronic Textiles', *Fibers*. Multidisciplinary Digital Publishing Institute, 6(2), p. 34. doi: 10.3390/fib6020034.

International Electrotechnical Committee (2018) *Strategic business plan -Wearable*

electronic devices and technologies-SMB/6488/SBP. Available at:

<https://www.iec.ch/public/miscfiles/sbp/124.pdf>.

Járó, M. (1990) 'Gold embroidery and fabrics in europe: XI – XIV centuries', *Gold Bulletin*. Springer-Verlag, 23(2), pp. 40–57. doi: 10.1007/BF03214711.

Koncar, V. (2016) 'Introduction to smart textiles and their applications', in Koncar, V. (ed.) *Smart Textiles and their Applications*. 1st edn. Oxford: Woodhead Publishing (Woodhead Publishing Series in Textiles), pp. 1–8. doi: <https://doi.org/10.1016/B978-0-08-100574-3.00001-1>.

Kwon, S. *et al.* (2018) 'Weavable and Highly Efficient Organic Light-Emitting Fibers for Wearable Electronics: A Scalable, Low-Temperature Process', *Nano Letters*. American Chemical Society, 18(1), pp. 347–356. doi: 10.1021/acs.nanolett.7b04204.

Mbise, E., Dias, T. and Hurley, W. (2015) 'Design and manufacture of heated textiles', *Electronic Textiles*. Woodhead Publishing, pp. 117–132. doi: 10.1016/B978-0-08-100201-8.00007-2.

Münzenrieder, N. *et al.* (2017) 'Oxide Thin-Film Transistors on Fibers for Smart Textiles', *Technologies*. Multidisciplinary Digital Publishing Institute, 5(2), p. 31. doi: 10.3390/technologies5020031.

Post, E. R. *et al.* (2000) 'E-broidery: design and fabrication of textile-based computing', *IBM Systems Journal*, pp. 840–860. doi: 10.1147/sj.393.0840.

Postrel, V. (2017) *E-Textiles & Interiors*. Available at: <https://vpostrel.com/articles/e-textiles-interiors> (Accessed: 1 March 2019).

Rein, M. *et al.* (2018) 'Diode fibres for fabric-based optical communications', *Nature*. Springer US, 560(7717), pp. 214–218. doi: 10.1038/s41586-018-0390-x.

Simon, E. P. *et al.* (2012) 'Development of a multi-terminal crimp package for smart textile integration', in *2012 4th Electronic System-Integration Technology Conference*. IEEE, pp. 1–6. doi: 10.1109/ESTC.2012.6542057.

Starner, T. *et al.* (1995) *Wearable Computing and Augmented Reality*. Available at: <https://pdfs.semanticscholar.org/c04a/eb6910c8d0e7cae03afdaa38120b449fdacf.pdf> (Accessed: 2 March 2019).

Starner, T. *et al.* (1996) *Augmented Reality Through Wearable Computing*. Available at:

<https://www.cc.gatech.edu/~thad/p/journal/augmented-reality-through-wearable-computing.pdf> (Accessed: 2 March 2019).

Stoppa, M. and Chiolerio, A. (2014) 'Wearable Electronics and Smart Textiles: A Critical Review', *Sensors*. doi: 10.3390/s140711957.

Tao, X. (2001) 'Smart technology for textiles and clothing – introduction and overview', in Tao, X. (ed.) *Smart Fibres, Fabrics and Clothing*. Woodhead Publishing, pp. 1–6. doi: 10.1533/9781855737600.1.

Teslasuit (2017) *Detailed wearables classification by Teslasuit team* | Teslasuit blog.

Available at: <https://teslasuit.io/blog/wearables/detailed-wearables-classification-by-teslasuit-team> (Accessed: 28 February 2019).

The New York Times (1884) *Electric Girls*, *The New York Times*. Available at: <https://www.nytimes.com/1884/04/26/archives/electric-girls.html>.

Thorp, E. O. (1998) 'The invention of the first wearable computer', in *Digest of Papers. Second International Symposium on Wearable Computers (Cat. No.98EX215)*. IEEE Comput. Soc, pp. 4–8. doi: 10.1109/ISWC.1998.729523.

Toprakci, H. A. K. and Ghosh, T. K. (2015) 'Textile Sensors', in *Handbook of Smart Textiles*. Singapore: Springer Singapore, pp. 357–379. doi: 10.1007/978-981-4451-45-1_37.

Wagner, M. (2013) 'Automotive applications of smart textiles', *Multidisciplinary Know-How for Smart-Textiles Developers*. Woodhead Publishing, pp. 444–467. doi: 10.1533/9780857093530.3.444.

Zysset, C. *et al.* (2010) 'Woven electronic textiles: An enabling technology for health-care monitoring in clothing', *Proc. 5th Int. Workshop Ubiquit. Health Wellness*, pp. 1–4.

Available at:

http://www.researchgate.net/publication/228905737_Woven_Electronic_Textiles_An_Enabling_Technology_for_Health-Care_Monitoring_in_Clothing/file/9c960527a7a4f82fa2.pdf.

Zysset, C. *et al.* (2012) 'Integration Method for Electronics in Woven Textiles', *IEEE Transactions on Components, Packaging and Manufacturing Technology*, 2(7), pp. 1107–1117. doi: 10.1109/TCPMT.2012.2189770.

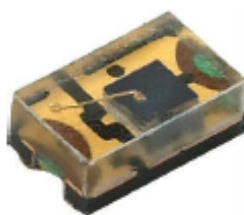
Annex 2 – Full specifications of the photodiodes

2.1 TEMD 7000×01 photodiode


www.vishay.com
TEMD7000X01

Vishay Semiconductors

Silicon PIN Photodiode



DESCRIPTION

TEMD7000X01 is a high speed and high sensitive PIN photodiode. It is a miniature surface mount device (SMD) including the chip with a 0.23 mm² sensitive area detecting visible and near infrared radiation.

FEATURES

- Package type: surface mount
- Package form: 0805
- Dimensions (L x W x H in mm): 2 x 1.25 x 0.85
- Radiant sensitive area (in mm²): 0.23
- High photo sensitivity
- High radiant sensitivity
- Suitable for visible and near infrared radiation
- Fast response times
- Angle of half sensitivity: $\varphi = \pm 60^\circ$
- Floor life: 168 h, MSL 3, according to J-STD-020
- Lead (Pb)-free reflow soldering
- AEC-Q101 qualified
- Material categorization: for definitions of compliance please see www.vishay.com/doc?99912

AUTOMOTIVE


RoHS
COMPLIANT
HALOGEN
FREE
GREEN
(Pb-free)

APPLICATIONS

- High speed photo detector

PRODUCT SUMMARY

COMPONENT	I_{rs} (μA)	φ (deg)	$\lambda_{0.1}$ (nm)
TEMD7000X01	3	± 60	350 to 1120

Note

- Test conditions see table "Basic Characteristics"

ORDERING INFORMATION

ORDERING CODE	PACKAGING	REMARKS	PACKAGE FORM
TEMD7000X01	Tape and reel	MOQ: 3000 pcs, 3000 pcs/reel	0805

Note

- MOQ: minimum order quantity

ABSOLUTE MAXIMUM RATINGS ($T_{amb} = 25^\circ\text{C}$, unless otherwise specified)

PARAMETER	TEST CONDITION	SYMBOL	VALUE	UNIT
Reverse voltage		V_R	60	V
Power dissipation	$T_{amb} \leq 25^\circ\text{C}$	P_V	215	mW
Junction temperature		T_J	100	$^\circ\text{C}$
Operating temperature range		T_{amb}	-40 to +100	$^\circ\text{C}$
Storage temperature range		T_{stg}	-40 to +100	$^\circ\text{C}$
Soldering temperature	Acc. reflow solder profile fig. 8	T_{sd}	260	$^\circ\text{C}$
Thermal resistance junction / ambient	Acc. J-STD-051	R_{thJA}	270	K/W



www.vishay.com

TEM7000X01

Vishay Semiconductors

BASIC CHARACTERISTICS ($T_{amb} = 25\text{ }^{\circ}\text{C}$, unless otherwise specified)						
PARAMETER	TEST CONDITION	SYMBOL	MIN.	TYP.	MAX.	UNIT
Forward voltage	$I_F = 50\text{ mA}$	V_F		1		V
Breakdown voltage	$I_R = 100\text{ }\mu\text{A}$, $E = 0$	$V_{(BR)}$	60			V
Reverse dark current	$V_R = 10\text{ V}$, $E = 0$	I_{r0}		1	3	nA
Diode capacitance	$V_R = 0\text{ V}$, $f = 1\text{ MHz}$, $E = 0$	C_D		4		pF
	$V_R = 5\text{ V}$, $f = 1\text{ MHz}$, $E = 0$	C_D		1.3		pF
Open circuit voltage	$E_0 = 1\text{ mW/cm}^2$, $\lambda = 950\text{ nm}$	V_o		350		mV
Temperature coefficient of V_o	$E_0 = 1\text{ mW/cm}^2$, $\lambda = 950\text{ nm}$	TK_{V_o}		-2.6		mV/K
Short circuit current	$E_0 = 1\text{ mW/cm}^2$, $\lambda = 950\text{ nm}$	I_k		3		μA
Temperature coefficient of I_k	$E_0 = 1\text{ mW/cm}^2$, $\lambda = 950\text{ nm}$	TK_{I_k}		0.1		%/K
Reverse light current	$E_0 = 1\text{ mW/cm}^2$, $\lambda = 950\text{ nm}$, $V_R = 5\text{ V}$	I_{r2}	2.4	3	3.6	μA
Angle of half sensitivity		φ		± 60		deg
Wavelength of peak sensitivity		λ_p		900		nm
Range of spectral bandwidth		$\lambda_{0.1}$		350 to 1120		nm
Rise time	$V_R = 10\text{ V}$, $R_L = 1\text{ k}\Omega$, $\lambda = 820\text{ nm}$	t_r		100		ns
Fall time	$V_R = 10\text{ V}$, $R_L = 1\text{ k}\Omega$, $\lambda = 820\text{ nm}$	t_f		100		ns

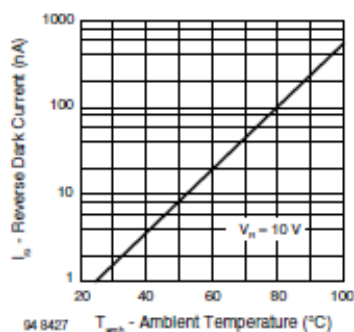
BASIC CHARACTERISTICS ($T_{amb} = 25\text{ }^{\circ}\text{C}$, unless otherwise specified)

Fig. 1 - Reverse Dark Current vs. Ambient Temperature

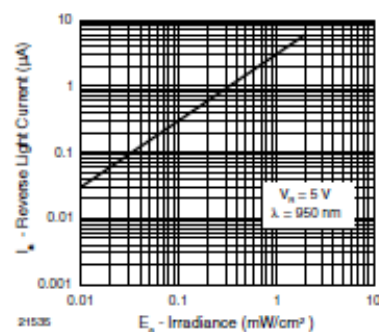


Fig. 3 - Reverse Light Current vs. Irradiance

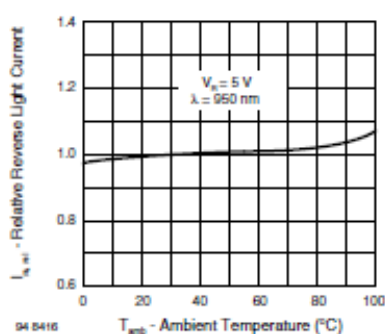


Fig. 2 - Relative Reverse Light Current vs. Ambient Temperature

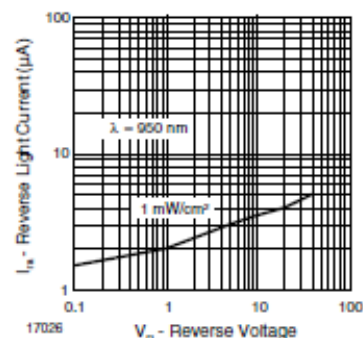


Fig. 4 - Reverse Light Current vs. Reverse Voltage


www.vishay.com

TEMD7000X01

Vishay Semiconductors

REFLOW SOLDER PROFILE

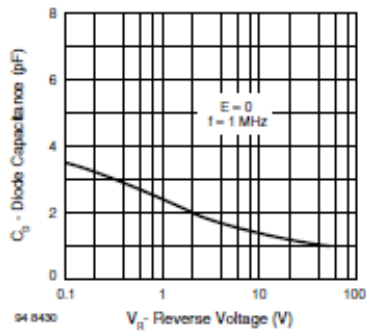


Fig. 5 - Diode Capacitance vs. Reverse Voltage

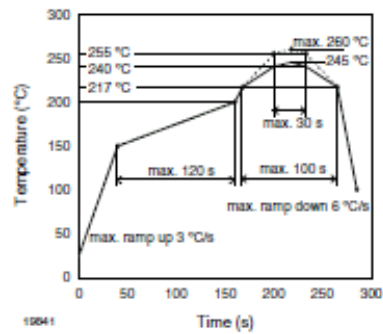


Fig. 8 - Lead (Pb)-free Reflow Solder Profile acc. J-STD-020

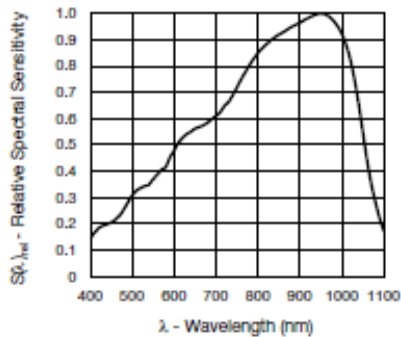


Fig. 6 - Relative Spectral Sensitivity vs. Wavelength

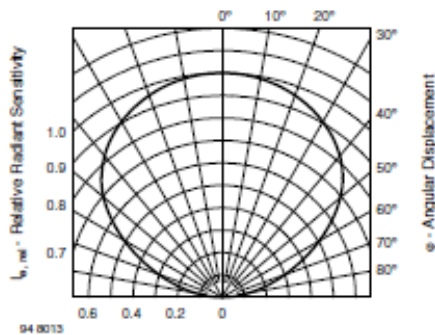


Fig. 7 - Relative Radiant Sensitivity vs. Angular Displacement

DRYPACK

Devices are packed in moisture barrier bags (MBB) to prevent the products from moisture absorption during transportation and storage. Each bag contains a desiccant.

FLOOR LIFE

Floor life (time between soldering and removing from MBB) must not exceed the time indicated on MBB label:

Floor life: 168 h

Conditions: $T_{amb} < 30\text{ °C}$, $RH < 60\%$

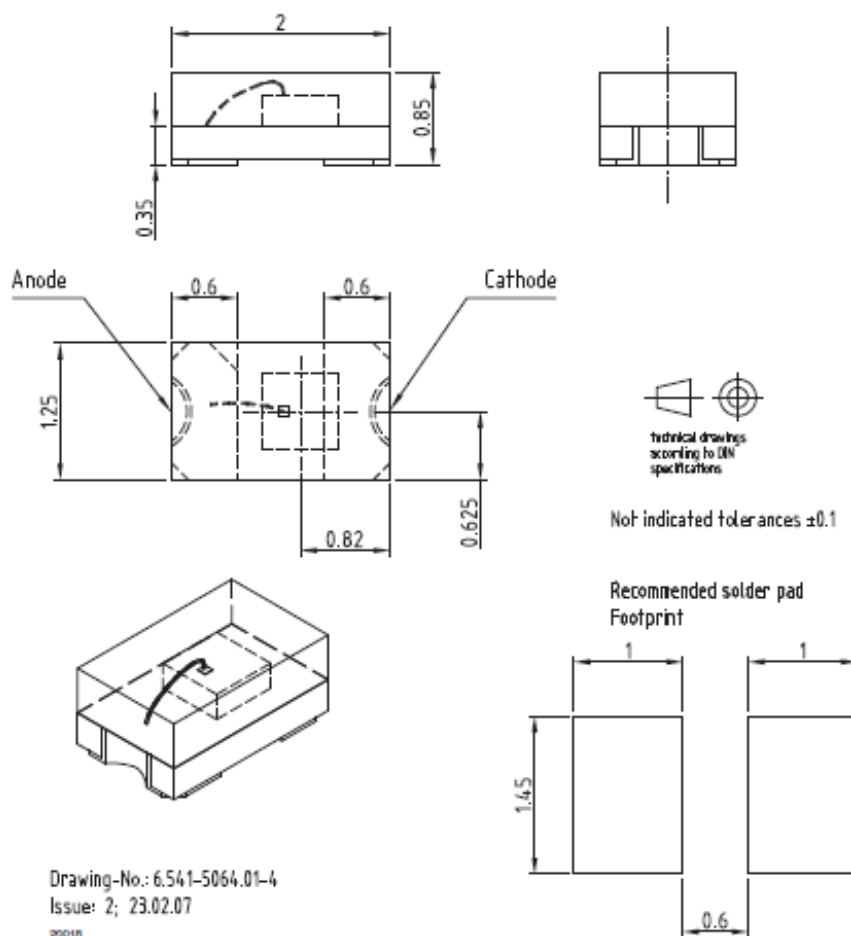
Moisture sensitivity level 3, according to J-STD-020.

DRYING

In case of moisture absorption devices should be baked before soldering. Conditions see J-STD-020 or label. Devices taped on reel dry using recommended conditions 192 h at $40\text{ °C} (+5\text{ °C})$, $RH < 5\%$.


www.vishay.com
TEMD7000X01

Vishay Semiconductors

PACKAGE DIMENSIONS in millimeters

Rev. 1.6, 18-Feb-15

4

Document Number: 81951

For technical questions, contact: detectortechsupport@vishay.com

THIS DOCUMENT IS SUBJECT TO CHANGE WITHOUT NOTICE. THE PRODUCTS DESCRIBED HEREIN AND THIS DOCUMENT
ARE SUBJECT TO SPECIFIC DISCLAIMERS, SET FORTH AT www.vishay.com/doc291000

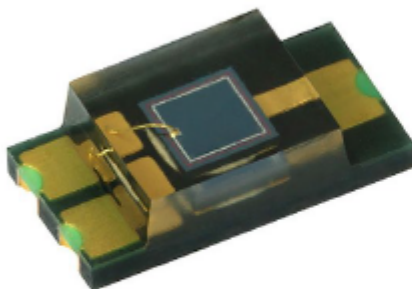
2.2 VEMD 6060×01 photodiode


www.vishay.com

VEMD6060X01

Vishay Semiconductors

Silicon PIN Photodiode



DESCRIPTION

VEMD6060X01 is a high speed and high sensitive PIN photodiode with excellent I_{ra} linearity. It is a small surface mount device (SMD) including the chip with a 0.85 mm² sensitive area detecting visible and near infrared radiation.

FEATURES

- Package type: surface mount
- Package form: 1206
- Dimensions (L x W x H in mm): 4 x 2 x 1.05
- Radiant sensitive area (In mm²): 0.85
- High photo sensitivity
- High radiant sensitivity
- Excellent I_{ra} linearity
- Suitable for visible and near Infrared radiation
- Fast response times
- Angle of half sensitivity: $\varphi = \pm 70^\circ$
- Floor life: 72 h, MSL 4, according to J-STD-020
- Lead (Pb)-free reflow soldering
- AEC-Q101 qualified
- Material categorization: for definitions of compliance please see www.vishay.com/doc?99912

AUTOMOTIVE



RoHS
COMPLIANT
HALOGEN
FREE
GREEN
JE-30841

APPLICATIONS

- High speed photo detector
- Small signal detection
- Proximity sensors

PRODUCT SUMMARY

COMPONENT	I_{ra} (μA)	φ (deg)	$\lambda_{0.1}$ (nm)
VEMD6060X01	5	± 70	380 to 1070

Note

- Test conditions see table "Basic Characteristics"

ORDERING INFORMATION

ORDERING CODE	PACKAGING	REMARKS	PACKAGE FORM
VEMD6060X01	Tape and reel	MOQ: 3000 pcs, 3000 pcs/reel	1206

Note

- MOQ: minimum order quantity

ABSOLUTE MAXIMUM RATINGS ($T_{amb} = 25^\circ\text{C}$, unless otherwise specified)

PARAMETER	TEST CONDITION	SYMBOL	VALUE	UNIT
Reverse voltage		V_R	20	V
Power dissipation	$T_{amb} \leq 25^\circ\text{C}$	P_V	215	mW
Junction temperature		T_J	110	$^\circ\text{C}$
Operating temperature range		T_{amb}	-40 to +110	$^\circ\text{C}$
Storage temperature range		T_{stg}	-40 to +110	$^\circ\text{C}$
Soldering temperature	According to reflow solder profile fig. 8	T_{sd}	260	$^\circ\text{C}$
Thermal resistance junction / ambient	According to EIA / JESD51	R_{thJA}	270	K/W

Rev. 1.0, 14-Jan-16

1

Document Number: 84296

For technical questions, contact: detector.techsupport@vishay.com

THIS DOCUMENT IS SUBJECT TO CHANGE WITHOUT NOTICE. THE PRODUCTS DESCRIBED HEREIN AND THIS DOCUMENT ARE SUBJECT TO SPECIFIC DISCLAIMERS, SET FORTH AT www.vishay.com/doc?91000



BASIC CHARACTERISTICS ($T_{amb} = 25^{\circ}\text{C}$, unless otherwise specified)						
PARAMETER	TEST CONDITION	SYMBOL	MIN.	TYP.	MAX.	UNIT
Forward voltage	$I_F = 50\text{ mA}$	V_F	-	0.85	1.1	V
Breakdown voltage	$I_R = 100\text{ }\mu\text{A}$, $E = 0$	V_{BR}	20	-	-	V
Reverse dark current	$V_R = 10\text{ V}$, $E = 0$	I_{RD}	-	0.03	5	nA
Diode capacitance	$V_R = 0\text{ V}$, $f = 1\text{ MHz}$, $E = 0$	C_D	-	11	-	pF
	$V_R = 5\text{ V}$, $f = 1\text{ MHz}$, $E = 0$	C_D	-	4.8	-	pF
Open circuit voltage	$E_0 = 1\text{ mW/cm}^2$, $\lambda = 950\text{ nm}$	V_O	-	360	-	mV
Temperature coefficient of V_O	$E_0 = 1\text{ mW/cm}^2$, $\lambda = 950\text{ nm}$	TK_{V_O}	-	-3.1	-	mV/K
Short circuit current	$E_0 = 1\text{ mW/cm}^2$, $\lambda = 950\text{ nm}$	I_k	-	5	-	μA
Temperature coefficient of I_k	$E_0 = 1\text{ mW/cm}^2$, $\lambda = 835\text{ nm}$	TK_{I_k}	-	0.1	-	%/K
Reverse light current	$E_0 = 1\text{ mW/cm}^2$, $\lambda = 950\text{ nm}$, $V_R = 5\text{ V}$	I_{RL}	3.5	5	6.5	μA
	$E_0 = 1\text{ mW/cm}^2$, $\lambda = 890\text{ nm}$, $V_R = 5\text{ V}$	I_{RL}	-	7	-	μA
Angle of half sensitivity		ϕ	-	± 70	-	deg
Wavelength of peak sensitivity		λ_p	-	820	-	nm
Range of spectral bandwidth		$\lambda_{0.1}$	-	380 to 1070	-	nm
Rise time	$V_R = 10\text{ V}$, $R_L = 50\text{ }\Omega$, $\lambda = 830\text{ nm}$	t_r	-	60	-	ns
Fall time	$V_R = 10\text{ V}$, $R_L = 50\text{ }\Omega$, $\lambda = 830\text{ nm}$	t_f	-	50	-	ns

BASIC CHARACTERISTICS ($T_{amb} = 25^{\circ}\text{C}$, unless otherwise specified)

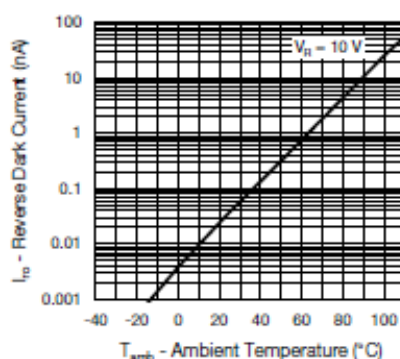


Fig. 1 - Reverse Dark Current vs. Ambient Temperature

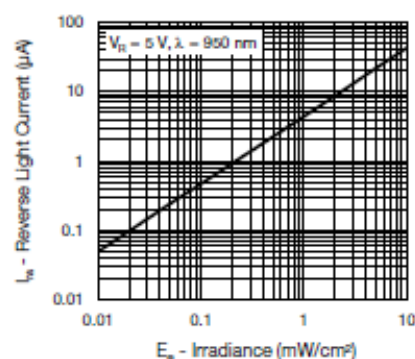


Fig. 3 - Reverse Light Current vs. Irradiance

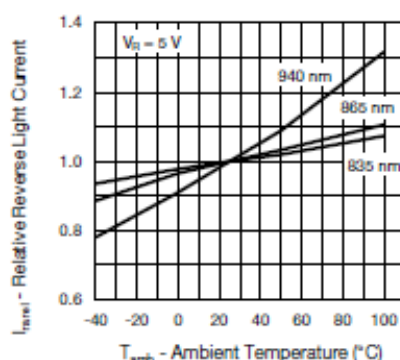


Fig. 2 - Relative Reverse Light Current vs. Ambient Temperature

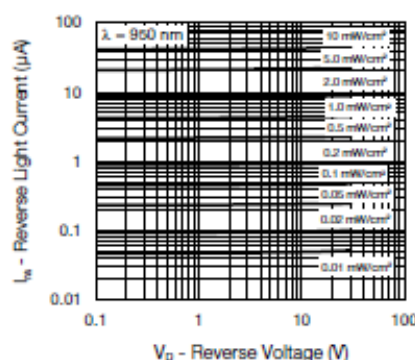


Fig. 4 - Reverse Light Current vs. Reverse Voltage


www.vishay.com
VEMD6060X01

Vishay Semiconductors

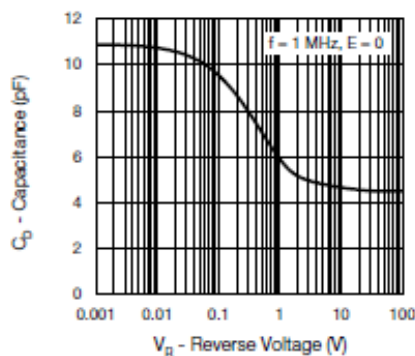


Fig. 5 - Diode Capacitance vs. Reverse Voltage

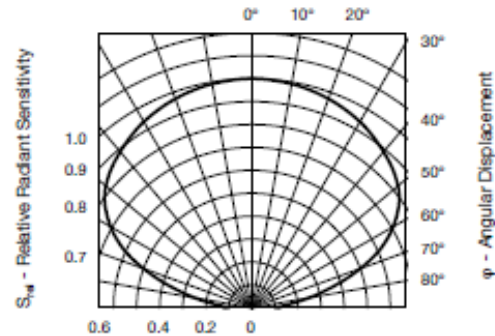


Fig. 7 - Relative Radiant Sensitivity vs. Angular Displacement

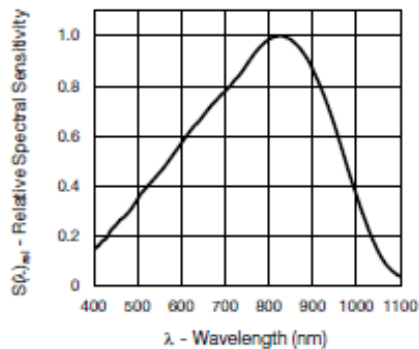
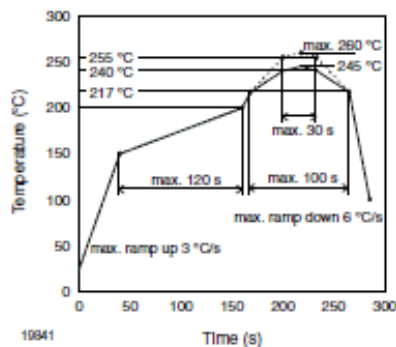


Fig. 6 - Relative Spectral Sensitivity vs. Wavelength

REFLOW SOLDER PROFILEFig. 8 - Lead (Pb)-free Reflow Solder Profile
According to J-STD-020**DRYPACK**

Devices are packed in moisture barrier bags (MBB) to prevent the products from moisture absorption during transportation and storage. Each bag contains a desiccant.

FLOOR LIFE

Floor life (time between soldering and removing from MBB) must not exceed the time indicated on MBB label:

Floor life: 72 h

Conditions: $T_{amb} < 30\text{ }^{\circ}\text{C}$, $RH < 60\%$

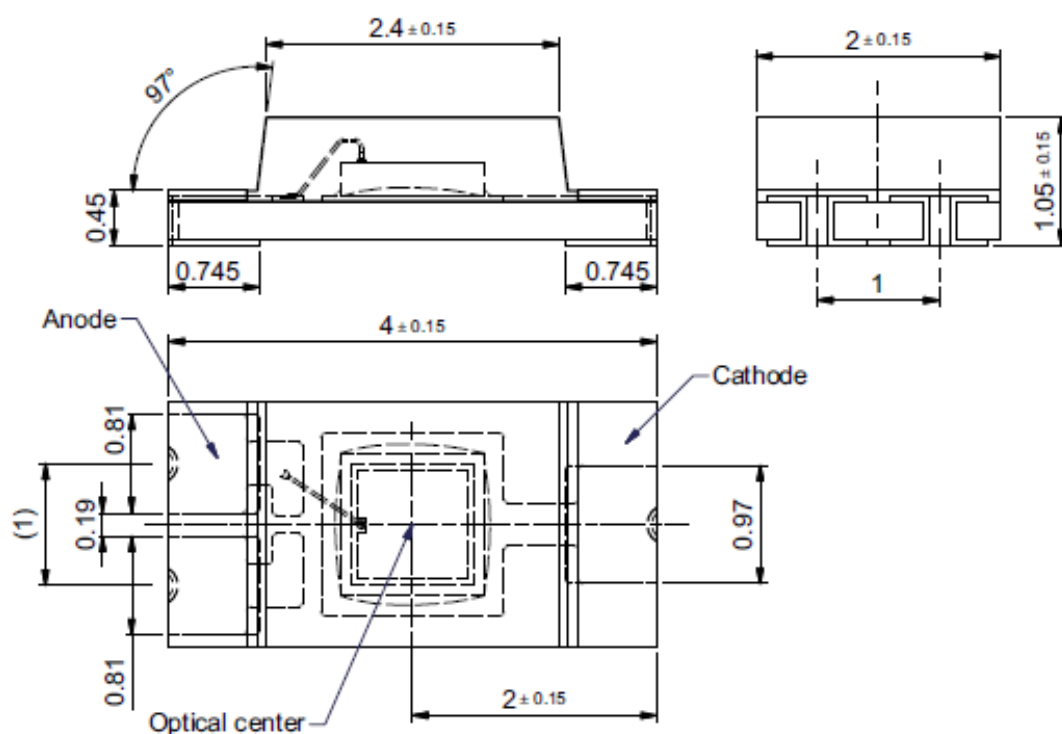
Moisture sensitivity level 4, according to J-STD-020.

DRYING

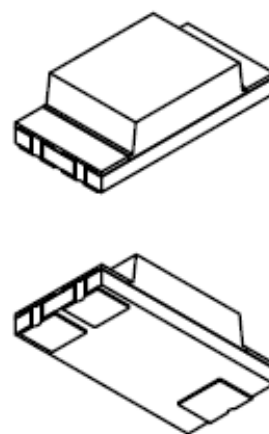
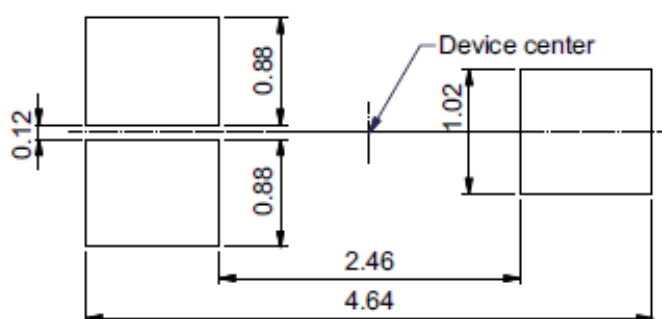
In case of moisture absorption devices should be baked before soldering. Conditions see J-STD-020 or label. Devices taped on reel dry using recommended conditions 192 h at $40\text{ }^{\circ}\text{C}$ ($\pm 5\text{ }^{\circ}\text{C}$), $RH < 5\%$.


www.vishay.com
VEMD6060X01

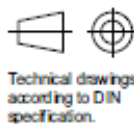
Vishay Semiconductors

PACKAGE DIMENSIONS in millimeters

Recommended solder pad footprint



Drawing-No. 6.541-5100.01-4
Preliminary issue 04.07.2013

Not indicated tolerances $\pm 0.1\text{mm}$

Rev. 1.0, 14-Jan-16

4

Document Number: 84296

For technical questions, contact: detectortechsupport@vishay.com

THIS DOCUMENT IS SUBJECT TO CHANGE WITHOUT NOTICE. THE PRODUCTS DESCRIBED HEREIN AND THIS DOCUMENT
ARE SUBJECT TO SPECIFIC DISCLAIMERS, SET FORTH AT www.vishay.com/doc?91000

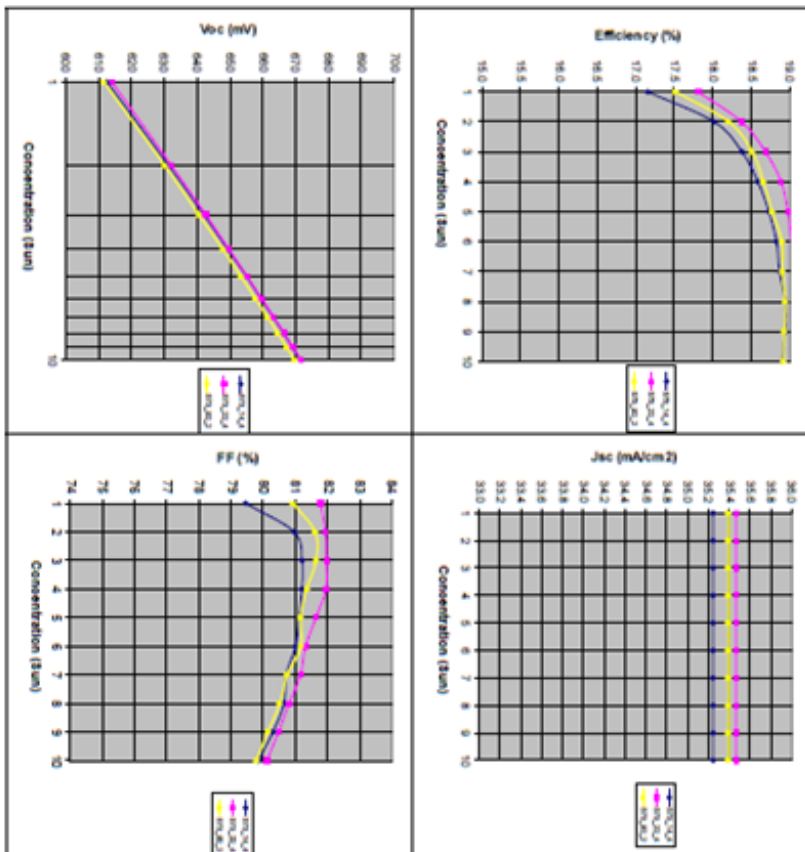
Annex 3 – Test report provided by the manufacturer for the solar cells before cutting

673_14.4									
Conc. (Sun)	Efficiency (%)	Voc (mV)	FF (%)	Jsc (mA/cm ²)	R _s (ohm)	Imp (I)	Vmp (mV)	R _{sh} (ohm)	R _{eq} (ohm)
1	17.18	612.6	79.46	34.25	0.0048	0.391	621.1	68	68
2	18.02	631.4	80.96	34.25	0.0048	0.774	628.5	82	82
3	18.38	642.1	81.21	34.25	0.0048	1.164	642.3	72	72
4	18.48	648.4	81.20	34.25	0.0048	1.661	644.3	69	69
6	18.73	664.0	81.12	34.25	0.0048	1.926	662.3	68	68
7	18.83	669.4	81.01	34.25	0.0048	2.317	663.8	71	71
8	18.87	680.2	80.72	34.25	0.0048	2.723	660.7	112	112
9	18.84	688.4	80.65	34.25	0.0048	3.088	667.5	143	143
10	18.80	691.6	79.86	34.25	0.0048	3.886	666.3	74	74

673_22.4									
Conc. (Sun)	Efficiency (%)	Voc (mV)	FF (%)	Jsc (mA/cm ²)	R _s (ohm)	Imp (I)	Vmp (mV)	R _{sh} (ohm)	R _{eq} (ohm)
1	17.81	614.1	81.79	34.47	0.0078	0.398	623.0	218	218
2	18.37	632.3	81.94	34.47	0.0080	0.798	640.4	214	214
3	18.68	642.7	81.97	34.47	0.0083	1.189	644.2	138	138
4	18.89	648.8	81.96	34.47	0.0086	1.680	659.8	64	64
6	18.87	665.5	81.64	34.47	0.0083	1.998	657.3	84	84
7	19.03	669.7	81.32	34.47	0.0083	2.334	664.4	154	154
8	19.09	683.4	81.16	34.47	0.0067	2.746	662.9	81	81
9	19.10	688.6	80.81	34.47	0.0062	3.100	668.8	138	138
10	19.09	691.8	80.11	34.47	0.0067	3.804	666.2	146	146

673_82.2									
Conc. (Sun)	Efficiency (%)	Voc (mV)	FF (%)	Jsc (mA/cm ²)	R _s (ohm)	Imp (I)	Vmp (mV)	R _{sh} (ohm)	R _{eq} (ohm)
1	17.62	611.8	80.83	34.39	0.0046	0.319	623.8	113	113
2	18.21	630.2	81.62	34.39	0.0047	0.771	648.0	167	167
3	18.61	640.8	81.66	34.39	0.0076	1.168	648.0	82	82
4	18.68	647.8	81.36	34.39	0.0081	1.646	648.3	170	170
6	18.77	663.4	81.17	34.39	0.0066	1.939	649.8	98	98
7	18.80	667.8	81.18	34.39	0.0062	2.234	644.0	98	98
8	18.80	681.5	80.76	34.39	0.0069	2.710	644.4	147	147
9	18.84	684.6	80.62	34.39	0.0089	3.119	651.8	641	641
10	18.83	687.3	80.16	34.39	0.0081	3.489	644.6	81	81

673_MEAN DATA									
Conc. (Sun)	Efficiency (%)	Voc (mV)	FF (%)	Jsc (mA/cm ²)	R _s (ohm)	Imp (I)	Vmp (mV)	R _{sh} (ohm)	R _{eq} (ohm)
1	17.60	612.8	80.72	34.37	0.0040	0.282	629.3	130	130
2	18.20	631.8	81.61	34.37	0.0046	0.777	641.8	144	144
3	18.62	641.8	81.61	34.37	0.0046	1.164	642.1	67	67
4	18.71	649.0	81.61	34.37	0.0044	1.662	647.7	286	286
6	18.82	664.6	81.31	34.37	0.0062	1.844	649.7	339	339
7	18.82	668.8	81.17	34.37	0.0063	2.236	644.3	106	106
8	18.86	682.7	80.88	34.37	0.0068	2.728	642.7	103	103
9	18.90	686.8	80.68	34.37	0.0066	3.102	648.3	283	283
10	18.87	691.0	79.92	34.37	0.0060	3.891	643.8	118	118



Annex 4 – Material specification of the solder paste



Complete Solder Solutions

S965D500A6 Product Specification

Product Description

The EFD SolderPlusD 500 No-Clean (NC) solder pastes for micro-dot dispensing, features low flux residue, superior wetting, and up to eight (8) hours of tack time. This solder paste offers exceptional lot-to-lot consistency with excellent dispense resolution and reproducibility.

500 flux residue is colorless, transparent, hard, non-corrosive, inert, and designed to be left on your assembly. Cleaning is optional.

Quality

EFD solder pastes and fluxes meet or exceed IPC Joint Industry standards J-STD-004 for flux, J-STD-005 for paste, and J-STD-006A for alloy.

Material Properties

J-STD-004	
Classification	ROL1
Copper Mirror	No Breakthrough
Silver Chromate	Pass
Fluoride Spot	Pass
Corrosion	None
SIR 24 hours*	$1.1 \times 10^{10} \Omega$
SIR 96 hours*	$9.7 \times 10^9 \Omega$
SIR 168 hours*	$7.0 \times 10^9 \Omega$
J-STD-005	
Metal Content	84.5% +/- 0.5%
Viscosity at 25°C	450 +/- 50kcPs
Solderball Test	Preferred
Wetting Test	Pass
J-STD-006A	
Alloy	Sn96.5Ag3.0Cu0.5
Particle Size	Type VI (15-5 micron)
Melting Temp.	217-219°C
Bellcore GR-78	Compliant

Delivery

SolderPlus solder paste is shipped direct from our factory via next-day air service within three (3) business days of order receipt, excluding weekend deliveries. For the full range of packaging options, reference our Packaging Guide.

Storage and Handling

Store between 4° and 21°C (40° and 70°F). Do not Freeze. Allow four (4) hours at room temperature before using. Exposure to temperatures in excess of 27°C may cause flux separation and chemical decomposition. When not in use, containers should be kept closed.

Warranty

EFD solder pastes are warranted until expiration date shown on the product label when stored in accordance with recommended storage and handling.

Safety

Read the MSDS prior to use. Care should be taken to prevent accidental ingestion and contact with the eyes. Use adequate ventilation and avoid breathing soldering fumes. Wash hands thoroughly after use.

Technical Support

Our Product Specialists and Technical Service Team are available to evaluate your process requirements and develop a soldering solution with you.

Application Guidelines

Dispensing	
Best Working Environment	20°C to 25°C (68°F to 77°F) at 35% to 60% Relative Humidity
Dispensing Process	Ref: SolderPlus Dispensing Guide
Reflow	
Heating profile	Ref: page 2 of this specification
Cleaning	
Solvents	Ref: Flux Residue Removal Guide**
No Clean	Residue is designed to be left in place for typical applications.

* Nominal/Typical values

** EFD does not sell or recommend specific solvents but collaborates with any solvent vendor.

EFD, Inc. 40 Catamore Blvd, East Providence, RI 02914 U.S.A. www.efd-inc.com
 North and South America: Telephone: 401-431-7000 Fax: 401-431-7079 solden@efd-inc.com
 Europe: +44(0)1582 666334 Fax: +44 (0)1582 664227 europa@efd-inc.com
 China: Telephone: 862158542345-806 899 Fax: 862150317583 china@efd-inc.com

EFD-S965D500A6 REV A p1 of 2 ©2009 Norson Corporation

Reflow Profiling

EFD solder pastes produce high quality solder joints across a wide heating process range. As a rule, the shorter the profile, the better the solder paste will perform. There is no advantage to a profile centered within the time ranges given below for printed circuit board (PCB) reflow profiling.

The soldering process involves three inputs: surfaces to be soldered, solder paste, and heat. No single profile is ideal for all products and heating methods. A good profile will not exceed the maximum recommended reflow time at the hottest point on the product. The minimum cycle time to reflow a solder joint can be half a second with laser heating.

Preheat

Room temperature to 140°C: During preheat, low boiling point solvents and moisture are evaporated slowly to prevent spattering. The flux transitions from a gel state to a fluid state and spreads out on the product, covering the surfaces to be cleaned.

Activation

140°C to 217°C: The flux cleans the surfaces to be soldered. Excessive time in the activation range will use up available flux activity and may result in non-wetting, de-wetting, and other related solder defects.

Because of the variety among solderable devices and reflow equipment, it is often necessary to deviate from the guidelines given here. If you have questions, contact Technical Support at 800-338-4353.

A nitrogen atmosphere can be used to extend the activation window for products requiring very long reflow profiles.

Reflow

217°C up to 234-259°C and back down to 217°C:

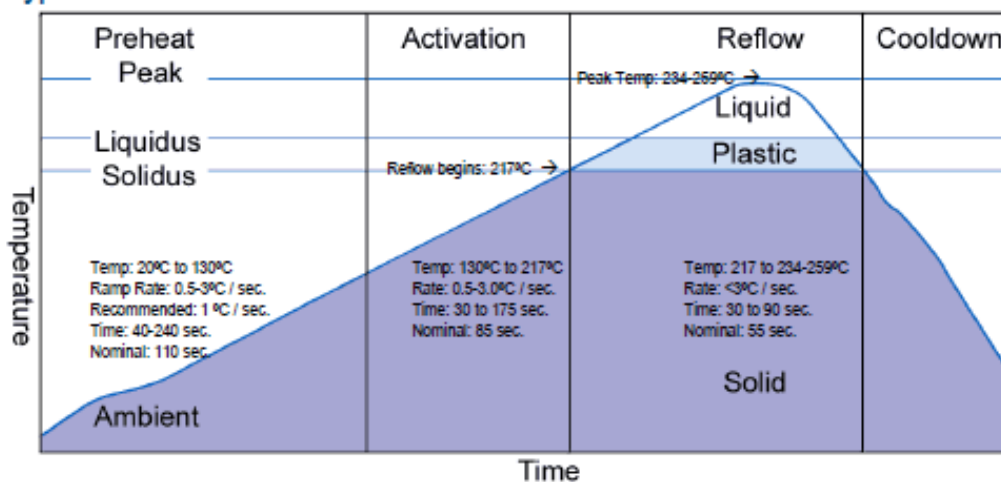
Soldering begins upon reaching the solidus temperature of the alloy being used. For maximum joint strength, a peak temperature of 15° to 40°C above the liquidus must be reached.

Cooldown

Cool to safe temperature prior to handling. Ramp rate: less than 4°C per second. Cooling too rapidly can cause Coefficient of Thermal Expansion (CTE) mismatch stress related damage.

NOTE: If you have problems with "tombstones" or unacceptable product temperature variation, temperature stabilization should start at 5° to 15°C below alloy solidus and end at 5° to 15°C above alloy solidus (10° to 30°C degree range). Ramp rate will usually need to be less than 1°C. Thermally uniform product may require as little as 5 seconds, while thermally diverse products may require over a minute.

Typical Printed Circuit Board Reflow Process



EFD, Inc. 40 Catamore Blvd, East Providence, RI 02914 U.S.A. www.efd-inc.com
 North and South America: Telephone: 401-431-7000 Fax: 401-431-7079 solder@efd-inc.com
 Europe: +44(0)1582 666334 Fax+44 (0)1582 664227 europa@efd-inc.com
 China: Telephone: 862158542345-806 899 Fax: 862150317583 china@efd-inc.com

EFD-SM525004S REV A p1 of 2 ©2009 Norson Corporation

Annex 5 -Material specifications of the encapsulation resins



Product Data Sheet

RESILIENT, CLEAR ENCAPSULANTS Multi-Cure® 9001-E-V3 SERIES

DESCRIPTION

9001-E-V3 Series encapsulants are performance upgrades of the flexible "instant curing" Dymax 9001 UV/visible light curing encapsulant, with improved moisture, thermal cycle resistance and adhesion to various component substrates. Curing completely in as little as five seconds upon exposure to longwave UV and visible light, these materials are environmentally resistant with good ionic and electrical properties. Multi-Cure® 9001-E-V3 Series encapsulants display excellent adhesion to printed circuit boards and electronic components and are especially well suited for chip on board, chip on flex, and multi-chip modules.

UNCURED PROPERTIES (not specifications)

Solvent Content	None, 100% Solids	
Isocyanate Content	None	
Chemical Class	Modified Urethane	
Appearance	Liquid	
Color	Clear	
Solubility	Alcohols/Chlorinated Solvents/Ketones	
Viscosity (20 rpm)	4,500 cP (nominal)	ASTM D-2556
	17,000 cP (nominal)	ASTM D-2556
	50,000 cP (nominal)	ASTM D-2556

CURED PROPERTIES (not specifications)

PHYSICAL		
Durometer Hardness	D45 (nominal)	ASTM D-2240
Elongation at Break	150%	ASTM D-638
Tensile at Break	750 psi	ASTM D-638
Modulus of Elasticity	2,500 psi	ASTM D-638
Water Absorption (24 h)	1.0%	ASTM D-570
Boiling Water Absorption (2 h)	2.6%	ASTM D-570
Thermal Limit	150°C	DSTM D-200*
Glass Transition, T _g	30°C	ASTM E-831
Coefficient of Thermal Expansion, α ₁	95 x 10 ⁻⁶ in/in/°C	ASTM E-831
Coefficient of Thermal Expansion, α ₂	180 x 10 ⁻⁶ in/in/°C	ASTM E-831
Linear Shrinkage	2%	ASTM D-2556

*DSTM Refers to Dymax Standard Test Method

Thermal Shear Stress (-55°C to 125°C) on:

Aluminum	16.4 psi	Ionic Purity:	
FR-4	16.9 psi	Extractable Chloride	<10 ppm
Gold	17.0 psi	Sodium	<10 ppm
Silicon	17.5 psi	Potassium	<10 ppm
Solder	16.0 psi	Fluoride	<10 ppm

RELIABILITY

Thermal Shock (0.25 mil wire)	>2,000 cycles (-40°C to 125°C)
Humidity	>1,000 h, 85°C/85% RH
Autoclave	>1,000 h

DYMAX Corporation - 318 Industrial Lane - Torrington, CT 06790 - Phone: 860.482.1010 - Fax: 860.496.0608 - E-mail: info@dymax.com - www.dymax.com

DYMAX Europe GmbH - Trakehner Strasse 3 - D-60487 Frankfurt am Main - Germany - Phone: 0049.69.7165.3568 - Fax: 0049.69.7165.3830 - E-mail: dymaxinfo@dymax.de - www.dymax.de

DYMAX UV Adhesives & Equipment (Shenzhen) Ltd - Unit 807, Talfook Building, No. 9 Shi Hua Road, Futian Free Trade Zone, Shenzhen, China 518038 - Phone: 86.755.83485759
Fax: 86.755.83485760 - E-mail: dymaxasia@dymax.com - www.dymax.com.cn

DYMAX Asia (HK) - Unit 1005, 10/F., Camarvon Plaza, No. 20 Camarvon Road, T.S.T., Kowloon, Hong Kong - Phone: 852.2460.7038 - Fax: 852.2460.7017 - E-mail: dymaxasia@dymax.com
www.dymax.com.cn



Product Data Sheet

9001 E-Series, 09-21-09

ELECTRICAL

Dielectric Strength	500 Volts/Mil	ASTM D-1304
Volume Resistivity	555×10^{12} ohm cm	ASTM D-1304
Surface Resistivity	$6,300 \times 10^{12}$ ohm	ASTM D-1304
Dissipation Factor, 1 MHz	0.046 (23°C)	ASTM D-1304
Dielectric Constant, 1 MHz	3.27 (23°C)	ASTM D-1304

HOW TO CURE WITH UV/VISIBLE LIGHT & IR:**I. Clear adhesive completely exposed to UV/Visible light:**

Exposure Time	UV/visible Lamp	Light Intensity	Distance	Spectral Output
30 sec	Light-Welder® 5000-EC	150 mW/cm ²	3 inches	300-500 nm

Multi-Cure® 9001-E-V3 Series encapsulants cure upon exposure to high intensity UV/Visible light in wavelengths between 300-500 nm in 10-30 seconds. The speed of light cure depends on the thickness of the encapsulant layer and the intensity from the light source.

II. Heat cure shadowed areas following UV exposure:

Heat may be used as a secondary cure mechanism when some encapsulant is shielded from light. Light cure must be done prior to heat cure. Any of the following schedules may be used:

Minimum Adhesive Temperature	Time
110°C (225°F)	60 Minutes
120°C (250°F)	30 Minutes
150°C (300°F)	15 Minutes

DISPENSING AND HANDLING ADHESIVE

Avoid prolonged exposure to ambient fluorescing lighting. Failing to do so may cause the 9001-E-V3 Series encapsulants to polymerize prematurely.

Multi-Cure® 9001-E-V3 Series encapsulants may be dispensed from a variety of automatic bench-top syringe applicators or other equipment. Skin contact should be avoided. Use barrier hand cream. Wear impervious gloves. Do not wear absorbent gloves. Adhesive may be removed with basic soap and water. Avoid eye contact. Wipe excess adhesive with paper towels and remove residue with isopropanol.

STORAGE AND SHELF LIFE

Store material in a cool, dark place when not in use. Do not expose to UV light or sunlight. Material may polymerize upon prolonged exposure to ambient light. Replace lid immediately after use. Product has a one-year shelf life when stored below 90°F in the original, unopened container. These products do not support fungal or bacterial growth.

CAUTION

For industrial use only. Avoid breathing vapors. Avoid contact with eyes and clothing. In case of skin contact, immediately flush with water for at least 15 minutes; for eyes, get medical attention. Wash clothing before reuse. Keep out of reach of children. Do not take internally. If swallowed, vomiting should be induced at once and a physician called. For specific information, refer to the product's Material Safety Data Sheet before use.

© 2009 Dymax Corporation

The data contained in this bulletin which represents typical results, is furnished for information only, and is believed to be reliable. We cannot assume responsibility for results obtained by others over whose methods we have no control. It is the user's responsibility to determine suitability for the user's purpose of any product or method mentioned herein and to adopt such precautions as may be advisable for the protection of property and persons against any hazards that may be involved in the handling and use thereof. Nothing in this bulletin is to be interpreted as a representation of freedom from domination of patents owned by others or a license under a Dymax Corporation patent. We recommend that each prospective user test the proposed application before repetitive use, using the data as a guide. For specific information, refer to Material Safety Data Sheet before use.

REV 09-21-09

DYMAX Corporation - 318 Industrial Lane - Torrington, CT 06790 - Phone: 860.482.1010 - Fax: 860.496.0508 - E-mail: info@dymax.com - www.dymax.com

DYMAX Europe GmbH - Traikheiner Strasse 3 - D-60487 Frankfurt am Main - Germany - Phone: 0049.69.7165.3568 - Fax: 0049.69.7165.3830 - E-mail: dymaxinfo@dymax.de - www.dymax.de

DYMAX UV Adhesives & Equipment (Shenzhen) Ltd - Unit 807, Taifook Building, No. 9 Shi Hua Road, Futian Free Trade Zone, Shenzhen, China 518038 - Phone: 86.755.83485759
Fax: 86.755.83485760 - E-mail: dymaxasia@dymax.com - www.dymax.com.cn

DYMAX Asia (HK) - Unit 1006, 10/F., Camarvon Plaza, No. 20 Camarvon Road, T.S.T., Kowloon, Hong Kong - Phone: 852.2460.7038 - Fax: 852.2460.7017 - E-mail: dymaxasia@dymax.com
www.dymax.com.cn



OPTICAL ADHESIVES

OP-29 Product Data Sheet

OP-29

Multi-Purpose, Light-Curable Optical Adhesive

APPLICATIONS

- Tacking
- Bonding
- Potting
- Sealing

FEATURES

- UV Light Cure
- One Component, No Mixing Required
- Solvent Free
- Medium Viscosity for Gap Filling

OTHER FEATURES

- Optically Clear
- Resilient
- Resists Yellowing
- Flexible
- Low Stress

Dymax OP-29 cures upon exposure to UV light and is designed for rapid optical assembly. Dymax OP-29 materials contain no nonreactive solvents and cure upon exposure to light. Their ability to cure in seconds enables faster processing, greater output, and lower processing costs. When cured with Dymax light-curing spot lamps, focused-beam lamps, or flood lamps, they deliver optimum speed and performance for optical assembly. Dymax lamps offer the optimum balance of UV and visible light for the fastest, deepest cures. This product is in full compliance with the RoHS Directives 2002/95/EC and 2003/11/EC.

UNCURED PROPERTIES *

Property	Value	Test Method
Solvent Content	No Nonreactive Solvents	N/A
Chemical Class	Acrylated Urethane	N/A
Appearance	Clear Liquid	N/A
Soluble In	Organic Solvents	N/A
Density, g/ml	1.05	ASTM D1875
Viscosity, cP (20 rpm)	2,500 (nominal)	ASTM D1084

CURED MECHANICAL PROPERTIES *

Property	Value	Test Method
Durometer Hardness	D60	ASTM D2240
Tensile at Break, MPa [psi]	22 [3,200]	ASTM D638
Elongation at Break, %	110	ASTM D638
Modulus of Elasticity, MPa [psi]	234 [34,000]	ASTM D638
Glass Transition T _g , °C	64	DSTM 256 [‡]

OTHER CURED PROPERTIES *

Property	Value	Test Method
Refractive Index (20°C)	1.50	ASTM D542
Boiling Water Absorption, % (2 h)	3.9	ASTM D570
Water Absorption, % (25°C, 24 h)	1.3	ASTM D570
Linear Shrinkage, %	0.79	ASTM D2566

* Not Specifications

N/A Not Applicable

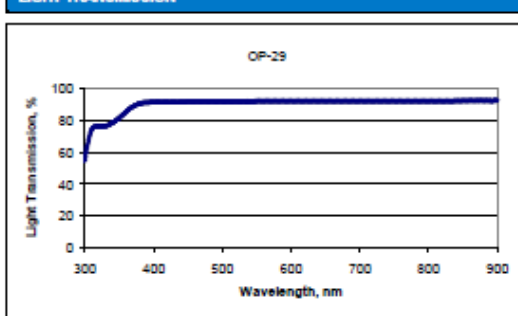
‡ DSTM Refers to Dymax Standard Test Method

ADHESION

Substrate	Recommendation
Glass	✓
Metals	✓
Plastics	o

✓ Recommended o Limited Applications
st Requires Surface Treatment (e.g. plasma, corona treatment, etc.)

LIGHT TRANSMISSION **



** Measured at 0.03 mm (0.001 in) per DSTM-501[‡]



© 2005-2014 Dymax Corporation. All rights reserved. All trademarks in this guide, except where noted, are the property of, or used under license by Dymax Corporation, U.S.A.

Technical data provided is of a general nature and is based on laboratory test conditions. Dymax does not warrant the data contained in this bulletin. Any warranty applicable to the product, its application and use is strictly limited to that contained in Dymax standard Conditions of Sale. Dymax does not assume responsibility for test or performance results obtained by users. It is the user's responsibility to determine the suitability for the product application and purpose and the suitability for use in the user's intended manufacturing apparatus and methods. The user should adopt such precautions and use guidelines as may be reasonably advisable or necessary for the protection of property and persons. Nothing in this communication shall act as a representation that the product use or application will not infringe on a patent owned by someone other than Dymax or act as a grant of license under any Dymax Corporation Patent. Dymax recommends that each user adequately test its proposed use and application before actual repetitive use, using the data in this communication as a general guideline.

Technical Data Collection Prior to 2006

Rev. 01/10/2014

Dymax Corporation
860.452.1010
info@dymax.com
www.dymax.com

Dymax Oligomers & Coatings
860.526.7006
oligomers@coatings@dymax.com
www.dymax-co.com

Dymax Europe GmbH
+49 (0) 811.962.7900
info_de@dymax.com
www.dymax.de

Dymax UV Adhesives & Equipment (Shanghai) Co Ltd
+86.755.83485759
dymaxasia@dymax.com
www.dymax-co.com.cn

Dymax UV Adhesives & Equipment (Shanghai) Co Ltd
+86.21.57285759
dymaxasia@dymax.com
www.dymax.com.cn

Dymax Asia (H.K.) Limited
+852.2480.7038
dymaxasia@dymax.com
www.dymax-co.com.hk

Dymax Korea LLC
82.2.794.3434
info@dymax.kr
www.dymax.com.kr



OPTICAL ADHESIVES OP-29 Product Data Sheet

CURING GUIDELINES

Fixture time is defined as the time to develop a shear strength of 0.1 N/mm² [10 psi] between glass slides. Actual cure time typically is to 5 times fixture time.

Dymax Curing System (Intensity)	Fixture Time or Belt Speed ^A
2000-EC (50 mW/cm ²) ^B	3 s
5000-EC (200 mW/cm ²) ^B	2 s
BlueWave [®] 75 (5.0 W/cm ²) ^B	1.4 s
BlueWave [®] 200 (10 W/cm ²) ^B	1.2 s
UVCS Conveyor with one 5000-EC (200 mW/cm ²) ^C	7.9 m/min [26 ft/min]
UVCS Conveyor with Fusion F300S (2.5 W/cm ²) ^C	8.2 m/min [27 ft/min]

A Curing through light-blocking substrates may require longer cure times if they obstruct wavelengths used for light curing (320-400 nm for UV light curing, 320-450 nm for UV/Visible light curing). These fixture times/belt speeds are typical for curing thin films through 100% light-transmitting substrates.

B Intensity was measured over the UVA range (320-395 nm) using a Dymax ACCU-CAL[™] 50 Radiometer.

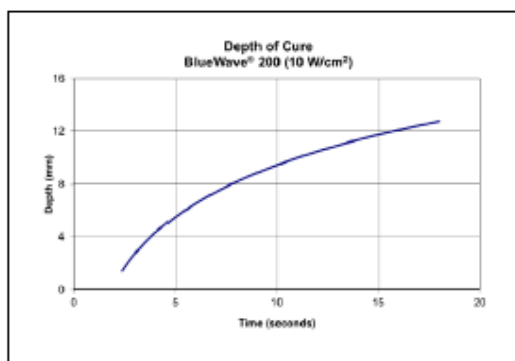
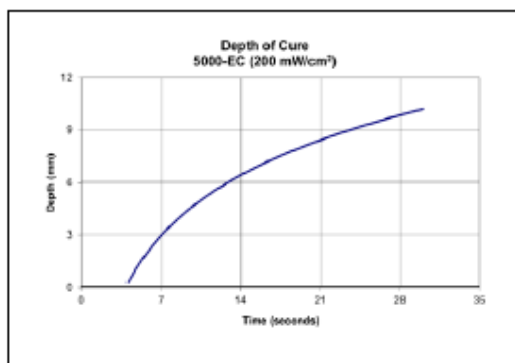
C At 53 mm [2.1 in] focal distance. Maximum speed of conveyor is 8.2 m/min [27 ft/min]. Intensity was measured over the UVA range (320-395 nm) using the Dymax ACCU-CAL[™] 100 Radiometer.

Full cure is best determined empirically by curing at different times and intensities, and measuring the corresponding change in cured properties such as tackiness, adhesion, hardness, etc. Full cure is defined as the point at which more light exposure no longer improves cured properties. Higher intensities or longer cures (up to 5x) generally will not degrade Dymax light-curable materials.

Dymax recommends that customers employ a safety factor by curing longer and/or at higher intensities than required for full cure. Although Dymax Application Engineering can provide technical support and assist with process development, each customer ultimately must determine and qualify the appropriate curing parameters required for their unique application.

DEPTH OF CURE

The graphs below show the increase in depth of cure as a function of exposure time with two different lamps at different intensities. A 9.5 mm [0.37 in] diameter specimen was cured in a polypropylene mold and cooled to room temperature. It was then released from the mold and the cure depth was measured.



intertronics**adhere**TM
better bonding from intertronics[Click to view gallery](#)**opti-tec****OPT 5012****Low Viscosity, Clear Epoxy
Adhesive / Encapsulant**

Opti-tec 5012 is a two component, low viscosity epoxy with very high optical clarity. It has a long pot life and can be cured at room temperature or at 80°C for 90 minutes. Opti-tec 5012 is designed for potting, encapsulation and adhesion of components where high optical clarity, good wetting and low viscosity are important.

Opti-tec 5012 can be used for bonding glass, quartz, metal and many plastics. It finds uses in assembly and repair of glass items where a clear adhesive is required.

High optical clarity, water white with excellent resistance to yellowing

Excellent transmission down to 300 nm

Low viscosity (500 cps)

Long pot life

Cures within 48 hours at room temperature. Cure can be achieved in 90 minutes at 80°C.

Opti-tec 5012 has high surface energy. This and its low viscosity allows it to readily wet and wick between surfaces. It develops strong adhesion to most materials used in optics, including metals, ceramics, glass and most plastics.

Good impact and thermal shock resistance, with low internal stresses due to low shrinkage on cure

Opti-tec 5012 is a hard, glass-like material after cure and can be polished

Good chemical and moisture resistance with a very low exotherm, suitable for sensitive potting and encapsulation applications

Opti-tec 5012 features low fluorescence

- Optical assembly, optical filters, lenses, prisms
- Glass bonding
- Plastic & glass fibre optics

- Opto-electronics, photonics, LED
- Optical encapsulation & glob topping, casting, potting
- Repair of glass, wood, ceramic
- Potting or encapsulation where high optical clarity is required: geology samples, relics and artefacts, tissue samples

Typical Properties

Mix ratio	100:35 resin to hardener
Mixed viscosity	0.5-1.0 Pa.s (500-1000 cps) @ 25°C
Colour	Water white
Specific gravity	1.05

Pot life	4 hours @ 23°C (< 25 g mix)	100g
	8 hours @ 23°C (< 4 g mix)	
	Max suggested mix	

Cure schedule	Bondline temperature	Time
	25°C	48 hours
	80°C	90 mins

Note: Optimal cured properties are achieved by curing at a bondline temperature of 80°C.

Cured properties

(90 minutes @ 80°C)

Glass transition temperature (T _g)	70°C
Hardness, Shore D	82
Temperature range	-60 to 200°C
CTE	50-60 ppm/°C
Lap shear strength (Al/Al)	3000 N
Optical transmission	>97% @ 300-900 nm; excellent to 2500 nm
Refractive index	1.56 est.
Dielectric strength	20kV/mm est.
Dielectric constant	3.1 est.
Volume resistivity	>10 ¹⁴ est.
Shelf life	12 months in original sealed containers

**OPT 4200**

Optically Clear Polyurethane Encapsulant & Potting Compound

Opti-tec™ 4200 is a clear, water-white polyurethane resin designed for the encapsulation of electronics, LEDs, electrical products and other items where high transparency and aesthetics are important. Opti-tec 4200 has excellent non-yellowing colour stability, due to the incorporation of both UV resistant base materials and the addition of UV stabilisers and antioxidants.

Opti-tec 4200 is used for a range of applications from high value LED panels to decorative giftware (e.g. flower impregnation). It is also an excellent resin for the doming of badges, labels and decals.

Opti-tec 4200 is available in a harder version (**Opti-tec 4210**) and a translucent milky-white version (**Opti-tec 4220**).

Clear, water-white, non-yellowing

Excellent long term UV stability

Scratch and mark resistant

Non-toxic

Easy to mix and process

Very low viscosity

Excellent penetration and air release properties

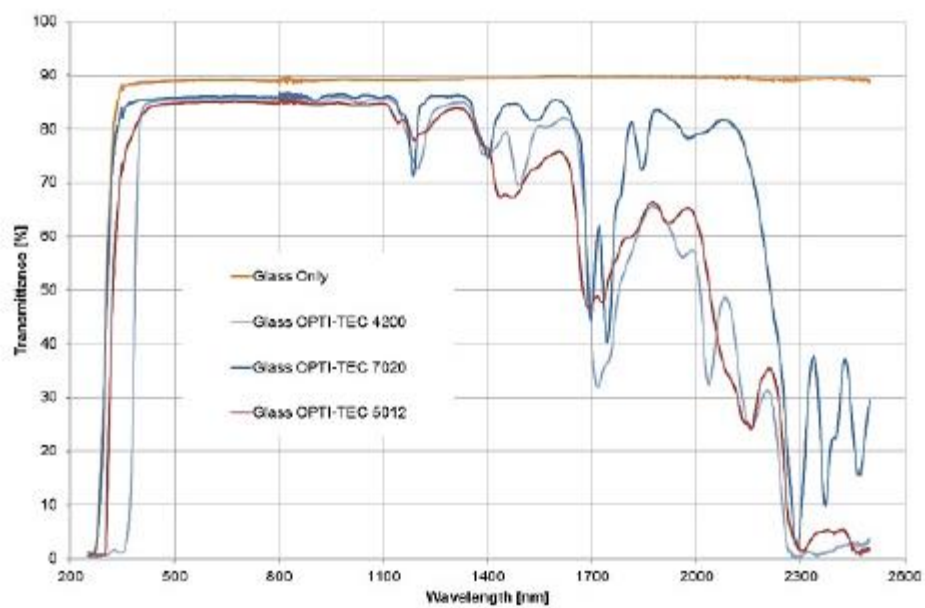
Low shrinkage

Low exotherm

- LED protection – LED bars, LED arrays, luminaires
- Electronics potting
- Dome coating of labels and badges
- High quality, clear casting

	Resin	Hardener	Mixed
Colour	Clear	Clear	Clear
Specific gravity (g/ml)	1.06	1.16	1.11
Viscosity mPa.s @ 25°C	600	600	600
Mix ratio by weight	0.92:1		
Mix ratio by volume	1:1		
Curing*			
Pot life	10 minutes		
Gel time	20 minutes		
Tack free cure	40 minutes		
Minimum cure schedule	36 hours @ 20-25°C 4 hours @ 40°C 2 hours @ 60°C		
* typical values – will vary according to mass, film thickness and application. Higher cure temperatures will result in greater cure shrinkage and exotherm.			
Cured properties			
Shore hardness	A75		
Operating temperature (application & geometry dependant)	-55 to +120°C		
Thermal conductivity	< 0.21 W/mK		
Tensile strength	~ 15 mPa		

Elongation at break	100%
Compressive yield strength	< 10 mPa
Coefficient of linear expansion	100-150 pp/m°C
Volume resistivity	< 1.3×10^{12} ohm.cm
Surface resistivity	< 1.4×10^{12} ohm
Electric strength	20 kV/mm
Water absorption	1.17% (30 days @ 25°C)
Refractive index	1.47-1.48
Opti-tec 4200 is RoHS compliant and contains 0% REACH SVHC	



Optical transmission of Opti-tec 4200, Opti-tec 7020, Opti-tec 5012

**opti-tec****Opti-tec 7020**

Optically Clear Silicone Potting Compound

Opti-tec™ 7020 Optically Clear Silicone Rubber Potting Compound is a two part, clear liquid silicone elastomer which will cure at room temperature or can be accelerated at elevated temperatures. It has a low viscosity, which allows for ease of flow around complex parts, providing electrical insulation and shock resistance. Its combination of transparency, non-yellowing and compliance makes it suitable for encapsulation of sensitive electronic or opto-electronic parts (e.g. LEDs), protecting the components from vibration, moisture and atmospheric contaminants.

Optically clear

Compliant

Room or low temperature cure

Non-yellowing catalyst system

Low shrinkage

Excellent for protecting LEDs and solar applications

Convenient 10:1 mixing ratio for use in automatic dispensing equipment or hand mixing

Low viscosity which allows for ease of flow around complex parts, providing electrical insulation and shock resistance

Contains no solvents

Has a chemical composition which provides hydrolytic stability and reversion resistance. It is an addition cure silicone with a platinum catalyst.

- Optical assembly
- Opto-electronics, photonics, LEDs
- Optical encapsulation & glob topping, casting, potting
- Solar panels
- Electronics potting

Instructions

Opti-tec 7020 is available in twinpacks or in bulk.

For bulk, weigh 10 parts of Part A to 1 part of Part B. Allowable tolerance on the measured weight for either Part A or Part B is $\pm 2.5\%$. The mixing container should be 4 to 5 times larger than the volume of silicone. Use stainless steel, HDPE, polypropylene, etc. Using clean tools, thoroughly mix the A and B components.



The twinpack sachet is a clear film sachet, with the resin and hardener separated by a removable clip and rail divider. [Click here for twinpack mixing instructions.](#)

Care should be taken to avoid excessive aeration. For many applications, natural degassing will be sufficient. If degassing is required, intermittently evacuate at 20-40 mbar for 15-30 minutes. Leave for a few minutes after releasing the vacuum to allow surface bubbles to collapse.

Cure begins as soon as the components are mixed in the recommended ratio. Complete cure is normally achieved in 16 to 24 hours at ambient temperatures of 20-30°C. Cure can be accelerated by heating to 50-120°C.

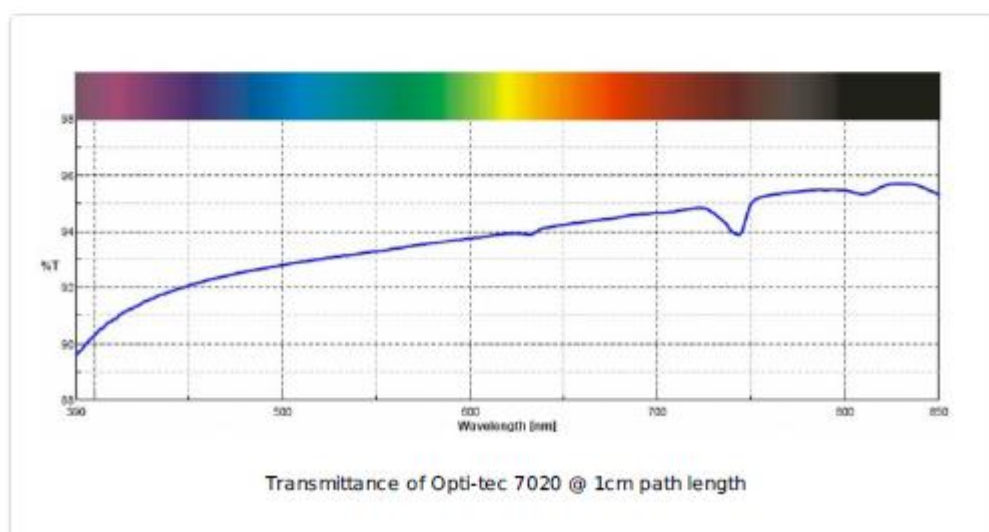
Uncured properties

Colour	Part A – clear
	Part B – clear
	Mixed – clear; colourless
Viscosity (mPa.s)	Part A – 4000
	Part B – 500
	Mixed – easily pourable
Specific gravity	Part A – 1.02
	Part B – 1.01
Mix ratio	10:1 Part A to Part B
Pot life (@ 23°C)	4 hours
Cure schedule (approx maximum time)	25°C – 20 hours
	100°C – 60 mins

Cured properties (1 hour @ 100°C)

Hardness, Shore A	40
-------------------	----

Temperature range	-60 to 200°C
Tensile strength	4.8 MPa
Elongation at break	100%
Linear shrinkage	< 0.1%
CTE (ppm/°C)	275
Dielectric strength (kV/mm)*	20
Dielectric constant @ 1000Hz	2.69
Dissipation factor @ 1000Hz	0.0006
Volume resistivity (ohm-cm)	1.7×10^{15}
Thermal conductivity (W/m K)	0.18
Specific heat (kJ/kg)	1.255
Refractive index @ 589nm	1.405
Transmittance @ 400nm	90.3%
*ASTM D149-09 Method A	



Annex 6 – Specifications of the UV lamp

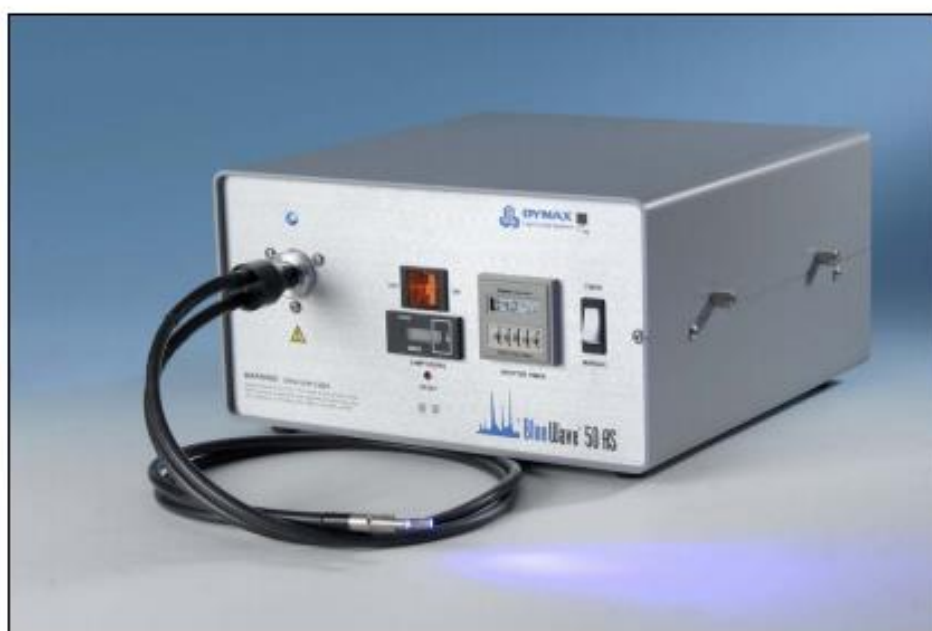


Adhesives • UV Curing Systems

Product Bulletin

BlueWave[™] 50 AS UV Light Curing Spot Lamp

The BlueWave[™] 50 AS UV light curing spot lamp is economical and simple to operate. It emits primarily UVA and blue visible light (300-450 nm) and is designed for curing UV adhesives, coatings and encapsulants. The BlueWave 50 AS contains an integral shutter which can be actuated by a foot pedal or PLC making it ideal for both manual and automated processes. A solid-state power supply provides consistent performance at any voltage (90-263V, 47-63 Hz). A proprietary "Cool Blue[™] Filter" protects liquid-filled lightguides from degradation, virtually eliminating the need to replace lightguides. Low initial cost, long lasting liquid lightguides, and 2,000-4,000 hour bulb life make the BlueWave 50 AS one of the most economical UV light curing spot lamps on the market.



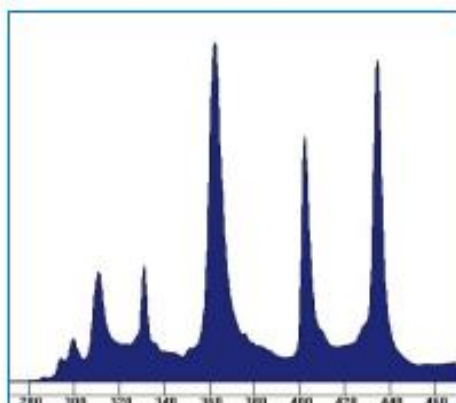
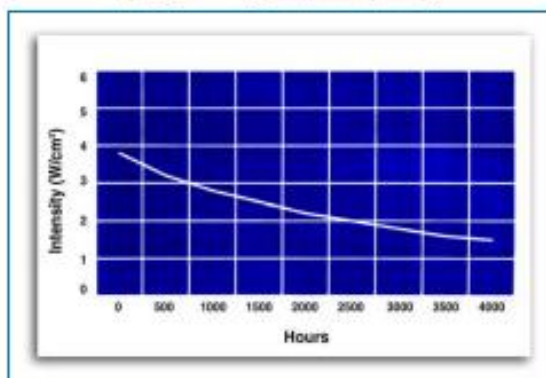
FEATURES	
3,000 mW/cm ² nominal ¹	2,000 hour bulb warranty (up to 4,000 hour life expectancy)
Solid state power supply (100-260V, 50-60 Hz)	Fast bulb replacement
Proprietary "Cool Blue [™] Filter" virtually eliminates liquid lightguide degradation	Wide range of lightguides available (liquid/fiber, single/multi-pole, various lengths)
Digital shutter timer (manual and timed modes)	Foot switch or PLC controlled shutter

¹ As measured through a 5 mm liquid lightguide with an ACCU-CAL[™] 50 Radiometer (320-395 nm)

SPECIFICATIONS

UV Output	3,000 mW/cm ² nominal
Power Requirements	90-265, 47-63 Hz
Power Supply	Solid State, 50 Watt
Bulb	50 Watt short arc mercury; fast bulb replacement
Reflector	Elliptical; glass with dichroic coating to reflect UV and minimize IR
Shutter Timer	Digital LCD timer up to 99.99 seconds; manual or time shutter
Shutter Activation	Foot switch or user supplied switching mechanism
Cooling	Filtered, dual-fan arrangement; thermally controlled to maintain proper lamp temperature
Hour Meter	Digital LCD
Housing Dimensions	12" x 11.5" x 6.5" (30.6 cm x 29.2 cm x 16.5 cm)
Weight	12 lbs. (5.4 kg)
System Warranty	1 year from purchase
Bulb Warranty	2,000 hours (no intensity warranty during 2,000 hours, only lighting)
Part Number	39370
Replacement Bulb PN	5120
Recommended Lightguides (sold separately)	5720 (5 mm x 1 M liquid-filled lightguide) 3,000 mW/cm ² nominal 5721 (5 mm x 1.5 M liquid-filled lightguide) 2,600 mW/cm ² nominal 5722 (8 mm x 1 M liquid-filled lightguide) 2,000 mW/cm ² nominal

SPECTRAL DISTRIBUTION

TYPICAL INTENSITY VS. TIME
(using a 5 mm lightguide, sold separately)

For further assistance with adhesive and equipment selection, contact your DYMAX Applications Engineer.

In the U.S. Call: 877.396.2988
In North and South America Call: 860.482.1010
In Europe Call: 0049.69.7165.3568
In Asia Call: 852.2460.7038

www.dymax.com

©2006, 2007 DYMAX Corporation

Please note that most dispensing and curing system applications are unique. DYMAX does not warrant the fitness of the product for the intended application. Any warranty applicable to the product, its application and use is strictly limited to that contained in DYMAX's standard Conditions of Sale. DYMAX recommends that any intended application be evaluated and tested by the user to insure that desired performance criteria are satisfied. DYMAX is willing to assist users in their performance testing and evaluation by offering equipment trial rental and testing programs to assist in such testing and evaluation. Data sheets are available for valve controllers or pressure pots upon request. LIT101 1/1/02/007

DYMAX Corporation - 318 Industrial Lane - Torrington, CT 06790 - Phone: 860.482.1010 - Fax: 860.496.0928 - E-mail: info@dymax.com - www.dymax.com

DYMAX Europe GmbH - Treibacher Strasse 3 - D-60487 Frankfurt am Main - Germany - Phone: 0049.69.7165.3568 - Fax: 0049.69.7165.3830 - E-mail: dymaxinfo@dymax.de - www.dymax.de

DYMAX Asia (HK) - Unit 1006, 10/F., Camarvon Plaza, No. 20, Camarvon Road, T.S.T., Kowloon, Hong Kong - Phone: 852.2460.7038 - Fax: 852.2460.7017 - E-mail: simon_ung@dymax.com - www.dymax.com.hk

DYMAX® Light-Weld®, Light-Weld™, Multi-Cure®, Ultra Light-Weld®, MEDV-CL-100®, MD® and SPEEDYMAX® are trademarks of DYMAX Corporation.



Annex 7 – Details of the knit braiding machine



MC-D

High-speed knit braiders for the production of non-elongation cords for technical applications

Machines tresseuses à crochet à haute vitesse, pour la production de cordes sans élongation pour des applications techniques

Máquinas trenzadoras de punto de alta velocidad para la producción de cuerdas sin elongación para aplicaciones técnicas



Complete line for the production of cords and ropes to be used for technical applications.

Non elongation cords and ropes.

For curtains and other technical applications.

TECHNICAL SPECIFICATIONS

- Design change by yarn crossing regulation.
- Cylinder diameter: from 1 up to 15 mm.
- Interchangeable cylinders from 4 up to 16 needles.
- Number of spindles: 1.
- Gauge and quantity of needles according to sample.
- Working system by means of latch needles.
- Run-proof product (lock stitch).
- Possibility to work from all kind of yarns.
- Direct feeding from bobbins or cones (from creel – see options).
- Electronic stop motion device.
- Density regulation system.
- Possibility to insert rigid core inside.
- Free take off of product (Standard).
- Digital meter counters with pre-selection.
- Security general stop.
- Security and protection system under EC regulation.

OPTIONAL EQUIPMENTS

- Different creels and pitch are available in function of samples to produce.
- Different cylinders and thread guide sets are available.
- Take off of product into spools (parallel spooling).
- Take off of product into spools (crossing spooling).

Ligne complète pour la production de cordes et cordons pour leurs applications techniques.

Cordes et cordons sans élongation.

Pour des applications en rideaux et autres applications techniques.

DONNÉES TECHNIQUES

- Changement de dessins par réglage du croisement des fils.
- Diamètre de cylindre: de 1 jusqu'à 15 mm.
- Cylindres interchangeables de 4 jusqu'à 16 aiguilles.
- Nombre de broches: 1.
- Jauge et quantité d'aiguilles selon échantillon.
- Système de travail avec aiguilles à languette.
- Obtention de produit indémallable.
- Apte pour tout type de fil.
- Alimentation directe à partir de cônes ou bobines (à partir de cantre – voir options).
- Arrêts électroniques pour casses des fils.
- Système de régulation de la densité.
- Possibilité d'incorporation d'âme central rigide.
- Sortie libre du produit (standard).
- Compteurs digitaux de mètres avec présélection.
- Arrêt général de sécurité.
- Système de sécurité et protection selon normative CE.

ÉQUIPEMENTS OPTIONNELS

- Toute sorte de cantres et écartements disponibles selon échantillon à produire.
- Jeu de cylindres et guide fils additionnels disponibles.
- Système de bobinage parallèle du produit final.
- Système de bobinage croisé du produit final.

Linea completa para la producción de cuerdas y cordones para aplicaciones técnicas.

Cuerdas y cordones sin elongación.

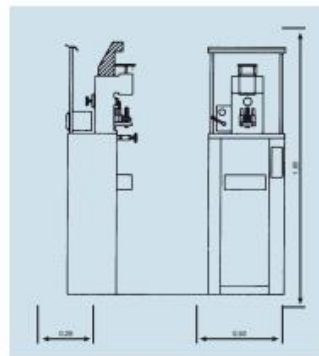
Para cortinería y otras aplicaciones técnicas.

CARACTERÍSTICAS TÉCNICAS

- Cambio de diseño por regulación de cruce de hilos.
- Diámetro de cilindro: desde 1 hasta 15 mm.
- Cilindros intercambiables desde 4 hasta 16 agujas.
- Número de husos: 1.
- Galga y cantidad de agujas según muestra.
- Sistema de trabajo mediante agujas de lengüeta.
- Producto indesmallable.
- Posibilidad de utilización de todo tipo de hilado.
- Alimentación directa desde conos o bobinas (desde fileta – ver opciones).
- Paros electrónicos por rotura de hilos.
- Sistema de regulación de densidad.
- Posibilidad de incorporación de alma central rígida.
- Salida libre del producto (estándar).
- Contadores digitales de metros a preselección.
- Paro general de la máquina.
- Sistema de seguridad y protección bajo normativa CE.

DISPOSITIVOS OPCIONALES

- Varias filetas y ecartamientos disponibles según muestras a fabricar.
- Cilindros y juego de guía-hilos disponibles.
- Sistema de encarretado paralelo del producto final.
- Sistema de encarretado cruzado del producto final.



Copyright By Rius. This brochure contains photos and technical data for information only, without contractual engagement. Rius reserves the right to introduce any modifications in the design and/or equipment.
Copyright By Rius. Les photos et données contenues dans ce catalogue, seront considérées à titre indicatif et ne représentent pas une obligation contractuelle. Rius se réserve le droit d'introduire modifications au design ou équipement.
Copyright By Rius. Las imágenes y datos contenidos en este catálogo, serán contemplados a título indicativo y no revisten obligación contractual. Rius se reserva el derecho a introducir modificaciones de diseño y/o equipamiento.



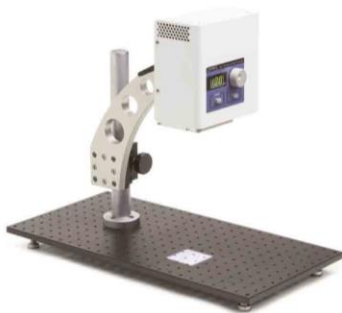
CONSTRUCCIONES METALÚRGICAS ESPECIALES, S.A.

Ctra. Manresa-Solsona, km. 4'2 • Polígon Industrial "Pla dels Vinyats" • E-08250 Sant Joan De Vilatorrada (BARCELONA)

Tel.: 34 - 938 76 44 22* • Fax: 34 - 938 76 41 49 • E-mail: vrc@rius-comatex.com • www.rius-comatex.com

Annex 8 – Full specification and calibration certificate for the solar simulator

LSH-7320 LED Solar Simulator



- Output beam size: 2 in. x 2 in. (51 mm x 51 mm)
- Factory certified IEC ABA Rated
- Variable output adjustment from 0.0 to 1.1 sun
- Fast turn on time; <100 ms via USB or external trigger
- 10,000 hour LED lifetime - no bulb replacement required
- Flexible mounting orientation
- PV cell placement indicator
- USB 2.0

The compact and easy to use LSH-7320 incorporates the benefits of LED technology in a value-priced, flexible solar simulator. The completely independent head includes all controls, LEDs, and optics allowing researchers flexible mounting and orientation options. External remote on/off triggering and long lamp life make remote mounting practical and bring LED technology to applications requiring only ABA ratings.

Benefits of LEDs

Unlike typical lamp based solar simulators, LED based solar simulators have lamp lifetimes that can exceed 10,000 hours and do not require a long warm up time. Shuttering can be accomplished by simply turning the output on and off; no mechanical shutter is required. Careful attention to the design and the use of solid state LEDs allow the LSH-7320 to be oriented in any position to fit your application needs.

Why Class ABA?

If your application doesn't require the highest level of uniformity of illumination, a Class ABA system may work for you. Class ABA systems still provide the highest spectral match performance (Class A) as defined by the most recent standards from the IEC.

Put Our Expertise to Work

Leveraging Oriel's deep application and market understanding, the LSH-7320 Class ABA LED solar simulator was designed to provide high performance in a rugged design. Oriel is a world leader in solar simulator technology and our products are renowned for their value and strong after-sales support.

ORIEL
INSTRUMENTS
A Newport Corporation Brand

Newport. Family of Brands – ILX Lightwave® • New Focus™ • Ophir® • Oriel® Instruments • Richardson Gratings™ • Spectra-Physics® • Spiricon®

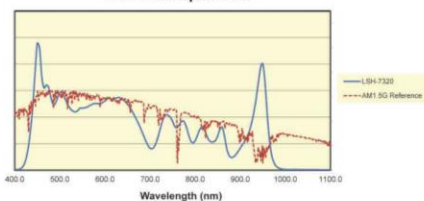
LSH-7320 LED Solar Simulator

LSH-7320 SOLAR SIMULATOR SPECIFICATIONS¹

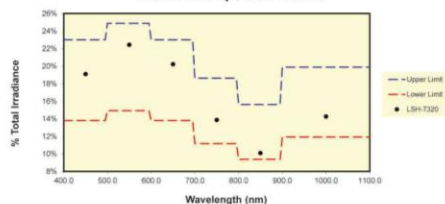
Illumination Area	2 inches x 2 inches (51 mm x 51 mm)
Total Power Output	110 mW/cm ² (1.1 sun)
Variable Output Control	0.1 to 1.1 sun
Wavelength Range	400nm - 1100nm
Temporal Stability	A - IEC 60904-9 2007
Uniformity Classification	B - IEC 60904-9 2007
Spectral Match	A - IEC 60904-9 2007
Working Plane Adjustment	12 inches; 305 mm
Alignment	Laser diode based optical alignment
Z Axis Head Adjustment from Base	7.5 inches - 17.75 inches (190 mm - 450 mm)
Head Rotation ²	0 - 360°
Remote Interface	USB 2.0 (B-Type) or BNC TTL for ON/OFF
TTL Turn On/Off Transition Time	10ms
Weight	
Head (on vertical assembly stand)	9.3 lbs (4.2 kg)
Stand	9.0 lbs (4.1 kg)
Power Supply	1.8 lbs (0.8 kg)
Dimensions	
Height (on vertical assembly stand)	15.25 - 25.5 inches (387 - 648 mm)
Width	7.25 inches (184 mm)
Depth	14.0 inches (362 mm)
Operating Temperature Range	10°C to 40°C
Storage Temperature Range	-40°C to 70°C
Humidity	<85%, relative, non-condensing
Compliance	CE, RoHS
Power Requirements	100-240 VAC, 47-63 Hz, 2.8A max
CE Certification	EN 61626-1:2013, EN 61010-1, EN 62471

NOTES: 1) All values are specified after a five minute warm up period.
2) Indents on mounting plate at 0°, 90°, 180°, and 270° orientations.

LSH-7320 Spectrum



LSH-7320 Spectral Match



Oriel
INSTRUMENTS
A Newport Corporation Brand

150 Long Beach Blvd., Stratford, CT 06615, USA

PHONE: 1-800-714-5393 FAX: 1-203-378-2457 EMAIL: oriel.sales@newport.com

www.newport.com/oriel

PHONE
Belgium +32-(0)800-11 257
China +86-10-6267-0065
France +33-(0)1-60-91-68-68
Japan +81-3-3794-5511
Taiwan +886-(0)2-2508-4977

EMAIL
belgium@newport.com
china@newport.com
france@newport.com
spectra-physics@splasers.co.jp
sales@newport.com.tw

PHONE
Irvine, CA, USA +1-800-222-6440
Netherlands +31-(0)30 6592111
United Kingdom +44-1235-432-710
Germany / Austria / Switzerland +49-(0)6151-708-0

EMAIL
sales@newport.com
netherlands@newport.com
uk@newport.com
germany@newport.com

Newport Corporation, Irvine and Santa Clara, California and Franklin, Massachusetts; Eury and Beaune-La-Rolande, France; Stahnsdorf, Germany and Wuxi, China have all been certified compliant with ISO 9001 by the British Standards Institution.

Newport Corporation, Global Headquarters
1791 Deere Avenue, Irvine, CA 92606, USA

Complete listings for all global office locations are available online at www.newport.com/contact

PHONE: 1-800-222-6440 1-949-863-3144
EMAIL: sales@newport.com

© 2014 Newport Corporation. All rights reserved. Oriel and the Newport logo are registered trademarks of Newport Corporation.

LSH-7320 REV07 110414

Newport Family of Brands – ILX Lightwave® • New Focus™ • Ophir® • Oriel® Instruments • Richardson Gratings™ • Spectra-Physics® • Spiricon®

Newport
Spectra Solutions
Newport Corporation
11550 East Frontage Rd
Bozeman, MT 59715
Tel: 800.459.9459
www.newport.com/newport
FAX: 94.0545155

PERFORMANCE VALIDATION CERTIFICATE
ORIEL® LSH-7320 CLASS ABA SOLAR SIMULATOR

Model # LSH-7320 **Serial #** 732012349

Performance validation of Spectral Match:
The current system is within the acceptable limits of Class A spectral match under the IEC¹, ASTM², and JIS³ standards.

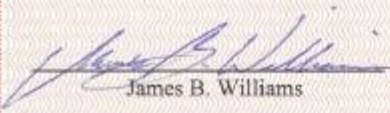
Performance validation of Non-uniformity of irradiance:
IEC¹ non-uniformity of irradiance of this system is 2.37%
ASTM² non-uniformity of irradiance of this system is 2.37%
JIS³ non-uniformity of irradiance of this system is 1.49%

Performance validation of Temporal instability of irradiance:
The IEC¹ short-term temporal instability of irradiance of this system is 0.15%
The IEC¹ long-term temporal instability of irradiance of this system is 0.38%

THE LSH-7320 SERIAL# 732012349 MEETS
CLASS A IEC, ASTM, AND JIS SPECTRAL MATCH,
CLASS B IEC, ASTM, AND JIS NON-UNIFORMITY OF IRRADIANCE, AND
CLASS A IEC TEMPORAL INSTABILITY OF IRRADIANCE.

REFERENCING THE FOLLOWING STANDARDS:

1. IEC 60904-9 Ed.2 (2007) Photovoltaic devices - Part 9: Solar simulator performance requirements.
2. ASTM E927-05: Standard Specifications for Solar Simulation for Photovoltaic Testing
3. JIS (Japanese Industrial Standard) C8912 (2005) Solar simulators for crystalline solar cells and modules

Certified by:

James B. Williams

Date: 2018-JAN-17